WILEY-VCH

Edited by
Alberto Piqué and Pere Serra

Laser Printing of Functional Materials

3D Microfabrication, Electronics and Biomedicine

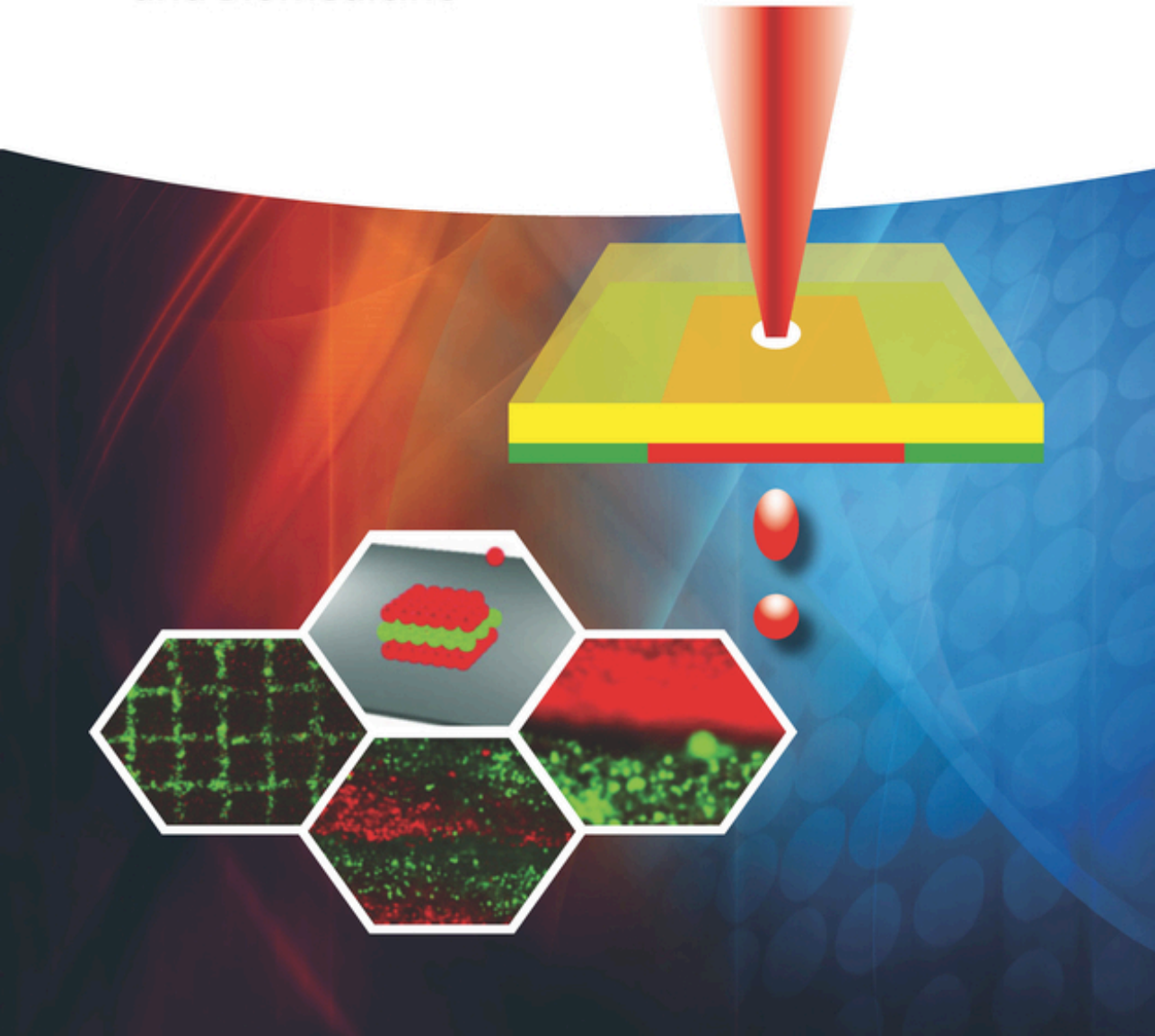

Laser Printing of Functional Materials

Laser Printing of Functional Materials

3D Microfabrication, Electronics and Biomedicine

Edited by Alberto Piqué and Pere Serra

WILEY-VCH

Editors
Dr. Alberto Piqué
Materials Science and Technology
Division, Code 6360
U.S. Naval Research Laboratory
4555 Overlook Ave. SW
Washington, DC 20375
United States

Prof. Pere Serra
Universitat de Barcelona
Departament de Física Aplicada
Martí i Franquès, 1
08028 Barcelona
Spain

Cover
Biotechnology & Bioengineering, 109 (7), Koch L, Deiwick A, Schlie S, Michael S, Gruene M, Coger V, *et al.*, Skin tissue generation by laser cell printing, 1855–63, Copyright (2012), with permission from John Wiley and Sons.

All books published by **Wiley-VCH** are carefully produced. Nevertheless, authors, editors, and publisher do not warrant the information contained in these books, including this book, to be free of errors. Readers are advised to keep in mind that statements, data, illustrations, procedural details or other items may inadvertently be inaccurate.

Library of Congress Card No.:
applied for

British Library Cataloguing-in-Publication Data
A catalogue record for this book is available from the British Library.

Bibliographic information published by the Deutsche Nationalbibliothek
The Deutsche Nationalbibliothek lists this publication in the Deutsche Nationalbibliografie; detailed bibliographic data are available on the Internet at <http://dnb.d-nb.de>.

© 2018 Wiley-VCH Verlag GmbH & Co. KGaA, Boschstr. 12, 69469 Weinheim, Germany

All rights reserved (including those of translation into other languages). No part of this book may be reproduced in any form – by photoprinting, microfilm, or any other means – nor transmitted or translated into a machine language without written permission from the publishers. Registered names, trademarks, etc. used in this book, even when not specifically marked as such, are not to be considered unprotected by law.

Print ISBN: 978-3-527-34212-9
ePDF ISBN: 978-3-527-80513-6
ePub ISBN: 978-3-527-80511-2
Mobi ISBN: 978-3-527-80512-9
oBook ISBN: 978-3-527-80510-5

Cover Design Bluesea Design, McLeese Lake, Canada
Typesetting SPi Global, Chennai, India
Printing and Binding

Printed on acid-free paper

10 9 8 7 6 5 4 3 2 1

Contents

Preface *xv*

Part I Fundamentals *1*

1 Introduction to Laser-Induced Transfer and Other Associated Processes *3*
Pere Serra and Alberto Piqué
1.1 LIFT and Its Derivatives *3*
1.2 The Laser Transfer Universe *5*
1.3 Book Organization and Chapter Overview *8*
1.4 Looking Ahead *12*
Acknowledgments *13*
References *13*

2 Origins of Laser-Induced Transfer Processes *17*
Christina Kryou and Ioanna Zergioti
2.1 Introduction *17*
2.2 Early Work in Laser-Induced Transfer *17*
2.3 Overview of Laser-Induced Forward Transfer *19*
2.3.1 Transferring Metals and Other Materials with Laser-Induced Forward Transfer (LIFT) *21*
2.3.2 Limitations of the Basic LIFT Technique *22*
2.3.3 The Role of the Donor Substrate *22*
2.3.4 Use of a Dynamic Release Layer (DRL)-LIFT *24*
2.3.5 LIFT with Ultrashort Laser Pulses *25*
2.4 Other Laser-Based Transfer Techniques Inspired by LIFT *27*
2.4.1 Matrix-Assisted Pulsed Laser Evaporation-Direct Write (MAPLE-DW) Technique *27*
2.4.2 LIFT of Composite Matrix-Based Materials *27*
2.4.3 Hydrogen-Assisted LIFT *28*
2.4.4 Long-Pulsed LIFT *28*
2.4.5 Laser Molecular Implantation *29*
2.4.6 Laser-Induced Thermal Imaging *30*

2.5 Other Studies on LIFT *31*
2.6 Conclusions *31*
References *32*

3 LIFT Using a Dynamic Release Layer *37*
Alexandra Palla Papavlu and Thomas Lippert
3.1 Introduction *37*
3.2 Absorbing Release Layer – Triazene Polymer *40*
3.3 Front- and Backside Ablation of the Triazene Polymer *42*
3.4 Examples of Materials Transferred by TP-LIFT *43*
3.5 First Demonstration of Devices: OLEDs and Sensors *47*
3.5.1 Organic Light Emitting Diode (OLEDs) *47*
3.5.2 Sensors *49*
3.6 Variation of the DRL Approach: Reactive LIFT *52*
3.7 Conclusions and Perspectives *54*
Acknowledgments *55*
Conflict of Interest *55*
References *55*

4 Laser-Induced Forward Transfer of Fluids *63*
Juan M. Fernández-Pradas, Pol Sopeña, and Pere Serra
4.1 Introduction to the LIFT of Fluids *63*
4.1.1 Origin *64*
4.1.2 Principle of Operation *65*
4.1.3 Developments *66*
4.2 Mechanisms of Fluid Ejection and Deposition *67*
4.2.1 Jet Formation *67*
4.2.2 Droplet Deposition *69*
4.3 Printing Droplets through LIFT *72*
4.3.1 Role of the Laser Parameters *72*
4.3.2 Role of the Fluid Properties *76*
4.3.3 Setup Parameters *76*
4.4 Printing Lines and Patterns with LIFT *78*
4.5 Summary *81*
Acknowledgments *82*
References *82*

5 Advances in Blister-Actuated Laser-Induced Forward Transfer (BA-LIFT) *91*
Emre Turkoz, Romain Fardel, and Craig B. Arnold
5.1 Introduction *91*
5.2 BA-LIFT Basics *93*
5.3 Why BA-LIFT? *94*
5.4 Blister Formation *97*
5.4.1 Dynamics of Blister Formation *97*
5.4.2 Finite Element Modeling of Blister Formation *102*

5.5 Jet Formation and Expansion *105*
5.5.1 Computational Fluid Dynamics Model *106*
5.5.2 Effect of the Laser Energy *108*
5.5.3 Effect of the Ink Film Properties *111*
5.6 Application to the Transfer of Delicate Materials *113*
5.7 Conclusions *117*
References *117*

6 Film-Free LIFT (FF-LIFT) *123*
Salvatore Surdo, Alberto Diaspro, and Martí Duocastella
6.1 Introduction *123*
6.2 Rheological Considerations in Traditional LIFT of Liquids *125*
6.2.1 The Challenges behind the Preparation of a Thin Liquid Film *125*
6.2.1.1 The Role of Spontaneous Instabilities *126*
6.2.1.2 The Role of External Instabilities *128*
6.2.2 Technologies for Thin-Film Preparation *129*
6.2.3 Wetting of the Receiver Substrate *130*
6.3 Fundamentals of Film-Free LIFT *131*
6.3.1 Cavitation-Induced Phenomena for Printing *131*
6.3.2 Jet Formation in Film-Free LIFT *132*
6.3.3 Differences with LIFT of Liquids *134*
6.4 Implementation and Optical Considerations *135*
6.4.1 Laser Source *135*
6.4.2 Forward (Inverted) versus Backward (Upright) Systems *136*
6.4.3 Spherical Aberration and Chromatic Dispersion *137*
6.5 Applications *138*
6.5.1 Film-Free LIFT for Printing Biomaterials *139*
6.5.2 Film-Free LIFT for Micro-Optical Element Fabrication *140*
6.6 Conclusions and Future Outlook *141*
References *142*

Part II The Role of the Laser–Material Interaction in LIFT *147*

7 Laser-Induced Forward Transfer of Metals *149*
David A. Willis
7.1 Introduction, Background, and Overview *149*
7.2 Modeling, Simulation, and Experimental Studies of the Transfer Process *151*
7.2.1 Thermal Processes: Film Heating, Removal, Transfer, and Deposition *151*
7.2.2 Parametric Effects *153*
7.2.2.1 Laser Fluence and Film Thickness *154*
7.2.2.2 Donor-Film Gap Spacing *156*
7.2.2.3 Pulse Width *157*

7.2.3 Droplet-Mode Deposition *160*
7.2.4 Characterization of Deposited Structures: Adhesion, Composition, and Electrical Resistivity *163*
7.3 Advanced Modeling of LIFT *165*
7.4 Research Needs and Future Directions *167*
7.5 Conclusions *169*
References *170*

8 LIFT of Solid Films (Ceramics and Polymers) *175*
Ben Mills, Daniel J. Heath, Matthias Feinaeugle, and Robert W. Eason
8.1 Introduction *175*
8.2 Assisted Release Processes *176*
8.2.1 Optimization of LIFT Transfer of Ceramics via Laser Pulse Interference *176*
8.2.1.1 Standing-Wave Interference from Multiple Layers *176*
8.2.1.2 Ballistic Laser-Assisted Solid Transfer (BLAST) *177*
8.2.2 LIFT Printing of Premachined Ceramic Microdisks *180*
8.2.3 Spatial Beam Shaping for Patterned LIFT of Polymer Films *181*
8.3 Shadowgraphy Studies and Assisted Capture *184*
8.3.1 Shadowgraphic Studies of the Transfer of Ceramic Thin Films *184*
8.3.2 Application of Polymers as Compliant Receivers *186*
8.4 Applications in Energy Harvesting *188*
8.4.1 LIFT of Chalcogenide Thin Films *189*
8.4.2 Fabrication of a Thermoelectric Generator on a Polymer-Coated Substrate *190*
8.5 Laser-Induced Backward Transfer (LIBT) of Nanoimprinted Polymer *193*
8.5.1 Unstructured Carrier Substrate *195*
8.5.2 Structured Carrier Substrate *195*
8.6 Conclusions *197*
Acknowledgments *197*
References *197*

9 Laser-Induced Forward Transfer of Soft Materials *199*
Zhengyi Zhang, Ruitong Xiong, and Yong Huang
9.1 Introduction *199*
9.2 Background *200*
9.3 Jetting Dynamics during Laser Printing of Soft Materials *201*
9.3.1 Jet Formation Dynamics during Laser Printing of Newtonian Glycerol Solutions *202*
9.3.1.1 Typical Jetting Regimes *202*
9.3.1.2 Jetting Regime as Function of Fluid Properties and Laser Fluence *204*
9.3.1.3 Jettability Phase Diagram *206*
9.3.2 Jet Formation Dynamics during Laser Printing of Viscoelastic Alginate Solutions *208*
9.3.2.1 Ink Coating Preparation and Design of Experiments *208*
9.3.2.2 Typical Jetting Regimes *209*

9.3.2.3 General Observation of the Jetting Dynamics *212*
9.3.2.4 Effects of Laser Fluence on Jetting Dynamics *212*
9.3.2.5 Effects of Alginate Concentration on Jetting Dynamics *214*
9.3.2.6 Jettability Phase Diagram *215*
9.4 Laser Printing Applications Using Optimized Printing Conditions *218*
9.5 Conclusions and Future Work *220*
Acknowledgments *221*
References *222*

10 Congruent LIFT with High-Viscosity Nanopastes *227*
Raymond C.Y. Auyeung, Heungsoo Kim, and Alberto Piqué
10.1 Introduction *227*
10.2 Congruent LIFT (or LDT) *229*
10.3 Applications *235*
10.4 Achieving Congruent Laser Transfers *242*
10.5 Issues and Challenges *245*
10.6 Summary *246*
Acknowledgment *247*
References *247*

11 Laser Printing of Nanoparticles *251*
Urs Zywietz, Tim Fischer, Andrey Evlyukhin, Carsten Reinhardt, and Boris Chichkov
11.1 Introduction, Setup, and Motivation *251*
11.2 Laser-Induced Transfer *252*
11.3 Materials for Laser Printing of Nanoparticles *254*
11.4 Laser Printing from Bulk-Silicon and Silicon Films *254*
11.5 Magnetic Resonances of Silicon Particles *261*
11.6 Laser Printing from Prestructured Films *261*
11.7 Applications: Sensing, Metasurfaces, and Additive Manufacturing *263*
11.8 Outlook *266*
References *266*

Part III Applications *269*

12 Laser Printing of Electronic Materials *271*
Philippe Delaporte, Anne-Patricia Alloncle, and Thomas Lippert
12.1 Introduction and Context *271*
12.2 Organic Thin-Film Transistor *272*
12.2.1 Operation and Characteristics of OTFTs *272*
12.2.2 Laser Printing of the Semiconductor Layer *275*
12.2.3 Laser Printing of Dielectric Layers *277*
12.2.4 Laser Printing of Conducting Layers *279*

12.2.5 Single-Step Printing of Full OTFT Device *279*
12.3 Organic Light-Emitting Diode *281*
12.4 Passive Components *285*
12.5 Interconnection and Heterogeneous Integration *287*
12.6 Conclusion *290*
References *291*

13 Laser Printing of Chemical and Biological Sensors *299*
Ioanna Zergioti
13.1 Introduction *299*
13.2 Conventional Printing Methods for the Fabrication of Chemical and Biological Sensors *300*
13.2.1 Contact Printing Methods *301*
13.2.1.1 Pin Printing Approach *301*
13.2.1.2 Microcontact Printing (or Microstamping) Technique *302*
13.2.1.3 Nanotip Printing *303*
13.2.2 Noncontact Printing Methods *303*
13.2.2.1 Photochemistry-Based Printing *303*
13.2.2.2 Inkjet Printing Technique *304*
13.2.2.3 Electrospray Deposition (ESD) *304*
13.3 Laser-Based Printing Techniques: Introduction *305*
13.3.1 Laser-Induced Forward Transfer *305*
13.3.2 LIFT of Liquid Films *307*
13.4 Applications of Direct Laser Printing *308*
13.4.1 Biosensors *308*
13.4.1.1 Background *308*
13.4.1.2 Printing of Biological Materials for Biosensors *309*
13.4.2 Chemical Sensors *316*
13.5 Conclusions *319*
List of Abbreviations *319*
References *320*

14 Laser Printing of Proteins and Biomaterials *329*
Alexandra Palla Papavlu, Valentina Dinca, and Maria Dinescu
14.1 Introduction *329*
14.2 LIFT of DNA in Solid and Liquid Phase *332*
14.3 LIFT of Biomolecules *333*
14.3.1 Streptavidin and Avidin–Biotin Complex *333*
14.3.2 Amyloid Peptides *337*
14.3.3 Odorant-Binding Proteins *339*
14.3.4 Liposomes *340*
14.4 Conclusions and Perspectives *343*
Acknowledgments *343*
Conflict of Interest *343*
References *344*

15 Laser-Assisted Bioprinting of Cells for Tissue Engineering *349*
Olivia Kérourédan, Murielle Rémy, Hugo Oliveira, Fabien Guillemot, and Raphaël Devillard
15.1 Laser-Assisted Bioprinting of Cells *349*
15.1.1 The History of Cell Bioprinting and Advantages of Laser-Assisted Bioprinting for Tissue Engineering *349*
15.1.2 Technical Specifications of Laser-Assisted Bioprinting of Cells *353*
15.1.3 Effect of Laser Process and Printing Parameters on Cell Behavior *356*
15.2 Laser-Assisted Bioprinting for Cell Biology Studies *358*
15.2.1 Study of Cell–Cell and Cell–Microenvironment Interactions *358*
15.2.2 Cancer Research *359*
15.3 Laser-Assisted Bioprinting for Tissue-Engineering Applications *359*
15.3.1 Skin *360*
15.3.2 Blood Vessels *362*
15.3.3 Heart *364*
15.3.4 Bone *365*
15.3.5 Nervous System *367*
15.4 Conclusion *368*
References *369*

16 Industrial, Large-Area, and High-Throughput LIFT/LIBT Digital Printing *375*
Guido Hennig, Gerhard Hochstein, and Thomas Baldermann
16.1 Introduction *375*
16.1.1 State of the Art in Digital Printing *376*
16.1.2 History of Lasersonic® LIFT *376*
16.2 Potential Markets and their Technical Demands on Lasersonic® LIFT *377*
16.2.1 Digital Printing Market Expectations and Challenges *377*
16.2.2 Demands on a LIFT/LIBT Printing Unit for Special Printing Markets *378*
16.3 Lasersonic® LIFT/LIBT Printing Method *379*
16.3.1 LIFT for Absorbing and LIBT for Transparent Inks *379*
16.4 Optical Concept and Pulse Control of the Lasersonic® Printing Machine *382*
16.4.1 Ultrafast Pulse Modulation at High Power Level *382*
16.4.2 Time Schemes *383*
16.4.3 Data Flow *385*
16.4.4 Ultrafast Scan of the Laser Beam *385*
16.5 The Four-Color Lasersonic® Printing Machine *387*
16.5.1 Large-Area, High-Throughput LIFT/LIBT Inline R2R Printing System *387*

16.5.2 Printing Heads for Absorptive (Black) and for Transparent (Colored) Inks *388*
16.5.3 Inking Units *390*
16.5.4 Synthetic Approaches to the Absorption Layer of the LIBT Donor Surface *392*
16.6 Print Experiments and Results *392*
16.7 Discussion of Effects *397*
16.7.1 LIFT Process with Continuous-Wave Laser Source and Fast Modulation *397*
16.7.2 Special Test Pattern to Study the Transfer Behavior at High Pixel Rate *399*
16.8 Future Directions *401*
16.9 Summary *402*
Acknowledgments *403*
References *403*

17 LIFT of 3D Metal Structures *405*
Ralph Pohl, Claas W. Visser, and Gert-willem Römer
17.1 Introduction *405*
17.2 Basic Aspects of LIFT of Metals for 3D Structures *407*
17.2.1 Ejection Regimes of Pure Metal Picosecond LIFT *408*
17.2.1.1 Velocity of the Ejected Donor Material *409*
17.2.1.2 Origin of Fragments in Cap-Ejection Regime *409*
17.2.2 Droplet Impact and Solidification *411*
17.3 Properties of LIFT-Printed Freestanding Metal Pillars *413*
17.3.1 Reproducibility *414*
17.3.2 Metallurgical Microstructure *416*
17.3.3 Mechanical Properties *417*
17.3.4 Electrical Properties *418*
17.3.5 Inclined Pillars *420*
17.4 Demonstrators and Potential Applications *420*
17.5 Conclusions and Outlook *423*
References *423*

18 Laser Transfer of Entire Structures and Functional Devices *427*
Alberto Piqué, Nicholas A. Charipar, Raymond C. Y. Auyeung, Scott A. Mathews, and Heungsoo Kim
18.1 Introduction *427*
18.2 Early Demonstrations of LIFT of Entire Structures *428*
18.3 Process Dynamics *431*
18.3.1 Lase-and-Place *432*
18.4 Laser Transfer of Intact Structures *435*
18.4.1 Laser Transfer of Metal Foils for Electrical Interconnects *436*
18.5 Laser Transfer of Components for Embedded Electronics *437*

18.6 Outlook *438*
18.7 Summary *440*
Acknowledgments *441*
References *441*

Index *445*

Preface

This book aims to serve as a reference on the fundamentals and applications of laser-induced forward transfer (LIFT) processes. All the chapter contributors are active members in the LIFT community, with several chapters written by some of the early adopters of the technique. Given the current attention and interest generated by additive manufacturing or AM, it is quite exciting to see LIFT being "rediscovered" given its potential as a meso- to microscale AM process. It was with this in mind that we embarked on this project with the goal of bringing together the leading LIFT researchers to share their findings in this book.

The organization of this book follows a practical approach: begin with an analysis of the LIFT process and how it has been adapted to work with almost any class of material and then discuss its broad range of applications. Our aim is not to provide an all-encompassing treatise on the subject but rather present a review of the present status of the technique with the goal of encouraging its further development, which might lead to new, not yet reported applications.

We are indebted to all the chapter authors in this book who have generously contributed their time and expertise in preparing their monographs. Most of them are old friends, while some are new members of the growing LIFT community. It has been a pleasure working with all of them in this project and we want to thank each one for their input, comments, suggestions, and support. We hope this book helps to provide a window to the intriguing phenomena of laser transfer and printing while encouraging the development of many more new and exciting applications.

Washington, DC, USA — *Alberto Piqué*
Barcelona, Spain — *Pere Serra*

Part I

Fundamentals

1

Introduction to Laser-Induced Transfer and Other Associated Processes

Pere Serra[1] *and Alberto Piqué*[2]

[1] *Universitat de Barcelona, Departament de Física Aplicada, Institute of Nanoscience and Nanotechnology, Martí i Franquès 1, 08028 Barcelona, Spain*
[2] *Materials Science and Technology Division, Code 6360, U.S. Naval Research Laboratory, 4555 Overlook Ave. SW, Washington, DC 20375, USA*

Digital manufacturing emerges as a new production paradigm that is transforming the future of the manufacturing industry on both the small and the large scale [1]. Despite that this new fabrication methodology is still far from being completely consolidated, there is little doubt now that the trend toward digitization is unstoppable and that almost no industrial field will remain immune to its influence in the next years. Thanks to the capabilities of the present-day computers and CAD software, as well as to unprecedented advances in serial production technologies, digital manufacturing makes possible a truly fast transition from an idea to its realization. This integrated approach provides in turn a new concept with a high degree of flexibility in that it allows to easily incorporate design changes into the final product. All these benefits have enabled digital manufacturing in such diverse industries as electronics, energy harvesting, packaging, decoration, textile manufacturing, medical instrumentation, or regenerative medicine.

Most digital manufacturing technologies are in fact "direct-writing" technologies, that is, they allow processing materials in a serial manner following a pattern previously recorded as a digital file [2]. The direct-writing approach makes patterning possible with high resolution and control in the flexible way just described. These technologies can be either subtractive, such as laser and water jet cutting, or additive, such as stereolithography and inkjet printing. Furthermore, they are sometimes assisted by other techniques that, instead of removing or adding new material, simply modify some of the properties of an already manufactured product, also in a digital way; laser sintering and laser curing are good examples of this.

1.1 LIFT and Its Derivatives

"Laser printing" is a quite general term that applies to a rather large set of additive direct-writing techniques whose principle of operation relies on a laser-induced

Laser Printing of Functional Materials: 3D Microfabrication, Electronics and Biomedicine,
First Edition. Edited by Alberto Piqué and Pere Serra.
© 2018 Wiley-VCH Verlag GmbH & Co. KGaA. Published 2018 by Wiley-VCH Verlag GmbH & Co. KGaA.

transfer process: a controlled amount of material is transferred from a donor system to a receiving substrate by means of laser irradiation [3]. The relative displacement of the laser beam with respect to the receiver (and eventually the donor) makes patterning possible. The most common laser printing approach is known as laser-induced forward transfer (LIFT), a technique that works according to the described principle of operation with the donor system being a thin film and the laser source usually a pulsed laser. In more detail, an optical system focuses a pulsed laser beam onto a thin film of the donor material through its supporting substrate, which needs to be transparent to the laser radiation. Under the influence of a laser pulse, a tiny portion of the donor material is ejected toward the receiving substrate as sketched in Figure 1.1, which results in the formation of a pixel/voxel on that substrate. Through the repetition of this process at different positions in the donor/receiver system, any pattern can be produced.

The donor material in LIFT can be either solid [4, 5] or liquid [6, 7]. In the earliest versions of the technique (some of which date as far back as the mid-1960s [8–10]), the donor material was always solid. In those instances, transfers took place in the gas phase with the irradiated material completely vaporized [11] or in the liquid phase if melted (totally or partially). Accordingly, deposition occurred in the receiving substrate through recondensation of the vapor in the first case and through resolidification of the molten voxel in the second [4, 5]. Those transfer modes were especially suited for the printing of metals, for which extremely high resolutions were achieved [12]. However, it was found out later that transfer from solid films was also possible in the solid state, that is, without any phase change of the donor material. In that case, transfer proceeded through the laser-induced ejection of a "flyer" that was projected away from the donor film and toward the receiving substrate, where it landed, giving way to the formation of a voxel. That transfer mechanism not only allowed printing

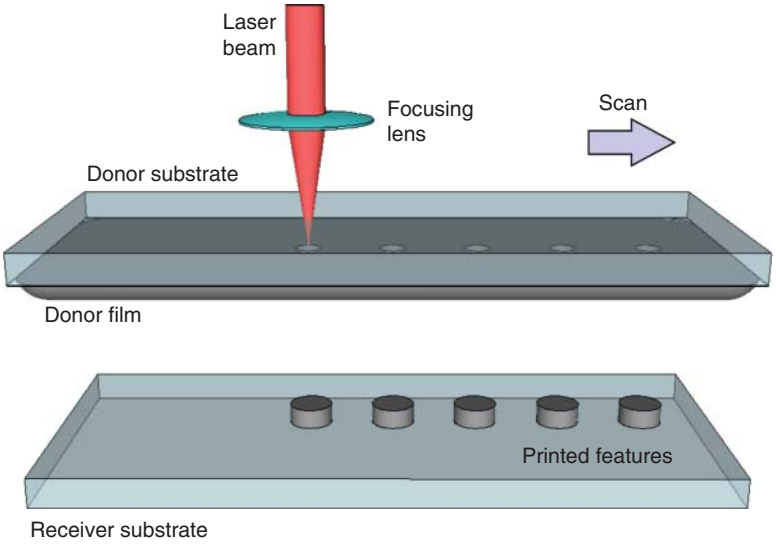

Figure 1.1 Principle of operation of the LIFT technique.

materials that would irreversibly change or decompose if melted or vaporized, such as complex ceramics [13], but also made possible to transfer stacks of different materials [14], especially interesting for the fabrication of multilayered devices. Even more than that, entire components such as surface-mounted devices and bare dies can be successfully transferred through LIFT [15].

LIFT can also work with liquid donor films. In this case, the material to print is previously dissolved or suspended in an ink that is transferred as a whole. The principle of operation of the technique is the same as with solid donor films (Figure 1.1), with the printing outcome now being a sessile droplet of the ink. Further evaporation of the ink solvents leads to the formation of the resulting pixel on the receiving substrate. The main difference with the LIFT of solids relies on the transfer mechanism: the ink is projected away from the donor film through a high-speed liquid jet that results from the expansion and collapse of a laser-induced cavitation bubble [16]. The LIFT of liquids is remarkably similar to inkjet printing regarding both transfer mechanism and printing outcome, but with significant advantages over it. Probably the most prominent is that LIFT presents fewer restrictions concerning the rheology of the printable inks: LIFT admits a substantially broader range of viscosities [17] and sizes of the particles loading the ink [18] compared to inkjet printing. Thus, such technologically interesting materials as high-solid-content inks and nanostructured materials can be successfully printed through LIFT. Furthermore, since those transfers also proceed without any significant phase change of the printed material, LIFT from liquid donor films can be used to print very sensitive materials such as biomolecules [19, 20] or living cells and tissue [21–23], which makes the technique especially suited for biosensing and tissue engineering applications.

In spite of its dominant position in the laser printing techniques universe, LIFT is not the only option to carry out laser-induced transfer. One alternative is laser-induced backward transfer (LIBT), wherein the donor film is irradiated directly, either at normal incidence through a transparent receiving substrate [2, 24] or at oblique incidence with flexible receiving substrates [25], and the irradiated material is propelled in a direction opposite to that of the incident laser beam. This approach is more restrictive and probably more difficult to set up compared to LIFT, but it has proved to be very convenient for the large-area and large-throughput printing of liquid inks [25]. Another novel departure from the traditional LIFT scheme is usually known as film-free laser printing [26]. This approach, which works only with liquid inks transparent to the laser radiation, requires the use of very short laser pulses. However, it presents the advantage of allowing to carry out transfers directly from the ink contained in a reservoir, without the need of preparing a thin film. Film-free laser printing can operate in both forward and backward configurations.

1.2 The Laser Transfer Universe

The concept of imparting kinetic energy to a solid using laser pulses can be traced back to research on the use of lasers for rocket propulsion applications

and launching of thin films to study matter under the effects of hypervelocities (>1 km/s) [27]. Early studies in the 1970s revealed that the plasma generated during the laser-induced breakdown of air near a surface would impinge on and transfer momentum to the surface [28, 29]. The use of pulsed lasers to accelerate small objects such as thin films has since then been explored to investigate means for propulsion of micro-rockets [30] and the effects of micrometeorites to simulate the effects of space debris on satellites [31–33]. These works focused on the efficiency of the release and launch process but share many similarities with LIFT.

The straight forwardness of the laser release and launch process and its relative simplicity in implementation attracted much attention in the graphics industry for digital printing tools [10]. In fact, Levene *et al*. reported in 1970 the laser-induced transfer of material across an air gap for the purposes of printing characters, recording of graphics, or marking applications [34]. The material transferred consisted of black ink from a polyethylene-backed typewriter ribbon and colored dies from a Mylar substrate across up to 100 μm gaps using a Nd:YAG laser ($\lambda = 1.06$ μm). Although the objective of this work was to develop a laser-based printing or marking process (the authors referred to it as material transfer recording), it was prescient in many ways including its reporting of not only forward but also backward transfers (called reverse transfer by the authors) and on proposing a simple physical model based on the melting and vaporization of the transferred material as a function of the laser pulse energy. Unfortunately, the authors did not apply their technique to any other types of materials, and their work went unnoticed until the late 1990s when their article began being cited within the printing and image science community. The laser forward-transfer process had to wait until 1986 to be rediscovered, this time with metals, with the work by Bohandy *et al*., who reported on the deposition of copper metal patterns using pulses from a UV laser ($\lambda = 193$ nm) and proposed a physical model more detailed but similar to Levene's to describe the process [4]. Furthermore, it was Bohandy's group who coined the term LIFT (for laser-induced forward transfer) to denote the process, which is essentially the subject of this book.

It was with LIFT that the use of lasers to achieve the controlled transfer of a specific material from a donor to a receiving substrate became widespread to the point that the acronym itself began to be used by some as a verb describing the process as in "LIFT-ing" a given material or ink. The success of LIFT also gave rise to numerous derivatives, all laser-based and all with their own acronym aiming at differentiating themselves from the basic technique. This book does not include all these LIFT derivatives since their discussion is beyond the scope of this volume. However, the remaining of this Introduction will provide a brief examination of some of these laser transfer techniques and include those relevant references where the reader will be able to find more details.

Early on, applications in the graphics industry motivated the use of laser transfer processes for image recording as evidenced by Levene's work. In these applications, the transfer process involves the conversion of light into heat when IR laser pulses are absorbed by IR-absorbing dye pigments dispersed in a translucent binder. Ultrafast heating of the absorbing dyes causes their decomposition, vapor generation, and thermal stresses leading to thermal ablation. These

processes known as laser ablative transfer or LAT involve delamination, rupture, and launch of the film from its carrier when the pressure of the generated gases trapped in the absorbing layer exceeds a threshold determined by the nature and thickness of the absorbing layer and laser parameters, that is, wavelength, pulse width, fluence, and so on. With LAT, it is possible to print high-resolution full-color graphics using a dry, noncontact printing process. Analysis of the LAT process was undertaken in the 1990s to determine its mechanism and optimize its operation by D. Dlott's group at the University of Illinois at Urbana Champaign. They reported various key findings including measuring heating rates and peak temperatures using dyes as molecular thermometers [35, 36] and applying ultrafast microscopy of shock waves generated with ps laser pulses [37, 38]. LAT can also be used to print nonabsorbing layers by incorporating a sacrificial laser absorbing layer first referred by Dlott's group as the dynamic release layer or DRL [39]. Finally, using a metal DRL and ps laser pulses, LAT can be achieved at low fluences ($<10\,mJ/cm^2$) by vaporizing the thin aluminum interlayer instead of the dyes, generating color images at ultrahigh speed and high resolution [40].

Another class of laser transfer techniques owe their development to the need to find alternatives for the generation of patterns, given the cost and complexity of conventional vacuum deposition and photolithography-based process. In many instances, these laser transfer derivatives were developed to address a specific class of material(s) for a given application as in the case of the organic semiconductor molecules used for organic electronic devices and organic light-emitting diodes (OLEDs). These materials present serious challenges when applied as liquid layers for large-area printing and would benefit from a dry printing process. These needs have given rise to several techniques based on laser transfer, which have meet with various levels of success. One of these techniques known as laser-induced thermal imaging or LITI was originally developed at DuPont by Blanchet's group for printing conducting polymers for organic electronics [41]. In LITI, the precoated donor and receiving films are in contact and held together using vacuum. A IR cw laser is aimed through the donor film at a thin absorbing layer for conversion of the light into heat, which vaporizes an intermediate organic layer with the resulting gas implanting a third layer comprising the conductive polymer onto the receiving film. This thermal transfer method relies on release/adhesion mechanisms rather than ablation of the conductive polymer (or organic semiconductor) layers, allowing them to remain continuous rather than undergoing irreversible damage (as with ablation). LITI was further developed by the 3 M Corporation for the fabrication of LCD color filters and OLED emitters [42], and beginning in 2000, 3 M partnered with Samsung SDI to jointly develop the process for active-matrix organic light-emitting diode (AMOLED) displays [43]. The use of LITI in the fabrication of AMOLED displays, which are commonly used in smartphones, represents the most successful example to date of the commercial application of laser transfer techniques. Interesting enough, given the commercial success of LITI, other consumer product companies have developed their own versions of laser transfer technologies such as laser-induced patternwise sublimation or LIPS, which has been developed by Sony Corporation. Using LIPS, RGB pixels are patterned for OLED applications, which have been used by the Display Device

Development group at Sony Corporation to fabricate a 27.3-inch AMOLED display [44]. For heat-sensitive organic materials, LITI and LIPS might cause their damage, and the use of more efficient light-absorbing layers based on loosely connected silver nanoparticles has been investigated. This technique named nanomaterial-enabled laser transfer or NELT allows the laser printing of patterns of the OLED tris-(8-hydroxyquinoline)Al, better known as Alq_3, without damage [45]. These laser transfer techniques for organic electronics are highly proprietary, each being the subject of numerous patents, and require the use of multilayer, complex, and, in most cases, proprietary donor films, which has limited their use by the general LIFT community.

The implantation of intact polymer molecules using a laser transfer process has been reported by H. Fukumura's group from Tohuku University. The technique known as laser molecular implantation or LMI is used for the implantation of fluorescent molecules into polymer films at precise locations and depths [46]. In LMI, the laser passes through a transparent polymer serving as the receiving substrate, such as poly(butyl methacrylate) or PBMA, or poly(ethyl methacrylate) or PEMA, which is in contact with an absorbing polymer film containing the organic molecules to be implanted, such as pyrene [47] or photochromic molecules [48]. More recently, there have been reports on laser-implanted coumarin C545 with a process called laser-induced molecular implantation technique (LIMIT) for organic electronics and optical device applications [49]. Both LMI and LIMIT are very similar, and their use is limited to applications requiring the implantation of specific molecules on a polymer matrix just below its surface, and as such, they have not found widespread use.

As a last example of laser-mediated transfers of a material or sample, it is worth considering the process used for laser pressure catapulting or LPC. This process has been used to procure single cells or small regions comprised of homogeneous cells for subsequent molecular analysis using UV laser pulses [50]. LPC is a noncontact cell or tissue capture technique that in combination with microdissection allows the rapid preparation of samples for cell or tissue analysis. LPC can also be used for the collection of chromosomes and chromosome subfragments for gene research applications [51]. Later reports have demonstrated the use of LPC for the transfer of living cells from a microdissected cell culture, which are viable enough to be recultivated [52, 53]. The drawback of LPC is that it requires a donor film prepared by microdissection, which, given their limited size, prevents this technique from its use in transferring much larger numbers of cells as for tissue engineering applications.

1.3 Book Organization and Chapter Overview

The aim of this book is to provide an extensive overview of the topic of laser printing of functional materials. As pointed out in the preceding sections, the editors are aware that the 18 chapters of this book have not covered all the existing laser-induced transfer techniques. Instead of attempting to cover the entire field, we have preferred to focus on LIFT and its most closely related

technologies, paying special attention to their principles of operation and transfer mechanisms, without forgetting their potential and applications. In other words, we have carefully selected the most popular approaches to laser printing and aimed to provide an in-depth treatment of all of them. This book is the result of contributions by international leading experts in the field, both from the academia and from the industry, thus providing a broad perspective of the present and future of these technologies.

This book is organized into three main parts. The first one deals with the fundamentals of laser printing. In this part, the main techniques are presented and described in detail, alongside the mechanisms of transfer involved in each of them, but with no special focus on any material in particular.

In Chapter 2, by C. Kryou and I. Zergioti, the authors provide an overview of the main laser-induced transfer processes and their historical origin. This chapter serves as an introduction to the techniques that will be later analyzed in more detail, outlining their main characteristics as well as some important instrumental issues. In this chapter, the authors also introduce some of the approaches to laser printing away from the mainstream. Since these approaches are not considered in the rest of this book, by presenting them here, the authors provide the interested reader with the appropriate references for further investigation.

We devote Chapter 3, by A. Palla Papavlu and T. Lippert, to a common variation to traditional LIFT: the use of a DRL. The transfer of very sensitive materials, as well as materials transparent to the laser radiation, is usually carried out through an intermediate absorbing film. The laser pulse is absorbed within that film, which provides the donor material with the thrust required for transfer without the sensitive material being exposed to the potentially harmful laser radiation. In this chapter, the authors focus their discussion on the use of triazene polymers, by which absorption can be easily tuned to several convenient laser wavelengths and by which decomposition products upon laser irradiation are very efficient in propelling the donor material.

In Chapter 4, by J.M. Fernández-Pradas *et al*., the authors introduce the general elements of the LIFT of fluids, probably the most widespread laser-based technique for printing inks. The authors describe the principle of operation of this particular approach to LIFT and discuss the mechanisms of liquid transfer, with their characteristic jetting dynamics. In this chapter, the authors also investigate the influence of the main process parameters on the morphology of the printed features and their correlation with the different possible transfer dynamics. Finally, the chapter considers some of the issues related with the printing of continuous patterns.

We return to the laser printing of fluids in Chapter 5, by E. Turkoz *et al*., where the authors present another approach to LIFT with an intermediate layer: blister-actuated laser-induced forward transfer (BA-LIFT). In contrast to the strategy presented in Chapter 3, in this case, the laser-absorbing layer does not decompose completely. Upon absorption of the laser pulse, only a fraction of the relatively thick polymeric layer is ablated. The expansion of the trapped ablation products results in a blister in that layer, which provides the donor material with the required impulse for transfer. The mechanisms of liquid ejection are discussed and analyzed in detail both experimentally and through computational methods.

In Chapter 6, by S. Surdo *et al*., the authors depart from the LIFT scheme to present film-free laser printing (or film-free LIFT), a technique that makes possible the transfer of liquids from bulk material. After discussing the problems associated with the preparation of a thin liquid film, the authors present the principle of operation of this relatively new approach and analyze in detail the mechanisms of material transfer, with a special emphasis on the differences with traditional LIFT. In this chapter, the authors also consider important instrumental aspects, as well as the different configurations through which film-free LIFT can be carried out (forward and backward). Finally, the chapter provides some examples of applications.

The second part of this book focuses on the laser–material interaction in laser printing, emphasizing those aspects that are specific to each kind of material (metals, ceramics, etc.). This part is organized according to a general materials classification.

We start this part with a complete overview of the LIFT of metals in Chapter 7, by D.A. Willis. After a general introduction highlighting the thermal nature of metal ablation, Willis reviews the main experimental and computational studies on the mechanisms of metal transfer through LIFT and the influence of the different process parameters on them. In this chapter, special attention is paid to a particular mode of deposition apparently specific to the LIFT of metals: droplet deposition. This remarkable transfer mode has allowed printing of the smallest features ever attained through laser-based processes.

In Chapter 8, by B. Mills *et al*., the authors discuss the laser transfer of materials from solid films, an alternative particularly interesting for printing ceramics and polymers. In contrast to metals, in this case, the material is not melted, but rather transferred as a solid flyer that is propelled from the solid donor film upon absorption of the laser pulse. The authors discuss the importance of laser beam shaping in this particular approach and analyze the main issues associated with its transfer dynamics, which appears to be quite different from most of the other laser printing approaches. Although most of the chapter is devoted to LIFT, it also includes some discussion on the LIBT of nanoimprinted polymers.

Chapter 9, by Z. Zhang *et al*., discusses LIFT of soft materials. After having introduced the LIFT of fluids in Chapter 4, the focus of attention in this chapter is aimed toward non-Newtonian fluids, with a transfer dynamics sensibly different from that analyzed in the first part of this book. The authors analyze the particular jetting behavior of these fluids, with special attention to the influence of their viscoelastic properties on the dynamics. It is remarkably interesting in this case how those viscoelastic properties make possible to build 3D structures through LIFT by means of stacking successive layers of material.

In Chapter 10, by R.C.Y. Auyeung *et al*., the authors discuss LIFT of high-viscosity nanopastes, a particular type of inks that somehow combine some of the most relevant elements encountered in Chapters 8 and 9. On the one hand, a relatively soft material can be transferred, and on the other hand, as a congruent flyer. This approach, also known as laser decal transfer (LDT), indeed makes it possible to transfer complex geometries with a single laser pulse. Furthermore, it allows achieving conformal deposition, which makes it

especially suited for electrical contacts, for example. Similarly to the LIFT of soft materials, 3D printing through multilayer stacks is also possible.

In Chapter 11, by U. Zywietz *et al*., the authors expand on the droplet deposition mode presented in Chapter 7 for the LIFT of metals with the aim of printing nanoparticles. In fact, the authors show that LIFT in that mode is also possible with semiconductors and demonstrate that extremely small features can indeed be obtained in that way. This chapter also explores alternatives to the traditional mode: a backward configuration for the transfer of individual nanoparticles, as well as the possibility of printing more complex patterns from prestructured films.

The last part of this book is devoted to applications. As many other digital printing techniques, laser-induced transfer can be used in a wide range of applications, some of them well consolidated in the industry and others still prospective. In this part, we present a rather comprehensive list of examples of application of laser printing and discuss the main advantages and bottlenecks of these techniques regarding their industrial implementation.

The first application that we consider is the laser printing of electronic materials, to which Chapter 12, by P. Delaporte *et al*., is devoted. Although the chapter extensively discusses the fabrication of organic devices (thin-film transistors and light-emitting diodes), the transfer of inorganic materials (dielectrics and conductive metals, especially) is also covered. The authors present examples of successful printing of electronic materials in both solid and liquid states, as well as printing of multistack structures. In addition to the feasibility of laser-induced transfer for the fabrication of electronic devices, the chapter considers issues related to the further industrialization of the technology, such as the process speed.

In Chapter 13, by I. Zergioti, the feasibility of laser printing for producing chemical and biological sensors is explored. After an overview on the most conventional printing techniques, the authors introduce LIFT of sensing materials. The chapter reviews the different approaches of laser printing for sensor fabrication, both in the solid state and in the liquid state, and with a broad variety of materials (inorganic, organic, biomolecules, nanostructured materials), to finally provide proofs of concept of functional sensors fabricated through laser-induced transfer processes.

Strongly related with the previous chapter, in Chapter 14, by A. Palla Papavlu *et al*., the authors consider the laser printing of proteins and biomaterials. Some of these materials can indeed be used for the fabrication of biosensors; however, there are many other interesting applications that require depositing biological materials with high resolution and control: cell growth and development studies, diagnostic tests, basic studies of biomolecule interactions, drug delivery, etc. The chapter discusses all these applications with a special focus on the particularities related with the laser-induced transfer of each type of biomolecule.

In Chapter 15, by O. Kérourédan *et al*., the authors make a step forward on the scale of biological complexity toward the laser printing of cells for tissue engineering applications. After an introduction to the subject of bioprinting, the authors focus their attention on the laser transfer of living cells and the influence

of the diverse process parameters on cell viability and behavior. In the frame of this investigation, it is especially important to provide analysis of cell–cell and cell–microenvironment interactions, issues that the chapter discusses alongside the remarkable problem of vascularization, essential for the correct development of printed tissues. Finally, the chapter reviews some studies on the laser printing of the most relevant tissues for regenerative medicine applications.

Chapter 16, by G. Hennig *et al*., provides a complete analysis on the industrial perspectives of laser printing, with a special focus on Lasersonic®, probably the largest printing machine based on LIFT/LIBT technologies to date. In this chapter, the authors review the state of the art of laser printing technologies in the industrial arena and discuss in all detail the main instrumental issues to be considered in the setting up of an industrial-scale printing machine. This is, in consequence, the chapter with strongest engineering focus in this book, which should serve as a bridge between the research and the development stage.

Chapter 17, by R. Pohl *et al*., returns to the LIFT of metals, this time to carry out 3D printing. The ejection of extremely small metallic droplets described in Chapters 7 and 11 can be exploited to generate 3D structures. The process requires the fine-tuning of the laser parameters, as well as a detailed knowledge of the transfer dynamics, acquired through time-resolved imaging techniques. High-aspect-ratio freestanding pillars are generated through stacking successive melted droplets, which solidify immediately upon landing on the growing pillar. These elements constitute the building blocks that will be used later to produce more complex 3D structures.

The last chapter of this book, Chapter 18, by A. Piqué *et al*., is devoted to the laser transfer of entire structures and functional devices. Instead of using laser printing techniques to transfer materials with the aim of manufacturing devices, in this chapter, the authors take advantage of the principle of operation of LIFT to propel entire structures and devices. The LDT technique presented in Chapter 10 can be successfully used to print interconnects in electronic circuits, for example. But the same scheme allows the transfer of small integrated devices, such as surface-mounted devices or bare dies, which can be positioned with high accuracy and control on the required positions in a more complex circuit.

1.4 Looking Ahead

As this brief introduction shows, laser transfer techniques have evolved significantly and found widespread use in many fields. Furthermore, with the advent of LIFT, these techniques have given rise to a community of practitioners who continue investigating its mechanisms and exploring its applications. This book is an attempt to document the origin and evolution of LIFT and all its variations while providing a snapshot of the broad range of present-day applications for which LIFT provides practical solutions. We cannot predict where LIFT will take us in 5 or 10 years from now, but we hope that the discussions presented by the authors of all the chapters in this book serve to lay the groundwork for the next generation of LIFT-based techniques and their new applications.

Acknowledgments

AP would like to acknowledge the support of the Office of Naval Research (ONR) through the Naval Research Laboratory Basic Research Program.

References

1 Holmström, J., Holweg, M., Khajavi, S.H., and Partanen, J. (2016) The direct digital manufacturing (r)evolution: definition of a research agenda. *Oper. Manage. Res.*, **9**, 1–10.
2 Hon, K.K.B., Li, L., and Hutchings, I.M. (2008) Direct writing technology-advances and developments. *CIRP Ann. Manuf. Technol.*, **57**, 601–620.
3 Arnold, C.B., Serra, P., and Piqué, A. (2007) Laser direct-write techniques for printing of complex materials. *MRS Bull.*, **32**, 23–31.
4 Bohandy, J., Kim, B.F., and Adrian, F.J. (1986) Metal deposition from a supported metal film using an excimer laser. *J. Appl. Phys.*, **60**, 1538–1539.
5 Bohandy, J., Kim, B.F., Adrian, F.J., and Jette, A.N. (1988) Metal-deposition at 532 nm using a laser transfer technique. *J. Appl. Phys.*, **63**, 1158–1162.
6 Piqué, A., Fitz-Gerald, J., Chrisey, D.B. *et al* (2000) Direct writing of electronic materials using a new laser assisted transfer/annealing technique. *Proc. SPIE*, **3933**, 105–112.
7 Fernández-Pradas, J.M., Colina, M., Serra, P., Domínguez, J., and Morenza, J.L. (2004) Laser-induced forward transfer of biomolecules. *Thin Solid Films*, **453–454**, 27–30.
8 Brisbane, A.D. (1966) Method for vapour depositing a material in the form of a pattern. Great Britain Patent GB 1, 138,084, filed Jul. 22, 1966 and issued Dec. 27, 1968.
9 Brisbane, A.D. (1967) Pattern deposit by laser. US Patent US 3, 560,258, filed May 31, 1967 and issued Feb. 2, 1971.
10 Braudy, R.S. (1969) Laser writing. *Proc. IEEE*, **57**, 1771–1772.
11 Papazoglou, D.G., Karaiskou, A., Zergioti, I., and Fotakis, C. (2002) Shadowgraphic imaging of the sub-ps laser-induced forward transfer process. *Appl. Phys. Lett.*, **81**, 1594–1596.
12 Willis, D.A. and Grosu, V. (2005) Microdroplet deposition by laser-induced forward transfer. *Appl. Phys. Lett.*, **86**, 244103.
13 Sones, C.L., Feinaeugle, M., Sposito, A., Gholipour, B., and Eason, R.W. (2012) Laser-induced forward transfer-printing of focused ion beam pre-machined crystalline magneto-optic yttrium iron garnet micro-discs. *Opt. Express*, **20**, 15171–15179.
14 Shaw-Stewart, J., Lippert, T., Nagel, M., Nüesch, F., and Wokaun, A. (2012) Red-green-blue polymer light-emitting diode pixels printed by optimized laser-induced forward transfer. *Appl. Phys. Lett.*, **100**, 203303.
15 Piqué, A., Mathews, S.A., Pratap, B., Auyeung, R.C.Y., Karns, B.J., and Lakeou, S. (2006) Embedding electronic circuits bylaser direct-write. *Microelectron. Eng.*, **83**, 2527–2533.

16 Duocastella, M., Fernández-Pradas, J.M., Morenza, J.L., and Serra, P. (2009) Time-resolved imaging of the laser forward transfer of liquids. *J. Appl. Phys.*, **106**, 084907.
17 Florian, C., Piazza, S., Diaspro, A., Serra, P., and Duocastella, M. (2016) Direct laser printing of tailored polymeric microlenses. *ACS Appl. Mater. Interfaces*, **8**, 17028–17032.
18 Papazoglou, S., Tsouti, V., Chatzandroulis, S., and Zergioti, I. (2016) Direct laser printing of graphene oxide for resistive chemosensors. *Opt. Laser Technol.*, **82**, 163–169.
19 Serra, P., Colina, M., Fernández Pradas, J.M., Sevilla, L., and Morenza, J.L. (2004) Preparation of functional DNA microarrays through laser-induced forward transfer. *Appl. Phys. Lett.*, **85**, 1639–1641.
20 Dinca, V., Farsari, M., Kafetzopoulos, D., Popescu, A., Dinescu, M., and Fotakis, C. (2008) Patterning parameters for biomolecules microarrays constructed with nanosecond and femtosecond UV lasers. *Thin Solid Films*, **516**, 6504–6511.
21 Kattamis, N.T., Purnick, P.E., Weiss, R., and Arnold, C.B. (2007) Thick film laser induced forward transfer for deposition of thermally and mechanically sensitive materials. *Appl. Phys. Lett.*, **91**, 171120.
22 Guillemot, F., Souquet, A., Catros, S., Guillotin, B., Lopez, J., Faucon, M., Pippenger, B., Bareille, R., Rémy, M., Bellance, S., Chabassier, P., Fricain, J.C., and Amédée, J. (2010) High-throughput laser printing of cells and biomaterials for tissue engineering. *Acta Biomater.*, **6**, 2494–2500.
23 Gruene, M., Deiwick, A., Koch, L., Schlie, S., Unger, C., Hofmann, N., Bernemann, I., Glasmacher, B., and Chichkov, B. (2010) Laser printing of stem cells for biofabrication of scaffold-free autologous grafts. *Tissue Eng. Part C Methods*, **17**, 79–87.
24 Papakonstantinou, P., Vainos, N.A., and Fotakis, C. (1999) Microfabrication by UV femtosecond laser ablation of Pt, Cr and indium oxide thin films. *Appl. Surf. Sci.*, **151**, 159–170.
25 Hennig, G., Baldermann, T., Nussbaum, C., Rossier, M., Brockelt, A., Schuler, L., and Hochstein, G. (2012) Lasersonic® LIFTprocess for large area digital printing. *J. Laser Micro/Nanoeng.*, **7**, 299–305.
26 Duocastella, M., Patrascioiu, A., Fernández-Pradas, J.M., Morenza, J.L., and Serra, P. (2010) Film-free laser forward printing of transparent and weakly absorbing liquids. *Opt. Express*, **18**, 21815–21825.
27 Pirri, A.N., Monsler, M.J., and Nebolsine, P.E. (1974) Propulsion by absorption of laser radiation. *AIAA J.*, **12** (9), 1254–1261.
28 Pirri, A.N., Schlier, R., and Northam, D. (1972) Momentum transfer and plasma formation above a surface with a high-power CO_2 laser. *Appl. Phys. Lett.*, **21**, 79. doi: 10.1063/1.1654297
29 Douglas-Hamilton, D.H., Kantrowitz, A.R., and Reilly, D.A. (1978) Laser assisted propulsion research. *Prog. Astronaut. Aeronaut.*, **61**, 271–278.
30 Phipps, C.R., Luke, J.R., McDuff, G.G., and Lippert, T. (2003) Laser-driven micro-rocket. *Appl. Phys. A*, **77**, 193–201.

31 Roybal, R., Tlomak, P., Stein, C., and Stokes, H. (1999) Simulated space debris impact experiments on toughened laminated thin solar cell cover glass. *Int. J. Impact Eng.*, **23** (1), 811–821. doi: 10.1016/S0734-743X(99)00126-8

32 Greenaway, M.W. and Field, J.E. (2004) The development of a laser-driven flyer system. *AIP Conf. Proc.*, **706**, 1389. doi: 10.1063/1.1780497

33 Yu, H., Fedotov, V., Baek, W., and Yo, J.J. (2014) Towards controlled flyer acceleration by a laser-driven mini flyer. *Appl. Phys. A*, **115**, 971. doi: 10.1007/s00339-013-7916-8

34 Levene, M.L., Scott, R.D., and Siryj, B.W. (1970) Material transfer recording. *Appl. Opt.*, **9**, 2260–2265.

35 Lee, I.-Y.S., Wen, X., Tolbert, W.A., Dlott, D.D., Doxtader, M., and Arnold, D.R. (1992) Direct measurement of polymer temperature during laser ablation using a molecular thermometer. *J. Appl. Phys.*, **72** (6), 2440–2448.

36 Chen, S., Lee, I.-Y.S., Tolbert, W.A., Wen, X., and Dlott, D.D. (1992) Applications of ultrafast temperature jump spectroscopy to condensed phase molecular dynamics. *J. Phys. Chem.*, **96** (18), 7178–7186.

37 Lee, I.-Y.S., Tolbert, W.A., Dlott, D.D., Doxtader, M.M., Foley, D.M., Arnold, D.R., and Willis, E.W. (1992) Dynamics of laser ablation transfer imaging investigated by ultrafast microscopy. *J. Imaging Sci. Technol.*, **36** (2), 180–187.

38 Lee, I.-Y.S., Hill, J.R., and Dlott, D.D. (1994) Ultrafast microscopy of shock waves using a shock target array with an optical nanogauge. *J. Appl. Phys.*, **75** (10), 4975–4983.

39 Tolbert, W.A., Lee, I.-Y.S., Doxtader, M.M., Ellis, E.W., and Dlott, D.D. (1993) High-speed color imaging by laser ablation transfer with a dynamic release layer: fundamental mechanisms. *J. Imaging Sci. Technol.*, **37** (4), 411–422.

40 Tolbert, W.A., Lee, I.-Y.S., Wen, X., Dlott, D.D., Doxtader, M.M., and Ellis, E.W. (1993) Laser ablation transfer imaging using picosecond optical pulses: ultra-high speed, lower threshold and high resolution. *J. Imaging Sci. Technol.*, **37** (5), 485–489.

41 Blanchet, G.B., Loo, Y.L., Rogers, J.A., Gao, F., and Fincher, C.R. (2003) Large area, high resolution, dry printing of conducting polymers for organic electronics. *Appl. Phys. Lett.*, **82** (3), 463–465.

42 Wolk, M.B., Baetzold, J., Bellmann, E., Hoffend, T.R. Jr., Lamansky, S., Li, Y., Roberts, R.R., Savvateev, V., Staral, J.S., and Tolbert, W.A. (2004) Laser thermal patterning of OLED materials. *Proc. SPIE*, **5519** art. no. 03, 12–23.

43 Chin, B.D., Suh, M.C., Kim, M.H., Kang, T.M., Yang, N.C., Song, M.W., Lee, S.T., Kwon, H.H., and Chung, H.K. (2003) High efficiency AMOLED using hybrid of small molecule and polymer materials pattered by laser transfer. *J. Inf. Disp.*, **4** (3), 1–5.

44 Hirano, T., Matsuo, K., Kohinata, K., Hanawa, K., Matsumi, T., Matsuda, E., Matsuura, R., Ishibashi, T., Yoshida, A., and Sasaoka, T. (2007) Novel laser transfer technology for manufacturing large-sized OLED displays. *SID Int. Symp.*, **38** (2), 1592–1595.

45 Ko, S.H., Pan, H., Ryu, S.G., Misra, N., Grigoropoulos, C.P., and Park, H.K. (2008) Nanomaterial enabled laser transfer for organic light emitting material direct writing. *Appl. Phys. Lett.*, **93**, 151110.

46 Fukumura, H., Kohji, Y., and Masuhara, H. (1996) Laser implantation of fluorescent molecules into polymer films. *Appl. Surf. Sci.*, **96-98**, 569–571.
47 Fukumura, H., Kohji, Y., Nagasawa, K.-I., and Masuhara, H. (1994) Laser implantation of pyrene molecules into poly(methyl methacrylate) films. *J. Am. Chem. Soc.*, **116** (22), 10304–10305.
48 Fukumura, H., Uji-i, H., Banjo, H., Masuhara, H., Karnakis, D.M., Ichinose, N., Kawanishi, S., Uchida, K., and Irie, M. (1998) Laser implantation of photochromic molecules into polymer films: a new approach towards molecular device fabrication. *Appl. Surf. Sci.*, **127-129**, 761–766.
49 Kishimoto, M., Hobley, J., Goto, M., and Fukumura, H. (2001) Microscopic laser patterning of functional organic molecules. *Adv. Mater.*, **13** (15), 1155–1158.
50 Schütze, K., Pösl, H., and Lahr, G. (1998) Laser micromanipulation systems as universal tools in cellular and molecular biology and in medicine. *Cell. Mol. Biol. (Noisy-le-Grand, France)*, **44** (5), 735–746.
51 Kubickova, S., Cernohorska, H., Musilova, P., and Rubes, J. (2002) The use of laser microdissection for the preparation of chromosome-specific painting probes in farm animals. *Chromosome Res.*, **10** (7), 571–577.
52 Stich, M., Thalhammer, S., Burgemeister, R., Friedemann, G., Ehnle, S., Lüthy, C., and Schütze, K. (2003) Live cell catapulting and recultivation. *Pathol. Res. Pract.*, **199** (6), 405–409.
53 Vogel, A., Horneffer, V., Lorenz, K., Linz, N., Hüttmann, G., and Gebert, A. (2007) Principles of laser microdissection and catapulting of histologic specimens and live cells. *Methods Cell Biol.*, **82**, 153–205.

2

Origins of Laser-Induced Transfer Processes

Christina Kryou and Ioanna Zergioti

National Technical University of Athens, Physics Department, Heroon Polytehneiou 9, 15780 Zografou, Athens, Greece

2.1 Introduction

The development and use of laser-induced transfer processes have grown steadily over the past 20 years. Due to its simplicity, this technique is becoming widely used for deposition of a broad variety of materials for many microfabrication applications. This chapter describes the evolution of the laser forward-transfer method from the early 1970s, its historical origins, and presents some of the early achievements, until 2001 when the laser-induced forward transfer (LIFT) technique was well stablished in the laser materials processing community. Generally, laser-induced transfer processes are promising laser-based microfabrication techniques, which enable the transfer and deposition of high-resolution structures comprising a wide range of materials without affecting their properties.

This chapter is concerned primarily with the initial findings on the technique and its potential for the direct writing of microscale and nanoscale structures of a broad variety of materials, providing an overview of LIFT and some alternative approaches that derive from this technique as well. LIFT has several experimental requirements that can have significant effects on the quality of the transferred patterns and on the operational characteristics of the printed devices, and these aspects will also be discussed in detail in the following sections, aiming to highlight the effectiveness of the technique in material processing applications.

2.2 Early Work in Laser-Induced Transfer

The LIFT technique was first described in the late 1960s and was further developed in the mid-1980s. In 1970, the first demonstration of laser-induced transfer of material across an air gap can be found in the work reported by Levene *et al*. [1] entitled "Material transfer recording," and the motivation of this research group was to develop a laser-based printing process. The material to be transferred consisted of black ink from polyethylene-backed typewriter ribbon and colored dyes from Mylar substrate across gaps up to 100 μm wide using an Nd:

Laser Printing of Functional Materials: 3D Microfabrication, Electronics and Biomedicine,
First Edition. Edited by Alberto Piqué and Pere Serra.
© 2018 Wiley-VCH Verlag GmbH & Co. KGaA. Published 2018 by Wiley-VCH Verlag GmbH & Co. KGaA.

YAG laser ($\lambda = 1.064\,\mu m$). They proposed a simple model based on the melting and vaporization of the material to be transferred with regard to the influence of the laser fluence. Their work was predictive in "labeling" the clarity and high writing speed of the technique. Moreover, an early experiment using argon laser has been mentioned by Braudy [2]. Levene *et al*. mentioned that using a more powerful Nd^{+3}: YAG laser could be an effective method to transfer materials for image recording either in the forward or in the backward direction both in contact and noncontact onto a transparent substrate. This laser-based printing process described an inherently noncontact, printing system with instant imaging capabilities that did not require any additional chemical process. In their experiment, line patterns were transferred with widths ranging from less than 30 μm to more than 130 μm using an Nd: YAG laser, depending on the spot size at focus and the air gap between the donor and the receiving substrate. In more detail, with an air gap of about 100–200 μm, they reported that the deposited lines presented a less sharp outline followed by some randomly distributed debris as illustrated in Figure 2.1a,b. Further experiments were accomplished with a reverse transfer setup [2] (as shown, also, in Figure 2.1c,d. To investigate the differences between the two approaches of material deposition via ablation transfer for the printing in the forward direction and for a given coating thickness, the transferred material was either completely removed above a certain laser fluence threshold or not at all. The experiments were further expanded to PET (poly(ethylene terephthalate)) foil-supported dyes and ink materials, suggesting that the laser-assisted material transfer recording is not restricted to a black carbon ribbon system.

The description of a process similar to LIFT was first reported in a US Patent filed in 1971, by Brisbane [3], for a laser-driven transfer method that was proposed as a new deposition method for the direct writing of different metals to a glass substrate for the graphic industry. The invention provided the principle of the technique whereby a sharply defined platinum interconnection pattern could be directly "written" on a semiconductor cellular substrate by placing a film of a vaporizable material (platinum) disposed on a glass plate opposite to the substrate.

In a US Patent filed in 1971 [4], further improvements in the printing system aimed for a laser imaging application close to that reported earlier. More specifically, the donor layer was coated on a transparent substrate that

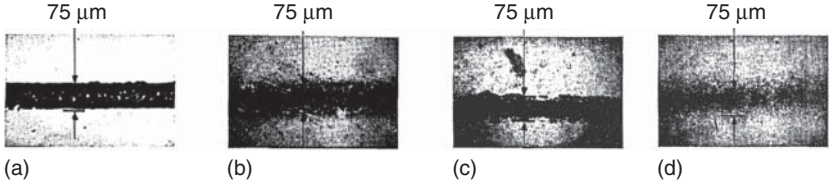

Figure 2.1 (a) Forward transfer, in contact, (b) forward transfer across a gap, (c) reverse transfer, in contact, (d) reverse transfer across a gap. (Levene *et al*. 1970 [1]. Reproduced with permission of OSA Publishing.)

comprised heat-absorbing carbon black particles and was dispersed in a self-oxidizing binder consisting of nitrocellulose. While the laser pulse heated the energy-absorbing particles, a burst of the energetic binder matrix occurred. As a result, this led to the coating elimination, leaving a clear area on the receiver substrate that was compatible to a positive image. In more detail, the transferred material created an image recording when the receiver was positioned as a support in close proximity to the donor layer. Following, a laser pulse was focused to heat the matrix binder and initiate the ignition.

In 1976, a slight extension of the laser transfer method was reported by Peterson J.O.H. for the preparation of planographic printing plates [5]. More specifically, the donor substrate coating comprised a cross-linkable prepolymer resin along with a thermos triggered cross-linker agent. Afterward, a laser-responsive ignition generated the transfer of the prepolymer resin coating along with the cross-linking agent, while the cross-linking reaction was produced by the heat generated during the laser irradiation and the exothermic decomposition of the binder. Finally, the deposited polymer components were enclosed after thermal curing on the receiving plate, which could be used for the copy printing process. This research indicates that by using a relevant material system, laterally well-regulated functional modules such as printing plates for graphic arts could be directly fabricated by laser-assisted material transfer techniques.

Laser-assisted deposition of metals was first reported by Osgood [6] in 1983, using the term "laser-initiated chemistry," where initially UV photolysis of gas-phase precursors was utilized to deposit metals [7, 8]. In a related study, using a focused continuous-wave laser, submicrometer reactions zones were formed, thus producing highly localized laser chemistry [6]. At this period, the term "direct writing" was used to present and describe the types of laser processes that could be carried out without the need of masks or molds in one single step, for the transfer of a wide variety of materials.

2.3 Overview of Laser-Induced Forward Transfer

The LIFT technique [9], as schematically shown in Figure 2.2, includes the transfer of materials from a donor substrate. The donor substrate is coated onto one side of a transparent carrier and is placed in close proximity to a receiver substrate. Material transfer from the donor to the receiver substrate takes place when a laser pulse of adequate intensity is focused through the carrier onto the carrier–donor interface. Absorption of the laser energy heats the donor material, and forward transfer typically occurs when ablation at the carrier–donor interface provides an explosive thrust [10]. This method allows for two-dimensional and three-dimensional direct write of a broad variety of materials at scales from submicron [11] to 0.5 mm, is easily integrated with micromachining methods [12], and can be also achieved in ambient atmosphere.

The term "LIFT" was first proposed by Bohandy *et al*. [9] to describe a method for repairing damaged photomasks. They reported the deposition of copper

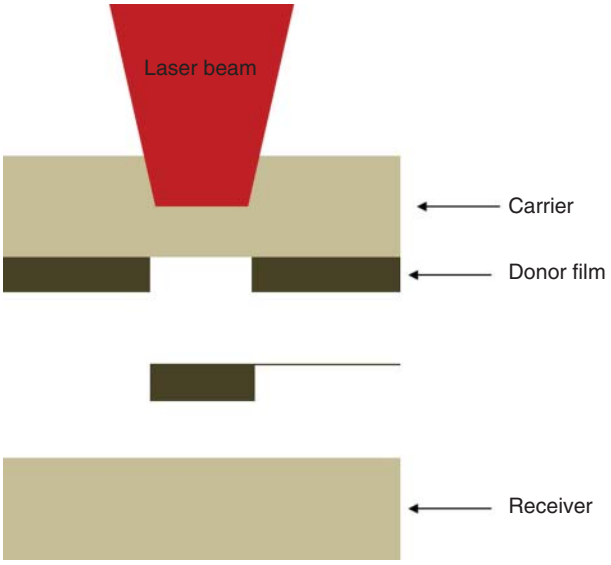

Figure 2.2 Conventional laser-induced forward transfer (LIFT) method.

metal patterns via laser forward transfer inside a vacuum chamber. Excimer laser pulses ($\lambda = 193$ nm, 15 ns) were focused with a cylindrical lens to a 25 mm long by 50 μm wide line on a source substrate containing a thin copper film. The Cu was deposited onto silicon and fused-silica substrates, while electrical characterization demonstrated resistivities ranging between 3 and 50 times the value for bulk copper with good adhesion behavior that passed simple tape tests. Bohandy and his group proposed a model similar to Levene's [1] to describe the process in more detail. Briefly, the process includes the following steps: (i) the laser radiation heats the interface of the film and the donor substrate, (ii) a resulting melt front propagates through the film until it reaches the free surface, (iii) the material at the interface is superheated beyond its boiling point until (iv) the resulting vapor-induced pressure at the interface catapults the molten film toward the receiver substrate [10]. Moreover, the same group, 1 year later, demonstrated that this technique could be applied in air under atmospheric pressure without the need for a vacuum chamber [13].

This primary experiment was considered as a milestone of LIFT technology for the direct printing of conducting lines. One of the main advantages of LIFT relies on the fact that the size of the transferred metal deposits correlates closely with the size and shape of the laser focal spot. Many mechanistic models of the laser-induced forward propulsion of metal patterns involve heating, melting, and vaporization processes of the metal film induced by the laser irradiation. Regarding inorganic nonmetallic materials, the LIFT of silicon nanoparticles was examined with respect to potential applications in device fabrication [14] using a Nd: YAG laser (1064 nm, 5–7 ns pulse width), while for the preparation of the donor substrates, Si nanoparticles were transferred on glass substrates by vertical pulsed

laser deposition (VPLD). According to the experiment in gas atmosphere, strong morphological variations of the transferred Si structures were observed.

2.3.1 Transferring Metals and Other Materials with Laser-Induced Forward Transfer (LIFT)

The LIFT technique rapidly gained acceptance and was utilized for a broad variety of single-element materials, mainly metals such as copper [13], gold [13, 15], aluminum [16], vanadium [17], chromium [11], tungsten [18, 19], and Ge/Se thin-film structures [20]. It is worth mentioning some results of LIFT for oxide compounds such as Al_2O_3 and $YBa_2Cu_3O_7$ high-temperature superconductors [21, 22], obtained in previous studies; however, the quality of these transferred materials was not as desirable as those deposited by conventional film growth techniques.

Generally, to successfully obtain the desired pattern, that is, uniform transfer with good spatial resolution and morphology on the receiver substrate, with the basic LIFT technique, the following steps should be taken into account: (i) the thickness of the donor film should not exceed 100 nm, (ii) the laser wavelength that is used should be strongly absorbed by the donor film, (iii) the donor substrate should be in close proximity or in contact with the receiver substrate, and (iv) the laser fluence should just exceed the threshold fluence to detach the film from the donor substrate toward the receiver substrate. This last condition (threshold fluence) is important in order to control the quality of the material to be transferred, because if high-energy fluences are applied, it is possible to cause excessive vaporization, due to the eruptive transfer. As a result, the morphology and resolution of the deposited film are affected.

A later variation of the LIFT technique employed an organic precursor compound rather than a pure metal for transfer [23]. It is worth mentioning, as it was indicated in this work, that the laser forward-transfer process can take advantage of the photoinduced decomposition of a precursor at the donor/coating interface to catapult the remnant of the film forward and create a metal pattern. By irradiating the transferred material with additional laser pulses, a thin (<100 nm) but grainy palladium coating was generated, on which a thicker metal layer could be developed by means of electroless plating in a two-step process, enabling the selective deposition of metal patterns. However, their initial aim was to report that the LIFT technique can be used to deposit a metal–organic precursor of the desired material, which once transferred can be then decomposed into its final form.

At this point, it is worth mentioning the first industrial application reported by Poon and Tam [24] entitled "Laser-induced forward transfer of carbon and chromium films in gases of one atmosphere pressure." Using the LIFT technique, they deposited patterned spots of carbon and chromium metals with specific thickness as well as compared ambient gas of air versus helium at one atmosphere pressure. Particularly, in this experiment, a focused pulsed laser of high repetition was used to produce structured spots from the "emitting" surface (donor substrate) to the "collecting" surface (receiver substrate) during the deposition with

high spatial resolution. The application of interest was to increase the roughness of the hard disk surface and enhance the antistitching behavior.

2.3.2 Limitations of the Basic LIFT Technique

The original LIFT technique was limited, despite its successful application in the transfer of thin metal layers, because of several shortcomings. For instance, to produce solid-metal films on the donor ribbon, it required "vacuum deposition techniques" and other expensive processes for the deposition. Apart from this, the main disadvantage of the primary version of the LIFT technique was the phase changes of materials (i.e., melting or vaporization) caused during transfer. As a consequence, the material's properties could be affected dramatically (e.g., oxidation of metals). Moreover, during the LIFT process, the melting and the solidification of the transferred material result in the formation of interfaces between adjacent regions of the material, which could cause detrimental effects in the electrical properties of the patterned structure under fabrication.

Furthermore, the original LIFT technique was not appropriate, until then, for the transfer of ceramics and other inorganic phases given the decomposition and the irreversible phase changes that these materials tend to encounter with melting and solidification. The main reason for the aforementioned limitations derived from the reliance of the basic LIFT technique on phase transformations of the material under laser transfer. It was considered difficult for these transformations to occur without any changes in the material under transfer. The key to overcome the aforementioned obstacles was to optimize the donor preparation. It was a crucial step, and it was regarded as a breakthrough since many types of materials, mainly complex multicomponent and multiphase systems, would incur irreversible changes upon melting, which could degrade their desirable properties (i.e., phase, structure, electrical behavior). Finally, the main objective was to make this technique compatible with a broad variety of materials.

2.3.3 The Role of the Donor Substrate

As mentioned earlier, the key for the successful deposition of materials by the LIFT technique is the donor substrate and its preparation. The main advantages provided by the donor substrate to the LIFT technique reside in the fact that the donor substrate and its preparation are a totally independent part of the process both from the laser source and the target (receiver substrate). Hence, it can easily be modified without requiring complex procedures to the basic setup and components. Furthermore, since it is a totally independent step of the process, main issues, such as elimination of contaminations with the receiver substrate, phase changes of the transferred material, and removal of the donor substrate to allow direct interaction of the laser beam with the acceptor substrate, are easily succeeded. Since the type of the material in the donor substrate can easily be changed (i.e., heterogeneous multilayers, composites, liquid dispersions, and complex fluids), the nature of the laser interaction with the material of the donor substrate can be adapted almost endlessly.

Briefly, there are many processing methods for the deposition of homogeneous wet films with high cross-directional uniformity. Therefore, a film having a uniform thickness can be readily obtained on a substrate having a great area by employing spin coating, blade coating, slot-die coating, dip coating, and drawdown rods methods. Spin coating is the most common film-formation method for applying thin films (a few nm to a few μm) evenly across the surface of a substrate by coating (casting) a solution of the desired material in a solvent while the substrate is rotating. It is used for coating substrates with a wide variety of materials including photoresists, insulators, organic semiconductors, synthetic metals, nanomaterials, metal and metal-oxide precursors, transparent conductive oxides.

Blade coating, also known as doctor blading is also a processing method for the fabrication of large-area films on flexible substrates. The blade coating method has seen an increasing attraction for the fabrication of small lab-scale devices, especially for active layers and electrodes [25, 26]. In the doctor blading process, a well-mixed slurry consisting of a suspension of material particles along with other additives (such as binders or dispersants) is placed on a substrate beyond the doctor blade. When a constant relative movement is established between the blade and the substrate, the slurry spreads on the substrate to form a thin sheet, which results in a gel layer upon drying. The doctor blading can operate at speeds up to several meters per minute, and it is suitable to coat substrates with a very wide range of wet-film thicknesses ranging from 20 to several hundred microns [27].

Another processing method for the deposition of uniform wet film on a substrate is the noncontact slot-die coating process. This process can handle a broad range of viscosities between less than 1 mPa s and several thousand pascal seconds while the coating speed has a similar wide spectrum between less than 1 m/min and more than 600 m/min. The slot-die approach provides many benefits, such as higher line speed capability and greater coat weight uniformity [28, 29].

As a popular alternative to spin coating, dip-coating methods are frequently employed to produce thin films from sol–gel precursors for research purposes, where they are generally used for applying films onto flat or cylindrical substrates [30]. The final product may incorporate the substrate and the coating, or the coating may be peeled off to form an object that consists solely of the dried or solidified coating. Recently, a new method was designed to draw down sample coatings with a high degree of reproducibility. Specifically, drawdown rods provide the ability to fine-tune coating thickness quickly and easily, without altering the chemistry of the coating material and without time-consuming and expensive changeovers [31, 32]. The most common film-formation methods for applying thin films for research purposes are spin coating and blade coating methods. All the others are used, mainly, in the industry.

In the following sections, several derivatives to the basic LIFT process based on different donor substrate arrangements will be presented to illustrate this point.

2.3.4 Use of a Dynamic Release Layer (DRL)-LIFT

An early variation to overcome some of LIFT's constraints employed multilayered films. This variation of the LIFT technique was originally intended for high-speed laser color printing applications and was called "laser ablation transfer" (LAT). The layers can be formed by depositing, through vacuum or spin coating technique, an intermediate laser-absorbing film on the transparent support, followed by a second layer including the material to be transferred. This thin intermediate laser-absorbing film is called the dynamic release layer (DRL) [33]. The deposited intermediate laser-absorbing film could have (20–100) nm thick thin-film metal layers from vacuum or polymer layers up to 1 μm in thickness from spin coating technique. Using metallic laser-absorbing films, laser energies above the ablation threshold result in melting and vaporization of the metal in a similar way as in LIFT. In case of polymeric laser-absorbing layers, the pulsed laser tends to cause both photochemical and photothermal decomposition of the organic molecules into vapor by-products. Under the right circumstances, it is possible for the material under transfer to avoid exposure to the incident laser pulse and undergo minimum heating from the laser-absorbing layer.

Consequently, materials showing weak absorption to the laser radiation or materials that could be damaged by their interaction with the laser pulse can be transferred by this process. An optimization of the type of laser absorbing layer (DRL), its thickness, the incident laser energy, pulse shape, and the thickness of the second layer is needed in order for the deposition to be successful with minimum interaction of the incident laser with the transferred materials. A schematic of laser forward-transfer laser-absorbing layer is shown in Figure 2.3. The use of Teflon AF and poly(methacrylonitrile) as intermediate laser-absorbing

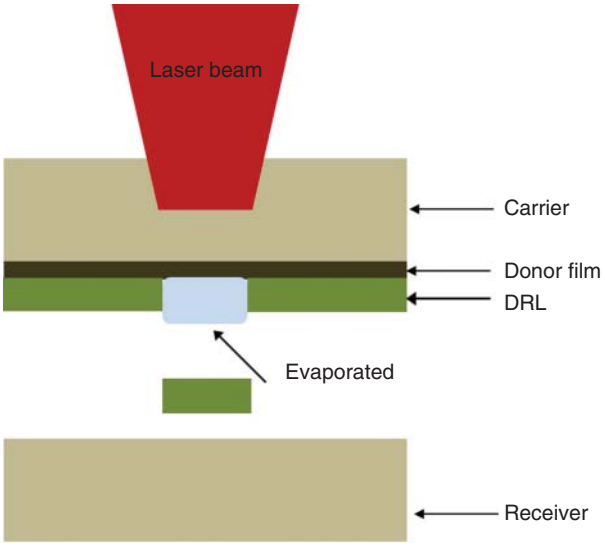

Figure 2.3 Dynamic release layer (DRL)-assisted LIFT method.

film for the transfer of gold and aluminum thin films was reported to enable the deposition at lower laser energies compared to those required for transferring the metal films without DRL [34].

2.3.5 LIFT with Ultrashort Laser Pulses

In 1993, Tolbert *et al*. [33] described the LIFT technique with a laser-absorbing layer (DRL) and showed for the first time that pulse duration has an effect on the transfer method. It is specified, by their experiment, that picosecond laser pulses are more efficient and effective in ablating the multilayered films than nanosecond pulses, with a laser fluence threshold that is an order of magnitude smaller. Our group, later [35, 36] reported, for the first time, the direct microdeposition of high-quality patterns using laser forward transfer without the use of DRL with subpicosecond laser pulses. Ultrafast laser pulses in the subpicosecond regime are known to have precise breakdown thresholds and minimal thermal diffusion in metals, uncontrollable melting processes are prevented, and therefore, they offer advantages of precision micromachining and microdeposition applications. Specifically, chromium metal and indium oxide microstructures were laser transferred using 500 fs KrF excimer ($\lambda = 248$ nm) laser pulses in a low vacuum environment (0.1 Torr). In this study, the deposition of highly reproducible, well-adhered structures of submicron size was reported, to demonstrate the fabrication of binary-amplitude and multilevel optical structures. The experiment exploited all the advantages over conventional methods including simplicity in terms of vacuum handling, deposition purity, position selectivity, and high-accuracy sub-micrometer pattern transfer.

The ability to deposit patterns, with sub-micrometer resolution, provided LIFT the opportunity to be incorporated in various applications in the field of microelectronics as well as in the optoelectronics fabrication industries [11]. Figure 2.4 shows a complex pixelated pattern produced by the deposition from a 400 nm thick chromium donor layer with a high lateral resolution of the individual square Cr deposit features of about 3 μm × 3 μm.

Furthermore, Figure 2.5 depicts a multilevel computer-generated holographic structure on glass, comprising three layers of Cr selectively deposited on appropriate areas on a glass plate. It is worth mentioning that in this first demonstration of this method, the deposited diffractive structures were shown to produce a high-quality computer-generated hologram.

Moreover, experiments with a nanosecond excimer laser as the ablating beam did not yield deposited features of quality comparable with the femtosecond laser results.

Other studies of fs-LIFT technique using ultrafast shadowgraphy [37] and stroboscopic Schlieren imaging [38] demonstrated that the high spatial resolution observed with fs-LIFT was due to the highly directional nature of the transfer with narrow angular divergence. Given the highly localized interaction of the fs laser pulse with the material on the donor substrate and the limited heat diffusion prior to ejection, it is possible to transfer extremely sensitive materials such as biomaterials mostly intact [39].

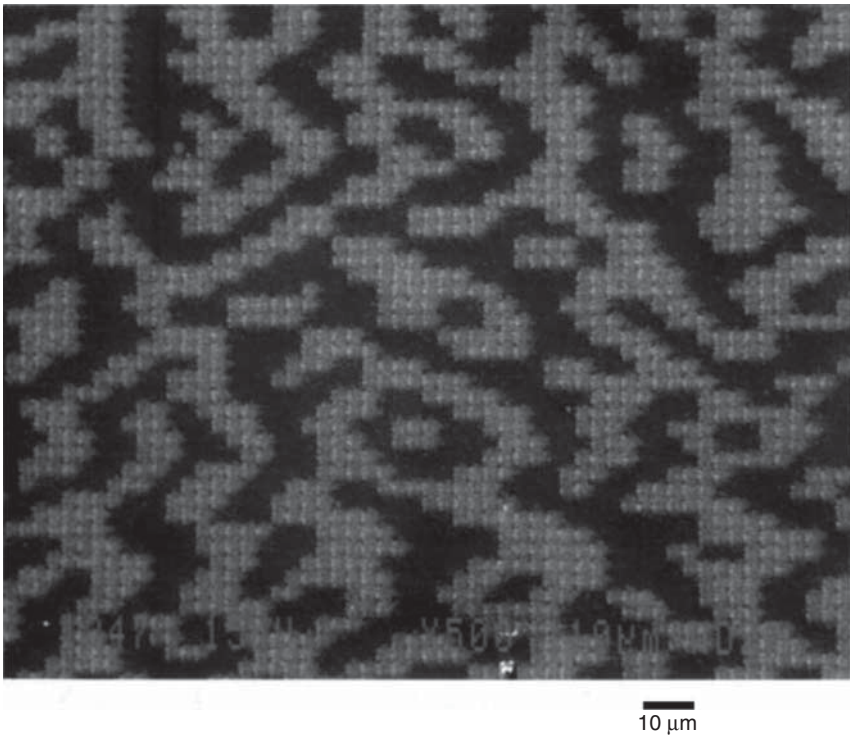

Figure 2.4 Scanning electron micrograph of a computer-generated holographic complex pixelated pattern produced by the deposition from a 400 nm thick chromium donor layer of Cr deposit features of about 3 μm × 3 μm. (Zergioti *et al*. 1998 [11]. Reproduced with permission of Springer.)

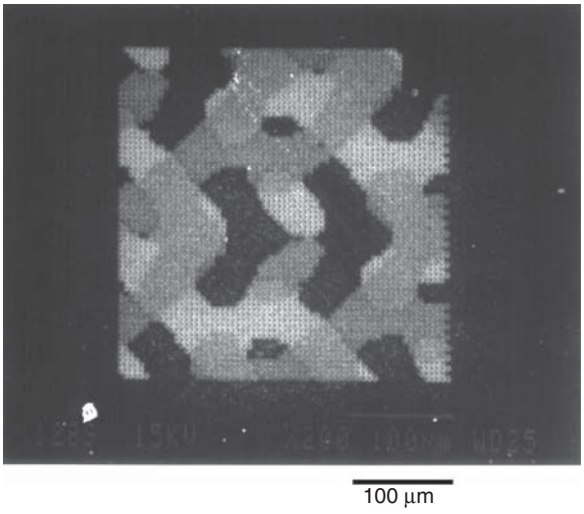

Figure 2.5 Scanning electron micrograph of a computer-generated multilevel computer-generated holographic structure on glass, comprising three layers of Cr selectively deposited on appropriate areas on a glass plate. (Zergioti *et al*. 1998 [11]. Reproduced with permission of Springer.)

2.4 Other Laser-Based Transfer Techniques Inspired by LIFT

2.4.1 Matrix-Assisted Pulsed Laser Evaporation-Direct Write (MAPLE-DW) Technique

The "matrix-assisted pulsed laser evaporation-direct write"(MAPLE-DW) technique, as proposed by Piqué *et al*. [12] combines the established matrix-assisted pulsed laser evaporation (MAPLE) [40] and the LIFT technique for the microdeposition of a variety of materials. MAPLE-DW was originally developed as a technique to rapidly prototype mesoscopic passive electronic devices such as interconnects, resistors, and capacitors [40–43]. This technology falls under the category of the "direct-write" approaches because it can be used to rapidly form any pattern with the aid of a CAD/CAM system, which enables this tool to rapidly fabricate complex structures without the aid of masks or molds. It also provides higher flexibility regarding the selection of the donor material compared to the original LIFT process, as it limits the effect of the incident laser pulse on the donor material and therefore prevents the transferred structure from damage. The material to be transferred is mixed in a laser-absorbent matrix (i.e., frozen solvents or organic binders), and the laser is used to vaporize the matrix. The donor substrate consists of a transparent carrier coated with a suspension or dispersion of the particulate transfer material that can be either powders or small particles or even a suspension of biomaterials including viable cells. Following, a focused laser pulse is directed through the backside of the donor substrate, and as a result, the focused laser pulse (usually in the UV range) interacts preferably with the matrix components, which are then vaporized, due to localized heating from electronic and vibrational excitations, to form the pressure that is necessary to propel the mixed transfer material away from the quartz support toward a receiver substrate positioned some micrometers away. However, to obtain the functionality of the particulate materials after deposition, often further improvements are necessary to obtain device compatibility (i.e., laser sintering, thermal annealing) for the bonding of conductive powders [44]. For the fabrication of more demanding devices, such as biodevices and sensors, MAPLE-DW has been proven to be a promising approach for LIFT deposition [45]. For example, solutions or suspensions of active proteins, including enzymes and antibodies, could be laser transferred by this method, and test assays consisting of microarrays with different immobilized proteins have been demonstrated by staining with fluorescently tagged complementary proteins [46].

2.4.2 LIFT of Composite Matrix-Based Materials

Another modification of the basic LIFT technique relies on the transfer of materials in powder form mixed with organic binders. The mixtures are then applied as a uniform coating on the transparent donor substrate to form a film. One of the advantages of this process is based on the transfer of thicker films from the donor substrate that can be achieved at lower laser fluences than with LIFT of homogeneous films. Another advantage of this approach is that the composite

film is transferred in the solid phase, thus avoiding the melting and recondensation steps that occur in conventional LIFT. This alternative LIFT technique has been used for the laser direct write of diamond nanopowders [47], ferroelectric ($BaTiO_3$ and $SrTiO_3$) and ferrite ($Y_3Fe_5O_{12}$) micron-sized powders [12, 48]. However, the adhesion of the transferred layers may be poor with the organic binder still present after the transfer; hence, a chemical treatment is necessary to remove the binder and achieve some degree of densification. The use of LIFT with donor substrates containing organic binders can be applied to the direct transfer of many complex material formulations such as rheological systems [49, 50]. It is worth mentioning, at this point, that this modified laser forward-transfer technique was named MAPLE-DW, in reference to the direct-write of powders or particles dispersed in a liquid. MAPLE-DW originated with the idea for the transfer of powder materials mixed with organic binders. Later, as organic and biological materials were tested, the matrix was no longer a solid but instead a water-based liquid or gel; hence, this terminology is no longer used.

2.4.3 Hydrogen-Assisted LIFT

Toet *et al*. [51] proposed an alternative to use the LIFT technique without direct ablation of the material to be transferred. In this procedure, the donor film is hydrogenated amorphous silicon (a-Si:H). The thrust for forward transfer is produced from the explosive release of hydrogen when the a-Si:H film is melted at the carrier–donor interface. The material in the donor substrate is then transferred in a mixture of molten droplets and particles and is deposited as a poly-Si pixel in the receiver substrate. This technique is also known as hydrogen-assisted laser-induced forward transfer (HA-LIFT). The a-Si:H films may also be utilized as an intermediate laser-absorbing film for the transfer deposition of other donor materials, for example, metals [52]. However, as the HA-LIFT approach releases only the hydrogen from the a-Si:H film and transfers the Si, contamination of the deposited film with poly-Si is a crucial point that has not been addressed yet.

2.4.4 Long-Pulsed LIFT

Long-pulsed LIFT (LP-LIFT) represents yet another variation of the LIFT technique. This approach, which was reported by Kántor *et al*. [53], compared to conventional LIFT, employs laser pulses in the order of microseconds or longer instead of subnanosecond laser pulses. For the LP-LIFT, the donor and the receiver substrates are in close proximity. By heating the donor film, the expanding donor material tightly contacts the receiver. Due to the long pulse durations used, the donor material is kept at high temperature for a relatively long time. The donor material anneals to the receiver and is bonded locally when the layers are separated.

Kántor *et al*. [54, 55] demonstrated the transfer of a 5 μm tungsten in solid phase by means of an IR laser ($\lambda = 1.064$ μm). The deposited material presented few signs of melting and adhered well to the receiver substrate. Unfortunately, the threshold of pulse duration for transfer was about 500 μs, and shorter pulses did not result in successful transfer (as well as the usual LIFT fluence threshold). It is considered that LP-LIFT is a thermal process, relying on annealing to achieve

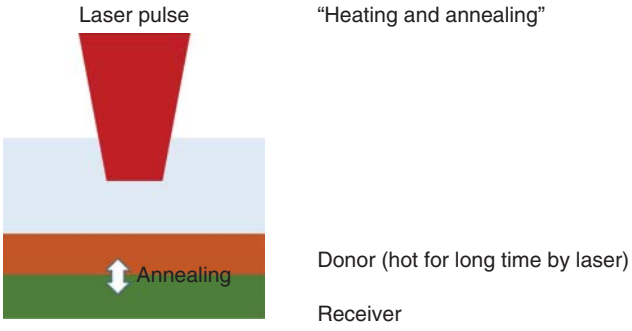

Figure 2.6 Schematic of LP-LIFT. Donor is annealed to the receiver.

Figure 2.7 Schematic of LP-LIFT. Donor and receiver substrates are separated and the annealed regions remain to the receiver.

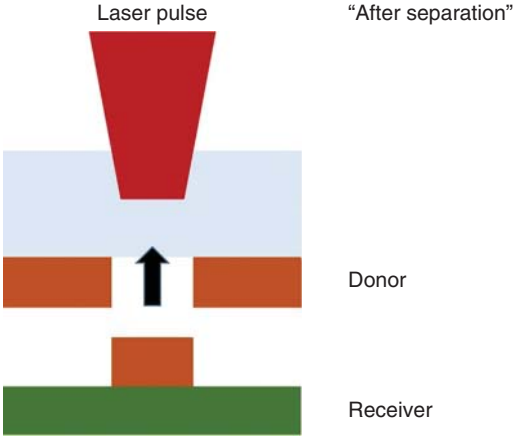

solid-phase forward transfer. This condition shows that it is an attractive technique to deposit a wide range of materials able to withstand significant heating. However, the variety of materials for deposition are restricted due to the thermal process. Figure 2.6 shows a schematic of LP-LIFT where the donor and receiver substrates are in contact.

Figure 2.7 shows a schematic of LP-LIFT where the two substrates are separated.

2.4.5 Laser Molecular Implantation

Laser molecular implantation (LMI) has been demonstrated by Fukumura *et al*. [56], in 1994, and is also known as *laser-induced molecular implantation technique* (LIMIT) [57–59]. The difference between LIMIT and other laser-based methods is that no donor film transfer is observed in this technique. This laser transfer technique aims at the transfer of single dopant molecules instead of complete donor layers. The molecules are implanted in a thin polymer film (donor film), which is kept in close contact to the receiving film. The material of the receiving film is similar to the undoped source. The absorption of the

incident laser beam depends on the doping concentration of the polymer and increases with higher doping concentration. In contrast to the LIFT technique, the source (donor film) is not heated directly, but the absorbed energy is used to activate the dopant molecules. The donor film (dopant molecule) can be then catapulted with a high kinetic energy from the expanded polymer into the receiver substrate (undoped polymer). Nevertheless, the mechanism of the preliminary process in the irradiated transfer material leading to ablation and the interactions between the particles of the material occurring after the ejection are still under investigation. Lastly, this technique works in forward- [59] and backward-transfer [56] geometries; in other words, the donor and the receiver polymer films are interchangeable.

LMI has also been utilized to implant a broad variety of organic molecules into polymer films. A particularly successful field of research has been the implantation of photochromic molecules to form optical devices and rewritable memories [57, 60]. This method has also been combined with the triazene polymer (TP) used for DRL applications [57]. In this experiment, the TP was doped with pyrene to form the source film. Recent research has focused on producing submicron patterns of organic molecules on polymer films and other organic substrates [60].

2.4.6 Laser-Induced Thermal Imaging

Laser-induced thermal imaging (LITI) is another laser-based technique, designed for the printing of a broad class of materials (i.e., conducting polymers) [61] for industrial applications. In a similar way as with DRL-LIFT, it is necessary to incorporate an intermediate absorbing layer between the donor substrate and the material to be transferred in order to protect the material during the deposition. This intermediate absorbing film is a metallic layer and, in the literature, is also called as a light-to-heat conversion (LTHC). LITI process is well suited for use in the manufacturing of high-precision industrial applications, where high resolution, absolute placement accuracy, and large format imaging are all required. LITI technique is considered as a digital patterning technique with a wide range of applications including the printing of digital color proofs, LCD color filters for flat-panel displays, patterning of organic electronic materials for OLEDs and organic transistors, patterning of multilayered organic light-emitting diode (OLED) stacks as well as other potential applications. In contrast to DRL-LIFT, in this technique, the intermediate absorbing layer is not ablated but is designed to absorb the incident laser beam and heat up sufficiently to decompose the surrounding particles. The main steps in the LITI process include deposition of the material to be transferred onto a donor film, precise optical alignment of a large-format laser imaging system to receiver substrate, treatment of the donor film (lamination) onto the target substrate, and patterning of the transfer material onto the substrate by selective exposure of the donor-transfer material-receptor stack to laser radiation.

The LITI process is considered important because of its use in the industry by companies such as Samsung SDI, in 2000, to jointly develop the process for active-matrix organic light-emitting diode (AMOLED) prototype devices [62]. Advantages of LITI over other patterning methods include its applicability to a

broad spectrum of OLED material sets, high patterning accuracy, and ability to pattern multilayer structures in a single step. It is possible that LITI introduces thermal defects in the OLED materials during patterning, but by fine-tuning the process conditions, donor structure, and OLED composition, occurrence of such defects can be eliminated.

2.5 Other Studies on LIFT

Following the early demonstrations described earlier, a wide variety of metals, [12, 23, 53, 63–70] among others, polymers [71], oxides [11, 65, 67], semiconductors [16], superconductors [22], diamond [47], have been successfully deposited through the LIFT technique. Many of these experiments have noticed the same, strict dependence of the process on the applied fluence in the early reports.

Nakata and Okada [72] have analyzed how the ablated atoms and emissive particles acted, through LIFT, based on the laser fluence. They measured atomic velocities of up to 2 km/s, while the emissive particles were much slower, traveling at around 100 m/s. The interaction of the transferred material with the receiver substrate was also investigated, where it was observed that high-energy particles were reflected off the substrate.

2.6 Conclusions

In this chapter, a general overview regarding the early stages of the LIFT processes is presented. The main topic of this chapter was to analyze the origins of laser-induced transfer. This technique first appeared in the early 1970s, was further described in 1986, and was later extended to a process with many variations. In summary, the LIFT historical origins, as well as the early achievements of this technique and results from the most fundamental state of the art, have been presented. Finally, LIFT is a promising technique for many applications since the variety of the transferred materials has also steadily increased from single inorganic compounds such as metals, to imaging dyes and inks, and further to functional multilayers and highly complex and sensitive biological systems.

List of Abbreviations

CVD	Chemical vapor deposition
DRL	Dynamic release layer
HA-LIFT	Hydrogen-assisted laser-induced forward transfer
HMDS	Hexamethyldisilane
LAT	Laser ablation transfer
LIFT	Laser-induced forward transfer
LMI	Laser molecular implantation
LP-LIFT	Long-pulsed LIFT
LTHC	Light-to-heat conversion

MAPLE	Matrix-assisted pulsed laser evaporation
MAPLE-DW	Matrix-assisted pulsed laser evaporation-direct write
PLD	Pulsed laser deposition
VPLD	Vertical pulsed laser deposition

References

1 Levene, M.L., Scott, R.D., and Siryj, B.W. (1970) Material transfer recording. *Appl. Opt.*, **9** (10), 2260–2265.
2 Braudy, R.S. (1969) Laser writing. *Proc. IEEE*, **57**, 1771–1772.
3 Brisbane, A.D. (1971) Pattern deposit by laser. US Patent 3,560,258
4 Roberts, D.L. (1971) Laser recording technique using combustible blow-off. US Patent 3, 787, 210, The National cash Register Comp., Dayton, filed Sep. 30, 1971
5 Peterson, J.O.H. (1974) Printing plate by laser transfer. US Patent 3, 964, 398, Scott Paper Comp., Philadelphia, filed Jan. 17, 1974
6 Osgood, R.M. Jr. (1983) Material deposition and removal using laser-initiated chemistry. *J. Phys.*, **44**, C5-133–C5-138.
7 Deutsch, T.F., Ehrlich, D.J., and Osgood, R.M. Jr. (1979) Laser photodeposition of metal films with microscopic features. *Appl. Phys. Lett.*, **35** (2), 175–177.
8 Ehrlich, D.J., Osgood, R.M. Jr., and Deutsch, T.F. (1981) Spatially delineated growth of metal films via photochemical pronucleation. *Appl. Phys. Lett.*, **38** (11), 946.
9 Bohandy, J., Kim, B., and Adrian, F.J. (1986) Metal deposition from a supported metal film using an excimer laser. *J. Appl. Phys.*, **60** (4), 1538–1539.
10 Adrian, F.J., Bohandy, J., Kim, B.F., Jette, A.N., and Thompson, P. (1987) A study of the mechanism of metal deposition by the laser induced forward transfer process. *J. Vac. Sci. Technol., B*, **5**, 1490.
11 Zergioti, I., Mailis, S., Vainos, N.A., Papakonstantinou, P., Kalpouzos, C., Grigoropoulos, C.P., and Fotakis, C. (1998) Microdeposition of metal and oxide structures using ultrashort laser pulses. *Appl. Phys. A*, **66**, 579.
12 Piqué, A., Chrisey, D.B., Auyeung, R.C.Y., Fitz-Gerald, J., Wu, H.D., McGill, R.A., Lakeou, S., Wu, P.K., Nyuyen, V., and Duignan, M. (1999) A novel laser transfer process for direct writing of electronic and sensor materials. *Appl. Phys. A*, **69** (Suppl), S279–S284.
13 Bohandy, J., Kim, B., Adrian, F.J., and Jette, A.N. (1988) Metal deposition at 532 nm using a laser transfer technique. *J. Appl. Phys.*, **63**, 1158.
14 Rigout, M.L.A., Niu, H., Qin, C., Zhang, L., Li, C., Bai, X., and Fan, N. (1998) Fabrication and photoluminescence of hyper branched silicon nanowire networks on silicon substrates by laser-induced forward transfer. *Nanotechnology*, **19**, 245303.
15 Baseman, R.J., Froberg, N.M., Andreshak, J.C., and Schlesinger, Z. (1990) Minimum fluence for laser blow-off of thin gold films at 248 and 532 nm. *Appl. Phys. Lett.*, **56**, 1412.
16 Mogyorósi, P., Szörényi, T., Bali, K., Tóth, Z., and Hevesi, I. (1989) Pulsed laser ablative deposition of thin metal films. *Appl. Surf. Sci.*, **36**, 157.

17 Schultze, V. and Wagner, M. (1991) Laser-induced forward transfer of aluminium. *Appl. Surf. Sci.*, **52**, 303.

18 Tóth, Z., Szörényi, T., and Tóth, A.L. (1993) Ar+ laser-induced forward transfer (LIFT): a novel method for micrometer-size surface patterning. *Appl. Surf. Sci.*, **69**, 317.

19 Kántor, Z., Tóth, Z., Szörényi, T., and Tóth, A.L. (1994) Deposition of micrometer-sized tungsten patterns by laser transfer technique. *Appl. Phys. Lett.*, **64**, 3506.

20 Tóth, Z. and Szörényi, T. (1991) Pulsed laser processing of Ge/Se thin film structures. *Appl. Phys. A*, **52**, 273.

21 Greer, J.A. and Parker, T.E. (1988) Basic mechanisms and application of the laser-induced forward transfer for high-Tc superconducting thin film deposition. *SPIE Proc.*, **998**, 113–125.

22 Fogarassy, E., Fuchs, C., Kerherve, F., Hauchecorne, G., and Perriere, J. (1989) Laser-induced forward transfer of high-Tc YBaCuO and BiSrCaCuO superconducting thin films. *J. Appl. Phys.*, **66**, 457.

23 Esrom, H., Zhang, J.-Y., Kogelschatz, U., and Pedraza, A.J. (1995) New approach of a laser-induced forward transfer for deposition of patterned thin metal films. *Appl. Surf. Sci.*, **86**, 202.

24 Poon, C.C. and Tam, A.C. (1996) Summaries of papers presented at the conference on lasers and electro-optics. CLEO, Anaheim, CA, USA, June 2–7, 1996

25 Krantz, J., Richter, M., Spallek, S., Spiecker, E., and Brabec, C. (2011) Solution-processed metallic nanowire electrodes as indium tin oxide replacement for thin-film solar cells. *Adv. Funct. Mater.*, **21**, 4784–4787.

26 Chang, Y.-H., Tseng, S.-R., Chen, C.-Y., Meng, H.-F., Chen, E.-C., Horng, S.-F., and Hsu, C.-S. (2009) Polymer solar cell by blade coating. *Org. Electron.*, **10**, 741–746.

27 Berni, A., Mennig, M., and Schmidt, H. (2004) *Sol-gel technologies for glass producers and users*, Springer Science and Business Media, New York.

28 Hösel, M, Krebs, FC (2013) Large-scale roll-to-roll fabrication of organic solar cells for energy production. PhD thesis

29 Han, G.H., Lee, S.H., Ahn, W.-G., Nam, J., and Jung, H.W. (2013) Effect of shim configuration on flow dynamics and operabilitywindows in stripe slot coating process. *J. Coat. Technol. Res.*, **11** (1), pp. 19–29.

30 Scriven, L.E. (1988) Physics and applications of dip coating and spin coating. Better Ceramics Through Chemistry III: Symposium held Reno, NV, April 5–8, 1988, pp. 717–729.

31 Hakovirta, M., Aksoy, B., and Hakovirta, J. (2015) Self-assembled micro-structured sensors for food safety in paper based food packaging. *Mater. Sci. Eng., C*, **53**, 331–335.

32 Prasath Balamurugan, G., Pukadyil, R.N., Nielsen, K.E., Brandys, F.A., and Thompson, M.R. (2013) Role of a micro-patterned adhesive interface on the performance of thermoformable multi-layered decorative polymeric film laminates. *Int. J. Adhes. Adhes.*, **44**, 78–90.

33 Tolbert, W.A., Lee, I.Y.S., Doxtader, M.M., Ellis, E.W., and Dlott, D.D. (1993) High-speed color imaging by laser ablation transfer with a dynamic release layer: fundamental mechanisms. *J. Imaging Sci. Technol.*, **37**, 411.

34 Lätsch, S., Hiraoka, H., Nieveen, W., and Bargon, J. (1994) Interface study on laser-induced material transfer from polymer and quartz surfaces. *Appl. Surf. Sci.*, **81**, 183.

35 Zergioti, I., Mailis, S., Vainos, N.A., Fotakis, C., Chen, S., and Grigoropoulos, C.P. (1998) Microdeposition of metals by femtosecond excimer laser. *Appl. Surf. Sci.*, **127–129**, 601.

36 Karaiskou, A., Zergioti, I., Fotakis, C., Kapsetaki, M., and Kafetzopoulos, D. (2003) Microfabrication of biomaterials by the sub-ps laser-induced forward transfer process. *Appl. Surf. Sci.*, **208–209** (15), 245–249.

37 Papazoglou, D.G., Karaiskou, A., Zergioti, I., and Fotakis, C. (2002) Shadowgraphic imaging of the sub-ps laser-induced forward transfer process. *Appl. Phys. Lett.*, **81**, 1594–1596.

38 Zergioti, I., Papazoglou, D.G., Karaiskou, A., Fotakis, C., Gamaly, E., and Rode, A. (2003) A comparative schlieren imaging study between ns and sub-ps laser forward transfer of Cr. *Appl. Surf. Sci.*, **208–209**, 177–180.

39 Karaiskou, A., Zergioti, I., Fotakis, C., Kapsetaki, M., and Kafetzopoulos, D. (2003) Microfabrication of biomaterials by the sub-ps laser-induced forward transfer process. *Appl. Surf. Sci.*, **208–9**, 245–249.

40 Pique, A., Chrisey, D.B., Auyeung, R.C.Y. *et al.* (1999) *SPIE Proc.*, **3618**, 330–339.

41 Modi, R., Wu, H.D., Auyeung, R.C.Y., Gilmore, C.M., and Chrisey, D.B. (2001) Direct writing of polymer thick film resistors using a novel laser transfer technique. *J. Mater. Res.*, **16** (11), 3214–3222.

42 Pique, A., Chrisey, D.B., Fitz-Gerald, J.M., McGill, R.A., Auyeung, R.C.Y., Wu, H.D., Lakeou, S., Nyuyen, V., Chung, R., and Duignan, M. (2000) Direct writing of electronic and sensor materials using a laser transfer technique. *J. Mater. Res.*, **15** (9), 1872–1875.

43 Young, D., Wu, H.D., Auyeung, R.C.Y., Modi, R., Fitz-Gerald, J., Piqué, A., and Chrisey, D.B. (2001) Dielectric properties of oxide structures by a laser-based direct-writing method. *J. Mater. Res.*, **16** (6), 1720–1725.

44 Chrisey, D.B., Pique, A., Modi, R., Wu, H.D., Auyeung, R.C.Y., and Young, H.D. (2000) Direct writing of conformal mesoscopic electronic devices by MAPLE-DW. *Appl. Surf. Sci.*, **168**, 345–352.

45 Ringeisen, B.R., Chrisey, D.B., Piqué, A., Young, H.D., Modi, R., Bucaro, M., Jones-Meehan, J., and Spargo, B.J. (2002) Generation of mesoscopic patterns of viable Escherichia doli by ambient laser transfer. *Biomaterials*, **23**, 161–166.

46 Wu, P.K., Ringeisen, B.R., Callahan, J., Brooks, M., Bubb, D.M., Wu, H.D., Piqué, A., Spargo, B., Mc Gill, R.A., and Chrisey, D.B. (2001) The deposition, structure, pattern deposition of biomaterial thin films by matrix-assisted pulsed-laser evaporation (MAPLE) and MAPLE direct write. *Thin Solid Films*, **398–399**, 607–614.

47 Pimenov, S.M., Shafeev, G.A., Smolin, A.A., Konov, V.I., and Vodolaga, B.K. (1995) Laser-induced forward transfer of ultra-fine diamond particles for selective deposition of diamond films. *Appl. Surf. Sci.*, **86**, 208.

48 Piqué, A., Chrisey, D.B., Auyeung, R.C.Y., Lakeou, S., Chung, R., McGill, R.A., Wu, P.K., Duignan, M., Fitz-Gerald, J., and Wu, H.D. (1999) *SPIE Proc.*, **3618**, 330–333.

49 Piqué, A., Fitz-Gerald, J., Chrisey, D.B., Auyeung, R.C.Y., Wu, H.D., Lakeou, S., and McGill, R.A. (2000) Direct writing of electronic materials using a new laser assisted transfer/annealing technique. *SPIE Proc.*, **3933**, 105–112.

50 Auyeung, R.C.Y., Wu, H.D., Modi, R., Piqué, A., Fitz-gerald, J.M., Young, H.D., Lakeou, S., Chung, R., and Chrisey, D.B. (2000) Matrix assisted laser transfer of electronic materials for direct write applications. *SPIE Proc.*, **4088**, 393–396.

51 Toet, D., Smith, P., Sigmon, T., and Thompson, M. (1999) Laser-assisted transfer of silicon by explosive hydrogen release. *Appl. Phys. Lett.*, **74** (15), 2170–2172.

52 Toet, D., Smith, P., Sigmon, T., and Thompson, M. (2000b) Spatially selective materials deposition by hydrogen-assisted laser-induced transfer. *Appl. Phys. Lett.*, **77** (2), 307–309.

53 Kántor, Z., Toth, Z., and Szorenyi, T. (1994a) Metal pattern deposition by laser-induced forward transfer. *Appl. Surf. Sci.*, **86**, 196–201.

54 Kántor, Z. and Szorenyi, T. (1995) Dynamics of long-pulse laser transfer of micrometer-sized metal patterns as followed by time-resolved measurements of reflectivity and transmittance. *J. Appl. Phys.*, **78** (4), 2775–2781.

55 Kántor, Z., Toth, Z., Szorenyi, T., and Toth, A. (1994b) Deposition of micrometer-sized tungsten patterns by laser transfer technique. *Appl. Phys. Lett.*, **64** (25), 3506–3508.

56 Fukumura, H., Kohji, Y., Nagasawa, K.-I., and Masuhara, H. (1994) Laser implantation of pyrene molecules into poly(methyl methacrylate) films. *Am. Chem. Soc.*, **116**, 10304–10305.

57 Karnakis, D., Lippert, T., Ichinose, N., Kawanishi, S., and Fukumura, H. (1998b) Laser induced molecular transfer using ablation of a triazene-polymer. *Appl. Surf. Sci.*, **127–129**, 781–786.

58 Okada, T., Hatanaka, K., Hobley, J., Fukumura, H., and Kishimoto, M. (2001) Laser-induced molecular implantation at the focus of an objective lens: a comparative study among anthracene derivatives. In Technical Digest. CLEO/Pacific Rim 2001. 4th Pacific Rim Conference on Lasers and Electro-Optics (Cat. No.01TH8557), Chiba, Japan, pp. 56-57

59 Fukumura, H., Kohji, Y., and Masuhara, H. (1996) Laser implantation of fluorescent molecules into polymer films. *Appl. Surf. Sci.*, **96–98**, 569–571.

60 Goto, M., Kawanishi, S., and Fukumura, H. (2000) Implantation of organic molecules into biotissue by pulsed laser irradiation. *Jpn. J. Appl. Phys.*, **38**, L87–L88.

61 Blanchet, G., Loo, Y.-L., Rogers, J., Gao, F., and Fincher, C. (2003) Large area, high resolution, dry printing of conducting polymers for organic electronic. *Appl. Phys. Lett.*, **82** (3), 463–465.

62 Wolk, M.B., Baetzold, J., Bellmann, E., Hoffend, T.R. Jr., Lamansky, S., Li, Y., Roberts, R.R., Savvateev, V., Staral, J.S., and Tolbert, W.A. (2004) in *Organic Light-Emitting Materials and Devices VIII*, vol. **5519** (eds Z.H. Kafafi and P.A. Lane), InTech, pp. 12–23. ISBN: 0-8194-5942.

63 Koundourakis, G., Rochstuhl, C., Papazoglou, D., Klini, A., Zergioti, I., Vainos, N., and Fotakis, C. (2001) Laser printing of active optical microstructures. *Appl. Phys. Lett.*, **78** (7), 868–870.

64 Germain, C., Charron, L., Lilge, L., and Tsui, Y. (2007) Electrodes for microfluidic devices produced by laser induced forward transfer. *Appl. Surf. Sci.*, **253**, 8328–8333.

65 Mailis, S., Zergioti, I., Koundourakis, G., Ikiades, A., Patentalaki, A., Papakonstantinou, P., Vainos, N., and Fotakis, C. (1999) Etching and printing of diffractive optical microstructures by a femtosecond excimer laser. *Appl. Opt.*, **38** (11), 2301–2308.

66 Mogyorosi, P., Szorenyi, T., Ball, K., Toth, Z., and Hevesi, I. (1989) Pulsed laser ablative deposition of thin metal films. *Appl. Surf. Sci.*, **36**, 157–163.

67 Papakonstantinou, P., Vainos, N., and Fotakis, C. (1999) Microfabrication by uv femtosecond laser ablation of pt, cr and indium oxide thin films. *Appl. Surf. Sci.*, **151**, 159–170.

68 Toth, Z., Kantor, Z., Mogyorosi, P., and Szorenyi, T. (1990) Surface pattering by pulsed laser induced transfer of metals and compounds. *SPIE Proc.*, **1279**, 150–157.

69 Bahnisch, R., Gross, W., and Menscig, A. (2000) Singlr-shot, high repetition rate metallic pattern transfer. *Microelectron. Eng.*, **50**, 541–546.

70 Sano, T., Yamada, H., Nakayama, T., and Miyamoto, I. (2002) Experimental investigation of laser induced forward transfer process of metal thin films. *Appl. Surf. Sci.*, **186**, 221–226.

71 Lee, I., Tolbert, W., Dlott, D., Doxtader, M., Foley, D., Arnold, D., and Ellis, E. (1992) Dynamics of laser ablation transfer imaging investigated by ultrafast microscopy. *J. Imaging Sci. Technol.*, **36** (2), 180–187.

72 Nakata, Y. and Okada, T. (1999) Time-resolved microscope imaging of the laser-induced forward transfer process. *Appl. Phys. A*, **69**, S275–S278.

3

LIFT Using a Dynamic Release Layer

Alexandra Palla Papavlu [1,2] and Thomas Lippert [1,3]

[1] Paul Scherrer Institute, Research with Neutrons and Muons Division, 5232 Villigen, Switzerland
[2] National Institute for Lasers, Plasma and Radiation Physics, Atomistilor 409, 077125 Magurele, Romania
[3] ETH Zürich, Laboratory of Inorganic Chemistry, Department of Chemistry and Applied Biosciences, Vladimir-Prelog-Weg 1-5/10, 8093, Zürich, Switzerland

3.1 Introduction

In the past years, polymer processing aiming at direct patterning and printing has witnessed an exponential growth, in particular in the rapidly growing field of flexible microelectronics, which demands fast and reliable patterning and printing technologies. The ability to develop miniaturized devices based on soft materials such as polymers combined or integrated with microfabricated substrates represents a key factor in one of the most important sectors of the microelectronics industry, with applications ranging from sensors to organic light-emitting diodes (OLEDs). However, there are still major issues concerning polymer patterning and printing and integration into devices due to their easy degradation or loss of their surface functionality, which is key to achieving the desired properties. In order to prevent this drawback, a variety of methods and approaches have been developed for polymer patterning and printing, from simple dispensing or soaking techniques to localized contact and noncontact patterning methods.

Spin coating has been used for several decades for the deposition of thin films. A typical process involves dispensing a small quantity of a fluid (a polymer dissolved in a proper solvent) onto the spinning substrate. Centripetal acceleration will cause most of the fluid to spread (also over the edge of the substrate), leaving a thin polymer film on the surface. The final film thickness and other properties will depend on the nature of the fluid (viscosity, drying rate, percent of the solid in the solution, surface tension, etc.) and the parameters chosen for the spinning process. Spin coating is a technique that offers a high degree of reproducibility [1]. However, it presents some disadvantages, that is, the lack of material efficiency. Typical spin coating processes utilize only 2–5% of the material dispensed onto the substrate [2], while the remaining 95–98% is propelled into the coating bowl and disposed of. Another disadvantage is the size of the substrates, that is, as the substrate size gets larger, the throughput of the spin coating process decreases. Large substrates cannot be spun at a sufficiently high rate in order to allow the film to thin and dry in a timely manner, which results in a decreased throughput.

Laser Printing of Functional Materials: 3D Microfabrication, Electronics and Biomedicine,
First Edition. Edited by Alberto Piqué and Pere Serra.
© 2018 Wiley-VCH Verlag GmbH & Co. KGaA. Published 2018 by Wiley-VCH Verlag GmbH & Co. KGaA.

Another relatively easy process, spray coating, is the process of coating an object with a liquid spray of a polymer or any other fluid. Spray coating technology uses a spray produced by forcing a fluid under high pressure through a small nozzle (spray tip) making aerosols. The fluid emerges as a narrow sheet at a high speed. The friction between the fluid and the air disrupts the sheet, breaking it into fragments initially and ultimately into droplets. One of the advantages of this technique is that it allows a high production rate.

The main disadvantages of this technique are the limited control over the amount of fluid flow and that airless spray coating technologies are generally not considered to be capable of providing a very high finish quality [3]. In addition, another limitation of this process and also of the spin coating technique is that they do not offer lateral resolution and only complete layers can be obtained.

Inkjet printing is a noncontact patterning method, which provides a versatile and low-cost microfabrication capability. This noncontact digital technology can be used to pattern a variety of liquids including polymers, proteins, and various solvents onto different substrates, rigid or flexible, rough or smooth. The advantages of this technique are the high accuracy and resolution and that it does not require a master template [4]. However, among the most important limitations of inkjet printing, we enumerate clogging of the print heads and the reduced velocity.

Due to the fact that the aforementioned approaches do not meet all requirements, that is, precise positioning, repeatability, control of polymer layer thickness and roughness, novel techniques, which overcome these limitations, are developed. These techniques are mainly based on lasers.

Shortly after the discovery of lasers, researchers began irradiating every possible target material and phase. Three years after the discovery of laser, Breech and Cross [5] studied the laser vaporization and excitation of atoms from solid surfaces, while in 1965, Smith and Turner [6] deposited the first thin films using a ruby laser. Starting with that moment, laser ablation became more and more popular for the deposition of various materials as thin films.

Pulsed laser deposition (PLD) involves the interaction of a laser beam with a target material (solid or liquid) resulting in a plasma plume that transports the ablated species to a substrate, where a thin film is formed. PLD offers many advantages [7, 8]; however, it cannot be used for all types of polymers, biopolymers, and proteins, because the high laser fluences can result in photochemical or thermal decomposition. Even at relatively low fluences, some polymers are very photosensitive. To reduce the photochemical decomposition from the direct interaction of the UV laser light with organic and polymeric materials, a more gentle approach has to be used.

As an alternative to conventional deposition techniques, matrix-assisted pulsed laser evaporation (MAPLE) has proved to be an attractive method for the deposition of organic thin films [7, 9]. MAPLE is similar to PLD, but has a different target preparation procedure. In MAPLE, a material, for example, a polymer or a biomolecule, is dissolved in a solvent in concentrations of 0.1–5%, and the mixture is frozen, resulting in a solid target. Ideally, only the solvent will absorb the laser radiation. When the laser light irradiates the target, the solvent

is evaporated and the dissolved material (the organic material or the polymer) is collected on a substrate, in the same way as for PLD.

The laser methods described earlier are well suited for obtaining thin films of controlled thickness and roughness on different types of substrates. However, for precise patterning, that is, positioning soft materials onto different substrates with lateral resolution, different approaches must be considered.

One of these approaches (also based on an ablation process) is laser-induced forward transfer (LIFT, see Chapter 1 for a detailed description of this and other direct-write techniques). Briefly, in LIFT, the laser irradiates the material of interest (which is in thin-film form) through its transparent support, pushing the material toward the receiving substrate (placed parallelly and in close proximity). Only the material that is irradiated will be transferred, the laser spot defining the lateral shape of the deposition. The technique first appeared as a new deposition method for the direct writing of different dried inks to a glass substrate for the graphic industry [10–12]. At that point, it was called laser writing (LW) or material laser recording (MLR). However, the first report on LIFT was the "direct writing" of copper metal patterns onto fused-silica plates using a 193 nm ArF excimer laser [13, 14]. Based on this work, in the following years, several alternatives to LIFT were developed. These alternatives include reducing the transferred material pattern size [15] but also the transfer of complex materials, that is, soft, sensitive materials, which may be easily damaged by the laser pulses and result in the loss of functionality, for example, in the case of proteins.

Therefore, in order to reduce the risk of damaging the layer or the surface of the layer to be transferred and to improve the process efficiency, the donor substrate can be precoated with an intermediate layer, which is called dynamic release layer (DRL) [16] or sacrificial layer. To this day, many alternatives to the DRL–LIFT were developed, each with a different name; however, all are based on the same principle, that is, a locally confined laser energy to transfer the material of interest. The addition of an intermediate layer was initially used as a thermally activated DRL and then as a matrix in a process known as *matrix-assisted pulsed laser evaporation-direct write* (MAPLE-DW), a version of MAPLE for high-resolution patterning (see Chapters 1 and 2) [17]. In the MAPLE-DW technique, the material to transfer is embedded into a matrix, for example, a sacrificial polymer layer, usually a Matrigel or a gelatin layer. During MAPLE-DW, the matrix is evaporated due to the heat caused by the absorbed laser beam, which subsequently releases the material to transfer onto a receiving substrate.

Further on, researchers have used metallic layers (Ti, Au, Pt, Cr,) [18–22] as DRLs, which are especially useful for the transfer of biomolecules as they are biocompatible and easy to process. For example, in [23, 24], the authors use thin (50–100 nm) metal films to transfer different types of cells in a medium. They name the method absorbing film assisted-LIFT (AFA-LIFT) (see Chapter 4 for a detailed description). The principle of this process relies on using laser beams with a penetration depth smaller than the thickness of the sacrificial metallic layer. Upon laser irradiation, the metallic sacrificial layer thermally expands, and a volume of the suspension (in this case, the donor is a biological ink) is propelled to a receiver substrate [25]. Although successful for bio-applications, the main disadvantage of the metallic DRLs is related to contamination of the

transferred material as a result of the ablation process, that is, hot volatilized products. This can be detrimental in applications aiming at the fabrication of organic micro devices, as micro- and nanosized particles resulting from the laser ablation process may hinder the performance of the devices. In order to mitigate this effect, more recently, the use of thin and thick polymer layers as DRLs has been proposed. In [26, 27], the authors propose the use of thick (several micrometers) polyimide absorbing layers to transfer various materials in liquid phase (e.g., embryonic stem cells, 9-anthracenemethanol, and tris8-hydroxyquinolinealuminum Alq_3 organic luminophores). The authors name this process blister-actuated laser-induced forward transfer (BA-LIFT, see Chapter 5). The transfer mechanism in BA-LIFT relies on the absorption of the laser within a thin part of the polyimide DRL, near the donor–substrate interface, and the formation of a rapidly expanding blister of high-pressure decomposition products. Below a critical laser energy, the blister deforms plastically; however, it remains sealed, and the material to transfer continues to move toward the receiving substrate enabling a "clean" transfer, without contamination from the ablation products.

Another approach consists in the use of a photodecomposing polymer, that is, a triazene polymer (TP), which can minimize contamination and, in addition, can be applied to transfer both solid- and liquid-phase materials, unlike BA-LIFT, which is mostly used for transfer of liquid-phase materials. The TP in the laser molecular implantation (LMI) process [28] was eventually followed by the use of triazene as a propellant in the hollowing and transfer of polymethyl methacrylate [29]. This led to the use of the TP as a DRL in the printing of other sensitive materials (see Section 3.4).

This chapter reviews the LIFT process assisted by a UV degradable photopolymer as DRL (i.e., TP), from fundamentals to the application of the process for the transfer of a wide range of materials. In addition, a detailed analysis of the characteristics and process parameters of the TP-assisted LIFT process are reviewed, with emphasis on the possible applications of TP-LIFT in sensors or OLEDs.

3.2 Absorbing Release Layer – Triazene Polymer

Polymers that incorporate the triazene unit into the backbone were developed in the early 1990s, specifically for laser ablation [30]. The TPs contain aryl-triazene chromophores where a conjugated π system spreads over the three nitrogens and the benzene ring [31]. The chemical structure of the TPs is shown in Figure 3.1.

These polymers were initially studied for applications as resist for high-resolution microlithography [32]. However, regardless their large number of advantages, for example, formation of high-quality films, stability to storage, and one-step synthesis [26], these polymers are very sensitive to acids [33], which are used in industrial applications for the following lithography processing steps. Therefore, further alterations were considered in order to improve the quality of the ablation process and broaden their usage in applications such as micro-optics and laser-plasma thrusters for microsatellites [34].

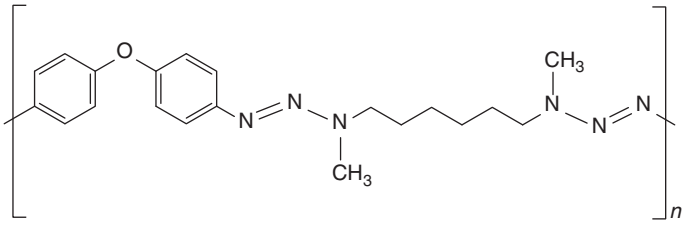

Figure 3.1 Chemical structure of the triazene polymer, which was used for most LIFT experiments.

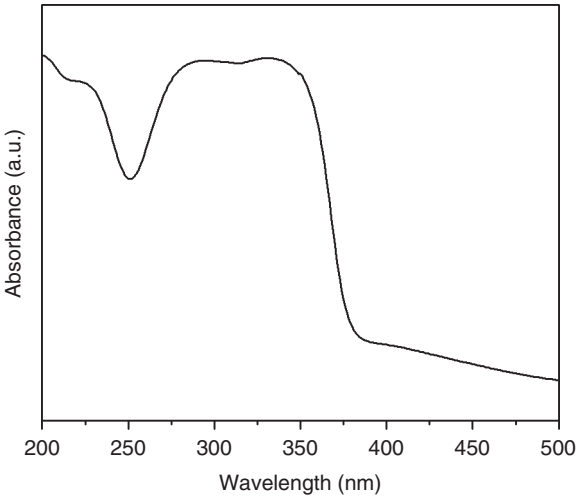

Figure 3.2 UV–vis absorption spectrum of a typical triazene polymer thin film, spin coated from chlorobenzene:cyclohexanone (1 : 1) solution.

A unique advantage of these polymers is the possibility to adjust the absorption maximum from 290 to 360 nm, making them appealing for irradiation with different wavelengths and different lasers. In the UV–vis absorption spectrum of a typical TP thin film (Figure 3.2), two distinct absorption maxima can be distinguished, one around 200 nm, which can be assigned to the aromatic system, and one around 330 nm, which corresponds to the triazene unit [35].

These two well-separated absorption regions led to numerous studies focused on the influence of different laser wavelengths on the ablation behavior. Higher ablation rates have been determined for irradiation wavelengths that excite the triazene system (266, 308, and 355 nm) compared to the ablation rates for shorter wavelengths (248 and 193 nm) [36]. In addition, a clear and well-defined ablation threshold fluence of 25 mJ/cm^2 ($\pm$5 mJ/cm^2) was observed for TP at an irradiation wavelength of 308 nm, while for irradiation with 248 nm, a much broader range of 16–28 mJ/cm^2 has been measured. For irradiation at 248 nm, carbonization of the polymer was detected upon irradiation, whereas the surface of the polymer remained unchanged after several laser pulses for irradiation with 308 nm [37].

In the following section, an overview of front- and backside ablation of the TP is presented. Although there is a multitude of laser wavelengths for which the ablation behavior has been studied, here we will only review TP ablation with the

XeCl laser operating at 308 nm. This is due to the fact that most of the studies in the literature focused on the transfer of functional materials (in solid and liquid phase) by LIFT were carried out with the XeCl laser, and the TP has the highest ablation rate and low threshold fluence at this wavelength (308 nm).

3.3 Front- and Backside Ablation of the Triazene Polymer

Front- and backside ablation behavior of the TP (Figure 3.3) has been studied in [38], by applying a time-resolved imaging technique (shadowgraphy) in order to gain information on the dynamic mechanism of the TP-assisted LIFT process. The experimental setup for such investigations consists in adding a camera with a microscopic objective perpendicular to the laser beam, that is, parallel to the sample surface, with the focus at the ablation spot. Illumination was obtained either by a probe laser pumping a fluorescent dye (rhodamine) or by a white-light nanosecond flash lamp placed on the camera axis on the opposite sample side. The delay between the pump and the probe laser pulses/flashlamp was set by a delay generator. Each picture was recorded with a different pulse and corresponds to a new position on the sample.

A sequence of photos taken for front-side ablation of a 500 nm thick TP layer for an irradiation fluence of 110 Jm/cm^2 is presented in Figure 3.4a. In comparison, a sequence of photos taken for backside ablation of a 460 nm thick TP film and for the same laser fluence (i.e., 110 mJ/cm^2) is shown in Figure 3.4b. In the case of front-side ablation, the film surface is on the right, while the laser pulse comes from the left, and in the case of backside ablation, the film surface is on the left, and the laser also comes from the left. In both figures, two propagating features can clearly be distinguished. The first feature is attributed to the shock wave caused by the pressure and temperature jump at the ablation spot, where a large amount of gas is released during the laser pulse. The second observable feature is different for the two cases of ablation: (i) in the case of front-side ablation, it is most probably formed by gaseous decomposition products from the polymer and (ii) in the case of backside ablation, the product front corresponds to an opaque object ejected from the substrate, that is, a flyer. In the case of front-side ablation, no particles are visible in the ablation plume, which confirms a clean and debris-free ablation of the triazene observed previously [39, 40]. In contrast, in the case of backside ablation, the presence of the flyer indicates that

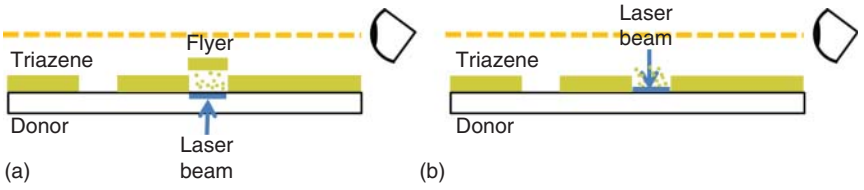

Figure 3.3 Schematic drawing of (a) backside ablation of a triazene polymer layer and (b) front-side ablation of a triazene polymer layer.

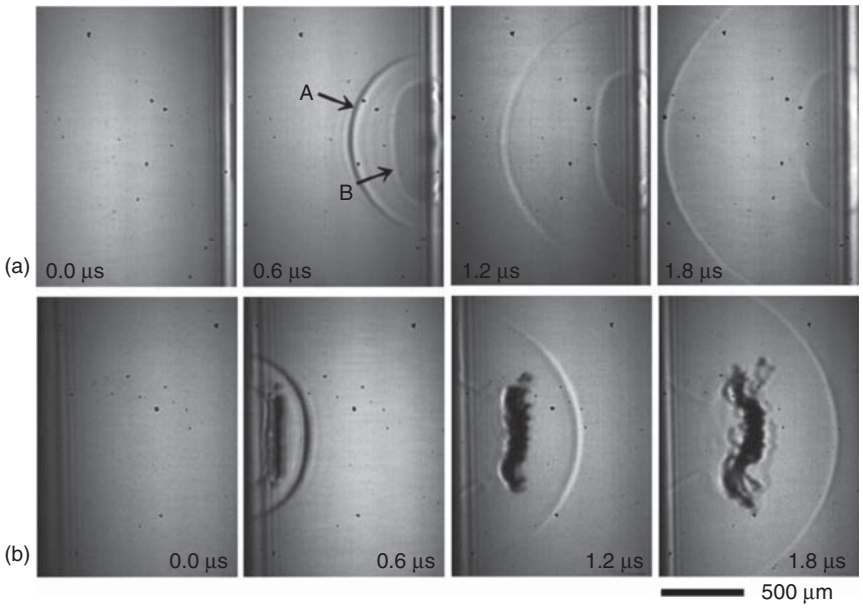

Figure 3.4 Sequence of photos taken for (a) front-side ablation of a 500 nm triazene polymer film at 110 mJ/cm^2 laser fluence; (b) backside ablation of a 460 nm triazene polymer film at 110 mJ/cm^2 laser fluence. (Fardel *et al*. 2009 [38]. Reproduced with permission of Elsevier.)

the entire triazene layer is not ablated by a single laser pulse at this fluence. The flyer consists of undecomposed polymer, which is ejected by the pressure thrust created during ablation and decomposition of the underlying part. In addition, the application of shadowgraphy for the study of the dynamics of TP-LIFT provided additional information, that is, on the flyer velocity, which when combined with the laser pulse length and the thermal effects gave insight into the energy generated by this process [41, 42]. Further work focused on a thermal analytical model has contributed to understanding the TP-LIFT process (at 308 nm) fundamentals [43]. The thermal model has been used to evaluate how fast the thermal energy is lost into the quartz substrates, and in the case of backside ablation, it is found that almost 50% is lost during the pulse length. In addition, in [44], the authors calculate the total energy transferred from the laser beam to the ablation species from the velocity of the shock wave. They found that a fraction of the laser energy was converted into mechanical energy (20–60%), while the remaining energy consumption occurred as thermal heat and mechanical loss into the substrate. In addition, the shock wave generated upon backside ablation was two times weaker than in the case of front-side ablation [44].

3.4 Examples of Materials Transferred by TP-LIFT

Aryltriazene polymers as sacrificial polymer release layers protect the transfer layer from the incident UV irradiation or generated heat, thus allowing highly

sensitive materials to be gently transferred and deposited. In addition, small and volatile organic fragments are formed by the laser-triggered photopolymer decomposition, and therefore, only a minimum of contamination of the transferred deposits may be expected. This is a substantial advantage compared to metal absorbing layers, which are known to be codeposited with the transferred material after laser-induced volatilization during the LIFT process [45, 46].

The use of aryltriazene photopolymers as sacrificial layers in LIFT applications was demonstrated with various highly sensitive materials in solid phase, including metals (i.e., Al) and oxides (such as $Ca_3Co_4O_9$), but also "soft" materials (some in liquid phase), that is, liposomes or cells. A list of the most representative materials is compiled in Table 3.1.

In [29], the first transfer of a polymethyl methacrylate polymer layer (as thin solid films) is reported, which opened up new possibilities for sensor fabrication where chemically selective polymers should be precisely deposited onto microsensor structures. In addition to the resolution requirement, the deposited polymer patterns should maintain their surface intact, that is, not alter their surface chemistry. Homogeneous, well-defined, and hole-free polyethyleneimine (PEI), polyepichlorohydrin (PECH), and polyisobutylene (PIB) pixels with low surface roughness were deposited from donors with triazene photopolymer

Table 3.1 Materials deposited through TP-LIFT.

Material	Laser and pulse length	Substrate	References
Mammalian cells	ArF (193 nm), ns	Glass	[47]
Quantum dots	ArF (193 nm), ns	Glass wafers coated with ITO	[48]
Liposomes	ArF (193 nm), ns	Glass	[49]
$Gd_3Ga_5O_{12}$	Ti:sapphire (800 nm), fs	Si wafer	[50]
Al	XeCl (308 nm), ns	Glass	[39, 51]
Polyisobutylene, polyethylenimine, polyepichlorohydrin	XeCl (308 nm), ns Nd:YAG (355 nm), ns	Glass, Al interdigitated transducers	[52–56]
Ag paste	Nd:YAG (355 nm), ps	Glass	[57]
Polystyrene microbeads	XeCl (308 nm), ns	Thermanox coverslips	[58, 59]
Single-walled carbon nanotubes	XeCl (308 nm), ns	Pt interdigitated transducers	[60]
Semiconducting oligomer	KrF (248 nm), ns Nd:YAG (355 nm), ps	Si/SiO_2	[61]
$Ca_3Co_4O_9$	XeCl (308 nm), ns	PDMS	[62]
Gelatine dyed with eosin	XeCl (308 nm), ns	Glass	[39]
OLED (Al/MEH-PPV)	XeCl (308 nm), ns	ITO-covered glass	[63, 64]
Polymer light-emitting diodes (Al/PFN)	XeCl (308 nm), ns	Glass/ITO/PEDOT:PSS/PVK	[65]
Methylcellulose	XeCl (308 nm), ns	Glass	[39]
$SnCl_2(acac)_2 \rightarrow SnO_2$	XeCl (308 nm), ns	Pt electrodes	[66, 67]

layers with thicknesses in the range of 60–300 nm after process optimization [52, 53]. LIFT of PEI, PIB, and PECH pixels onto surface acoustic-wave (SAW) structures allowed measurement of different chemical analytes [54, 55].

In addition, with TP-LIFT, it was possible to fabricate microarrays of polystyrene microbeads (PS-μbeads) on Thermanox coverslip surfaces without any specific immobilization process. For this, a XeCl excimer laser (with a top hat beam profile) was shaped using a $2 \times 2\,mm^2$ rectangular aperture and demagnified four times to ablate square PS-pixels of $500 \times 500\,\mu m^2$. TP layers of 100 nm were used as DRL to propel close-packed monolayers of PS-μbeads, very adherent to the Thermanox substrates and which do not suffer any chemical decomposition during transfer [58, 59]. A sequence of pictures taken for backside ablation of a PS-microbeads pixel on top of a 100 nm thick TP layer together with the corresponding SEM images of the pixel and its surface morphology are shown in Figure 3.5. The fact that these arrays can be produced cost-effective and time-effective with a minimum sample volume required suggests that TP-LIFT is a promising technique for transferring PS-bead pixels, which can therefore be applied in biochip applications.

The use of the TP as DRL also enables the accurate LIFT deposition of metal films. Aluminum film pixels ($500\,\mu m \times 500\,\mu m$, 80 nm thin) transferred from a quartz substrate coated with a 350 nm thick triazene layer showed clear-cut edges and a homogeneous layer morphology without traces of splashing or debris outside the pixel area for laser fluences in the range of 490–570 mJ/cm^2 [39]. It has been found that the mechanical as well as the thermophysical material properties of the transfer layer and carrier substrate have significant effects on the transfer results. In addition, the transfer dynamics of Al layers has been investigated by nanosecond time-resolved imaging techniques [51, 68]. The shadowgraphy data show that the Al flyer is completely destroyed by the shock wave when high laser fluences are applied, while in the case of low laser fluences (after 2 μs), only slight bending at the edges of the flyer may be observed [51, 68].

In [47], the transfer of viable neuroblast cells using a 193 nm ArF laser was reported. LIFT was carried out with 90, 110, and 140 nm thick sacrificial TP as DRL, and ribbons of B35 neuroblast cells were transferred from a donor to a receiver substrate over a gap of 150 μm above the threshold fluence for cell transfer of 50 mJ/cm^2. The biocompatibility of the TP was assessed with different cell lines, for example, osteoblasts, myoblasts, and endothelial cells, and the results indicated very good adhesion. In addition, 48 h post transfer, the cells showed intact preservation of nuclei with well-developed axonal extensions, demonstrating that the technique is applicable in creating patterns of viable cells at low fluences.

Further on, in [49], the authors report the transfer of a biomembrane model system, that is, liposomes in solution (liquid-phase TP-LIFT) in regular patterns onto glass substrates (detailed information is presented in Chapter 14). After a careful optimization of the laser transfer parameters, for example, influence of target–substrate distance, thickness of the applied TP layer, and laser fluence on the pattern sizes and shape, clearly circular, well-defined patterns can be obtained for relatively low laser fluences in the range of 40–60 mJ/cm^2. The fact that these biomembrane patterns can be obtained in a time-effective manner

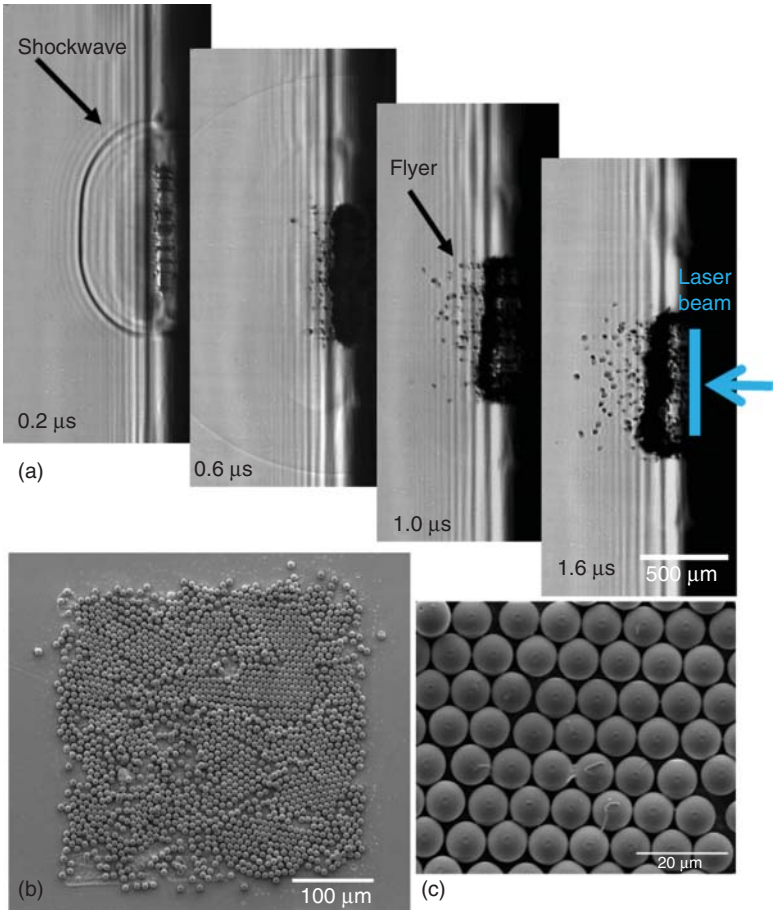

Figure 3.5 (a) Sequence of pictures taken for backside ablation of a PS-microbead pixel on top of a 100 nm thick triazene polymer layer at 1.5 J/cm^2 laser fluence. (b) SEM image of a PS-microbead pixel transferred at 2.25 J/cm^2 laser fluence. (c) SEM image of the surface morphology of the PS-microbeads transferred at 1.5 J/cm^2 laser fluence. (Palla-Papavlu *et al*. 2010 [58]. Reproduced with permission of AIP.)

and with a minimum sample volume suggests that they can be ultimately applied in biosensors or drug delivery systems.

Another interesting application of TP-LIFT is the successful transfer of semiconducting multispectral nanocrystal quantum dots (NCQDs) into laterally patterned arrays [48]. A 40 nm thick TP layer was used for the transfer of CdSe nanoquantum dots (5 and 6 nm in diameter) onto ITO-coated substrates. A 6 × 6 red and yellow array with pixel sizes of 800 µm was demonstrated. Photoluminescence of the NCQDs before and after transfer was found to be nearly unchanged, indicating the conservation of material functionality during the transfer.

Finally, to prove the validity of the photopolymer-based LIFT approach, working miniaturized model OLED devices have been fabricated for the first time

using LIFT [63]. Detailed information of the fabrication of OLEDs by TP-LIFT is given in Section 3.5.1 and also in Chapter 12.

3.5 First Demonstration of Devices: OLEDs and Sensors

In the previous sections of this chapter, some of the advantages and limitations preventing the adoption of TP-LIFT in printing different materials have been presented. Although TP-LIFT has been extensively used to transfer a wide range of materials, for material integration into functional devices, a trade-off between the various experimental parameters and limitations of the technique must be taken into account. If for the fabrication of OLEDs, complete functional layers must be transferred, the transfer can take place with the metal electrode sandwiched between the TP-DRL and the electroluminescent polymer, thus additionally protecting the electroluminescent polymer; in the case of polymers for sensor applications, the process is even more "delicate." When transferring polymers for sensing applications, the surface of the polymer that is in contact with the TP as DRL is actually the sensing surface, and no damage, contamination, or functionalization of the surface should take place during or post transfer. Here, we will only briefly present the main results of TP-LIFT for the fabrication of functional OLEDs and sensors (for both examples, the transfer is carried out from solid donor layers). Please refer to Chapters 12 and 13 for detailed description of LIFT for microdevice fabrication (Chapter 12), that is, OLEDs, thin-film transistors, and sensors and biosensors (Chapter 13).

3.5.1 Organic Light Emitting Diode (OLEDs)

The first work on the transfer of OLED devices was undertaken in 2007 [63]. This was one of the biggest breakthroughs in the field of LIFT, not just for OLEDs. Good functionality and pixel morphology were observed, as shown in Figure 3.6.

The devices reported in [63] were realized in the simplest architecture, that is, an electroluminescent material sandwiched between an anode and a cathode. The anode was a transparent tin-doped indium oxide (ITO), which was used as receiving substrate onto which an aluminum/MEH-PPV (poly[2-methoxy-5-(2-ethylhexyloxy)-1,4-phenylenevinylene]) bilayer was LIFTed. The bilayer, that is, the cathode and the electroluminescent materials Al/MEH-PPV with thickness of 80 nm Al and 90 nm MEH-PPV were deposited onto a 100 nm thick TP layer. The laser fluence applied for the successful transfer was of 250 mJ/cm^2 (308 nm XeCl laser). Bilayer transfers were carried out with the donor and receiver substrates in as close contact as possible. Small cracks in the devices were a minor problem, but a larger problem was the reproducibility. On a single sample, about eight pixels could be deposited on the two ITO edges. Even at the same fluence, huge variations in pixel morphology could be observed on a single substrate, and from sample to sample, the variation was even larger. However, the characterization of the transferred pixels by luminance and emission spectroscopy revealed the same characteristics as those of a similar device made by well-established techniques.

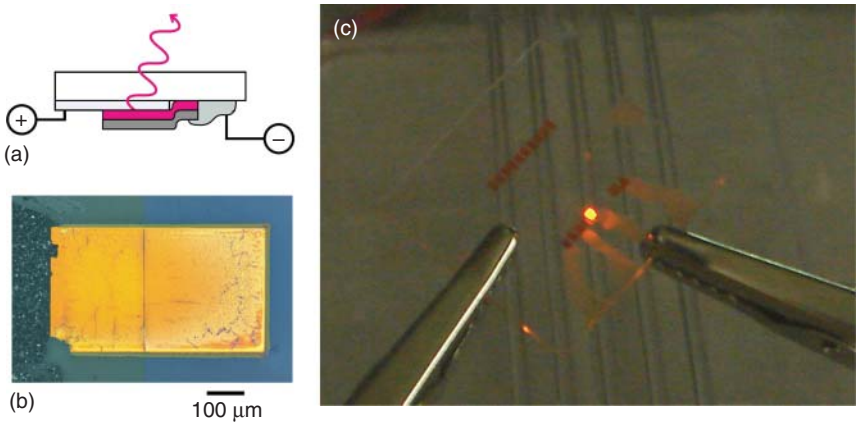

Figure 3.6 (a) Scheme of the device architecture with two electrodes (ITO anode and Al cathode) and the MEH-PPV light-emitting layer. (b) Al/MEH-PPV transferred onto the ITO substrate. (c) Image of the successful operation of one of the transferred devices. (Fardel *et al*. 2007 [63]. Reproduced with permission of AIP.)

The fact that sensitive materials such as MEH-PPV could be transferred without altering the functional properties proves that the LIFT technique with a TP as sacrificial layer is very well suited to the transfer of sensitive materials.

Later works [64, 65] have shown that by optimizing the laser transfer process, optimized devices could be fabricated.

In [64], the functionality of the OLEDs has been improved by modifying charge injection in the devices. This has been realized by adjusting both the cathode and anode by adding additional layers, that is, electron-injecting and hole-transporting layers. The scheme of the TP-LIFT for the fabrication of OLED pixels/devices is shown in Figure 3.7a. In addition, in [64], it has been shown that by adding a thin film of poly(3,4-ethylenedioxythiophene) polystyrene sulfonate (PEDOT:PSS) onto the ITO receiver substrate, it was possible to achieve a "softer" transfer, that is, to reduce the laser fluence required for the transfer, that is, from 250 to 80 mJ/cm^2. The authors suggest that this effect is due to the stronger attractive force interactions between the flyer and the PEDOT:PSS layer. The transferred pixels exhibited far superior and more reliable device characteristics compared to the devices LIFTed onto plain ITO. Finally, the LIFTed pixels were compared with the conventionally fabricated devices. The overall performance of the LIFTed poly(ethylene)oxide (PEO)-containing pixels was slightly lower than for conventional devices, possibly because of oxygen and water damage by combining the substrates together in air, but the plain MEH-PPV device showed elevated performance, presumably mainly due to the different light-emitting polymers (LEP)/Al interface [69]. An example of two working devices fabricated by LIFT that showed the distinctive orange-red electroluminescence is presented in Figure 3.7b.

In addition, further optimization and refinement of the LIFT process itself, that is, controlling the gap between the donor and the receiver, the usage of the TP layers thicker than 150 nm, together with carrying out all laser transfer in

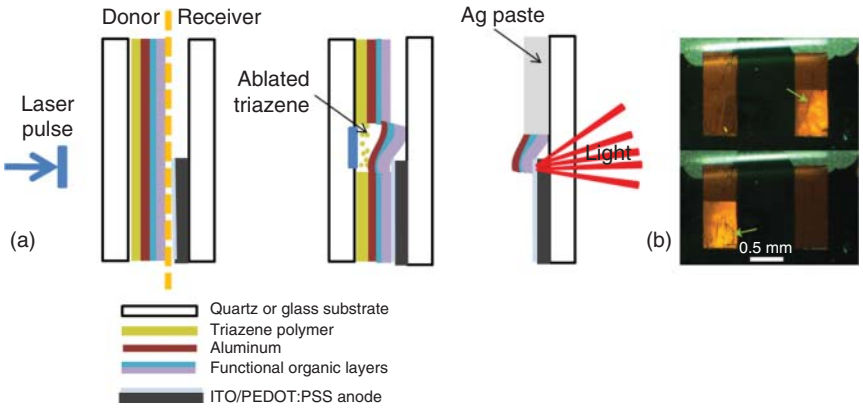

Figure 3.7 (a) Scheme of the TP-LIFT for fabricating an OLED pixel/device. (b) Electroluminescence from two LIFTed devices with the architecture ITO/PEDOT:PSS/MEH-PPV:PEO/Al. The light-emitting section of the diodes is the lower half, where the aluminum cathode overlaps with the ITO anode. (Shaw-Stewart *et al*. 2011 [64]. Reproduced with permission of ACS Publications.)

a controlled atmosphere (vacuum), led to the successful fabrication of three-color OLEDs (see Chapter 14).

Further works have focused on varying the processing parameters together with the characteristics of LIFT for improving the OLED device performances. One of the main issues related to LIFT assisted by a TP layer is of solvent orthogonality of the different polymers in adjacent layers. In order to solve this issue, a strict orthogonality in the solubility of different materials or subsequent selective cross-linking of previously solution-deposited layers is required. Therefore, for the fabrication of OLEDs by sequential LIFT, poly[(9,9-bis(3′-(*N*,*N*-dimethylamino)propyl)-2,7-fluorene)-alt-2,7-(9,9-diocty-fluorene)] (PFN) was chosen, which could be dissolved in methanol:DMF (dimethylformamide) (99 : 1) solution and directly spin coated on top of the TP layer (insoluble in that solution). However, the sequential LIFT of PFN and Al single layers to fabricate a functioning PFN PLED was very positive, but the device characteristics were much poorer than the PFN conventional device and the normal bilayer LIFTed PFN pixel, with a much higher operating voltage and poorer efficiency. A positive fact was that the electroluminescence spectrum was completely unchanged, suggesting that the chemical structure was unaltered. In addition, the adsorption of a layer of *tert*-butyl acrylate (TBA) onto the aluminum cathodes led to a significant improvement in device performances. The TBA layer was used with the purpose of promoting electron injection from the aluminum cathode, thus increasing the device efficiency [64].

3.5.2 Sensors

Another breakthrough in the field of TP-LIFT is the successful demonstration of chemical sensors for the detection of volatile organic compounds (VOCs) and warfare agents. For detailed information on sensor fabrication by LIFT,

please refer to Chapter 13. Several polymers have been checked from the point of view of their properties in the form of thin films: PIB, PEI, and polyepichlorohydrin (PECH). PEI with the molecular formula $(C_6H_{21}N_5)_n$, PECH $[CH(CH_2Cl)CH_2O]_n$, and PIB $[CH_2(CH_3)_2]_n$ are used for the detection of the nerve agent sarin (GB), simulants such as dimethyl methyl phosphonate (DMMP), and also hydrocarbons (acetone) and esters (i.e., ethyl acetate). The ability of the polymers to form weak hydrogen bonds with the target analyte molecules is the most basic functionality prescribing the polymers' utility in the design of a useful chemical warfare agent detector.

The most common and studied type of chemical detectors are the SAW sensors due to their remarkable performances in terms of high sensitivity, portability, low cost, and easy deployment [70, 71, 80]. These devices are based on a SAW resonator, solidly mounted resonator (SMR), or a delay line, where the propagation path is coated with a chemically interactive membrane, that is, a polymer designed to detect a specific analyte. The main issue related to the development of performant SAW resonators for the detection of toxic and chemical species is the poor reliability caused by the lack of accuracy in placing the polymer membranes onto the SAW devices. The sensitivity of the SAW resonators is dependent on the amount of vapor adsorbed by the surface of the polymer overlayer and also by the SAW's inherent ability to respond to the physical changes in the overlaying film. Therefore, it is very important to precisely place the polymer coating and moreover for the coating to have the correct thickness and roughness and desired functionality on the surface.

PIB, PEI, and PECH were deposited by laser-based methods as chemical interactive membranes onto the SAW sensor structures. Preliminary work on the DRL-LIFT of different chemoselective polymers, that is, PEI, PIB, and PECH, has shown that a careful optimization of different transfer parameters, that is, the laser fluence, donor film morphology, single- and multiple-pixel deposition, is critical for the successful microfabrication of the chemical sensors based on SAW devices [52, 53]. Additional studies have shown that a separation distance between the donor and the receiver substrates results in damage of the transferred material [69]. All transfer experiments were therefore carried out in close contact between the donor and the receiver. The studies reported in [52, 53] have shown that in order to minimize scattering and diffraction of the SAW devices, it is important to (i) improve the polymer pixel morphology by using TP as a DRL compared to the LIFT process without a DRL; (ii) use the 308 nm wavelength (it yields better results, i.e., clean-cut pixels) instead of 266 nm irradiation; (iii) use polymer films with thicknesses below 60 nm. Optical microscopy images of PIB, PECH, and PEI polymers transferred by LIFT onto different types of SAW devices are shown in Figure 3.8a,b.

In addition to sensor fabrication by TP-LIFT, a sealed chamber containing electronic oscillators, one for each sensor, was designed and fabricated. In order to obtain an optimized and complete measuring system, resonators without any coating were provided as reference. The TP-LIFT-coated SAW and SMR sensors were tested to evaluate the performances with respect to sensitivity, resolution, and response time. The first measurements were carried out onto single SAW and SMR sensors by using the Network Analyzer in order to track the frequency

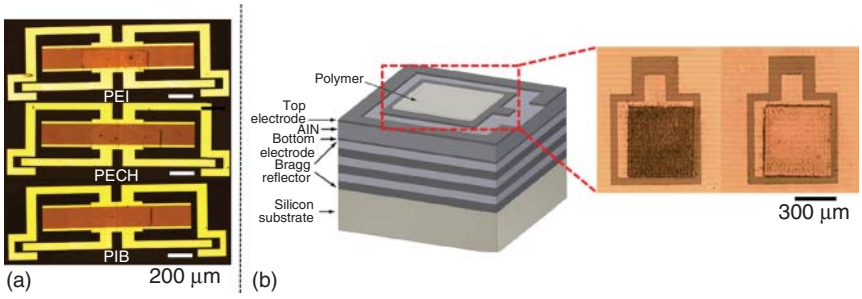

Figure 3.8 (a) Optical microscopy images of PIB (bottom), PECH (middle), and PEI (top) polymers transferred by LIFT onto two-port SAW devices. Dinca *et al*. 2013 [72]. Reproduced with permission from Romanian Reports in Physics.) (b) Schematic drawing of the SMR (left side) and optical microscopy images of SMR devices coated with PEI polymer deposited at 400 mJ/cm^2 (left) and 300 mJ/cm^2 (right) laser fluence. (Cannata *et al*. 2012 [55]. Reproduced with permission of Elsevier.)

shifts of the resonance peak due to various concentrations of different analytes. The devices under test were placed in a sealed chamber where the total gas flow was kept constant and the analyte concentrations were in the range of parts per million. The responses of the PEI, PIB, and PECH coated devices to different concentrations of DMMP, GB, ethyl acetate, and acetone were evaluated. The tests carried out with the SAW resonators [54] showed good performances of the SAW sensor fabricated by TP-LIFT, in particular for DMMP and GB. The obtained sensitivities for DMMP are similar to the results reported in the literature where the same polymers were used, however, deposited on the surface of the sensors with more mature and well-established techniques (airbrush, spray coating, screen printing) [73, 74], proving thus that the TP-LIFT process does not strongly alter the surface chemistry of the polymers. In addition, a remarkable result is the sensitivity obtained for sarin (~650 Hz/ppm) that is one order of magnitude higher than those obtained using DMMP (~66 Hz/ppm). The lowest concentration of measured GB was lower than the median lethal dose (18 ppm). The time responses of the three sensors for two concentrations of ethyl acetate (EtOAc) together with the response curve for PECH, PEI, and PIB sensors upon exposure to different concentrations of DMMP are shown in Figure 3.9a,b.

Furthermore, when exposing the SMR devices to different concentrations of DMMP [54], that is, between 22 and 127 ppm, fast and reversible responses are obtained, with the highest sensitivity obtained for PEI and followed by PIB and PECH. The frequency response of an SMR before and after deposition of 13 nm thick PECH film and the response curves of coated SMR sensors (PEI, PIB, and PECH polymers) for DMMP are presented in Figure 3.9c,d.

The SMR has several advantages, that is, the simple and well-known planar fabrication technologies and the small size of resonator. Moreover, the use of Bragg reflector ensures a robust design allowing simple and straightforward polymer depositions by LIFT. Finally, considering the flexibility and the micron-scale lateral resolution obtainable by LIFT and the possibility to integrate a large number

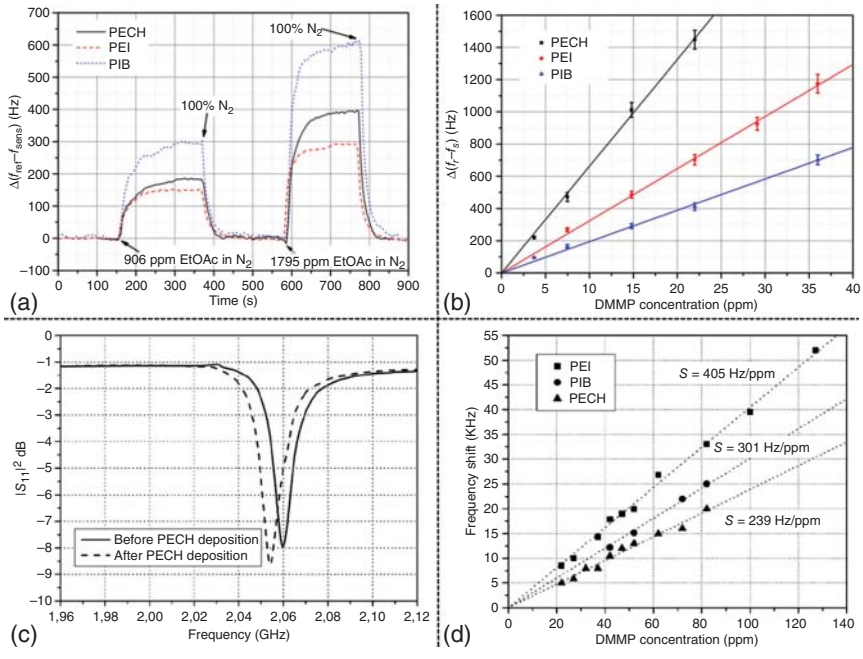

Figure 3.9 (a) Time response of the three SAW sensors for two concentrations of EtOAc. (b) Response curve for PECH, PEI, and PIB sensors upon exposure to different concentrations of DMMP. (Di Pietrantonio *et al*. 2012 [54]. Reproduced with permission of Elsevier.) (c) Frequency response of an SMR before and after deposition of 13 nm thick PECH film. (d) Response curves of coated SMR sensors (PEI, PIB, and PECH polymers) for DMMP. (Cannata *et al*. 2012 [55]. Reproduced with permission of Elsevier.)

of SMRs on a single silicon chip, the proposed solution is an excellent candidate for implementation of sensor arrays using different sensitive polymers.

3.6 Variation of the DRL Approach: Reactive LIFT

In recent years, sensor development and improvement received great attention from industry and research. A direct-writing technique such as LIFT is a promising method for commercial sensor coating. It is solvent free, and a large variety of materials can be transferred with high lateral resolution onto nearly every substrate. It would be a promising alternative to replace, for example, photolithographic steps or inkjet printing. One other advantage is that large-area donor substrate can be prepared by different well-established methods such as spin coating, sputtering, evaporation, or drop casting [75, 76].

A new approach, that is, reactive LIFT (rLIFT), has been evaluated as an alternative method to LIFT, which allows the integration of metal-oxide semiconductor materials, that is, SnO_2 for their use in microsensors. In rLIFT, the donors are UV-absorbing metal complex precursors (i.e., metal acetylacetonates), which upon absorption of the laser light partially decompose to SnO_2 [77], thus making the transfer layer a DRL. Solution-based precursors are in particular appealing

due to their low deposition (growing) temperatures, which make them suitable for flexible substrates, and good potential for scaling-up. During the past decade, a large number of metal oxides have been prepared from metal acetylacetonates, for example, TiO_2, In_2O_3, SnO_2 [78] and more recently ZnO nanowires [79]. rLIFT is a unique technique that combines the advantages of the low decomposition temperatures of the acetylacetonates together with the spatial resolution of the laser-based method. The transformation of the metal precursor to SnO_2 takes place partially during laser transfer as a result of the photochemical and thermal processes, which in this particular case are an advantage as they shorten the fabrication process. Therefore, rLIFT has proven great potential for the integration of active materials into micro-sensing devices.

In recent works [67], the rLIFT technique was demonstrated for the fabrication of SnO_{2-} and Pd:SnO_2-based gas sensors. The donors were UV-absorbing metal acetylacetonates spin coated onto fused-silica substrates. The UV–vis absorption spectrum of a typical $SnCl_2(acac)_2$ thin film with a thickness of 900 nm used as a donor in the rLIFT experiment together with the chemical structure of the $SnCl_2(acac)_2$ is shown in Figure 3.10. Previous studies have shown that by a careful choice of the transfer parameters, regular, well-defined SnO_2 pixels could be printed onto glass substrates from donor films of metal complex precursors. The laser fluence was an important parameter to achieve a regular, debris-free transfer and therefore was investigated thoroughly. The range of laser fluences for which successful transfers were obtained, that is, SnO_2 pixels with a surface structure comparable to the donor film, was 200–400 mJ/cm^2. The transferred pixels were in the range of 900 nm–1 μm thickness, as determined by measuring their height with a profilometer.

In [67], the authors have shown that rLIFT was an appropriate technique for fabricating efficient SnO_{2-} and Pd:SnO_2-based sensors. An example of a SnO_2 sensor printed by rLIFT is shown in Figure 3.11a. Measuring the base resistance of the rLIFTed sensors in dry and humid air, it was concluded that the SnO_2 transferred pixels have a resistance in a suitable range for sensing applications.

Further on, analyzing the sensor responses toward C_2H_5OH revealed that the laser-transferred SnO_2 pixels had a very high response, and most of the

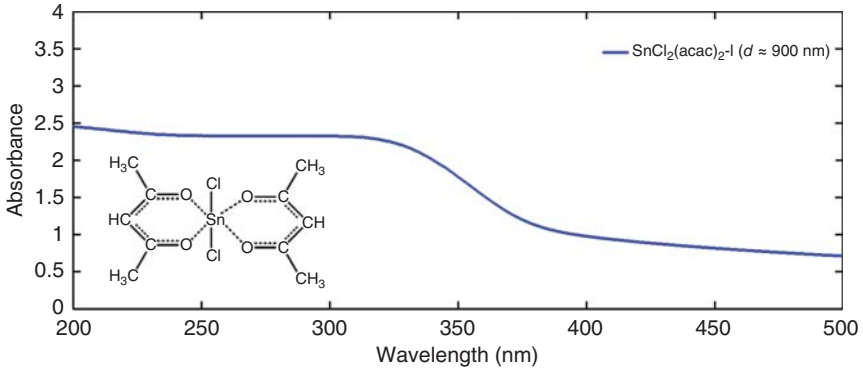

Figure 3.10 UV–vis absorption spectrum of a typical $SnCl_2(acac)_2$ thin film with a thickness of 900 nm. Inset: Chemical structure of $SnCl_2(acac)_2$.

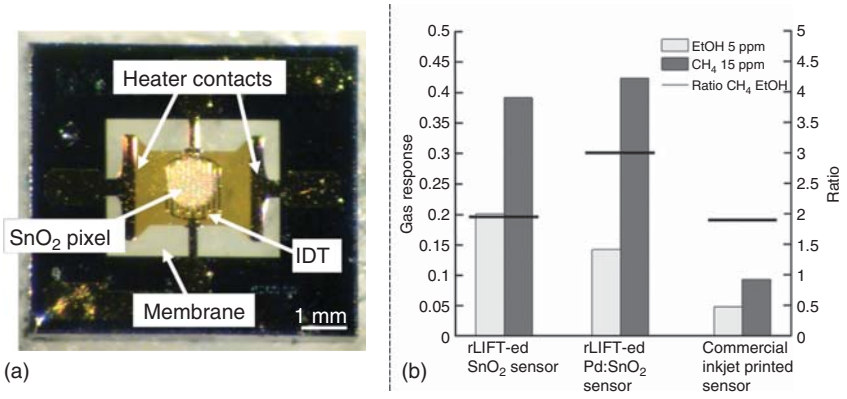

Figure 3.11 (a) SnO_2 rLIFTed pixel onto a commercial Microsens semiconductor gas sensor (MSGS) structure. (b) Sensor responses to 5 ppm of ethanol (at 350 °C) and 15 ppm of methane (at 500 °C). (Palla-Papavlu *et al*. 2016 [67]. https://www.ncbi.nlm.nih.gov/pmc/articles/PMC4846859/. Used under CC BY 4.0.)

sensor-like pads were close to saturation even when exposed to 10 ppm of C_2H_5OH. The rLIFTed sensor-like pads were stable over approximately 1 year.

Another key analyte for SnO_2 gas sensors was the detection of CH_4. With the rLIFTed SnO_2 pixels, 50 ppm CH_4 could be detected in dry air. Moreover, a comparison between the SnO_2 sensors fabricated by rLIFT and sensors fabricated by drop casting the metal complex precursor onto the sensor-like pads was carried out. The sensor responses were much lower in comparison with the rLIFTed sensors. Therefore, it can be assumed that the rLIFT process was the key factor to achieve SnO_2 pixels with high gas responses. The high response toward C_2H_5OH and CH_4 determined on the sensor-like pads was successfully confirmed. The sensor response of the SnO_2 rLIFTed sensors had four times better performance than the commercial inkjet printed sensors using the SnO_2 and the same sensing structure. In addition, the Pd-doped SnO_2 rLIFTed showed four times better response toward CH_4 than the commercial inkjet printed sensor. The sensor responses to 5 ppm of ethanol and 15 ppm of methane are shown in Figure 3.11b. The black line in Figure 3.11b indicates the ratio ($S[CH_4]/S[C_2H_5OH]$) between the two sensitivities to visualize the influence of Pd doping. This suggested that rLIFT could be a competitive alternative to commercial printing techniques, that is, sputtering or inkjet printing for fabricating high-performance sensors.

3.7 Conclusions and Perspectives

Applications in the field of microelectronics require processing techniques that allow material patterning and printing with high spatial resolution and reproducibility. LIFT has been classified as an emerging additive printing technique, competing with more mature techniques, such as inkjet or screen printing. From the first reports on this technique 30 years ago to the present day, several modifications to LIFT were developed, which try to accommodate different material

phases, that is, from liquid to solid, and also their integration into functional devices. These modifications include, for example, the addition of a DRL, which would facilitate (and protect) the intact transfer of materials.

In this chapter, we focus on the LIFT process assisted by a TP as a DRL and show some of the advantages and limitations preventing the adoption of this technique in patterning and printing of solid- and liquid-phase materials and devices (sensors and OLEDs). TP-LIFT, as an additive manufacturing process, offers advantages that make it an ideal technique in applications aiming at non-traditional manufacturing, where high resolution and high printing speed would open up the possibilities for competitive patterning and printing of materials.

In this context, the potential for additive printing is to be more economical and more environmentally friendly than the current methods. However, patterning and printing by TP-LIFT and LIFT in general still present challenges, and new ways to deliver both structural and functional materials in liquid or solid form need to be addressed.

Acknowledgments

Financial support from the Paul Scherrer Institute, the Commission for Technology and Innovation CTI (project no. 16713.1 PFNM-NM) and the European Commission – Seventh Framework Program (FP7-ICT project no. 247868, eLIFT) is gratefully acknowledged.

Conflict of Interest

The authors declare no competing interests.

References

1 Caliendo, C., Fratoddi, I., Russo, M.V., and Sterzo, C.L. (2003) Response of a Pt-polyyne membrane in surface acoustic wave sensors: experimental and theoretical approach. *J. Appl. Phys.*, **93** (12), 10071–10077.
2 Haaland, P., McKibben, J., and Paradi, M. (1995) Fundamental constraints on thin film coatings for flat-panel display manufacturing. 2nd Display Manufacturing Technology Conference, pp. 79–81.
3 Bruening, M. and Dotzauer, D. (2009) Polymer films: just spray it. *Nat. Mater.*, **8**, 449–450.
4 de Gans, B.J., Duineveld, P.C., and Schubert, U.S. (2004) Inkjet printing of polymers: state of the art and future developments. *Adv. Mater.*, **16** (3), 203–213.
5 Breech, F. and Cross, L. (1962) Optical microemission stimulated by a ruby MASER. *Appl. Spectrosc.*, **16**, 59.
6 Smith, H.M. and Turner, A.F. (1965) Vacuum deposited thin films using a ruby laser. *Appl. Opt.*, **4**, 147–148.

7 Chrisey, D.B., Piqué, A., McGill, R.A., Horwitz, J.S., Ringeisen, B.R., Bubb, D.M., and Wu, P.K. (2003) Laser deposition of polymer and biomaterial films. *Chem. Rev.*, **103** (2), 553–576.

8 Brodoceanu, D., Scarisoreanu, N.D., Filipescu, (.M.).M., Epurescu, G.N., Matei, D.G., Verardi, P., Craciun, F., and Dinescu, M. (2004) Pulsed Laser deposition of oxide thin films, in *Plasma Production by Laser Ablation* (eds S. Gammino, A.M. Mezzasalma, F. Neri, and L. Torrisi), World Scientific, pp. 41–46.

9 Schou, J. (2009) Physical aspects of the pulsed laser deposition technique: the stoichiometric transfer of material from target to film. *Appl. Surf. Sci.*, **255**, 5191–5198.

10 Braudy, R.S. (1969) Laser writing. *Proc. IEEE*, **57**, 1771–1772.

11 Brisbane, A.D. (1971) Pattern deposit by laser. U.S. Patent 3,560,258, filled and issued May 31, 1967 issued Feb 2, 1971.

12 Levene, M.L., Scott, R.D., and Siryj, B.W. (1970) Material transfer recording. *Appl. Opt.*, **9** (10), 2260–2265.

13 Bohandy, J., Kim, B.F., and Adrian, F.J. (1986) Metal deposition from a supported metal film using an excimer laser. *J. Appl. Phys.*, **60** (4), 1538–1539.

14 Bohandy, J., Kim, B.F., Adrian, F.J., and Jette, A.N. (1988) Metal deposition at 532 nm using a laser transfer technique. *J. Appl. Phys.*, **63** (4), 1158–1162.

15 Sametoglu, V., Sauer, V.T.K., and Tsui, Y.Y. (2013) Production of 70-nm cr dots by laser-induced forward transfer. *Opt. Express*, **21** (15), 18525–18531.

16 Tolbert, W.A., Lee, I.-Y.S., Doxtader, M.M., Ellis, E.W., and Dlott, D.D. (1993) High-speed color imaging by laser ablation transfer with a dynamic release layer: fundamental mechanisms. *J. Imaging Sci. Technol.*, **37** (4), 411–421.

17 Piqué, A., Chrisey, D.B., Auyeung, R.C.Y., Fitz-Gerald, J., Wu, H.D., McGill, R.A., Lakeou, S., Wu, P.K., Nguyen, V., and Duignan, M. (1999) A novel laser transfer process for direct writing of electronic and sensor materials. *Appl. Phys. A*, **69** (7), S279–S284.

18 Dinca, V., Fardel, R., Di Pietrantonio, F., Cannatà, D., Benetti, M., Verona, E., Palla-Papavlu, A., Dinescu, M., and Lippert, T. (2010) Laser induced forward transfer: an approach to single-step polymer microsensor fabrication. *Sens. Lett.*, **8** (3), 436–440.

19 Boutopoulos, C., Tsouti, V., Goustouridis, D., Chatzandroulis, S., and Zergiotti, I. (2008) Liquid phase direct laser printing of polymers for chemical sensing applications. *Appl. Phys. Lett.*, **93**, 191109.

20 Fitz-Gerald, J.M., Pique, A., Chrisey, D.B., Rack, P.D., Zeleznik, M., Auyeung, R.C.Y., and Lakeou, S. (2000) Laser direct writing of phosphor screens for high-definition displays. *Appl. Phys. Lett.*, **76** (11), 1386–1388.

21 Fernande-Pradas, J.M., Colina, M., Serra, P., Dominguez, J., and Morenza, J.L. (2004) laser-induced forward transfer of biomolecules. *Thin Solid Films*, **453–454**, 27–30.

22 Barron, J.A., Wu, P., Ladouceur, H.D., and Ringeisen, B.R. (2004) Biological laser printing: a novel technique for creating heterogeneous 3-dimensional cell patterns. *Biomed. Microdevices*, **6** (2), 139–147.

23 Hopp, B., Smausz, T., Zs, A., Kresz, N., Zs, B., and Chrisey, D. (2004) Absorbing film assisted laser induced forward transfer of fungi (Trichoderma conidia). *J. Appl. Phys.*, **96** (6), 3478–3481.

24 Hopp, B., Smausz, T., Kresz, N., Barna, N., Bor, Z., Kolozsvári, L., Chrisey, D.B., Szabó, A., and Nógrádi, A. (2005) Survival and proliferative ability of various living cell types after laser-induced forward transfer. *Tissue Eng.*, **11**, 1817–1823.

25 Hopp, B., Smausz, T., Szabo, G., Kolozsvari, L., Kafetzopoulos, D., Fotakis, C., and Nogradi, A. (2013) Femtosecond laser printing of living cells using absorbing film-assisted laser-induced forward transfer. *Opt. Eng.*, **51** (1), 014302.

26 Kattamis, N.T., McDaniel, N.D., Bernhard, S., and Arnold, C.B. (2009) Laser direct write printing of sensitive and robust light emitting organic molecules. *Appl. Phys. Lett.*, **94**, 103306.

27 Kattamis, N.T., Purnick, P.E., Weiss, R., and Arnold, C.B. (2007) Thick film laser induced forward transfer for deposition of thermally and mechanically sensitive materials. *Appl. Phys. Lett.*, **91**, 171120.

28 Fukumura, H., Kohji, Y., Nagasawa, K.-I., and Masuhara, H. (1994) Laser implantation of pyrene molecules into poly(methyl methacrylate) films. *J. Am. Chem. Soc.*, **116** (22), 10304–10305.

29 Mito, T., Tsujita, T., Masuhara, H., Hayashi, N., and Suzuki, K. (2001) Hollowing and transfer of polymethyl methacrylate film propelled by laser ablation of triazeno polymer film. *Jpn. J. Appl. Phys.*, **40** (2-8A), L805–L806.

30 Lippert, T., Wokaun, A., Stebani, J., Nuyken, O., and Ihlemann, J. (1993) Triazene polymers designed for excimer laser ablation. *Angew. Makromol. Chem.*, **206**, 97–110.

31 Stebani, J., Nuyken, O., Lippert, T., and Wokaun, A. (1993) Synthesis and characterization of a novel photosensitive triazene polymer. *Makromol. Chem. Rapid Commun.*, **14**, 365.

32 Lippert, T., Yabe, A., and Wokaun, A. (1997) Laser ablation of doped polymer systems. *Adv. Mater.*, **9** (2), 105–119.

33 Lippert, T., Wei, J., Wokaun, A., Hoogen, N., and Nuyken, O. (2000) Development and structuring of combined positive–negative/negative–positive resists using laser ablation as positive dry etching technique. *Macromol. Mater. Eng.*, **283**, 140–143.

34 Lippert, T., David, C., Dickinson, J.T., Hauer, M., Kogelschatz, U., Langford, S.C., Nuyken, O., Robert, J., and Wokaun, A. (2001) Structure property relations of photoreactive polymers designed for laser ablation. *J. Photochem. Photobiol., A*, **145**, 145–157.

35 Lippert, T. (2009) UV Laser ablation of polymers: from structuring to thin film deposition, in *Laser-Surface Interactions for New Materials Production Tailoring Structure and Properties*, Springer Series in Materials Chemistry, vol. **130** (eds A. Miotello and P.M. Ossi), Springer-Verlag, Berlin, pp. 141–175.

36 Lippert, T. and Dickinson, J.T. (2003) Chemical and spectroscopic aspects of polymer ablation- special features and novel directions. *Chem. Rev.*, **103**, 453–485.

37 Lippert, T., Nakamura, T., Niino, H., and Yabe, A. (1997) Laser induced chemical and physical modifications of polymer films: dependence on the irradiation wavelength. *Appl. Surf. Sci.*, **110**, 227–231.

38 Fardel, R., Nagel, M., Nuesch, F., Lippert, T., and Wokaun, A. (2009) Shadowgraphy investigation of laser-induced forward transfer: front side and back side ablation of the triazene polymer sacrificial layer. *Appl. Surf. Sci.*, **255**, 5430–5434.

39 Fardel, R., Nagel, M., Nuesch, F., Lippert, T., and Wokaun, A. (2007) Laser forward transfer using a sacrificial layer: influence of the material properties. *Appl. Surf. Sci.*, **254**, 1322–1326.

40 Fardel, R., Feurer, P., Lippert, T., Nagel, M., Nuesch, F., and Wokaun, A. (2007) Laser ablation of aryltriazene photopolymer films: effects of polymer structure on ablation properties. *Appl. Surf. Sci.*, **254**, 1332–1337.

41 Hauer, M., Funk, D., Lippert, T., and Wokaun, A. (2003) Laser ablation of polymers studied by ns-interferometry and ns-shadowgraphy measurements. *Appl. Surf. Sci.*, **208–209**, 107–112.

42 Hauer, M., Funk, D., Lippert, T., and Wokaun, A. (2005) Time resolved techniques as probes for the laser ablation process. *Opt. Lasers Eng.*, **43** (3–5), 545–556.

43 Fardel, R., Nagel, M., Nuesch, F., Lippert, T., Wokaun, A., and Luk'yanchuk, B. (2008) Influence of thermal diffusion on the laser ablation of thin polymer films. *Appl. Phys. A*, **90**, 661–667.

44 Fardel, R., Nagel, M., Nuesch, F., Lippert, T., and Wokaun, A. (2009) Energy balance in a laser-induced forward transfer process studied by shadowgraphy. *J. Phys. Chem. C*, **113**, 11628–11633.

45 Rapp, L., Cibert, C., Nenon, S., Alloncle, A.P., Nagel, M., Lippert, T., Videlot-Ackermann, C., Fages, F., and Delaporte, P. (2011) Improvement in semiconductor laser printing using a sacrificial protecting layer for organic thin-film transistors fabrication. *Appl. Surf. Sci.*, **257**, 5245–5249.

46 Nagel, M. and Lippert, T. (2012) Laser-Induced Forward Transfer for the fabrication of devices, in *Nanomaterials: Processing and Characterization with Lasers* (eds S.C. Singh, H. Zeng, C. Guo, and C. Weiping), Wiley-VCH Verlag GmBH, pp. 255–316.

47 Doraiswamy, A., Narayan, R., Lippert, T., Urech, L., Wokaun, A., Nagel, M., Hopp, B., Dinescu, M., Modi, R., Auyeung, R., and Chrisey, D. (2006) Excimer laser forward transfer of mammalian cells using a novel triazene absorbing layer. *Appl. Surf. Sci.*, **252**, 4743–4747.

48 Xu, J., Liu, J., Cui, D., Gerhold, M., Wang, A., Nagel, M., and Lippert, T. (2007) Laser-assisted forward transfer of multi-spectral nanocrystal quantum dot emitters. *Nanotechnology*, **18**, 025403.

49 Palla-Papavlu, A., Paraico, I., Shaw-Stewart, J., Dinca, V., Savopol, T., Kovacs, E., Lippert, T., Wokaun, A., and Dinescu, M. (2011) Liposome micropatterning based on laser-induced forward transfer. *Appl. Phys. A Mater. Sci. Process.*, **102** (3), 651–659.

50 Banks, D., Kaur, K., Gazia, R., Fardel, R., Nagel, M., Lippert, T., and Eason, R. (2008) Triazene photopolymer dynamic release layer-assisted femtosecond laser-induced forward transfer with an active carrier substrate. *EPL (Europhys. Lett.)*, **83**, 38003.

51 Mattle, T., Shaw-Stewart, J., Schneider, C.W., Lippert, T., and Wokaun, A. (2012) Laser induced forward transfer aluminum layers: process investigation by time resolved imaging. *Appl. Surf. Sci.*, **258**, 9352–9354.

52 Dinca, V., Palla-Papavlu, A., Dinescu, M., Shaw-Stewart, J., Lippert, T., Di Pietrantonio, F., Cannata, D., Benetti, M., and Verona, E. (2010) Polymer pixel enhancement by laser-induced forward transfer for sensor applications. *Appl. Phys. A*, **101**, 559–565.

53 Dinca, V., Palla-Papavlu, A., Matei, A., Luculescu, C., Dinescu, M., Lippert, T., Di Pietrantonio, F., Cannata, D., Benetti, M., and Verona, E. (2010) A comparative study of DRL-lift and lift on integrated polyisobutylene polymer matrices. *Appl. Phys. A*, **101**, 429–434.

54 Di Pietrantonio, F., Benetti, M., Cannata, D., Verona, E., Palla-Papavlu, A., Dinca, V., Dinescu, M., Mattle, T., and Lippert, T. (2012) Volatile toxic compound detection by surface acoustic wave sensor array coated with chemoselective polymers deposited by laser induced forward transfer: application to sarin. *Sens. Actuators, B*, **174**, 158–167.

55 Cannata, D., Benetti, M., Di Pietrantonio, F., Verona, E., Palla-Papavlu, A., Dinca, V., Dinescu, M., and Lippert, T. (2012) Nerve agent simulant detection by solidly mounted resonators (SMRs) polymer coated using laser induced forward transfer (LIFT) technique. *Sens. Actuators, B*, **173**, 32–39.

56 Dinca, V., Mattle, T., Palla-Papavlu, A., Rusen, L., Luculescu, C., Lippert, T., and Dinescu, M. (2013) Polyethyleneimine patterns obtained by laser-transfer assisted by a Dynamic Release Layer onto Themanox soft substrates for cell adhesion study. *Appl. Surf. Sci.*, **278**, 190–197.

57 Inui, T., Mandamparambil, R., Araki, T., Abbel, R., Koga, H., Nogia, M., and Suganuma, K. (2015) Laser-induced forward transfer of high-viscosity silver precursor ink for non-contact printed electronics. *RSC Adv.*, **5**, 77942–77947.

58 Palla-Papavlu, A., Dinca, V., Paraico, I., Moldovan, A., Shaw-Stewart, J., Schneider, C.W., Kovacs, E., Lippert, T., and Dinescu, M. (2010) Microfabrication of polystyrene microbead arrays by laser induced forward transfer. *J. Appl. Phys.*, **108**, 033111–033116.

59 Palla-Papavlu, A., Dinca, V., Luculescu, C., Shaw-Stewart, J., Nagel, M., and Dinescu, M. (2010) Laser induced forward transfer of soft materials. *J. Opt.*, **12**, 124114–124119.

60 Palla-Papavlu, A., Dinescu, M., Wokaun, A., and Lippert, T. (2014) Laser-induced forward transfer of single-walled carbon nanotubes. *Appl. Phys. A*, **117**, 371–376.

61 Rapp, L., Diallo, A.K., Nénon, S., Alloncle, A.P., Videlot-Ackermann, C., Fages, F., Nagel, M., Lippert, T., and Delaporte, P. (2012) Laser printing of a semiconducting oligomer as active layer in organic thin film transistors: Impact of a protecting triazene layer. *Thin Solid Films*, **520**, 3043–3047.

62 Chen, J., Palla-Papavlu, A., Li, Y., Chen, L., Dobeli, M., Stender, D., Populoh, S., Weidenkaff, A., Schenider, C.W., Wokaun, A., and Lippert, T. (2014) Laser direct deposition and direct-writing of thermoelectric misfit cobaltite thin films. *Appl. Phys. Lett.*, **104**, 231907.

63 Fardel, R., Nagel, M., Nüesch, F., Lippert, T., and Wokaun, A. (2007) Fabrication of organic light-emitting diode pixels by laser-assisted forward transfer. *Appl. Phys. Lett.*, **91**, 061103.

64 Shaw-Stewart, J., Lippert, T., Nagel, M., Nuesch, F., and Wokaun, A. (2011) Laser-induced forward transfer of polymer light-emitting pixels with increased charge injection. *ACS Appl. Mater. Interfaces*, **3**, 309–316.

65 Shaw-Stewart, J., Lippert, T., Nagel, M., Nuesch, F., and Wokaun, A. (2012) Sequential printing by laser-induced forward transfer to fabricate a polymer light-emitting diode pixel. *ACS Appl. Mater. Interfaces*, **4**, 3535–3541.

66 Mattle, T., Hintennach, A., Lippert, T., and Wokaun, A. (2013) Laser induced forward transfer of SnO_2 for sensing applications using different precursors systems. *Appl. Phys. A*, **110**, 309–316.

67 Palla-Papavlu, A., Mattle, T., Temmel, S., Lehmann, U., Hintennach, A., Grisel, A., Wokaun, A., and Lippert, T. (2016) Highly sensitive SnO_2 sensor via reactive laser-induced transfer. *Sci. Rep.*, **6**, 25144.

68 Shaw-Stewart J., Lippert T., Nagel M., Nuesch F., and Wokaun A. (2010) Laser-induced forward transfer using Triazene polymer dynamic releaser layer. AIP Conference Proceedings, vol. 1278, pp. 789–799.

69 Shaw-Stewart, J.R.H. (2012) Optimizing the fabrication of organic light-emitting diodes by laser-induced forward transfer. PhD thesis. ETH.

70 Ballantine, D.S., White, R.M., Martin, S.J., Ricco, A.J., Frye, G.C., Zellers, E.T., and Wohltjen, H. (1997) *Acoustic Wave Sensors: Theory, Design, and Physico-Chemical Applications*, John Wiley & Sons, Inc., New York, ISBN: 978-0-12-077460-9.

71 Martin, S.J., Frye, G.C., Spates, J.J., and Butler, M.A. (1996) Gas sensing with acoustic devices. Proceedings of IEEE Ultrasonics Symposium, vol. 421, pp. 423–434.

72 Dinescu, M., Matei, A., Dinca, V., Palla-Papavlu, A., Di Pietrantonio, F., Cannata, D., Benetti, M., Verona, E., and Lippert, T. (2013) Laser processing of organic materials: applications in tissue engineering and chemical sensing. *Rom. Rep. Phys.*, **65** (3), 1019–1031.

73 Ballantine, D.S., Rose, S.L., Grate, J.W., and Wohltjen, H. (1986) Correlation of surface acoustic wave device coating responses with solubility properties and chemical structure using pattern recognition. *Anal. Chem.*, **58** (14), 3058–3066.

74 Rose-Pehrsson, S.L., Grate, J.W., Ballantine, D.S., and Jurs, P.C. (1988) Detection of hazardous vapors including mixtures using pattern recognition analysis of responses from surface acoustic wave devices. *Anal. Chem.*, **60**, 2801–2811.

75 Kaur, K.S., Feinaeugle, M., Banks, D.P., Ou, J.Y., Di Pietrantonio, F., Verona, E., Sones, C.L., and Eason, R.W. (2011) Laser-induced forward transfer of focused ion beam pre-machined donors. *Appl. Surf. Sci.*, **257** (15), 6650–6653.

76 Palla-Papavlu, A., Constantinescu, C., Dinca, V., Matei, A., Moldovan, A., Mitu, B., and Dinescu, M. (2010) Polyisobutylene thin films obtained by matrix assisted pulsed laser evaporation for sensors applications. *Sens. Lett.*, **8** (3), 502–506.

77 Pinna, N., Garnweitner, G., Antonietti, M., and Niederberger, M. (2005) A general nonaqueous route to binary metal oxide nanocrystals involving a C-C bond cleavage. *J. Am. Chem. Soc.*, **127** (15), 5608–5612.
78 Niederberger, M., Garnweitner, G., Krumeich, F., Nesper, R., Colfen, H., and Antonietti, M. (2004) Tailoring the surface and solubility properties of nanocrystalline titania by a nonaqueous in situ functionalization process. *Chem. Mater.*, **16** (7), 1202–1208.
79 Wu, J.M., Chen, Y.-R., and Kao, W.T. (2014) Ultrafine ZnO nanoparticles/nanowires synthesized on a flexible and transparent substrate: formation, water molecules, and surface defect effects. *ACS Appl. Mater. Interfaces*, **6**, 487–494.
80 Benetti, M., Cannata, D., D'Amico, A., Di Pietrantonio, F., Macagnano, A., and Verona, E. (2004) SAW sensors on AlN/diamond/Si structures. Proceedings of IEEE Sensors, vol. 752, pp. 753–756.

4

Laser-Induced Forward Transfer of Fluids

Juan M. Fernández-Pradas, Pol Sopeña, and Pere Serra

Universitat de Barcelona, Departament de Física Aplicada, IN2UB, Martí i Franquès 1, 08028 Barcelona, Spain

4.1 Introduction to the LIFT of Fluids

The laser-induced forward-transfer (LIFT) technique, typically applied to the local deposition of solid materials from thin solid-film precursors, can also be applied to the deposition of liquid droplets from thin liquid films [1]. The setup and the principle of operation are basically the same as explained in the previous chapters (Chapters 1–3); however, the mechanisms of material ejection and deposition are sensibly different because of the handling of fluid materials. In this case, the fluid state of the donor material is intended to be preserved during the whole deposition process, avoiding material vaporization. Since no melting and vaporization are required, low energy densities are enough to promote the transfer of material with insignificant thermal damage.

LIFT has emerged as a direct-write technique able to print inks for digital manufacturing ready to face the challenges proposed by the rapidly changing markets [2, 3]. In this sense, direct-write techniques appear as an interesting alternative for solving the difficulties that traditional methods based on the use of masks or molds present for manufacturing products on demand. Most of these direct-write techniques, with inkjet and dip-pen technologies as the most commonly used, rely on the transfer of individual droplets, and thus, they are well suited to print patterns of different materials directly from digital files wherein the pixels positions are defined [3]. One of the main advantages of LIFT over other direct-write techniques is its capacity for transferring a wide variety of inks without special formulation requirements. This can make LIFT very competitive in many instances, since it allows using already existing inks that had been initially designed for other well-established techniques instead of requiring totally new formulations, which can definitely impact the cost of the final product. Furthermore, LIFT does not involve nozzles for achieving the desired resolution, so that it presents practically no restrictions concerning the printable viscosities and no clogging issues. This in turn results in practically no limitations regarding the size of the particles loading the ink. They can contain particles with dimensions ranging from nanometers to few hundred micrometers [2].

Laser Printing of Functional Materials: 3D Microfabrication, Electronics and Biomedicine,
First Edition. Edited by Alberto Piqué and Pere Serra.
© 2018 Wiley-VCH Verlag GmbH & Co. KGaA. Published 2018 by Wiley-VCH Verlag GmbH & Co. KGaA.

In this chapter, a general overview of the LIFT technique for the deposition of fluids is provided. The review starts with a very short introduction to the origins of LIFT and to the evolution that led to the use of fluids instead of solids. Then, the basic principle of operation and further developments are described before reviewing the main mechanisms involved in the ejection and deposition of fluids. Afterward, the role of the different parameters is analyzed and discussed on the basis of their effects on the ejection and deposition processes. Finally, the issues appearing during the printing of continuous lines and areas are described together with solution proposals that finally resulted in real improvements for the future application of the technique in industrial production processes.

4.1.1 Origin

In the late 1960s, lasers were already devised as tools for the direct writing of patterns from donor thin films in a configuration that is very similar to that of LIFT [4–7, see Chapter 2 for details]. Until then, laser applications had been basically focused on their capability for material removal. New uses extended the abilities of lasers not only to remove material but also to transfer it onto a different surface. One of the main claimed advantages was the direct printing of patterns without the need of masks. Thus, the process of pattern transfer could be simplified; the required manufacture of a mask and all the processes of mask placement, alignment, and removal could be avoided. Apparently without any knowledge about the prior work, the same idea appeared again as a new technique in 1986 in a paper by Bohandy *et al*. [8]. This technique was named LIFT for the first time in a subsequent paper in 1987 [9]. In all these previous works, the donor thin-film precursor from which the material is transferred was in solid state and in contact with the receiver substrate [5, 7, 8] or with a small gap below 100 μm [4–7]. The process was performed in vacuum conditions [4, 6, 8] or in air under atmospheric conditions [5, 7] depending on the approach proposed from each group.

Research in the LIFT technique grew up after its revival in 1986. The first studies were mostly focused on the transfer of metals [8–13], though other inorganic materials such as oxides [14–16] and superconductors [17] were also successfully transferred through LIFT. However, the LIFT process from solid donor thin films was not suitable for the transfer of delicate materials that are prone to decomposition or modification if melted or vaporized. In order to overcome this issue, matrix-assisted pulsed-laser evaporation-direct write (MAPLE-DW) was proposed in 1999 by Piqué *et al*. [18]. The main innovation introduced with respect to LIFT was that that the donor material was embedded inside a matrix of an organic binder or a polymer ideally highly absorbent of the laser radiation. This decomposed into volatile components, and the material of interest was deposited alone on the receiving substrate [18, 19].

The use of fluids as a matrix for the transfer of delicate materials appeared as a natural evolution of MAPLE-DW [20, 21]. The fluid acts as a protector against thermal damage and as the transfer vector of the material that is dissolved or suspended in it. Cells, as well as many biomolecules, for example, require a wet environment for their survival and do not withstand high temperatures. Hence, this evolution opened the possibility to transfer biological material such as proteins

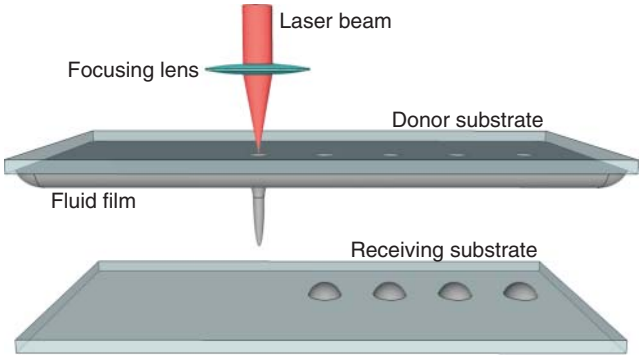

Figure 4.1 Sketch of a LIFT setup for printing fluids from a donor film onto a receiving substrate.

or cells for biomedical applications [21–25]. Nonetheless, the interest of the LIFT of fluids was not restricted to printing biological or biomedical materials [26–29], but it also extended to materials for electronic applications [30–32], the graphic arts industry [2], and other functional materials [33–36].

4.1.2 Principle of Operation

The setup required for the LIFT of fluids is basically the same as that for traditional LIFT with solid donor films. Figure 4.1 shows a sketch of the typical arrangement of the main elements. The laser source is usually a pulsed laser system delivering pulses of several nanoseconds in duration or below. The laser wavelength is not, in general, a restrictive parameter but must be in accordance with the donor substrate and the donor thin-film absorption properties. The laser pulses are guided through an optical system that ends with a lens, which focuses the laser radiation in the interface between the donor substrate and the donor thin film at fluences high enough to promote the transfer process. Consequently, the donor substrate must be transparent to the laser radiation. Hence, the donor substrate can be made of glass for laser wavelengths in the visible or the near-infrared range. However, quartz or fused-silica substrates must be used for UV wavelengths. Other materials, such as flexible organic substrates in roll-to-roll production, can also be used provided that they are transparent to the laser radiation. On the other hand, the laser radiation should be absorbed by the donor thin film. Thus, at least one component of the fluid must be absorbing. Nevertheless, it is also possible to transfer nonabsorbing fluids by placing an absorbing layer between the transparent substrate and the thin donor film (see Chapter 3 for details). Metallic (titanium, gold) thin films with thicknesses around tenths of nanometers, as well as polymeric layers of a few microns thickness, have been typically used for absorption purposes. The fluid to be transferred is spread on the donor substrate to form a uniform layer with a thickness that usually ranges from 10 to 100 μm.

The receiving substrate surface is placed in front and parallel to the free fluid surface. The gap between them must be large enough to prevent unwanted transfer of fluid by contact. However, it is not such a critical parameter for the transfer

of fluids as it is for solids, as we describe in Section 4.3.3. This is an important advantage for the future setting up of the technique in industrial processes. Typical gap distances used in laboratory experiments range from few tens of microns up to few millimeters. Motion stages can be used to move the donor and receiving substrates in order to produce patterns, or, alternatively, laser scanners based on galvanometric mirrors or rotating polygons can also be used to scan the laser beam along the donor layer. Lines and patterns can be generated by sequentially printing individual droplets similarly to many other digital printing techniques. The LIFT process of fluids does not require vacuum equipment and is perfectly compatible with clean-room facilities.

The same setup used for LIFT can also be used for surface treatment or micromachining purposes by simply removing the donor substrate system and adjusting the focus of the laser beam to get the desired result. Thus, a LIFT setup can be implemented in a production line as a complete tool for additive, subtractive, and modification purposes.

4.1.3 Developments

The transfer of fluids with a laser by means of an approach based on LIFT has received many different names in the literature (see Chapters 1 and 2 for details). Thus, as described in the previous section, the LIFT of fluids started under the name of MAPLE-DW due to the evolution of the last to the use of fluid matrices [21, 37, 38]. Biomolecules and cells were one of the first materials to be transferred with fluid donor layers, and thus, some groups adopted the name of biological laser printing (BioLP) for the technique [26, 39–41]. In some cases, when an absorbing layer was used, the term absorbing film assisted–LIFT (AFA-LIFT) was used [42, 43], although others kept the simple original name of LIFT [27–36]. Later, the same technique applied to the printing of cells can be found under the name of laser-assisted bioprinting (LAB) [44, 45].

In the approach proposed as blister-actuated LIFT (BA-LIFT), the ejection of the donor fluid is performed in a configuration similar to that of LIFT with an absorption layer but without producing the complete ablation of the absorption layer [46, 47]. In this case, the evaporated material remains encapsulated between the donor substrate and the absorbing layer and does not interact directly with the fluid. The expansion of the evaporated material produces a rapid deformation of the absorbing layer that transfers its momentum to the fluid layer. The technique has special interest for the deposition of very sensitive materials since the fluid can be deposited without any trace of contamination from the absorbing layer. A detailed description of BA-LIFT can be found in Chapter 5.

The rheological properties of extremely high viscosity fluids or pastes allow the use of structured light to promote the ejection of material from the donor layer reproducing the shape of the incident light. The technique receives the name of laser decal transfer (LDT) [48–50] and shares with LIFT the same setup and principle of operation but with an intercalated mask or a spatial light modulator device for structuring the laser beam light. In this way, three-dimensional structures can be directly printed through LDT. In spite of LDT also corresponding to the LIFT of fluids, the mechanisms involved are substantially different from those

of the LIFT of fluids with low and moderate viscosities. Thus, they are treated separately in Chapter 10.

The film-free laser printing (FF-LP) technique appeared as an alternative to LIFT for the ejection of fluids directly from a reservoir, avoiding the step of spreading a thin film on the donor substrate [51–54]. As with LDT, this version of the LIFT of fluids deserves a chapter on its own, Chapter 6.

4.2 Mechanisms of Fluid Ejection and Deposition

The localized absorption of the laser radiation in the fluid in the vicinity of the donor substrate interface or in the dedicated absorption layer promotes different regimes in the dynamics of fluid transfer depending on the different laser radiation parameters, as well as on the fluid characteristics. This section is devoted to the different ejection and deposition dynamics that can take place during a LIFT event, with special emphasis on the jetting regime that allows the formation of well-defined droplets on the receiving substrate, that is, the optimum printing conditions.

4.2.1 Jet Formation

The onset of the deposition process starts with the absorption of the laser radiation that promotes a quick vaporization of the absorbing agent. Thus, a vapor bubble is generated, thereby expanding against the surrounding fluid. The particular dynamics of both bubble and displaced fluid have been unveiled by means of time-resolved imaging for different fluids and irradiation conditions [45, 47, 55–68]. Figure 4.2 shows a series of images of the ejection process that result in the formation of a long and stable jet. The high pressure inside the bubble promotes its rapid expansion during the first microseconds after the laser pulse. Concomitant with its expansion, a protrusion is formed in the fluid layer as the vapor pressure pushes the liquid surrounding the bubble. When the bubble starts collapsing, a thin needle-like jet develops on top of this protrusion. While the bubble collapses, the jet continues advancing in the axial direction toward the receiving substrate. The contact of the needle-like jet, which can achieve an extremely high aspect ratio (widths of a few microns versus lengths of few millimeters), with the receiving substrate triggers the deposition of the droplet, a process that lasts until the jet breakup [55, 56].

The bubble expansion is anisotropic and elongated in the direction perpendicular to the donor surface. On one side, the bubble is constrained by the rigid donor substrate, so that it expands pushing the fluid around and below it. Since it is much easier for the bubble to displace the liquid close to the free surface than that surrounding it, a pressure gradient develops between the lateral contour of the bubble near the substrate and its pole adjacent to the free surface. This promotes a flux of fluid along the bubble walls and toward the pole. The streamlines converge in the pole and generate a high-pressure stagnation point. This pressure relaxes with the formation of a very thin needle-like jet. The bubble continues expanding while the internal vapor pressure is higher than the outward

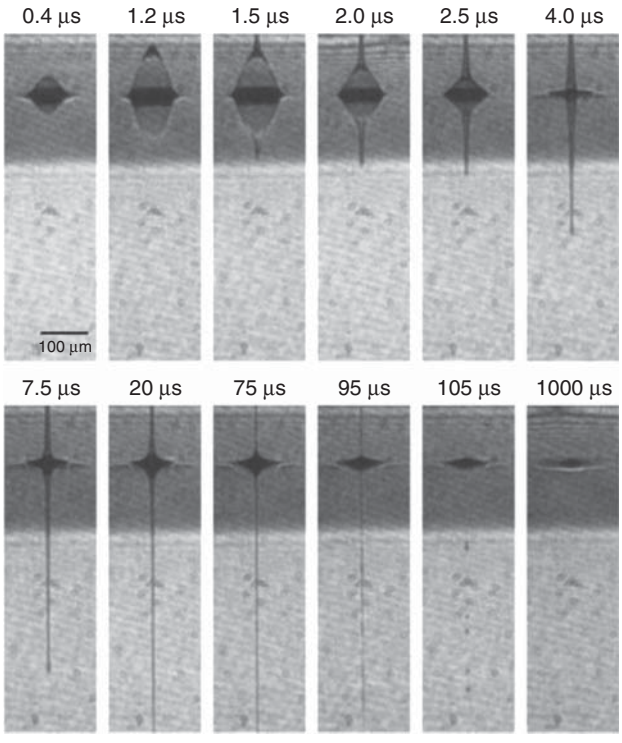

Figure 4.2 Stop-action movie of the dynamics of long and stable jet formation in LIFT at different delay times with respect to the laser pulse. The corresponding delay time is indicated above each image, and the image exposure time is always 100 ns. In all of the frames, the laser impinges from above. The transferred solution corresponds to a mixture of water and glycerol. (Duocastella *et al*. 2008 [55]. Reproduced with permission of Springer.)

pressure plus the capillary force. Afterward, the bubble starts collapsing. The jet, though, has enough inertia and continues moving toward the acceptor substrate at speeds that usually range from tens to few hundreds of meters per second [56] depending on the laser fluence and fluid properties. The jet finally breaks due to the Plateau–Rayleigh instability caused by surface tension effects [69].

In some cases, time-resolved imaging studies of the LIFT process revealed the emergence of a new thicker jet several microseconds after the first needle-like jet was formed [58, 64]. This second fluid ejection is caused by the rebound expansion of the vapor bubble, a typical process for cavitation bubbles [70]. This double-jet formation was also observed for FF-LIFT [51, 53]. Time-resolved studies of the FF-LIFT ejection process [71, 72] unveiled the direct correlation between the bubble second expansion and the second jet apparition and gave clues to explain the evolution of the cavitation bubble during collapse and re-expansion. In fact, the overpressure generated on the bubble pole due to the flow of fluid from its sides generates the already observed forward jet but also an inward counter-jet that propagates in the opposite direction [73]. Thus, the counter-jet penetrates the bubble transforming it into a torus. After collapse,

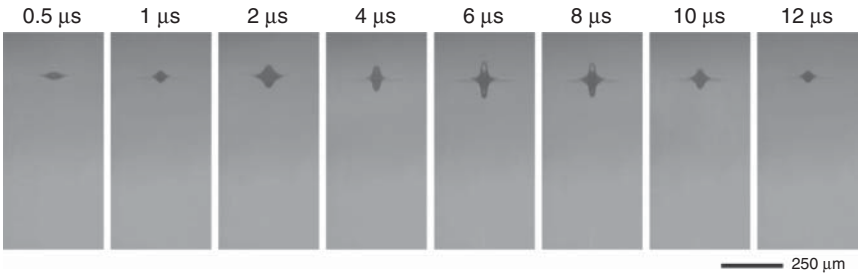

Figure 4.3 Stop-action movie of the jetting dynamics corresponding to a LIFT event with insufficient laser pulse energy for transfer to occur. The jet retracts before reaching the receiving substrate. The corresponding delay time after the laser pulse is indicated above each image, and the image exposure time is always 100 ns. In all of the frames, the laser impinges from above. The transferred solution corresponds to a mixture of water and glycerol.

the second expansion of the torus-shaped bubble promotes the formation of a new jet thicker than the first. Following similar mechanisms as those explained earlier, the fluid overpressure is generated now on the circular pole of the torus instead of the single pole of the sphere. Consequently, the second jet emerges with cylindrical shape that is rapidly transformed in a thick jet.

If the laser fluence is not high enough, the first needle-like jet can retract before breaking (Figure 4.3). In this case, the capillary forces are able to counteract the small jet inertia and do not allow its further growth. On the contrary, if the laser fluence is too high, the needle-like jet becomes unstable and turbulent. For even higher fluences, the pressure inside the vapor bubble is high enough to overcome the capillary forces and produce the bubble burst (Figure 4.4).

4.2.2 Droplet Deposition

As stated earlier, the best conditions for depositing single droplets correspond to those wherein the fluid is ejected as long and stable jets. This in turn provides LIFT with considerable tolerance in the donor/receiver gap, which impacts positively its further setting up in a production line.

Although the speed of the jet reaches values from tens to few hundred meters per second, the deposition process and droplet formation are gentle enough to

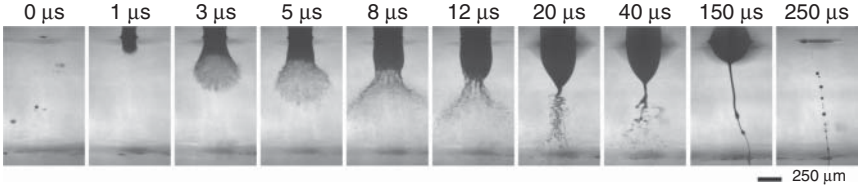

Figure 4.4 Stop-action movie of the transfer dynamics corresponding to a LIFT event with excessive laser pulse energy. The bubble bursts before the jet can develop, which results in undesired splashing on the receiving substrate. The corresponding delay time after the laser pulse is indicated above each image, and the image exposure time is always 100 ns. In all of the frames, the laser impinges from above. The transferred solution corresponds to a commercial silver ink.

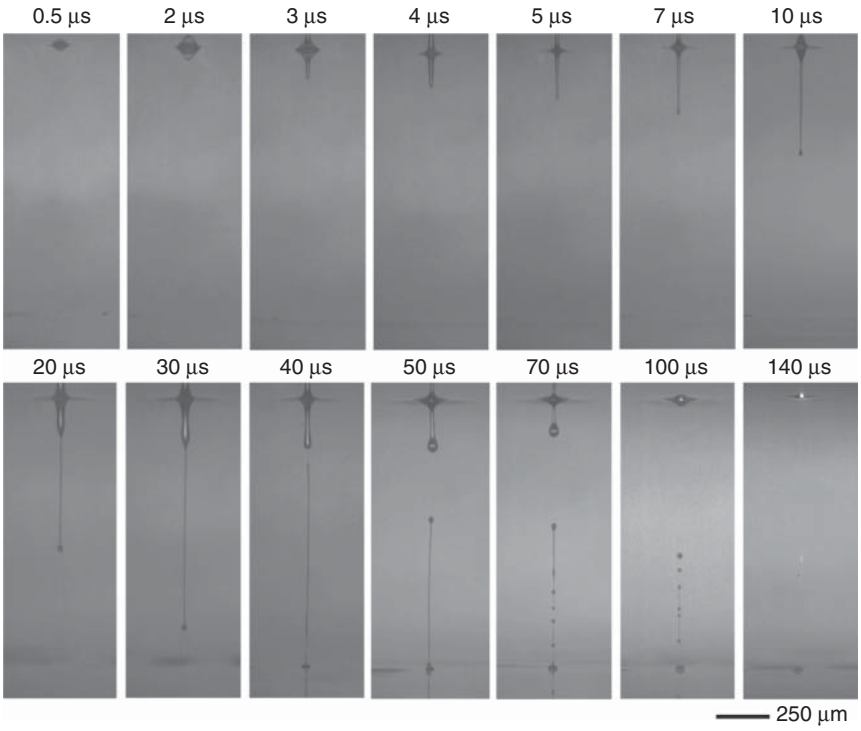

Figure 4.5 Stop-action movie of the jetting dynamics corresponding to a LIFT event resulting in the formation of circular sessile droplets. It can be observed that transfer proceeds through the contact of the jet with the receiving substrate. The corresponding delay time after the laser pulse is indicated above each image, and the image exposure time is always 100 ns. In all of the frames, the laser impinges from above. The transferred solution corresponds to a mixture of water and glycerol.

avoid splashing in most instances [57]. Figure 4.5 shows a stop-action movie of droplets deposition in the jetting regime for a water and glycerol solution (50% v/v). After the absorption of the laser pulse, the jet is formed according to the previous description (Section 4.2.1). When the jet contacts the receptor surface, the liquid spreads through a dynamics that resembles that of a drop impacting on a dry surface at moderate speed [74, 75]. In this process, the area occupied by the fluid rapidly increases beyond the jet diameter. Viscous frictional forces act against the fluid inertia until the spreading stops. Meanwhile, the jet continues feeding the growing droplet and increasing its volume. The further growth of the bubble follows a dynamics similar to that found in experiments of adding liquid at moderate rates into a sessile drop [76]. At this moment, the volume increase is accompanied by an increase of the contact angle. This likely occurs, whereas the contact angle is below the critical advancing contact angle [77]. It has been observed that when gently feeding an individual droplet on a flat surface, it can stay in a metastable state between two contact angle values, the receding and

advancing contact angles. In the case that this critical angle is overcome, the fluid spreads again and the contact angle diminishes [58]. All along the droplet feeding process, the jet becomes thinner and thinner until Plateau–Rayleigh instabilities cause the jet breakup [69]. Subsequently, the dome-shaped droplet spreads again in a relaxation process that takes some milliseconds until it reaches its final size that depends on the wettability of the fluid on the receiver surface.

In the previous paragraphs, we have described the most common dynamics taking place in the LIFT of fluids. However, other transfer dynamics are possible depending on the operating configurations. For instance, when the receiving substrate is placed at a distance smaller than the maximum bubble height, the bubble can contact the receiving substrate surface before the jet could be developed [65, 78, 79], and in spite of the corresponding dynamics being completely different from that described before, this instance can also lead to the deposition of circular droplets. Figure 4.6 shows a stop-action movie for this case, wherein it is clear that the bubble expands and impacts the receiving surface. After the impact, the bubble starts collapsing from its end in contact with the surface until a bridge is finally formed. The breakup of the bridge results in the formation of dome-shaped droplets with nice round profiles [78]. However, because of the different deposition dynamics, droplets are usually more flattened and acquire a lower contact angle than those deposited through the jet contact mechanism. In the case of deposition through bubble contact, the initial droplet dimensions coincide with that of the contact area of the bubble, but later the droplet suffers a receding process until it attains its final size. Thus, droplets deposited through bubble contact get a final contact angle close to the critical receding contact angle. Conversely, in the case of droplets deposited through the jet contact mechanism, since they relax from an advancing motion, the resulting contact angle is closer to the advancing critical contact angle. Consequently, droplets of the same fluid deposited on the same receiver substrate can reach different contact angles depending on the mechanisms through which they have been transferred. Thus, droplets deposited through jet contact benefit from better resolution. However, the bubble contact mechanism has been proved adequate for sticking droplets on superhydrophobic surfaces [65]. The high speed of the fluid at impact makes possible to wet superhydrophobic surfaces following the Wenzel wetting mechanism [80], which has also been revealed effective for the fabrication of high-quality microlenses [81].

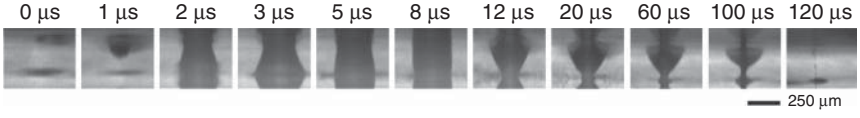

Figure 4.6 Stop-action movie of the dynamics corresponding to a LIFT event resulting in the formation of circular sessile droplets through contact of the expanding bubble with the receiving substrate. The corresponding delay time after the laser pulse is indicated above each image, and the image exposure time is always 100 ns. In all of the frames, the laser impinges from above. The transferred solution corresponds to a commercial silver ink. (Sopeña *et al*. 2017 [36]. Reproduced with permission of Elsevier.)

4.3 Printing Droplets through LIFT

In the LIFT of fluids, each single laser pulse results in a single transfer event that ends with the printing of an individual droplet on the receiving substrate. The main mechanisms leading to the printing of droplets have been described in the previous section. In this section, we focus the attention on the outcome of the printing process, and thus, we analyze the influence that the main parameters involved in a LIFT event have on the morphology of the deposited droplets.

Before starting with the analysis of each particular parameter, it seems convenient, though, to have a brief discussion about the size of the printed droplets and the influence of the receiving substrate on them. It is clear with any printing technique that the diameter and contact angle of the sessile droplets strongly depend on the wetting properties of the printed fluid on the substrate. It is not so clear, though, for their volume. In the case of inkjet printing, for example, since the droplet that will be finally printed is generated in flight from the breakup of a jet, the droplet volume is independent of the nature of that substrate. LIFT is also a jet-based technique. However, since droplet formation proceeds through the contact of the jet with the receiving substrate, the volume of the resulting droplet can also depend in this case on the properties of the receiver, as we clearly showed in [81]. Both droplet diameter and droplet volume have been traditionally used in the literature to characterize the dimensions of the printing outcomes.

4.3.1 Role of the Laser Parameters

Lasers with many different wavelengths, from the UV to the near-IR, have been used for successfully printing fluids through LIFT. The only requirements for the laser wavelength is that the donor substrate must be transparent to it while it has to be absorbed either by the ink or by the specific absorbing layer (indispensable for transparent inks). Hence, the use of an absorbing layer permits the use of multiple types of lasers practically without restriction.

The laser pulse duration is not a very restrictive parameter either. Typically, pulses from Nd:YAG or excimer lasers with duration of some nanoseconds are used [21–23, 26–29, 32–34, 36–45, 47, 55–60, 62, 64–68, 70, 78, 79, 82]. Nevertheless, the LIFT of fluids can also be performed successfully with much shorter laser pulses [30, 31, 35, 61, 83, 84]. A direct comparison between nanosecond and femtosecond laser pulses showed that smaller droplets could be deposited in the femtosecond case; however, transfer with nanosecond pulses accepted larger gaps between the donor and the receiving substrates [83].

The laser parameters that probably play the most significant role in the transfer of fluids by LIFT are the pulse energy and the laser beam size in the absorbing region. Studies on the influence of the laser pulse energy for different fluids [29, 32, 82, 85–90] reveal the existence of a threshold below which no deposition is obtained. For energies just above that threshold, circular droplets are deposited (Figure 4.7), with their size increasing with pulse energy. However, if the pulse energy is too high, the fluid is deposited in irregular shapes, with satellites around it and even in total splashing. All these features can be qualitatively correlated with the ejection and deposition dynamics presented in Section

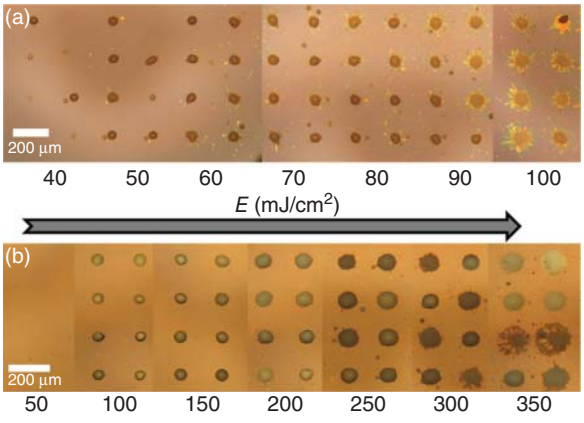

Figure 4.7 Optical microscopy image of LIFT-printed droplets of silver nanoparticles ink for different energies from (a) Ag NPs ink/quartz donor substrate, (b) Ag NPs ink/Ti/quartz donor substrate. (Makrygianni *et al*. 2014 [32]. Reproduced with permission of Elsevier.)

4.2. When the energy is below the threshold, the jet or protrusion produced by the bubble expansion cannot reach the receiving substrate before retraction (the threshold, therefore, depends on the donor/receiver gap). Thus, no droplet is deposited. Above the energy threshold, droplet deposition proceeds through contact of the thin and stable jet with the receiver substrate; the jet can gently transfer liquid onto the substrate until breakup. If the speed of the jet is too high, though, the transfer is not so gentle, and any instability can result in the ejection of secondary droplets, thus resulting in the irregular shapes and satellites observed at relatively high pulse energies [66]. At the highest energies, the internal pressure of the vapor bubble can overcome the capillary forces in the fluid and produce a burst of liquid that results in the presence of splashing in the receiving substrate.

The dimensions of the beam in the absorbing region also influence the deposition results [86–88, 91]. At a given pulse energy, smaller amounts of fluid can be deposited by reducing the spot size. Additionally, the energy threshold for deposition decreases with laser spot size. Hence, the smallest droplets can be obtained near the threshold and using the smallest possible beam size [86, 87]. With this approach, LIFT has been proved to be able to deposit very small volumes of around 10 fl [82] that lead to the formation of droplets with diameters below 10 µm [59, 82].

In spite of the complex dynamics of fluid ejection and deposition involving jet formation, a linear relationship between the deposited volume and the pulse energy has been found in several studies using Gaussian laser beams [56, 59, 60, 62, 78, 82, 86, 87, 89, 90, 92]. Figure 4.8 shows the results of one of those studies wherein that linear relationship can be clearly identified for different laser spot sizes. Thus, the deposited volume (V) follows the empirical law

$$V = K(E - E_0) \tag{4.1}$$

where E is the pulse energy, and the parameters K and E_0 can be obtained from the linear fit of the experimental points. K can be identified as an efficiency parameter of the transfer process. It is worth noting that it presents very similar values for all the series presented in Figure 4.8 except for those points corresponding to the highest focusing of the laser beam. On the other hand, the values of E_0 for the

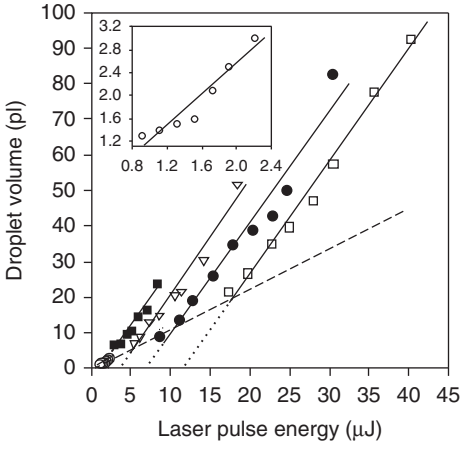

Figure 4.8 Plot of the transferred droplet volume versus laser pulse energy for a water and glycerol solution deposited with different laser beam dimensions (ω_x and ω_y correspond to the major and minor radii of an elliptical laser beam): (○) $\omega_x = \omega_y = 11$ μm; (■) $\omega_x = 31$ μm, $\omega_y = 25$ μm; (∇) $\omega_x = 51$ μm, $\omega_y = 36$ μm; (•) $\omega_x = 73$ μm, $\omega_y = 47$ μm; (□) $\omega_x = 95$ μm, $\omega_y = 64$ μm; (–) linear fit. The insert corresponds to a magnification of the points corresponding to the smallest beam dimensions. (Colina *et al*. 2006 [86]. Reproduced with permission of American Institute of Physics.)

different series are perfectly correlated with the laser beam dimensions, thus a fluence threshold F_0 can be inferred from this correlation [86]. F_0 corresponds to the peak fluence of a Gaussian beam with pulse energy E_0, and it has been identified as the minimum fluence required to generate the cavitation bubble that starts fluid impulsion. However, the formation of the cavitation bubble does not grant deposition (the behavior shown in Figure 4.3 is a good example of this), which explains why the threshold for droplet printing is higher than E_0.

Equation (4.1) requires some additional considerations. Figure 4.9a shows a cross section of the fluence distribution of a pulsed Gaussian beam that would lead to fluid deposition. For this to occur, its energy E must be higher than E_0 and thus its fluence peak F_p higher than F_0; in this plot, therefore, the "volume" below the solid curve is E (it must be taken into account that the laser beam profile has cylindrical symmetry and that, in consequence, the area in the plot actually corresponds to a volume). On the other hand, the dashed curve corresponds to the profile of a pulse whose fluence peak is F_0 and accordingly its energy is E_0 (the

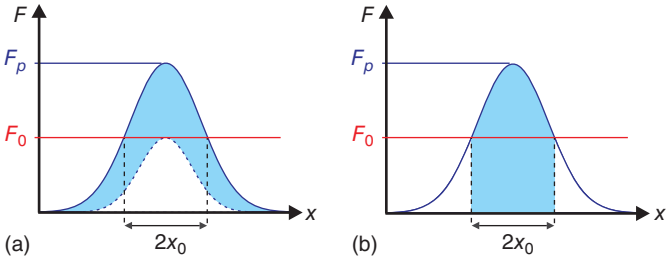

Figure 4.9 Cross section of the three-dimensional plot of the local fluence function along the *fluence-x* plane for a laser pulse in which the fluence peak is higher than F_o. (a) The volume corresponding to the shaded area equals $E–E_o$, and the dashed line corresponds to a laser pulse of total energy equal to E_o. (b) The volume corresponding to the shaded area equals E_{eff}. (Duocastella *et al*. 2012 [62]. Reproduced with permission of Springer.)

volume in white below the dashed curve). Consequently, the shaded region corresponds to $E - E_0$, which is the amount of energy directly correlated with the deposited volume through Eq. (4.1). It is straightforward to prove, though, that the "volume" of the shaded area in Figure 4.9a is exactly the same as that in the shaded area of Figure 4.9b [62], which provides an interpretation for Eq. (4.1): only the portion of laser beam with fluence above the threshold F_o is effective ($E_{\text{eff}} = E - E_o$) in propelling the liquid.

The final volume of deposited liquid is, according to Eq. (4.1), proportional to E_{eff}. Figure 4.10 shows this proportionality for the series in Figure 4.8, corresponding to different spot sizes. Remarkably, all the points are aligned along the same line. This behavior is compatible with a model proposed in [86] according to which the deposited volume would equal the volume of a cylinder in the donor thin film whose base corresponds to the area of the region wherein the local fluence is higher than F_0 and whose height corresponds to the donor film thickness. The model correctly predicts the volume of the printed droplets for low pulse energies ($E < 3.5E_0$) whenever the diameter of the beam is considerably larger than the thickness of the donor film and fails otherwise [62]. It has to be noted that under these conditions, the model allows to roughly estimate the K parameter in Eq. (4.1). In fact, for a donor film with thickness d, the volume of the cylinder V_c can be approximated by

$$V_c \cong \frac{0.57d}{F_0} E_{\text{eff}} \tag{4.2}$$

Consequently, whenever the cylinder model applies, the K parameter is independent of the laser beam dimensions, which is in good agreement with the observations.

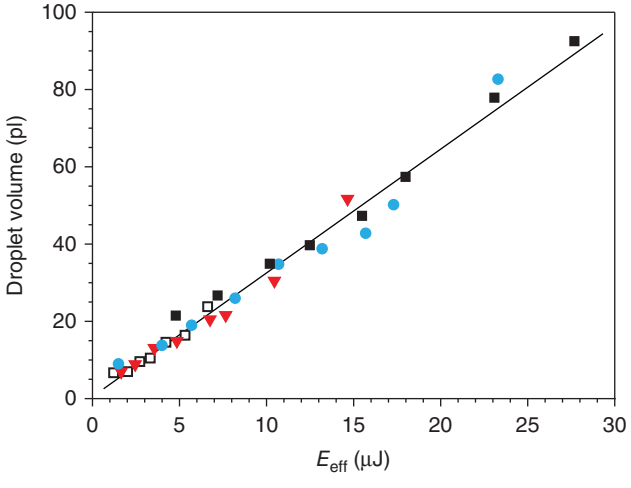

Figure 4.10 Plot of the droplet volume versus E_{eff} for the results in Figure 4.8 corresponding to the LIFT of a water and glycerol solution with the following laser beam radii: (□) $\omega_x = 31$ μm, $\omega_y = 25$ μm; (▼) $\omega_x = 51$ μm, $\omega_y = 36$ μm; (●) $\omega_x = 73$ μm, $\omega_y = 47$ μm; (■) $\omega_x = 95$ μm, $\omega_y = 64$ μm; (–) linear fit. (Duocastella *et al*. 2012 [62]. Reproduced with permission of Springer.)

4.3.2 Role of the Fluid Properties

The LIFT technique benefits of its ability to operate with fluids with very different rheological properties. As already mentioned in Section 4.1, this permits the printing of fluid solutions with minimum formulation and represents a clear advantage over other additive direct-writing techniques such as inkjet printing or pin microspotting. However, the printing results certainly depend on the fluid properties.

Most of the fluid properties are intrinsic to the ink formulation and therefore cannot be varied without altering its composition. The only parameter associated to the liquid that can be controlled independently from the rest of fluid properties is the thickness of the donor layer (d). Comparative studies of droplets deposited from donors with different thickness show an increase of the deposited volume when using thicker donor layers [59, 60]. Whenever the cylinder model applies, Eq. (4.2) predicts a proportional increase of the K parameter with the donor layer thickness. Beyond the range of the model, the amount of printed liquid increases more rapidly, but nevertheless, a linear relationship between K and d is still found [60]. The threshold energy required for printing also increases with thickness: the bubble has to push a higher amount of fluid in front of it, and this requires additional energy. However, the fluence threshold F_0 does not change with thickness [60]: irrespective of the donor thickness, for a given liquid, the fluence required for bubble generation must be always the same.

Among the different characteristics of the fluid, viscosity has been the most widely studied and presents an important influence in the deposition behavior [59, 61, 64, 83, 93]. A broad range of fluid viscosities has been successfully printed through LIFT, from water-based solutions ($\sim 10^{-3}$ Pa s) to screen printing inks ($\sim 10^{2}$ Pa s) [61, 94]. However, no clear relationship between the deposited volume and viscosity has been found [59, 93]. For water and glycerol solutions, the trend of the deposited volume has a maximum at a given viscosity that depends on the laser fluence (Figure 4.11) [93], and a similar trend has been found for fluids based on alginate solutions [59]. Viscosity helps to stabilize the jet [61], which in turn makes the deposition of circular and uniform droplets more reproducible. This can be correlated with the jet dynamics. The jet speed decreases with increasing viscosity [59]. Therefore, jets develop under a more stable and laminar regime that leads to gentle deposition of circular droplets, without the presence of satellites and splashing. At very low viscosities (below $\sim$10 mPa s), bursting is prone to occur at fluences not far from the threshold, as internal cohesive forces are low and do not withstand the high pressures induced inside the expanding bubble [61]. Consequently, for liquids with low viscosity, the range of fluences leading to good printing outcomes is narrow, and the LIFT parameters must be carefully adjusted. With the increase in viscosity, the minimum energy required for deposition increases since the jet recoil occurs at shorter distances [64].

4.3.3 Setup Parameters

A minimum gap between the donor thin film and the receiving substrate must be kept in order to prevent any contact between them, which might cause the

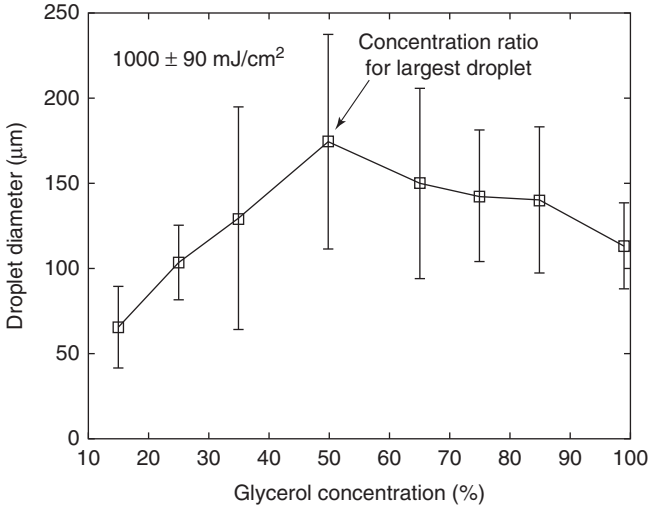

Figure 4.11 Plot of the droplet diameter as a function of glycerol concentration of water–glycerol solutions deposited by LIFT with spot diameter of 150 μm of an ArF excimer laser. (Lin *et al*. 2009 [93]. Reproduced with permission of AIP.)

uncontrolled massive transfer of fluid. Since jets generated in LIFT are stable during several millimeters of travel, transfer in the jetting regime allows some tolerance in the setting up of the gap between the donor and the receiver [57, 78, 83, 92, 95]. Thus, the gap can range from few tens of micrometers up to few millimeters, as it is shown in Figure 4.12. This degree of tolerance is really advantageous in view of a further industrial implementation of the technique in a production line. However, for small gaps and under certain operating conditions, the jet speed when impacting the receiving surface can be faster than for large gaps, and this can lead to the modification of the contact angle [31, 65], which in turn results in obtaining different droplet diameters. Even in the extreme case of very small gaps, when the bubble contacts the receiving substrate before the jet is formed, a droplet can be deposited [78]. In this case, although the deposition mechanism is substantially different, the volume transferred is similar to that for larger gaps. However, the final dimensions of the droplets are different because of the different contact angles. Consequently, the gap between the donor and the receiver can influence the wetting of the fluid on the receiving surface [33, 65, 96].

When the fluid is transparent to the laser radiation, an absorption layer must be used. Remarkable differences in the transfer of fluids have been observed when comparing LIFT performed with and without a specific absorbing layer [31, 32, 66]. Results from different studies show that the use of an absorbing layer helps to better control the deposition process. The range of laser fluences leading to the deposition of circular droplets without splashing or satellites is sensibly wider when an absorption layer is used (Figure 4.7). In fact, the generated jet attains higher speeds when LIFT is performed without absorption layer [66], and as pointed out in Section 4.2.1, high speeds promote turbulent jets that produce irregular deposits and satellites.

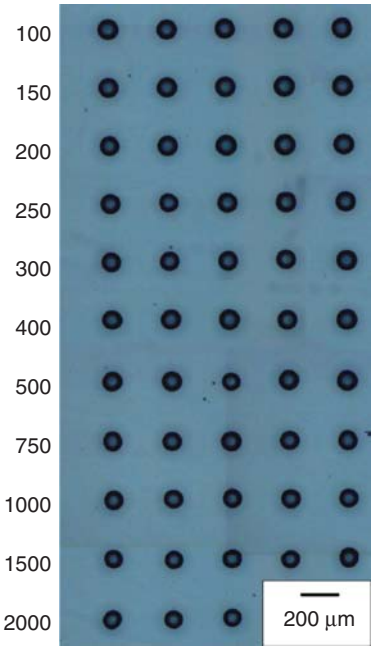

Figure 4.12 Optical microscope image of a microarray of droplets obtained through LIFT at constant laser pulse energy and at different donor–receiver gaps. The separation distance is indicated on the left, in micrometers. The transferred solution corresponds to a mixture of water and glycerol. (Serra *et al*. 2009 [92]. Reproduced with permission of Elsevier.)

4.4 Printing Lines and Patterns with LIFT

LIFT is a drop-on-demand technique. As described in the preceding sections, in LIFT, every single laser pulse promotes the deposition of a single droplet. For the printing of complex patterns, both donor and receiving substrates have to be translated to the position wherein a droplet has to be deposited. Alternatively, the laser beam can be scanned along the donor film in order to sequentially print the desired pattern. However, that pattern does not correspond to a set of isolated droplets in general. Rather, it is usually composed of continuous lines and areas, and this requires printing adjacent droplets with an optimum overlap between them. This is not always a trivial task, not only for LIFT, but for any printing technique operating with fluids, since contiguous droplets must merge or coalesce adequately in order to get the desired shape. There is no universal recipe since the results depend on many variables and especially on the particular rheological properties of the ink as well as on its wetting properties on the specific substrate.

The production of continuous lines of conductive materials for electronic circuits is probably one of the most challenging instances wherein printing continuous patterns is required. Just a single discontinuity in one point of a line can compromise the operation of the full device. Thus, most of the works on printing continuous patterns have been focused on printing lines of silver conductive inks [31, 32, 97–100]. Nevertheless, patterns of water-based solutions have also attracted considerable attention due to their interest in sensors and biomedical applications [35, 96, 101, 102].

The width of the printed lines is controlled through the droplet size, and their morphology strongly depends on the overlap between adjacent droplets.

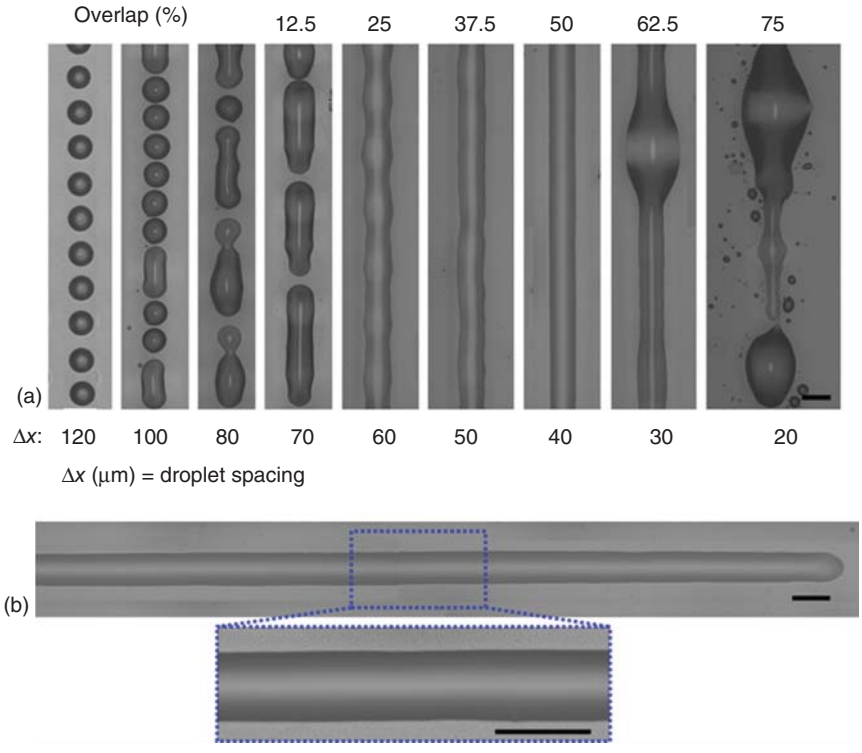

Figure 4.13 Optical microscopy image of (a) LIFT-printed droplets of a water–glycerol solution at different separation distance, Δx, and (b) 2 mm uniform line printed at 40 μm droplet separation distance; inset: area of the uniform line printed at 40 μm droplet spacing. Printing direction is (a) from top to bottom, and (b) from left to right. The transferred solution corresponds to a mixture of water and glycerol. Scale bar is 100 μm. (Palla-Papavlu *et al*. 2013 [101]. Reproduced with permission of Springer.)

Figure 4.13 shows a typical evolution of lines printed with different overlap for a water and glycerol solution. When the distance between consecutive droplets (measured from center to center) is sensibly higher than the droplet diameter, isolated droplets are obtained. At distances close to the droplet diameter but without overlap, droplets are still isolated, but some pairs of droplets can appear merged as a consequence of an exceptional spreading of the droplet, which leads to coalescence. This can be caused by the instability of the laser pulse energy or by inhomogeneities in the receiving surface. For small overlaps, broken lines are produced. Continuous lines are observed when the overlap is higher than 25%. However, the lines present a scalloped morphology for overlaps below 50% in this case. The presence or absence of scalloping is related with the deposition dynamics [101]. It is found that for those water-based solutions, uniform lines are obtained when the droplet being deposited contacts the already deposited line during its initial expansion, and the jet continues feeding liquid to the line. The flow associated with the jet is much higher than the capillary flows developing within the growing line, and this prevents the pinning of the lateral contact line

that is responsible for the scalloped morphology. For high overlaps, though, bulges appear as a consequence of the development of instabilities within the already printed line. This phenomenon is not exclusive of LIFT [103–105], and its prevention is one of the main challenges for any printing technique. Because of the high content of liquid when the overlap is high, any irregularity in the contact line can grow due to the backward capillary flow arising from the pressure gradient between the front and the incipient bulge of the printed line. The bulge growth can continue until the bridge line connecting the bulge with the front is large enough for the viscous forces to interrupt the fluid flow. When the overlap is very high, the jet impacts directly on the printed line producing splashing.

The printing of uniform continuous lines is not usually an easy task because the window of the overlap parameter can be very narrow depending on the fluid composition. Hence, small deviations of any parameter can cause the emergence of defects in the line. In order to overcome these drawbacks, alternative approaches have been proposed [98–100]. The first proposes the printing of two sets of equally spaced droplets [98]. The first set of droplets is printed without overlap between them. Afterward, the printed droplets are dried before the second set of droplets is printed. This last set is printed with a shift respect to the first set corresponding to half the distance between consecutive droplets. The presence of the dry material mitigates the capillary flows producing bulging and allows the printing of continuous lines. However, the insertion of a drying step compromises the printing speed and complicates its setting up in a production line. Another approach corresponds to printing inside fluidic guides previously fabricated in the substrate [98]. The fluidic guide helps to confine the liquid inside it, preventing bulge formation. The guide must be filled with enough volume of liquid so that continuous lines are obtained, but an excessive amount of liquid can cause overflow beyond the guide walls. Fluidic guides are especially helpful for achieving complicated geometries with high resolution, such as sharp angles difficult to achieve with direct printing. Furthermore, as lasers can be used for ablation, the fluidics guides can be machined with the same laser that is later used for LIFT. Later on, the laser can also be used for sintering the deposited material in order to achieve the desired functional properties [99, 100]. In a complementary approach, and taking advantage of all the possibilities of the laser tool, LIFT can be performed first for printing continuous lines, and in a second step, selective laser ablation can be carried out for removing defects and/or decreasing the line width [99]. Conductive lines with a resolution of 1 μm in width have been produced on flexible substrates in this way.

LIFT can also be used for selectively covering areas [35, 96, 102]. In this case, LIFT offers the possibility to significantly decrease the contact angle between the fluid being printed and the receiving substrate by only changing the deposition conditions [96]. In general, the contact angle is influenced by the surface roughness of the receiving substrate. Droplets gently deposited with low-speed jets present contact angles similar to droplets deposited with a pipette [96]. In this case, the droplet can be suspended on the crest of the rough pattern, and the surface tension of the liquid impedes the fluid to fill up the valleys and completely cover all the surface (Cassie–Baxter wetting). However, the high pressure associated with fast jets generated by LIFT allows to overcome surface tension,

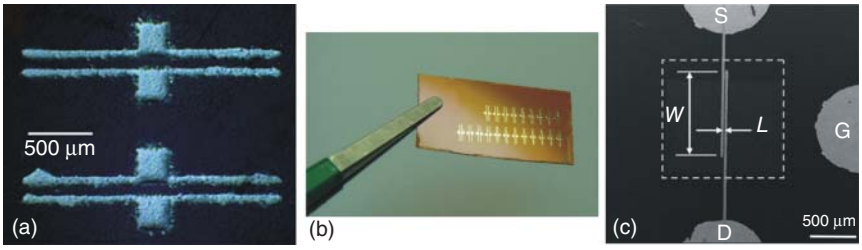

Figure 4.14 (a) Optical microscopy image of LIFT-printed AgNP electrodes on PI with 70 μm width and 2 mm length. (Zacharatos *et al*. 2016 [100]. Reproduced with permission of Elsevier.) (b) Image of sample consisting of 21 pairs of electrodes with spacing between electrode pairs of 50, 100, and 200 μm. (Zacharatos *et al*. 2016 [100]. Reproduced with permission of Elsevier.) (c) SEM image of a pentacene TFT with top-contact geometry ($L = 10$ μm, $W = 1000$ μm). The electrodes were printed with LIFT [97]. The pentacene layer corresponds to the area enclosed by the broken-line square. S represents the source, D represents the drain, and G represents the gate. (Kim *et al*. 2009 [97]. Reproduced with permission of Springer.)

and the fluid can enter the valleys covering the whole surface (Wenzel wetting). This limits the coffee-ring effect during drying and permits a more uniform distribution of the material [35, 65]. In this way, sensors with materials deposited with LIFT exhibit better performance than others deposited with other traditional techniques [33, 34, 102]. Examples of lines and areas of conductive inks printed through LIFT are shown in Figure 4.14.

Undesired features such as satellites, misaligned or irregular droplets appear when LIFT is pushed to the limit, for example, when operating with extremely high repetition rates in order to get the highest production yields [2, 106]. As described in the preceding sections, the ejection and deposition dynamics take several microseconds to occur. However, different ejection dynamics have been observed through time-resolved imaging when multiple cavitation bubbles are generated at a short distance between each other in a short time interval [107, 108]. Bubbles expanding simultaneously at a close distance interact, and as a result of this interaction, the induced jets are deflected from the forward direction, and new jets can appear in random directions [107, 109]. All these features can lead to uncontrollable deposition. Consequently, special care must be taken when printing through LIFT at very high speed in order to prevent undesired effects such as the ones described here.

4.5 Summary

LIFT is a feasible technique for printing fluids. Round and uniform droplets with volumes ranging from femtoliters to nanoliters can be successfully printed from fluid donor layers with almost no restriction concerning the rheological properties of the printed ink. Thus, a broad range of materials can be printed through LIFT in a digital way without requiring complex ink formulations.

In the LIFT of fluids, the absorption of the laser pulse generates a vapor bubble in the liquid donor film, from which expansion and further collapse a jet emerges

and propagates toward the receiving substrate. The contact of the jet with that substrate results in the growth of a sessile droplet, the outcome of the printing event. Complex patterns can be printed through the repetition of this procedure combined with the relative translation of the donor/receiver system with respect to the laser beam.

Thanks to its versatility, the LIFT of fluids can find application in a number of fields, from the manufacturing of printed electronics devices to the growth of human tissue for regenerative medicine. In the following chapters, the reader can find details about those applications, as well as about the LIFT of particular fluids (complex fluids, soft materials, high viscosity) and alternative approaches (blister-assisted LIFT, FF-LP).

Acknowledgments

The authors would like to thank Mr Edgar Lendínez for his collaboration in the acquisition of time-resolved images of the LIFT deposition process. Works presented in this chapter have been funded by MINECO of the Spanish Government (Projects TEC2014-54544-C2-1-P and TEC2015-72425-EXP) and also by Fondo Europeo de Desarrollo Regional (FEDER).

References

1 Arnold, C.B., Serra, P., and Piqué, A. (2007) Laser direct-write techniques for printing of complex materials. *MRS Bull.*, **32**, 23–31.
2 Hennig, G., Baldermann, T., Nussbaum, C., Rossier, M., Brockelt, A., Schuler, L., and Hochstein, G. (2012) Lasersonic® LIFT process for large area digital printing. *J. Laser Micro/Nanoeng.*, **7**, 299–305.
3 Ru, C., Luo, J., Xie, S., and Sun, Y. (2014) A review of non-contact micro- and nano-printing technologies. *J. Micromech. Microeng.*, **24**, 053001.
4 Brisbane, A.D. (1966) Method for vapour depositing a material in the form of a pattern. Great Britain Patent GB1,138,084, filed July 22, 1966 and issued Dec 27, 1968.
5 Braudy, R.S. (1969) Laser writing. *Proc. IEEE*, **57**, 1771–1772.
6 Brisbane, A.D. (1967) Pattern deposit by laser. US Patent US3,560,258, filed May 31, 1967 and issued Feb 2, 1971.
7 Levene, M.L., Scott, R.D., and Siryj, B.W. (1970) Material transfer recording. *Appl. Opt.*, **9**, 2260–2265.
8 Bohandy, J., Kim, B.F., and Adrian, F.J. (1986) Metal deposition from a supported metal film using an excimer laser. *J. Appl. Phys.*, **60**, 1538–1539.
9 Adrian, F.J., Bohandy, J., Kim, B.F., Jette, A.N., and Thompson, P. (1987) A study of the mechanism of metal-deposition by the laser-induced forward transfer process. *J. Vac. Sci. Technol., B*, **5**, 1490–1494.
10 Bohandy, J., Kim, B.F., Adrian, F.J., and Jette, A.N. (1988) Metal-deposition at 532 nm using a laser transfer technique. *J. Appl. Phys.*, **63**, 1158–1162.

11 Schultze, V. and Wagner, M. (1991) Laser-induced forward transfer of aluminum. *Appl. Surf. Sci.*, **52**, 303–309.

12 Kántor, Z., Tóth, Z., and Szörényi, T. (1992) Laser induced forward transfer: the effect of support-film interface and film-to-substrate distance on transfer. *Appl. Phys. A Mater.*, **54**, 170–175.

13 Zergioti, I., Mailis, S., Vainos, N.A., Fotakis, C., Chen, S., and Grigoropoulos, C.P. (1998) Microdeposition of metals by femtosecond excimer laser. *Appl. Surf. Sci.*, **127–129**, 601–605.

14 Greer, J.A. and Parker, T.E. (1988) Laser-induced forward transfer of metal oxides to trim the frequency of surface acoustic wave resonator devices. Proceedings of SPIE, vol. 998, pp. 113–125.

15 Zergioti, I., Mailis, S., Vainos, N.A., Papakonstantinou, P., Kalpouzos, C., Grigoropoulos, C.P., and Fotakis, C. (1998) Microdeposition of metal and oxide structures using ultrashort laser pulses. *Appl. Phys. A Mater.*, **66**, 579–582.

16 Papakonstantinou, P., Vainos, N.A., and Fotakis, C. (1999) Microfabrication by UV femtosecond laser ablation of Pt, Cr and indium oxide thin films. *Appl. Surf. Sci.*, **151**, 159–170.

17 Fogarassy, E., Fuchs, C., Kerherve, F., Hauchecorne, G., and Perriere, J. (1989) Laser-induced forward transfer of high-Tc YBaCuO and BiSrCaCuO superconducting thin films. *J. Appl. Phys.*, **66**, 457–459.

18 Piqué, A., Chrisey, D.B., Auyeung, R.C.Y., Fitz-Gerald, J., Wu, H.D., McGill, R.A., Lakeou, S., Wu, P.K., Nguyen, V., and Duignan, M. (1999) A novel laser transfer process for direct writing of electronic and sensor materials. *Appl. Phys. A Mater.*, **69**, S279–S284.

19 Chrisey, D.B., Piqué, A., Fitz-Gerald, J., Auyeung, R.C.Y., McGill, R.A., Wu, H.D., Lakeou, S., and Duignan, M. (2000) New approach to laser direct writing active and passive mesoscopic circuit elements. *Appl. Surf. Sci.*, **154–155**, 593–600.

20 Fitz-Gerald, J.M., Piqué, A., Chrisey, D.B., Rack, P.D., Zeleznik, M., Auyeung, R.C.Y., and Lakeou, S. (2000) Laser direct writing of phosphor screens for high-definition displays. *Appl. Phys. Lett.*, **76**, 1386–1388.

21 Wu, P.K., Ringeisen, B.R., Callahan, J., Brooks, M., Bubb, D.M., Wu, H.D., Piqué, A., Spargo, B., McGill, R.A., and Chrisey, D.B. (2001) The deposition, structure, pattern deposition, and activity of biomaterial thin-films by matrix-assisted pulsed-laser evaporation (MAPLE) and MAPLE direct write. *Thin Solid Films*, **398–399**, 607–614.

22 Ringeisen, B.R., Chrisey, D.B., Piqué, A., Young, H.D., Modi, R., Bucaro, M., Jones-Meehan, J., and Spargo, B.J. (2002) Generation of mesoscopic patterns of viable *Escherichia coli* by ambient laser transfer. *Biomaterials*, **23**, 161–166.

23 Ringeisen, B.R., Wu, P.K., Kim, H., Piqué, A., Auyeung, R.Y.C., Young, H.D., Chrisey, D.B., and Krizman, D.B. (2002) Picoliter-scale protein microarrays by laser direct write. *Biotechnol. Progr.*, **18**, 1126–1129.

24 Skardal, A. and Atala, A. (2015) Biomaterials for integration with 3-D bioprinting. *Ann. Biomed. Eng.*, **43**, 730–746.

25 Nguyen, A.K. and Narayan, R.J. (2016) Liquid-phase laser induced forward transfer for complex organic inks and tissue engineering. *Ann. Biomed. Eng.*, **45**, 84–99.

26 Barron, J.A., Wu, P., Ladouceur, H.D., and Ringeisen, B.R. (2004) Biological laser printing: A novel technique for creating heterogeneous 3-dimensional cell patterns. *Biomed. Microdevices*, **6**, 139–147.

27 Fernández-Pradas, J.M., Colina, M., Serra, P., Domínguez, J., and Morenza, J.L. (2004) Laser-induced forward transfer of biomolecules. *Thin Solid Films*, **453–454**, 27–30.

28 Serra, P., Fernández-Pradas, J.M., Berthet, F.X., Colina, M., Elvira, J., and Morenza, J.L. (2004) Laser direct writing of biomolecule microarrays. *Appl. Phys. A Mater.*, **79**, 949–952.

29 Serra, P., Colina, M., Fernández-Pradas, J.M., Sevilla, L., and Morenza, J.L. (2004) Preparation of functional DNA microarrays through laser-induced forward transfer. *Appl. Phys. Lett.*, **85**, 1639–1641.

30 Rapp, L., Diallo, A.K., Alloncle, A.P., Videlot-Ackerman, C., Fages, F., and Delaporte, P. (2009) Pulsed-laser printing of organic thin film transistors. *Appl. Phys. Lett.*, **95**, 171109.

31 Rapp, L., Ailuno, J., Alloncle, A.P., and Delaporte, P. (2011) Pulsed-laser printing of silver nanoparticles ink: control of morphological properties. *Opt. Express*, **19**, 21563–21574.

32 Makrygianni, M., Kalpyris, I., Boutopoulos, C., and Zergioti, I. (2014) Laser induced forward transfer of Ag nanoparticles ink deposition and characterization. *Appl. Surf. Sci.*, **297**, 40–44.

33 Boutopoulos, C., Touloupakis, E., Pezzotti, I., Giardi, M.T., and Zergioti, I. (2011) Direct laser immobilization of photosynthetic material on screen printed electrodes for amperometric biosensor. *Appl. Phys. Lett.*, **98**, 093703/1–093703/3.

34 Touloupakis, E., Boutopoulos, C., Buonasera, K., Zergioti, I., and Giardi, M.T. (2012) A photosynthetic biosensor with enhanced electron transfer generation realized by laser printing technology. *Anal. Bioanal. Chem.*, **402**, 3237–3244.

35 Palla-Papavlu, A., Patrascioiu, A., Di Pietrantonio, F., Fernández-Pradas, J.M., Cannatà, D., Benetti, M., D'Auria, S., Verona, E., and Serra, P. (2014) Preparation of surface acoustic wave odor sensors by laser-induced forward transfer. *Sens. Actuators, B*, **192**, 369–377.

36 Sopeña, P., Fernández-Pradas, J.M., and Serra, P. (2017) Laser-induced forward transfer of low viscosity inks. *Appl. Surf. Sci.*, **418**, 530–535.

37 Wu, P.K., Ringeisen, B.R., Krizman, D.B., Frondoza, C.G., Brooks, M., Bubb, D.M., Auyeung, R.C.Y., Piqué, A., Spargo, B., McGill, R.A., and Chrisey, D.B. (2003) Laser transfer of biomaterials: Matrix-assisted pulsed laser evaporation (MAPLE) and MAPLE Direct Write. *Rev. Sci. Instrum.*, **74**, 2546–2557.

38 Chrisey, D.B., Piqué, A., McGill, R.A., Horwitz, J.S., Ringeisen, B.R., Bubb, D.M., and Wu, P.K. (2003) Laser deposition of polymer and biomaterial films. *Chem. Rev.*, **103**, 553–576.

39 Barron, J.A., Rosen, R., Jones-Meehan, J., Spargo, B.J., Belkin, S., and Ringeisen, B.R. (2004) Biological laser printing of genetically modified Escherichia coli for biosensor applications. *Biosens. Bioelectron.*, **20**, 246–252.

40 Barron, J.A., Spargo, B.J., and Ringeisen, B.R. (2004) Biological laser printing of three dimensional cellular structures. *Appl. Phys. A Mater.*, **79**, 1027–1030.

41 Guillemot, F., Souquet, A., Catros, S., Guillotin, B., Lopez, J., Faucon, M., Pippenger, B., Bareille, R., Rémy, M., Bellance, S., Chabassier, P., Fricain, J.C., and Amédée, J. (2010) High-throughput laser printing of cells and biomaterials for tissue engineering. *Acta Biomater.*, **6**, 2494–2500.

42 Hopp, B., Smausz, T., Antal, Z., Kresz, N., Bor, Z., and Chrisey, D. (2004) Absorbing film assisted laser induced forward transfer of fungi (Trichoderma conidia). *J. Appl. Phys.*, **96**, 3478–3488.

43 Hopp, B., Smausz, T., Kresz, N., Barna, N., Bor, Z., Kolozsvári, L., Chrisey, D.B., Szabó, A., and Nógrádi, A. (2005) Survival and proliferative ability of various living cell types after laser-induced forward transfer. *Tissue Eng.*, **11**, 1817–1823.

44 Guillemot, F., Souquet, A., Catros, S., and Guillotin, B. (2010) Laser assisted cell printing: principle, physical parameters versus cell fate and perspectives in tissue engineering. *Nanomedicine*, **5**, 507–515.

45 Ali, M., Pages, E., Ducom, A., Fontaine, A., and Guillemot, F. (2014) Controlling laser-induced jet formation for bioprinting mesenchymal stem cells with high viability and high resolution. *Biofabrication*, **6**, 045001.

46 Brown, M.S., Kattamis, N.T., and Arnold, C.B. (2010) Time-resolved study of polyimide absorption layers for blister-actuated laser-induced forward transfer. *J. Appl. Phys.*, **107**, 083103.

47 Brown, M.S., Kattamis, N.T., and Arnold, C.B. (2011) Time-resolved dynamics of laser-induced micro-jets from thin liquid films. *Microfluid. Nanofluid.*, **11**, 199–207.

48 Auyeung, R.C.Y., Kim, H., Birnbaum, A.J., Zalalutdinov, M., Mathews, S.A., and Piqué, A. (2009) Laser decal transfer of free standing microcantilevers and microbridges. *Appl. Phys. A Mater.*, **97**, 513–519.

49 Wang, J., Auyeung, R.C.Y., Kim, H., Charipar, N.A., and Piqué, A. (2010) Three-dimensional printing of interconnects by laser direct-write of silver nanopastes. *Adv. Mater.*, **22**, 4462–4466.

50 Auyeung, R.C.Y., Kim, H., Charipar, N.A., Birnbaum, A.J., Mathews, S.A., and Piqué, A. (2011) Laser forward transfer based on a spatial light modulator. *Appl. Phys. A Mater.*, **102**, 21–26.

51 Duocastella, M., Patrascioiu, A., Fernández-Pradas, J.M., Morenza, J.L., and Serra, P. (2010) Film-free laser forward printing of transparent and weakly absorbing liquids. *Opt. Express*, **18**, 21815.

52 Duocastella, M., Fernández-Pradas, J.M., Morenza, J.L., Zafra, D., and Serra, P. (2010) Novel laser printing technique for miniaturized biosensors preparation. *Sens. Actuators, B*, **145**, 596–600.

53 Patrascioiu, A., Fernández-Pradas, J.M., Morenza, J.L., and Serra, P. (2012) Microdroplet deposition through a film-free laser forward printing technique. *Appl. Surf. Sci.*, **258**, 9412–9416.

54 Desrus, H., Chassagne, B., Moizan, F., Devillard, R., Petit, S., Kling, R., and Catros, S. (2016) Effective parameters for film-free femtosecond laser assisted bioprinting. *Appl. Opt.*, **55**, 3879–3886.

55 Duocastella, M., Fernández-Pradas, J.M., Serra, P., and Morenza, J.L. (2008) Jet formation in the laser forward transfer of liquids. *Appl. Phys. A Mater.*, **93**, 453–456.

56 Duocastella, M., Fernández-Pradas, J.M., Morenza, J.L., and Serra, P. (2009) Time-resolved imaging of the laser forward transfer of liquids. *J. Appl. Phys.*, **106**, 084907.

57 Duocastella, M., Fernández-Pradas, J.M., Morenza, J.L., and Serra, P. (2010) Sessile droplet formation in the laser-induced forward transfer of liquids: A time-resolved imaging study. *Thin Solid Films*, **518**, 5321–5325.

58 Unger, C., Gruene, M., Koch, L., Koch, J., and Chichkov, B.N. (2010) Time-resolved imaging of hydrogel printing via laser-induced forward transfer. *Appl. Phys. A Mater.*, **103**, 271–277.

59 Gruene, M., Unger, C., Koch, L., Deiwick, A., and Chichkov, B.N. (2011) Dispensing pico to nanolitre of a natural hydrogel by laser-assisted bioprinting. *Biomed. Eng. Online*, **10**, 19/1–19/11.

60 Duocastella, M., Patrascioiu, A., Dinca, V., Fernández-Pradas, J.M., Morenza, J.L., and Serra, P. (2011) Study of liquid deposition during laser printing of liquids. *Appl. Surf. Sci.*, **257**, 5255–5258.

61 Dinca, V., Patrascioiu, A., Fernández-Pradas, J.M., Morenza, J.L., and Serra, P. (2012) Influence of solution properties in the laser forward transfer of liquids. *Appl. Surf. Sci.*, **258**, 9379–9384.

62 Duocastella, M., Patrascioiu, A., Fernández-Pradas, J.M., Morenza, J.L., and Serra, P. (2012) On the correlation between droplet volume and irradiation conditions in the laser forward transfer of liquids. *Appl. Phys. A Mater.*, **109**, 5–14.

63 Kuznetsov, A.I., Unger, C., Koch, J., and Chichkov, B.N. (2012) Laser-induced jet formation and droplet ejection from thin metal films. *Appl. Phys. A Mater.*, **106**, 479–487.

64 Yan, J., Huang, Y., Xu, C., and Chrisey, D.B. (2012) Effects of fluid properties and laser fluence on jet formation during laser direct writing of glycerol solution. *J. Appl. Phys.*, **112**, 083105.

65 Boutopoulos, C., Papageorgiou, D.P., Zergioti, I., and Papathanasiou, A.G. (2013) Sticking of droplets on slippery superhydrophobic surfaces by laser induced forward transfer. *Appl. Phys. Lett.*, **103**, 024104.

66 Boutopoulos, C., Kalpyris, I., Serpetzoglou, E., and Zergioti, I. (2014) Laser-induced forward transfer of silver nanoparticle ink: time-resolved imaging of the jetting dynamics and correlation with the printing quality. *Microfluid. Nanofluid.*, **16**, 493–500.

67 Zhang, Z., Xiong, R., Mei, R., Huang, Y., and Chrisey, D.B. (2015) Time-resolved imaging study of jetting dynamics during laser printing of viscoelastic alginate solutions. *Langmuir*, **31**, 6447–6456.

68 Zhang, Z., Xiong, R., Corr, D.T., and Huang, Y. (2016) Study of impingement types and printing quality during laser printing of viscoelastic alginate solutions. *Langmuir*, **32**, 3004–3014.

69 Eggers, J. (1997) Nonlinear dynamics and breakup of free-surface flows. *Rev. Mod. Phys.*, **69**, 865–929.

70 Mezel, C., Hallo, L., Souquet, A., Breil, J., Hebert, D., and Guillemot, F. (2009) Self-consistent modeling of jet formation process in the nanosecond laser pulse regime. *Phys. Plasmas*, **16**, 123112.

71 Patrascioiu, A., Fernández-Pradas, J.M., Palla-Papavlu, A., Morenza, J.L., and Serra, P. (2014) Laser-generated liquid microjets: correlation between bubble dynamics and liquid ejection. *Microfluid. Nanofluid.*, **16**, 55–63.

72 Patrascioiu, A., Fernández-Pradas, J.M., Morenza, J.L., and Serra, P. (2014) Film-free laser printing: jetting dynamics analyzed through time-resolved imaging. *Appl. Surf. Sci.*, **302**, 303–308.

73 Pearson, A., Cox, E., Blake, J.R., and Otto, S.R. (2004) Bubble interactions near a free surface. *Eng. Anal. Boundary Elem.*, **28**, 295–313.

74 Rioboo, R., Marengo, M., and Tropea, C. (2002) Time evolution of liquid drop impact onto solid, dry surfaces. *Exp. Fluids*, **33**, 112–124.

75 Roux, D.C.D. and Cooper-White, J.J. (2004) Dynamics of water spreading on a glass surface. *J. Colloid Interface Sci.*, **277**, 424–436.

76 Kwok, D.Y., Gietzelt, T., Grundke, K., Jacobasch, H.J., and Neumann, A.W. (1997) Contact angle measurements and contact angle interpretation. 1. Contact angle measurements by axisymmetric drop shape analysis and a goniometer sessile drop technique. *Langumir*, **13**, 2880–2894.

77 Gao, L.C. and McCarthy, T.J. (2006) Contact angle hysteresis explained. *Langmuir*, **22**, 6234–6237.

78 Duocastella, M., Fernández-Pradas, J.M., Morenza, J.L., and Serra, P. (2011) Droplet printing through bubble contact in the laser forward transfer of liquids. *Appl. Surf. Sci.*, **257**, 2825–2829.

79 Palla-Papavlu, A., Shaw-Stewart, J., Mattle, T., Dinca, V., Lippert, T., Wokaun, A., and Dinescu, M. (2013) Comparison of 193nm and 308nm laser liquid printing by shadowgraphy imaging. *Appl. Surf. Sci.*, **278**, 180–184.

80 Liu, B. and Lange, F.F. (2006) Pressure induced transition between superhydrophobicstates: configuration diagrams and effect of surface feature size. *J. Colloid Interface Sci.*, **298**, 899–909.

81 Florian, C., Piazza, S., Diaspro, A., Serra, P., and Duocastella, M. (2016) Direct laser printing of tailored polymeric microlenses. *ACS Appl. Mater. Interfaces*, **8**, 17028–17032.

82 Duocastella, M., Colina, M., Fernández-Pradas, J.M., Serra, P., and Morenza, J.L. (2007) Study of the laser-induced forward transfer of liquids for laser bioprinting. *Appl. Surf. Sci.*, **253**, 7855–7859.

83 Dinca, V., Farsari, M., Kafetzopoulos, D., Popescu, A., Dinescu, M., and Fotakis, C. (2008) Patterning parameters for biomolecules microarrays constructed with nanosecond and femtosecond UV lasers. *Thin Solid Films*, **516**, 6504–6511.

84 Dinca, V., Ranella, A., Farsari, M., Kafetzopoulos, D., Dinescu, M., Popescu, A., and Fotakis, C. (2008) Quantification of the activity of

biomolecules in microarrays obtained by direct laser transfer. *Biomed. Microdevices*, **10**, 719–725.

85 Barron, J.A., Young, H.D., Dlott, D.D., Darfler, M.M., Krizman, D.B., and Ringeisen, B.R. (2005) Printing of protein microarrays via a capillary-free fluid jetting mechanism. *Proteomics*, **5**, 4138–4144.

86 Colina, M., Duocastella, M., Fernández-Pradas, J.M., Serra, P., and Morenza, J.L. (2006) Laser-induced forward transfer of liquids: Study of the droplet ejection process. *J. Appl. Phys.*, **99**, 084909.

87 Duocastella, M., Fernández-Pradas, J.M., Domínguez, J., Serra, P., and Morenza, J.L. (2008) Printing biological solutions through laser-induced forward transfer. *Appl. Phys. A Mater.*, **93**, 941–945.

88 Boutopoulos, C., Andreakou, P., Kafetzopoulos, D., Chatzandroulis, S., and Zergioti, I. (2008) Direct laser printing of biotin microarrays on low temperature oxide on Si substrates. *Phys. Status Solidi A*, **205**, 2505–2508.

89 Fernández-Pradas, J.M., Duocastella, M., Colina, M., Serra, P., and Morenza, J.L. (2007) Production of miniaturized biosensors through laser-induced forward transfer. Proceedings of SPIE, vol. 6592, 65920R1-8.

90 Duocastella, M., Fernández-Pradas, J.M., Serra, P., and Morenza, J.L. (2008) Laser-induced forward transfer of liquids for miniaturized biosensors preparation. *J. Laser Micro/Nanoeng.*, **3**, 1–4.

91 Fernández-Pradas, J.M., Serra, P., Colina, M., and Morenza, J.L. (2004) Production of biomolecule microarrays through laser induced forward transfer. Proceedings of SPIE, vol. 5662, pp. 582–585.

92 Serra, P., Duocastella, M., Fernández-Pradas, J.M., and Morenza, J.L. (2009) Liquids microprinting through laser induced forward transfer. *Appl. Surf. Sci.*, **255**, 5342–5345.

93 Lin, Y., Huang, Y., and Chrisey, D.B. (2009) Droplet formation in matrix-assisted pulsed-laser evaporation direct writing of glycerol water solution. *J. Appl. Phys.*, **105**, 093111.

94 Munoz-Martina, D., Brasz, C.F., Chen, Y., Morales, M., Arnold, C.B., and Molpeceres, C. (2016) Laser-induced forward transfer of high-viscosity silver pastes. *Appl. Surf. Sci.*, **366**, 389–396.

95 Palla-Papavlu, A., Paraico, I., Shaw-Stewart, J., Dinca, V., Savopol, T., Kovacs, E., Lippert, T., Wokaun, A., and Dinescu, M. (2011) Liposome micropatterning based on laser-induced forward transfer. *Appl. Phys. A Mater.*, **102**, 651–659.

96 Touloupakis, E., Chatzipetrou, M., Boutopoulos, C., Gkouzou, A., and Zergioti, I. (2014) A polyphenol biosensor realized by laser printing technology. *Sens. Actuators, B*, **193**, 301–305.

97 Kim, H., Auyeung, R.C.Y., Lee, S.H., Huston, A.L., and Piqué, A. (2009) Laser forward transfer of silver electrodes for organic thin-film transistors. *Appl. Phys. A Mater.*, **96**, 441–445.

98 Florian, C., Caballero-Lucas, F., Fernández-Pradas, J.M., Artigas, R., Ogier, S., Karnakis, D., and Serra, P. (2015) Conductive silver ink printing through the laser-induced forward transfer technique. *Appl. Surf. Sci.*, **336**, 304–308.

99 Florian, C., Caballero-Lucas, F., Fernández-Pradas, J.M., Ogier, S., Winchester, L., Karnakis, D., Geremia, R., Artigas, R., and Serra, P. (2016)

Printing of silver conductive lines through laser-induced forward transfer. *Appl. Surf. Sci.*, **374**, 265–270.

100 Zacharatos, F., Makrygianni, M., Geremia, R., Biver, E., Karnakis, D., Leyder, S., Puerto, D., Delaporte, P., and Zergioti, I. (2016) Laser Direct Write micro-fabrication of large area electronics on flexible substrates. *Appl. Surf. Sci.*, **374**, 117–123.

101 Palla-Papavlu, A., Córdoba, C., Patrascioiu, A., Fernández-Pradas, J.M., Morenza, J.L., and Serra, P. (2013) Deposition and characterization of lines printed through laser-induced forward transfer. *Appl. Phys. A Mater.*, **110**, 751–755.

102 Di Pietrantonio, F., Benetti, M., Cannatà, D., Verona, E., Palla-Papavlu, A., Fernández-Pradas, J.M., Serra, P., Staiano, M., and D'Auria, S. (2015) A surface acoustic wave bio-nose for detection of volatile odorant molecules. *Biosens. Bioelectron.*, **67**, 516–523.

103 Gau, H., Herminghaus, S., Lenz, P., and Lipowsky, R. (1999) Liquid morphologies on structured surfaces: from microchannels to microchips. *Science*, **283**, 46–49.

104 Duineveld, P.C. (2003) The stability of ink-jet printed lines of liquid with zero receding contact angle on a homogeneous substrate. *J. Fluid Mech.*, **477**, 175–200.

105 Stringer, J. and Derby, B. (2010) Formation and stability of lines produced by inkjet printing. *Langmuir*, **26**, 10365–10372.

106 Puerto, D., Biver, E., Alloncle, A.P., and Delaporte, P. (2016) Single step high-speed printing of continuous silver lines by laser-induced forward transfer. *Appl. Surf. Sci.*, **374**, 183–189.

107 Patrascioiu, A., Florian, C., Fernández-Pradas, J.M., Morenza, J.L., Hennig, G., Delaporte, P., and Serra, P. (2014) Interaction between jets during laser-induced forward transfer. *Appl. Phys. Lett.*, **105**, 014101.

108 Biver, E., Rapp, L., Alloncle, A.P., and Delaporte, P. (2014) Multi-jets formation using laser forward transfer. *Appl. Surf. Sci.*, **302**, 153–158.

109 Brasz, C.F., Yang, J.H., and Arnold, C.B. (2015) Tilting of adjacent laser-induced liquid jets. *Microfluid. Nanofluid.*, **18**, 185–197.

5

Advances in Blister-Actuated Laser-Induced Forward Transfer (BA-LIFT)

Emre Turkoz, Romain Fardel, and Craig B. Arnold

Princeton University, Department of Mechanical and Aerospace Engineering, Princeton Institute for Science and Technology of Materials, D410 Engineering Quadrangle/Bowen Hall Rm 320, Princeton, NJ 80544, USA

Blister-actuated laser-induced forward transfer (BA-LIFT) is a laser printing technique that enables the deposition of liquid droplets with lateral resolution down to a few micrometers. BA-LIFT was developed to overcome some of the limitations of classical LIFT by enabling the transfer of sensitive materials, such as functional polymers and molecules, biomolecules, and living organisms, while retaining their functionality intact. BA-LIFT utilizes a laser pulse that is absorbed in a thick polymer layer, which undergoes plastic deformation and forms a rapidly expanding blister. With an ink layer coating the polymer layer, this blister expansion provides the impulse for jet formation and ultimately material transfer. BA-LIFT is different compared to other conventional LIFT processes because the ink itself is not directly exposed to the laser, either optically or thermally during this process due to the thickness of the polymer layer. The jet is formed purely due to mechanical deformation, making sure that the chemical composition of the ink remains intact and undisturbed. As a result, this strategy has great potential for the transfer of delicate materials and can be used in bio-related applications and organic electronics. This chapter aims to explain the developments in the BA-LIFT process. Time-resolved imaging studies are presented along with the advances in the modeling of the BA-LIFT.

5.1 Introduction

Laser-induced forward transfer (LIFT) is a laser printing technique that enables the simultaneous transfer and patterning of material from a donor to an acceptor substrate with a lateral resolution down to a few micrometers [1, 2]. As described in many chapters in this book, this technique has been used in various solid or liquid printing applications ranging from organic biomaterials [3–6] to metals [7–9]. In the case of liquid LIFT, transfer is initiated in the form of a liquid jet that draws liquid from the donor film onto the acceptor substrate. The coupling of the laser energy into the liquid, also called *ink*, is therefore a critical part of the process. Conventional LIFT techniques employ two distinct mechanisms for

Laser Printing of Functional Materials: 3D Microfabrication, Electronics and Biomedicine,
First Edition. Edited by Alberto Piqué and Pere Serra.
© 2018 Wiley-VCH Verlag GmbH & Co. KGaA. Published 2018 by Wiley-VCH Verlag GmbH & Co. KGaA.

that purpose: the first one relies on the absorption of the laser pulse directly into the ink and is called direct-matrix absorption (DMA). The other technique uses a dynamic release layer (DRL) to absorb the laser energy. There are numerous studies published that compare both techniques with different inks and DRL materials [10–12]. However, for many sensitive materials, direct exposure to the laser beam or to the heat associated with laser absorption leads to unacceptable damages. Using a metal DRL does shield the ink from laser radiation, but not from heat. In addition, ablated metal particles can contaminate the ink, which is unacceptable in particular applications. Polymer DRLs, such as triazene polymer, offer an alternative to the contamination issue, but the vaporization of the thin layer still has the potential to damage the most sensitive materials. Blister-actuated LIFT (BA-LIFT) has been developed to mitigate these issues by fully isolating the transfer liquid from the light and heat of the laser beam and from contamination of ablation products. These concerns are adressed in the literature [11], and it is shown according to nuclear magnetic resonance (NMR) spectroscopy and photoluminescence (PL) studies that BA-LIFT preserves the integrity of sensitive inks where the other techniques can be damaging [13].

BA-LIFT distinguishes itself from other liquid LIFT techniques by the use of a relatively thick (~1–10 μm) polymer layer between the ink and the transparent substrate, which absorbs the laser. Upon ablation of a portion of the polymer film, the expansion of trapped gasses results in a blister on the polymer layer. This polymer blister fulfills two purposes: it converts the laser and chemical energy released during laser ablation into a mechanical impulse that propels the ink. It also fully shields the ink from laser light, heat, and contamination by ablation products. The comparison of BA-LIFT with other conventional LIFT techniques is presented in [14]. There it is shown that BA-LIFT preserves the integrity of thermally and mechanically sensitive luminophores, whereas DMA and DRL techniques result in the degradation of the chemical integrity of these substances.

The mechanism for BA-LIFT along with an example is illustrated in Figure 5.1. The distinct feature of BA-LIFT, the presence of a relatively thick polymer layer (polyimide) between the glass slide and the donor ink film, is represented in yellow in Figure 5.1a,b. A blister is created upon irradiation with a UV laser pulse, which creates the impulse to drive the donor ink film (shown in blue) into a jet. The right-hand side of Figure 5.1 shows the evolution of this jet as a time sequence obtained by pump-probe microscopy [16].

In summary, BA-LIFT offers a platform to print liquids and suspensions by relying on the mechanical impulse created through the rapid expansion of a thin polymer layer. In BA-LIFT, direct laser–ink interaction is prevented with the utilization of the polymer layer. The details and applications of this process are given in this chapter. The experimental setup for BA-LIFT is very similar to setups for the conventional LIFT experiment. The details on polymer layer deposition and the experimental methods are given in Section 5.2. Time-resolved imaging of the BA-LIFT jetting is presented in Section 5.3. Blister formation on polymer layers is investigated extensively, and details of this process can be found in Section 5.4. Jet formation during BA-LIFT is investigated using computational fluid dynamics (CFD). The modeling effort is presented in Section 5.5. BA-LIFT is used to transfer delicate materials while not disrupting the chemical integrity of the inks.

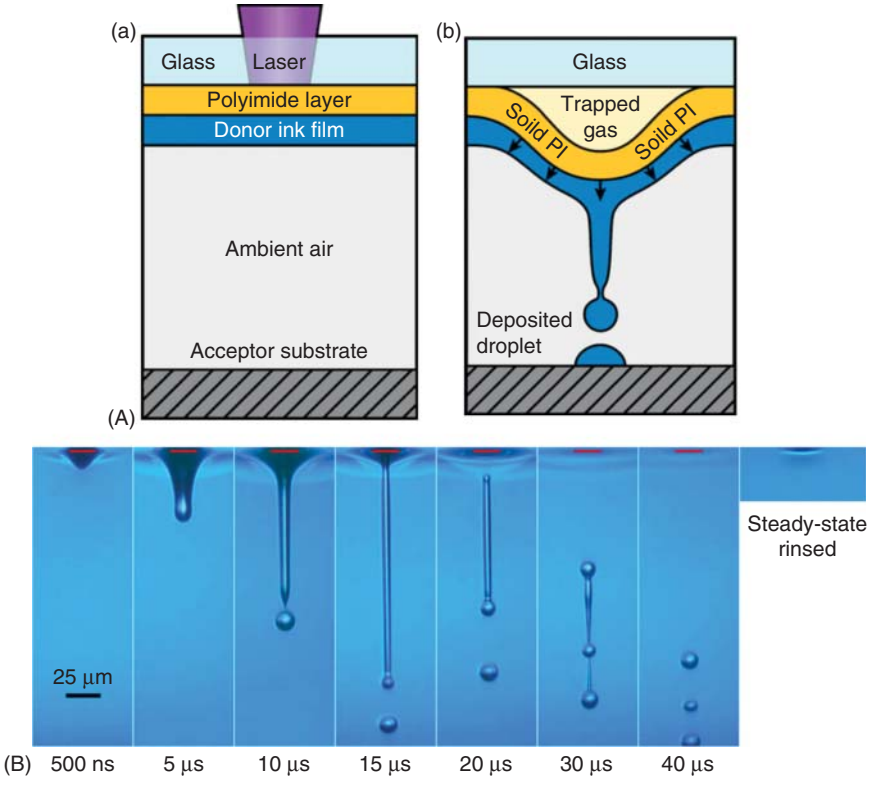

Figure 5.1 (A) Laser-induced forward transfer utilizing a polymer laser-absorbing layer: (a) the laser is absorbed within a thin layer of the polymer film, (b) ablating a confined pocket of gas and forcing the remaining film away from the glass as a rapidly expanding blister. If the impulse provided by the blister is sufficient, a small volume of ink is ejected onto an acceptor substrate [15]. (B) Transfers from a 10 µm film of NMP spread on 6 µm polyimide film initiated with a 20 µm beam at 1.3 J/cm^2 fluence. The vertical field of view is 200 µm, and the bars indicate the beam size and location [16]. (Brown *et al*. 2012 [15]. Reproduced with permission of Cambridge.)

An application for this is presented in Section 5.6. The chapter ends with the concluding remarks and directions for future work in Section 5.7.

5.2 BA-LIFT Basics

BA-LIFT works by the rapid creation of a blister from a polymer layer. The ideal polymer should strongly absorb the laser pulse within a short depth, undergo clean and efficient ablation, and deform plastically without rupturing. Additionally, this polymer should not dissolve in any solvent composing the ink. This last condition is also known as *solvent orthogonality*. One common polymer that satisfies all these criteria is polyimide [17]. Polyimide has the advantage of being among the most studied polymers for laser ablation, and its properties are well documented in the literature [17–19].

A polymer layer can be created by spin coating onto a glass microscope slides at various speeds to control layer thickness. In the specific case of polyimide, a precursor solution is applied and subsequent thermal processing is used to drive out excess solvent and complete the imidization process [12, 15, 16, 20]. After imidization and cross-linking, polyimide becomes practically insoluble and is therefore an ideal substrate on which water-based and organic inks are coated.

The laser used in the studies presented in this chapter is primarily a frequency-tripled Nd:YVO_4 laser, which has a wavelength of $\lambda = 355$ nm and a pulse duration of $\tau = 20$ ns; however, other laser wavelengths and pulse durations can be used provided they are absorbed in the polymer film leading to ablation of the material. Laser irradiation of polyimide with a nanosecond UV laser pulse results in decomposition of the polymer into fragments, notably gaseous species (CO, CO_2, HCN, and C_2H_2) [21, 22]. In the case of free-surface ablation, the ablation products are ejected from the surface under the action of the gas pressure. However, in the case of BA-LIFT, the rapid creation of ablated species confined between the intact portion of the film and the glass substrate leads to the buildup of pressure, which is released though the deformation of the remaining polyimide film into a blister. In order to achieve a proper blister, it is crucial that only a part of the film is ablated while the remaining layer stays intact. This *partial* ablation occurs when the penetration depth of the laser into the material, or more importantly the effective ablation depth, is smaller than the total thickness of the film.

For the experiments shown here, the thickness of the polyimide film is typically 3.5–7 μm, whereas the penetration or absorption depth, at which the incident intensity has dropped to $1/e$, is $d = 1/\alpha = 0.37$ μm. After 0.85 μm, the incident intensity has dropped to 10% of its initial value, which is well below the film thickness. The absorption depth allows us to estimate the residual intensity that is transmitted through the film. However, the absorption depth is not a good metric for the actual ablation depth [18]. In addition, the absorption process and optical reflection from the confined ablation plume make it difficult to model blister expansion for a given laser energy [23]. Therefore, experiments are critical for obtaining the specific details of blister formation and expansion.

5.3 Why BA-LIFT?

To appreciate the fundamental differences among different LIFT processes, it is instructive to perform time-resolved imaging [12]. In this study, we explored three different cases as described in Figure 5.2. The first case deals with a traditional titanium DRL layer, BA-LIFT is the second case, and the third case represents BA-LIFT where the blister ruptures due to excessive incident laser energy.

Time-resolved imaging studies require a 100 ns resolution to accurately capture the dynamics of the blister expansion and jet formation. Pump-probe imaging is performed by taking a single snapshot of a jet at particular time and shifting the delay between the pump and the probe to capture the whole sequence. All the BA-LIFT studies used a nanosecond flash lamp or diode along

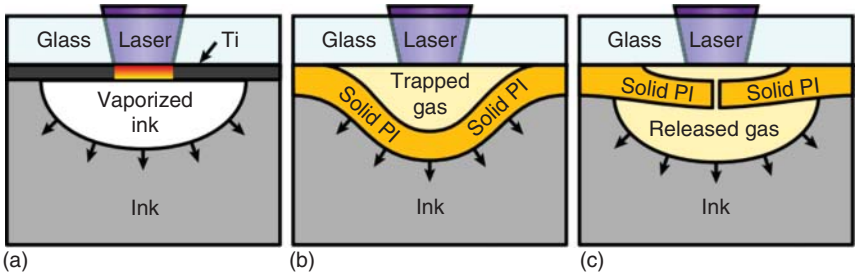

Figure 5.2 Mechanisms for laser-induced actuation of flow within the ink film. (a) Laser absorption within a Ti film that results in vaporization of the solvents in adjacent ink. (b) Laser absorption within a PI layer produces an expanding, sealed blister. (c) Laser absorption within a PI layer causes its rupture and releases high-pressure gases. (Brown *et al*. 2011 [12]. Reproduced with permission of Springer.)

with a charge-coupled device (CCD) camera connected to a delay generator and synchronized with the laser pulse. The delay between the lamp and the laser is adjusted to capture the snapshots of the formed jet. This method has become popularized in different studies [12, 20, 24–26] in the literature by many research groups. Some studies also employ a second laser and a beam expander to light the system [10, 27, 28].

With a metal absorber, the required energy to create jet formation is lower than that in the BA-LIFT cases. The resulting images are given in Figure 5.3.

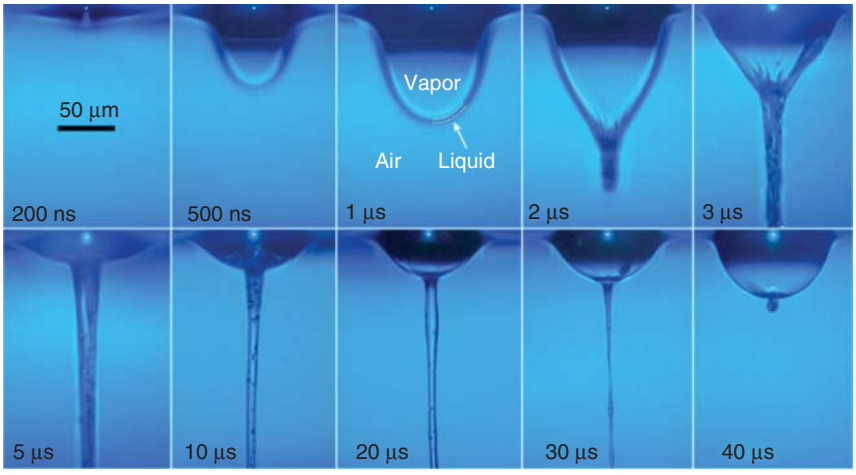

Figure 5.3 Time-resolved images of liquid ejection into the ambient air using a 50 nm titanium-absorbing layer. A 1.6 µJ laser pulse is focused into the titanium film to a spot size of 2.5 µm (indicated by a white marker), initiating liquid ejection from an adjacent 5 µm film [12]. Fluid motion is initiated by focusing a 1.6 µJ laser pulse into the titanium layer to a 2.5 µm Gaussian spot. This value is observed to be the threshold value for 5 µm liquid donor film using a 50 nm titanium metal absorber layer. The ink used in this study consists of an aqueous solution of glycerol (50% v/v) with Triton X-100 surfactant (1.4% v/v), a solution commonly employed in the literature [31, 32]. (Brown *et al*. 2011 [12]. Reproduced with permission of Springer.)

Absorption of the laser into the titanium layer causes rapid heating, which results in explosive boiling of the adjacent liquid and ejection of hot fragments of the metal film, which can contaminate the ink [11, 29]. This produces a high-pressure vapor cavity and drives the flow. Initial flow velocities are calculated around 200 m/s. In the fractured blister case, the ejection is propelled by the high-pressure gases discharged from the ruptured polyimide film. In this case, cavitation similar to the titanium DRL leads to jet formation, and the time-resolved images captured for this case look very similar (not shown here). The vapor cavity is observed to reach its maximum size in 1–2 μs. Because of the remnant momentum associated with the flow, the jet continues even after the cavity stops expanding. After the cavity collapses, it rebounds and undergoes a secondary expansion. This interesting phenomenon has been examined in the literature [30].

Cavitation bubble collapse near a rigid boundary has long been studied [33–35], and one of the key characteristics of this scenario is the presence of a re-entrant jet. As the bubble collapses, a secondary jet is initiated at the collapsing front and is directed toward the solid boundary. With high-resolution imaging, we are able to observe the existence of a re-entrant jet during both the titanium DRL and the fractured polyimide blister cases as shown in Figure 5.4.

In contrast, images from the BA-LIFT case with a nonruptured blister are presented in Figure 5.5. In this case, the jet formation mechanism is the rapid expansion of the blister as discussed earlier, rather than cavitation and collapse. By controlling the laser fluence on the polyimide-absorbing layer, it is possible to achieve blister expansion without fracture. There are no indications of cavitation within the liquid for the expanded blister actuated case. Instead, the ink on the expanding polyimide layer gains momentum, which causes the fluid to develop into a jet. The jet initially propagates with a constant velocity of approximately 25 m/s, and the propagation is maintained due to the momentum of the jet, which pulls additional ink from the surrounding liquid film. As the jet extends from the film, the diameter at the base slightly increases and the diameter around the jet midpoint starts to decrease. This eventually results in the breaking up of the jet into spherical droplets because of the Rayleigh–Plateau instability [37–39].

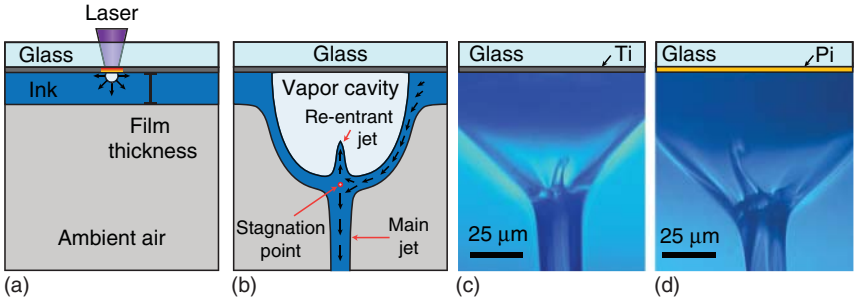

Figure 5.4 (a) Initial configuration of the problem. (b) Schematic of the re-entrant jet with vapor cavity. Close-up experimental images acquired at 5 μs of gas cavities formed during the ejection of liquid from a 5 μm film using (c) titanium (11.8 μJ) and (d) polyimide (7.3 μJ) absorbing layers with a 2.5 μm beam. Internal re-entrant jets (directed upwards) are clearly visible within the gas cavity [36].

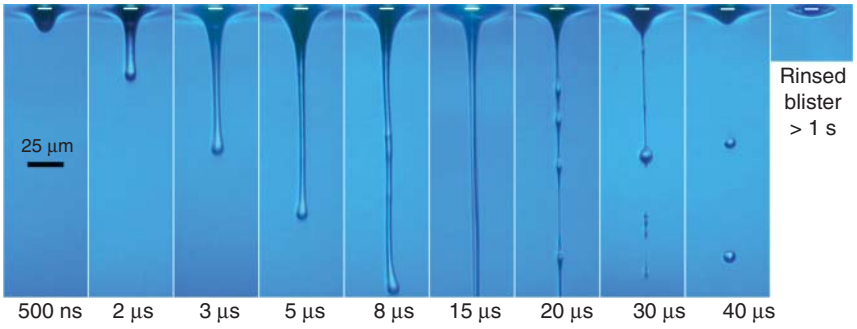

Figure 5.5 Time-resolved images of liquid jets expelled into the ambient air using a 7 μm expanded polyimide-absorbing layer. A 2.7 μJ laser pulse is focused into the polyimide film to a spot size of 10 μm (indicated by a white marker), producing a rapidly expanding, sealed blister, which initiates liquid ejection from an adjacent 5 μm film. The vertical field of view is ~200 μm. An image (>1 s) of the blister, rinsed with residual liquid. (Brown *et al*. 2011 [12]. Reproduced with permission of Springer.)

5.4 Blister Formation

5.4.1 Dynamics of Blister Formation

Blister formation can be experimentally examined in detail by making use of time-resolved imaging and optical microscopy [16]. Blister expansion in time is shown in Figure 5.6a for blisters formed on a 3.5 μm polyimide film with a 20 μm top hat beam at the fluence value of 2.6 J/cm^2. Similarly, Figure 5.6b shows the results for blisters formed on a 6 μm film with a 20 μm beam at 4.3 J/cm^2. Top plots present the volume and the exterior surface area given as a fraction of their equilibrium value with time. Here the equilibrium volume corresponds to the blister volume long after irradiation with the laser pulse. Bottom images represent blister expansion at various stages. Same trends, which are not reported here, are also obtained for a 10 μm beam diameter. Spot sizes given here are evaluated as the full width at $1/e^2$. A side product of the laser ablation is plasma generation, which appears as white flashes in Figure 5.6.

The blister undergoes rapid expansion (~100 μs) under the effect of the pressurized trapped gases. As the blister expands, stresses in the film begin to build, and the internal pressure drops due to the quenching of the gaseous products. Cooling of the products takes place because the blister volume is expanding [16]. Energy dissipates on the deforming polyimide, which results in the delamination of the thin film from the glass. At the ablation spot, the film delaminates from the substrate, and when the pressure created by the gaseous products is no longer able to overcome the elastic stress in the film, blister acceleration ceases. After the blister reaches its peak, it starts to spring back, and the total volume decreases. First by approximately 150 ns, the internal pressure causes the sides of the blister to bow out, which makes the blister take a rather blunted shape. By approximately 500 ns, the blister takes the more uniformly rounded shape. The expansion velocity for the 6 μm film case is calculated as approximately 400–500 m/s, whereas

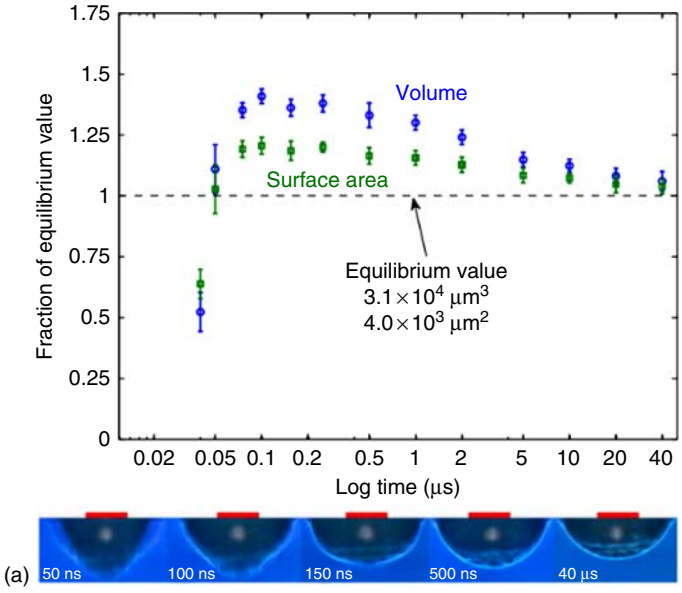

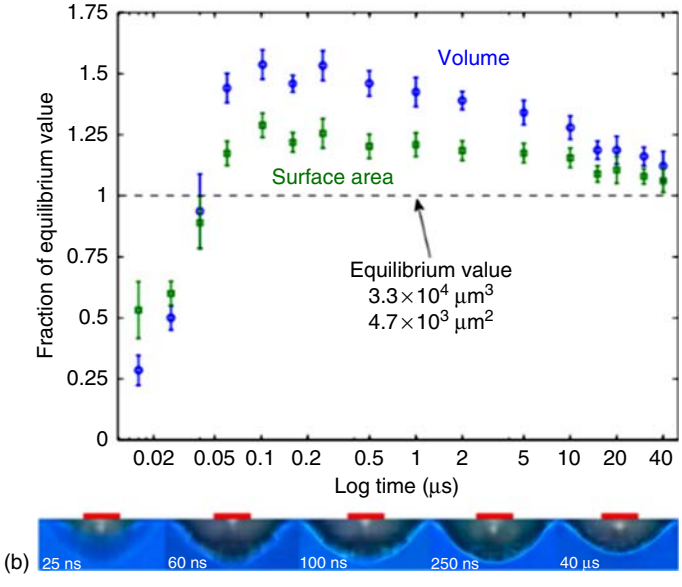

Figure 5.6 (a) Time response of blisters formed on 3.5 μm thick polyimide film with a 20 μm top hat beam (2.6 J/cm^2). (b) Time response of blisters formed on 6 μm thick polyimide film with a 20 μm top hat beam (4.3 J/cm^2). In these cases, a 10 μm *N*-methyl-2-pyrrolidone (NMP) ink is used. (Top) Volume and surface area versus time. Error bars indicate the ±1 standard deviation in the values. (Bottom) Sample images of the blisters at several times. The bar indicates the 20 μm beam diameter.

for the 3.5 μm film, the obtained velocity is approximately 800–1200 m/s. This difference exists because a thicker film requires more energy to be dissipated into the stretching and bending as compared to a thinner film, and it implies that film thickness should affect the ink ejection characteristics.

After the initial expansion of the blister, a gradual contraction is observed as depicted in Figure 5.6. This contraction continues for approximately 50 μs. This contraction can be attributed to a further reduction in pressure caused by the cooling of the trapped gas. Heat equation is solved to evaluate the temperature of gaseous products with time. A simple examination can be performed by solving the heat equation in 1D. The equation is formulated as

$$\rho c_p \frac{\partial T}{\partial t} = \frac{\partial}{\partial x}\left(k \frac{\partial T}{\partial x}\right) \tag{5.1}$$

which can be easily solved numerically. The required density (ρ), specific heat (c_p), and thermal conductivity (k) values are given in Table 5.1. The gas density is approximated by assuming that the experimentally measured blister volume is filled with a mass of vapor equal to the estimated mass of ablated polyimide [21]. In this simple 1D model, the blister is modeled as a 20 μm slab of gas, initially at the elevated temperature T_H and sandwiched between a semi-infinite domain of glass and a 3 μm layer of polyimide layer. The polyimide layer is in contact with ambient air, which has a temperature of T_C. It is evaluated that the thermal decay has the same trend as the volume and surface area reduction. The results of this study show that the thermal decay takes place around the same time as the experimentally measured blister contraction, indicating that the cooling can be the reason for the observed phenomenon [16].

The evolution of blister height with time for different beam size, fluence, and film thickness values is given in Figure 5.7a. Blister size is crucial in determining the amount of ink to be ejected. It is important to understand how the blister size varies with changing parameters such as film thickness, laser beam diameter, and fluence. This study shows that the blister height and width monotonically increase with increasing laser fluence above the ablation threshold of 0.1 J/cm^2 for 355 nm Nd:YAG lasers. The increase in height with fluence is given in Figure 5.7b. The reason for this increase in blister size is the increase in the mass of vaporized polyimide, increasing ablation depth (thereby thinning the remaining blister material), and the increase in the temperature of the trapped gaseous products [40]. Similarly, holding fluence constant and increasing the laser beam diameter

Table 5.1 Material properties used in the solution of the 1D heat equation [16].

	ρ (kg/m^3)	c_p (J/kg K)	k (W/m K)
Air	1.184	1012	0.025
Polyimide	1420	1089	0.15
Gas	25	1100	0.1
Glass	2500	879	0.94

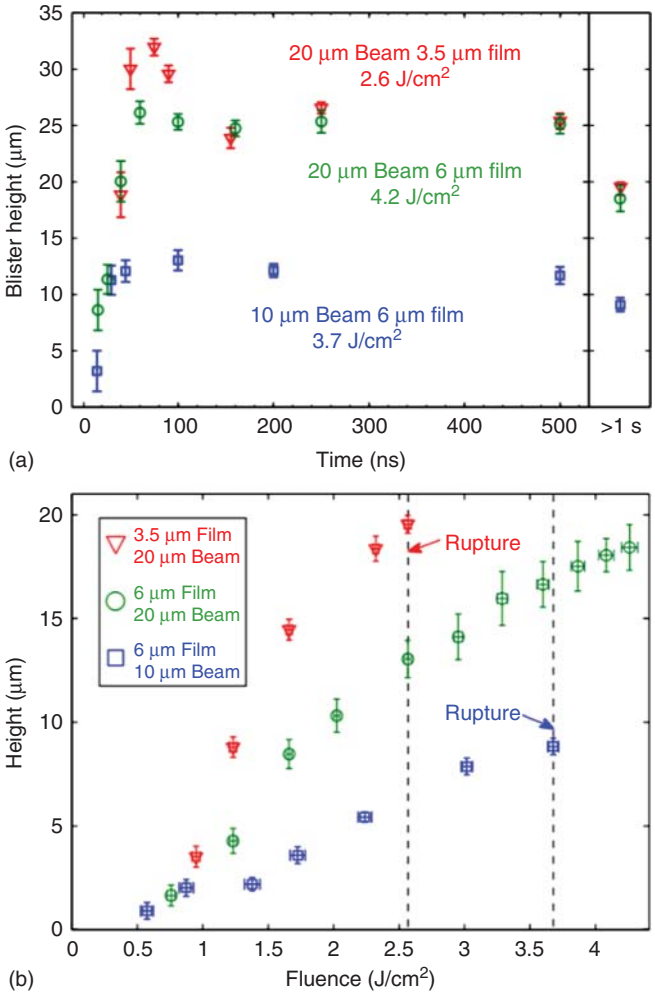

Figure 5.7 (a) Evolution of blister height during the initial period of rapid expansion. An overshoot and oscillation are visible in the blisters formed with a 20 μm beam. The effect is more pronounced with the thinner film. Steady-state blister heights are shown for reference. (b) Blister height versus laser fluence for different combinations of film thickness and beam size. The vertical dashed lines indicate the blister rupture fluence for each case. (Brown *et al*. 2010 [16]. Reproduced with permission of American Institute of Physics.)

produces a larger area over which the polyimide is vaporized and a larger blister. For instance, it is observed that increasing the beam diameter from 10 to 20 μm results in nearly doubled blister heights.

The shapes of the blisters reflect the relative contributions of stretching versus bending stress as depicted in Figure 5.8a. When blister dimensions (width and height) are small relative to the film thickness, bending stresses dominate, and the blister takes on a pointed shape. This is apparent in Figure 5.8a for 6 μm film with a 10 μm beam. As blister dimensions get larger, stretching becomes dominant

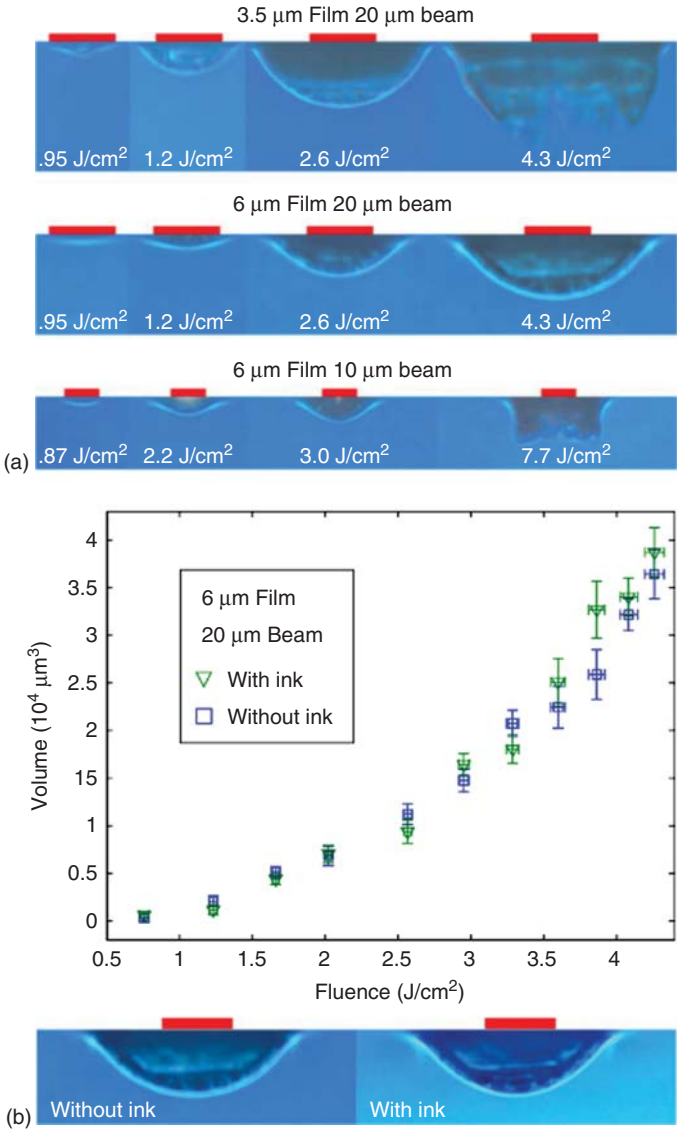

Figure 5.8 (a) Images of blisters formed at several fluences for different combinations of film thickness and beam size. The bars indicate the beam diameter (10 or 20 μm). (b) Blisters formed on 6 μm polyimide film with a 20 μm beam (4.3 J/cm^2) with and without a 10 μm liquid film of NMP. (Top) Blister volume as a function of fluence for blisters formed with and without an ink layer. Both curves overlap significantly indicating the minimal effect of the ink layer on the blister size. (Bottom) No noticeable difference in the shape between blisters formed with and without a liquid layer. The bars indicate the 20 μm beam diameter.

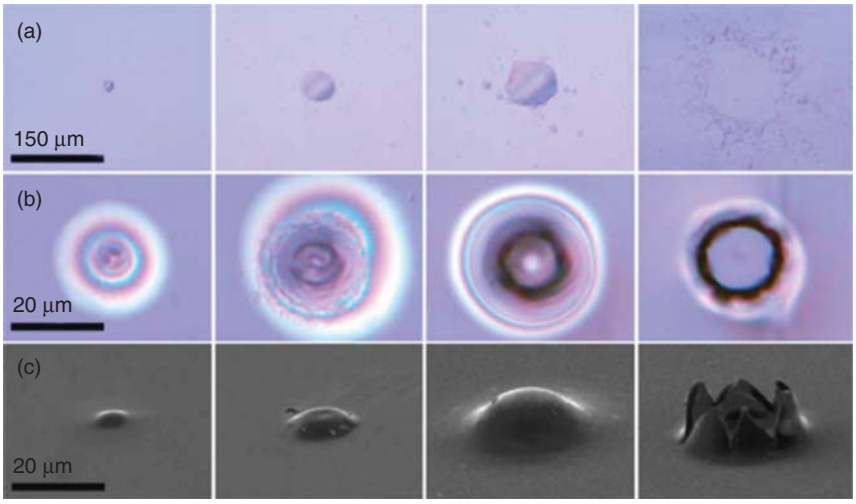

Figure 5.9 (a) Optical microscopy images of laser-transferred droplets taken at 5, 7, 11, and 31 μJ from left to right. (b) Associated microscopy images of polyimide film. (c) SEM images of polyimide film taken at an angle of 70°. (Kattamis *et al*. 2007 [14]. Reproduced with permission of AIP.)

[41]. This results in spherical cap blister shapes. An example case is shown in Figure 5.8 for 3.5 μm film with the 20 μm beam.

Blister formation under different energies is observed under optical microscope and secondary electron microscope (SEM) as presented in Figure 5.9. As noted before, when laser fluence exceeds the critical value, rupture takes place and the blister opens like a flower [42]. However, such a regime is typically avoided in experiements to preserve the benefits of BA-LIFT in comparison to more traditional LIFT approaches.

5.4.2 Finite Element Modeling of Blister Formation

A modeling effort for the finite element simulation of blister deformation during the BA-LIFT process is given in [43]. This study captures initial expansion of the blister subject to the incident laser. The strain rates associated with the process are on the order of 10^5–10^7 s^{-1}, which makes the material properties given in data sheets not applicable. We resolved this issue by introducing a parameter mapping strategy that would account for temperature-dependent material properties. The strategy is forming a constant by bundling the material properties that vary with temperature together and setting the value of this constant so that the numerically evaluated blister profile fits the experimentally observed blister shape. ANSYS software for finite element analysis (FEA) is used to implement the proposed model. The model in this study is developed using 7 μm blisters and verified on the formation of 3 μm blisters. Details of this process are elaborated next.

We begin with the Peirce equation to evaluate the dynamic flow stress:

$$\sigma_y = \sigma_{y0}\left(1 + \frac{\dot{\epsilon}_{pl}}{\gamma}\right)^m \tag{5.2}$$

where σ_{y0} is the static yield stress, γ is the material viscosity parameter, and m is the strain-rate-hardening parameter. These last two parameters are considered free-fitting parameters and are determined using the parameter map analysis. The plastic strain rate ($\dot{\epsilon}_{pl}$) is calculated using the finite element software (in this case, ANSYS). The driving force for the blister growth is the pressure change between the polymer layer and the glass substrate. The pressure change in between is formulated as

$$P_t = P_{t-\Delta t}\left(\frac{V_{t-\Delta t}}{V_t}\right)^{\frac{c_p}{c_v}} + \eta\frac{1}{V_t}\int_{t-\Delta t}^{t} I(Fl,t)dt \tag{5.3}$$

which indicates the combination of an adiabatic increase and an increase due to the laser power. Here $I(Fl,t)$ is the instantaneous laser power, and the integral extends over time. The functional form is Gaussian in time t, and the integral of this function over the entire pulse length is equal to the laser energy.

The second term on the right-hand side of this equation is derived from the following formulas. We start with the simple relation that connects the temperature increase to the heat added:

$$\Delta T = \frac{\Delta Q}{mc_v} \tag{5.4}$$

where ΔQ is the heat added, m is the mass of the gas, and c_v is the specific heat at constant volume. The pressure change can be evaluated using the equation of state:

$$\Delta P = \frac{mR\Delta T}{MV} \tag{5.5}$$

where R is the universal gas constant, M is the molar mass of the gas, and V is its volume. Inserting (5.4) into (5.5) yields

$$\Delta P = \frac{R\Delta Q}{MVc_v} \tag{5.6}$$

In this system, the heat transfer takes place due to the laser; therefore, we need a formula for the energy deposited with the laser, so that the change in pressure can be expressed in terms of this deposited energy. The amount of laser energy converted into the thermal energy can be formulated as

$$\Delta Q = k\int I(Fl,t)dt \tag{5.7}$$

where k is the conversion efficiency of laser energy to thermal energy in the gas. Inserting (5.7) into (5.6) yields

$$\Delta P = \frac{kR}{Mc_v}\frac{1}{V}\int I(Fl,t)dt \tag{5.8}$$

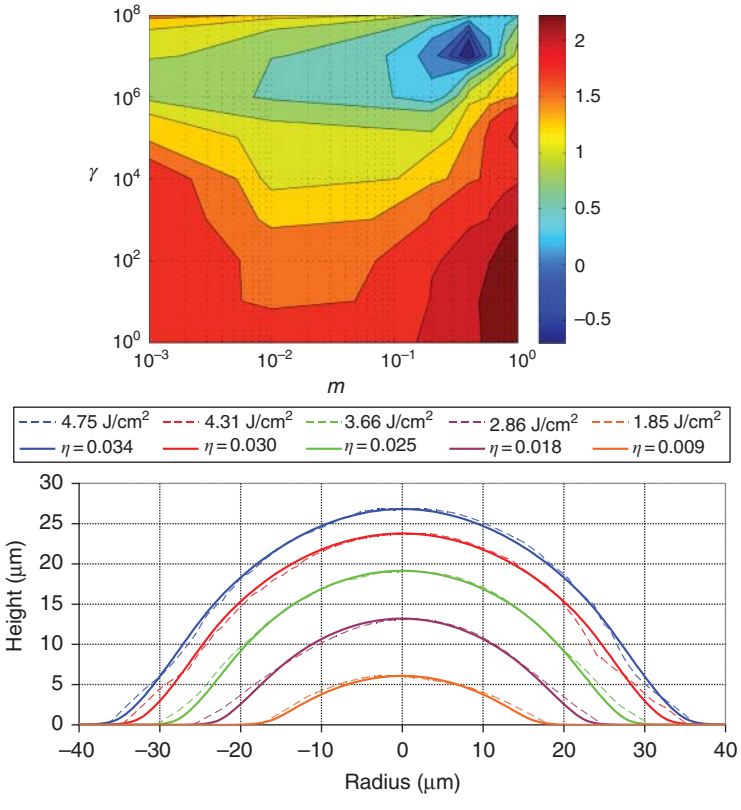

Figure 5.10 (a) Parameter map evaluated to find γ and m to evaluate the dynamic flow stress, σ_y, by choosing the values that yield the minimum average residual sum of squares (RSS). (b) The blister formation as evaluated via finite element simulations. The parameter η is varied to equate the numerically evaluated blister height to the experimental result [43]. Dashed lines denote the experimental profile, whereas solid lines denote the fitted blister profiles. (Kattamis *et al*. 2011 [43]. Reproduced with permission of Cambridge University Press.)

It can be observed that this expression constitutes the second term on the right-hand side of (5.3) with setting $\eta = kR/Mc_v$. During the fitting procedure, η is varied to ensure that numerically evaluated blister heights match the experimentally observed blister heights. The correct selection of this parameter can be verified by comparing experimental and numerical results. This is shown in Figure 5.10 along with the calculated and measured blister shapes.

Time-dependent formation of the blister can be monitored experimentally, and an empirical formula is determined [15]. While the finite element model gives accurate results, an empirical formula for the blister formation is important if the focus is the jet formation dynamics. The inflated blister's shape is represented with a displacement function as

$$\delta = X(r, E) \cdot T(t) \tag{5.9}$$

which is the product of a spatial component $X(r, E)$ and a temporal component $T(t)$. Here r denotes the radial coordinate, and E denotes the laser pulse energy.

The spatial function represents the final shape of the blister as a function of laser energy. The temporal component is a normalized function that does not depend on laser energy. The spatial function has the form

$$X(r,E) = H_0(E)\left(1 - \left(\frac{r}{R_0(E)}\right)^2\right)^C \tag{5.10}$$

where $H_0(E)$ is the blister height, $R_0(E)$ is the blister radius. Both of these parameters are functions of laser energy. The coefficient C depends on whether the blister formation mechanism is stretching or bending. The two limiting cases are pure stretching ($C = 1$) and pure bending ($C = 2$). This expression is fit to each steady-state (500 ns) blister profile generated with different laser energies. It is found in [15] that C has an energy-independent average value of 1.25 ± 0.185 with blister height and radius fitted to the following functions:

$$H_0(E) = -0.0093E^2 + 2.5708E - 9.2618 \tag{5.11}$$

and

$$R_0(E) = 18.117\ln(E) - 12.887 \tag{5.12}$$

where values obtained from these expressions are in micrometers. It should be noted that this profile is fitted to blisters that are generated on a 7 μm polyimide layer. The form of the function may change for different thickness values. The temporal function is the evolution of its blister height normalized by its steady-state value. It is observed from our experiments that the blister expands rapidly during the initial 50–100 ns and reaches a constant height within 150–250 ns. This behavior is observed to be energy independent, and we empirically determine the temporal function:

$$T(t) = \frac{2}{\pi}\arctan(t/\tau) \tag{5.13}$$

where $\tau = 2.359 \times 10^{-8}$ s, and it is the time for the blister to reach 50% of its maximum height. This value is obtained by fitting the given form of the function into the experimental data. Evolution of the temporal function and the change in steady-state blister height with varying energy levels are given in Figure 5.11.

Equation (5.9) and the corresponding equations are very important as they describe the deforming solid boundary, which leads to jet formation in the fluids. In the following sections, we use this as a boundary condition for fluid flow simulations.

5.5 Jet Formation and Expansion

The jet formation mechanism in BA-LIFT is the rapid mechanical deformation due to the expanding blister. This fact makes the process easier to simulate than traditional LIFT processes because the flow characteristics can be obtained without dealing with the complications associated with cavitation. That being said, some effort has been dedicated to model conventional LIFT processes. A recent

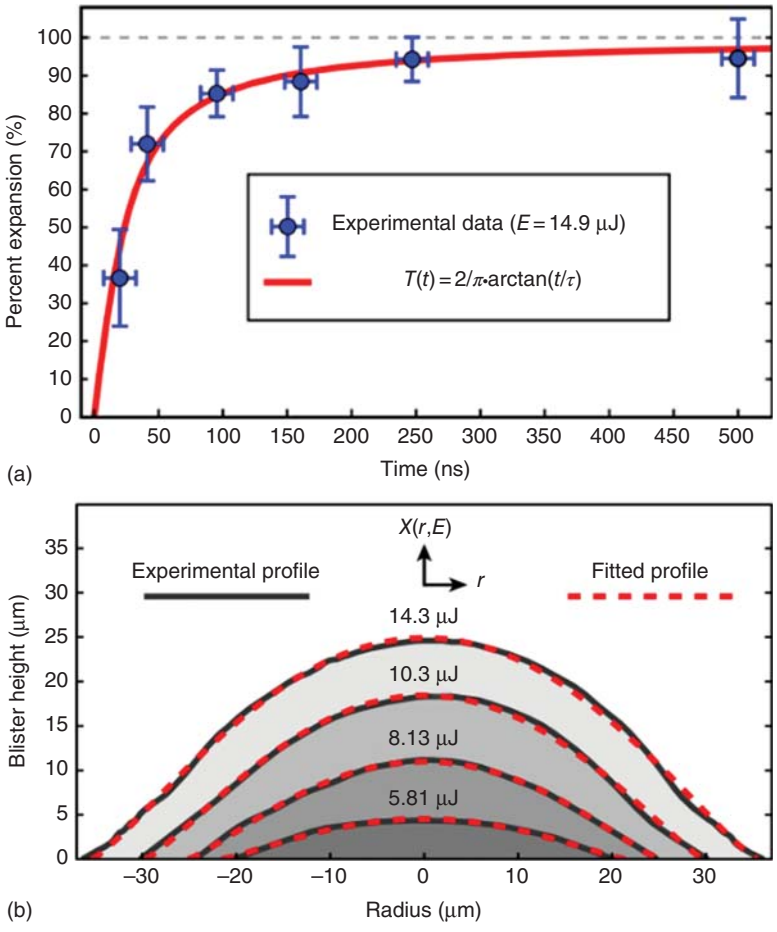

Figure 5.11 Results from the empirical formula for blister profile. (a) The normalized temporal evolution of blister height initiated with a 14.9 μJ laser pulse. Each data point represents the average of five measurements, and the vertical bars indicate ±1 standard deviation. A fit is also shown on the plot. (b) Experimentally measured blister profiles (solid lines) shown with their associated fits (dashed lines). (Brown *et al*. 2012 [15]. Reproduced with permission of Cambridge University Press.)

example is [45], where the jet formation of a hydrogel layer under a Titanium DRL is simulated. An extension of this model to biomaterials is presented in [46]. Another approach for LIFT modeling is based on the two-temperature model to evaluate the temperature and stress levels during the absorption of the laser pulse [27, 47].

5.5.1 Computational Fluid Dynamics Model

Modeling of the BA-LIFT process, where the ejection mechanism is the rapid mechanical deformation of the solid boundary, is performed in [15]. The purpose of such numerical analysis is to develop a platform whereby parametric studies

can be performed and optimum conditions can be evaluated for jet printing. The governing equations for the jet formation of Newtonian fluids during BA-LIFT are the well-known Navier–Stokes equations for incompressible flows with the addition of the surface tension term. First, the continuity equation is expressed as

$$\frac{\partial \rho}{\partial t} + \nabla \cdot (\rho \mathbf{u}) = 0 \tag{5.14}$$

The incompressibility condition is written as

$$\nabla \cdot \mathbf{u} = 0 \tag{5.15}$$

The equation of motion:

$$\rho \left(\frac{\partial \mathbf{u}}{\partial t} + \mathbf{u} \cdot \nabla \mathbf{u} \right) = -\nabla p + \rho \mathbf{g} + \mu \nabla^2 \mathbf{u} + \gamma \kappa \delta_s \mathbf{n} \tag{5.16}$$

where ρ, $\mathbf{u}$, and μ are the density, velocity, and the dynamic viscosity, respectively. The last term in the given equation is the contribution from surface tension, with γ denoting the surface tension coefficient, κ and $\mathbf{n}$ the curvature and normal vector to the interface. The Dirac delta function (δ_s) denotes that the surface tension term is applied only at the interface. The continuity equation is necessary in addition to the incompressibility condition because we are dealing with a two-phase flow (air and ink), and the numerical scheme solves for the fluid motion in two phases with different densities. Inserting the incompressibility equation into the continuity equation results in

$$\frac{D\rho}{Dt} = 0 \tag{5.17}$$

which can be considered an advection equation for the fluid density.

In multiphase flows, the interface can be represented in various ways. Two widely used techniques are the level-set method [48] and the volume-of-fluid (VOF) method [49]. Simulations that are presented with this chapter are performed using the VOF method because the mass is conserved intrinsically, and the topological changes are handled easily [50]. Within this scheme, the density can be defined as

$$\rho(c) = c\rho_1 + (1 - c)\rho_2 \tag{5.18}$$

where ρ_1 and ρ_2 are the densities of the first and second fluids. The interface is represented implicitly with the VOF method, which uses a volume fraction field $c(x, t)$ varying between 0 for a cell filled with the first phase (air) and 1 for the second phase (liquid). A phase-dependent viscosity is defined similarly.

Boundary conditions are derived empirically from experiments. The deformation of the boundary is performed by imposing a boundary condition for blister deformation. These conditions are presented in Section 5.4.2. The time-dependent vertical velocity is specified as

$$V_b(r, t, E) = \dot{h}_b = X(r, E)\dot{(}T)(t) = X(r, E)\frac{2/(\pi\tau)}{1 + (t/\tau)^2} \tag{5.19}$$

where the dots denote time derivatives, and h_b, X, and T are defined in Eqs (5.10), (5.11), and (5.13).

The specific numerical scheme depends on the solver code used to perform simulations. Results presented in this chapter are obtained using Gerris [51] and CFD-ACE+ (ESI Group, Paris, France) (ESI CFD Inc. [52]). Compared to models previously developed for LIFT processes [45], the modeling of the BA-LIFT process does not include the solution of the energy equation because the energy absorption is limited to the interface between the polyimide layer and the glass substrate and has already been accounted for in Eq. (5.19). In addition, the low thermal conductivity of the polyimide makes it possible to neglect the heating of the ink during jet formation [11].

5.5.2 Effect of the Laser Energy

Parametric studies are performed in [15] to investigate the effects of ink properties on jet formation. The liquid layer investigated in this numerical study is NMP similar to the ink used in the experimental measurements of Figure 5.5. Properties of this liquid are taken as: $\mu = 1.7$ mPa s, $\rho = 1030$ kg m^{-3}, $\gamma = 40.79$ mN m^{-1}. The ejections take place into a background of air ($\mu = 18.46$ mPa s, $\rho = 1.1614$ kg m^{-3}).

The correlation between the simulation and experiments is presented with two cases given in Figure 5.12. This figure shows experimentally and numerically produced jets. Figure 5.12a,b shows the close correspondence between the experimental and numerical results for 5.4 μJ laser pulse. Figure 5.12c,d shows the correspondence between results for a higher laser energy of 7.7 μJ. The configuration on the right shows the status of the jet at 8 μs with a glass acceptor surface 150 μm below the donor substrate. This close correspondence is significant considering that there are no additional free parameters included in simulations.

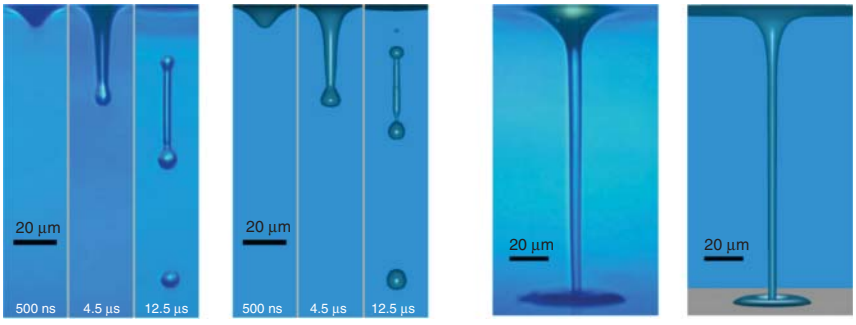

Figure 5.12 (a) Experimentally acquired images and (b) rendered computational results of fluid ejections from a 5 μm donor film of NMP using a 5.4 μJ laser pulse. The ejected fluid volume extracted from the last experimental image (1.2×10^{-15} m^3) compares favorably with that from the simulated ejection (1.0×10^{-15} m^3). Image frames are 134 μm high. (c) Experimentally acquired image of a jet ejected from a 5 μm donor film of NMP-acquired 8 μs after a 7.7 μJ laser pulse. The jet impacts with an acceptor substrate (glass slide) located 150 μm below the donor substrate. (d) Rendered image of a simulated ejection at 8 μs corresponding to the experimental conditions. A 45° contact angle is imposed at the acceptor–substrate boundary to match the experiment. (Brown *et al*. 2012 [15]. Reproduced with permission of Cambridge University Press.)

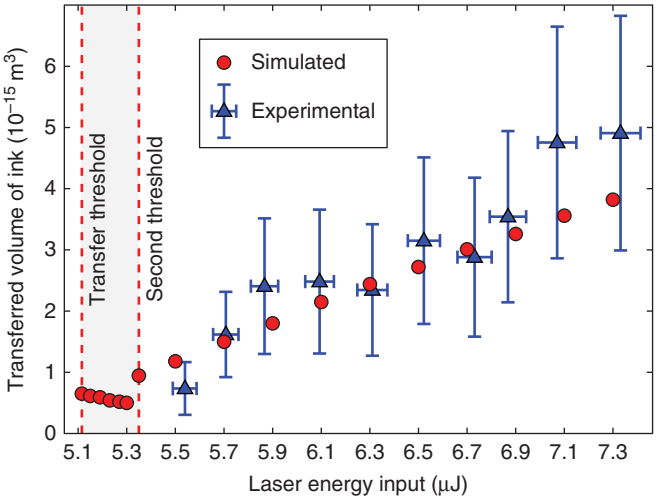

Figure 5.13 Plot of experimentally measured and simulated volumes of ink transferred as a function of laser energy. Each experimental data point represents the average of volumes measured from 10 transferred droplets, and the vertical error bars indicate the ±1 standard deviation. The horizontal error bars indicate the ±1 standard deviation in the shot-to-shot variation of laser energy. (Brown *et al*. 2012 [15]. Reproduced with permission of Cambridge University Press.)

The quantitative correlation is also examined by comparing the transferred volume of ink between experiments and simulations. This comparison is presented in Figure 5.13, which focuses on a smaller range of laser energies near the threshold energy. This threshold laser energy, below which no fluid is transferred, is experimentally observed at 5.5 μJ. This value compares favorably with the threshold energy (5.115 μJ) predicted by the simulations. In the simulations, a second threshold energy is observed, below which all secondary droplets are reabsorbed by the ink film rather than being transferred. Beyond the threshold, both data sets exhibit a similar dependence on laser energy, with the simulated data points located well within the uncertainty of the experimental measurements. This validates the accuracy of the computational model in resolving the dependence of the ejection process on laser energy input.

Different regimes of droplet formation during the process with changing energy are presented in Figure 5.14. The earlier time dynamics ($t \leq 300$ ns) of the jetting process follow the same qualitative trends with increasing energy, whereas the longer-time behavior differs. Below the threshold at 5.1 μJ, the jet's kinetic energy is insufficient for the droplet to detach from the ink film as shown in Figure 5.14a. Between 5.1 μJ and 5.115 μJ, a droplet is detached from the ink, but its velocity is in the direction of the liquid film. At the threshold, only 15 nJ higher than 5.1 μJ, the pinch-off of the droplet is observed at 8.5 μs. At this energy level, a smaller satellite droplet is observed to be forming. This satellite droplet has a velocity toward the ink film and does not result in transfer (Figure 5.14b). It is important to notice that this energy level denotes a hard threshold, and 5.114 μJ energy does not result in the transfer of the droplet.

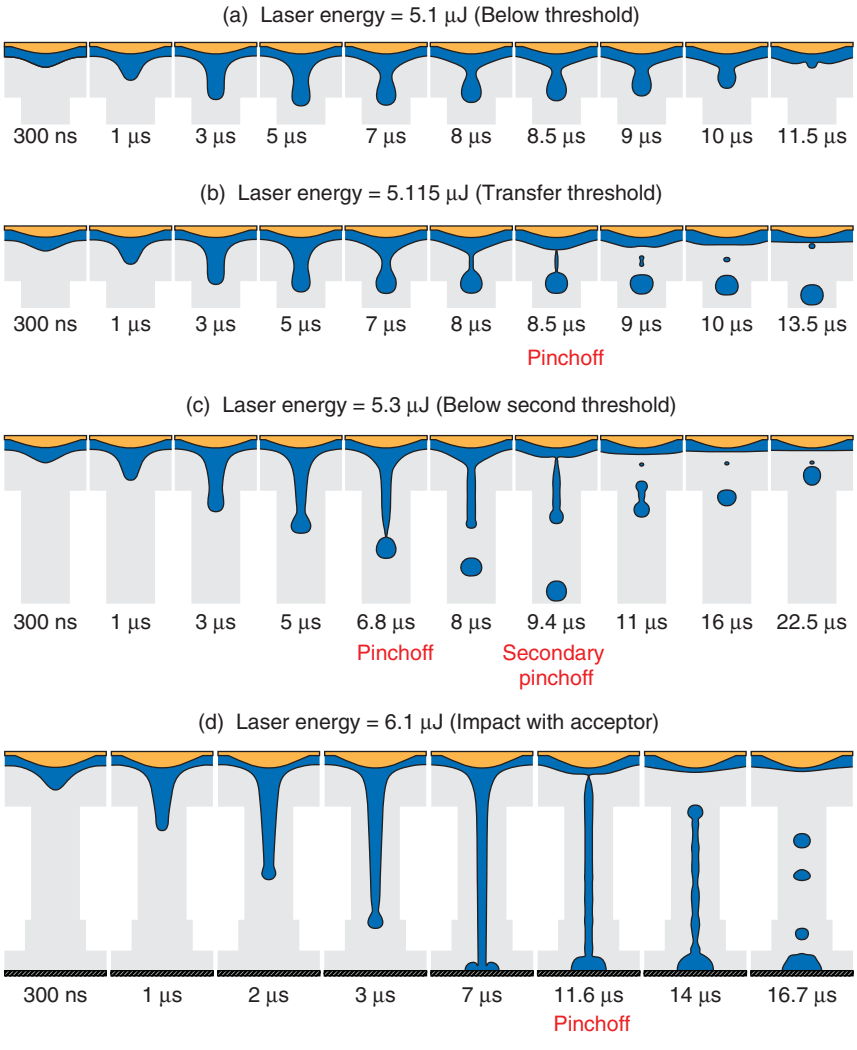

Figure 5.14 Simulation results for blister-actuated flows using standard ink properties initiated with laser energy inputs of: (a) $E = 5.1$ μJ (below threshold), (b) $E = 5.115$ μJ (transfer threshold), (c) $E = 5.3$ μJ (below second threshold), (d) $E = 6.1$ μJ (impact with acceptor). (Brown *et al*. 2012 [15]. Reproduced with permission of Cambridge University Press.)

At this point, it is useful to go back to Figure 5.13 and examine the change in transferred volume with energy. The jet formation is due to a phenomenon called Rayleigh–Plateau instability [39]. A general trend of the droplet formation through this instability is that the droplets produced scale with the jet diameter [53]. Between two thresholds (5.115–5.3 μJ), as laser energy is increased beyond the threshold, the jets become more elongated and narrower at their tip before the instability is initiated (Figure 5.13c). The satellite droplets attain a velocity in the direction of the liquid film. These two effects combine to produce a decrease in transferred volume with increasing laser energy between thresholds.

However, beyond the second threshold, the satellite droplets are ejected with positive velocity. This results in a sharp increase in the ejected volume as depicted in Figure 5.13. Beyond the second threshold, the deposited volume increases approximately linearly with laser energy. A case for higher laser energies ($E = 6.1$ μJ) is presented in Figure 5.14d with an acceptor surface. It is seen that the jet reaches the acceptor surface before pinch-off takes place.

5.5.3 Effect of the Ink Film Properties

For high-resolution printing purposes, the narrow range of laser energies between two thresholds is ideal because this produces the smallest deposited volumes and minimizes the mechanical stress applied on the ink by the rapid blister formation. Therefore, it is important to determine how this threshold regime changes as ink properties are varied. A parametric study is performed in [15] to investigate the effects of the ink properties on the threshold laser energy and transferred volume. The results of this study are presented in Figure 5.15. The other parameters of the ink are kept constant as the values of NMP while performing the parametric study.

Figure 5.15a shows that for film thicknesses smaller than 2.5 μm, the threshold energy decreases with increasing film thickness. On the other hand, for thicknesses larger than 2.5 μm, the threshold laser energy increases linearly with increasing film thickness. This difference in the trend can be attributed to the competing factors during jet formation. For film thicknesses large compared to the blister width, the dependence on the film thickness is dominated by how much the initial impulse is transferred to the free surface. For example, the ratio of the initial free-surface velocity to the blister expansion velocity increases from 61% for a 10 μm film to 76% for a 5 μm film. With a 2.5 μm film, the two velocities are nearly equal. Here it is important to note that reducing film thickness enhances the influence of viscous stresses on the evolution of the flow. As the film thickness decreases, the boundary layer spans the film thickness in less time and the energy required to shear the liquid increases. At 2.5 μm film thickness, the increase in viscous resistance offsets the improvement to the coupling between the blister and the free surface, which results in a local minimum in the laser energy required for transfer.

Figure 5.15b shows the threshold laser energy increases with ink viscosity with a linear dependence. The mechanism for the linear relation between the threshold laser energy and viscosity is not currently understood; however, the general increase in threshold energy versus viscosity is consistent with the additional energy required to induce jet formation. On the other hand, the volume transferred at this threshold decreases. This decrease can be attributed to the thinning in jet diameter with increasing viscosity.

Figure 5.15c shows that the laser energy input required for transfer increases with the surface tension, exhibiting a power-law behavior with an exponent of 0.3130. In addition, the volume transferred decreases with decreasing surface tension, suggesting that there would be no transfer if the surface tension could be reduced to zero. This leads to an optimization idea for high-resolution printing, which utilizes the phenomenon that the surface tension of liquids decreases

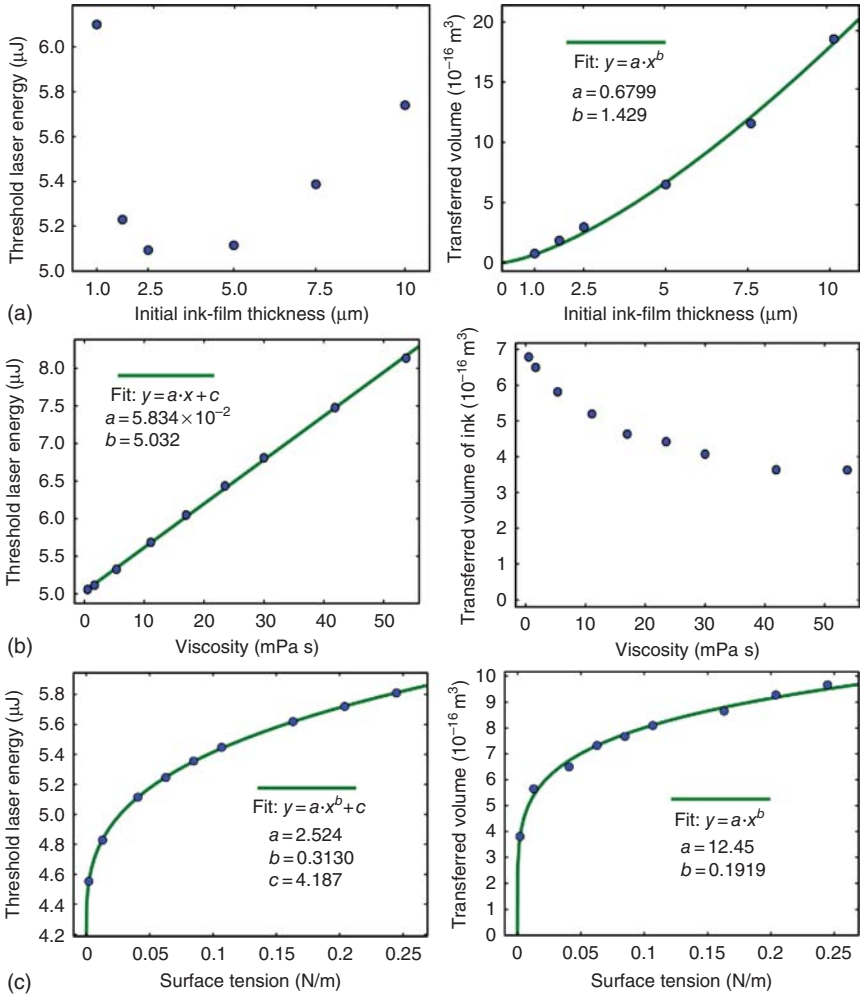

Figure 5.15 Results of the numerical parametric studies. Transferred volume and threshold energy values with varying parameters are presented. (Brown *et al*. 2012 [15]. Reproduced with permission of Cambridge University Press.)

with increasing temperature. Using this trend, high-resolution printing may be improved by heating.

The reasoning behind this power-law trend can be explained using the energy balance. Conservation of the total energy for the entire system can be written as

$$\Delta E_T = \Delta E_k + \Delta E_s + \Delta E_d = 0 \tag{5.20}$$

where ΔE_k is the change in kinetic energy, ΔE_s is the change in surface energy, and ΔE_d is the energy dissipated by heat. This equation means that any decrease in kinetic energy is balanced by the increase in surface energy or dissipated heat. Here it is useful to examine how the kinetic energy changes with increasing laser beam energy. Kinetic energy of the fluid (remnant kinetic energy) can

be evaluated as a function of increasing laser energy, and it has been shown that the remnant kinetic energy scales as $E_k(t_0) \sim (E - E_{\text{th}})^{4.5}$, where E_{th} is the threshold energy for blister formation (not pinch-off) [44]. Using the same approach and defining $\overline{E} \equiv E - E_{\text{th}}$, the remnant kinetic energy scales with $E_k(t_0) \sim \overline{E}^{4.5}$. The surface tension results can be explained by observing that the same relation holds with the pinch-off energy ($\overline{E}_{\text{th}}$) and using $E_k(t_0) \sim \overline{E}^{4.5}$. Taking the conservation of energy formula given earlier into account, it can be said that the energy spent on the dissipation is very low because NMP has a low viscosity. Therefore, we can assume that all the initial kinetic energy is converted to surface energy ($\Delta E_s = \gamma \Delta A$, where ΔA is the increase in surface area). This leads to the following relation between the remnant kinetic energy and the surface energy:

$$E_k(t_0) \sim \overline{E}_{\text{th}}^{4.5} \sim \gamma \Delta A \tag{5.21}$$

It is observed from simulation results in [44] that ΔA is relatively independent of $\overline{E}_{\text{th}}$, which implies that $\overline{E}_{\text{th}}^{4.5} \sim \gamma$. Solving for $\overline{E}_{\text{th}}$ yields

$$\overline{E}_{\text{th}} \sim \gamma^{0.22} \tag{5.22}$$

which agrees with the measured exponent.

The effect of the ink density is not given in Figure 5.15 because its effect is negligible. Since the flow is modeled as incompressible and the boundary deformation is prescribed depending on the beam energy, the fluid's density has little influence on the velocity field that develops during blister's initial expansion. The influence of density is effective through the scaling of viscous (μ/ρ) and surface tension (γ/ρ) forces. This is verified by comparing the simulation results in which the surface tension, viscosity, and fluid densities are jointly varied by a factor of 1000. Both the jet length and its tip velocity differ by less than 0.4% at 2 μs.

5.6 Application to the Transfer of Delicate Materials

In the introduction of this chapter, we argued that BA-LIFT provides the ability to transfer materials without damaging their properties, and we demonstrate this point with regard to organic luminophores. Such materials will exhibit changes in their optical emission as well as chemical signatures when exposed to UV irradiation or excessive temperatures. In a prior work [11], we compared the PL and NMR spectra from different luminophores transferred using the three different LIFT techniques shown in Figure 5.16.

The transferred materials used in this study are blue 9-anthracenemethanol (AM) and the rather robust green tris(8-hydroxyquinoline)aluminum (Alq_3). These luminophores are added to the NMP, which has been employed in other studies as explained in the previous sections, at a concentration of 30 mg/ml to form the inks without significantly affecting its rheological properties. The substrate used is glass for the direct laser absorption into the ink case. The donor substrate for the metal-absorbing layer is comprised of glass slides with a 50 nm

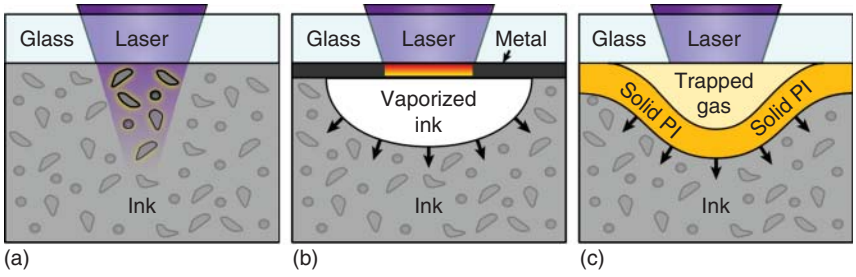

Figure 5.16 Variations of LIFT. (a) Absorption directly within the ink. (b) Laser absorption within a metal-film absorbing layer results in vaporization of the adjacent ink, producing a high-pressure vapor cavity. (c) Laser absorption within a polymer-film absorbing layer produces a rapidly expanding, sealed blister [36].

sputter-coated layer of titanium. The BA-LIFT process is performed with a 6 μm layer of polyimide. All the substrates are coated with a 10 μm thick ink using a wire coater.

The material degradation is investigated by analyzing the printed droplets using each technique. Different fluence values are used to ensure similar droplet sizes for each technique. For PL studies, transferred material is washed off the acceptor surfaces using acetonitrile into quartz cuvettes. Results of the PL study are presented in Figure 5.17. Degradation is clearly apparent for AM that is deposited by DMA as indicated by the modified peak structure in the spectrum. However, titanium DRL and BA-LIFT both show similar emission as the control sample. Conversely, the more robust Alq_3 does not appear to be affected by any of the LIFT conditions.

More detailed structural and chemical analysis is done with NMR studies, and again, the transferred materials are washed off, this time with 1/2 ml of deuterated acetone. Results of this study on AM are given in Figure 5.18. In the case of Alq_3, both PL results and NMR results show that there is no damage at the integrity of the transferred droplet. However, in the case of AM, there are clear indications of new peaks in the NMR spectrum corresponding to decomposition products created during the LIFT process. We see such peaks in the DMA LIFT. In contrast to the PL measurements where the titanium DRL showed no damage, the NMR clearly shows decomposition products in the transferred materials. Notably such peaks are not present in the BA-LIFT, verifying the ability to transfer delicate materials without damage.

Additional studies have been performed on the optoelectronic properties of organic electronic devices fabricated via BA-LIFT in addition to NMR and PL analyses. An example is presented in [13]. In this study, the fabrication of devices with ionic transition metal complexes (iTMCs) is performed using BA-LIFT. One of these devices is a tris(4,4′-di-*tert*-butyl-2,2′-bipyridyl)ruthenium, $[Ru(dtb\text{-}bpy)_3]^{2+}(PF_6^-)_2$ (Complex 1), electroluminescent device. Another sample is prepared using bis(5-trifluoromethyl,2-(2′,4′-difluorophenyl)pyridyl), (4,4′-di-*tert*-butyl-2,2′-bipyridyl) iridium, $[Ir(F_5\text{-}mppy)_2(dtb\text{-}bpy)](PF_6)$. Both of these samples are prepared according to the guidelines presented in the literature [54, 55].

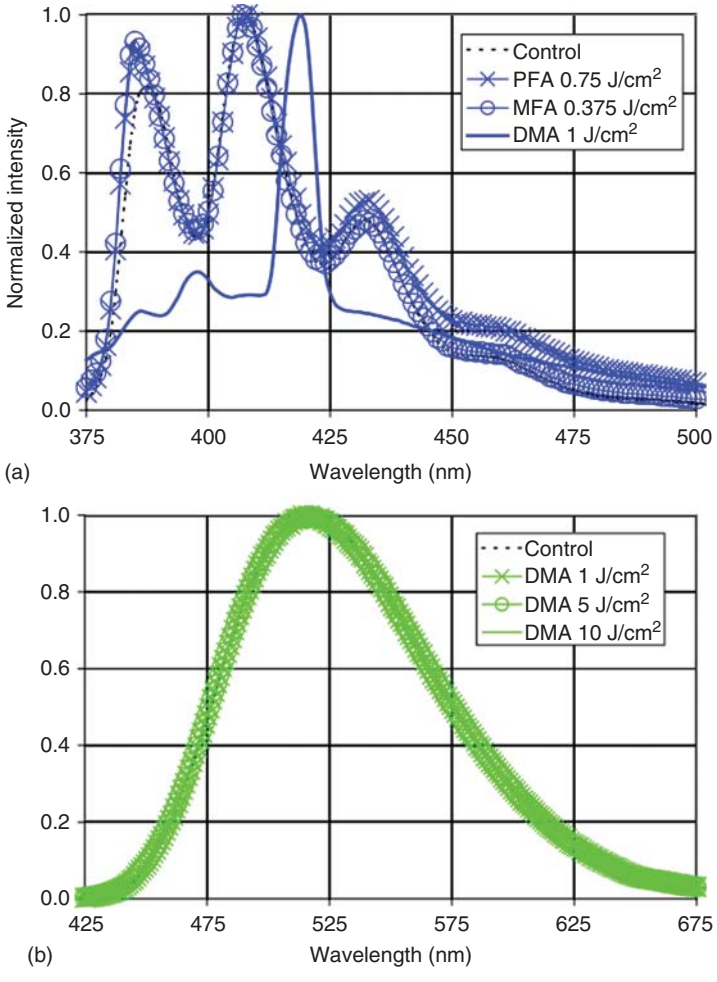

Figure 5.17 Photoluminescence spectra of (a) AM showing significant damage when printed via DMA (1 J/cm^2) but no apparent damage using either metal-film absorber (MFA) (0.375 J/cm^2) or polymer-film absorber (PFA or BA-LIFT) (0.75 J/cm^2). An undamaged spectrum of (b) Alq_3 material printed via DMA transferred at higher fluences can be seen for the Alq_3 molecule. (Kattamis *et al*. 2009 [11]. Reproduced with permission of American Institute of Phyiscs.)

An image of the working device is given in Figure 5.19. It is seen that the pixels emit bright electroluminescence in ambient conditions under forward bias (Figure 5.19b). Uniformity of the electroluminescence is an indication that the integrity of the ITO layer is preserved during the BA-LIFT process, since damage would prevent the uniform charge transfer along the layer.

PL measurements are performed with an Hg lamp, and the emission spectra are recorded with a colorimeter. The emission spectrum of a Complex 1 film via PL is shown in 5.19c. It is seen that the PL spectrum of the BA-LIFT-printed luminophore matches the nonprinted control solution. Both curves also exhibit the same peak wavelength at 630 nm. This value is similar to those reported in the

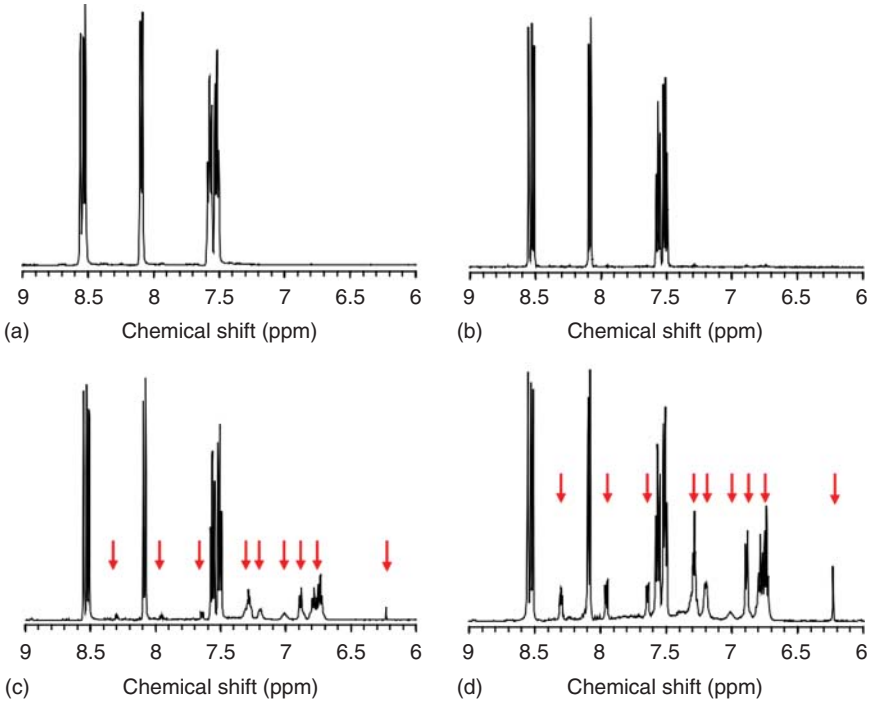

Figure 5.18 NMR spectra of AM for (a) control and printed using (b) BA-LIFT, (c) titanium DRL, and (d) direct-matrix absorption. Arrows indicate the degradation products present in the corresponding techniques. No peaks exist in control or polymer absorptive layer. (Kattamis *et al*. 2009 [11]. Reproduced with permission of American Institute of Phyiscs.)

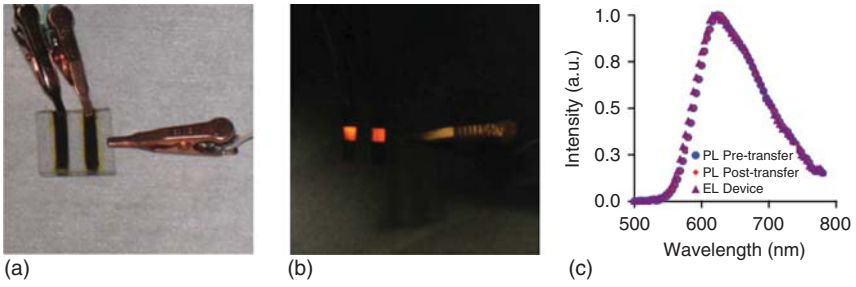

Figure 5.19 (a) Image of the LED (12.5 × 12.5 mm^2) under room light illumination. (b) Device operation under ambient conditions depicting two 2.5 × 2.5 mm^2 orange–red pixels. (c) Posttransfer PL and device EL match the pretransfer solution PL. (Kattamis *et al*. 2011 [13]. Reproduced with permission of Elsevier.)

literature [54, 56, 57]. Since both the shape and the peak wavelength of the curve match with the examples in the literature, we can conclude that the properties of the molecule are not altered during the BA-LIFT process. Furthermore, similar results are observed for the devices fabricated in nitrogen environments via spin coating [54, 56]. Electrical performance of these devices are also evaluated and

shown that the performance matches that of other devices in the literature. It is seen from these studies that use of a polymer layer prevents damage to the ink, and device performance is not adversely affected.

5.7 Conclusions

In this chapter, we have shown the underlying physics and applications of BA-LIFT, a technique developed as an alternative to conventional LIFT processes. BA-LIFT relies on the mechanical impulse created by an expanding blister to induce jet formation in a liquid or multiphase ink. Since the incident laser energy is absorbed in a shallow region of the thick polymer film, the associated blister maintains thermal and optical insulation between the laser and the ink. Expansion of the blister is investigated through time-resolved imaging, and the underlying physics is examined using finite element simulations. In addition, empirical blister formation formulas are derived from time-resolved images, which are used as boundary condition for analytical and computational studies performed to examine the jet formation.

Time-resolved images and developed CFD models can provide details on the jet formation process and shed light on the importance of different parameters on the transfer process. Parametric studies are performed to investigate jet properties at different transfer regimes and provide users with a greater understanding of how to control the process to optimize the transfer. Most notably, BA-LIFT is demonstrated to be a suitable technique for the transfer of sensitive materials, since it prevents degradation and damage to chemically, thermally, or optically delicate materials.

References

1 Adrian, F., Bohandy, J., Kim, B., Jette, A.N., and Thompson, P. (1987) A study of the mechanism of metal deposition by the laser-induced forward transfer process. *J. Vac. Sci. Technol., B*, **5** (5), 1490–1494.

2 Esrom, H., Zhang, J.Y., Kogelschatz, U., and Pedraza, A.J. (1995) New approach of a laser-induced forward transfer for deposition of patterned thin metal films. *Appl. Surf. Sci.*, **86** (1), 202–207.

3 Serra, P., Colina, M., Fernández-Pradas, J.M., Sevilla, L., and Morenza, J.L. (2004) Preparation of functional DNA microarrays through laser-induced forward transfer. *Appl. Phys. Lett.*, **85** (9), 1639–1641.

4 Hopp, B., Smausz, T., Antal, Z., Kresz, N., Bor, Z., and Chrisey, D. (2004) Absorbing film assisted laser induced forward transfer of fungi (trichoderma conidia). *J. Appl. Phys.*, **96**, 3478–3481.

5 Hopp, B., Smausz, T., Kresz, N., Barna, N., Bor, Z., Kolozsvári, L., Chrisey, D.B., Szabó, A., and Nógrádi, A. (2005) Survival and proliferative ability of various living cell types after laser-induced forward transfer. *Tissue Eng.*, **11** (11-12), 1817–1823.

6 Colina, M., Serra, P., Fernández-Pradas, J.M., Sevilla, L., and Morenza, J.L. (2005) Dna deposition through laser induced forward transfer. *Biosens. Bioelectron.*, **20** (8), 1638–1642.

7 Schultze, V. and Wagner, M. (1991) Laser-induced forward transfer of aluminium. *Appl. Surf. Sci.*, **52** (4), 303–309.

8 Banks, D.P., Grivas, C., Mills, J.D., Eason, R.W., and Zergioti, I. (2006) Nano-droplets deposited in microarrays by femtosecond Ti:sapphire laser-induced forward transfer. *Appl. Phys. Lett.*, **89** (193107), 1–3.

9 Yamada, H., Sano, T., Nakayama, T., and Miyamoto, I. (2002) Optimization of laser-induced forward transfer process of metal thin films. *Appl. Surf. Sci.*, **197**, 411–415.

10 Boutopoulos, C., Kalpyris, I., Serpetzoglou, E., and Zergioti, I. (2014) Laser-induced forward transfer of silver nanoparticle ink: time-resolved imaging of the jetting dynamics and correlation with the printing quality. *Microfluid. Nanofluid.*, **16** (3), 493–500.

11 Kattamis, N.T., McDaniel, N.D., Bernhard, S., and Arnold, C.B. (2009) Laser direct write printing of sensitive and robust light emitting organic molecules. *Appl. Phys. Lett.*, **94** (103306), 1–3.

12 Brown, M.S., Kattamis, N.T., and Arnold, C.B. (2011) Time-resolved dynamics of laser-induced micro-jets from thin liquid films. *Microfluid. Nanofluid.*, **11** (2), 199–207.

13 Kattamis, N.T., McDaniel, N.D., Bernhard, S., and Arnold, C.B. (2011) Ambient laser direct-write printing of a patterned organo-metallic electroluminescent device. *Org. Electron.*, **12** (7), 1152–1158.

14 Kattamis, N.T., Purnick, P.E., Weiss, R., and Arnold, C.B. (2007) Thick film laser induced forward transfer for deposition of thermally and mechanically sensitive materials. *Appl. Phys. Lett.*, **91** (171120), 1–3.

15 Brown, M.S., Brasz, C.F., Ventikos, Y., and Arnold, C.B. (2012) Impulsively actuated jets from thin liquid films for high-resolution printing applications. *J. Fluid Mech.*, **709**, 341–370.

16 Brown, M.S., Kattamis, N.T., and Arnold, C.B. (2010) Time-resolved study of polyimide absorption layers for blister-actuated laser-induced forward transfer. *J. Appl. Phys.*, **107** (083103), 1–8.

17 Urech, L. and Lippert, T. (2010) Photoablation of polymer materials, in *Photochemistry and Photophysics of Polymer Materials* (ed. N.S. Allen), John Wiley & Sons, Inc., Hoboken, NJ, pp. 541–568, doi: 10.1002/9780470594179.ch14.

18 Lippert, T., Hauer, M., Phipps, C.R., and Wokaun, A. (2003) Fundamentals and applications of polymers designed for laser ablation. *Appl. Phys. A: Mater. Sci. Process.*, **77**, 259–264, doi: 10.1007/s00339-003-2111-y.

19 Lippert, T. (2010) UV laser ablation of polymers: from structuring to thin film deposition, in *Laser-Surface Interactions for New Materials Production*, Springer-Verlag, Berlin Heidelberg, pp 141–175, doi: 10.1007/978-3-642-03307-0_7.

20 Brasz, C.F., Yang, J.H., and Arnold, C.B. (2015) Tilting of adjacent laser-induced liquid jets. *Microfluid. Nanofluid.*, **18** (2), 185–197.

21 Brannon, J.H., Lankard, J., Baise, A., Burns, F., and Kaufman, J. (1985) Excimer laser etching of polyimide. *J. Appl. Phys.*, **58** (5), 2036–2043.

22 Ortelli, E.E., Geiger, F., Lippert, T., Wei, J., and Wokaun, A. (2000) UV-laser-induced decomposition of Kapton studied by infrared spectroscopy. *Macromolecules*, **33** (14), 5090–5097.

23 Dwivedi, A. (2007) Recent advances in pulsed laser ablated plasma plumes: a review. *Surf. Rev. Lett.*, **14** (01), 57–69.

24 Feinaeugle, M., Alloncle, A., Delaporte, P., Sones, C., and Eason, R. (2012) Time-resolved shadowgraph imaging of femtosecond laser-induced forward transfer of solid materials. *Appl. Surf. Sci.*, **258** (22), 8475–8483.

25 Biver, E., Rapp, L., Alloncle, A.P., Serra, P., and Delaporte, P. (2014) High-speed multi-jets printing using laser forward transfer: time-resolved study of the ejection dynamics. *Opt. Express*, **22** (14), 17 122–17 134.

26 Puerto, D., Biver, E., Alloncle, A.P., and Delaporte, P. (2016) Single step high-speed printing of continuous silver lines by laser-induced forward transfer. *Appl. Surf. Sci.*, **374**, 183–189.

27 Pohl, R., Visser, C.W., Römer, G.W., Lohse, D., Sun, C., Huis, B. et al. (2015) Ejection regimes in picosecond laser-induced forward transfer of metals. *Phys. Rev. Appl.*, **3** (024001), 1–9.

28 Desrus, H., Chassagne, B., Catros, S., Artigues, C., Devillard, R., Petit, S., Deloison, F., Frricain, J., Guillemot, F., and Kling, R. (2016) Laser assisted bioprinting using a femtosecond laser with and without a gold transductive layer: a parametric study. SPIE BiOS, International Society for Optics and Photonics, 970600, pp. 1–18.

29 Smausz, T., Hopp, B., Kecskemeti, G., and Bor, Z. (2006) Study on metal microparticle content of the material transferred with absorbing film assisted laser induced forward transfer when using silver absorbing layer. *Appl. Surf. Sci.*, **252** (13), 4738–4742.

30 Akhatov, I., Lindau, O., Topolnikov, A., Mettin, R., Vakhitova, N., and Lauterborn, W. (2001) Collapse and rebound of a laser-induced cavitation bubble. *Phys. Fluids (1994-present)*, **13** (10), 2805–2819.

31 Colina, M., Duocastella, M., Fernández-Pradas, J.M., Serra, P., and Morenza, J.L. (2006) Laser-induced forward transfer of liquids: study of the droplet ejection process. *J. Appl. Phys.*, **99** (084909), 1–7.

32 Duocastella, M., Fernández-Pradas, J., Serra, P., and Morenza, J. (2008) Jet formation in the laser forward transfer of liquids. *Appl. Phys. A*, **93** (2), 453–456.

33 Benjamin, T.B. and Ellis, A.T. (1966) The collapse of cavitation bubbles and the pressures thereby produced against solid boundaries. *Philos. Trans. R. Soc. London, Ser. A*, **260** (1110), 221–240.

34 Plesset, M.S. and Chapman, R.B. (1971) Collapse of an initially spherical vapour cavity in the neighbourhood of a solid boundary. *J. Fluid Mech.*, **47** (2), 283–290.

35 Blake, J.R. and Gibson, D. (1987) Cavitation bubbles near boundaries. *Annu. Rev. Fluid Mech.*, **19** (1), 99–123.

36 Brown, M.S. (2011) Experimental and numerical study of laser-induced forward transfer printing of liquids. PhD thesis. Princeton University.

37 Plateau, J.A.F. (1873) *Statique expérimentale et théorique des liquides soumis aux seules forces moléculaires*, vol. **2**, Gauthier-Villars.

38 Strutt, J.W. and Rayleigh, L. (1878) On the instability of jets. *Proc. London Math. Soc.*, **10** (4), 4–13.

39 Eggers, J. (1997) Nonlinear dynamics and breakup of free-surface flows. *Rev. Mod. Phys.*, **69** (3), 865–929.

40 Dreyfus, R. (1992) CN temperatures above laser ablated polyimide. *Appl. Phys. A*, **55** (4), 335–339.

41 Arjun, A. and Wan, K.T. (2005) Derivation of the strain energy release rate G from first principles for the pressurized blister test. *Int. J. Adhes. Adhes.*, **25** (1), 13–18.

42 Gu, J., Tay, E., Lim, P., and Lim, P. (2002) Micro-humps formed in excimer laser ablation of polyimide using mask projection system. *Appl. Phys. A*, **74** (4), 487–491.

43 Kattamis, N.T., Brown, M.S., and Arnold, C.B. (2011) Finite element analysis of blister formation in laser-induced forward transfer. *J. Mater. Res.*, **26** (18), 2438–2449.

44 Brasz, C.F., Arnold, C.B., Stone, H.A., and Lister, J.R. (2015) Early-time free-surface flow driven by a deforming boundary. *J. Fluid Mech.*, **767**, 811–841.

45 Mézel, C., Hallo, L., Souquet, A., Breil, J., Hébert, D., and Guillemot, F. (2009) Self-consistent modeling of jet formation process in the nanosecond laser pulse regime. *Phys. Plasmas (1994-present)*, **16** (123112), 1–7.

46 Mézel, C., Souquet, A., Hallo, L., and Guillemot, F. (2010) Bioprinting by laser-induced forward transfer for tissue engineering applications: jet formation modeling. *Biofabrication*, **2** (1), 014 103.

47 Shugaev, M.V. and Bulgakova, N.M. (2010) Thermodynamic and stress analysis of laser-induced forward transfer of metals. *Appl. Phys. A*, **101** (1), 103–109.

48 Sethian, J.A. (1996) A fast marching level set method for monotonically advancing fronts. *Proc. Natl. Acad. Sci. U.S.A.*, **93** (4), 1591–1595.

49 Hirt, C.W. and Nichols, B.D. (1981) Volume of fluid (VOF) method for the dynamics of free boundaries. *J. Comput. Phys.*, **39** (1), 201–225.

50 Kleefsman, K., Fekken, G., Veldman, A., Iwanowski, B., and Buchner, B. (2005) A volume-of-fluid based simulation method for wave impact problems. *J. Comput. Phys.*, **206** (1), 363–393.

51 Popinet, S. (2003) Gerris: a tree-based adaptive solver for the incompressible Euler equations in complex geometries. *J. Comput. Phys.*, **190** (2), 572–600.

52 ESI, RD (2004) *CFD-ACE+, Version 2007.2. 25*, ESI R&D Inc., Huntsville, AL.

53 Teng, H., Kinoshita, C., and Masutani, S. (1995) Prediction of droplet size from the breakup of cylindrical liquid jets. *Int. J. Multiphase Flow*, **21** (1), 129–136.

54 Bernhard, S., Barron, J.A., Houston, P.L., Abruna, H.D., Ruglovksy, J.L., Gao, X., and Malliaras, G.G. (2002) Electroluminescence in ruthenium (II) complexes. *J. Am. Chem. Soc.*, **124** (45), 13 624–13 628.

55 Slinker, J.D., Koh, C.Y., Malliaras, G.G., Lowry, M.S., and Bernhard, S. (2005) Green electroluminescence from an ionic iridium complex. *Appl. Phys. Lett.*, **86** (17), 173506.

56 Handy, E.S., Pal, A.J., and Rubner, M.F. (1999) Solid-state light-emitting devices based on the tris-chelated ruthenium (II) complex. 2. tris (bipyridyl) ruthenium (II) as a high-brightness emitter. *J. Am. Chem. Soc.*, **121** (14), 3525–3528.

57 Balzani, V., Barigelletti, F., and De Cola, L. (1990) Metal complexes as light absorption and light emission sensitizers, in *Photoinduced Electron Transfer II*, Springer-Verlag, pp. 31–71.

6

Film-Free LIFT (FF-LIFT)

Salvatore Surdo, Alberto Diaspro, and Martí Duocastella

Department of Nanophysics, Istituto Italiano di Tecnologia, Via Morego 30, 16163 Genova, Italy

6.1 Introduction

The control of inorganic matter into an ever-decreasing size has enabled the technological revolution of the past decades, with developments ranging from computers to medical tools. Arguably, behind these advances lies photolithography, the de facto standard micro/nanofabrication technique [1]. Despite unrivaled results in terms of parallelization, resolution, and feature size, photolithography is highly optimized for a short parameter space, namely few materials (metals or semiconductors) and even fewer substrates (flat silicon or glass). All these intrinsic constraints of photolithography are incompatible with novel key applications such as lab-on-a-chip [2], tissue engineering [3], gene sequencing [4], or organic electronics [5], which demand for the heterogeneous integration of a wide variety of functional materials, including polymers, proteins, or living organisms, at the micro- and nanoscale. Compatibility with flexible substrates or uneven or rough surfaces is also required. Therefore, the big challenge ahead of us is the development of fabrication tools that enable to translate the same degree of control achievable with photolithography into organic or biological matter.

With the previous points in mind, the ideal fabrication technique of the twenty-first century should combine characteristics such as high speed and high lateral resolution, with a total compatibility with a wide range of complex materials. Unfortunately, current techniques capable of patterning functional materials, including inkjet printing [6], dip-pen lithography [7], or soft lithography [8, 9], can only accommodate some of these demands. Within this context, laser-induced forward transfer (LIFT) appears as a much versatile approach for micro- and nanofabrication [10, 11]. LIFT is a printing technique that uses laser pulses to transfer material from a donor film onto a receiver substrate placed in close proximity to the donor film (Figure 6.1a and Chapter 1). An air gap between the donor film and the substrate prevents potential contamination of the transferred material. Notably, since LIFT does not require the use of nozzles, it can print a wider variety of materials compared to inkjet printing, ranging from highly viscous inks [12, 13] to even materials in solid form [14–16].

Laser Printing of Functional Materials: 3D Microfabrication, Electronics and Biomedicine,
First Edition. Edited by Alberto Piqué and Pere Serra.
© 2018 Wiley-VCH Verlag GmbH & Co. KGaA. Published 2018 by Wiley-VCH Verlag GmbH & Co. KGaA.

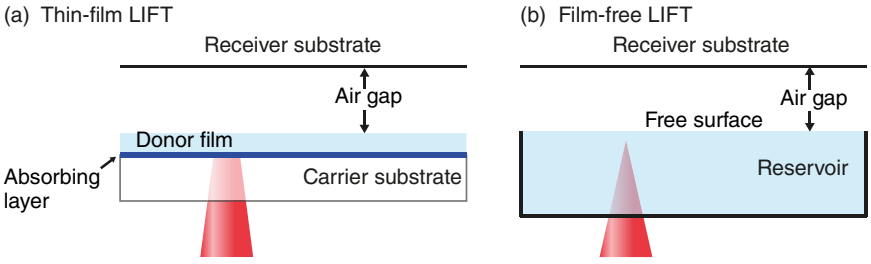

Figure 6.1 Scheme of traditional LIFT of liquids (a) and film-free LIFT (b).

Despite resolutions typically limited to about 1 μm, the possibility to monitor *in situ* the printing process coupled with the high directionality of lasers opens the door to unique features. For instance, one could pick up a specific cell or biomolecule from the donor film and deposit it on a targeted area of a substrate. Importantly, LIFT is implemented in a laser direct-write system. Thus, the same setup used for LIFT can be used to ablate or modify a material, complementing the additive nature of LIFT with other laser processing modalities such as laser ablation [17, 18], photostimulation [19], or even optical transfection [20].

A natural consequence of the versatility of LIFT is the requirement to optimize the printing process depending on the targeted material. In other words, the conditions needed to print a metal completely differ from those used for printing a prepolymer in terms of parameters such as laser wavelength, pulse duration, fluence, or separation distance between the donor film and the receiver substrate. A particularly delicate situation of significant importance arises when the printing material (ink) is a liquid transparent to commercially available laser wavelengths. This is the case of most biological materials, which are usually prepared in aqueous solutions. Therefore, optimizing the laser printing of transparent liquids is necessary for the use of this technique in bioapplications ranging from DNA or protein microarrays [21, 22] to the growing field of biosensors [23, 24]. There are two aspects, though, that have typically limited the use of LIFT in this instance. The first one is the need to promote laser absorption. This is usually done by intercalating an absorbing layer or dynamic release layer (DRL) between the donor film and the carrier substrate [25–32]. Thus, the laser radiation is absorbed in the DRL upon which it volatilizes, generating the thrust necessary to propel the targeted material into the receiver substrate. The DRL has the additional advantage of preventing the direct exposure of the material of interest to the laser irradiation. However, the quest of an ideal DRL has been proved challenging. Traces of most materials used as DRL, including titanium or chromium, are found in the deposited material. Alternative approaches such as the use of explosive polymers that fully decompose with the laser irradiation [33, 34] (Chapter 3), or the use of thick polymers that mechanically deform [35–37] (Chapter 5), can mitigate the contamination caused by the DRL. But even if contamination caused by the DRL could be fully eliminated, there would still be a second problem in the laser printing of transparent liquids: the preparation of a liquid film over large areas. Importantly, the uniformity of the liquid film is directly correlated to the quality of the printing process, for example, different film thicknesses can result in

different amounts of deposited material under the same laser conditions. Because of the difficulty in the preparation of liquid films and their inherent instability, a technique that could operate under the same principles of traditional LIFT but without the need to prepare the liquid in thin form would be highly advantageous. This prompted the development of film-free laser printing or film-free LIFT (FF-LIFT), a technique that can directly transfer transparent liquids contained in a reservoir (Figure 6.1b)[38, 39].

In this chapter, we discuss in detail the current problems related to the preparation of liquid films in LIFT, from fundamental aspects to practical problems. We then introduce FF-LIFT, explain its physical principles, and describe the different modalities in which the technique can be implemented. We discuss important experimental factors that can affect the quality of the printing process, such as spherical aberration or optical absorption of the liquid, and finally, we give examples of applications in which FF-LIFT has been successfully used.

6.2 Rheological Considerations in Traditional LIFT of Liquids

The uniformity of the donor film has a direct influence on the outcome of the LIFT printing process. Indeed, parameters such as feature size, energy threshold for printing, printing area, and reproducibility are strongly affected by the local thickness of the liquid film. In this section, we discuss which are the main factors that impact the uniformity of thin liquid films and describe the existing technologies available for liquid film preparation. We also highlight the key aspects to be considered when selecting a receiver substrate.

6.2.1 The Challenges behind the Preparation of a Thin Liquid Film

Ideally, in traditional LIFT of liquids, one would like to have thin films with high temporal stability and spatial uniformity over large areas ($\sim mm^2$). Despite the preparation of a liquid film being simple and straightforward, this task can be highly challenging. In fact, thin liquid films are often subjected to several instabilities that compromise their spatiotemporal uniformity [40]. Depending on the mechanism that triggers these instabilities, two main groups can be recognized. The first one involves spontaneous instabilities, namely the intrinsic tendency of a thin liquid film to break into smaller droplets (Figure 6.2a). Typical examples are the Rayleigh–Taylor instability, caused by gravity forces that destabilize a suspended (facing down) film, and liquid dewetting, in which the liquid film is ruptured due to its tendency to withdraw from a "hostile" surface [41, 42]. The second group of instabilities encompasses those induced by external agents (Figure 6.2b) [43], as in the case of capillary waves, that is, pressure waves traveling along the phase boundary of the liquid. Eventually, when the external perturbation ceases, these nonuniformities may vanish due to viscous dissipation. For a given magnitude or frequency of the perturbation, though, the instabilities could also result in permanent film breakup.

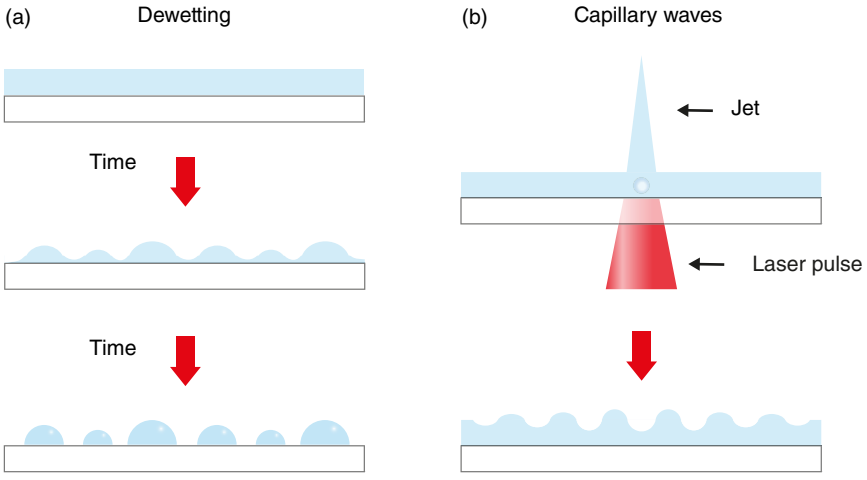

Figure 6.2 Sketch of spontaneous (a) and externally induced (b) instabilities that can affect the spatiotemporal uniformity of a thin liquid donor film.

The occurrence of liquid film instabilities strongly depends on several rheological parameters of the printed material or ink, namely surface tension (γ), mass density (ρ), vapor pressure, and viscosity (υ), as well as on the morphology (e.g., surface roughness) and chemistry (e.g., level of hydrophobicity) of the carrier substrate. Because there exists an interplay between all these parameters, understanding how they affect the donor preparation is not an easy task. To simplify the study, it is useful to distinguish two main stages in which liquid nonuniformities can appear during LIFT. The first one includes the initial preparation of the liquid film, and it is dominated by spontaneous instabilities. The second stage occurs once a uniform film is obtained and involves the formation of capillary waves induced by the laser pulses that act as the external perturbing agent. A more detailed description of each of these stages is presented next.

6.2.1.1 The Role of Spontaneous Instabilities

To understand the challenges behind the initial preparation of a thin liquid film, it is necessary to first clarify the meaning of the term *thin*. In the context of printing liquids with LIFT, we consider "thin" those films with a thickness in the interval of 5–50 µm. Within this length scale, gravity and consequently the Rayleigh–Taylor instability are negligible. Thus, liquid dewetting is the only potential source of spontaneous liquid instabilities. Importantly, liquid dewetting occurs for films below a critical thickness e_C given by the equation

$$e_C = 2k^{-1} \sin\left(\frac{\theta_E}{2}\right) \tag{6.1}$$

where $k^{-1} = (\gamma/\rho g)^{1/2}$ is the capillary length, and γ, ρ, g, and θ_E are the ink surface tension, density, gravitational constant, and equilibrium contact angle, respectively [44]. From Eq. (6.1), it is possible to unveil the main parameters that affect film stability, which as stated earlier, are not limited to the ink rheology, but also include the chemical and morphological properties of the carrier substrate.

Table 6.1 Contact angle θ_E of water on metals, oxides, and polymers and the corresponding critical thickness e_C below which dewetting occurs.

Material	θ_E (°)	e_C
Metal	~0	~100 nm
Oxide (e.g., glass)	~10–30	~1–10 μm
Polymer	~60–110	~50–500 μm

For the sake of simplicity, we limit the discussion on donor film dewetting to two inks, water ($\gamma_{H_2O} = 73$ mN/m, $\rho_{H_2O} = 1 \times 10^3$ kg/m^3, and $\upsilon_{H_2O} = 1$ mPa s) and glycerol ($\gamma_{glyc} = 63$ mN/m, $\rho_{glyc} = 1.3 \times 10^3$ kg/m^3, and $\upsilon_{glyc} = 1.5$ Pa s). Note that these two inks are widely used as model systems in LIFT [45, 46]. Table 6.1 presents a list of the critical thickness e_C for various materials used in LIFT. As expected, only when the wettability between the liquid and the carrier substrate is high, it is possible to obtain stable films with a thickness suitable for LIFT.

Even if the critical thickness of the two model inks can be, in many cases of practical interest (e.g., metal absorbing layers), well below the typical thickness used in LIFT, the risk of dewetting cannot be completely averted. First of all, any imperfections of the absorbing layer can induce local instabilities that trigger the rupture of the film. To avoid this problem, it is imperative to have clean and uniform carrier substrates. Moreover, several metals oxidize upon exposure to air resulting in a thin oxide film that reduces ink wettability. Thus, inert noble metals such as Au are, a priori, more suitable for LIFT. Finally, because liquid evaporation decreases the film thickness d_0, at least locally, the film stability is limited overtime, until $d_0 < e_C$. Therefore, the kinetics of film evaporation determines the temporal window during which the donor film remains stable and suitable for printing.

The liquid film evaporation rate (m_E) can be estimated for a model case, namely the liquid evaporation at the free vapor–liquid interface. This phenomenon is governed by the general form of Dalton's law that can be written as

$$m_E = h_M S \frac{(P_b - R_H P_{sat})}{RT} \tag{6.2}$$

where h_M is the mass transfer coefficient, S the surface area of the film, R_H the relative humidity, $R = R_0/m_v$ with R_0 the gas constant, m_v the vapor molar mass, T the temperature, P_b the vapor pressure, and P_{sat} the saturated vapor pressure. Importantly, h_M is a function of additional parameters among which the vapor diffusivity D and the velocity U of the surrounding air (convection) are the most relevant. Remarkably, Eq. (6.2) introduces an additional ink parameter, that is, the ink vapor pressure, which further limits the range of the ink candidates for LIFT. Indeed, the ideal ink should have a low evaporation rate. Note that many organic solvents, which typically feature excellent wettability over a wide variety of substrates, can be discarded as ink candidates because of their typically high vapor pressure. For a water film under standard laboratory conditions, $R_H = 60\%$,

$T = 293\,\mathrm{K}$, and U from 0.01 to 1 mm/s, the evaporation rate ranges from approximately 70 to 700 pg/m^2 s, which corresponds to a thickness reduction rate ranging from approximately 0.07 to 0.7 µm/s. Thus, a water film with a thickness of about 10 µm prepared on glass becomes unstable ($d_0 = e_C \approx 1\,\mu\mathrm{m}$) within a timescale ranging from tens of seconds to few minutes. This is impracticable for many applications and could limit future industrial implementations of LIFT. In contrast, a glycerol film exhibits good stability over time (evaporation rate $\ll$ nm/s) thanks to its low vapor pressure (~10 mPa) and high viscosity (1.5 Pa s). As detailed in the next sections, viscosity can be a drawback during the interaction of the liquid film with the laser irradiation. Highly viscous materials are also difficult to spread, and hence, in practice, it is difficult to prepare them in thin form. This is why glycerol is mainly used as an additive for decreasing the vapor pressure of aqueous solutions.

6.2.1.2 The Role of External Instabilities

Once a stable donor film is obtained, external agents can degrade the spatiotemporal stability of the liquid. In the case of LIFT, the irradiation of the film with laser pulses is the main external factor that can lead to liquid instabilities. Indeed, as a possible consequence of the liquid–matter interaction, capillary waves are usually generated [47]. The dynamics of these waves can degrade the performance of LIFT. For instance, when two laser pulses are fired in close temporal and spatial proximity, the presence of capillary waves induced by the first pulse can affect the printing process initiated by the second pulse [47, 48] (see Chapter 5 for details). To overcome this issue, the second pulse should be fired temporally or spatially separated from the first pulse. A quantification of the minimal separation (in time or space) between consecutive pulses for which interference by capillary waves is avoided can be estimated by using the lubrication approximation. In this case, capillary waves within a thin liquid layer decay exponentially with a relaxation time τ_C given by the equation

$$\tau_C = \frac{\mu \lambda^4}{\gamma d_0^3} \tag{6.3}$$

where μ is the absolute or dynamic viscosity of the ink, d_0 the film thickness, and λ the wavelength of the external disturbance with $\lambda < k^{-1}$ [44]. Thus, two pulses that are temporally separated by less than τ_C will interfere. This temporal separation can be easily transformed into a spatial distance by considering the propagation velocity of capillary waves U_c, which is given by

$$U_c = \frac{3}{2}\sqrt{\frac{2\pi\gamma}{\rho\lambda}} \tag{6.4}$$

Thus, the minimal spatial distance between two consecutive pulses (L_c), by combining Eq. (6.3) with Eq. (6.4), is

$$L_c = U_c \tau_c = \frac{3}{2}\mu\left(\frac{\lambda}{d_0}\right)^3 \sqrt{\frac{2\pi\lambda}{\rho\gamma}} \tag{6.5}$$

Under typical operational conditions, for example, $d_0 = 10\,\mu\mathrm{m}$ and $\lambda = 40\,\mu\mathrm{m}$ [47], τ_c for a water–glycerol mixture ranges from 35 µs for pure water to 40 ms

for pure glycerol, whereas the corresponding L_c would be 180 µm and 180 mm, respectively. A simple estimate of the maximum repetition rate of the printing process (*prr*) when the spatial separation between events is below L_c, as it occurs in most practical instances, would scale with $1/\tau_c$, which leads to 28 kHz for water and 25 Hz for glycerol. However, in this assumption, the temporal dynamics of the printing process have not been considered. Thus, the time required for liquid ejection, denoted as τ_e, further limits *prr*. In other words, $prr \sim 1/(\tau_c + \tau_e)$, where τ_e also depends on viscosity. These results further highlight the crucial role of the ink rheology on the performance of LIFT, which does not only affect the preparation of the liquid film but can also later alter the throughput of the technique.

Importantly, in the case of FF-LIFT, the values of L_c and τ_c can be greatly reduced. In fact, the damping effects in a bulk liquid help mitigating capillary wave effects [44]. Thus, the use of a film-free approach is less demanding in terms of the rheology of the inks to be printed.

6.2.2 Technologies for Thin-Film Preparation

Even if an ink with the ideal conditions required for LIFT printing was found, one should still look for the optimal existing technology that enables the spreading of the ink into a thin film. Several techniques are now available that enable controlled preparation of thin films at the 5–50 µm range required in LIFT. A brief description of the main features and properties of some of the most used techniques in LIFT is provided next.

Spin coating. In this approach, a small amount of ink is deposited on the center of a flat substrate, which is then rotated at high speed to uniformly spread the ink over the substrate surface (Figure 6.3a) [49, 50]. During the rotation step, solvents that are present in the ink totally or partially evaporate, leading to a film whose thickness depends on both the rotation speed (ω) and the ink viscosity (υ). In particular, the film thickness decreases with ω, whereas, it increases with υ. Therefore, the use of spin coating further limits the range of available inks for LIFT. This is particularly crucial for polymer inks, since they usually feature high viscosity that limits the minimum thickness of feasible films. Furthermore, this method is not appropriate for water-based inks since a fine control of the water evaporation rate is difficult.

Dip coating. This technique is based on a two-step process (Figure 6.3b). First, the carrier substrate over which the liquid has to be prepared is immersed in the ink. Second, the substrate is withdrawn at constant speed [50]. During this second step, a thin layer of ink deposits on the substrate, and the retracting speed determines the final thickness. In general (for Newtonian fluids, as the model solutions considered earlier), the faster the withdrawal process, the thicker the resulting film. Compared to spin coating, this method is compatible with water-based films and features a simpler implementation. For highly viscous inks, though, the uniformity of the film can be compromised.

Blade coating. This method is probably the most used in LIFT thanks to its ease of implementation and limited cost [27, 45]. Initially, a tiny amount of ink is placed in an outer marginal region of a flat substrate. After that, a blade is used

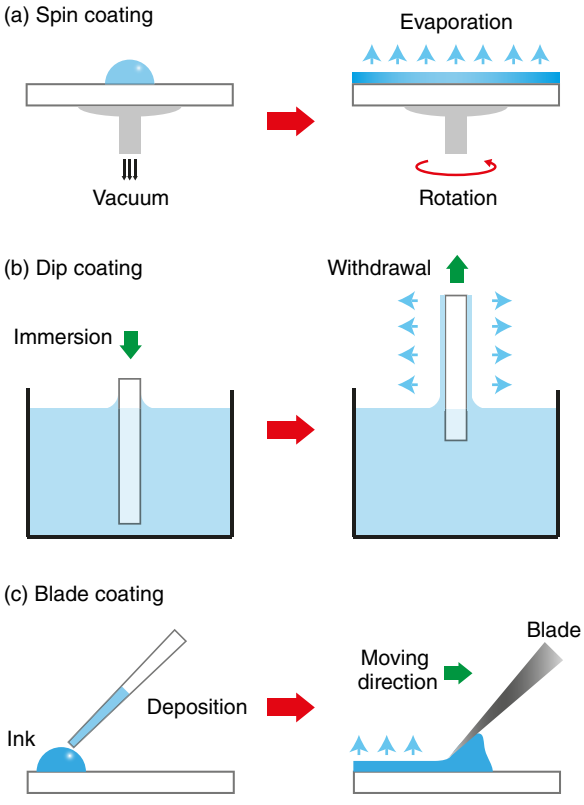

Figure 6.3 Schematic representation of the main existing technologies for the preparation of thin liquid films: (a) spin coating, (b) dip coating, and (c) blade coating.

to coat the entire substrate with the ink (Figure 6.3c). Because the gap between the blade and the substrate sets the final thickness of the coating, uniform films are feasible regardless of the ink viscosity. Despite its simplicity, any variations of the coating speed compromise the film uniformity.

6.2.3 Wetting of the Receiver Substrate

There is an additional key factor to be considered in LIFT, and that ultimately dictates the outcome of this printing process: the properties of the receiver substrate. Indeed, the amount of ink deposited on the receiver substrate does not exclusively depend on the rheological properties of the ink or the laser parameters, but it can also be affected by the wetting of the receiver substrate. In LIFT, the printing process is mediated by the formation of a jet that impacts upon the receiver substrate (Chapter 4). Thus, the jet–receiver interaction (wettability, adhesion forces) determines aspects as relevant as the laser fluence threshold required for printing [51] or the final amount of deposited material [52]. As a result, an ink that presents rheological properties optimal for the preparation of the donor film may not necessarily result in good printing. For instance, the addition of surfactants in the liquid to be printed can facilitate liquid wettability on the carrier substrate and thus enables the preparation of stable liquid films. However, the decrease of the surface tension of the ink can also promote wetting on

the receiver substrate, resulting in printed droplets with a diameter or volume larger than the ones obtained without the use of surfactant, which is detrimental in terms of printing resolution. This limitation is the consequence of the intrinsic dependence of the LIFT performance on the entire carrier/donor/receiver system. In other words, in traditional LIFT, there is a fundamental coupling between the receiver substrate and the carrier/donor system in terms of the ink properties. Thus, the choice of the ink will always be a trade-off between the optimal ink for the receiver substrate and the ideal rheological properties of the ink for its preparation in film form. In this scenario, the reader can catch a glimpse of the great potential of FF-LIFT, where the ink simply stays in a reservoir, and its rheology can be optimized only with respect to the receiver substrate. Therefore, the film-free approach provides LIFT with the ability to tune the ink with respect to a targeted application rather than to optimize the ink for its suitability as a donor film.

6.3 Fundamentals of Film-Free LIFT

The intrinsic instability of a liquid film and the technical problems associated with the preparation of materials in film form led to the development of a novel laser printing technique capable of depositing a liquid directly from a reservoir. The technique, called film-free LIFT or FF-LIFT, is based on a very simple premise: focus a laser beam underneath the free surface of a liquid contained in a reservoir in order to provide the thrust for liquid ejection. A receiver substrate, placed in close proximity to the free surface, is then used to collect the fraction of liquid ejected. Naturally, the laser beam must be absorbed in a localized area beneath the liquid-free surface for FF-LIFT to properly work. This imposes certain requirements on the optical properties of the liquid of interest or on the laser used, as it is discussed in Section 6.4. But assuming that one can deliver an amount of controlled laser energy within a small volume of a fluid, what is the mechanism that can lead to liquid ejection? What are the fundamental parameters that drive liquid motion? An answer to these questions, with particular emphasis in the differences between FF-LIFT and traditional LIFT, is presented next.

6.3.1 Cavitation-Induced Phenomena for Printing

First, we need to consider how to promote significant liquid ejection or large liquid transport using a laser. This essential step for printing is challenging to implement in practice, and it usually imposes strong requirements on the laser system or liquids to be printed. For instance, in highly light-absorbent liquids, laser-induced temperature gradients can drive large-scale fluid flows [53]. This mechanism, though, is incompatible with biological solutions, which are typically transparent to the laser radiation. In contrast, liquid actuation by cavitation bubbles fulfills the requirements desired in a laser printing technique, namely the possibility to operate with a large amount of liquids (provided they are transparent to the laser radiation) and control of the printed material by means of the

laser parameters. Indeed, laser-induced cavitation constitutes the fundamental mechanism of FF-LIFT.

The typical sequence of events in the formation of laser cavitation bubbles starts when a laser pulse is focused within a liquid. Provided the laser intensity is high enough (see Section 6.4), optical breakdown in the liquid can be induced [54, 55]. In analogy to the well-known electrical breakdown of a dielectric under strong electric fields, the molecules of a fluid can be ionized in the presence of laser radiation. As a consequence, a confined and hot plasma can be formed that explosively expands at a velocity faster than the speed of sound in the liquid (i.e., shock wave), resulting in the generation of a cavitation bubble [56, 57]. More importantly, the evolution of this bubble, including its initial growth and final collapse, can induce powerful fluid flows. Depending on the particular conditions of cavitation bubble formation, different scenarios can develop. In particular, when the bubble is generated close to a free surface, a jet perpendicular to the surface is formed, which transports a fraction of liquid away from the surface [58]. The formation of these cavitation jets dictates the outcome of the printing process in FF-LIFT. Thus, it is paramount to understand the interplay between cavitation bubble and jet formation in this printing technique.

6.3.2 Jet Formation in Film-Free LIFT

The initial dynamics of jet formation in FF-LIFT is dependent on only one parameter, the so-called standoff distance d_γ, defined as [59]:

$$d_\gamma = \frac{h}{R_{\max}} \tag{6.4}$$

where $R_{\max}$ is the maximum bubble radius (depends on the laser pulse energy absorbed), and h is the distance from the free surface to the initial bubble centroid. In general, if $d_\gamma > 0.8$, the cavitation bubble is far from the free surface for its given $R_{\max}$, and only a small protrusion in the surface is formed, which impedes proper printing. In addition, if $d_\gamma < 0.3$, bubble bursting can occur prior to jet formation, resulting in splashing in the receiver substrate. Thus, the suitable range for printing in FF-LIFT is usually $0.3 < d_\gamma < 0.8$ [60, 61]. Note that surface tension does not affect the initial formation of a jet, since bubble growth and collapse are inertia-dominated processes. At this stage, the Weber number, which describes the importance of inertial over surface tension forces, is typically large, up to 10^4 [60]. Moreover, viscosity is also found to have little effects at this initial stage [62]. Indeed, inviscid models have been found to be in good agreement with the experimental observations [36, 58, 59].

Figure 6.4 presents a temporal sequence of the jet dynamics in an FF-LIFT experiment with $d_\gamma \sim 0.6$[60]. Simulations obtained with computational fluid dynamics (CFDs) are also shown for comparison [62]. Despite the different temporal and spatial scales for experiment and simulation, the overall dynamics show a remarkable good agreement. After bubble formation, the cavitation bubble grows caused by hot gases created during plasma formation (Figure 6.4a). Notably, the growing is asymmetrical, due to the presence of the free surface that disrupts the symmetry of bubble expansion and results in a pressure gradient

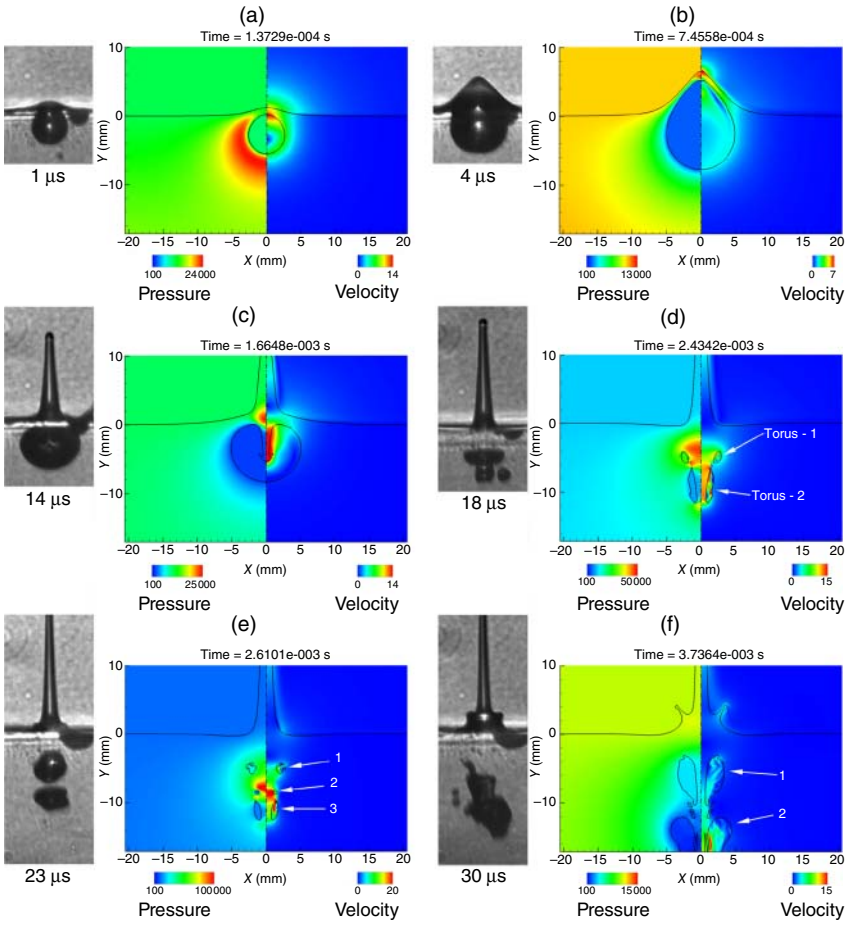

Figure 6.4 Investigation of the dynamics of FF-LIFT. Time-resolved images depicting the cavitation formation and jet evolution in a solution of water and glycerol, for $d_\gamma = 0.6$ (grayscale images) (Patrascioiu *et al*. 2014 [60]. Reproduced with permission of Springer.) and numerical simulations of the same process depicting the pressure map and velocity field. (Koukouvinis *et al*. 2016 [62]. Reproduced with permission of American Institute of Physics.)

around the bubble. In other words, because it is easier for the bubble to expand against the free surface than against the bulk liquid, a pressure gradient around the bubble is formed (Figure 6.4b). As a consequence, fluid flows are generated that move toward the bubble tip, resulting in the development of a jet. Moreover, bubble expansion causes a decrease in the inner bubble pressure, which finally produces the collapse of the bubble (Figure 6.4c). During this phase, a second jet is formed that moves downward. This second jet, also called counter-jet, passes through the bubble and impacts its bottom surface. At this point, a second gas pocket is formed that detaches from the initial bubble (Figure 6.4d). Note that the initial bubble remains toroidal due to the counter-jet piercing, as clearly appreciated in the simulation. The two bubbles then initiate an expansion phase

followed by collapse (Figure 6.4e). Interestingly, during the expansion phase of the toroidal bubble, the same situation as described previously occurs, namely the formation of a pressure gradient around the bubble and the consequent flow of liquid toward the low-pressure region, that is, the free surface. In this case, given the toroidal shape of the bubble, a corona or bulge is formed (Figure 6.4f). Depending on the experimental conditions, this corona could be disrupted due to surface tension forces (as observed in the simulations, where the *We* number decreases to a value of approximately 50 [62]) or could progress unperturbed (as in the experiment). In the case that inertial forces overcome viscous effects, both jet and corona continue advancing, until impacting the receiver substrate (not shown). At a low laser fluence (just above the threshold for printing), though, the corona may not reach the receiver substrate, even if the jet is energetic enough to do so. This would explain the steep transition observed in the amount of printed volume as the laser fluence increases [38]. Finally, instabilities created by surface tension (Plateau–Rayleigh instability) produce jet breakup [63]. Importantly, during jet propagation, viscosity also plays a crucial role, since it helps jet stability and hence can prevent the formation of satellite droplets during printing. Note that stable jets are highly desirable since they provide flexibility in the positioning of the receiver substrate relative to the liquid surface.

6.3.3 Differences with LIFT of Liquids

As described in Chapter 4, traditional LIFT of liquids is also a printing process based on cavitation jets. Thus, it comes as no surprise that the dynamics between this technique and FF-LIFT regarding cavitation bubble generation and jet development are similar. However, there are distinct peculiarities of FF-LIFT that are worth detailing. First, the corona or bulge observed in FF-LIFT is not typically identified in time-resolved imaging studies of LIFT [35, 48, 64–67]. A possible interpretation of this fact is the use of a thin liquid film in LIFT (5–20 μm), which would prevent a full development of the counter-jet and the consequent creation of the toroidal bubble. Indeed, in LIFT, the counter-jet would hit the bottom of the donor substrate and dissipate its energy during impact, truncating the further development of the corona. For liquid films with a thickness above 50 μm, though, the formation of the corona can be clearly distinguished [68–71]. Thus, in agreement with the aforementioned interpretation, the film thickness plays a crucial role in corona formation. Regarding the typical absence of corona in LIFT, this technique would seem preferable over FF-LIFT for printing small volumes. Nevertheless, the use of low laser fluences in FF-LIFT, probably under conditions in which the corona did not reach the substrate, resulted in the smallest liquid droplets printed to date [39].

A second important difference between FF-LIFT and LIFT is the propagation and dissipation of capillary waves (Section 6.2). Due to the large reservoir used in FF-LIFT, capillary waves can be quickly dissipated, and thus, a second laser pulse fired in close vicinity to the first one could lead to suitable printing. This contrasts with LIFT, in which the presence of capillary waves impedes the proper development of closely spaced jets [47, 48]. In fact, in LIFT printing of highly viscous prepolymers, the minimum lateral distance between two laser shots that

resulted in proper printing was about 50 µm [51]. In this case, the time required to completely dissipate the capillary waves was of the order of minutes. Therefore, FF-LIFT appears more suitable for high-throughput printing.

Finally, a more subtle difference between the two techniques concerns the level of understanding of the dynamics of each process. Notably, the formation of bubbles near a free surface is a phenomenon that has been widely studied in fluid mechanics, experimentally as well as computationally. Indeed, literature dating back to more than 30 years ago already studied this problem, given its direct link to cavitation erosion. Thus, the extensive knowledge of the mechanisms of FF-LIFT facilitates the search of optimization pathways for this technique. Instead, the configuration used in the LIFT of liquids is more recent, and parts of the mechanisms that lead to bubble collapse are more challenging to explore. In addition, the particular conditions of LIFT (in particular, the initial formation of the cavitation bubble) also make the computational study of this phenomenon difficult. On the other hand, this can be regarded as an opportunity for scientists in the field of fluid mechanics, for which LIFT represents a very interesting boundary value problem.

6.4 Implementation and Optical Considerations

In this section, we list the main elements to be considered for the successful implementation of FF-LIFT. In more detail, we discuss the two possible configurations that enable successful printing with this technique and the potential limitations of each of them. We also describe the most suitable laser sources in FF-LIFT, the typical laser intensities required, as well as the optical considerations of both focusing optics and liquid.

6.4.1 Laser Source

What is the suitable laser source for FF-LIFT? To answer this question, one must consider the intensity required to induce optical breakdown in a liquid. This value depends on the optical properties of the liquid as well as on laser pulse duration, wavelength, and focusing optics. For water at a wavelength of approximately 1 µm, the intensity value necessary to reach optical breakdown with nanosecond pulses (6 ns) is approximately 1×10^{11} W/cm^2, whereas for picosecond (30 ps) and femtosecond pulses (300 fs), the intensity increases to approximately 5×10^{11} W/cm^2 and 30×10^{11} W/cm^2, respectively [54, 72]. Despite the increase in intensity as the pulse duration decreases, for a given wavelength and focusing optics, the energy per pulse required to induce optical breakdown with femtosecond pulses (10 s of nJ) is significantly lower than for nanosecond pulses (mJ). Moreover, multiphoton absorption induced by femtosecond pulses facilitates the generation of seed electrons. These electrons are necessary for avalanche ionization and plasma formation (optical breakdown). In the case of nanosecond pulses, the seed electrons are generated by defects in the material, which are stochastically distributed. In contrast, femtosecond pulses enable the deterministic formation of optical breakdown in a liquid and

hence a much higher reproducibility of the printing process than in the case of nanosecond pulses. Combined with the low energy per pulse needed with femtosecond pulses, one can generally state that ultrafast lasers are the most appropriate laser source to perform FF-LIFT.

6.4.2 Forward (Inverted) versus Backward (Upright) Systems

FF-LIFT can be implemented in two different layouts, as shown in Figure 6.5. In the first configuration, known as *forward* [38, 61, 73], the liquid is ejected in the direction of beam propagation. Thus, the laser beam enters the bottom part of the reservoir and passes through the liquid until being focused just beneath the liquid-free surface. Because of the long distance the beam has to travel through the liquid, the liquid optical properties play a crucial role. Indeed, not only liquid absorption has to be very low, but also the chromatic dispersion of the medium has to be small in order to preserve the temporal duration of the laser pulse and the consequent high intensity in the focal volume required to induce optical breakdown. In addition, the reservoir has to be transparent to the laser beam, and ideally, it should have the same refractive index as the liquid in order to prevent unwanted reflections.

In the second configuration of FF-LIFT, known as *backward*, the liquid is ejected in the direction contrary to laser propagation. In particular, the laser beam first passes through the receiver substrate, it crosses the air gap between the receiver and the liquid film, and then it is focused beneath the liquid-free surface. Because the laser beam only travels through the liquid over a short distance, chromatic dispersion effects are significantly reduced compared to the forward implementation. In addition, the reservoir can be optically opaque without affecting the performance of the technique. In contrast, the receiver substrate must be transparent and present low chromatic dispersion.

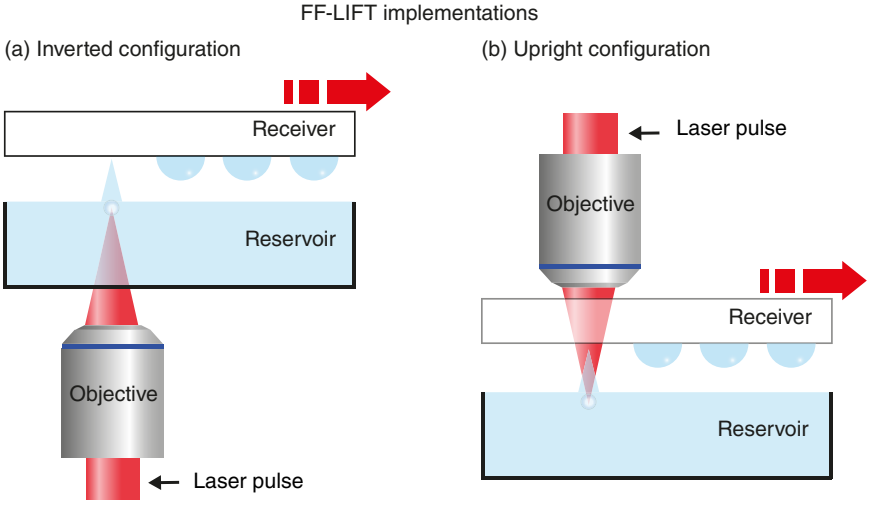

Figure 6.5 Schematic of two different implementations of FF-LIFT. (a) Inverted or forward configuration and (b) upright or backward configuration.

This strongly limits the potential use of FF-LIFT with many technologically significant substrates, such as silicon or metals, which are opaque but widely used in applications as relevant as lab-on-a-chip [2] or surface patterning [45]. Furthermore, the inevitable mismatch between the refractive index of air and that of the liquid will result in significant loss of intensity within the laser focal volume.

Considering the previous differences between the forward and backward configurations, what would be the suitable system to implement? This strongly depends on the particular demands of a given application. There is, though, an additional aspect that has not been discussed yet and that will probably determine the final system of choice for most users. In both forward and backward FF-LIFT, the reservoir has to be placed upside up. Consequently, the forward implementation requires a beam coming from below the reservoir, that is, an inverted optical system. This is more commonly found in life science laboratories. In contrast, the backward implementation needs an upright optical system, which is the standard system used for laser materials processing.

6.4.3 Spherical Aberration and Chromatic Dispersion

The focal point of a focusing lens (microscope objective) is usually designed to be an aplanatic point. In other words, the focus of most optical systems is designed to present minimal coma and spherical aberrations. However, if a planar dielectric with a different refractive index is placed within the optical path of the focusing length (between the lens and the focus), the aplanatic conditions are no longer fulfilled, and one can observe spherical aberration. The immediate consequence is the axial elongation of the focal volume. In FF-LIFT, the liquid plays the role of the dielectric, and hence, spherical aberration will have to be considered. Indeed, the elongation of the focal volume decreases the overall laser intensity and degrades the control in the positioning of cavitation bubble formation.

By using geometrical optics and Snell's law, it is possible to derive an expression for the lateral spherical aberration (A_s) induced by a planar dielectric. Considering A_s to be defined by the separation between the marginal and paraxial focus (the effective spreading of the focal volume) yields [74]:

$$A_s \cong d{\cdot}n_r \left[-\frac{(\tan\alpha)^2}{2}(1 - n_r^2) + \frac{3(\tan\alpha)^4}{8}(1 - n_r^2)^2 \right] \tag{6.5}$$

where $n_r = n_0/n$ is the ratio of the refractive index of the medium (typically air) relative to the liquid, d is the physical distance travelled by the laser beam within the liquid (in the case of forward configuration, it should also include the thickness of the reservoir, considering it has the same refractive index as the liquid), and $\tan\alpha = \omega_0/f$, with ω_0 being the beam waist at the entrance of the focusing lens with focal length f. Note that $\tan\alpha$ is proportional to the numerical aperture (NA) of the focusing optics. From this equation, it can be observed that A_s scales with the NA of the system and with the distance the beam travels within the liquid (Table 6.2). Thus, the forward configuration will in general produce a more significant elongation of the focal volume than the backward layout. In addition, low NA optics will usually lead to better focus confinement, as

Table 6.2 Spherical aberration A_s induced when focusing light using air microscope objectives with different NA and considering that a liquid with thickness *d* is placed before the system focus. In all cases, the liquid is assumed to be water, with a refractive index of 1.33.

d (μm)	NA	A_s (μm)
100	0.3	1.6
400	0.3	6.3
1000	0.3	16
100	0.5	4.8
400	0.5	19
1000	0.5	48

experimentally demonstrated [61]. There exists, though, the possibility to greatly minimize spherical aberration in the forward configuration. This can be achieved by using a dipping objective, for example, a water-dipping objective. In this case, if both liquid and reservoir match the operational refractive index of the objective, for example, water, no spherical aberration would be induced.

Another important optical property of the medium that can affect the printing process is the refractive index dependency with wavelength. Indeed, the relative large wavelength bandwidth of femtosecond pulses makes them prone to chromatic dispersion, and consequent pulse stretching, when passing through different media. In addition, as a consequence of chromatic aberration, the effective intensity in the laser focus may be reduced. The chromatic dispersion of a medium is typically characterized with the Abbe number or constringence (symbol V), which specifies the variations in the refractive index of a medium for a specific spectral range. In particular, $V = (n_D - 1)/(n_F - n_C)$, where n_D, $n_{F,}$ and n_C are the refractive indices of the material at the wavelengths 589.3, 486.1, and 656.3 nm, respectively. The Abbe number can be found in tables. Typically, materials with $V < 50$ are considered dispersive ($V = 34$ for polycarbonate plastics), whereas low-dispersive materials can reach $V > 70$, such as phosphate crown glasses. For water, $V = 50$, and hence, the amount of chromatic dispersion in FF-LIFT, particularly in the forward configuration, can be significant.

6.5 Applications

Traditional LIFT of liquids with a DRL is arguably the most widely used version of this printing approach. However, the possibility offered by FF-LIFT to decouple the requirements of the ink regarding the receiver substrate from those needed to prepare a liquid film could be advantageous in several fields. To illustrate the potential benefits of this technique, in this section, we present two selected examples of applications in which FF-LIFT can be successfully implemented.

6.5.1 Film-Free LIFT for Printing Biomaterials

A potential niche market for LIFT is the controlled deposition of biological materials such as DNA, [27, 75] proteins, [76–78], and even living cells [26, 28, 30, 37]. Compared to alternative strategies such as inkjet printing or pin spotting, LIFT offers unique features that render this technique particularly suitable for the growing fields of biomolecule microarrays or biosensors. Indeed, LIFT enables the printing of volumes as small as femtoliters while preserving a high throughput. In addition, it is possible to visually inspect the donor film during the printing process. This makes possible to irradiate only a targeted area of the donor film. For instance, if the donor film contains cells, one can select the cells to be ejected toward the receiver substrate. However, the problems related to the preparation of the liquid film are particularly excruciating in the case of biological materials. Notably, biological solutions are often transparent to the common laser radiations – the use of UV lasers is not recommended since it could alter the biological materials (e.g., denaturation of DNA) – and thus, an intermediate absorbing layer or DRL, usually a metal, is utilized to enhance the light absorption and induce liquid ejection. The use of an absorbing layer, though, can lead to sample contamination by micro/nanometallic particles. For instance, DNA damage and cell toxicity could be induced by metallic contaminants [79, 80]. Although the use of a polyimide intermediate layer, as in the case of blister-actuated LIFT, solves this problem [37] (Chapter 5), the risk of liquid dewetting for thin films prepared on polymers (Section 6.2.1.1) is very high, and hence, only specific materials with very low surface tension can be used in practice. Note that it is also possible to use ultrashort laser pulses in LIFT to induce material ejection from weakly absorbing materials without DRL. However, this option is difficult to implement in practice due to the small thickness of the liquid film and the refractive index mismatch between the ink and the carrier substrate. Indeed, in this case, the control of the laser focus beneath the free surface of the liquid film is utterly challenging not only due to spherical aberration and the intrinsic depth of field of the focusing optics (which also exist in FF-LIFT), but especially for the change (jump) in the focus position when traversing two materials each with a different refractive index.

Within this framework, the possibility offered by FF-LIFT to directly deposit the biological material from a reservoir is of clear advantage. Because no absorbing layer is needed, contamination can be greatly reduced. Moreover, by obviating the liquid film, one can save time, prevent potential contamination during the preparation of the liquid film, and more importantly, skip the tight requirements on the rheology of the ink necessary to obtain a spatiotemporal stable thin film. In fact, FF-LIFT could be used with liquids that present a relatively high vapor pressure, provided the laser focus beneath the free surface is adjusted to compensate for liquid evaporation. As stated in Section 6.2.1.1, such inks are incompatible with LIFT, since liquid evaporation can lead to dewetting issues.

The feasibility of FF-LIFT for the fabrication of miniaturized optical biosensors has been recently demonstrated [39]. In this case, the biosensor consisted of a microarray printed on a poly-L-lysine-coated microscope slide with FF-LIFT and containing mouse and rabbit immunoglobulin G (IgG) solutions

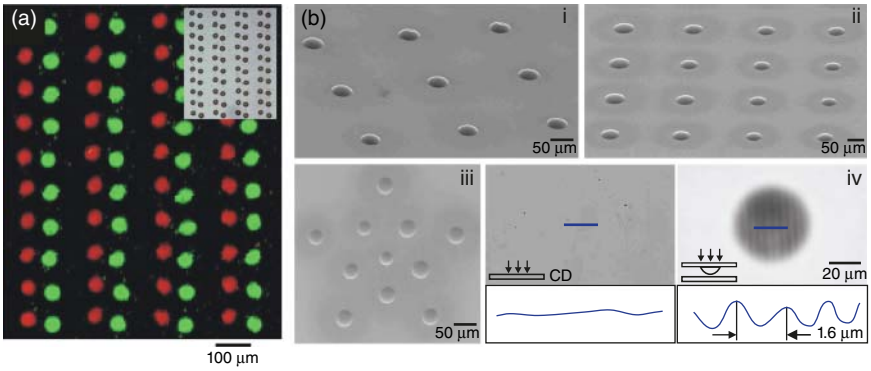

Figure 6.6 Applications of FF-LIFT (a) Fluorescence image of a fabricated biosensors consisting of a microarray of mouse IgG and rabbit IgG after immunoassay with specific anti-IgG. The inset shows an optical microscopy image of the same array. (Duocastella *et al*. 2010 [39]. Reproduced from Elsevier.) (b) Laser printing applied to the realization of polymeric microlenses. Scanning electronic microscopy (SEM) images of polymer microlenses fabricated on (i) polydimethylsiloxane and (ii) glass. (iii) SEM image of a star-shaped pattern of microlenses. (iv) Optical microscopy image of the surface of a CD (line pitch 1.6 µm) without and with the microlens on top. In the latter, the lines of the CD can be observed, which demonstrates the effective enhancement in the resolution of the system. (Florian *et al*. 2016 [51]. Reproduced from American Chemical Society.)

(Figure 6.6a). Notably, both solutions were directly printed from a 100 µl cylindrical plastic container. After an immunoassay with tagged antibodies, fluorescence microscopy revealed high specific binding for each printed solution. This result demonstrates the ability of accurately placing undamaged proteins onto solid substrates using FF-LIFT. Furthermore, FF-LIFT has been successfully exploited for printing DNA molecules for a hybridization assay [39]. Two DNA solutions were printed by FF-LIFT, directly form a reservoir, each one containing a single human cDNA clone insert: the mitogen-activated protein kinase 3 gene (MAPK3) and the v-ets avian erythroblastosis virus E26 oncogenehomolog 2 (ETS2), respectively. After a standard hybridization protocol, with the complementary strands of the cDNAs tagged with a different fluorochrome (Cy5 for MAPK3 and Cy3 for ETS2), fluorescence images demonstrated the specific binding of each cDNA strand to its perfect complementary. This further confirms the feasibility of FF-LIFT for printing biomolecules.

6.5.2 Film-Free LIFT for Micro-Optical Element Fabrication

The fabrication of micro-optical components plays a key role in the development of functional devices such as detectors, energy-harvesting systems, or CMOS cameras. With the advance of additive manufacturing processes and the trend toward customized production units, methods capable of directly fabricating user-defined microlenses or microlens arrays without masks or molds appear particularly suitable. Given the intrinsic compatibility of LIFT with highly

viscous inks such as those traditionally used for microlens fabrication, this technique seems to be an ideal tool of choice for this purpose. In addition, the use of liquid printing techniques has a natural advantage over the methods that operate with solid materials, because surface tension provides liquid droplets with a perfectly spherical shape. This has prompted the use of LIFT for the successful printing of liquid microlenses that provide an enhancement of the focusing capabilities of a laser system and enable deep subwavelength laser nanopatterning [45]. Moreover, LIFT has recently been used for the fabrication of polymeric lenses with tailored geometry and size (Figure 6.6b) [51]. In both cases, the potential advantages of LIFT can be hampered by two serious constraints of this technique. First, the requirement of an absorbing layer can result in debris (micro/nanoparticles) inside the fabricated lens. As a result, the optical quality of the microlenses can be severely deteriorated. Second, the wettability of the microlenses with the receiver substrate dictates the optical properties of the lenses, namely the radius of curvature. Indeed, to obtain lenses with high curvature, one requires inks that present a poor wettability with the receiver substrate. Given the restricted number of available inks with desired optical qualities, an ink with poor wettability on the receiver will typically have poor wettability in most materials, and hence, the preparation of such an ink in film form will be challenging. In contrast, FF-LIFT has the potential to solve all these problems. Indeed, the possibility to generate micro-optical components without an absorbing layer can prevent contamination issues. Furthermore, printing inks with poor wettability is no longer a problem, because the ink can be directly handled from a reservoir or container.

6.6 Conclusions and Future Outlook

The use of FF-LIFT enables the printing of weakly absorbing liquids with high resolution and high speed over extended surfaces. The large experimental parameter space that comes with this technique is due to the possibility to directly deposit the liquid from a reservoir. This contrasts with traditional LIFT, in which the material of interest has to be spread into a thin film. Indeed, the outcome of LIFT is seriously affected by the spatial uniformity and temporal stability of the liquid donor film. As a consequence, LIFT is restricted to liquids with specific rheology, which may not be fully compatible with a targeted application.

The operational principle of FF-LIFT, based on cavitation jetting and corona formation, provides remote control of liquid ejection by simply tuning the laser parameters or the distance between the laser focus and the free surface. These unique characteristics can be exploited in a myriad of novel and fascinating applications such as biosensing, micro-optics, and tissue engineering. As FF-LIFT continues to be developed and we learn more about the fundamentals of liquid–laser interactions, interesting possibilities will continue to emerge, offering new opportunities for laser-based additive manufacturing technologies.

References

1 Mack, C.A. (2007) *Fundamental Principles of Optical Lithography : the Science of Microfabrication*, Wiley, Chichester, West Sussex, England; Hoboken, NJ.

2 Dittrich, P.S. and Manz, A. (2006) Lab-on-a-chip: microfluidics in drug discovery. *Nat. Rev. Drug Discovery*, **5** (3), 210–218.

3 Billiet, T., Vandenhaute, M., Schelfhout, J. *et al.* (2012) A review of trends and limitations in hydrogel-rapid prototyping for tissue engineering. *Biomaterials*, **33** (26), 6020–6041.

4 Mardis, E.R. (2008) Next-generation DNA sequencing methods. *Annu. Rev. Genomics Hum. Genet.*, **9** (1), 387–402.

5 Menard, E., Meitl, M.A., Sun, Y. *et al.* (2007) Micro- and nanopatterning techniques for organic electronic and optoelectronic systems. *Chem. Rev.*, **107** (4), 1117–1160.

6 Singh, M., Haverinen, H.M., Dhagat, P., and Jabbour, G.E. (2010) Inkjet printing-process and its applications. *Adv. Mater.*, **22** (6), 673–685.

7 Piner, R.D., Zhu, J., Xu, F. *et al.* (1999) Dip-Pen Nanolithography. *Science*, **283** (5402), 661–663.

8 Quake, S.R. and Scherer, A. (2000) From micro- to nanofabrication with soft materials. *Science*, **290** (5496), 1536–1540.

9 Guo, L.J. (2007) Nanoimprint lithography: methods and material requirements. *Adv. Mater.*, **19** (4), 495–513.

10 Arnold, C.B., Serra, P., and Piqué, A. (2007) Laser direct-write techniques for printing of complex materials. *MRS Bull.*, **32**, 23–31.

11 Delaporte, P. and Alloncle, A.-P. (2016) Laser-induced forward transfer: a high resolution additive manufacturing technology. *Opt. Laser Technol.*, **78**, 33–41.

12 Wang, J., Auyeung, R.C.Y., Kim, H. *et al.* (2010) Three-dimensional printing of interconnects by laser direct-write of silver nanopastes. *Adv. Mater.*, **22** (40), 4462–4466.

13 Kim, H., Duocastella, M., Charipar, K.M. *et al.* (2013) Laser printing of conformal and multi-level 3D interconnects. *Appl. Phys. A*, **113** (1), 5–8.

14 Willis, D.A. and Grosu, V. (2005) Microdroplet deposition by laser-induced forward transfer. *Appl. Phys. Lett.*, **86** (24), 244103.

15 Banks, D.P., Grivas, C., Mills, J.D. *et al.* (2006) Nanodroplets deposited in microarrays by femtosecond Ti : sapphire laser-induced forward transfer. *Appl. Phys. Lett.*, **89** (19), 193107.

16 Tseng, M.L., Wu, P.C., Sun, S. *et al.* (2012) Fabrication of multilayer metamaterials by femtosecond laser-induced forward-transfer technique. *Laser Photonics Rev.*, **6** (5), 702–707.

17 Surdo, S., Piazza, S., Ceseracciu, L. *et al.* (2016) Towards nanopatterning by femtosecond laser ablation of pre-stretched elastomers. *Appl. Surf. Sci.*, **374** (30), 151–156.

18 Heisterkamp, A., Maxwell, I.Z., Mazur, E. *et al.* (2005) Pulse energy dependence of subcellular dissection by femtosecond laser pulses. *Opt. Express*, **13** (10), 3690–3696.

19 Boyden, E.S., Zhang, F., Bamberg, E. *et al.* (2005) Millisecond-timescale, genetically targeted optical control of neural activity. *Nat. Neurosci.*, **8** (9), 1263–1268.

20 Antkowiak, M., Torres-Mapa, M.L., Stevenson, D.J. *et al.* (2013) Femtosecond optical transfection of individual mammalian cells. *Nat. Protoc.*, **8** (6), 1216–1233.

21 Heller, M.J. (2002) DNA microarray technology: devices, systems, and applications. *Annu. Rev. Biomed. Eng.*, **4** (1), 129–153.

22 Hall, D.A., Ptacek, J., and Snyder, M. (2007) Protein microarray technology. *Mech. Ageing Dev.*, **128** (1), 161–167.

23 Wang, J. (2005) Carbon-nanotube based electrochemical biosensors: a review. *Electroanalysis*, **17** (1), 7–14.

24 Fan, X., White, I.M., Shopova, S.I. *et al.* (2008) Sensitive optical biosensors for unlabeled targets: a review. *Anal. Chim. Acta*, **620** (1–2), 8–26.

25 Hopp, B., Smausz, T., Antal, Z. *et al.* (2004) Absorbing film assisted laser induced forward transfer of fungi (Trichoderma conidia). *J. Appl. Phys.*, **96** (6), 3478–3481.

26 Hopp, B., Smausz, T., Kresz, N. *et al.* (2005) Survival and proliferative ability of various living cell types after laser-induced forward transfer. *Tissue Eng.*, **11** (11–12), 1817–1823.

27 Fernández-Pradas, J.M., Colina, M., Serra, P. *et al.* (2004) Laser-induced forward transfer of biomolecules. *Thin Solid Films*, **453–454**, 27–30.

28 Guillotin, B., Souquet, A., Catros, S. *et al.* (2010) Laser assisted bioprinting of engineered tissue with high cell density and microscale organization. *Biomaterials*, **31** (28), 7250–7256.

29 Guillotin, B. and Guillemot, F. (2011) Cell patterning technologies for organotypic tissue fabrication. *Trends Biotechnol.*, **29** (4), 183–190.

30 Barron, J.A., Wu, P., Ladouceur, H.D., and Ringeisen, B.R. (2004) Biological laser printing: a novel technique for creating heterogeneous 3-dimensional cell patterns. *Biomed. Microdevices*, **6** (2), 139–147.

31 Barron, J.A., Ringeisen, B.R., Kim, H. *et al.* (2004) Application of laser printing to mammalian cells. *Thin Solid Films*, **453–454**, 383–387.

32 Dinca, V., Farsari, M., Kafetzopoulos, D. *et al.* (2008) Patterning parameters for biomolecules microarrays constructed with nanosecond and femtosecond UV lasers. *Thin Solid Films*, **516** (18), 6504–6511.

33 Fardel, R., Nagel, M., Nüesch, F. *et al.* (2007) Laser forward transfer using a sacrificial layer: Influence of the material properties. *Appl. Surf. Sci.*, **254** (4), 1322–1326.

34 Banks, D.P., Kaur, K., Gazia, R. *et al.* (2008) Triazene photopolymer dynamic release layer-assisted femtosecond laser-induced forward transfer with an active carrier substrate. *Europhys. Lett. Assoc.*, **83** (3), 38003.

35 Brown, M.S., Kattamis, N.T., and Arnold, C.B. (2011) Time-resolved dynamics of laser-induced micro-jets from thin liquid films. *Microfluid. Nanofluid.*, **11** (2), 199–207.

36 Brown, M.S., Brasz, C.F., Ventikos, Y., and Arnold, C.B. (2012) Impulsively actuated jets from thin liquid films for high-resolution printing applications. *J. Fluid Mech.*, **709**, 341–370.

37 Kattamis, N.T., Purnick, P.E., Weiss, R., and Arnold, C.B. (2007) Thick film laser induced forward transfer for deposition of thermally and mechanically sensitive materials. *Appl. Phys. Lett.*, **91** (17), 171120.

38 Duocastella, M., Patrascioiu, A., Fernández-Pradas, J.M. *et al.* (2010) Film-free laser forward printing of transparent and weakly absorbing liquids. *Opt. Express*, **18** (21), 21815–21825.

39 Duocastella, M., Fernández-Pradas, J.M., Morenza, J.L. *et al.* (2010) Novel laser printing technique for miniaturized biosensors preparation. *Sens. Actuators, B*, **145** (1), 596–600.

40 Craster, R.V. and Matar, O.K. (2009) Dynamics and stability of thin liquid films. *Rev. Mod. Phys.*, **81** (3), 1131–1198.

41 Bestehorn, M. and Merkt, D. (2006) Regular surface patterns on Rayleigh-Taylor unstable evaporating films heated from below. *Phys. Rev. Lett.*, **97** (12), 127802.

42 Bonn, D., Eggers, J., Indekeu, J., and Meunier, J. (2009) Wetting and spreading. *Rev. Mod. Phys.*, **81** (2), 739–805.

43 H-C, Chang (1994) Wave evolution on a falling film. *Annu. Rev. Fluid Mech.*, **26** (1), 103–136.

44 de Gennes, P.-G., Brochard-Wyart, F., and Quéré, D. (2004) *Capillarity and Wetting Phenomena*, Springer-Verlag, New York, Inc.

45 Duocastella, M., Florian, C., Serra, P., and Diaspro, A. (2015) Sub-wavelength laser nanopatterning using droplet lenses. *Sci. Rep.*, **5**, 16199.

46 Duocastella, M., Fernández-Pradas, J.M., Morenza, J.L., and Serra, P. (2010) Sessile droplet formation in the laser-induced forward transfer of liquids: A time-resolved imaging study. *Thin Solid Films*, **518**, 5321–5325.

47 Brasz, C.F., Yang, J.H., and Arnold, C.B. (2014) Tilting of adjacent laser-induced liquid jets. *Microfluid. Nanofluid.*, **18** (2), 185–197.

48 Biver, E., Rapp, L., Alloncle, A.-P. *et al.* (2014) High-speed multi-jets printing using laser forward transfer: time-resolved study of the ejection dynamics. *Opt. Express*, **22** (14), 17122–17134.

49 Hall, D.B., Underhill, P., and Torkelson, J.M. (1998) Spin coating of thin and ultrathin polymer films. *Polym. Eng. Sci.*, **38** (12), 2039–2045.

50 Scriven, L.E. (1988) Physics and Applications of Dip Coating and Spin Coating. *MRS Online Proc. Libr.*, **121**, 717–729.

51 Florian, C., Piazza, S., Diaspro, A. *et al.* (2016) Direct laser printing of tailored polymeric microlenses. *ACS Appl. Mater. Interfaces*, **8** (27), 17028–17032.

52 Duocastella, M., Fernández-Pradas, J.M., Morenza, J.L., and Serra, P. (2011) Droplet printing through bubble contact in the laser forward transfer of liquids. *Appl. Surf. Sci.*, **257** (7), 2825–2829.

53 Delville, J.-P., Robert de Saint Vincent, M., Schroll, R.D. *et al.* (2009) Laser microfluidics: fluid actuation by light. *J. Opt. A: Pure Appl. Opt.*, **11** (3), 034015.

54 Vogel, A., Noack, J., Nahen, K. *et al.* (1999) Energy balance of optical breakdown in water at nanosecond to femtosecond time scales. *Appl. Phys. B*, **68** (2), 271–280.

55 Vogel, A., Nahen, K., Theisen, D., and Noack, J. (1996) Plasma formation in water by picosecond and nanosecond Nd:YAC laser pulses – Part I: Optical breakdown at threshold and superthreshold irradiance. *IEEE J. Sel. Top. Quantum Electron.*, **2** (4), 847–860.

56 Vogel, A., Busch, S., and Parlitz, U. (1996) Shock wave emission and cavitation bubble generation by picosecond and nanosecond optical breakdown in water. *J. Acoust. Soc. Am.*, **100** (1), 148–165.

57 Schaffer, C.B., Nishimura, N., Glezer, E.N. *et al.* (2002) Dynamics of femtosecond laser-induced breakdown in water from femtoseconds to microseconds. *Opt. Express*, **10** (3), 196–203.

58 Robinson, P.B., Blake, J.R., Kodama, T. *et al.* (2001) Interaction of cavitation bubbles with a free surface. *J. Appl. Phys.*, **89** (12), 8225–8237.

59 Pearson, A., Cox, E., Blake, J.R., and Otto, S.R. (2004) Bubble interactions near a free surface. *Eng. Anal. Boundary Elem.*, **28** (4), 295–313.

60 Patrascioiu, Fernandez-Pradas, J. M., Palla-Papavlu, *et al.* (2014) Laser-generated liquid microjets : correlation between bubble dynamics and liquid ejection. *Microfluid. Nanofluid.*, **16** (1–2), 55–63.

61 Desrus, H., Chassagne, B., Moizan, F. *et al.* (2016) Effective parameters for film-free femtosecond laser assisted bioprinting. *Appl. Opt.*, **55** (14), 3879–3886.

62 Koukouvinis, P., Gavaises, M., Supponen, O., and Farhat, M. (2016) Simulation of bubble expansion and collapse in the vicinity of a free surface. *Phys. Fluids*, **28** (5), 051203.

63 Eggers, J. and Villermaux, E. (2008) Physics of liquid jets. *Rep. Prog. Phys.*, **71** (3), 036601.

64 Duocastella, M., Fernández-Pradas, J.M., Serra, P., and Morenza, J.L. (2008) Jet formation in the laser forward transfer of liquids. *Appl. Phys. A*, **93** (2), 453–456.

65 Duocastella, M., Patrascioiu, A., Dinca, V. *et al.* (2011) Study of liquid deposition during laser printing of liquids. *Appl. Surf. Sci.*, **257** (12), 5255–5258.

66 Boutopoulos, C., Kalpyris, I., Serpetzoglou, E., and Zergioti, I. (2014) Laser-induced forward transfer of silver nanoparticle ink: Time-resolved imaging of the jetting dynamics and correlation with the printing quality. *Microfluid. Nanofluid.*, **16** (3), 493–500.

67 Brown, M.S., Kattamis, N.T., and Arnold, C.B. (2010) Time-resolved study of polyimide absorption layers for blister-actuated laser-induced forward transfer. *J. Appl. Phys.*, **107** (8), 083103.

68 Unger, C., Gruene, M., Koch, L. *et al.* (2011) Time-resolved imaging of hydrogel printing via laser-induced forward transfer. *Appl. Phys. A*, **103** (2), 271–277.

69 Gruene, M., Unger, C., Koch, L. *et al.* (2011) Dispensing pico to nanolitre of a natural hydrogel by laser-assisted bioprinting. *Biomed. Eng. Online*, **10** (1), 19.

70 Yan, J., Huang, Y., Xu, C., and Chrisey, D.B. (2012) Effects of fluid properties and laser fluence on jet formation during laser direct writing of glycerol solution. *J. Appl. Phys.*, **112** (8), 083105.

71 Zhang, Z., Xiong, R., Mei, R. *et al.* (2015) Time-resolved imaging study of jetting dynamics during laser printing of viscoelastic alginate solutions. *Langmuir*, **31** (23), 6447–6456.

72 Vogel, A., Linz, N., Freidank, S., and Paltauf, G. (2008) Femtosecond-laser-induced nanocavitation in water: Implications for optical breakdown threshold and cell surgery. *Phys. Rev. Lett.*, **100** (3), 038102.

73 Patrascioiu, A., Duocastella, M., Fernández-Pradas, J.M. *et al.* (2011) Liquids microprinting through a novel film-free femtosecond laser based technique. *Appl. Surf. Sci.*, **257** (12), 5190–5194.

74 Iwaniuk, D., Rastogi, P., and Hack, E. (2011) Correcting spherical aberrations induced by an unknown medium through determination of its refractive index and thickness. *Opt. Express*, **19** (20), 19407–19414.

75 Colina, M., Serra, P., Fernández-Pradas, J.M. *et al.* (2005) DNA deposition through laser induced forward transfer. *Biosens. Bioelectron.*, **20**, 1638–1642.

76 Zergioti, I., Karaiskou, A., Papazoglou, D.G. *et al.* (2005) Femtosecond laser microprinting of biomaterials. *Appl. Phys. Lett.*, **86** (16), 163902.

77 Serra, P., Fernández-Pradas, J.M., Berthet, F.X. *et al.* (2004) Laser direct writing of biomolecule microarrays. *Appl. Phys. A*, **79** (4–6), 949–952.

78 Duocastella, M., Fernández-Pradas, J.M., Domínguez, J. *et al.* (2008) Printing biological solutions through laser-induced forward transfer. *Appl. Phys. A*, **93** (4), 941–945.

79 Papageorgiou, I., Brown, C., Schins, R. *et al.* (2007) The effect of nano- and micron-sized particles of cobalt-chromium alloy on human fibroblasts in vitro. *Biomaterials*, **28** (19), 2946–2958.

80 Kroll, A., Pillukat, M.H., Hahn, D., and Schnekenburger, J. (2009) Current in vitro methods in nanoparticle risk assessment: Limitations and challenges. *Eur. J. Pharm. Biopharm.*, **72** (2), 370–377.

Part II

The Role of the Laser–Material Interaction in LIFT

7

Laser-Induced Forward Transfer of Metals

David A. Willis

Southern Methodist University, Bobby B. Lyle School of Engineering, Department of Mechanical Engineering, 3101 Dyer Street, Dallas, TX 75205, USA

7.1 Introduction, Background, and Overview

Laser-induced forward transfer (LIFT) of metals is a physical microdeposition process that uses a laser beam as an energy source for transferring material from a "donor" substrate to a "target" substrate, as shown in Figure 7.1. The donor substrate is a transparent material such as glass and oriented such that the donor material is in close proximity to the target substrate. The two substrates are separated by a gap, Δz, which can range from zero (contact mode) to hundreds of microns, with the gap maintained by a spacer. The laser is focused through the donor substrate and absorbed in the metal film near the donor substrate/film interface. The absorbed laser energy heats the film to a threshold level where it is energized and propelled to the target substrate, where it is deposited. Patterns of the deposit can be formed on the target substrate by a number of methods, including controlling the path of the sample with respect to a tightly focused laser beam or by irradiating a large area of the film with a patterned laser beam. Methods of patterning the beam include cylindrical lenses [1], spatial light modulators [2, 3] (see also Chapter 10), self-assembled microbead lenses [4], masking [5], and prepatterned donor films [6–8]. Metal films are coated onto the donor substrate by methods such as sputtering, which allows careful control of the donor film thickness and uniformity. Metal films used for LIFT are usually coated to a thickness ranging from tens of nanometers (nm) to micrometers (μm). The deposited feature characteristics depend upon the gap spacing, Δz; donor film thickness, t; laser spot size, $2\omega_o$; laser pulse width, τ_p; and laser fluence, F. Pulse widths used for LIFT range from femtoseconds (fs) to milliseconds (ms), although LIFT of metals normally uses nanosecond (ns) or shorter pulses in order to minimize thermal diffusion from the laser spot, which provides additional control over the resolution.

LIFT is a subset of the more general topic of laser-induced transfer, the origins of which are reviewed in Chapter 2. The first report of LIFT as described in this book was by Bohandy *et al.*, in which copper was deposited using an excimer laser

Laser Printing of Functional Materials: 3D Microfabrication, Electronics and Biomedicine,
First Edition. Edited by Alberto Piqué and Pere Serra.
© 2018 Wiley-VCH Verlag GmbH & Co. KGaA. Published 2018 by Wiley-VCH Verlag GmbH & Co. KGaA.

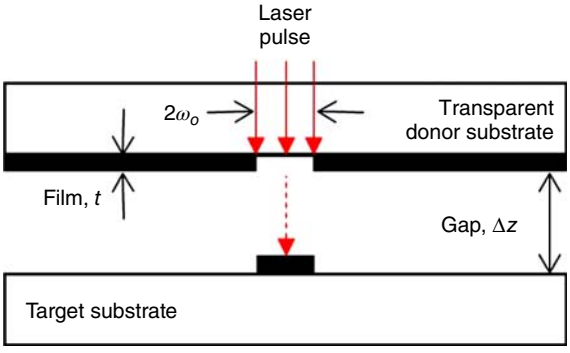

Figure 7.1 Schematic of LIFT of metals including laser heating, transfer, and deposition on a target substrate. The focused laser spot locally heats the metal film at the interface with a transparent donor substrate. The metal is energized at the laser focal spot, propelled across a gap, and deposited on a target substrate.

[1]. Since then, LIFT has been studied for a wide range of materials and applications. Materials that have been transferred with LIFT and its variations include semiconductors [9] (see also Chapter 12), polymers [10] (see also Chapter 8), superconductors [11], electronic pastes/inks and sensing materials [12, 13] (see also Chapters 10, 12, and 13), and biological materials [14, 15] (see also Chapters 14 and 15).

LIFT of metals is a single-step process that does not require additional steps, unless postdeposition sintering is desired. Since deposition occurs only in the path of the laser, LIFT can be highly localized and used for fabricating micro- and nanostructures. Such capability is useful for rapid prototyping and fabrication of microdevices. While other localized direct-write deposition methods exist, such as inkjet, screen printing, aerosol jet, and selective laser sintering, LIFT has a much higher resolution [16]. While UV photolysis is capable of depositing metals with spatial selectivity, LIFT can accomplish this without organometallic precursors [1]. The resolution of LIFT has now reached the sub-500 nm range [17, 18] and can be as small as 70 nm using fs laser pulses [19]. In addition to the resolution, spatial selectivity, and variety of materials that can be transferred, LIFT can be performed with or without vacuum conditions and does not require a cleanroom. Since the laser does not interact directly with the target substrate, the target can be a low-melting-point material, allowing deposition onto polymers and glasses with minimal risk of damage [20]. LIFT of metals has been explored for applications in electronics and optics including diffractive optics [21–23], waveguide fabrication [24, 25], surface texturing [26], and deposition of electrical conductors in various applications such as electrodes for microfluidics [27], contact pads for solder [28], through-silicon vias [16], silicon solar cell line metallization [29], and repair and tuning of electronic components [28]. More recently, LIFT has been explored for microscale 3D printing [30–33], which is explored in detail in Chapter 17.

LIFT of metals has challenges not encountered with other materials due to the high thermal diffusivity and short optical absorption depth of metals. Since metal films easily absorb optical radiation over a wide wavelength range, they are less sensitive to laser wavelength compared to other materials and do not require a dynamic release layer for absorbing the laser (see, e.g., Chapter 3). Thus, laser irradiation is absorbed directly by the donor film, and the film thermal properties dominate the behavior of the LIFT process. However, this also leads to challenges

with LIFT of metals since the film must go through solid–liquid and liquid–vapor phase change for transfer and deposition. Thus, deposits suffer from splashing of the molten phase, nonuniformity of the deposit, voids, and oxides. Improved understanding of the roles and the interaction of the many process variables (Δz, t, ω_o, τ_p, F) will allow for improved process control and tailored design of LIFT for specific applications.

The following review will discuss LIFT of metals, with an emphasis on the laser absorption, heat transfer, and related process parameters that control LIFT. Following a discussion of the fundamental laser–material interactions, early experimental and numerical studies will be reviewed, followed by more recent developments such as droplet-based transfer and lift-off and advanced numerical models.

7.2 Modeling, Simulation, and Experimental Studies of the Transfer Process

The use of LIFT for transferring metals involves direct laser heating at the interface between the film and the donor substrate. Due to the short optical absorption depth, the laser energy is initially confined to a shallow region near the metal film/substrate interface. This localized heating can result in melting and liquid–vapor phase change at the interface, which drives the transfer process. However, the behavior of the transfer process is also controlled by thermal diffusion away from the laser absorption zone. Thus, the relative size of the donor film thickness and the thermal diffusion length are important for understanding how transfer will occur.

7.2.1 Thermal Processes: Film Heating, Removal, Transfer, and Deposition

The LIFT process begins with absorption of laser energy at the interface between the donor substrate and the donor film. Since the donor substrate is usually a type of glass, it is very transparent and has low thermal conductivity. Thus, most of the energy is absorbed at the donor substrate/film interface and conducted into the metal film, which has a much higher conductivity than the donor substrate. In most instances, the film thickness, t, is much smaller than the laser spot size, and the heat conduction is one-dimensional in the z-direction (Figure 7.2). The temperature rise in the film is governed by the heat diffusion equation, given as [34]

$$\nabla \cdot (k \nabla T) + \dot{q} = \rho C_p \frac{\partial T}{\partial \tau} \tag{7.1}$$

where $\dot{q}$ is the rate of volumetric heat generation due to absorption of laser energy, k is the thermal conductivity, ρ is the density, C_p is the specific heat, and τ is time. The rate of volumetric heat generation is given as

$$\dot{q} = \gamma(1 - R_2)(1 - R_1) I_o e^{-\gamma z} \tag{7.2}$$

where γ is the optical absorption coefficient, z is the axial coordinate, and R_1 and R_2 are the reflectivity values of the of the donor substrate/air interface and the

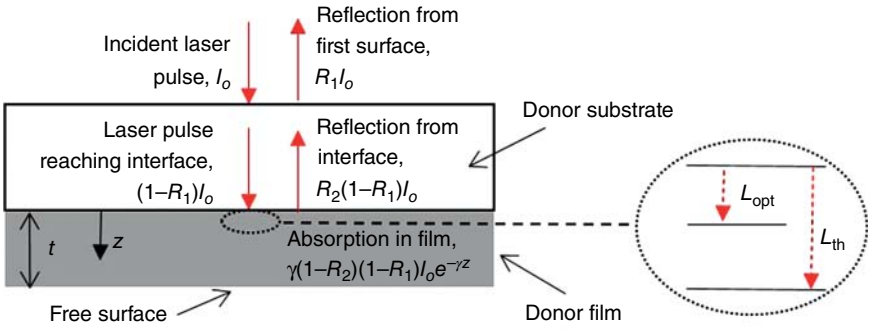

Figure 7.2 Absorption of laser energy in the metal donor film showing the confinement of the absorbed laser energy at the interface between the donor substrate and the film. The relative sizes of the film thickness, t, thermal diffusion length, L_{th}, and optical absorption depth, L_{opt}, are critical to the behavior of the LIFT process.

donor substrate/film interface, respectively. The incident laser irradiance, I_o, is the time-dependent heat flux from the laser, which may also be a function of spatial coordinates, such as the case for TEM_{00} lasers with a Gaussian distribution. As shown in Figure 7.2, L_{opt} is the absorption depth, given by Eq. (7.3),

$$L_{opt} = \frac{1}{\gamma} \tag{7.3}$$

which is the depth at which the absorbed laser intensity has decayed to a value of e^{-1}. For metals, the absorption depth is typically on the order of 10–20 nm for wavelengths ranging from ultraviolet to near-infrared [35]. Thus, most of the irradiation is absorbed within a small distance of the interface. Although the laser irradiance, I_o, is the parameter that controls the rate of heating, most studies specify the laser fluence in joule per square centimeter out of convenience.

The thermal diffusion length is the distance the temperature disturbance propagates within a given timescale and can be approximated as [36]

$$L_{th} = 2\sqrt{\alpha\tau} \tag{7.4}$$

where α is the thermal diffusivity of the metal, and τ is a timescale, such as the laser pulse width. As will be seen in the literature review, the resulting processes that occur during and after laser heating are a result of the relative magnitudes of t, L_{th}, and L_{opt}.

When modeling heat transfer with Eq. (7.1), knowledge of the location of the solid–melt interface is required. One method that is commonly used for this purpose is the enthalpy formulation, in which the heat conduction equation is reformulated in terms of the enthalpy of the material. The enthalpy method provides a simple method of tracking the melt interface in a fixed grid numerical model and allows multiple phase-change processes to be modeled simultaneously. The numerical details of the enthalpy method are beyond the scope of this review, but the reader is referred to some excellent references on the topic [37, 38]. Equation (7.1) must be combined with appropriate boundary conditions at the donor substrate/film interface and the free surface. At the free surface, the convective and

radiative heat losses are negligible since they are several orders of magnitude smaller than the absorbed laser irradiance due to the short timescales involved [39, 40]. Thus, it is common to assume an adiabatic boundary condition at the free surface. At the donor substrate/film interface ($z = 0$), the conduction losses into the substrate are often neglected since the metal film has a much higher conductivity than the substrate, although accounting for substrate conduction is relatively simple to implement with numerical models.

If the laser fluence is sufficiently high, then more complex boundary conditions at $z = 0$ are required to accurately model the heating process. For example, if the fluence is sufficiently high, melting will occur, with the melt interface growing from the donor substrate/film interface toward the free surface of the film. Even higher fluences will cause liquid–vapor phase change of the film, gasification of the donor substrate at the interface, mechanical exfoliation, or some other mechanism, which will provide enough pressure to drive the donor film away from its substrate. Similarly to laser ablation processes, a threshold fluence exists, below which no material is removed, and this threshold depends on the film thickness. However, unlike ablation, the laser irradiation region is "confined" at the donor film/substrate interface, complicating the removal process. Hence, for very thick films, some studies reported that the film could not be removed even for the highest fluences used in experiments [22]. As will be discussed in this review, the boundary condition at $z = 0$ may not be the same under all combinations of laser and material parameters, which is the emphasis of much of the research on LIFT.

7.2.2 Parametric Effects

This section reviews the studies on the various parameters that influence LIFT of metals, organized in terms of laser fluence, film thickness, donor–acceptor gap spacing, and pulse width. Laser fluence is an important parameter since it will control the maximum temperature at the film/donor substrate interface, thus influencing the pressure driving the molten phase during transfer. For metals, the contrast in thermal diffusivity between the donor substrate and the metal film is high, such that a negligible amount of heat is lost to the substrate. However, for nonmetals, the loss of heat to the substrate can be significant, which raises the threshold fluence required for the removal of the donor material.

During LIFT of metals, the film begins as a solid phase, which must pass through the molten state before transfer. This is in contrast to other LIFT techniques, such as LIFT of liquids, in which the donor film remains in the liquid state prior to and after transfer. Since metals have a high thermal diffusivity, this further complicates matters since large melt zones are formed, which can limit spatial resolution and cause spattering of melt around the deposit. Metal films are thus more sensitive to laser pulse width, compared to other materials, since the relative size of L_{th} and t is controlled by the combination of laser pulse width and thermal diffusivity. Another reason that pulse width is more significant for LIFT of metals is that other LIFT techniques, such as LIFT of liquids and LIFT using a dynamic release layer, are not sensitive to pulse width (see, e.g., the reviews by Piqué *et al*. [41] and Delaporte and Alloncle [42]). In the case

of liquids, for example, the process is much more dependent on vapor bubble nucleation dynamics and jet formation, which are less sensitive to laser pulse width.

7.2.2.1 Laser Fluence and Film Thickness

The first report of LIFT used a 193 nm excimer laser with a 15 ns pulse width to transfer copper from a 0.41 μm thick copper film on a fused-silica substrate to a silicon target in vacuum [1]. The laser was focused to a spot size of 2.5 mm × 50 μm by a cylindrical lens. The films were maintained in close contact with the target substrate, with a gap of less than 10 μm. At the lowest energy level used (60 mJ), copper lines were transferred but consisted of sporadic clusters of copper, as shown in the scanning electron microscope (SEM) images in Figure 7.3. With increasing energy levels, more uniform lines were formed,

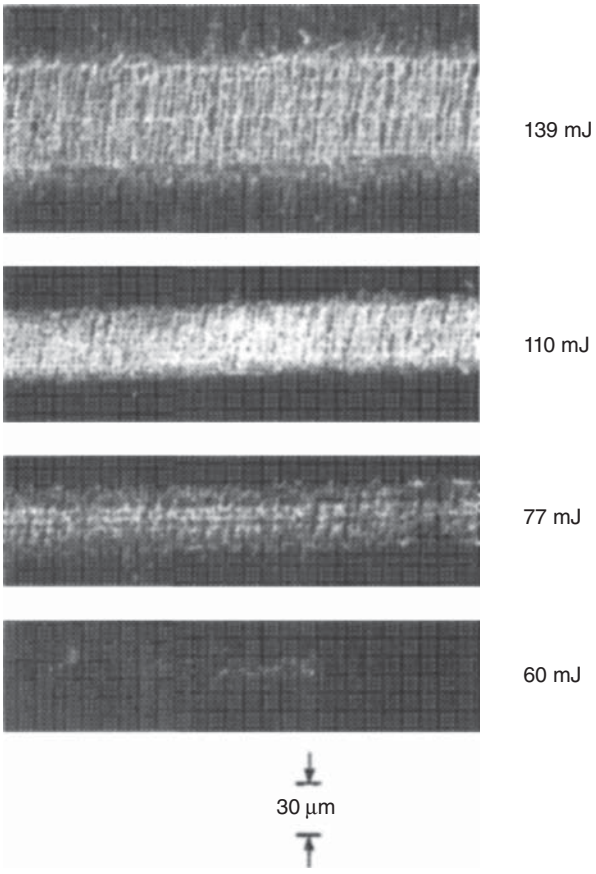

Figure 7.3 First LIFT results reported by Bohandy *et al*. [1] showing copper lines deposited on a silicon target using a 193 nm, 15 ns excimer laser. At low pulse energy, the deposited lines were not consistent. As the laser pulse energy increased, the line quality and uniformity improved. However, at the highest energy, the resolution was degraded due to spreading of the deposited material. (Bohandy *et al*. 1986 [1]. Reproduced with permission of AIP.)

which replicated the rectangular laser pattern. At a laser energy of 110 mJ, copper lines with a width of 40 μm were transferred, which were relatively clean, but above this energy, the deposited line width increased to sizes wider than the laser spot due to splattering.

Follow-up studies by the same research group performed numerical modeling and experiments to better understand the LIFT process. Adrian *et al*. [39] developed a one-dimensional thermal model to study the temperature profile in the films during the laser heating and melting process based on the parameters used by Bohandy *et al*. [1]. Their model indicated that the process proceeds by laser absorption in the metal film, heat transfer through the film, and melting, which propagates from the donor substrate/film interface toward the free surface. At or near the time at which the solid–liquid interface reaches the free surface, the substrate/film interface is near the metal boiling point. Adrian *et al*. [39] hypothesized that vaporization begins at the interface, building up enough pressure to propel the molten metal to the target.

Baseman *et al*. [43] studied the minimum fluences for the removal of gold films using Nd:YAG (532 nm, 15 ns) and excimer (248 nm, 25 ns) laser pulses with uniform beam irradiance. Calculations to understand their experimental results indicated that for films with thickness values less than the thermal diffusion length ($t < L_{th}$), the films were nearly isothermal across the thickness. For all thicknesses studied, the interface temperatures were near or above the normal boiling point at the end of the laser pulse, supporting a boiling process as the removal mechanism. Schultze and Wagner performed detailed numerical modeling and proposed two modes of deposition based on the results [6, 40]. The first mode occurs during LIFT of thin films and/or moderate laser fluences, for which the time needed for melting through the metal film is less than the time required for the interface to reach the normal boiling point. Under these conditions, film removal and transfer occur when the fluence is sufficient for the interface temperature to reach the normal boiling point, and approximately 1 atm of pressure is required to remove the film. The second mode of transfer occurs during LIFT of thicker films and/or higher fluences, under which conditions it is possible for the normal boiling point to be reached before the melt front reaches the free surface. Under such situations, the molten metal at the donor substrate/film interface becomes superheated, allowing higher interface pressures to be reached. For Gaussian irradiance beams, the highest pressure will be in the center of the laser spot. The radial variation of pressure causes the removed material to expand radially, with deposited patterns spreading by as much as 2.5 times larger than the ablated spot size [6]. However, for fluences near the threshold value, the transferred feature size closely replicated the laser focal spot size.

Boiling at the donor substrate/film interface has also been supported by experimental evidence. Two studies have reported nonuniform removal of the donor film when uniform irradiance patterns were used for LIFT [40, 44]. Both studies showed that for threshold fluences, film removal occurred in the form of small isolated locations. This is consistent with a boiling process, as all boiling processes begin with vapor growth from isolated nucleation sites [34]. During boiling processes at low heat fluxes, such as near-threshold fluences in LIFT, boiling

proceeds from isolated nucleation spots with no merging of bubbles. At higher heat fluxes, more nucleation sites will become activated, and vapor bubbles will tend to merge together before removal from the substrate. This may explain why the nonuniform removal is only observed near the threshold fluence.

Bohandy *et al*. [45] studied LIFT of copper and silver films on fused silica using a Nd:YAG laser (532 nm, 10–15 ns). The laser was focused to smaller spot sizes, approximately 50 μm, in order to study the possibility of achieving high spatial resolution of the deposits. Copper lines were formed by manually translating the micrometer stages on which the samples were mounted. The study found that the feature size of the deposits scaled with the laser spot size, with deposits as small as 15 μm obtained. They noted that the best-quality deposits occur for low fluence and thin donor films, as the uniformity of the films was best under these conditions. This is consistent with the first mode of removal proposed by Schultze and Wagner [6, 40] in which the solid–liquid interface reaches the free surface prior to the donor substrate/film interface temperature reaching the normal boiling point. For a fixed film thickness, the transferred deposit size could be varied by as much as a factor of 3 depending upon the fluence. High fluences resulted in large amounts of melt transferred with significant radial spattering. For thinner films at a fixed fluence, the deposited material size was reduced significantly. Under all cases studied, the deposited material was thinner in the center than on the edges, which was attributed to the fact that the center of the laser beam will have the highest irradiance. The center of the heated region will have the highest temperature, which when deposited will heat the target substrate, lower the sticking coefficient, and reduce further deposition in the center of the deposit. This preferential deposition at the edges of the deposit has been observed in other studies for both nanosecond pulses [39] and sub-nanosecond pulses [23].

Zergioti *et al*. [21, 22] observed many of the same phenomena on a shorter timescale using 500 fs pulses. This work studied LIFT of chromium films of 40, 80, and 200 nm thicknesses. The best transfers were obtained using thin films and low laser fluences. The threshold laser fluence also increased with film thickness, with measured values of 80 mJ/cm^2 for 40 nm films and 100 mJ/cm^2 for 80 nm films [23]. For the thickest films (200 nm), however, no transfer was achieved at the highest fluence in the study (500 mJ/cm^2).

7.2.2.2 Donor-Film Gap Spacing

After the film is removed from the donor substrate, the removed material travels across the gap, Δz, and is deposited onto the target substrate. Thus, the gap between the donor film and the target substrate will have a significant influence on the resolution and quality of the LIFT process. The first studies of LIFT of metals performed the process with the donor film and target substrate in contact or near contact, with $\Delta z < 10$ μm. Even in near-contact mode, Schultze and Wagner [6] observed spreading of deposited material in the radiation direction due to the radial variation of pressure. When the gap spacing is increased beyond this level, the transferred material will tend to spread due to expanding vapor plumes and collisions of particles.

Zergioti *et al*. [22] measured the deposited feature size for 500 fs LIFT of chromium films. For small gap spacing ($\Delta z < 50$ μm), the feature size did not

spread significantly, with deposit sizes remaining approximately the same size as the laser spot. When the gap spacing was 100 μm and higher, the feature size increased to values larger than the laser spot size. At the highest gap reported ($\Delta z = 300$ μm), the deposited features spread to as much as 10 times the laser spot size. While the pulse width was much shorter than used in other studies, the phenomenon appears to be consistent, with larger gaps providing distance for the removed material to spread prior to being deposited.

Nakata and Okada [46] performed LIFT of gold films ($t = 20$, 100, 500 nm) from SiO_2 donor substrates using a pulsed dye laser (9 ns) and studied ablation plumes using time-resolved laser-induced fluorescence and thermal emission. Most experiments were performed without the target substrate in place in order to view the plume. Under vacuum conditions, atoms lefts the surface at speeds higher than 2 km/s, while large particles traveled much slower, around 100 m/s. Similar results were observed in air, but with lower divergence of the plume. Strong forward peaking of the ablated material was observed near the threshold fluence, with the angular divergence increasing as a function of fluence for the emissive particles. The spreading of the atoms and emissive particles was smaller for thinner films, which is consistent with other studies showing that the best deposition occurs when using thinner films. Similar directionality of transferred material has been observed in other studies at shorter pulse durations [47]. When the target substrate was inserted, large gap spacing ($\Delta z = 500$ μm) resulted in reflection of particles and poor adhesion, while small gaps ($\Delta z = 70$ μm) resulted in good adhesion of deposits.

Sano *et al*. [48, 49] measured the spread of transferred gold and nickel films during LIFT with a 30 ns excimer laser (248 nm). For small gaps between the donor film and the target substrate, $\Delta z < 100$ μm, a nonlinear increase in the spread of deposit size was measured [49]. However, for larger gaps ($\Delta z > 100$ μm), a linear dependence was measured [48]. Time-resolved intensified CCD imaging and shadowgraph imaging showed that at optimum fluence (0.8 J/cm^2), the removed material remains tightly packed with little spread, but at higher fluences (1.5 J/cm^2), the removed material begins spreading within hundreds of nanosecond and moves much faster. The difference was attributed to the fact that higher fluence causes higher driving pressure at the interface, resulting in higher velocities and spreading of the material upon impact with the target substrate. The authors also compared the effect of the target substrate on the plume dynamics. Without a target substrate in place, the plume is highly directional, but when the target substrate is used, the plume is directed transversely, increasing spreading of the deposit [49], consistent with Schultze and Wagner's earlier work in contact mode [6].

7.2.2.3 Pulse Width

LIFT of metals has been performed with pulse widths from as long as milliseconds to as short as femtoseconds. In general, many of the same behaviors are observed with all pulse widths, as noted in the discussion on the effects of laser fluence, donor film thickness, and gap spacing. Pulse width has a more pronounced effect during LIFT of metals when compared to other materials, since the high thermal diffusivity leads to a larger heat affected zone. The relative

scale between L_{th} and t is responsible for the two modes of transfer observed by Schultze and Wagner with nanosecond pulses [6, 40]. As will be shown in this review, this same effect is also observed with shorter pulses since it is controlled by the relative magnitude of L_{th} and t. Shorter values of L_{th} will confine the absorbed laser energy and thus lead to a reduction of threshold fluences and reduced feature size. When sub-nanosecond pulses are used, nonlinear effects in the donor substrate may also be observed.

The thermal diffusion length according to Eq. (7.4) is on the order of microns when using nanosecond laser pulse widths. With shorter pulses, this length decreases to much smaller scales, meaning that less of the absorbed laser energy is lost to thermal conduction, reducing the amount of energy required for ablation. This is directly observed during LIFT, as the threshold fluence for material transfer is significantly reduced with shorter pulses. For the nanosecond pulses, the thresholds tend to be approximately 1 J/cm^2 or larger depending on the film material, thickness, and laser wavelength, while for picosecond pulses, the threshold fluences are typically of the order of 100 mJ/cm^2. Bera *et al*. [18] performed a threshold study with two different laser pulse widths during LIFT of 100 nm aluminum films. The threshold fluence for LIFT with 25 ns pulses was 1.3 J/cm^2, while for LIFT with 45 fs pulses, the threshold was reduced to 0.23 J/cm^2, an order of magnitude reduction. While other studies show similar results, it is difficult to compare the numerous studies because each uses a different combination of film thickness, laser wavelength, and film materials.

The series of studies by Zergioti *et al*. [21, 22] and Papakonstantinou *et al*. [23] were the first on LIFT using sub-nanosecond laser pulses. Their work used 500 fs excimer (248 nm) laser pulses to transfer chromium and platinum films, and they were able to consistently achieve smaller deposit features than observed in nanosecond LIFT. For fluences slightly above the threshold value, they were able to achieve features smaller than the laser spot size. The threshold fluences for chromium films were 80 and 100 mJ/cm^2 for 40 and 80 nm films, respectively. For 30–40 nm platinum films, the threshold fluence was 150 mJ/cm^2.

Bullock and Bolton [50] investigated the role of absorption in the glass substrate during picosecond LIFT of aluminum from BK-7 glass. This work measured the laser beam energy transmitted through the donor substrate as a function of laser energy and pulse width for pulses ranging from 2.0 to 3.6 ps. The work found that the glass donor substrate was damaged at high fluence due to laser-induced avalanche and multiphoton ionization, which limited the transmitted laser fluence and hence the velocity of the emitted vapor plume. The authors noted that this was a method of controlling the ablation plume velocity.

Zergioti *et al*. [47] compared pulse width effects during LIFT of 40 nm chromium films using an excimer laser (248 nm). The laser fluence was held constant at 330 mJ/cm^2 in order to compare two pulse widths, 30 ns and 500 fs. Plumes generated by LIFT were observed with a time-resolved Schlieren apparatus. The 30 ns pulses showed hemispherical spreading of ejected material and 350 m/s velocity. The material ejected during LIFT using 500 fs pulses emitted in a highly directional manner with high velocity (460 m/s) and low divergence (3°). By keeping the fluence constant, the effect of pulse width was observed to have effects on the relative length scales of film thickness and thermal diffusion

length. For the 30 ns pulses, the melt front has time to propagate through the film thickness, resulting in melting and vaporization of the film. The vaporized film will expand as most laser ablation vapor plumes, with significant spreading of material as it travels across the gap. The 500 fs pulses confine the laser energy to a very small region due to the shorter thermal diffusion length, which is approximately equal to the optical absorption depth ($L_{th} \sim L_{opt}$). The confinement of absorbed energy causes a buildup of pressure that induces a shock wave that removes the film, resulting in a more directional removal of the material.

When using longer pulses and high-melting-point materials such as tungsten, LIFT in contact mode can be performed in the solid phase such that the transferred material replicates the shape and size of the laser spot. Such effects have been observed with millisecond, microsecond [51–53], and nanosecond [54] laser pulses. In this process, the metal film bulges and contacts the target substrate during laser heating [52]. The bulging and exfoliation occur when the stresses due to thermal expansion of the solid exceed the adhesion strength between the donor substrate and the film [55]. Since the film touches the target substrate during laser heating, the hot film causes softening of the target substrate, allowing for good adhesion.

In another study [56] using molybdenum films, the effect of the relative size of the thermal diffusion length was performed by controlling the film thickness and pulse width independently. When the film thickness was held constant at $t = 430$ nm and the pulse duration was varied from 20–330 ns, no difference was observed between LIFT mode heating and heating from the thin film side (free surface). This was a result of the film being uniformly heated since $L_{th} > t$ for this timescale. The same effect could be observed for 10 ps pulses if very thin films, less than 50 nm, were used. However, when using molybdenum and other refractory metals, if the film thickness is significantly larger than the thermal diffusion length (i.e., when short pulses are used), a different phenomenon occurs [56–64]. Heise *et al*. [57, 58] used 10 ps, 1064 nm laser pulses to study laser heating of thin films through the donor substrate and found that the films are punched out in a disk of material with no obvious evaporation or melting effects. This is now commonly referred to as laser "lift-off" [57]. The measured threshold for removing films was less than that required to melt and vaporize the donor film. Below the threshold for punching out the film, the film showed a bump on the surface. Time-resolved measurements of the film bulging during 660 fs laser heating of molybdenum films were performed using ultrafast pump–probe shadowgraph [60, 61]. Results showed that film deformation began on the order of 400 ps after the heating laser pulse, with complete removal after about 15 ns.

Bartl *et al*. developed a time-resolved shadowgraph apparatus for studying lift-off of molybdenum films using picosecond laser pulses and a fast camera that allowed sequential imaging of the removed disk [62]. Using 5 ps pulses at low fluences ($0.28 < F < 0.62$ J/cm^2), the molybdenum was removed in a complete disk that traveled with an average velocity of 45 m/s. At higher fluences ($F > 0.62$ J/cm^2), the disk was removed in the shape of a ring due to a hole forming in the center of the disk. SEM imaging of the removed disk showed a hole with molten edges and droplets surrounding the hole. The disk traveled at an average velocity of 63 m/s, but the removed droplets traveled much faster,

at 207 m/s. Further studies using 10 ps pulses under similar conditions were able to measure the time at which the disk separated from the donor substrate, which occurred 21 ns after laser heating [63], consistent with the time for lift-off measured by Domke *et al*. [60, 61].

The cause of the initial bulge formation in the refractory metal films that leads to lift-off is still a topic of study. Initial studies hypothesized that the process was driven by confined vaporization or phase explosion at the donor substrate/film interface, followed by expansion of the gas phase [57, 58]. More recent studies, including numerical modeling, have indicated that thermal expansion during laser heating causes a pressure wave in the film. This ultrafast pressure wave results in a shock wave, which causes the film to bulge and eventually tear from the donor substrate [64, 65]. Since refractory metals have high melting and boiling points, the later arguments appear to be more realistic. Since the laser energy is confined to a shallow region during ultrashort laser heating, stresses that exceed the strength of the interface may be reached before the interface reaches temperatures and pressures required for transfer driven by vaporization at the interface. Further studies are needed, however, to better understand the processing conditions and materials under which lift-off will occur.

7.2.3 Droplet-Mode Deposition

The resolution of the transferred deposits in LIFT is typically limited by the spot size of the laser beam; however, recent works have shown that subspot size deposits can be achieved by careful control of laser fluence. Willis and Grosu [66] utilized a Nd:YAG laser beam (1064 nm, 7 ns FWHM) focused onto 1 μm aluminum and nickel films on glass substrates. This work showed that by controlling the fluence of a Gaussian beam, the spatial resolution of LIFT could be maintained well below the focal spot size even with a nanosecond laser pulse. In this work, the laser was focused to a spot size of approximately 25 μm, but individual droplets of approximately 3 μm diameter were deposited at the transfer threshold in both contact and noncontact configurations (Figure 7.4). Imaging of the donor film after laser irradiation indicated that droplets originated from a single raised section in the center of the donor film. This would not be expected for LIFT driven by a boiling process at the donor substrate/film interface. Figure 7.4b shows SEM images of an aluminum donor film at a fluence slightly below the transfer threshold. Droplets can clearly be observed, which froze on the donor film, preventing them from being transferred. The droplets are raised above the surface and sit on top a jet of aluminum, which has resolidified. Figure 7.4c is a close up of one of these droplets, which was smaller due to a lower fluence, and the jet can be observed. The authors explained the process as the result of volumetric expansion of the aluminum as it transitions from the solid to liquid state. Since the melting begins at the donor substrate/film interface, the expansion is constrained until the melt front reaches the free surface. Once reaching the free surface, the melt was ejected through a small opening in the center of the laser spot where the temperature was the highest.

The earlier works by Zergioti *et al*. [21, 22] and Papakonstantinou *et al*. [23] performed detailed studies of femtosecond excimer LIFT of chromium

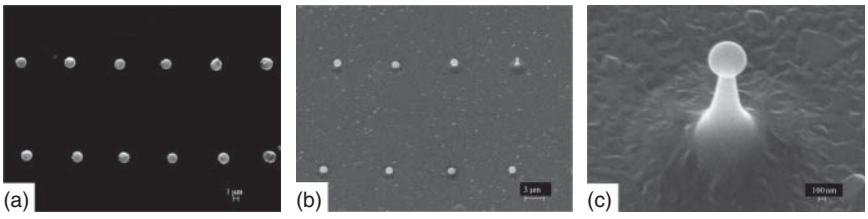

Figure 7.4 SEM images showing results of nanosecond LIFT of aluminum. (a) Aluminum microdroplets transferred to a glass target substrate (scale bar is 1 μm) [66]. Each droplet resulted from a single laser pulse. (b) Aluminum donor film after laser irradiation below the transfer threshold, showing droplets which did not leave the donor. (c) Closeup view of one of the droplets from the upper right of image (b) showing a resolidified jet with a droplet on top (scale bar is 100 nm). (Willis and Grosu 2005 [66]. Reproduced with permission of American Institute of Physics.)

and platinum films and observed that for thin films and low laser fluences, micron-sized "dots" that were smaller than the laser spot size could be deposited. Although the physical process for this form of deposition was not discussed, atomic force microscopy (AFM) images of the donor film after transfer of platinum dots indicated a crater-like removal in the area in which the dot was removed, indicating possibly an explosive type removal. Another earlier work by Tien *et al*. studied 1 ps LIFT of aluminum films using a Nd:glass laser and were able to deposit aluminum "dots" with diameters of the order of 0.8 μm [67]. The diameter of the dots was smaller than the laser waist of 3 μm, however, SEM images of the donor film after LIFT was complete showed a hole with a droplet in the center, which appears to be the source of the transferred dot, similar to that observed by Willis and Grosu [66]. This was distinctly different than the crater observed by Zergioti's work. Tien *et al*. noted that the dot transfer occurred slightly above the melting fluence and explained the process in terms of "compression" of the heated metal at the interface, with a pressure gradient forming, which accelerates the metal film toward the target [67].

Further studies of the droplet-based LIFT process were performed using femtosecond laser pulses [17, 68]. The work by Yang *et al*. used 148 fs laser pulses on 80 nm copper films and showed that a similar process could be used to deposit material in droplet form [68]. However, AFM imaging of the droplet and the donor film after transfer indicated that a different process was responsible for driving the droplet from the film. Figure 7.5 shows an AFM image of a droplet at the transfer threshold and an image of the donor film after ejection. The donor film shows a crater-like morphology distinctly different than that observed in nanosecond and picosecond LIFT in droplet transfer mode [66, 67]. The authors believed that the droplet ejection was a result of superheating of the molten copper film at the donor substrate/film interface to near the critical temperature, resulting in explosive boiling in a confined volume. This could explain why a crater-like spot was observed on the donor film after ejection rather than a jet of material.

Banks *et al*. [17] also achieved droplet-based LIFT of chromium films using femtosecond laser pulses and performed a detailed study of the transferred

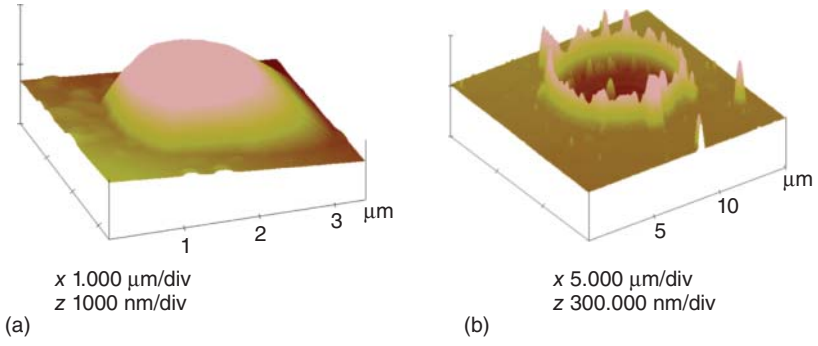

Figure 7.5 Images showing transferred droplet (a) and donor film (b) after LIFT. The donor film shows a crater from which the droplet was removed, rather than a jetting mechanism observed in other studies. (Panels (a) and (b): Yang *et al*. 2006 [68]. Reproduced with permission of American Institute of Physics)

droplet features as a function of laser fluence. Their study used a 110 fs laser with top-hat irradiance and demonstrated feature sizes that were smaller than the laser spot size and smaller than the laser wavelength of 800 nm. At the threshold for transferring droplets, approximately 325 mJ/cm^2, single droplets were transferred, which were attributed to the melt-motion mechanism proposed by Willis and Grosu [66]. Above a second threshold (~345 mJ/cm^2), both the droplet diameter and variation in droplet diameter increased as a function of fluence, which was attributed to vaporization at the donor substrate/film interface that propelled the melt from the substrate. A third threshold was observed at 380 mJ/cm^2, above which multiple droplets were ejected for each laser pulse, with an exponential increase in the number of droplets with fluence. The multiple droplets per laser pulse were explained as a result of explosive phase change at the donor substrate/film interface. Thus, the study by Banks *et al*. [17] provides evidence of both of the proposed modes of droplet formation in LIFT: that driven by melt through of a thin film from a confined region and vaporization and/or explosive phase change at the interface.

Although the cause of droplet formation is still under investigation, more recent studies have shed light by characterizing the process with time-resolved imaging. Giesbers *et al*. [69] used time-resolved imaging to measure the velocity of copper droplets deposited by 15 ns laser pulses with 355 nm wavelength. Shadowgraph images were obtained using 500 ps probing laser pulses, allowing high time resolution and captured direct observation of liquid jets from which droplets are formed. At low fluences (1.77 J/cm^2), a single droplet leaves the jet, which occurs on the order of 400 ns after laser heating. Similarly to the previous studies [17], the number of droplets ejected during the process increased with laser fluence. Giesbers *et al*. [69] observed this was a result of jet instability at higher fluences caused by higher jet velocity leading to reduced deposit resolution. In addition to the instability, the jet velocity at high fluence was highly variable, which led to a wider range of number of droplets deposited for a given laser pulse. Double-pulse images

measured droplet velocities ranging from 20 m/s at low fluence to 80 m/s at high fluence.

Pohl *et al*. [70] also used time-resolved shadowgraph imaging to investigate LIFT of gold films using 6 ns Nd:YAG (532 nm) laser pulses. Liquid jets were observed, which at low fluence resulted in ejection of single droplets after a long time delay, somewhere between 300 and 800 ns after laser heating. Double-exposure imaging measured droplet velocity on the order of 10 m/s, comparable to that measured by Giesbers *et al*. [69]. As the fluence increased, the number of droplets and the variability in number of droplets increased, making the process less repeatable. At fluences above 400 mJ/cm^2, a bubble of molten gold is formed above the donor substrate surface, rather than a jet, which decomposes into multiple droplets. The observed bubble is similar to that observed in the studies of femtosecond LIFT of gold, although it is not clear if the mechanisms are the same. Kuznetsov *et al*. [71] studied LIFT of gold films using 30 fs pulses and observed both nanobump formation at low fluences and jetting with ejection of droplets at higher fluences. At low fluences, the nanobumps were consistent with melting in which volumetric expansion during solid–liquid phase change pushes the film away from the donor substrate. The droplet formation observed at higher fluences is consistent with cavitation-induced jetting with a counter-jet, similar to that observed with LIFT of liquid films using nanosecond laser pulses [70].

Zenou *et al*. [72] studied the jetting phenomena induced by 400 ps pulses and measured the velocity of droplets formed by LIFT using an electronic circuit. When the droplet deposited by LIFT arrived on the target substrate, it completed an electronic circuit and allowed the time of deposition to be measured. Using the known gap spacing, the average droplet velocity was obtained. Measured droplet velocities were much higher than those reported in other studies, with some droplets reaching supersonic velocities.

Although droplet-based LIFT is still not well understood, it is quickly gaining ground as a method of microfabrication due to the high degree of control of droplet formation. The droplet-based deposition mechanism holds great promise since it is not only simple to implement but can also be used with a wide range laser pulse widths and materials. It can also achieve spatial resolution ranging from sub-100 nm to μm. Thus, droplet-based LIFT of metals is being explored for the fabrication of metal circuits [69], vias [16, 67], ITO- and $FeSi_2$-based photonic structures [73, 74], and now microscale 3D printing [30–33]. Microscale 3D printing is a particularly interesting application of LIFT of metals, since it can achieve resolution not available with other 3D metal printing methods. The reader is referred to Chapter 17, in which the subject of 3D printing of metals by LIFT is explored in more detail.

7.2.4 Characterization of Deposited Structures: Adhesion, Composition, and Electrical Resistivity

When forming structures, that is, patterns other than a deposit by a single laser pulse, the laser beam and the donor film are usually moved relative to each other

in order to form connected, and sometimes overlapping, deposits. Since each laser pulse results in a deposit that will usually solidify prior to the next arriving deposit, the structures consists of numerous interfaces, which can include grain boundaries, oxide layers, and voids [75]. Oxide layers can be present either due to the presence of oxides on the original donor film or as a result of oxidation during transfer and deposition if the process is performed in ambient air. Making a continuous pattern in this manner is further complicated by the high surface tension of metals, which will cause them to bead up into droplets on the target substrate. Schultze and Wagner [6] were able to overcome this problem by prepatterning the donor film with lithography and using LIFT to transfer the entire pattern with a uniform irradiance pattern in contact mode ($\Delta z = 0$). At high fluences, the deposited material formed droplets that did not resemble the donor film pattern. At fluences slightly above the threshold, the film pattern was replicated on the target substrate since the transferred material quickly solidified before hydrodynamic effects allowed the deposits to form droplets. Another method of controlling interfaces was performed in droplet mode by Kuznetsov *et al*. [71]. When droplets were deposited onto a glass substrate in near contact ($\Delta z = 10\,\mu m$), the droplets did not have time to solidify before the next droplet arrived due to the low conductivity of the glass target substrate. When the glass substrate was coated with a high-conductivity coating, the droplet quickly solidified before the next drop arrived, allowing 3D structures to be built up. When droplet-mode deposition is used for LIFT, the resulting roughness of the deposit is of the same order as the transferred droplet size [75]. An effective method of reducing the surface roughness and the percentage of voids is to utilize laser remelting of the deposited structure with a second laser process. Berg *et al*. [75] showed that pulses with hundreds of nanosecond duration could remelt the deposited structures without ablation and reduce surface roughness to as low as 0.2 μm and void density to as low as 0.9%. Droplet volume can also be used to control surface roughness, which can be controlled by the donor film thickness. Using small droplets can reduce surface roughness, although this can come at the expense of increased oxidation and reduced position accuracy [20].

Adhesion of deposits generated by LIFT has been observed to be generally of good quality, although little has been performed in quantitative terms. The most common test is the "Scotch tape" test in which a piece of tape is applied to the deposit and then pulled away from the sample. Well-adhering deposits will stick to the target substrate rather than be pulled away with the tape. While this method can be used to make quantitative measurements of adhesion (if designed properly) [76], most researchers use it only as a qualitative measure of adhesion [1, 22].

Electrical resistivity is important for many applications of LIFT of metals and is one of the more commonly quantified aspects other than the shape and size of the deposit. In the original study by Bohandy *et al.* [1], copper was deposited on fused silica, and the resistivity of the lines was measured using a four-point probe. The resistivity values ranged from 3 to 50 times that of bulk copper. X-ray fluorescence of the deposited copper in this same study indicated that pure copper was deposited, although that was expected since the deposition was performed in vacuum. In a follow-up study, Bohandy *et al*. [45] performed deposition of copper

in air onto fused-silica substrates. X-ray fluorescence indicated no oxidation of the copper deposit despite processing in ambient air, with electrical resistivity measurements indicating values 80 times that of bulk copper. Oosterhuis *et al*. [16] also deposited copper conductor lines and measured the resistivity to be five times that of bulk copper. Röder and Köhler [29] reported X-ray photoelectron spectroscopy of nickel that was transferred by LIFT from soda-lime donor substrates. The nickel deposits had sodium on top of the deposited features, which was explained as a result of gasification of the donor glass substrate, which drives the LIFT process.

Grant-Jacob *et al*. [77] fabricated copper wires on silica using LIFT with femtosecond laser pulses. The copper wires had resistivity values 17 times larger than the bulk value, with measured values of approximately $1.72 \times 10^8\ \Omega\,\mathrm{m}$. Energy dispersive X-ray spectroscopy of the wire indicated a ratio of copper to oxygen atoms of 2 : 1, indicating oxidation of the copper during the deposition process. The authors also note that as most resistivity measurements, an assumption must be made regarding the cross-sectional areas of the wires, which are not uniform in the LIFT process. The cross-sectional dimensions in their work varied by as much as 23% [77].

While the wide range of electrical resistivity values can be viewed as a drawback to LIFT of metals, a positive aspect of this is that the electrical properties of the deposited structures can be tuned by adjusting the process parameters. Large gaps will result at longer exposure times to air, thus increasing oxidation and the resulting resistivity [78]. The same study showed that resistivity increases as droplet size decreases due to the higher surface-area-to-volume ratio, but that high-velocity droplets can break down the oxide layers upon impact and reduce resistivity.

7.3 Advanced Modeling of LIFT

Modeling of the LIFT process has had limited success due to the complexity of the processes involved. Many of the early works were successful at explaining the basic aspects of LIFT induced by high-power nanosecond laser pulses using a combination of experiments and simple one-dimensional heat conduction models. For example, the early works by Bohandy's research group [1, 39] showed that LIFT was initiated by heating the metal films to temperatures near the boiling point, followed by buildup of pressure at the interface, which removed the material in a mixture of liquid and vapor. Since these early works were published, many new phenomena have been observed, including droplet-based deposition at low fluences and removal and transfer of the film due to lift-off of a disk at low fluences. Few numerical models extend beyond one-dimensional conduction models. The following is a brief review of some of the modeling efforts that have tried to explain some of these phenomena.

Grosu and Willis [79] used a volume-of-fluid model to study nanosecond LIFT of aluminum films with a goal of explaining how droplet-based deposition begins. The model included transient volumetric absorption of the Gaussian Nd:YAG laser beam, solid–liquid phase change, and volumetric expansion of

the aluminum when melting. The model also included convective terms in the energy equation and solved the Navier–Stokes equations for fluid motion in the molten film. Phase change was modeled using the enthalpy formulation, which eliminates the need for interface tracking. At a fluence just above the melting threshold, volumetric expansion resulted in a protrusion of the molten film at the center of the laser spot where the melt front reached the free surface. The melt front reached the free surface at approximately 35 ns, at which time only the center of the free surface is molten due to the Gaussian irradiance pattern, forming a small opening through which pressurized molten aluminum can escape. However, the peak temperature during the process, which occurs at the interface between the donor substrate and the donor film, was approximately 1755 K, at a time of 10 ns. This value is much lower than the normal boiling point of aluminum, eliminating the possibility of vaporization as a source of droplet ejection. The protrusion caused by volumetric expansion remained after solidification, with an appearance similar to that observed in experiments below the droplet ejection threshold, although the model was unable to capture the jet and droplet formation. The model did not incorporate surface tension gradients, which may influence the formation of the molten jet.

Röder and Köhler [29] developed a transient two-dimensional thermal model to study nanosecond LIFT of nickel films from glass substrates. The LIFT model included temperature-dependent thermal properties, melting of the nickel film, and vaporization of the glass phase. The model assumed evaporation of the glass in the range from 1780 to 3073 K (the boiling point of quartz) and was used to determine the "blow-off time" of the nickel films based on pressure buildup in the vaporized glass. When the model calculated gas pressure greater than the strength of the nickel film, the nickel layer was assumed to blow off from the substrate. The strength of the nickel film was either the surface tension of the liquid phase for completely molten films or the yield strength if the nickel film was not completely molten. The model results for blow-off time compared well with experimental measurements for various pulse energies and film thicknesses. Their results are in contrast to prior studies showing that experimentally measured threshold fluences for transfer agree with the numerical models showing that the temperature at the donor substrate/film interface is at or near the boiling point of the metal film. Perhaps the discrepancy is from the fact that the work by Röder and Köhler [29] used nickel for the donor film and glass for the donor substrate, which have similar boiling points.

Shugaev and Bulgakova developed a one-dimensional model of coupled heat transfer and stress waves in metal films during femtosecond LIFT [80]. The study used a two-temperature model of heat transfer, with one equation for absorption and diffusion of laser energy by electrons and a second equation for the transient temperature rise of the lattice due to coupling effects with electrons. One-dimensional stress waves resulting from thermal expansion were modeled in gold, chromium, and zinc films, and the model was able to qualitatively explain the results observed in the experiments for each of these materials [81]. Gold tends to be transferred in a mixture of molten metal with nanocrystals, chromium as a single liquid droplet, and zinc as a mixture of vapor and droplets [81].

Sotrop *et al*. developed a numerical model of the low fluence lift-off process in molybdenum films [65]. Their model included two-temperature thermal

transport for electrons and lattice, elastic and plastic stress in the donor film, and adhesion between the donor substrate and the film. The model was able to capture the bulging of the molybdenum film due to an ultrafast thermal expansion and subsequent shock-wave propagation. Results of their model demonstrated that vaporization and gas expansion at the donor substrate/film interface are not required for removing molybdenum films from the donor substrate.

Advanced numerical modeling of LIFT processes is an area that requires further advancement. Few models have extended beyond one-dimensional heat transfer studies for nanosecond LIFT, and effects such as surface tension gradients and liquid–vapor phase change at the interface need to be studied further. For short pulses (ps, fs), there are even fewer models due to the wide range of complex, and often coupled, phenomena that may occur. Shorter pulses lead to highly nonequilibrium heat transfer and phase-change processes, stress waves, and nonlinear laser absorption phenomena. These processes are still under investigation by the laser processing community [82] but have not yet been studied in detail for LIFT.

7.4 Research Needs and Future Directions

A number of topics remain to be addressed for LIFT of metals, particularly in the area of basic thermal-fluid processes. For LIFT at high fluences, material removal and transfer appear to be driven by vapor formation and the resulting buildup of pressure at the donor substrate/film interface. For nanosecond laser pulses, this appears to occur at a well-defined temperature, often attributed to the normal boiling temperature or a value slightly higher. Work with nanosecond pulses demonstrates that the transfer may occur in two modes: one in which the film melts through prior to the interface reaching the boiling point (thin films and/or low fluences, often with $t \sim L_{th}$), the other in which the interface reaches the boiling point before melt-through occurs (thicker films and/or high fluences) [6, 40]. The first mode results in transfer that closely resembles the laser outline, as shown in the left-hand inset of Figure 7.6e. The second mode causes spreading significantly beyond the laser spot size due to the high pressure buildup at the interface, as shown in the right-hand inset of Figure 7.6e for LIFT of aluminum films [6]. LIFT at high fluences is qualitatively understood, at least for longer pulses, from the viewpoint that experimental results agree with conduction and melting models to explain the difference in transfer behavior shown in Figure 7.6e. The actual interface temperature and vapor pressure driving the process are not well understood, and further research on short timescale vaporization and boiling kinetics would improve the ability to predict LIFT thresholds in this regime. In addition to the removal mechanisms, the ability to model the material transfer and deposition is limited due to the complex physical processes. Transfer and deposition involve two-phase fluid flow, compressible-gas dynamics, and fluid–solid interaction at the target substrate. Since vapor-driven LIFT may also occur on shorter timescales, femtosecond and picosecond LIFT would also benefit from research on these topics.

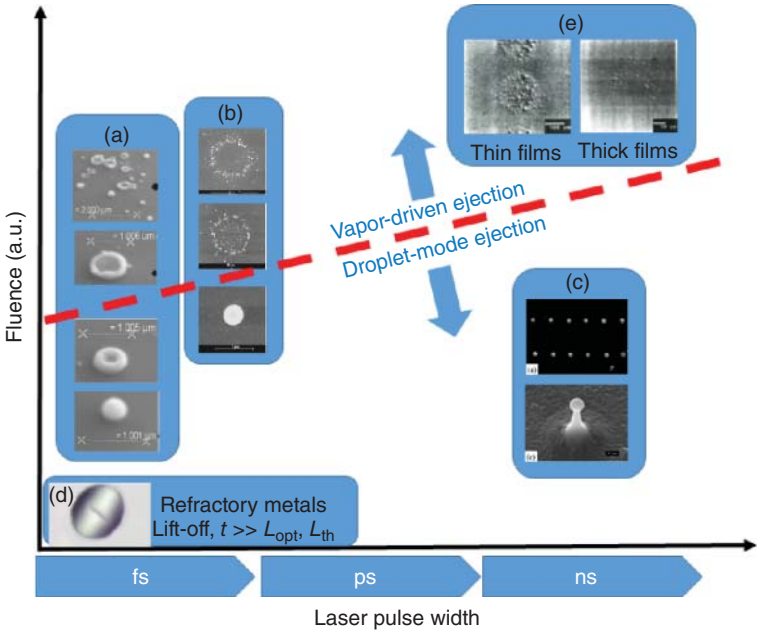

Figure 7.6 Transfer regimes of LIFT as a function of timescale and fluence. (Panel (a): Banks *et al*. 2006 [17]. Reproduced with permission of American Institute of Physics. Panel (b): Yang *et al*. 2006 [68]. Reproduced with permission of American Institute of Physics. Panel (c): Willis and Grosu 2005 [66]. Reproduced with permission of American Institute of Physics. Panel (d): Heise *et al*. 2012 [58]. Reproduced with permission of IOP Publishing. Panel (e): Schultze and Wagner 1991 [6]. Reproduced with permission of Elsevier.)

The most promising aspect of LIFT of metals, and where most future research efforts should focus, is low-fluence processing. Low-fluence LIFT includes droplet-based LIFT, Figure 7.6a–c, and laser lift-off, Figure 7.6d, in which the film is removed in a single piece. Low-fluence LIFT is rich with interesting thermal-fluid phenomena and is promising for a number of applications. This regime provides highly controllable material removal and transfer, fine printing resolution, and high repeatability. Such capabilities are powerful since current 3D printing methods are limited to printing of low-melting-point metals [31], while LIFT is capable of printing any metal. Early studies using LIFT for the fabrication of 3D structures show great promise [20, 30, 31], but challenges remain. For example, these early works have developed significant empirical knowledge, providing information such as angular spreading and droplet deformation behavior as a function of laser fluence for a specific laser/material combination [78]. However, the driving process that initiates melt ejection is not understood, as it appears to be a complex interaction between surface tension gradients, thermal expansion, and possibly vapor pressure at higher fluences. Even for femtosecond laser pulses, there appears to be a gradual transition from droplet-mode ejection to vapor-driven ejection [17, 68], as shown in Figure 7.6a,b. Thus, vaporization and boiling appear to participate even at this timescale, which requires further research in order to predict interface

temperatures and vapor pressure. Numerical models that are able to capture heat transfer, solid–liquid phase change, liquid–vapor phase change, surface tension gradients, thermal expansion, and the resulting fluid flow would allow an improved understanding of droplet-mode LIFT from the femtosecond to nanosecond timescales. By better understanding the fundamental mechanisms of the droplet-based LIFT, improved control of the deposited feature sizes is anticipated. Such control will lead to advances in applications of LIFT, such as control of deposition size and uniformity for three-dimensional printing applications, improved electrical resistivity for electronics applications, and improved optical resolution for photonics.

Laser lift-off is another regime of low-fluence LIFT that requires further investigation. It is not clear under what conditions lift-off occurs, although it appears to be limited to refractory metals with femtosecond and picosecond laser pulses. For lift-off, most of the studies are limited to molybdenum films, thus limiting the breadth of knowledge on the topic. More studies are needed to better understand the range of materials and parameters under which lift-off occurs. Due to the shorter timescale, coupled thermomechanical processes appear to be responsible, rather than purely thermal processes. Since the films are removed at thresholds below that required for melting the entire film thickness, material is removed as a solid disk due to some form of mechanical exfoliation from the remainder of the donor film. However, the basic initiation mechanism (i.e., localized vaporization vs thermal expansion, or a combination of both) that causes the ejection of the disk is still an open question [57, 58, 64, 65]. A clearer understanding will allow for prediction of transfer behavior of films based on their melting temperature, thermomechanical properties, and laser parameters. Delineating the various contributing factors will require creative experimental studies and advanced numerical modeling, providing numerous research opportunities.

7.5 Conclusions

LIFT of metals has been under development for 30 years now and has been studied under a wide range of processing conditions. This chapter has reviewed the fundamental thermal processes, including laser absorption, heat transfer, and phase change, which drive LIFT of metals. Additionally, this chapter reviewed the various experimental and numerical studies that have investigated the process parameters that are important for LIFT of metals. These studies have led to the evolution of LIFT of metals from a simple technique able to transfer large amounts of melt by a vapor-pressure-driven process to new techniques that have high levels of control of spatial resolution. These new techniques, droplet-mode transfer and lift-off, are rapidly advancing and expanding the capabilities of LIFT of metals. However, many opportunities for research remain in these new areas. Our understanding of ultrashort laser material interactions is limited, and further research in this area is required to better understand the strong coupling between laser-induced thermal processes in a confined geometry and the resulting mechanical stress waves, which can become important on short timescales.

References

1 Bohandy, J., Kim, B.F., and Adrian, F.J. (1986) Metal deposition from a supported metal film using an excimer laser. *J. Appl. Phys.*, **60** (4), 1538–1539.

2 Auyeung, R.C.Y., Kim, H., Charipar, N.A., Birnbaum, A.J., Mathews, S.A., and Piqué, A. (2011) Laser forward transfer based on a spatial light modulator. *Appl. Phys. A*, **102** (1), 21–26.

3 Pohl, R., Jansink, M., Römer, G.R.B.E., and Huis in' t Veld, A.J. (2015) Solid-phase laser-induced forward transfer of variable shapes using a liquid-crystal spatial light modulator. *Appl. Phys. A*, **120** (2), 427–434.

4 Othon, C.M., Laracuente, A., Ladouceur, H.D., and Ringeisen, B.R. (2008) Sub-micron parallel laser direct-write. *Appl. Surf. Sci.*, **255** (5), 3407–3413.

5 Rapp, L., Constantinescu, C., Larmande, Y., Alloncle, A.P., and Delaport, P. (2014) Smart beam shaping for the deposition of solid polymeric material by laser forward transfer. *Appl. Phys. A*, **117** (1), 333–339.

6 Schultze, V. and Wagner, M. (1991) Laser-induced forward transfer of aluminum. *Appl. Surf. Sci.*, **52** (4), 303–309.

7 Sametoglu, V., Sauer, V., and Tsui, Y.Y. (2013) Nanoscale laser-induced forward transfer through patterned Cr films. *Appl. Phys. A*, **110** (4), 823–827.

8 Kuznetsov, A.I., Evlyukhin, A.B., Gonçalves, M.R., Reinhardt, C., Koroleva, A., Arnedillo, M.L., Kiyan, R., Marti, O., and Chichkov, B.N. (2011) Laser fabrication of large-scale nanoparticle arrays for sensing applications. *ACS Nano*, **5** (6), 4843–4849.

9 Mogyorósi, P., Szörényi, T., Bali, K., Tóth, Z., and Hevesi, I. (1989) Pulsed laser ablative deposition of thin metal films. *Appl. Surf. Sci.*, **36** (1), 157–163.

10 Boutopoulos, C., Tsouti, V., Goustouridis, D., Chatzandroulis, S., and Zergioti, I. (2008) Liquid phase direct laser printing of polymers for chemical sensing applications. *Appl. Phys. Lett.*, **93** (19), 191109.

11 Fogarassy, E. (1990) Basic mechanisms and application of the laser-induced forward transfer for high-Tc superconducting thin film deposition. *Proc. SPIE*, **1394**, 169–179.

12 Auyeung, R.C.Y., Kim, H., Mathews, S.A., and Piqué, A. (2007) Laser direct-write of metallic nanoparticle inks. *J. Laser Micro/Nanoeng.*, **2** (1), 21–25.

13 Munoz-Martin, D., Brasz, C.F., Chen, Y., Morales, M., Arnold, C.B., and Molpeceres, C. (2016) Laser-induced forward transfer of high-viscosity silver pastes. *Appl. Surf. Sci.*, **366**, 389–396.

14 Barron, J.A., Spargo, B.J., and Ringeisen, B.R. (2004) Biological laser printing of three dimensional cellular structures. *Appl. Phys. A*, **79** (4), 1027–1030.

15 Kattamis, N.T., Purnick, P.E., Weiss, R., and Arnold, C.B. (2007) Thick film laser induced forward transfer for deposition of thermally and mechanically sensitive materials. *Appl. Phys. Lett.*, **91** (17), 171120.

16 Oosterhuis, G., Prenen, A., and Huis in't Veld, A.J. (2012) Laser induced forward transfer of interconnects for 3D integration. *ECS Trans.*, **41** (43), 81–90.

17 Banks, D.P., Grivas, C., Mills, J.D., Eason, R.W., and Zergioti, I. (2006) Nanodroplets deposited in microarrays by femtosecond Ti:sapphire laser-induced forward transfer. *Appl. Phys. Lett.*, **89** (19), 193107.

18 Bera, S., Sabbah, A.J., Yarbrough, J.M., Allen, C.G., Winters, B., Durfee, C.G., and Squier, J.A. (2007) Optimization study of the femtosecond laser-induced forward transfer with thin aluminum films. *Appl. Opt.*, **46** (21), 4650–4659.

19 Sametoglu, V., Sauer, V.T.K., and Tsui, Y.Y. (2013) Production of 70-nm Cr dots by laser-induced forward transfer. *Opt. Express*, **21** (15), 18525–18531.

20 Zenou, M., Sa'ar, A., and Kotler, Z. (2015) Digital laser printing of aluminum micro-structure on thermally sensitive substrates. *J. Phys. D*, **48** (20), 205303.

21 Zergioti, I., Mailis, S., Vainos, N.A., Fotakis, C., Chen, S., and Grigoropoulos, C.P. (1998) Microdeposition of metals by femtosecond excimer laser. *Appl. Surf. Sci.*, **127–129**, 601–605.

22 Zergioti, I., Mailis, S., Vainos, N.A., Papakonstantinou, P., Kalpouzos, C., Grigoropoulos, C.P., and Fotakis, C. (1998) Microdeposition of metal and oxide structures using ultrashort laser pulses. *Appl. Phys. A*, **66** (5), 579–582.

23 Papakonstantinou, P., Vainos, N.A., and Fotakis, C. (1999) Microfabrication by UV femtosecond laser ablation of Pt, Cr, and indium oxide thin films. *Appl. Surf. Sci.*, **151** (3-4), 159–170.

24 Sones, C.L., Kaur, K.S., Ganguly, P., Banks, D.P., Ying, Y.J., Eason, R.W., and Mailis, S. (2010) Laser-induced-forward-transfer: a rapid prototyping tool for fabrication of photonic devices. *Appl. Phys. A*, **101** (2), 333–338.

25 Tseng, M.L., Chang, C.M., Chen, B.H., Huang, Y.-W., Chu, C.H., Chung, K.S., Liu, Y.J., Tsai, H.G., Chu, N.-N., Huang, D.-W., Chiang, H.-P., and Tsai, D.P. (2012) Fabrication of plasmonic devices using femtosecond laser-induced forward transfer technique. *Nanotechnology*, **23** (44), 1–9.

26 Tan, B., Venkatakrishnam, K., and Tok, K.G. (2003) Selective surface texturing using femtosecond pulses laser induced forward transfer. *Appl. Surf. Sci.*, **207** (1-4), 365–371.

27 Germain, C., Charron, L., Lilge, L., and Tsui, Y.Y. (2007) Electrodes for microfluidic devices produced by laser induced forward transfer. *Appl. Surf. Sci.*, **253** (19), 8328–8333.

28 Bähnisch, R., Groß, W., and Menschig, A. (2000) Single-shot, high repetition rate metallic pattern transfer. *Microelectron. Eng.*, **50** (1-4), 541–546.

29 Röder, T.C. and Köhler, J.R. (2012) Physical model for the laser induced forward transfer process. *Appl. Phys. Lett.*, **100** (7), 071603.

30 Visser, C.W., Pohl, R., Sun, C., Römer, G.-W., Huis in 't Veld, B., and Lohse, D. (2015) Toward 3D printing of pure metals by laser-induced forward transfer. *Adv. Mater.*, **27** (27), 4087–4092.

31 Zenou, M., Sa'ar, A., and Kotler, Z. (2015) Laser transfer of metals and metal alloys for digital microfabrication of 3D objects. *Small*, **11** (33), 4082–4089.

32 Zenou, M., Sa'ar, A., and Kotler, Z. (2015) Laser jetting of femto-liter metal droplets for high resolution 3D printed structures. *Sci. Rep.*, **5**, 17265.

33 Kuznetsov, A.I., Kiyan, R., and Chichkov, B.N. (2010) Laser fabrication of 2D and 3D metal nanoparticle structures and arrays. *Opt. Express*, **18** (20), 21198–21203.

34 Bergman, T.L., Lavine, A.S., Incropera, F.P., and DeWitt, D.P. (2011) 7th edn, in *Fundamentals of Heat and Mass Transfer*, John Wiley & Sons, Inc., Hoboken, NJ.

35 Von Allmen, M. and Blatter, A. (1998) *Laser-Beam Interactions with Materials*, 2nd edn, Spring-Verlag, Berlin, Heidelberg, New York.

36 Metev, S.M. and Veiko, V.P. (1998) *Laser-Assisted Micro-Technology*, 2nd edn, Springer-Verlag, Berlin, Heidelberg, New York.

37 Griffith, R. and Nassersharif, B. (1990) Comparison of one-dimensional interface-following and enthalpy methods for the numerical solution of phase change. *Numer. Heat Transfer, Part B*, **18** (2), 169–187.

38 Xu, X., Chen, G., and Song, K.H. (1999) Experimental and numerical investigation of heat transfer and phase change phenomena during excimer laser interaction. *Int. J. Heat Mass Transfer*, **42** (8), 1371–1382.

39 Adrian, F.J., Bohandy, J., Kim, B.F., Jette, A.N., and Thompson, P. (1987) A study of the mechanism of metal deposition by the laser-induced forward transfer process. *J. Vac. Sci. Technol., B*, **5** (5), 1490–1494.

40 Schultze, V. and Wagner, M. (1991) Blow-off of aluminum films. *Appl. Phys. A*, **53** (3), 241–248.

41 Piqué, A., Auyeung, R.C.Y., Kim, H., Charipar, N.A., and Mathews, S.A. (2016) Laser 3D micro-manufacturing. *J. Phys. D*, **49** (22), 223001.

42 Delaporte, P. and Alloncle, A.-P. (2016) Laser-induced forward transfer: a high resolution additive manufacturing technology. *Opt. Laser Technol.*, **78**, 33–41.

43 Baseman, R.J., Froberg, N.M., Andreshak, J.C., and Schlesinger, Z. (1990) Minimum fluence for laser blow-off of thin gold films at 248 and 532 nm. *Appl. Phys. Lett.*, **56** (15), 1412–1414.

44 Baseman, R.J. and Andreshak, J.C. (1988) Threshold for single excimer laser pulse backside removal of thin metal films from optical quartz. *Mater. Res. Soc. Symp. Proc.*, **100**, 627–633.

45 Bohandy, J., Kim, B.F., Adrian, F.J., and Jette, A.N. (1988) Metal deposition at 532 nm using a laser transfer technique. *J. Appl. Phys.*, **63** (4), 1158–1162.

46 Nakata, Y. and Okada, T. (1999) Time-resolved microscopic imaging of the laser-induced forward transfer process. *Appl. Phys. A*, **69** (Suppl. 1), S275–S278.

47 Zergioti, I., Papazoglou, D.G., Karaiskou, A., Fotakis, C., Gamaly, E., and Rode, A. (2003) A comparative schlieren imaging study between ns and sub-ps laser forward transfer of Cr. *Appl. Surf. Sci.*, **208–209**, 177–180.

48 Sano, T., Miyamoto, I., Hayashi, H., and Ochi, H. (2000) Analysis of excimer laser patterning process of Cu thin film. *Proc. SPIE*, **3933**, 356–364.

49 Sano, T., Yamada, H., Nakayama, T., and Miyamoto, I. (2002) Experimental investigation of laser induced forward transfer process of metal thin films. *Appl. Surf. Sci.*, **186** (1-4), 221–226.

50 Bullock, A.B. and Bolton, P.R. (1999) Laser-induced back ablation of aluminum thin films using picosecond laser pulses. *J. Appl. Phys.*, **85** (1), 460–465.

51 Kántor, Z., Tóth, Z., Szörényi, T., and Tóth, A.L. (1994) Deposition of micrometer-sized tungsten patterns by laser transfer technique. *Appl. Phys. Lett.*, **64** (25), 3506–3508.

52 Kántor, Z., Tóth, Z., and Szörényi, T. (1995) Metal pattern deposition by laser-induced forward transfer. *Appl. Surf. Sci.*, **86** (1-4), 196–201.

53 Kántor, Z. and Szörényi, T. (1995) Dynamics of long-pulse laser transfer of micrometer-sized metal patterns as followed by time-resolved measurements of reflectivity and transmittance. *J. Appl. Phys.*, **78** (4), 2775–2781.

54 Tóth, Z., Solis, J., Afonso, C.N., Vega, F., and Szörényi, T. (1993) Time resolved reflectivity and transmission measurements during laser induced blow-off of thin metal films. *Appl. Surf. Sci.*, **69** (1-4), 330–334.

55 Veiko, V.P., Shakhno, E.A., Smirnov, V.N., Miaskovski, A.M., and Nikishin, G.D. (2006) Laser-induced film deposition by LIFT: physical mechanisms and applications. *Laser Part. Beams*, **24** (2), 203–209.

56 Domke, M., Nobile, L., Rapp, S., Eiselen, S., Sotrop, J., Huber, H., and Schmidt, M. (2014) Understanding thin film laser ablation: The role of the effective penetration depth and the film thickness. *Physics Procedia*, **56**, 1007–1014.

57 Heise, G., Englmaier, M., Hellwig, C., Kuznicki, T., Sarrach, S., and Huber, H.P. (2011) Laser ablation of thin molybdenum films on transparent substrates at low fluences. *Appl. Phys. A*, **102** (1), 173–178.

58 Heise, G., Domke, M., Konrad, J., Sarrach, S., Sotrop, J., and Huber, H.P. (2012) Laser lift-off initiated by direct induced ablation of different metal thin films with ultra-short laser pulses. *J. Phys. D*, **45** (31), 315303.

59 Domke, M., Rapp, S., and Huber, H.P. (2012) Ultra-fast movies resolve ultra-short pulse laser ablation and bump formation on thin molybdenum films. *Physics Procedia*, **39**, 717–725.

60 Domke, M., Rapp, S., Schmidt, M., and Huber, H.P. (2012) Ultra-fast movies of thin-film laser ablation. *Appl. Phys. A*, **109** (2), 409–420.

61 Domke, M., Rapp, S., Schmidt, M., and Huber, H.P. (2012) Ultrafast pump-probe microscopy with high temporal dynamic range. *Opt. Express*, **20** (9), 10330–10338.

62 Bartl, D., Michalowski, A., Hafner, M., Letsch, A., Nolte, S., and Tunnermann, A. (2013) Time-resolved study of back side ablated molybdenum thin films by ultrashort laser pulses. *Appl. Phys. A*, **110** (1), 227–233.

63 Bartl, D., Ametowobla, M., Schmid, F., Letsch, A., Hafner, S., and Tunnermann, A. (2013) Probing timescales during back side ablation of molybdenum thin films with optical and electrical measurement. *Opt. Express*, **21** (14), 16431–16443.

64 Domke, M., Felsl, D., Rapp, S., Sotrop, J., Huber, H., and Schmidt, M. (2015) Evidence of pressure waves in confined laser ablation. *J. Laser Micro/Nanoeng.*, **10** (2), 119–123.

65 Sotrop, J., Kersch, A., Domke, M., Heise, G., and Huber, H.P. (2013) Numerical simulation of ultrafast expansion as the driving mechanism for confined laser ablation with ultra-short laser pulses. *Appl. Phys. A*, **113** (2), 397–411.

66 Willis, D.A. and Grosu, V. (2005) Microdroplet deposition by laser-induced forward transfer. *Appl. Phys. Lett.*, **86** (24), 244103.

67 Tien, A.-C., Sacks, Z.S., and Mayer, F.J. (2001) Precision laser metallization. *Microelectron. Eng.*, **56** (3-4), 273–279.

68 Yang, L., Yang, C.-Y., Ni, X.-C., Wang, Z.-J., Jia, W., and Chai, L. (2006) Microdroplet deposition of copper film by femtosecond laser-induced forward transfer. *Appl. Phys. Lett.*, **89** (16), 161110.

69 Giesbers, M.P., Hoppenbrouwers, M.B., Smits, E.C.P., and Mandamparambil, R. (2014) Process optimization of LIFT through visualization: towards high resolution metal circuit printing. *Proc. SPIE*, **9135**, 91350Z.

70 Pohl, R., Visser, C.W., Römer, G.R.B.E., Sun, C., Huis in 't Veld, A.J., and Lohse, D. (2015) Imaging of the ejection process of nanosecond laser-induced forward transfer of gold. *J. Laser Micro/Nanoeng.*, **10** (2), 154–157.

71 Kuznetsov, A.I., Unger, C., Koch, J., and Chichkov, B.N. (2012) Laser-induced jet formation and droplet ejection from thin metal films. *Appl. Phys. A*, **106** (3), 479–487.

72 Zenou, M., Sa'ar, A., and Kotler, Z. (2015) Supersonic laser-induced jetting of aluminum micro-droplets. *Appl. Phys. Lett.*, **106** (18), 181905.

73 Narazaki, A., Kurosaki, R., Tadatake, S., Kawaguchi, Y., Watanabe, W., and Niino, H. (2012) On-demand preparation of microdot patterns by laser-induced dot transfer. *J. Laser Micro/Nanoeng.*, **7** (1), 77–80.

74 Narazaki, A., Kurosaki, R., Tadatake, S., Kawaguchi, Y., and Niino, H. (2014) On-demand deposition of functional oxide microdots by double-pulse laser-induced dot transfer. *J. Laser Micro/Nanoeng.*, **9** (1), 10–14.

75 Berg, Y., Zenou, M., Dolev, O., and Kotler, Z. (2015) Temporal pulse shaping for smoothing of printed metal surfaces. *Opt. Eng.*, **54** (1), 011010.

76 Campbell, D.S. (1970) in *Handbook of Thin Film Technology* (eds L.I. Maissel and R. Glang), McGraw-Hill, New York, pp. 3–50.

77 Grant-Jacob, J.A., Mills, B., Feinaeugle, M., Sones, C.L., Oosterhuis, G., Hoppenbrouwers, M.B., and Eason, R.W. (2013) Micron-scale copper wires printed using femtosecond laser-induced forward transfer with automated donor replenishment. *Opt. Mater. Express*, **3** (6), 747–754.

78 Zenou, M., Sa'ar, A., and Kotler, Z. (2016) Digital laser printing of metal/metal-oxide nano-composites with tunable electrical properties. *Nanotechnology*, **27** (1), 015203.

79 Grosu, V. and Willis, D.A. (2007) The effect of melting-induced volumetric expansion on initiation of laser-induced forward transfer. *Appl. Surf. Sci.*, **253** (10), 4759–4763.

80 Shugaev, M.V. and Bulgakova, N.M. (2010) Thermodynamic and stress analysis of laser-induced forward transfer of metals. *Appl. Phys. A*, **101** (1), 103–109.

81 Klini, A., Loukakos, P.A., Gray, D., Manousaki, A., and Fotakis, C. (2008) Laser induced forward transfer of metals by temporally shaped femtosecond laser pulses. *Opt. Express*, **16** (15), 11300–11309.

82 Shugaev, M.V., Wu, C., Armbruster, O., Naghilou, A., Brouwer, N., Ivanov, D.S., Derrien, T.J.-Y., Bulgakova, N.M., Kautek, W., Rethfeld, B., and Zhigilei, L.V. (2016) Fundamentals of ultrafast laser-material interaction. *MRS Bull.*, **41**, 960–968.

8

LIFT of Solid Films (Ceramics and Polymers)

Ben Mills, Daniel J. Heath, Matthias Feinaeugle, and Robert W. Eason

University of Southampton, Optoelectronics Research Centre, Building 46, Highfield, Southampton, Hants SO17 1BJ, UK

8.1 Introduction

The key components to successful LIFT implementation are (i) the removal of the donor from the carrier (the released donor often being referred to as a "flyer") and (ii) the capture of the flyer by the receiver. As there are an extremely wide range of experimental parameters, for both the laser (pulse energy, pulse length, wavelength, beam size, etc.) and the material (type, thickness, etc.), the process of optimization can often be time-consuming. Typically, for a chosen material, a range of donor thicknesses is explored over a range of laser pulse energies. Often, there is a narrow range of pulse energies (typically ±20%) that result in successful transfer. As a result of this complexity, many research groups focus on a subset of possible donor materials, and here we describe our work for LIFT printing of ceramic and polymer solid films. As explained in this chapter, this set of materials has many potential applications across photonics and electronics and therefore merit a full scientific investigation.

This chapter discusses donor release and capture, application to the fabrication of an energy-harvesting device, and a variant of LIFT called laser-induced backward transfer (LIBT, see Section 8.2.2.2). Specifically, Section 8.2 discusses a range of techniques for the optimization of the removal of the material, via laser interference, beam shaping, and premachining of the donor. Section 8.3 elucidates the transfer process via shadowgraphy (imaging of the donor in flight) and offers experimental and theoretical evidence for the usefulness of a compliant (i.e., soft and deformable) coating on the receiver substrate. End applications are always important, and therefore, in Section 8.4, we discuss a relevant application of thermoelectric materials, namely a microscale thermoelectric generator. Finally, in Section 8.5, we show how LIBT can enable subwavelength resolution patterning on the deposited material. A variety of laser systems are used in this chapter, namely a femtosecond laser system (Sections 8.2 and 8.5), KrF (Sections 8.3.2 and 8.4), and Nd:YAG (Section 8.3.1).

Laser Printing of Functional Materials: 3D Microfabrication, Electronics and Biomedicine,
First Edition. Edited by Alberto Piqué and Pere Serra.
© 2018 Wiley-VCH Verlag GmbH & Co. KGaA. Published 2018 by Wiley-VCH Verlag GmbH & Co. KGaA.

8.2 Assisted Release Processes

The LIFT technique relies on accurate and highly reliable removal of specific regions of the donor from the carrier substrate. Here, we discuss three methods that have been successfully applied to the LIFT of ceramic and polymer thin films. In Section 8.2.1, we discuss using interference of the incident laser pulse to create more useful intensity profiles. In Section 8.2.2, we describe the use of a focussed ion beam (FIB) for premachining of the donor substrate. Finally, in Section 8.2.3, we show the application of a digital micromirror device (DMD) for beam shaping.

8.2.1 Optimization of LIFT Transfer of Ceramics via Laser Pulse Interference

This section is divided into two subsections, each describing an approach for laser pulse interference-assisted LIFT, namely standing-wave interference from multiple layers and ballistic laser-assisted solid transfer (BLAST). More detailed analysis of these approaches is given in [1] and [2], respectively.

8.2.1.1 Standing-Wave Interference from Multiple Layers

An important realization is that, for certain conditions, a standing wave can exist during the LIFT process, due to the interference between backward- and forward-propagating components of the incident light waves that reflect off interfaces between the carrier, dynamic release layer (DRL, see Chapter 3), donor, air gap, and receiver [1]. The consequence is the potential for a large intensity modulation along the direction of laser propagation, leading to surprising variations in the required laser fluence for transfer and, under certain conditions, causing unexpected damage to the deposited material. In this section, the consequences of standing-wave effects on femtosecond pulse LIFT of transparent films are briefly explored. For the specific dependence on a variety of experimental factors, including the thicknesses of the donor, the DRL and air layers, and the receiver reflectivity, for simulated and experimental results, see [1].

For the simulations, nonconvergent incident light can be assumed; in other words, the fact that the laser is focused on the sample can be ignored. The resultant error is negligible, as the thickness of the donor is small (<1 μm) compared to the focal Rayleigh range (~100 μm), and makes the calculations considerably easier, as reflections are normal to the reflecting interfaces. Although the approach here is for monochromatic illumination, the laser source used for experimental comparison was a Coherent Legend F, pumped by a Coherent Mira 900, with central wavelength of 800 nm, bandwidth of 10 nm, pulse length of 150 fs, and pulse energy up to 2 mJ (the femtosecond laser system). The bandwidth of 10 nm is small compared to the standing-wave period (~100s nm), and therefore, the model still provides an acceptable level of accuracy.

To calculate the end result, each possible multiple reflection, from every interface, is calculated, where the interfaces are as shown in Figure 8.1. Although this might seem to lead to a very large set of calculations, as each of these multiple reflections results in a series of further multiple reflections, the calculation is, in

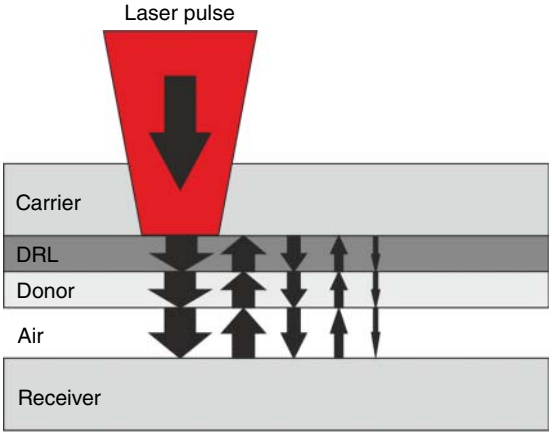

Figure 8.1 Schematic showing possible interference effects in the LIFT process.

fact, a series calculation that can be mathematically described by a single finite equation. For the full mathematical derivation, the reader should refer to [1]. Each interface results in a reflection of the pulse, where the reflected intensity depends on the refractive index difference between the two layers. If each layer thickness is not too large, the reflected pulse can interfere with the back end of the incident pulse. This interference effect can also occur for each subsequent reflection, depending on the physical length of the incident pulse and also the thickness of the DRL, donor, and air layer.

In practice, the interference effects are extremely dependent on the specific parameters used in the LIFT experiment, and therefore, for brevity, only a general discussion of the conclusions is presented here. The most important conclusion is the dramatic variation in the fluence in the DRL, when each of the layer thicknesses is changed. Due to the large effects that could be caused by small changes in the layer thicknesses, for example, 50% variations in DRL fluence for approximately 200 nm changes in the air layer thickness [1], careful selection of experimental parameters in order to minimize this effect can be an important consideration. This is because unintended variations in layer thickness, from, for example, inhomogeneities in sample fabrication, could result in different fluences on the donor across the sample width, simply from differing interference effects. In the case where the optimal transfer fluence is narrow, such effects could even result in certain regions of the sample failing to LIFT correctly.

8.2.1.2 Ballistic Laser-Assisted Solid Transfer (BLAST)

Successful removal of the flyer during LIFT is one of the most challenging aspects of the deposition technique, particularly in solid-phase LIFT, as the flyer must be detached from the thin film, ideally, however, with as little damage to the flyer itself or the surrounding donor material that remains on the carrier substrate. The difficulty here lies in the fact that a higher fluence is generally needed for the outer perimeter of the flyer, as compared to the central region, as the outer perimeter region must be released from the carrier substrate and sheared away from the surrounding donor material. It is therefore a reasonable argument that a structured laser pulse, where the fluence on the outer perimeter is greater than

that in the central region, could be a more appropriate beam profile than one with a uniform spatial intensity. In this section, an approach is presented where Fresnel diffraction is used to move toward a more appropriate spatial intensity profile for the LIFT of solid-phase material. Specifically, by using near-field diffraction from a circular aperture, a beam profile that has an intense outer ring is created for the LIFT process, leading to a more reproducible LIFTed deposit. The technique, described in this section, has been named BLAST [2].

While LIFT has a defined fluence threshold value, which depends on the donor film parameters such as thickness and absorption, a fluence below the threshold can nevertheless result in some level of donor modification. Specifically, there can be a small amount of vaporization of the donor material, but not enough to completely release the donor. Therefore, several below-threshold fluences can result in the delamination of the region of interest on the donor from the carrier, without the required sidewall or perimeter tearing, and hence, the donor is still physically attached to the carrier. To achieve transfer at this point, only the sidewalls must be disconnected, in this case, via a spatial intensity profile that has a considerably higher intensity profile at the outer perimeter. When this is achieved via BLAST, a less destructive transfer process results with an associated reduced probability of flyer damage. In practice, the higher-intensity outer ring is created via Fresnel diffraction from a circular aperture, as shown in Figure 8.2, which shows simulated spatial intensity profiles for a 10 μm diameter top-hat intensity profile for 800 nm wavelength light, at several distances from the aperture. By imaging a Fresnel-diffracted intensity profile onto the LIFT sample, some control of the relative intensity in the outer perimeter can be achieved. For small distances (Figure 8.2b), the outer ring is considerably more intense (~50%) than the interior average. However, for larger distances (Figure 8.2c,d), the interior intensity modulation becomes more substantial, leading to possible damage to the donor at the high-intensity interior modulations. Of interest, and demonstrated in the figure, is the sensitivity to distance, where there is significant change of the intensity profile over a distance of just 1 μm.

Pulses from the femtosecond laser system were focussed to a spot size of approximately 12 μm onto glass slides coated in films of chromium of 80 and 160 nm thicknesses. Silicon wafers were used as receivers, and donor–receiver separation was set to approximately 2 μm. Experiments were conducted under partial vacuum, at approximately 0.1 mbar. The threshold fluence for both donor thicknesses was found to be approximately 390 mJ/cm^2, which was in close agreement with other similar studies [3]. Delamination was found to occur at approximately 75% of the threshold value.

Figure 8.3 shows results from LIFT, using an intense outer ring that had approximately 5% higher intensity than the central region, for (a) a donor thickness of 80 nm using a single pulse at 90% of threshold fluence, (b) a donor thickness of 80 nm using 10 pulses at 80% of threshold fluence, and (c) a donor thickness of 160 nm using 10 pulses at 87% of threshold fluence. What is clear from the figure is that large numbers of pulses that are lower in intensity offer the potential for a considerably more effective deposition and that the technique of multiple-pulse BLAST enables lower-than-threshold fluences to be

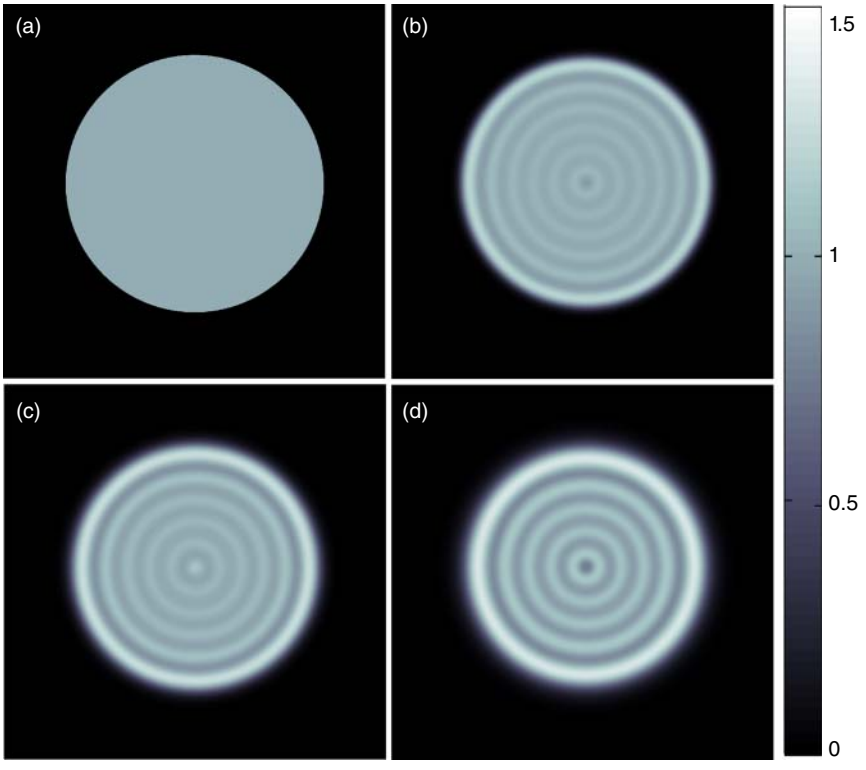

Figure 8.2 Simulated intensity profiles from a circular aperture of diameter 10 μm, for 800 nm light, for distances of (a) 0 nm, (b) 250 nm, (c) 500 nm, and (d) 1000 nm.

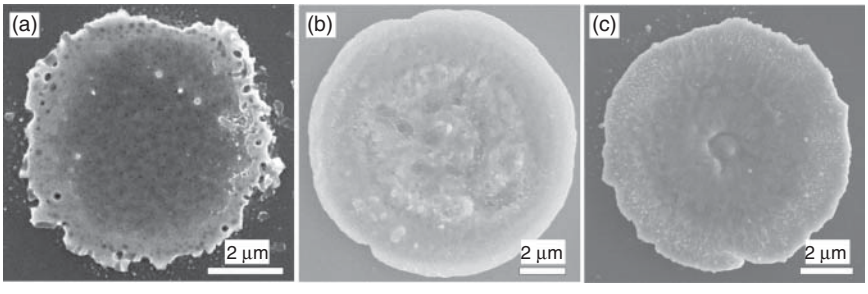

Figure 8.3 BLAST technique for (a) donor thickness 80 nm, single pulse at 90% of fluence threshold, (b) donor thickness 80 nm, 10 pulses at 80% of fluence threshold, and (c) donor thickness 160 nm, 10 pulses at 87% of fluence threshold.

used. The minimum and maximum transfer fluences that resulted in deposition were 75% and 95% of the threshold, corresponding to the use of between 2 and 30 laser pulses, with the most effective number of pulses found to be in the range of 5–10. These results show the potential benefit of using the BLAST technique for the deposition of heat-sensitive and fragile solid-phase donor films.

8.2.2 LIFT Printing of Premachined Ceramic Microdisks

In this section, a second option for optimization of the removal of the donor material is presented. This particular method relies on an external process, specifically use of a FIB to premachine the outer perimeter of the donor material intended for transfer, in order to reduce the amount of sidewall material that needs to be sheared from the donor substrate. While a DRL can enhance the donor–carrier separation process during LIFT, the separation of the donor–donor sidewall interface is not similarly enhanced. One possible application of this approach is to enable the use of donors that have thicknesses greater than a few microns, as this generally corresponds to the upper limit for more conventional LIFT. The approach presented in this section is discussed in more detail in [4] for ceramic microdisks and in [5] for LIFT of single-crystal microdisks of yttrium iron garnet, grown on yttrium aluminum garnet.

For this work, 1 μm thick donor films of zinc oxide, a piezoelectric material, was sputtered onto glass slides. FIB machining was used to etch 5 and 10 μm diameter circles, to a depth of 80% of the donor thickness, hence leaving 20% of the donor thickness at the donor–carrier interface. Typical machining times for the FIB were about 80 s per ring, and hence, this approach is more suited to low numbers of high-quality depositions. Depth values of greater than 100% were also investigated (corresponding to machining through the entire donor and into the carrier) but were not suitable, as this prevented the pressure buildup required for LIFT. Figure 8.4a shows a 5 μm diameter circle machined into the donor film to a depth of 80% of the donor thickness. Clearly shown is the excellent machining quality that can be achieved using a FIB.

Pulses from the femtosecond laser system with spot size of approximately 12 μm were used for the deposition onto silicon receivers, where the spot size was larger than the premachined ring, in order to minimize misalignment. The donor–receiver separation of approximately 1 μm was achieved using Mylar film. Figure 8.4 shows results that highlight the differences when (b) not using and (c) using premachining of the donor. While there is a difference in deposit size for these two examples, all other conditions were similar, and so the considerable difference in deposition quality is almost entirely a consequence of premachining. In the case of (c), the edge quality is considerably superior, and no surrounding debris is observed. Worthy of note is the much reduced threshold fluence for the premachined depositions, at approximately 450 mJ/cm^2, versus

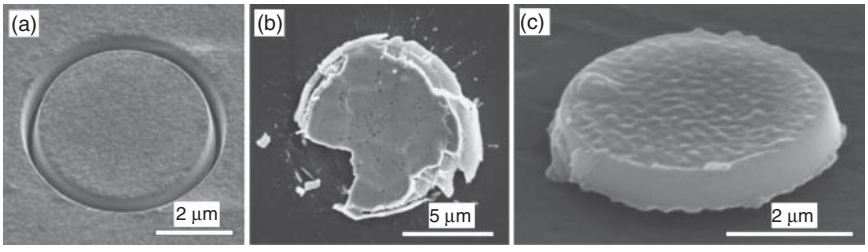

Figure 8.4 (a) Donor film, showing FIB machining of a circle of 80% depth of the donor film, and deposited zinc oxide material (b) not using and (c) using donor premachining.

approximately 1 J/cm^2 for the nonmachined donor regions, where the difference approximately corresponds to the required energy for the shearing of the sidewalls during the release process.

In conclusion, a method for significant improvement of the sidewalls of the deposited structure has been presented, which comes with the caveat of increased time and complexity of donor preparation. However, in applications where only small numbers of such deposits are required, then this approach may prove valuable.

8.2.3 Spatial Beam Shaping for Patterned LIFT of Polymer Films

In this section, we discuss how a DMD, acting as a variable illumination mask, can be used to assist in the removal of shaped regions of a polymer film, with features as small as 10 μm. Previous work has shown how a DMD can be used for laser ablation [6–8] and multiphoton polymerization [9].

Much of the research into LIFT to date has utilized laser pulses that have a Gaussian or "top-hat" spatial intensity beam profile. While there have been some successes using other approaches, such as "smart beam shaping" [10], custom masks [11], or overlapping deposits [12], the result by Auyeung *et al*. [13] showed the clear advantages of using a DMD as a beam shaper capable of variable illumination for silver nanopaste deposition using a 355 nm UV laser. In this section, we show a continuation and translation of the work by Piqué *et al*. [14] and demonstrate LIFT of a solid polymer film.

Pulses from the femtosecond laser system were shaped via diffraction from a DLP3000 DMD. The device itself consisted of an array of 608 by 684 square mirrors, each of width approximately 7.6 μm. Each individual mirror was able to be set, remotely, to either an "on" or "off" position, corresponding to an angle of +12° or −12° relative to the surface of the device. This remote control of each mirror position allowed specific binary patterns (the DMD pattern) to be loaded onto the DMD. If illuminated by incoherent light, the DMD would therefore only reflect parts of the beam that corresponded to mirrors in the "on" position, hence enabling direct control of the spatial intensity profile. Importantly, however, coherent laser light, as used here, resulted in the DMD acting as a diffraction grating. The effect was that multiple diffraction orders, each containing spatial frequency information on the DMD pattern, were created. However, simply collecting a single diffraction order with an objective lens, and imaging the light onto the sample, allowed the DMD pattern to be recreated as a spatial intensity pattern at the desired focal plane. As shown in Figure 8.5, the LIFT sample was positioned at this plane, and hence, the intensity pattern on the LIFT sample was a highly demagnified version of the DMD pattern. The angular orientation of the DMD mirrors allowed the device to be used in a blazed-grating arrangement, hence increasing the efficiency. A total of approximately 30% of the incident light was collected, where the losses corresponded to mirror reflectivity (∼88%), device coating (∼90%), diffraction losses, and other effects. For DMD-shaped experiments, either a 50× or a 20× objective was used.

The donor used was poly(methylmethacrylate), also known as *PMMA*, which was spin-coated to a thickness of approximately 1.3 μm. The carrier

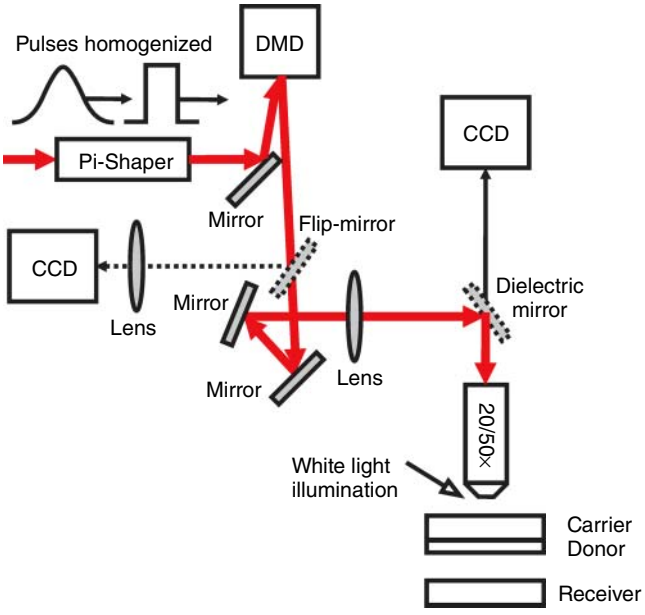

Figure 8.5 Experimental setup for the DMD-based LIFT of polymer films.

was a borosilicate glass slide. The receiver, also a borosilicate glass slide, had a approximately 10 µm thick PDMS layer, acting as a compliant receiver [15] (see Section 8.3.2). While a compliant receiver is not a requirement, it should be noted that PDMS-coated substrates are used extensively in lithography, MEMS devices, microelectronics, and microfluidics.

The LIFT of polymer films shaped as a series of alphabetic letters of different sizes was investigated, in order to determine the limit to the flyer complexity. Figure 8.6 shows a comparison of the deposition of letters ("O," "B," and "S"), chosen to illustrate objects of increasing spatial complexity, including open-ended structures, using (a–c) a 50× objective and fluence of 300 mJ/cm^2 and (d–f) a 20× objective and fluence of 270 mJ/cm^2. A DRL of (a–c) 30 nm gold and (d–f) 50 nm carbon was used to increase the laser absorption, but it should be noted that there was no noticeable difference between the effectiveness of the two DRL types (confirmed via additional measurements), other than a reduced amount of surface debris using carbon. While (d–f) clearly show high-fidelity transfer, (a–c) appear to be at a resolution limit for this particular material. This result was similarly evident from the rest of the deposited structures.

Of interest, therefore, is the limit to this technique. In order for a structure to be released from the donor, both the carrier–donor interface and the complete circumference of the donor must be separated. An important realization is that while the carrier–donor interface area is proportional to the size of the beam, the circumference is not, but it rather depends on the complexity of the pattern. Therefore, more complicated structures, such as those shown in Figure 8.6,

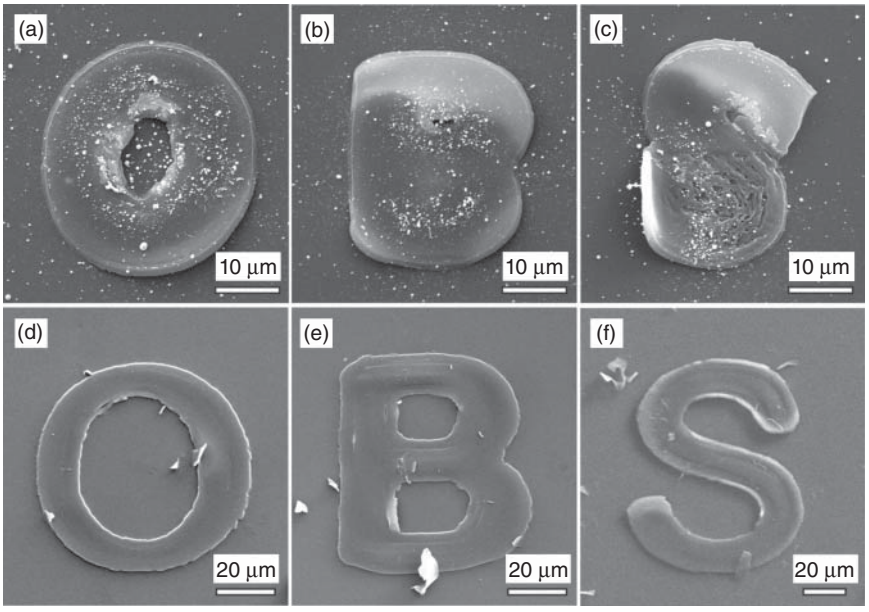

Figure 8.6 SEM images of approximately 1.3 μm thick polymer film deposits of letters ("O," "B," and "S") deposited via DMD-based LIFT using (a–c) 50× objective and (d–f) 20× objective.

likely require higher incident pulse energies compared to a similarly sized circular deposit. Another consideration is that the deposited structures match the projected intensity pattern in overall shape, but not line thickness, see (c) for example. We attribute this effect to the fact that there exists a minimum line thickness (~10 μm) that can be LIFT-removed out of the material, hence causing (b,c) to appear almost unrecognizable from the intended profile. This effect also caused corners to become more rounded. Figure 8.7 shows deposition of the letter "A" for a range of laser fluences, demonstrating an effective fluence window between 235 and 300 mJ/cm^2. Out of approximately 300 total depositions, 100% adherence was observed, even after sonication in water for 30 min.

In summary, DMD-based beam shaping for LIFT offers the potential for high-resolution, on-demand, printing of a range of materials. As discussed in Section 8.5, this approach to beam shaping can also be used for LIBT, hence synergizing strongly with subwavelength nanoimprinting approaches.

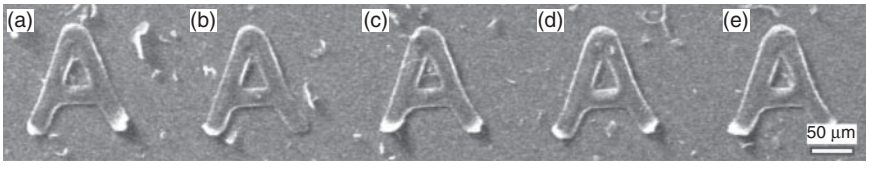

Figure 8.7 SEM images of structured deposition (letter "A"), for fluences of (a) 235 mJ/cm^2, (b) 251 mJ/cm^2, (c) 268 mJ/cm^2, (d) 284 mJ/cm^2, and (e) 300 mJ/cm^2.

8.3 Shadowgraphy Studies and Assisted Capture

There are two key components to a successful LIFT deposition. Firstly, the donor must be released correctly, and there exists several advanced techniques for optimizing this process, including those discussed in Section 8.2. Secondly, the donor must be captured correctly by the receiver. Due to the high speeds that can be experienced by the flyer, of order 1000 ms^{-1} in some cases [15], the impact forces can exceed material limits, resulting in fracture of the deposited sample. In fact, as discussed in Section 8.3.1, fracture can also occur immediately after release from the carrier. Here, some of the mechanisms that occur during both the flyer motion (Section 8.3.1) and the impact of the flyer on the receiver (Section 8.3.2) are quantified.

8.3.1 Shadowgraphic Studies of the Transfer of Ceramic Thin Films

In this section, the transfer mechanisms of solid-phase LIFT at atmospheric pressure is discussed, using experimental results from time-resolved shadowgraphy. The influence of the laser fluence is explained, using results from both the threshold fluence and above-threshold fluence. Time-resolved shadowgraphy provides a useful mechanism for observing the flyer in transit between the carrier and the receiver, hence providing information regarding the integrity and velocity of the flyer, under specific experimental conditions. Here, we discuss shadowgraphy of LIFT of solid ceramic donor materials, using a triazene polymer as a sacrificial DRL (see Chapter 3).

The rationale behind the use of a DRL is as follows. In conventional LIFT, the donor material absorbs the incident laser pulse energy, in order to act as its own propellant, which can, in some circumstances, lead to unavoidable damage to the deposited flyer. One solution to this problem is to use a sacrificial release layer that is positioned between the carrier and the donor that absorbs the laser pulse energy. Triazene polymer was studied in this context as a DRL material [16], due to its low ablation threshold and photolytic dissociation. Upon dissociation, the triazene releases nitrogen gas, hence providing the forward thrust that is required for LIFT. Understanding the effect of such DRLs, via shadowgraphy, is important to ensure optimum transfer with minimum donor damage.

Generally for LIFT, the distance between the donor and the receiver is on the order of microns, therefore making the imaging of the flyer, at 90° to the flyer trajectory, near impossible. Rather than image the actual LIFT process, that is, the release *and* the deposition, time-resolved shadowgraphy is generally used to only image the donor release and subsequent flight, without the presence of a receiver. The setup is shown in Figure 8.8. The delay generator controlled the timing for laser pulses generated from the XeCl excimer laser (Compex, Lambda Physik, 308 nm, 30 ns) that was used in these LIFT experiments, and the timings for the laser pulses generated from a second-harmonic Nd:YAG laser (532 nm, 6 ns) that was used for irradiation of a rhodomine dye that provided the illumination of the ejected flyer and released shock wave. Although the 532 nm pulses could have been used directly for flyer illumination, experience has shown that an incoherent light source is more effective. The camera, also triggered by the delay

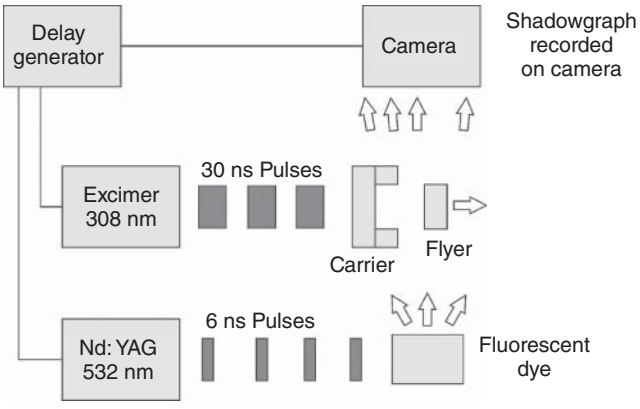

Figure 8.8 Schematic showing shadowgraphy setup.

generator, recorded the shadowgraph. Different delays therefore allowed the flyer to be imaged at different positions following release, hence providing images that show the progression of the flyer after release. It is important to note that *each shadowgraph corresponds to a different flyer*, and hence, shadowgraphy analysis assumes that the LIFT process is repeatable from pulse to pulse. Here, the samples used were 1 μm thick Yb:YAG ceramic film donors that were deposited via pulsed laser deposition [17] onto triazene-coated glass substrates.

Figure 8.9 shows time-resolved shadowgraphs of 1 μm Yb:YAG, for time steps of 400–2400 ns, for incident pulse energy of (a) 60 mJ/cm^2 and (b) 600 mJ/cm^2. Both the flyer and the shock wave released by the pressure step are clearly visible in all the shadowgraphs. For the higher pulse energy, the flyer speed is also higher and the shockwave is more pronounced and exists for a longer time period. At a delay time of 800 ns, the flyer has only just delaminated in (a) but has already moved approximately 500 μm in (b). This is likely due to the fact that the higher fluence decomposed a larger fraction of the depth of the DRL, hence releasing a larger volume of propellant gas.

In addition to laser fluence, donor thickness and DRL thickness also play a key role in the dynamics of the flyer. For example, if the ablation depth is greater than the DRL thickness, then damage may occur to the flyer. Alternatively, if the donor material thickness is increased, then the flight velocity may be lower, as

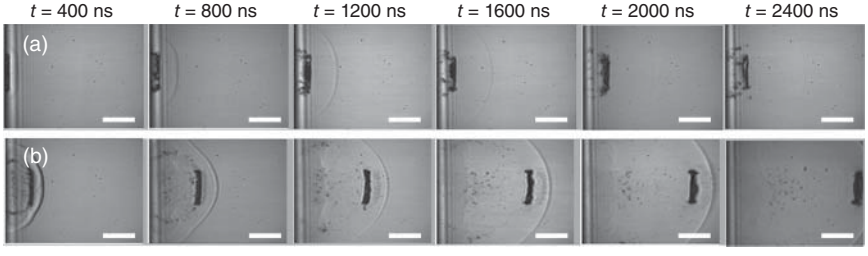

Figure 8.9 Shadowgraph images for 1 μm thick Yb:YAG donor for DRL thickness of 250 nm and fluence values of (a) 60 mJ/cm^2 and (b) 600 mJ/cm^2. White scale bars are 500 μm.

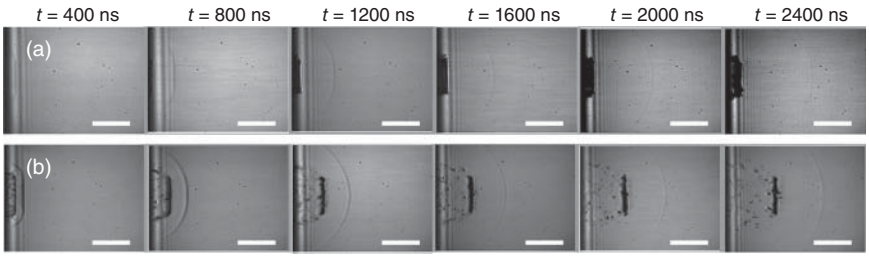

Figure 8.10 Shadowgraph images for 1 μm thick Yb:YAG donor for a fluence value of 100 mJ/cm^2 and DRL thicknesses of (a) 50 nm and (b) 350 nm. White scale bars are 500 μm.

the same initial impulse when converted into kinetic energy will correspond to a lower velocity, as well as a larger amount of energy used to shear the thicker donor material. For a thorough discussion regarding the interplay of these parameters, see [16]. The rest of this section only discusses the effect of DRL thickness.

Figure 8.10 shows shadowgraphy results for a laser fluence of 100 mJ/cm^2 for triazene thicknesses of (a) 50 nm and (b) 350 nm, for 1 μm thick Yb:YAG. Once again, the time delay is from 400 to 2400 ns. The clear, and expected, conclusion is that a thicker DRL provides the opportunity for a faster release, due to a larger volume of propellant gas. Specifically, according to the figure, a thicker DRL increases the flyer velocity, reduces the initial time before release, increases the amount of debris, and increases the chance of flyer disintegration. As the DRL thickness increases further, at some point the thickness will be greater than the absorption depth, leaving undissociated DRL material. As shown in (a), the 50 nm DRL appears to provide only enough explosive energy to delaminate the flier, rather than to propel it away from the donor substrate. As such, we suspect that 50 nm thickness corresponds approximately to the minimum DRL thickness that enables the release of the ceramic film.

In summary, the dependence on laser fluence and DRL thickness has been studied via time-resolved shadowgraphy. This approach allows significant understanding to be gained, for specific combinations of experimental parameters, and hence, shadowgraphy is considered as an important tool for optimizing the transfer process.

8.3.2 Application of Polymers as Compliant Receivers

In this section, experimental and theoretical results are used to demonstrate the efficacy of using a compliant coating on the receiver, to reduce the effects of impact on the flyer upon deposition on the receiver. While the total kinetic energy reduction that the flyer must experience cannot be changed by a coating on the receiver, the timescale over which it is reduced can be increased. More specifically, the maximum impulse (change in force per time period) can be reduced, allowing higher transfer velocities and more fragile flyers to be successfully transferred.

While the conclusion from the numerical model is discussed here, the theoretical derivation for the model [15] is beyond the scope of this section. Experimental results showing the difference between LIFT of 1 μm bismuth

telluride onto a bare glass slide and a PDMS-coated glass slide are shown and qualitatively agree with the theoretical model. As discussed in [15], the deposition process is strongly dependent on many experimental parameters and occurs over a very short time, meaning that the whole system is extremely nonlinear and very challenging to quantify precisely. Given the available computing power and the accuracy of the known material parameters (see [15] for a discussion on the reliability of values in the literature), qualitative agreement is all that can be currently achieved. Nonetheless, the results presented here offer potential for a significant improvement in the range of materials that can be deposited in an intact form via LIFT.

The collision of the flyer with the receiver can lead to material failure for certain transfer conditions and material properties. The flyer may experience plastic deformation caused by exceeding a certain stress limit or may bypass plastic deformation and simply fracture if brittle, such as the bismuth telluride shown in the section. In the model, the stress and strain of the flyer during the moments after impact are determined, including time-dependent shock waves. In order to judge whether the flyer experiences failure, the maximum force is noted and compared with known material limits. If the force at any time after impact exceeds the limit, then material failure is assumed to have occurred.

The simulation used finite-element analysis software (COMSOL Multiphysics) for a time up to 2 μs after the initial impact. The receiver, flyer, and polymer film were modeled as cylinders for symmetry reasons to reduce the number of spatial dimensions from 3 to 2. The flyer deformation and resulting stress were determined using constant values of Young's modulus, Poisson's ratio, and density of the layered materials, whereas in practice, these parameters can also depend on the stress/strain and temperature, all of which vary dramatically over the short timescales associated with flyer impact. The maximum receiver size, a consequence of using a mesh size of 1 nm, was 30 μm in radius with a thickness of 15 μm, meaning that the radius of the flyer was much smaller than that shown in the experimental results. The donor was assumed to be isotropic, which is a considerable oversimplification for materials such as crystals, and all materials were modeled as elastic bodies. The flyer was not able to be re-ejected from the receiver, but rather tightly bound to its surface. The simulation shows that the maximum forces experienced by flyer incident onto a receiver can be reduced by, at least, a factor of 3, when using a compliant receiver.

Experimentally, flyers of 1 μm thick bismuth telluride were transferred on polymer-coated receivers (see [18] for preparation practices), using 20 ns pulses from a KrF excimer laser. In this section, results for LIFT onto PDMS-coated receivers are discussed; for other receiver coatings, see [15]. Figure 8.11 shows deposition onto (a) uncoated glass, (b) 12 μm PDMS coating, (c) 100 μm PDMS coating, and (d) 12 μm PDMS coating but using above-threshold fluence. For all results, some degree of cracking along the edges was observed and therefore is most likely to have been formed during the donor release process via partial melting. The results show reduced damage when a PDMS coating was used, indicating that the use of a compliant receiver most likely reduces the maximum forces imparted on the flyer in the short time after impact with the receiver.

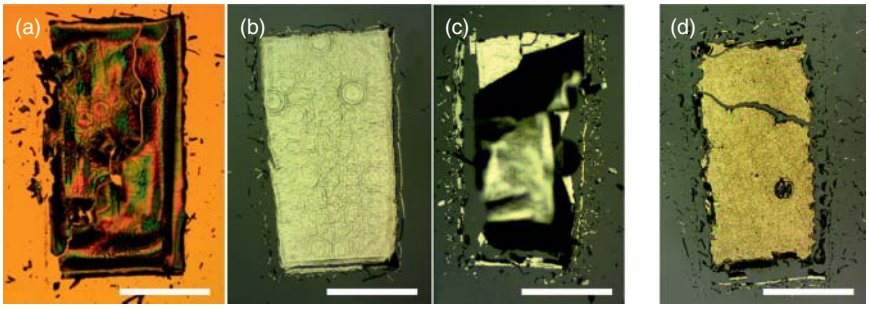

Figure 8.11 LIFT of 1 μm bismuth telluride with fluence 80 mJ/cm^2 for (a) uncoated glass, (b) 12 μm PDMS, (c) 100 μm PDMS, and (d) fluence 120 mJ/cm^2, and 12 μm PDMS. The scale bars are 200 μm.

Contradictory to the model, however, was the result for (c) 100 μm thick PDMS, which shows that the flyer appears significantly more damaged than the case of (b) 12 μm thick PDMS. In the model, a thicker compliant receiver layer generally corresponded to lower maximum stresses. As highlighted by (d), it is important to note that despite the PDMS coating, it is still important to use the correct fluence.

Despite the lack of complete agreement between experiment and theory, the overall conclusion from both experimental and theoretical approaches is that a PDMS-coated receiver can improve the prospect of successful LIFT. The use of a compliant receiver becomes even more important for fragile and structured flyers, as discussed in Section 8.2.3.

8.4 Applications in Energy Harvesting

Here, a particular application of the LIFT approach is discussed, namely the fabrication of a microscale thermoelectric generator, via deposition of chalcogenide thin films. Such small-sized energy-harvesting devices, including both thermoelectric and piezoelectric devices, have significant potential in the areas of microfabrication, as they have the potential to power microscale electrical components and offer the potential for "green" energy fabrication solutions. In this case, LIFT is an ideal fabrication technique as it enables the deposition of ceramic solid films with very minimal damage, while also being a noncontact approach that offers precise positional control and direct placement of devices.

Chalcogenides are a group of materials that have good prospects for a range of photonics [19] and electronics [20] applications and can have properties that enable them to be used for thermoelectric devices. The thermoelectric generator discussed here consisted of thermoelectric chalcogenides bismuth telluride, bismuth selenide, and bismuth antimony telluride and had a Seebeck coefficient of 0.17 mV/K and leg-pair resistance of 10 kΩ. The optimization of the depositing technique for the materials is shown in Section 8.4.1, and the fabrication of the device and corresponding measurements are presented in Section 8.4.2.

8.4.1 LIFT of Chalcogenide Thin Films

The deposition of intricate materials for the fabrication of devices such as an energy harvester is of interest for applications such as waste-energy recovery [21] and remote sensing [22]. The fabrication steps, however, are somewhat complicated, as a variety of materials must be precisely coassembled on a substrate, which may, in itself, need to be flexible in order to facilitate high-volume roll-to-roll production [23]. In addition, any degradation in the quality of the deposited material directly impacts on the efficiency of the fabricated device. Therefore, the chosen fabrication technique must be able to precisely deposit a range of materials, with almost perfect preservation of the initial material state. Here, the LIFT of thin films of bismuth telluride is studied in detail. For results showing the LIFT of bismuth selenide and bismuth antimony telluride, see [18]. Deposits of size 15 mm^2 were deposited onto polymer-coated substrates (see Section 8.3.2 for discussion on complaint receivers), and characterization showed that the polycrystalline structure of the films could be preserved, under certain LIFT conditions. Seebeck coefficients of the transferred films were found to be approximately 80% of their initial values, showing the efficacy of the LIFT of material that could be used for thermoelectric devices.

Experimentally, LIFT was achieved using a 20 ns pulse KrF excimer laser, central wavelength of 248 nm, pulse energy of 400 mJ, and repetition rate of 1 Hz. The laser beam passed through a rectangular aperture, in order to spatially shape each laser pulse. The laser pulses were focused at the interface between the UV transparent fused-silica carrier and the donor material. The donor films were deposited via RF sputtering using targets of Bi_2Te_3, $Bi_{0.5}Sb_{1.5}Te_3$, and Bi_2Se_3, with thicknesses of 0.27, 0.36, 1, and 1.4 μm. The receiver substrates were polymer-coated glass, with the polymer thickness approximately 130 μm, which acted as both a compliant receiver and an electrical insulator. Figure 8.12 shows transfer of bismuth telluride of thickness 1 μm, under an optimal transfer fluence of 90 mJ/cm^2.

In order to investigate the morphology of the deposited materials, X-ray diffraction data was compared in order to investigate the change induced via LIFT. A small broadening of the bismuth telluride peak was observed, suggesting that

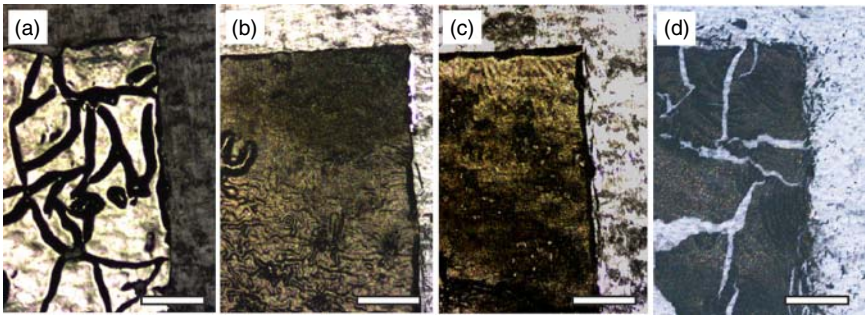

Figure 8.12 Microscope images of 1 μm thick bismuth telluride deposits for laser fluences of (a) 70 mJ/cm^2, (b) 100 mJ/cm^2, (c) 110 mJ/cm^2, and (d) 200 mJ/cm^2. Scale bars are 200 μm.

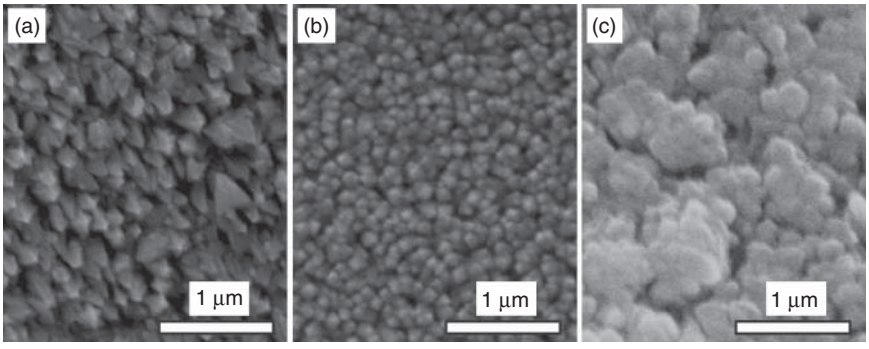

Figure 8.13 SEM images showing surfaces of bismuth telluride films of thicknesses (a) 270 nm, (b) 1 μm, and (c) 1.4 μm, before the LIFT process.

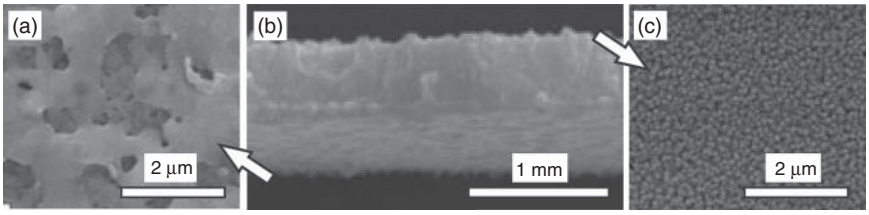

Figure 8.14 SEM images of (b) a side view of the 1 μm thick bismuth telluride deposit, with corresponding (a) bottom and (c) top surfaces. The laser irradiated the bottom surface.

a limited phase change of the material had occurred during the LIFT process, likely due to melting and resolidification in the absorbed region of the donor. For further analysis and the associated X-ray spectra, see [18]. SEM images of the bismuth telluride film before the LIFT process, for three difference thicknesses, are shown in Figure 8.13. This figure should be compared to Figure 8.14, which shows a side view and top and bottom surfaces of a deposited region of a bismuth telluride donor. As expected, the irradiated side shows significant morphological change, while the top surface, which was not directly exposed to any laser energy, has the original morphology. The extent of the damage, roughly corresponding to the absorption depth, is approximately 100 nm.

Measurements of the donor film (before LIFT) demonstrated a Seebeck coefficient of $-64 \pm 1\,\mu V/K$ (see [24, 25] for comparable values from the literature), whereas the deposited material (after LIFT) had a value of $-49 \pm 1\,\mu V/K$, hence showing an approximately 20% drop in efficiency upon transfer. The negative sign here is because bismuth telluride is an n-type semiconductor. The following section describes the assembly of LIFTed materials into a working thermoelectric device.

8.4.2 Fabrication of a Thermoelectric Generator on a Polymer-Coated Substrate

The device was constructed by depositing bismuth telluride (n-type) and bismuth antimony telluride (p-type) onto a PDMS-coated glass slide, connected in

series, with no further lithographic steps required. Such devices see applications in many areas, including temperature sensors, heating and cooling devices, and energy conversion, where a naturally occurring temperature gradient is present. The measured Seebeck coefficient was 0.17 mV/K, and resistance per leg pair was 10 kΩ.

Donors consisted of bismuth telluride and bismuth antimony telluride layers grown via sputtering onto fused-silica carriers. The receivers were microscope slides coated in approximately 5 μm of PDMS (see Section 8.3.2 for a discussion on compliant receivers). The LIFT process used single 20 ns laser pulses, at 248 nm, from a KrF excimer laser, where the fluences used for transfer were in the range 70–80 mJ/cm^2. As discussed in Section 8.4.1, an aperture was used, in order to spatially shape the laser pulses to a rectangular shape. The deposition of the two types of chalcogenides was carried out sequentially, as shown in Figure 8.15, where the p-type material (bismuth antimony telluride) was deposited first and the n-type material (bismuth telluride) was deposited second, hence electrically connecting the device.

The final device was characterized via use of two Peltier elements attached to opposite sides of the device, hence producing a temperature gradient and enabling the required voltage measurements to take place. The series connection layout between the n-type and p-type components ensures that the total device consisted of the sum of all component voltages, when a temperature gradient was applied, where typically the minimum practical output voltage for powering useful devices is on the order of millivolts. Figure 8.16 shows (a) the location of electrical contacts and the direction of the temperature gradient, (b) the complete device, and (c) a microscope image showing a contact between an n-type and p-type leg pair. As shown in the figure, the device was designed for planar operation, that is, the temperature gradient was in plane with the substrate, rather than in a perpendicular direction. In this work, typical temperatures of order 300 and 330 K were used for measurements.

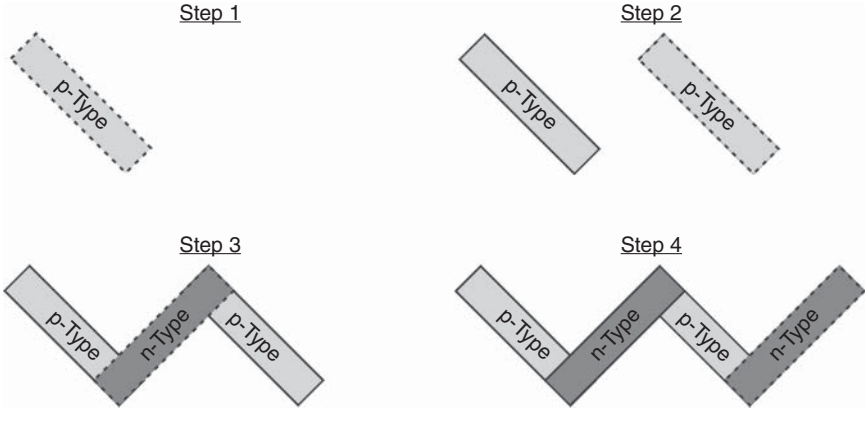

Figure 8.15 Schematic showing deposition steps used for LIFT for device fabrication. Actual device was 20 leg pairs (19 junctions).

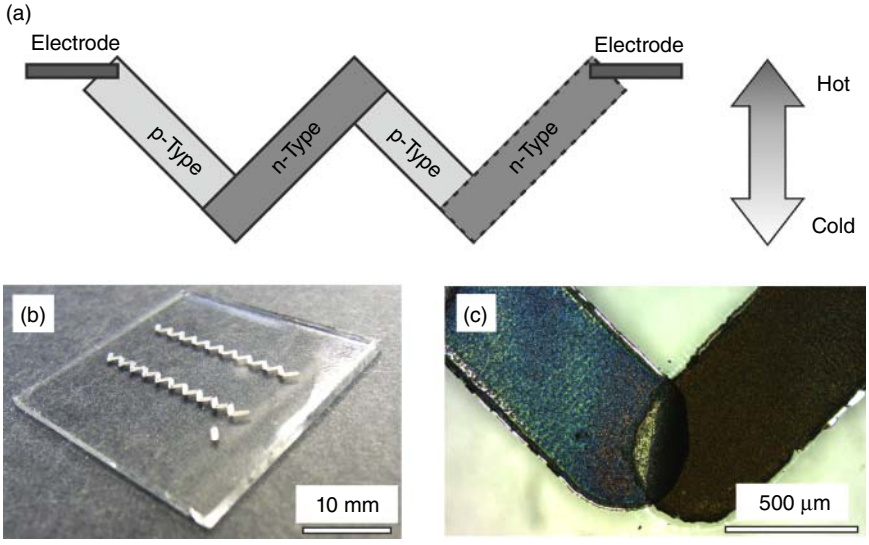

Figure 8.16 (a) Device schematic, (b) photo of fabricated device, and (c) image of n-type and p-type leg-pair contact.

Although other designs are possible, such as square profiles (where the n-type and p-type materials are exactly perpendicular to the temperature gradient) that use electrical connectors, the chosen design minimized additional fabrication steps, such as the addition of multiple electrical connectors, while sacrificing area efficiency, that is, the amount of energy extracted per unit area.

It was found that establishing an effective electrical and thermal contact at the junctions was a demanding fabrication step, as both n-type and p-type elements must be sufficiently connected to each other and to the substrate, which, in this case, relied on the mutual bonding induced via the LIFT process. To estimate the quality of this bonding, the resistance of single junctions was measured, and by taking into account the known resistance of the elements, the junction resistance was determined to be $10.3 \pm 0.5\,\text{k}\Omega$. In order to improve the junction connection, that is, to reduce the resistance, silver nanoparticle ink with particle size approximately 100 nm and gold conductive paint were manually dispensed onto the junctions. Once cured, these approaches resulted in a resistance drop down to $9.3 \pm 0.5\,\text{k}\Omega$.

The maximum Seebeck coefficient was measured to be $170\,\mu\text{V/K}$, which is similar to the theoretical value of $191\,\mu\text{V/K}$ [26]. As expected, increasing the number of junctions connected in series increased the measured voltage. Treatment of silver nanopaste reduced the Seebeck voltage by approximately a factor of 3, likely as a consequence of the migration of the silver nanoparticles into the thermoelectric materials, hence degrading their effectiveness, and also due to the shrinking associated with the curing process.

In conclusion, this work has demonstrated that the adhesion between n-type and p-type materials, and to the polymer substrate, is sufficient for manufacturing of such devices. It is not unrealistic to assume that the manufacturing

process could be scaled up to coveragence of many square centimeter total area. Overall, the performance of the presented device is comparable to those fabricated using other manufacturing processes, and when the fabrication speed and the nonrequirement of a clean-room environment are taken into account, the LIFT fabrication process clearly offers promise for future high-precision additive manufacturing applications.

8.5 Laser-Induced Backward Transfer (LIBT) of Nanoimprinted Polymer

In this section, results from a variant of LIFT, namely LIBT [27], are presented. In the case of LIFT, the laser pulse propagates through the transparent carrier and is absorbed by the donor, which is then propelled toward the receiver. In the case of LIBT, the laser pulse propagates through the transparent receiver and transparent donor and is absorbed by the carrier, which expands and propels the deposit toward the receiver. For LIBT, the propagation direction of the deposit is backward, with respect to the incident laser pulse. From the earlier discussion, it is clear that LIFT requires a carrier of sufficient transparency to the incoming laser pulse, while LIBT requires a transparent receiver and a transparent donor. Therefore, for example, LIBT can work with a nontransparent carrier, such as a bulk material. For more details on this variant, the reader is directed to Section 8.2.2.2.

Here, solid-phase LIBT of transparent photopolymers through use of an absorbing silicon carrier substrate is discussed, also including the use of a DMD, as a spatial light modulator (see Section 8.2.3), for producing shaped flyers via shaping pulses from the femtosecond laser system. In addition, a technique for subwavelength structuring of the deposited material is demonstrated. Minimum lateral size scales of approximately 6 μm are shown, with observed subwavelength features of approximately 140 nm via the imprinting of a silicon photonic waveguide structure. This combination of DMD-based shaping and nanoimprinting offers the potential for high-precision deposition on the nanoscale. In order for the subwavelength features to be maintained during transfer, a requirement is that the flyer must be in solid phase, as opposed to liquid phase; otherwise, the nanostructures would not survive transfer and deposition. For a more in-depth discussion, see [28]

While DMD-based modification of the pulse spatial intensity for applications to LIFT (see Section 8.2.3) has unlocked new regimes in microscale deposition, there exists a fundamental limit to the minimum resolution possible using this approach, specifically a resolution approximately equal to the laser wavelength, a direct consequence of the Rayleigh criterion. Therefore, alternate approaches are needed, in order to further improve the achievable resolution. In this section, such a technique is described and results are demonstrated. The key to this improvement in resolution is the fact that a different physical process is used for the deposition, hence bypassing the aforementioned wavelength-based resolution limit.

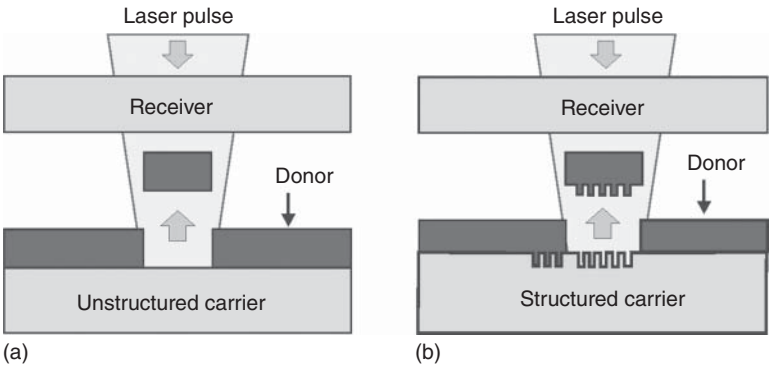

Figure 8.17 Schematic of LIBT using an (a) unstructured and (b) structured carrier substrate.

A schematic of the nanoimprinting approach is shown in Figure 8.17, which illustrates the difference between using (a) an unstructured and (b) a structured carrier substrate for LIBT. It is important to note that the surface of the deposit will not be an exact inverted replica of the initial carrier surface, as there will be a limitation to the minimum size and maximum aspect ratio that can be achieved, where these limits will also depend on the structure and material parameters.

In practice, carrier structures could be fabricated via techniques such as lithography, focused ion-beam milling, or UV-beam machining. The deposition of the donor material onto the structured carrier could be via techniques such as spin coating of liquid polymers or one of many vapor deposition processes. The specific combination of structuring method and deposition method will of course depend on both the nature of the features desired and the materials to be used. In certain cases, for example, the combination of silicon carrier and polymer donor presented in this section, the structured carrier can be reused, hence offering the potential for scale-up of this deposition process.

The nanostructuring of the deposited material at resolutions far below the diffraction limit offers great potential for applications in the electronics and photonics fields. In this work, we present the results from the intact transfer of solid deposits of photoresist material from a silicon carrier substrate that incorporated a prefabricated photonic waveguide relief structure. While photoresist was, in this case, used as a donor, nanoimprint LIBT is not limited to using this particular material, and the photoresist was only used here as a proof-of-principle demonstration. In nanoimprint LIBT, in comparison to UV lithography, the process does not require a clean-room environment, and the overall beam shape can be modified using a DMD, as opposed to the fabrication of a new mask as in the case of UV lithography. Other advantages over lithography include the noncontact nature, the possibility to use nonplanar receiver substrates, and the lack of postprocessing steps.

The experimental setup is almost identical to that shown in Figure 8.5, in Section 8.2.3, except that Section 8.2.3 corresponds to LIFT, while this section corresponds to LIBT, and so the sample geometry here is modified. Pulses from the femtosecond laser system were spatially homogenized before illumination onto the DMD, which was used to modify the spatial intensity profile of each

laser pulse. The patterned pulses were then focused on the sample, which was positioned using computer-controlled stages, using either a 50× or a 20× objective. Pulse energies were modified in order to determine the threshold intensity for optimum LIBT. The donors were fabricated via spin coating photoresists onto monocrystalline silicon wafers (unstructured carrier) and silicon-on-insulator chips (structured carrier). Receivers were 1 mm thick microscope slides that were uncoated or coated with a 10 μm thick PDMS layer. The donor–receiver spacing was set at approximately 5 μm, verified by interferometric measurements.

8.5.1 Unstructured Carrier Substrate

Donors with different thicknesses of S1813 deposited onto unstructured silicon wafers were used for LIBT, in order to investigate the capabilities of using only the DMD for control of the shape of the deposited material. The transfer fluences were observed to be approximately 475, 580, and 765 mJ/cm^2 for the donor thickness of 1.4, 1.85, and 2.25 μm. As expected, a higher fluence was required for the deposition of more complicated profiles, where complexity here is defined as the length of the outline (also referred to as the sidewall) of the shape compared to the area, where circles are therefore the lowest complexity shape and require the lowest fluence for transfer.

The results in Figure 8.18 illustrate a few examples of the achievable complexity offered by DMD-based pulse shaping for LIBT using an unstructured carrier. The figure shows examples of 1.4 μm thick S1813 transferred onto a PDMS-coated glass receiver, although deposition onto freestanding PDMS was also demonstrated, hence showing efficacy for the fabrication of thin devices and electronic structures on nonplanar substrates. The smallest features are approximately 6 μm, with a tapered border visible, formed during the donor release process. Importantly, there is very little observed debris. More than 90% of deposits remained adhered after a 30 min ultrasonic bath.

8.5.2 Structured Carrier Substrate

The carrier substrate used was a silicon-on-insulator chip containing photonic waveguide structures designed for IR wavelengths and hence an ideal resolution

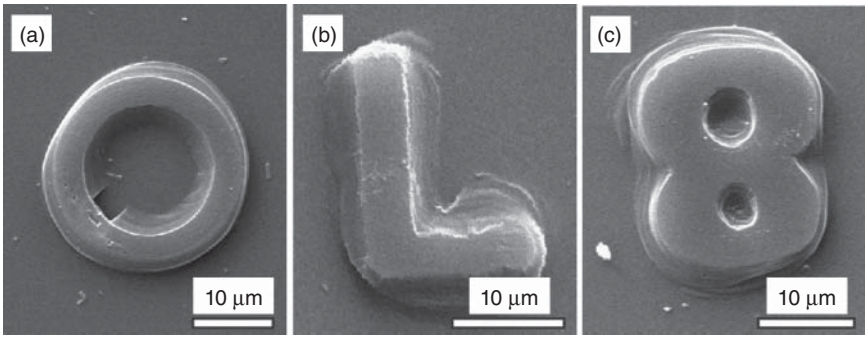

Figure 8.18 SEM images of DMD-based pulse shaping for LIBT using an unstructured carrier, with S1813 donor with 1.4 μm thickness.

test sample for nanoimprint LIBT as the structures were already characterized and offered a range of high-quality surface features. S1813 photoresist was spin-coated onto the structured carrier, where the parameters were carefully chosen to maximize conformity of the carrier by the donor material, hence replicating the structures with exceptional fidelity while forming a flat layer at the donor–air interface. Figure 8.19 shows a range of imprinted features, with resolution well below the diffraction limit for the laser wavelength used.

In summary, this section has demonstrated that LIBT and nanoimprint LIBT offer real potential for high-resolution nanoscale, localized deposition. While photopolymer was used here, other materials are almost certainly similarly effective. For fluences just above the transfer threshold, very little debris was observed, along with very limited damage to the uncovered structured carrier, indicating that the carrier could indeed be recoated with new donor material. Hence, nanoimprint LIBT also offers a path to scale-up manufacturing, for potential applications such as electronic and photonic devices.

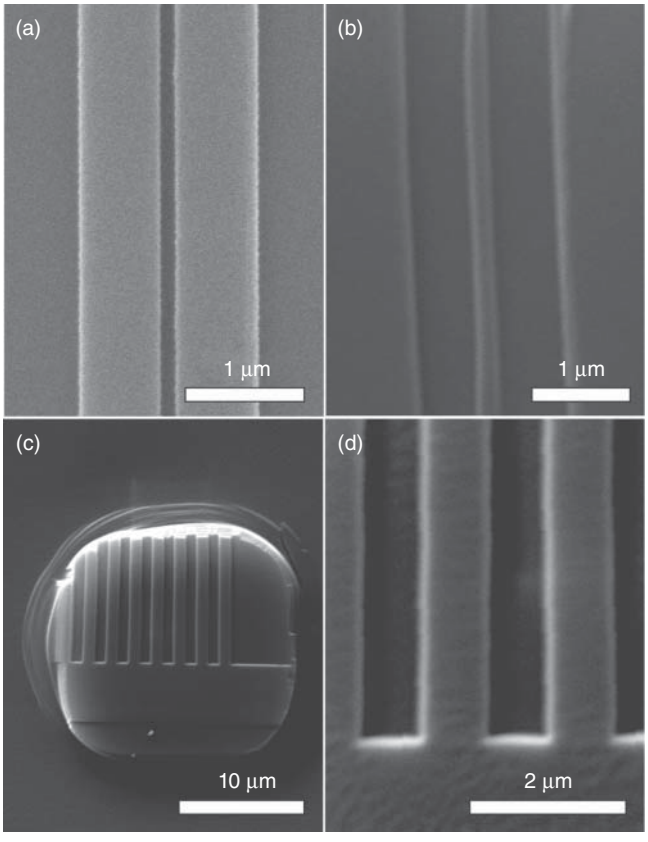

Figure 8.19 SEM images of (a) a region on a structured carrier feature, (b) LIBT deposition showing an inverted profile with central feature 140 nm wide and 220 nm high, (c) LIBT deposition showing an imprinted grating structure with fingers 900 nm wide and 220 nm high and (d) associated higher magnification image.

8.6 Conclusions

This chapter has discussed the importance of understanding and optimizing both the release and capture of the donor material, with particular emphasis on ceramic and polymer donors. Through optimizing these processes, there is potential for a considerably higher quality and more reliable LIFT process. Of course, it is also important to demonstrate the applications, and hence, the fabrication of a microscale energy-harvesting device was shown, with an efficiency matching those fabricated by more complex processes such as lithography. Finally, a modification to the geometry, into a "backward" orientation was explored, with results showing that subwavelength structuring is possible. The work to date has therefore opened up the potential for great advances in the use of LIFT and LIBT, for a very wide range of electronic and photonic applications. The next steps, as always, are the further refinement of parameters in order to advance the reliability, flexibility, and resolution of the technique.

Acknowledgments

The advancements demonstrated in this chapter have been made possible by many researchers. The authors would like to particularly thank Dave Banks, Collin Sones, John Mills, Kamalpreet Kaur, Thomas Lippert, and Alberto Sposito. The authors would like to gratefully acknowledge the support of the e-LIFT project (no. 247868-FP7-ICT-2009-4) and from the Engineering and Physical Sciences Research Council (EPSRC) under grant numbers EP/L022230/1, EP/J008052/1, and EP/N03368X/1.

References

1 Banks, D.P., Kaur, K., and Eason, R.W. (2009) *Appl. Opt.*, **48** (11), 2058–2066.
2 Banks, D.P., Grivas, C., Zergioti, I., and Eason, R.W. (2008) *Opt. Express*, **16** (5), 3249–3254.
3 Baseman, R. and Froberg, N. (1990) *Appl. Phys. Lett.*, **56**, 1412–1414.
4 Kaur, K.S., Feinaeugle, M., Banks, D.P., Ou, J.Y., Di Pietrantonio, F., Verona, E., Sones, C.L., and Eason, R.W. (2011) *Appl. Surf. Sci.*, **257**, 6650–6653.
5 Sones, C.L., Feinaeugle, M., Sposito, A., Gholipour, B., and Eason, R.W. (2012) *Opt. Express*, **20** (14), 15171–15179.
6 Mills, B., Feinäugle, M., Rizvi, N., and Eason, R.W. (2013) *J. Micromech. Microeng.*, **23**, 035005.
7 Mills, B., Heath, D.J., Feinäugle, M., Grant-Jacob, J.A., and Eason, R.W. (2014) *J. Laser Appl.*, **26** (4), 41501.
8 Heath, D.J., Mills, B., Feinäugle, M., and Eason, R.W. (2015) *Appl. Opt.*, **54** (16), 4984–4988.
9 Mills, B., Grant-Jacob, J.A., Feinäugle, M., and Eason, R.W. (2013) *Opt. Express*, **21** (12), 14853–14858.

10 Rapp, L., Constantinescu, C., Larmande, Y., Alloncle, A.P., and Delaporte, P. (2014) *Appl. Phys. A*, **117** (1), 1–7.
11 Ko, S.H., Pan, H., Ryu, S.G., Misra, N., Grigoropoulos, C.P., and Park, H.K. (2008) *Appl. Phys. Lett.*, **93** (15), 91–94.
12 Grant-Jacob, J., Mills, B., Feinäugle, M., Sones, C.L., Oosterhuis, G., Hoppenbrouwers, M.B., and Eason, R.W. (2013) *Opt. Mater. Express*, **3** (6), 747–754.
13 Auyeung, R.C.Y., Kim, H., Charipar, N.A., Birnbaum, A.J., Mathews, S.A., and Piqué, A. (2011) *Appl. Phys. A*, **102** (1), 21–26.
14 Piqué, A., Kim, H., Auyeung, R.C.Y., and Smith, A.T. (2013) *J. Imaging Sci. Technol.*, **57** (4), 40401–40404.
15 Feinäugle, M., Horak, P., Sones, C.L., Lippert, T., and Eason, R.W. (2014) *Appl. Phys. A*, **116** (4), 1939–1950.
16 Kaur, K.S., Fardel, R., May-Smith, T.C., Nagel, M., Banks, D.P., Grivas, C., Lippert, T., and Eason, R.W. (2009) *J. Appl. Phys.*, **105** (11), 113118–113119.
17 Sposito, A., Gregory, S.A., de Groot, P.A.J., and Eason, R.W. (2014) *J. Appl. Phys.*, **115**, 053102.
18 Feinaeugle, M., Sones, C.L., Koukharenko, E., Gholipour, B., Hewak, D.W., and Eason, R.W. (2013) *Appl. Phys. A.*, **112** (4), 1073–1079.
19 Elliott, G.R., Murugan, G.S., Wilkinson, J.S., Zervas, M.N., and Hewak, D.W. (2010) *Opt. Express*, **18**, 26720–26727.
20 Tseng, M.L., Chen, B.H., Chu, C.H., Chang, C.M., Lin, W.C., Chu, N.N., Mansuripur, M., Liu, A.Q., and Tsai, D.P. (2011) *Opt. Express*, **19**, 16975–16984.
21 Saqr, K.M. and Musa, M.N. (2009) *Therm. Sci.*, **13**, 165–174.
22 Zhu, D., Beeby, S., Tudor, J., and Harris, N. (2009). Power MEMS 2009, Washington, DC 201–204.
23 Organic Electronics Association (2011) *White Paper: OE-A Roadmap for Organic and Printed Electronics*, 4th edn, Organic Electronics Association, pp. 76–106.
24 Al Bayaz, A., Giani, A., Foucaran, A., Pascal-Delannoy, E., and Boyer, A. (2003) *Thin Solid Films*, **441**, 1–5.
25 Bottner, H., Nurnus, J., Gavrikov, A., Kuhner, G., Jagle, M., Kunzel, C., Eberhard, D., Plescher, G., Schubert, A., and Schlereth, K.H. (2004) *J. Micro-electromech. Syst.*, **13**, 414–420.
26 Feinäugle, M., Sones, C.L., Koukharenko, E., and Eason, R.W. (2013) *J. Smart Mater. Struct.*, **22** (11), 115023.
27 Papakonstantinou, P., Vainos, N.A., and Fotakis, C. (1999) *Appl. Surf. Sci.*, **151** (3), 159–170.
28 Feinäugle, M., Heath, D.J., Mills, B., Grant-Jacob, J.A., Mashanovich, G.Z., and Eason, R.W. (2016) *Appl. Phys. A Mater. Sci. Process.*, **122** (4), 1–5.

9

Laser-Induced Forward Transfer of Soft Materials

Zhengyi Zhang[1,2], *Ruitong Xiong*[2], *and Yong Huang*[2]

[1] *Huazhong University of Science and Technology, School of Naval Architecture and Ocean Engineering, 1037 Luoyu Road, Wuhan, Hubei 430074, China*
[2] *University of Florida, Department of Mechanical and Aerospace Engineering, 571 Gale Lemerand Drive, Gainesville, FL 32611, USA*

9.1 Introduction

Laser-induced forward transfer (LIFT), a versatile direct-write technique to deposit materials, has emerged as a promising orifice-free direct-write technique with a great variety of applications, such as microelectronics [1] and tissue engineering [2–9], to name a few. In particular, it has found increasing interest in printing two-dimensional (2D) or three-dimensional (3D) soft tissue constructs from soft materials [4, 10]. During LIFT, a laser beam passes through one side of a support, which is transparent to the laser beam and coated with a thin layer of soft build material to be printed on the other side. Sometimes, a sacrificial layer of energy-absorbing material is also coated between the support and the build material layer. Collectively, they are usually called the laser printing ribbon. The incident laser beam is focused on the interface between the support and the coating and sublimes part of the coating material, resulting in a high-temperature, high-pressure vapor or plasma bubble due to rapid localized heating. The bubble further expands and may eject some of the underneath coating material away from the quartz support as a liquid jet. Depending on the laser fluence and coating's rheological properties, the resulting jet may become a long, thin jet and then breakup into one or a few droplets or recoil back to the coating.

During a typical LIFT-based fabrication process [11], each structure is made in a voxel-by-voxel, then layer-by-layer manner. Within a given layer, each continuous feature is made of a number of printed droplets. The shape and size of printed droplets are largely affected by the properties of materials being transferred and/or operating conditions [12–14] and is ultimately determined by the jet formation process. As such, it is important to understand and further model the jet and droplet formation processes and the droplet landing/spreading process under different LIFT operating conditions when various electronic or biological soft build materials are printed. This will allow a better understanding of the LIFT process as well as a better control of the resulting printing quality and

Laser Printing of Functional Materials: 3D Microfabrication, Electronics and Biomedicine,
First Edition. Edited by Alberto Piqué and Pere Serra.
© 2018 Wiley-VCH Verlag GmbH & Co. KGaA. Published 2018 by Wiley-VCH Verlag GmbH & Co. KGaA.

feature resolution, laying down a solid foundation for the fabrication of functional 2D or 3D tissues using laser printing.

While the general jet formation and droplet deposition mechanisms have been discussed in Chapter 4, herein the effects of fluid properties and laser fluence on the jet formation process are reported during LIFT of soft materials, which include Newtonian glycerol and viscoelastic alginate solutions herein. Under identified optimal printing conditions, the feasibility of using laser printing for the freeform fabrication of 3D alginate and cellular tubes is further investigated, which can be considered as the first logical step toward successful organ printing.

9.2 Background

The jet formation mechanism in laser printing has been studied using time-resolved imaging analysis [15–18]. Depending on the applied laser fluence, three distinct working regimes have been identified: subthreshold (no material deposition), jetting (having well-defined jet formation), and plume (generating atomized droplets) [12, 16, 19, 20]. The well-defined jet formation regime is generally desired for better printing or direct writing. During this process, a bubble is first generated by absorbing the energy of the incident laser pulse, and then a needle-like jet is formed as the bubble expands, and finally, a long, thin jet is developed. In addition, some phenomena may accompany the formation of the well-defined jet: for example, the formation of a counter-jet inside the ribbon coating [16], a bulgy structure due to the possible lateral collapse of the jet [18], or droplets after jet breakup [21].

Jet morphology has been characterized in terms of the bubble size [21], jet diameter [16, 18], and jet breakup [18, 21]. Specifically, the effects of laser fluence on the jet morphology and jet velocity have been studied [16, 18, 19, 22], and the jet and plume velocities were found to increase with the laser fluence [16, 19]. In addition, the jet formation process has been evaluated under various operating conditions such as the sacrificial layer thickness [21], ribbon coating thickness [23], direct-writing height [15, 24], and laser beam dimensions [13, 21]. However, the investigation about the effects of fluid properties as well as the combined effects of laser fluence and fluid properties on the jet formation process is still largely elusive. In this study, time-resolved imaging analysis has been applied to investigate the individual and combined effects of fluid properties and laser fluence on the jet formation process to have a comprehensive understanding of the LIFT technology.

With the capability of printing various soft materials, laser printing has been implemented for the fabrication of 2D or 3D constructs/structures from various biomaterials as well as cellular bioinks [4, 10]. Some interesting 2D constructs include 2D branch and stem structures made from human umbilical vein endothelial cells (HUVECs) and human umbilical vein smooth muscle cells (HUVSMCs) to investigate the interaction between these two cells [25], and 2D chessboard-like cardiac patch comprised of HUVECs and human mesenchymal stem cells (hMSCs) for cardiac regeneration [26]. While 3D constructs are of ultimate interest, only few studies have been reported regarding

the freeform fabrication of complex and spatially heterogeneous 3D patterns. Multilayer hydrogel-cell planar structure has been fabricated by laser printing human adipose-derived stem cells (ASCs) and endothelial colony-forming cells (ECFCs), as individual droplets onto hyaluronic acid–fibrinogen hydrogel layer and then covered with another hydrogel layer to study cell–cell and cell–environment interactions [8]. Skin-like structure has been made by laser printing collagen-based NIH 3T3 fibroblast and human immortalized keratinocyte coatings to fabricate multilayered (with alternating cellular layers) and grid structures to investigate cell functions and tissue formation process in a 3D environment [27]. However, these structures are still not strictly 3D in nature, and there were no arbitrary material or geometry variations along the height direction. Toward 3D laser bioprinting, Yan *et al*. [11] and Xiong *et al*. [28] have attempted to laser print tubular alginate structures with some success, but the approach is yet to be further implemented for cellular construct fabrication.

9.3 Jetting Dynamics during Laser Printing of Soft Materials

To have a better understanding of the jetting dynamics during laser printing, the jet/droplet formation process during the laser printing of representative Newtonian glycerol and viscoelastic alginate bioinks has been investigated. The effects of the operating conditions such as the laser fluence and material properties (e.g., the glycerol/alginate concentration) on the jet formation performance have been evaluated. The glycerol and alginate solutions were selected as representative bioinks for their many fabrication applications. As shown in Figure 9.1, the LIFT apparatus had a laser delivery system, an argon fluoride (ArF) excimer laser (193 nm, 12 ns pulse duration, Coherent ExciStar, Santa Clara, CA), and a ribbon, which consisted of a quartz disk (Edmund optics,

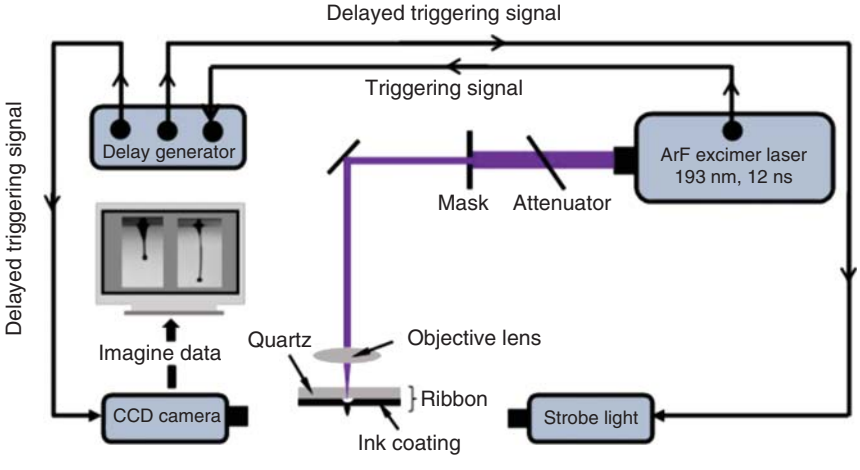

Figure 9.1 Schematic of experimental setup. (Zhang *et al*. 2015 [29]. Reproduced with permission of American Chemical Society.)

Barrington, NJ) and a thin layer of glycerol/alginate ink coating to be printed. The laser spot size was controlled at 150 μm in diameter, and its repetition rate was set as at 2 Hz. Laser fluence was measured and reported after considering a 15% transmission loss due to the quartz disk. The jet/droplet formation process was studied using a JetXpert imaging system (ImageXpert Inc., Nashua, NH) based on a time-resolved imaging method. After each laser firing, the trigger signal from the laser was used to control the imaging system in order to capture a frame of a droplet formation process after a certain delay time. For a given printing scenario, a series of images were taken using different delay times of different jets and compiled to represent the jet and droplet formation process.

9.3.1 Jet Formation Dynamics during Laser Printing of Newtonian Glycerol Solutions

Glycerol (Acros Organics, Fair Lawn, NJ, 99% pure) and deionized (DI) water were used to make the glycerol–water coating inks with different glycerol concentrations (v/v). The coating ink was controlled to be 100 μm. As shown in Table 9.1, two laser printing experiments have been conducted to appreciate the effects of laser fluence and glycerol concentration on the jetting dynamics, respectively.

9.3.1.1 Typical Jetting Regimes

Time-resolved imaging analysis was performed in this study to obtain a better understanding of the material transfer process during LIFT. Several events occur during a typical LIFT process: bubble formation, jet formation/breakup, and jet/droplet landing. During the direct-write process, the energy of the incident laser pulse is absorbed by the glycerol solution in the ribbon coating, producing a high-pressure and high-temperature bubble that further expands within the coating due to sublimation [12, 30]. Well-defined jets only form under certain operating conditions for a given glycerol solution. In particular, the jet formation process can be classified into four different scenarios depending on the laser fluence and the glycerol concentration: pluming/splashing (Figure 9.2), jetting with a bulgy shape (Figure 9.3a,b), well-defined jetting (9.3c,d), and no material transfer (Figure 9.3e). The background of these figures is composed of two different regions: the top portion corresponds to the ribbon and its coating and the lower part to the free space or ambient environment. There were some reflections of jetting phenomena on the ribbon, which acted as a mirror during imaging. The phenomena observed herein when the concentration changed are consistent with others reported or discussed when operating conditions varied [12, 16, 19, 20] during laser printing.

Table 9.1 Design of experiments.

Experiment no.	Glycerol concentration (v/v)	Laser fluence (mJ/cm^2)
1	15%, 25%, 35%, 50%, 65%, 75%, 85%, and 99%	717, 957, 1183, and 1433
2	15%, 25%, 35%, 50%, 65%, 75%, 85%, and 99%	717

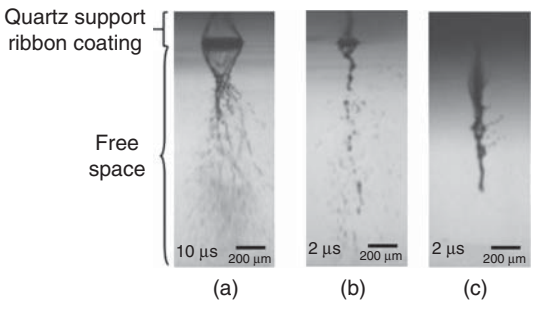

Figure 9.2 Pluming/splashing regime images obtained using low glycerol concentration solutions: (a) 15%, (b) 25%, and (c) 35%, all of them at a laser fluence of 717 mJ/cm^2. (Yan *et al*. 2012 [31]. Reproduced with permission of American Institute of Physics.)

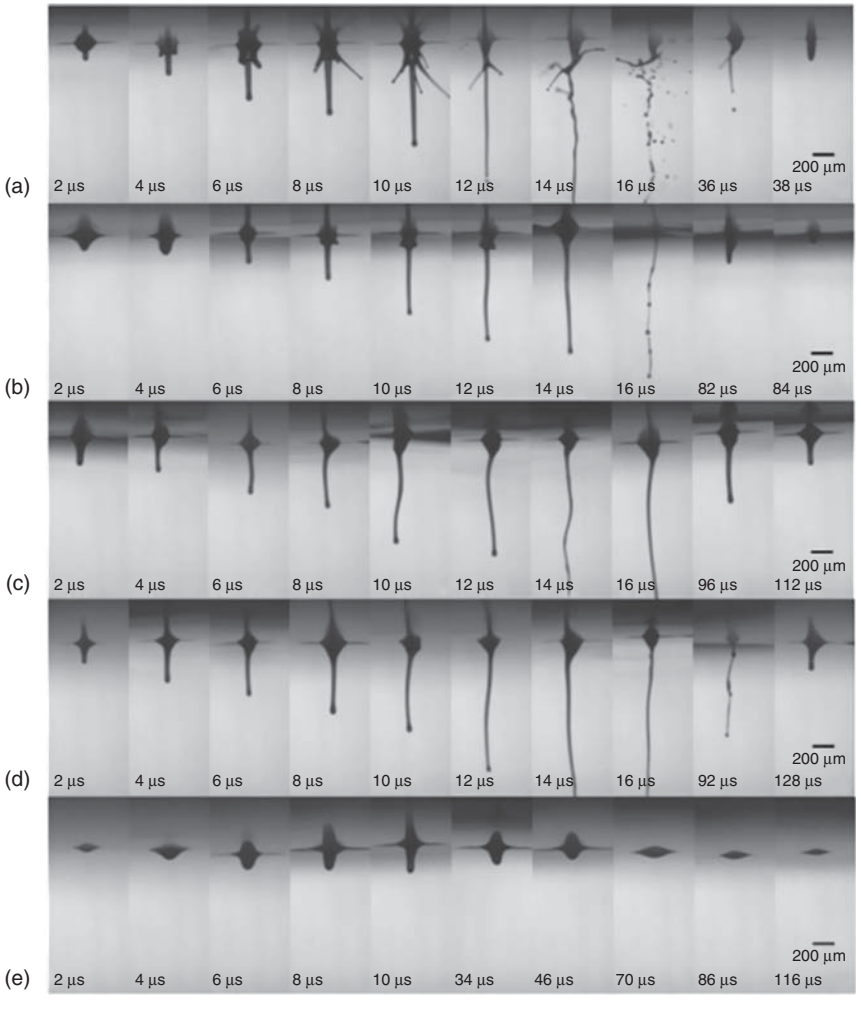

Figure 9.3 Different time-resolved images of some jetting regimes (laser fluence of 717 mJ/cm^2): (a) jetting with a bulgy shape when using 50% glycerol solution, (b) jetting with a bulgy shape when using 65% solution, (c) well-defined jetting when using 75% solution, (d) well-defined jetting when using 85% solution, and (e) no material transfer when using 99% solution. (Yan *et al*. 2012 [31]. Reproduced with permission of American Institute of Physics.)

9.3.1.2 Jetting Regime as Function of Fluid Properties and Laser Fluence

Jetting during LIFT is the result of the formation of a laser-induced vapor/plasma bubble inside the ribbon coating. As the absorbed laser energy raises the solution temperature in the laser focal volume above the boiling temperature, the heated fluidic coating material undergoes a metastable superheated state [32]. Any slight perturbation in the coating density may lead to the initiation of vapor nuclei in the superheated liquid, known as *homogeneous nucleation*; once vapor bubbles reach a critical size, their further growth is spontaneous and the superheated volume may explode [33], leading to phase explosion, a form of rapid evaporation. When the internal bubble pressure reaches a balance with that due to the ambient pressure and the surface tension, the bubble has its largest size. As the bubble continues to grow, the internal bubble pressure becomes lower than that due to the ambient environment and surface tension. Then it shrinks and eventually collapses.

In this study, it is considered that the laser pulse-induced phase explosion mostly contributes to the generation of vapor pressure, which ejects the coating material beneath to form a jet or jets. It should be pointed out that laser-induced thermoelastic stress [34] might also contribute to the jet formation in addition to phase explosion. The aforementioned scenario is also applicable to the sacrificial LIFT process, during which the bubble is induced by the expansion of a vapor or plasma resulting from the ablation of sacrificial film [35, 36].

The effect of glycerol concentration is shown in Figure 9.3 by printing different concentration glycerol solutions under a laser fluence of 717 mJ/cm^2. For the highest concentration solution (99%), the bubble pressure is not high enough to overcome the effect due to the ambient pressure and the surface tension, so no material is transferred. For the 85% and 75% solutions, a well-defined jet forms. The expanding bubble collapses outwards the coating instead of shrinking or collapsing inwards the coating. For the 65% and 50% solutions, a jet may form but with bulge(s) around it. As the laser-induced bubble expands, a high-pressure area forms between the bubble and the free surface. The formation of bulges is attributed to the collision of the liquid flows around the ablation spot [18] and/or the breakup of the main bubble when vapor bubble collapses inwards and/or bursts outwards the coating. This phenomenon is analogous to the evolution of cavitation bubble during ablation in liquid [37, 38]. For the 35%, 25%, and 15% solutions, splashing and bubble bursting clearly reveal the effect of a highly pressurized bubble, which bursts outwards the coating and even may atomize the coating being transferred.

The effect of laser fluence on the jet formation has also been studied herein, and similar phenomena have been observed as previously reported [16, 18, 19, 22]. Figure 9.4 shows some representative jetting regimes during LIFT using a 65% glycerol solution. Four jet formation regimes were also observed: no material transferring, well-defined jetting, jetting with a bulgy shape, and pluming/splashing as the applied laser fluence increased. The laser fluence determines the jet kinetic energy, and higher laser fluences result in a higher jet/droplet velocity [16, 19, 39]. The glycerol concentration affects the viscous dissipation energy and the capillary force. When the jet kinetic energy is higher than that

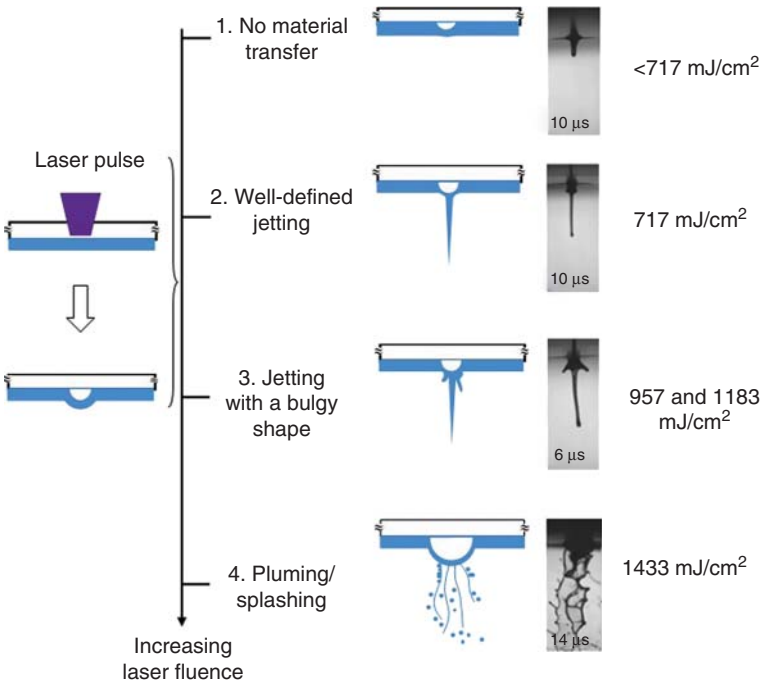

Figure 9.4 Jetting regimes during LIFT under different laser fluences (65% glycerol solution). (Yan *et al*. 2012 [31]. Reproduced with permission of American Institute of Physics.)

due to viscous dissipation, a jet forms; when the surface tension effect dominates and leads to the Rayleigh instability, the jet breaks up, forming flying droplet(s).

Under laser fluences lower than 717 mJ/cm^2 such as 478 mJ/cm^2, no material was transferred, and the bubble pressure did not exceed the pressure due to the surface tension of the ribbon coating and the ambient environment. This is a similar scenario as shown in Figure 9.3e. Under a laser fluence of 717 mJ/cm^2, a well-defined jet formed, as shown in Figure 9.3c,d. Under laser fluences of 957 and 1183 mJ/cm^2, the forming jet turned bulgy and curved as seen from Figure 9.3a,b. The higher the laser fluence, the more the coating material being transferred, resulting in a larger but less stable jet. When the applied laser fluence was even higher, such as 1433 mJ/cm^2, splashing occurred instead of a jet, similar to those shown in Figure 9.2. It should be noted that the laser fluence threshold for different jetting regimes varies as the coating solution changes.

In summary, jetting dynamics is a function of fluid properties such as the glycerol concentration and operating conditions such as the laser fluence. If the laser fluence is too low and/or the glycerol concentration is too high, it is less likely for a bubble to fully form and/or grow before it collapses [32]. There is no enough kinetic energy provided by the expanding bubble. Even when a jet can be formed, it retracts back after the bubble collapses. If the laser fluence is too high and/or the glycerol concentration is too low, it is also difficult to form a well-developed jet since dramatic bubble expansion may lead to a bulgy shape

[40] and even splashing [12, 18, 32]. Only under some selected conditions of glycerol concentration and laser fluence, as aforementioned, can a well-defined jet form.

9.3.1.3 Jettability Phase Diagram

Generally, the droplet formation process on the printing quality has been of great research interest during dropwise manufacturing, especially in terms of the printability [41] and the droplet formability [42, 43] during orifice-based jetting. During the jet/droplet formation process, capillary thinning and breakup of the free surface liquid filaments can be characterized by three main timescales: visco-capillary timescale $t_v = \eta_0 R/\sigma$, inertio-capillary or Rayleigh timescale $t_c = \sqrt{\rho R^3/\sigma}$, and λ, where η_0 is the zero-shear viscosity, R is the characteristic length, which is taken as the laser spot radius in this study (75 μm), σ is the surface tension, ρ is the density, and λ is the longest relaxation time, which is a characteristic time that relates to the motion of the polymer chains. For most viscoelastic soft materials, three material property-based dimensionless numbers can be derived based on the relative significance of these three timescales: the Ohnesorge number $Oh = \frac{t_v}{t_c} = \frac{\eta_0}{\sqrt{\rho\sigma R}}$, the elasto-capillary number $Ec = \frac{\lambda}{t_v} = \frac{\lambda\sigma}{\eta_0 R}$, and the intrinsic Deborah number $De_0 = \frac{\lambda}{t_c} = \sqrt{\frac{\lambda^2\sigma}{\rho R^3}}$. The Oh number represents the ratio of the viscous to inertial effects, and the De_0 or Ec number represents the elastic to viscous or inertial effects. It should be pointed out that the Ec number is a De_0 number with a characteristic process time of t_v for viscous-effect-dominated fluids.

For the breakup of Newtonian glycerol solutions, the elastic effects are negligible, and their jetting dynamics can be conveniently captured by the Ohnesorge number (Oh) solely [44]. It is noted that the Ohnesorge number only depends on the thermophysical properties (viscosity, density, and surface tension) of the fluid and the laser spot size.

As discussed, a good jet only forms under certain combinations of fluid properties and operating conditions. For given operating conditions such as the laser fluence in this study, a new nondimensional J number $\left(J = \frac{1}{Oh}\right)$, defined as the inverse of the Ohnesorge number, is proposed to evaluate the jettability during laser printing. It is noted that the inverse of the Ohnesorge number has also been proposed as a nondimensional Z number to quantify the fluid printability during inkjetting under a certain excitation voltage, and the printability was evaluated based on the single droplet formability, minimum stand-off distance (distance between the nozzle and the receiving substrate), positional accuracy, and maximum allowable jetting frequency [41]. Alternatively, J can also be interpreted as $J = \frac{t_c}{t_v}$, the ratio between the inertio-capillary or Rayleigh timescale t_c and visco-capillary timescale t_v.

Figure 9.5 illustrates the relationships among J, the visco-capillary and Rayleigh timescales, and the glycerol concentration under a laser fluence of 717 mJ/cm^2. As the glycerol concentration increases, the viscosity increases significantly while there are negligible variations in density and surface tension [12], resulting

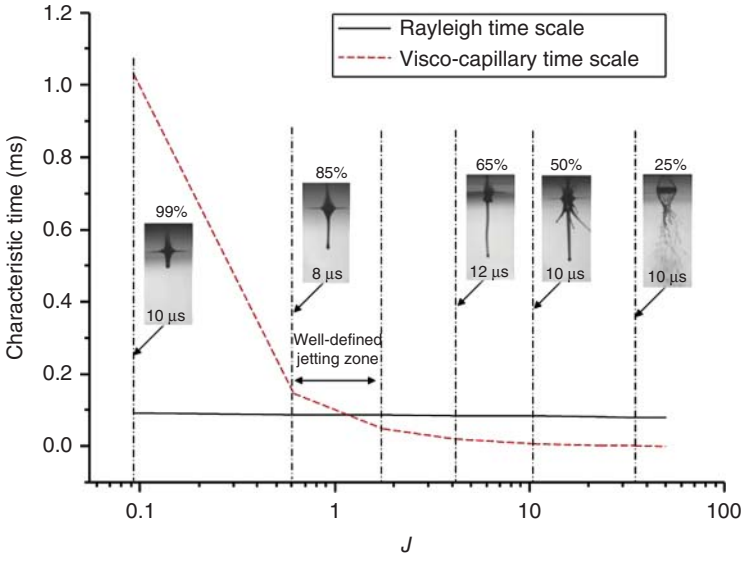

Figure 9.5 Jetting regimes and characteristic timescale variations versus the dimensionless parameter J under a laser fluence of 717 mJ/cm^2. (Yan *et al*. 2012 [31]. Reproduced with permission of American Institute of Physics.)

in a decreasing J. Due to the same reason, the visco-capillary timescale increases significantly while the Rayleigh timescale almost stays the same as the glycerol concentration decreases. As seen from Figure 9.5, at most time, no materials are transferred if the visco-capillary timescale is longer than the Rayleigh timescale. Once the visco-capillary timescale is smaller than the Rayleigh timescale with an 85% glycerol solution, well-defined jet forms; if the glycerol concentration further decreases, splashing may happen. As the J value decreases almost exponentially with the glycerol concentration, it is observed that a good jet forms at $0.09 \leq J \leq 1.76$ (corresponding to 75–85%) in this study under the laser fluence of 717 mJ/cm^2.

It should be noted that the jettability range varies as the laser fluence changes, which means the change of external forcing dynamics such as the jet velocity. Figure 9.6 illustrates different jetting regimes (no materials transferred, good jet forming, and splashing/bulgy) delineated using dashed lines based on the experimental observations in this study as the laser fluence varies. Figure 9.6a is based on the jettability number, J, while Figure 9.6b is based on the glycerol concentration. The dashed lines are for illustration only, and more experiments are needed in future studies to exactly determine the line positions. To better appreciate the jettability, a nondimensional number-based phase diagram, such as a diagram based on the Ohnesorge and Reynolds numbers for typical viscous fluids [44], is required by including the contributions from both the material properties and operating conditions.

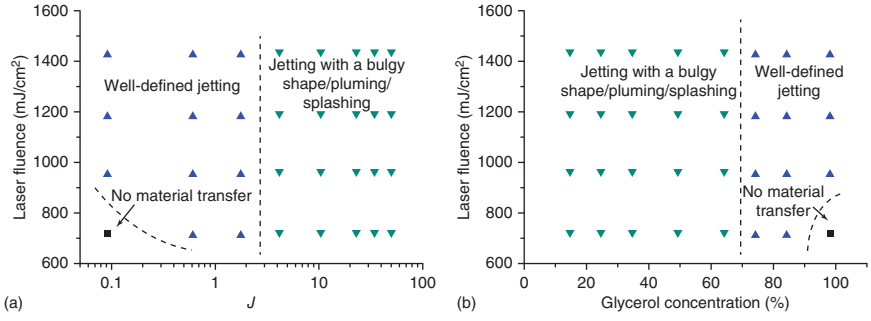

Figure 9.6 The influence of glycerol concentration and laser fluence on jet morphology and printability (dashed lines are for illustration only). (Yan *et al*. 2012 [31]. Reproduced with permission of American Institute of Physics.)

9.3.2 Jet Formation Dynamics during Laser Printing of Viscoelastic Alginate Solutions

9.3.2.1 Ink Coating Preparation and Design of Experiments

Sodium alginate (Sigma–Aldrich, St. Louis, MO) was dissolved in the deionized water to make coating inks with different alginate concentrations of 2%, 4%, 6%, and 8% (w/v). The material properties of the alginate solutions are shown in Table 9.2. Specifically, the shear viscosity was measured using a cup-and-bob rheometer (ARES, TA Instrument, New Castle, DE), and the surface tension was measured using a pendant drop method (DSA10-MK2, Krüss GmbH, Hamburg, Germany). The longest relaxation time was determined based on the elasto-capillary thinning mechanism $\left(\frac{D(t)}{D_0} \approx \left(\frac{G_1 D_0}{4\sigma}\right)^{1/3} \exp\left[-\frac{t}{3\lambda}\right]\right)$ [45] during dripping using a Photron camera (Photron Fastcam MC2.1, Photron, San Diego, CA), where $D(t)$ is the ligament diameter, D_0 is the initial ligament diameter, and G_1 is related to the elastic modulus. Then, the longest relaxation time was found based on the slope $\left(-\frac{1}{3\lambda}\right)$ of the log–log plot of $(D(t), t)$ during the pinch-off period. A power-law relaxation time model ($\lambda = 0.4[1 + 0.013(c/c^*)^{3.0}]$), determined based on the measurements of 0.5%–2.0% alginate solutions, was used to estimate the longest relaxation time of alginate solutions with concentrations of 4%, 6%, and 8%, where c is the alginate concentration and c^* is the critical coil overlap concentration. In addition, the specific viscosities as a function of alginate concentration were measured for alginate solutions with a concentration range of 0.01%–8.00%. Then other key viscoelastic properties of alginate solutions, including the intrinsic viscosity ($[\eta]$) [46], the critical coil overlap concentration (c^*), and the entanglement concentration (c_e), were determined as 220 ml/g, 0.32%, and 1.20%, respectively. Therefore, 2%, 4%, 6%, and 8% alginate solutions herein are considered semi-dilute entangled solutions. As shown in Table 9.3, two laser printing experiments have been conducted to appreciate the effects of laser fluence and alginate concentration on the jetting dynamics, respectively.

Table 9.2 Material properties and key nondimensional numbers of sodium alginate solutions.

Sodium alginate concentration (w/v)	Density ρ (g/cm^3)	Viscosity η_0 (cP)	Surface tension γ (mN/m)	Relaxation time (μs)	*Oh*	*Ec*
2%	1.020	139.5	44.6	1650	2.38	7.06
4%	1.040	855.8	44.5	10 462	15.04	7.01
6%	1.060	3 123.6	43.6	34 358	53.05	6.39
8%	1.080	8 278.9	42.7	80 893	140.76	5.56

Table 9.3 Design of experiments.

Experiment no.	Alginate concentration (w/v)	Laser fluence (mJ/cm^2)
1	2%	500, 700, 900, 1100, 1300, and 1500
	4%	900, 1100, 1300, 1500, 1700, and 1900
	6%	1100, 1300, 1500, 1700, 1900, 2100, and 2300
	8%	1300, 1500, 1700, 1900, 2100, 2300, 2500, 2700, and 2900
2	2%, 4%, 6%, and 8%	1100

9.3.2.2 Typical Jetting Regimes

Figure 9.7a illustrates a representative jet/droplet formation process observed at 130 μs during printing of a 4% alginate solution under a 1300 mJ/cm^2 laser fluence. Once a jet is formed, a primary droplet starts forming progressively at the head of the jet. Some key morphological features of the forming jet and droplet such as the ligament are depicted in Figure 9.7a. The jet velocity U herein was calculated by a linear fit of the jet head distance dependence on the measurement time [47]. The outmost droplet of the ligament is called primary droplet. Once the jet detaches from the quartz support, the trailing fluid behind the primary droplet is called tail. The breakup time represents the time of the first breakup taking place inside the field of view of the imaging system, and the breakup length means the ligament length measured when the first breakup is observed.

The jetting morphology and breakup mechanism during laser printing were investigated using time-resolved imaging. As shown in Figure 9.7, five different jetting regimes are observed during the laser printing of different alginate solutions under different laser fluences: pluming/splashing (Figure 9.7b), jetting with a bulgy shape (Figure 9.7c), well-defined jetting with an initial bulgy shape (Figure 9.7d), well-defined jetting (Figure 9.7e), and no material transfer (Figure 9.7f). Well-defined jetting with an initial bulgy shape is a special jetting scenario during viscoelastic fluid printing, meaning that a jet with an initial bulgy shape may develop into a well-defined jet during the later jetting stage.

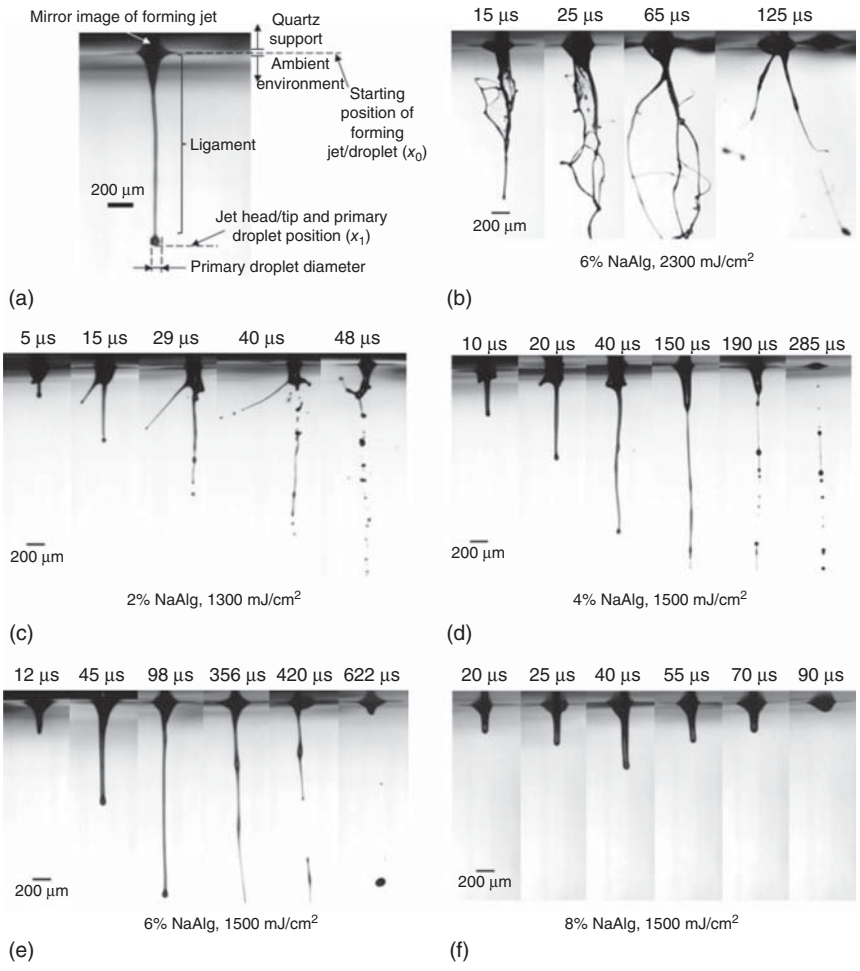

Figure 9.7 (a) Morphological features of a forming jet at 130 μs during printing 4% sodium alginate solution under a 1300 mJ/cm^2 laser fluence and representative images of the jet regimes: (b) pluming/splashing (6% alginate, 2300 mJ/cm^2), (c) jetting with a bulgy shape (2% alginate, 1300 mJ/cm^2), (d) well-defined jetting with an initial bulgy shape (4% alginate, 1500 mJ/cm^2), (e) well-defined jetting (6% alginate, 1500 mJ/cm^2), and (f) no material transfer (8% alginate, 1300 mJ/cm^2). (Zhang *et al*. 2015 [29]. Reproduced with permission of American Chemical Society.)

Only well-defined jetting with or without an initial bulgy shape is considered as desirable and evaluated in this study.

In order to further illustrate the morphological evolution of forming jets under different alginate concentrations and laser fluences, the jet head and primary droplet position within the field of view as well as the jetting regime type are presented as a function of laser fluence (Figure 9.8a with a 2% alginate solution) and alginate concentration (Figure 9.8b with a 1300 mJ/cm^2 laser fluence). Error bars in this study represent the plus or minus one-sigma variation. Some jetting images are presented to illustrate the jet morphology at some critical moments

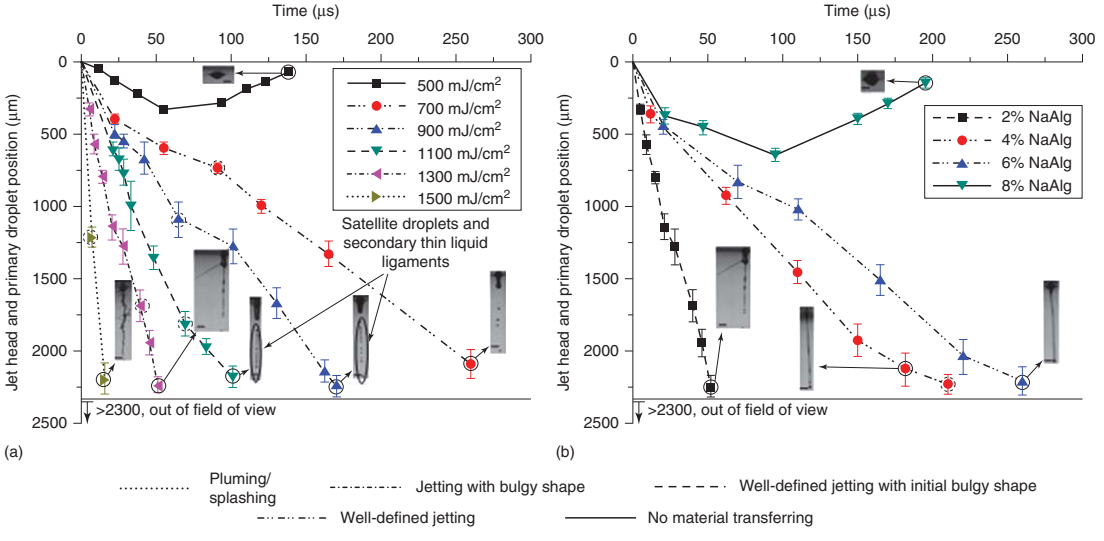

Figure 9.8 Jet/droplet morphological evolution under a) different laser fluences when printing a 2% alginate solution and b) different alginate concentrations when using a 1300 mJ/cm^2 laser fluence. (The scale bar is 400 μm, and the dashed circle indicates the jet breakup moment as observed.) (Zhang *et al*. 2015 [29]. Reproduced with permission of American Chemical Society.)

as indicated with the solid circles. It can be seen that the jet head and primary droplet position increases with the laser fluence, meaning a longer ligament length and a higher velocity under higher laser fluences if a jet can be formed. The jet head and primary droplet position decreases with the alginate concentration. This indicates that printing of higher concentration alginate solutions results in shorter ligament lengths and lower velocities. The jetting regime changes from no material transferred to well-defined jetting to well-defined jetting with an initial bulgy shape to jetting with a bulgy shape to pluming/splashing as the laser fluence increases or the alginate concentration decreases.

9.3.2.3 General Observation of the Jetting Dynamics

During laser printing of viscoelastic alginate solutions, most of the input laser energy is consumed for bubble expansion, eventually converting it into the viscous dissipation, elastic, surface, and kinetic energies of forming jets/droplets in this study. Once a jet is formed, it may break up differently due to the combined effects of liquid inertial, elastic, viscous, capillary, and ambient aerodynamic (gas inertia) forces acting on the jet. As the jet velocity increases, a jet may experience four different breakup mechanisms: Rayleigh breakup, first wind-induced breakup, second wind-induced breakup, and atomization mechanisms. Most liquid jet breakup can be attributed to the Rayleigh or Plateau–Rayleigh instability, a common mechanism during the breakup of cylindrical jets. Since the droplet formation process is not easily controllable under the second wind-induced and atomization mechanisms, they are not of interest during laser printing. Only the Rayleigh and first wind-induced breakups are expected for good droplet formation for laser printing.

For Rayleigh breakup, the inertio-capillary force is mainly responsible for the growth of perturbation, leading to pinch-off, and the aerodynamic force induced due to the relative motion between the liquid jet and ambient gas is negligible. When the aerodynamic force is large enough as the jet velocity increases, the growth rate of perturbation is enhanced via the aerodynamic force, and a higher growth rate leads to a faster breakup process and shorter breakup length [48, 49], indicating the first wind-induced breakup mechanism. The aerodynamic effect due to the surrounding gas is comparable to and can be as high as 10% [50] of the surface tension force. When the jet velocity further increases, a jet may experience the second wind-induced breakup and atomization mechanisms during which the growth of the perturbation is dominated by the aerodynamic force, and the most unstable perturbations turn out to be those with shorter wavelengths than those during Rayleigh breakup and first wind-induced breakup. The resulting drop size is much smaller than the jet diameter under the second wind-induced and atomization mechanisms [50, 51].

9.3.2.4 Effects of Laser Fluence on Jetting Dynamics

As seen from Figure 9.9a, the jet velocity of well-defined jets increases monotonically with the applied laser fluence for all the alginate solutions investigated since higher laser fluences introduce more energy into the system, resulting in a higher jet velocity. Similar observations were reported when laser printing alginate solutions [18] as well as Newtonian fluids and Newtonian fluid-based

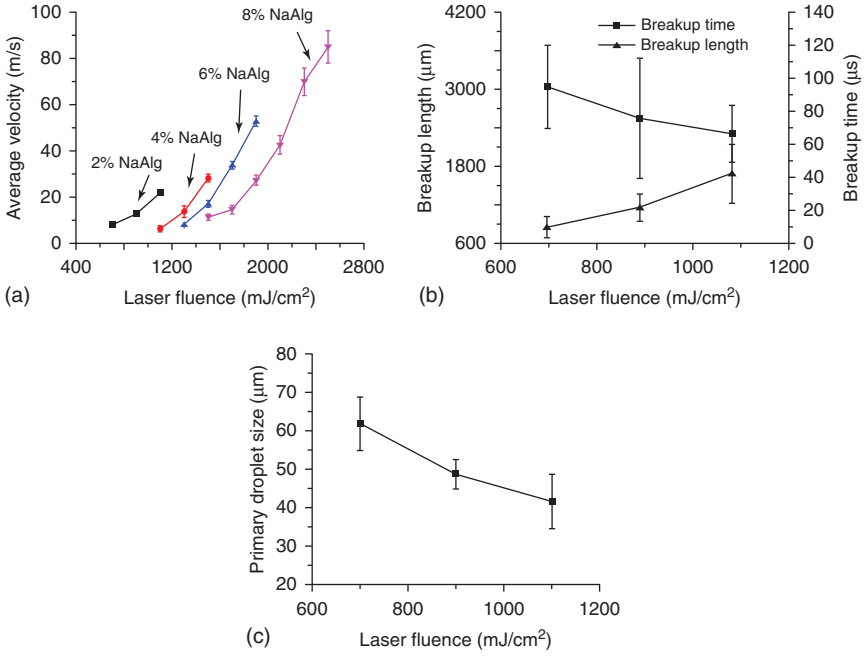

Figure 9.9 (a) Jet velocity of different alginate solutions, (b) breakup time and breakup length (2% alginate), and (c) primary droplet size (2% alginate) as a function of laser fluence. (Zhang *et al*. 2015 [29]. Reproduced with permission of American Chemical Society.)

suspensions such as silver-nanoparticle-loaded ethylene glycol, glycerol, and ethanol suspensions [47] and glycerol solutions [31]. It can also be seen from Figure 9.9a that the velocity change of any alginate solution is more sensitive to the laser fluence under higher laser fluences, demonstrating a shear-thinning behavior. This is different from that observed during the laser printing of Newtonian fluids and suspensions such as glycerol solutions [31] and glycerol-based suspensions [47], where the jet velocity increases nearly linearly with the laser fluence.

As observed from Figure 9.9a, the achievable velocity for well-defined jetting increases with the alginate concentration. For viscoelastic fluids, the storage modulus measures their stored energy, representing the elastic effect, while the loss modulus measures the energy dissipated as heat, representing the viscous effect. For alginate solutions [52], the storage and loss moduli increase with the alginate concentration, indicating the increase of elastic and viscous effects. As the concentration increases, the elastic and viscous effects increase while the surface tension decreases, which delays the perturbation growth on forming jets. As such, it suppresses jetting with a bulgy shape and splashing/pluming. Furthermore, as the jet velocity increases, the increased aerodynamic force induced by the faster relative motion between the fluid jet and the ambient gas is better balanced through the increased viscous and elastic forces of high-concentration alginate solutions. Thus, higher concentration alginate solutions can achieve a higher velocity while maintaining a well-defined jet.

Only the 2% alginate solution-related breakup observations are reported here since jets of other solutions except the breakup of 4% alginate solutions under 1100 mJ/cm^2 do not break up within the field of view. For the 2% alginate solution, the breakup time, as seen from Figure 9.9b, shows a decreasing tendency with the applied laser fluence, which is comparable with the observation during the laser printing of silver-nanoparticle-loaded Newtonian fluid-based suspensions [47]. At higher laser fluences, the jet velocity is higher, which may lead to a more elongated and narrower jet [53]. As such, the required breakup time may be shorter to break up a narrower jet as observed in this study. In addition, Figure 9.9b shows that the breakup length increases with the laser fluence, which is consistent with the breakup length observation during the nozzle jetting of viscoelastic polyethylene oxide (PEO) solutions [54].

It is found from Figure 9.9c that the primary droplet size decreases when the laser fluence increases. Narrower jets under higher laser fluences lead to the formation of smaller primary droplets. After primary droplets detach from the ligaments, growing perturbations further break up the flying ligaments into multiple satellite droplets and/or secondary liquid ligaments due to the Plateau–Rayleigh instabilities as shown in Figure 9.9a. It is noted that the droplet size after deposition [12] is different from the size of primary droplets, which may contribute together with other possible satellite droplets to the size of deposited droplets. Generally speaking, such satellite droplets, if they do not finally merge with their primary droplet, should be avoided during printing.

9.3.2.5 Effects of Alginate Concentration on Jetting Dynamics

Since the effects of alginate concentration on the jetting dynamics are only examined based on well-defined jets with their breakups observed within the field of view, only a few observations are presented here. It can be seen from Figure 9.10a that the jet velocity decreases as the alginate concentration increases. As aforementioned, both the elastic and viscous effects increase with the alginate concentration. When the concentration increases, the viscous dissipation during jetting increases, and the elastic energy stored in a jet also increases. As a result, the remaining jet kinetic energy decreases accordingly, resulting in a lower jet velocity. Such a trend is consistent with the observations during the laser printing of alginate solutions with different concentrations [55].

The effects of alginate concentration on the breakup time, breakup length, and primary droplet size are studied in terms of jets of 2% and 4% alginate solutions under a 1100 mJ/cm^2 laser fluence. As shown in Figure 9.10b, the breakup time increases while the breakup length decreases with the concentration. The increased viscous and elastic effects of higher concentration solutions resist the capillary effect and delay the breakup, leading to an increased breakup time [56]. This conclusion is in good agreement with the reported observations during the inkjet printing of cell-laden alginate solutions [57] and cellulose ester polymer solutions [58].

Coil overlap concentration represents the degree of entanglement among ploymer chains and is usually used to distiguish semi-dilute from dilute polymer solutions. For a solution with a concentration higher than its critical coil overlap concentration, it is reported that the ligament length at breakup decreases

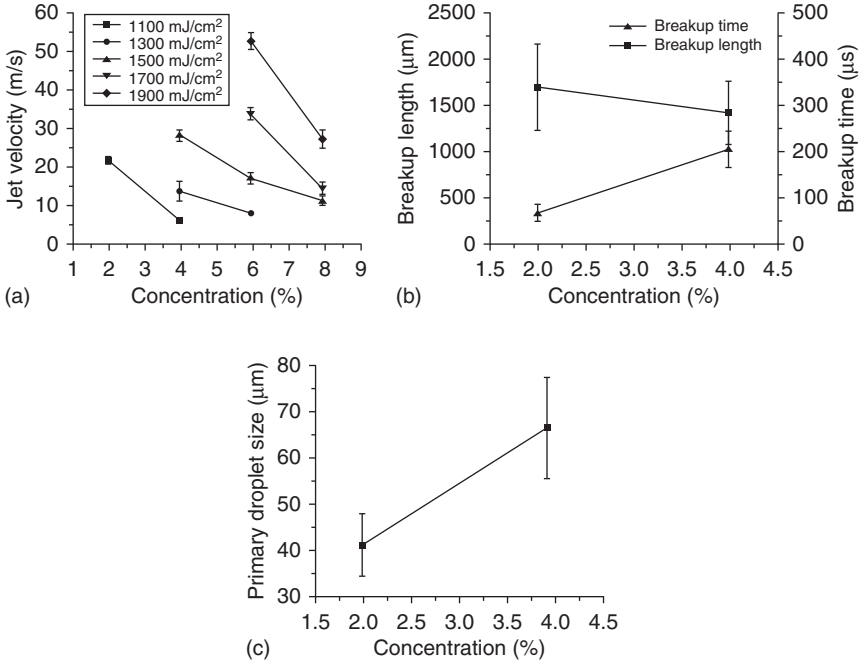

Figure 9.10 (a) Jet velocity as a function of alginate concentration, (b) breakup time and breakup length, and (c) size of the primary droplet size under a 1100 mJ/cm^2 laser fluence. (Zhang *et al*. 2015 [29]. Reproduced with permission of American Chemical Society.)

with the concentration during the inkjet printing of viscoelastic cellulose ester solutions [58]. Since 2% or higher concentrations of alginate solutions are higher than their coil overlap concentration as aforementioned, the higher the alginate concentration, the shorter the breakup length.

For 2% alginate solution jets, the primary droplet detaches from the jet head as a type of front pinching, and most material is still kept inside the ligament. For 4% alginate solution jets, the ligament thinning process is delayed by the increased viscoelastic effect of higher concentration alginate solutions. The pinch-off mechanism is a type of middle pinching and different from that during 2% alginate printing as seen from Figure 9.11. As a result, the breakup length is shorter, and the primary droplet is larger.

9.3.2.6 Jettability Phase Diagram

As observed, there is a specific laser fluence and/or alginate concentration range for the formation of desirable jetting. The jettability of Newtonian fluids has been evaluated using a nondimensional number J, the inverse of the Ohnesorge number (Oh), as discussed in Section 9.3.2.4, and the proposed J number, laser fluence, and glycerol concentration help distinguish different jet-forming regimes during the laser printing of Newtonian glycerol–water solutions [31]. Unfortunately, no dimensionless number-based jettability diagrams were proposed [31]. In addition, the alginate solution in this study, as a typical viscoelastic fluid, behaves significantly different during laser printing due to its

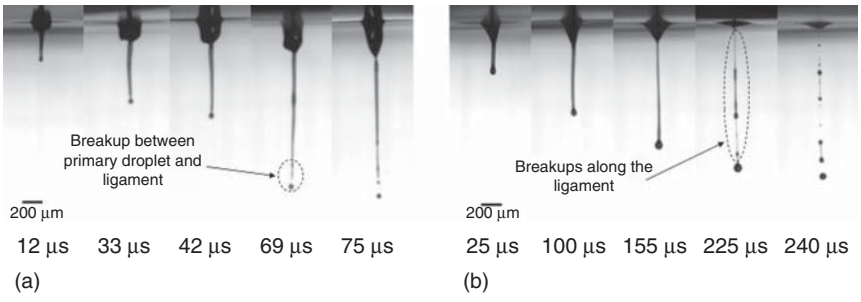

Figure 9.11 Different pinch-off locations for (a) 2% and (b) 4% alginate solutions. (Zhang *et al*. 2015 [29]. Reproduced with permission of American Chemical Society.)

elasticity and cannot be characterized by the proposed J number only. Polymer stretching-induced elastic effect affects jetting and delays the jet breakup time, so the elastic effect should be incorporated in jettability phase diagrams for the evaluation of alginate laser printing. Therefore, an additional elasticity-related nondimensional number, *Ec* or *De*, is required for the characterization of the jetting dynamics during laser printing of viscoelastic fluids [29]. Ideally, nondimensional number-based jettability diagrams, which represent various operating conditions and materials properties, are expected to fully capture the jetting dynamics during alginate laser printing. For the 2–8% sodium alginate solutions studied herein, $Oh > 1$, indicating that the thinning and breakup process is dominated by the viscous force. As such, the jet/droplet formation process should be better described by the *Oh* and *Ec* numbers. In addition, the Weber number $We = \frac{\rho R U^2}{\sigma}$, which represents inertial to capillary effects, is introduced as a process-dynamics-related dimensionless number to appreciate the jetting dynamics.

In order to illustrate the dependence of jetting regimes on the dimensionless numbers, the jetting regimes are mapped out in a 3D phase diagram in a (*We*, *Ec*, *Oh*) space as shown in Figure 9.12a by considering the contributions from both the process dynamics (*We*) and the material properties (*Ec* and *Oh*). As shown in Table 9.1, as the alginate concentration increases from 2% to 8%, the *Oh* number increases from 2.38 to 140.76 and the *Ec* number decreases from 7.06 to 5.56. Higher concentration alginate solutions, meaning more pronounced viscous and elastic effects, help suppress the growth of perturbations and produce well-defined jets, if formed.

For further illustration, four *We* number-defined planes in (*We*, *Oh*) and (*We*, *Ec*) spaces are drawn as mid-planes to distinguish two nearby jetting regimes as seen in Figure 9.12b,c. Herein the *We* number is determined based on velocity measurements, which is convenient for understanding the underlying physics. However, such velocity information should be predicted first for process planning. These two phase diagrams show five distinct jet formation regimes in both the (*We*, *Oh*) and (*We*, *Ec*) spaces. Similarly, it is noted that the *We* and *Oh* numbers were also selected to construct the dripping/jetting [59] and satellite droplet formation [49] phase diagrams. As the *We* number increases, the jetting behavior changes from no material transfer to well-defined jetting to

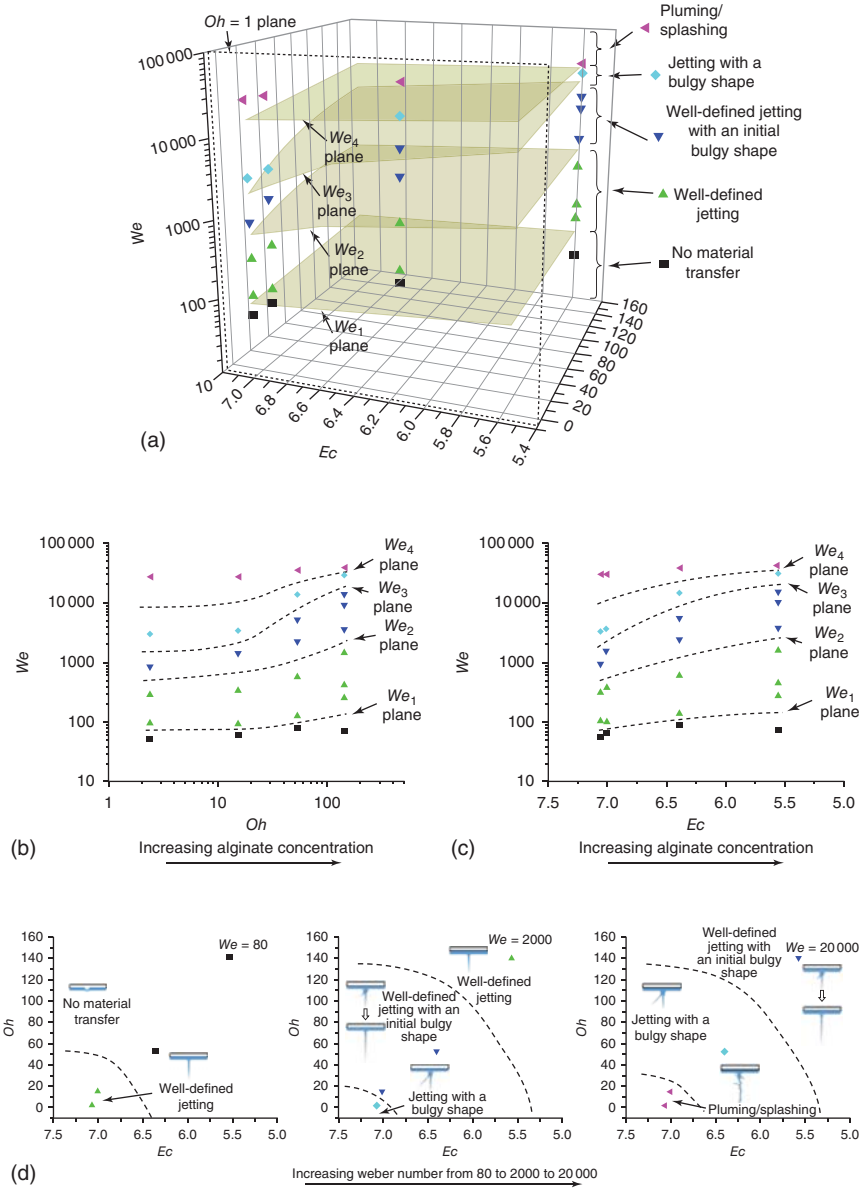

Figure 9.12 Jetting regime as a function of (a) *We*, *Oh*, and *Ec* numbers, (b) *We* and *Oh* numbers, (c) *We* and *Ec* numbers, and (d) *Oh* and *Ec* numbers. (Zhang *et al*. 2015 [29]. Reproduced with permission of American Chemical Society.)

well-defined jetting with an initial bulgy shape to jetting with a bulgy shape to pluming/splashing for both phase diagrams. As the *Oh* number increases or the *Ec* number decreases, which represents an increasing alginate concentration, the *We* number required for the jetting regime switch increases accordingly. For a given *We* number, increasing viscous and/or elastic effects help stabilize

jetting or even suppress the formation of jets as seen from Figure 9.12d, which illustrates the effect of material properties in a (*Oh*, *Ec*) space. A similar material property-based *Oh* and *De* (with applicable characteristic process times to be De_0 and *Ec*) space was also proposed to study the beads-on-a-string phenomenon during viscoelastic liquid bridge breakup [60].

It should be noted that the change of the *Ec* number of different alginate solutions is not only different (decreasing) but also relatively small when compared with the change of the *Oh* number, and this is determined by the alginate rheological properties as measured. For reference, the Reynolds numbers ($\frac{\rho LR}{\eta_0}$) of different solutions may change from smaller than 1 to larger than 1 when the laser fluence increases. For example, the Reynolds numbers change from 0.5 to 10.9 when the laser fluence increases during printing the 4% alginate solution, indicating an increasing significance of inertial over viscous forces.

9.4 Laser Printing Applications Using Optimized Printing Conditions

To demonstrate the potential of laser printing as an effective technique for the printing of soft materials, the resulting knowledge from the jetting dynamics study is further applied to the freeform fabrication of 3D Y-shaped tubes using two different bioinks: 8% alginate solution and 2% alginate-based suspension of mouse fibroblasts (NIH 3T3, ATCC, Rockville, MD). Laser printing of cells for tissue engineering has been discussed in detail in Chapter 15. Herein, Y-shaped tubes without and with cells have been printed since such tubes are the basic constituent of vascular structures [61]. Vascularization is often correctly identified as a main technological barrier for building 3D human organs [62]. Without adequate vascularization, tissue-engineered constructs and organs could not survive and undergo intensive apoptosis and necrosis, and the capability to print Y-shaped tubes is not only an enabling step but also a critical indicator of the overall feasibility of organ printing.

The detailed procedure for the fabrication of 3D Y-shaped tubes has been outlined by Xiong *et al*. [63]. Calcium-chloride-based solution was used to gel the deposited droplet during the laser printing of Y-shaped tubes. It is assumed that the gelation does not significantly change the printing quality, which was confirmed in the results as well. During 3D laser bioprinting, each structure/construct is printed in a layer-by-layer manner, and each layer is a continuous feature made from numerous printed droplets on a receiving substrate. In order to print 2D features for each layer, the receiving substrate needs to be moved laterally to control the position of the printed droplets. Once a layer is finished, the receiving substrate moves vertically accordingly to cooperate with the thickness of each deposited layer. For better construct printing quality, printing conditions were identified based on the approach proposed in a previous line-printing study [28]. Specifically, the optimal printing conditions considering the substrate velocity have been identified as 2125 mJ/cm^2 laser fluence (actual laser fluence as estimated after transmitting through the quartz

support), 100 mm/min substrate velocity, and 10 Hz laser pulse repetition rate for the 8% alginate solution [28]. Similarly, for cellular bioinks with a cell concentration of 5×10^6 cells/ml and 2% (w/v) alginate, 1445 mJ/cm^2 laser fluence (actual laser fluence as estimated after transmitting through the quartz support), 80 mm/min substrate velocity, and 10 Hz repetition rate are identified as optimal based on the resulting printing quality.

To vertically print Y-shaped constructs, which have a straight segment and two inclined overhang segments as shown in Figure 9.13a, consideration should

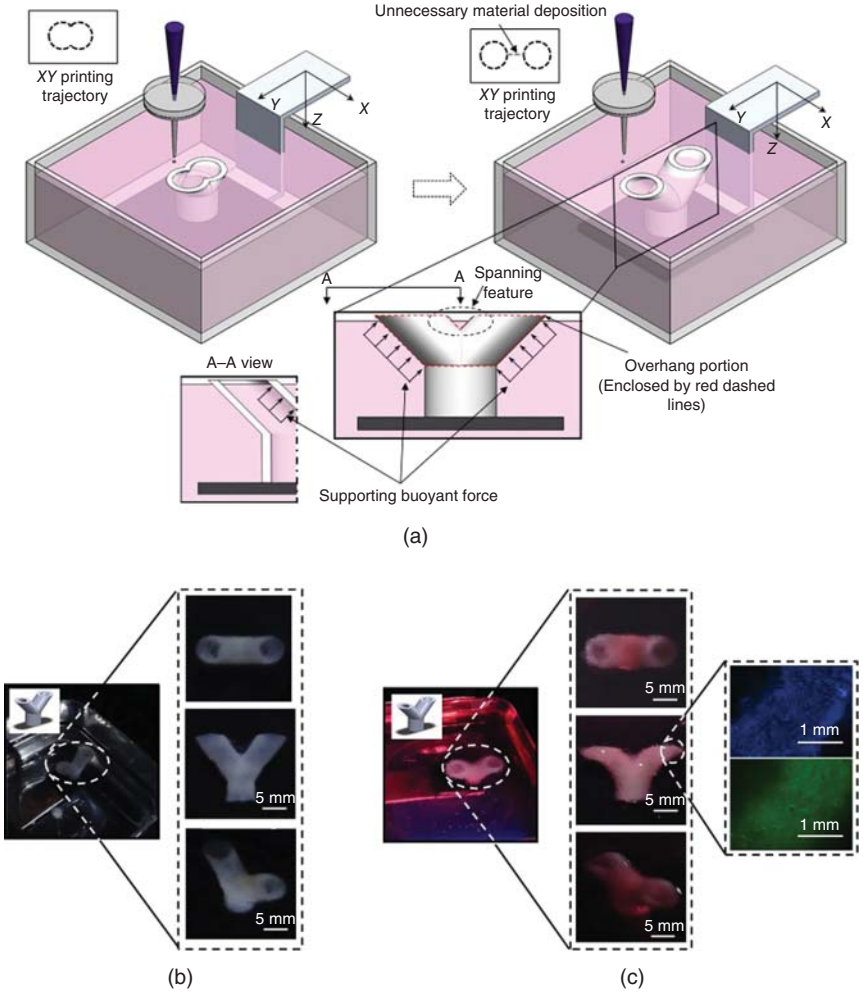

Figure 9.13 (a) Schematics of bifurcated construct printing (inset: a typical Y-shaped bifurcated structure), (b) representative images of Y-shaped alginate tubes printed using 8% sodium alginate solution (inset: different views of a printed Y-shaped alginate tube), and (c) Y-shaped cellular tubes printed with 2% alginate and 5×10^6 cells/ml bioink (left inset: different views of a printed Y-shaped cellular tube, and right inset: printed cells dyed in blue and living cells dyed in green). (Xiong *et al*. 2015 [63]. Reproduced with permission of Institute of Physics.)

be paid to overhang structures, which include a spanning feature at the saddle location. Since solid support requires additional work of postprocessing, the calcium chloride solution was used as a dual-purpose liquid support and cross-linking solution [64]. Besides gelling deposited materials, the cross-linking solution (calcium chloride solution herein) also serves as a support material by providing a buoyant force as shown in the inset of Figure 9.13a. When compared with the gravitational force, the buoyant force provided by the calcium chloride solution is significant and acts as an effective support together with the adhesive force from previously deposited gel materials to hold printed structures [64]. Therefore, the printing of overhang parts of Y-shaped tubes is permissible by printing layers slightly overhanging away from a previously printed layer. Figure 9.13b shows a representative Y-shaped alginate tubular construct with an inclination angle of 45° and a diameter of 5 mm. The Y-shaped tube has an average wall thickness of 1.4 ± 0.3 mm as measured based on the bottom straight portion and a total height of around 9.5 mm. With the help of supporting force provided by the calcium chloride solution, the two branch tubes are successfully fabricated and have an inclination angle of 45° approximately as designed. Figure 9.13c illustrates a printed Y-shaped cellular tube with a diameter of 5 mm, a total height of around 9.5 mm, and a wall thickness of 2.5 ± 0.3 mm. It has a well-defined morphology, while the wall thickness of Y-shaped cellular constructs is almost doubled by comparing it with that of alginate only tubes. This is attributed to the possible nonideal droplet formation process during the printing of bioinks containing cells.

Furthermore, several layers of printed cellular tubes were dissected and dyed to observe the printed cells. The right inset of Figure 9.13c shows all deposited cells in blue, which were dyed using Hoechst 33342 (Molecular Probes, Eugene, OR), and living cells in green, which were dyed using fluorescein diacetate (FDA) (Molecular Probes, Eugene, OR). Considering the control effect, the postprinting cell viability of printed constructs is 68.1% immediately after printing and 70.8% after 24 h of incubation. The cell viability is reasonable for effective bioprinting, and the observed increase of cell viability after incubation is attributed to the possible cell injury recovery and regular cell proliferation.

9.5 Conclusions and Future Work

This chapter has reviewed the effects of fluid properties as well as the combined effects of laser fluence and fluid properties on the jet formation process during laser printing of representative Newtonian glycerol and viscoelastic alginate solutions, respectively. A time-resolved imaging analysis-based approach has been implemented to investigate the jet formation process. The knowledge obtained from the jetting dynamics study has been further applied to investigate the feasibility of 3D alginate and cellular tubes using laser printing.

During the laser printing of Newtonian glycerol solutions, it is found that the jetting dynamics is a function of fluid properties such as the glycerol concentration and operating conditions such as the laser fluence. If the laser fluence is too

low and/or the glycerol concentration is too high, it is less likely for a bubble to lead to liquid ejection during its expansion/collapse cycle. There is not enough kinetic energy provided by the expanding bubble. Even when a jet can be formed, it retracts back after the bubble collapses. If the laser fluence is too high and/or the glycerol concentration is too low, it is also difficult to form a well-developed jet since dramatic bubble expansion may lead to a bulgy shape and even splashing. Only under some selected conditions of glycerol concentration and laser fluence, can a well-defined jet form. When a jetting fluid is given, its jettability (J) can be characterized as the inverse of Ohnesorge number. It is observed that a good jet forms at $0.09 \leq J \leq 1.76$ in this study under the laser fluence of 717 mJ/cm^2.

During the laser printing of viscoelastic alginate solutions, five jetting regimes are identified as follows: no material transfer, well-defined jetting, well-defined jetting with an initial bulgy shape, jetting with a bulgy shape, and pluming/splashing. Among them, well-defined jetting with and without an initial bulgy shape are the desirable jetting regimes. It is found that the jetting behavior changes from no material transfer to well-defined jetting to well-defined jetting with an initial bulgy shape to jetting with a bulgy shape to pluming/splashing when the laser fluence increases. When the alginate concentration increases, the jetting dynamics changes in an inverse order as the laser fluence increases. In particular, for the desirable well-defined jetting regimes, as the laser fluence increases, the jet velocity and breakup length increase while the breakup time and primary droplet size decrease; as the alginate concentration increases, the jet velocity and breakup length decrease while the breakup time and primary droplet size increase. Furthermore, Ohnesorge, elasto-capillary, and Weber number-based phase diagrams are presented to better appreciate the dependence of jetting regimes on the laser fluence and alginate concentration. Four Weber number-defined planes can be used to distinguish different jetting regimes. The increase of viscous and elastic effects helps stabilize the jetting process or even suppress the formation of jets.

Y-shaped tubes based on the knowledge obtained from the jetting dynamics study have been printed using two different bioinks: 8% alginate solution and 2% alginate-based mouse fibroblast suspension. It has been demonstrated that 3D cellular constructs with bifurcated overhang structures can be adequately fabricated under optimal printing conditions using laser printing. The printing of overhang and spanning structures can be achieved using a dual-purpose crosslinking solution, which functions as a support material. The postprinting cell viability measurements immediately after printing as well as after 24-h incubation are above 60% for printed Y-shaped fibroblast tubes.

Acknowledgments

The study was partially supported by the National Science Foundation (CMMI 1314830). The authors would like to acknowledge the contribution from and discussion with D. Chrisey, D. Corr, J. Yan., C. Xu, and Y. Lin over the years.

References

1 Piqué, A., Chrisey, D.B., Auyeung, R.C.Y., Fitz-Gerald, J., Wu, H.D., McGill, R.A., Lakeou, S., Wu, P.K., Nguyen, V., and Duignan, M. (1999) A novel laser transfer process for direct writing of electronic and sensor materials. *Appl. Phys. A*, **69** (1), S279–S284.

2 Ringeisen, B.R., Othon, C.M., Barron, J.A., Young, D., and Spargo, B.J. (2006) Jet-based methods to print living cells. *Biotechnol. J.*, **1** (9), 930–948.

3 Lin, Y., Huang, G., Huang, Y., Jeremy Tzeng, T.R., and Chrisey, D. (2010) Effect of laser fluence in laser-assisted direct writing of human colon cancer cell. *Rapid Prototyp. J.*, **16** (3), 202–208.

4 Schiele, N.R., Corr, D.T., Huang, Y., Raof, N.A., Xie, Y., and Chrisey, D.B. (2010) Laser-based direct-write techniques for cell printing. *Biofabrication*, **2** (3), 032001.

5 Lin, Y., Huang, Y., and Chrisey, D.B. (2011) Metallic foil-assisted laser cell printing. *J. Biomech. Eng.*, **133** (2), 025001.

6 Lin, Y. and Huang, Y. (2011) Laser-assisted fabrication of highly viscous alginate microsphere. *J. Appl. Phys.*, **109** (8), 083107.

7 Guillotin, B., Souquet, A., Catros, S., Duocastella, M., Pippenger, B., Bellance, S., Bareille, R., Rémy, M., Bordenave, L., Amédée, J., and Guillemot, F. (2010) Laser assisted bioprinting of engineered tissue with high cell density and microscale organization. *Biomaterials*, **31** (28), 7250–7256.

8 Gruene, M., Pflaum, M., Hess, C., Diamantouros, S., Schlie, S., Deiwick, A., Koch, L., Wilhelmi, M., Jockenhoevel, S., Haverich, A., and Chichkov, B. (2011) Laser printing of three-dimensional multicellular arrays for studies of cell–cell and cell–environment interactions. *Tissue Eng. Part C*, **17** (10), 973–982.

9 Ringeisen, B.R., Pirlo, R.K., Wu, P.K., Boland, T., Huang, Y., Sun, W., Hamid, Q., and Chrisey, D.B. (2013) Cell and organ printing turns 15: diverse research to commercial transitions. *MRS Bull.*, **38** (10), 834–843.

10 Riggs, B.C., Dias, A.D., Schiele, N.R., Cristescu, R., Huang, Y., Corr, D.T., and Chrisey, D.B. (2011) Matrix-assisted pulsed laser methods for biofabrication. *MRS Bull.*, **36** (12), 1043–1050.

11 Yan, J., Huang, Y., and Chrisey, D.B. (2013) Laser-assisted printing of alginate long tubes and annular constructs. *Biofabrication*, **5** (1), 015002.

12 Lin, Y., Huang, Y., and Chrisey, D.B. (2009) Droplet formation in matrix-assisted pulsed-laser evaporation direct writing of glycerol-water solution. *J. Appl. Phys.*, **105** (9), 093111.

13 Colina, M., Duocastella, M., Fernández-Pradas, J.M., Serra, P., and Morenza, J.L. (2006) Laser-induced forward transfer of liquids: study of the droplet ejection process. *J. Appl. Phys.*, **99** (8), 084909.

14 Duocastella, M., Kim, H., Serra, P., and Piqué, A. (2012) Optimization of laser printing of nanoparticle suspensions for microelectronic applications. *Appl. Phys. A*, **106** (3), 471–478.

15 Serra, P., Duocastella, M., Fernández-Pradas, J.M., and Morenza, J.L. (2009) Liquids microprinting through laser-induced forward transfer. *Appl. Surf. Sci.*, **255** (10), 5342–5345.

16 Duocastella, M., Fernández-Pradas, J.M., Morenza, J.L., and Serra, P. (2009) Time-resolved imaging of the laser forward transfer of liquids. *J. Appl. Phys.*, **106** (8), 084907.

17 Duocastella, M., Fernández-Pradas, J.M., Morenza, J.L., and Serra, P. (2010) Sessile droplet formation in the laser-induced forward transfer of liquids: a time-resolved imaging study. *Thin Solid Films*, **518** (18), 5321–5325.

18 Unger, C., Gruene, M., Koch, L., Koch, J., and Chichkov, B.N. (2011) Time-resolved imaging of hydrogel printing via laser-induced forward transfer. *Appl. Phys. A*, **103** (2), 271–277.

19 Young, D., Auyeung, R.C.Y., Piqué, A., Chrisey, D.B., and Dlott, D.D. (2002) Plume and jetting regimes in a laser based forward transfer process as observed by time-resolved optical microscopy. *Appl. Surf. Sci.*, **197**, 181–187.

20 Guillemot, F., Souquet, A., Catros, S., Guillotin, B., Lopez, J., Faucon, M., Pippenger, B., Bareille, R., Rémy, M., Bellance, S., and Chabassier, P. (2010) High-throughput laser printing of cells and biomaterials for tissue engineering. *Acta Biomater.*, **6** (7), 2494–2500.

21 Brown, M.S., Kattamis, N.T., and Arnold, C.B. (2010) Time-resolved study of polyimide absorption layers for blister-actuated laser-induced forward transfer. *J. Appl. Phys.*, **107** (8), 083103.

22 Brown, M.S., Kattamis, N.T., and Arnold, C.B. (2011) Time-resolved dynamics of laser-induced micro-jets from thin liquid films. *Microfluid. Nanofluid.*, **11** (2), 199–207.

23 Duocastella, M., Patrascioiu, A., Dinca, V., Fernández-Pradas, J.M., Morenza, J.L., and Serra, P. (2011) Study of liquid deposition during laser printing of liquids. *Appl. Surf. Sci.*, **257** (12), 5255–5258.

24 Duocastella, M., Colina, M., Fernández-Pradas, J.M., Serra, P., and Morenza, J.L. (2007) Study of the laser-induced forward transfer of liquids for laser bioprinting. *Appl. Surf. Sci.*, **253** (19), 7855–7859.

25 Wu, P.K. and Ringeisen, B.R. (2010) Development of human umbilical vein endothelial cell (HUVEC) and human umbilical vein smooth muscle cell (HUVSMC) branch/stem structures on hydrogel layers via biological laser printing (BioLP). *Biofabrication*, **2** (1), 014111.

26 Gaebel, R., Ma, N., Liu, J., Guan, J., Koch, L., Klopsch, C., Gruene, M., Toelk, A., Wang, W., Mark, P., and Wang, F. (2011) Patterning human stem cells and endothelial cells with laser printing for cardiac regeneration. *Biomaterials*, **32** (35), 9218–9230.

27 Koch, L., Deiwick, A., Schlie, S., Michael, S., Gruene, M., Coger, V., Zychlinski, D., Schambach, A., Reimers, K., Vogt, P.M., and Chichkov, B. (2012) Skin tissue generation by laser cell printing. *Biotechnol. Bioeng.*, **109** (7), 1855–1863.

28 Xiong, R., Zhang, Z., and Huang, Y. (2015) Identification of optimal printing conditions for laser printing of alginate tubular constructs. *J. Manuf. Processes*, **20**, 450–455.

29 Zhang, Z., Xiong, R., Mei, R., Huang, Y., and Chrisey, D.B. (2015) Time-resolved imaging study of jetting dynamics during laser printing of viscoelastic alginate solutions. *Langmuir*, **31** (23), 6447–6456.

30 Wang, W., Li, G., and Huang, Y. (2009) Modeling of bubble expansion-induced cell mechanical profile in laser-assisted cell direct writing. *J. Manuf. Sci. Eng.*, **131** (5), 051013.

31 Yan, J., Huang, Y., Xu, C., and Chrisey, D.B. (2012) Effects of fluid properties and laser fluence on jet formation during laser direct writing of glycerol solution. *J. Appl. Phys.*, **112** (8), 083105.

32 Xiong, R., Zhang, Z., Shen, J., Lin, Y., Huang, Y., and Chrisey, D.B. (2015) Bubble formation modeling during laser direct writing of glycerol solutions. *J. Micro Nano-Manuf.*, **3** (1), 011004.

33 Yoo, J.H., Borisov, O.V., Mao, X., and Russo, R.E. (2001) Existence of phase explosion during laser ablation and its effects on inductively coupled plasma-mass spectroscopy. *Anal. Chem.*, **73** (10), 2288–2293.

34 Wang, W., Lin, Y., and Huang, Y. (2011) Modeling of thermoelastic stress wave in laser-assisted cell direct writing. *J. Manuf. Sci. Eng.*, **133** (2), 024502.

35 Schaffer, C., Nishimura, N., Glezer, E., Kim, A., and Mazur, E. (2002) Dynamics of femtosecond laser-induced breakdown in water from femtoseconds to microseconds. *Opt. Express*, **10** (3), 196–203.

36 Brujan, E.A. and Vogel, A. (2006) Stress wave emission and cavitation bubble dynamics by nanosecond optical breakdown in a tissue phantom. *J. Fluid Mech.*, **558**, 281–308.

37 Lauterborn, W. and Ohl, C.D. (1997) Cavitation bubble dynamics. *Ultrason. Sonochem.*, **4** (2), 65–75.

38 Brujan, E.A., Ikeda, T., and Matsumoto, Y. (2005) Jet formation and shock wave emission during collapse of ultrasound-induced cavitation bubbles and their role in the therapeutic applications of high-intensity focused ultrasound. *Phys. Med. Biol.*, **50** (20), 4797–4810.

39 Kaur, K.S., Fardel, R., May-Smith, T.C., Nagel, M., Banks, D.P., Grivas, C., Lippert, T., and Eason, R.W. (2009) Shadowgraphic studies of triazene assisted laser-induced forward transfer of ceramic thin films. *J. Appl. Phys.*, **105** (11), 113119.

40 Barron, J.A., Young, H.D., Dlott, D.D., Darfler, M.M., Krizman, D.B., and Ringeisen, B.R. (2005) Printing of protein microarrays via a capillary-free fluid jetting mechanism. *Proteomics*, **5** (16), 4138–4144.

41 Jang, D., Kim, D., and Moon, J. (2009) Influence of fluid physical properties on ink-jet printability. *Langmuir*, **25** (5), 2629–2635.

42 Herran, C.L. and Huang, Y. (2012) Alginate microsphere fabrication using bipolar wave-based drop-on-demand jetting. *J. Manuf. Processes*, **14** (2), 98–106.

43 Herran, C.L., Huang, Y., and Chai, W. (2012) Performance evaluation of bipolar and tripolar excitations during nozzle-jetting-based alginate microsphere fabrication. *J. Micromech. Microeng.*, **22** (8), 085025.

44 McKinley, G.H. and Renardy, M. (2011) Wolfgang von ohnesorge. *Phys. Fluids A*, **23** (12), 127101.

45 Entov, V.M. and Hinch, E.J. (1997) Effect of a spectrum of relaxation times on the capillary thinning of a filament of elastic liquid. *J. Non-Newtonian Fluid Mech.*, **72** (1), 31–53.

46 Wolf, B.A. (2007) Polyelectrolytes revisited: reliable determination of intrinsic viscosities. *Macromol. Rapid Commun.*, **28** (2), 164–170.

47 Boutopoulos, C., Kalpyris, I., Serpetzoglou, E., and Zergioti, I. (2014) Laser-induced forward transfer of silver nanoparticle ink: time-resolved imaging of the jetting dynamics and correlation with the printing quality. *Microfluid. Nanofluid.*, **16** (3), 493–500.

48 Gordillo, J.M. and Pérez-Saborid, M. (2005) Aerodynamic effects in the break-up of liquid jets: on the first wind-induced break-up regime. *J. Fluid Mech.*, **541**, 1–20.

49 van Hoeve, W., Gekle, S., Snoeijer, J.H., Versluis, M., Brenner, M.P., and Lohse, D. (2010) Breakup of diminutive Rayleigh jets. *Phys. Fluids A*, **22** (12), 122003.

50 Lin, S.P. and Reitz, R.D. (1998) Drop and spray formation from a liquid jet. *Annu. Rev. Fluid Mech.*, **30** (1), 85–105.

51 Reitz, R.D. and Bracco, F.V. (1982) Mechanism of atomization of a liquid jet. *Phys. Fluids A*, **25** (10), 1730–1742.

52 Fu, S., Thacker, A., Sperger, D.M., Boni, R.L., Velankar, S., Munson, E.J., and Block, L.H. (2010) Rheological evaluation of inter-grade and inter-batch variability of sodium alginate. *AAPS PharmSciTecn*, **11** (4), 1662–1674.

53 Brown, M.S., Brasz, C.F., Ventikos, Y., and Arnold, C.B. (2012) Impulsively actuated jets from thin liquid films for high-resolution printing applications. *J. Fluid Mech.*, **709**, 341–370.

54 Mun, R.P., Byars, J.A., and Boger, D.V. (1998) The effects of polymer concentration and molecular weight on the breakup of laminar capillary jets. *J. Non-Newtonian Fluid Mech.*, **74** (1), 285–297.

55 Gruene, M., Unger, C., Koch, L., Deiwick, A., and Chichkov, B. (2011) Dispensing pico to nanolitre of a natural hydrogel by laser-assisted bioprinting. *Biomed. Eng. Online*, **10** (1), 19.

56 McKinley, G.H. (2005) Visco-elasto-capillary thinning and break-up of complex fluids. *Annu. Rheol. Rev.*, 1–48.

57 Xu, C., Zhang, M., Huang, Y., Ogale, A., Fu, J., and Markwald, R.R. (2014) Study of droplet formation process during drop-on-demand inkjetting of living cell-laden bioink. *Langmuir*, **30** (30), 9130–9138.

58 Xu, D., Sanchez-Romaguera, V., Barbosa, S., Travis, W., de Wit, J., Swan, P., and Yeates, S.G. (2007) Inkjet printing of polymer solutions and the role of chain entanglement. *J. Mater. Chem.*, **17** (46), 4902–4907.

59 Ambravaneswaran, B., Subramani, H.J., Phillips, S.D., and Basaran, O.A. (2004) Dripping-jetting transitions in a dripping faucet. *Phys. Rev. Lett.*, **93** (3), 034501.

60 Bhat, P.P., Appathurai, S., Harris, M.T., Pasquali, M., McKinley, G.H., and Basaran, O.A. (2010) Formation of beads-on-a-string structures during break-up of viscoelastic filaments. *Nat. Phys.*, **6** (8), 625–631.

61 Lalan, S., Pomerantseva, I., and Vacanti, J.P. (2001) Tissue engineering and its potential impact on surgery. *World J. Surg.*, **25** (11), 1458–1466.
62 Krogh, A. (1919) The number and distribution of capillaries in muscles with calculations of the oxygen pressure head necessary for supplying the tissue. *J. Physiol.*, **52** (6), 409–415.
63 Xiong, R., Zhang, Z., Chai, W., Huang, Y., and Chrisey, D.B. (2015) Freeform drop-on-demand laser printing of 3D alginate and cellular constructs. *Biofabrication*, **7** (4), 045011.
64 Christensen, K., Xu, C., Chai, W., Zhang, Z., Fu, J., and Huang, Y. (2015) Freeform inkjet printing of cellular structures with bifurcations. *Biotechnol. Bioeng.*, **112** (5), 1047–1055.

10

Congruent LIFT with High-Viscosity Nanopastes

Raymond C.Y. Auyeung, Heungsoo Kim, and Alberto Piqué

Materials Science and Technology Division, Code 6360, U.S. Naval Research Laboratory, 4555 Overlook Ave. SW, Washington, DC 20375, USA

10.1 Introduction

Ever since the laser-induced forward transfer (LIFT) technique was first used to print ink [1] and then copper patterns [2] onto a substrate, it has been demonstrated in a wide range of materials such as inorganics, organics, and multicomponent systems. Traditionally, LIFT employs a donor substrate of which one side is coated with a solid thin-film layer. The laser fluence (energy/area) that is required to propel a portion of this solid film layer from the donor across the gap to a receiving substrate typically causes some melting or vaporization of the donor material. Since LIFT takes place under ambient conditions, this can result in oxidation, decomposition, phase impurity, and, finally, degraded functional and morphological properties of the deposited donor material.

Many strategies ranging from modifying the design or nature of the donor layer to shortening the laser pulsewidth have been adopted in order to minimize the incident laser fluence, reduce phase transformation of the donor material, and preserve its functional properties [3]. For example, the donor layer design can first consist of a thin dynamic-release layer (DRL) that absorbs a significant portion of the laser energy and then covered with a second layer of the material to be transferred [4]. This geometry shields the donor material from overexposure to the laser energy and also aids in the transfer of material that is laser-transparent. A similar idea is to use a polymer layer (instead of a DRL) that swells into a sealed blister from absorption of laser energy (without decomposing) and ejects donor material [5]. This mechanical propulsion preserves the functional properties of the donor material and prevents contamination of the transfer with the polymer layer [6]. Further details of these two techniques are discussed in Chapter 3 (for LIFT with a DRL) and Chapter 5 (for LIFT via blister formation).

The nature of the donor layer can be modified using a LIFT-based technique called matrix pulsed laser evaporation-direct write (MAPLE-DW) [7], which is discussed further in Chapter 2. Briefly, MAPLE avoids phase transformations of the donor layer by dispersing powders in a laser-absorbing organic matrix or binder, but density and adhesion issues of the transferred material remained.

Laser Printing of Functional Materials: 3D Microfabrication, Electronics and Biomedicine,
First Edition. Edited by Alberto Piqué and Pere Serra.
© 2018 Wiley-VCH Verlag GmbH & Co. KGaA. Published 2018 by Wiley-VCH Verlag GmbH & Co. KGaA.

The MAPLE technique was soon extended to other rheological systems such as chemical precursors, inks, suspensions, sol–gel solutions, and cell cultures [8]. Because these transfer processes do not necessarily involve the evaporation of the matrix or binder, it was more suitable to use the more general term laser direct-write (LDW) to describe the laser transfer of these rheological systems.

The LDW process was used to transfer complex rheological systems for applications such as microbatteries [9, 10], photovoltaics [11] and polymer–ceramic membranes [12]. Previously, laser transfer of metals involved either a donor layer composed of a solid thin film or metal powder dispersed within a matrix. The first instance of using a metal-based rheological fluid as the donor layer was the LDW of a screen-printable silver ink onto polyimide [13] that demonstrated a resistivity of 40× bulk Ag.

The next advance in the LDW of metallic rheological systems was the use of a silver nanoparticle ink (size <100 nm) in the donor layer [14]. Narrow 20 μm wide silver lines with 0.5 μm heights were laser-printed onto polyimide and showed resistivities of 5–10× bulk Ag after oven or laser curing. However, the low viscosity of these inks resulted in height and width variation and satellite droplets around the transfers.

One application that requires features with uniform morphology without surrounding debris is the printing of thin-film-like patterns for the repair of thin-film transistor–liquid crystal displays (TFT-LCD). Typically, these repairs require printed features that are a few microns in width, a few hundred microns in length, and a few hundred nanometers high. A direct-write technique such as LDW was used to transfer features with this resolution and uniform morphology by using a single donor layer of highly viscous silver ink suspension (nanopaste). These laser printed features were uniform, well-defined, and highly congruent in size and shape to the incident laser spatial profile. As a result, this unique LDW process was named "laser decal transfer" (LDT) or congruent LIFT [15]. The LDT term will be used mainly in this chapter for the sake of brevity.

This is a new operating regime of LIFT in which the high congruence between the design and the transferred feature means that individual picture elements in the drawing (pixels) correspond to volume elements (voxels) in the printed feature, making this process a 3D digital microfabrication tool. This improvement in the quality of the transferred features and their design fidelity are unique features of congruent LIFT and are not available in other direct-write processes.

Other variations of LIFT have been used to create congruent transfers such as using a DRL in the donor substrate [16–18], ensuring a zero-gap distance between the receiver and the donor substrate [19, 20], and premachining the donor layer to minimize shearing of a solid film during LIFT [21]. Although these techniques have produced successful congruent transfers, they involve extraneous donor layers, restrictive donor–receiver geometries, or additional time-consuming steps in preparing the donor substrate. LDT simply employs a highly viscous nanoparticle donor layer, a uniform laser beam spatial profile, and standard LIFT protocol to produce congruent transfers.

In this chapter, the unique qualities of features made by LDT will be presented first followed by examples of printed structures and their functional properties. It will be shown that the serial LDT technique can be adapted into a parallel

processing regime that represents a paradigm shift in direct-write technologies. A more detailed characterization of the LDT process and its requirements will then be discussed, and the chapter will conclude with a summary of remaining issues with LDT and suggestions for future work.

10.2 Congruent LIFT (or LDT)

The laser system and experimental setup used to perform LDT are similar to those used in LIFT except that extra attention is paid to the laser beam spatial quality and properties of the donor layer. Laser pulses from a UV ($\lambda = 355$ nm) Nd:YVO_4 laser are spatially defined by a hard aperture (mask), which is imaged onto the donor substrate with a microscope objective. The donor substrate is typically a glass slide in which a well (typically few cm wide by 1–5 μm deep) has been etched. Silver nanopaste (NPS, nominal viscosity approximately 100 Pa s, 80 wt% solids loading, Harima Chemicals) is doctor-bladed into this well and allowed time for the volatile components to evaporate. Typically, the actual donor layer thickness after blading is about 50–80% of the well depth as measured by confocal microscopy. Laser transfers described in this chapter will essentially use this basic setup with some variations on the laser, mask, or microscope objective as will be noted later. A detailed video of the entire transfer process is presented in Ref. [22].

There are many properties of the LDT process and its adaptations that make it unique among LDW techniques. The intrinsic properties of the transfer process, methods of "engineering" LDT to specific applications, and some measured functional properties are summarized in Table 10.1 along with their corresponding references. The intrinsic properties of the transferred material in LDT will be discussed in this section. The engineered approaches and measured properties of the transfers will be discussed together in the next section, as these topics naturally lead to applications of LDT. Of course, many of these attributes are not mutually exclusive and can appear together in a demonstrated LDT feature.

The first demonstration of LDT [15] in 2008 already displayed many of the attributes listed in Table 10.1. Arrays of 2 and 5 μm squares were laser transferred onto glass and silicon substrates [15, 23] as shown in Figure 10.1a,b. The 2 μm square voxels were more sensitive to nonuniformities in the donor layer, and this sensitivity will be further discussed in Section 10.4. Note the relative absence of debris in the scanning electron microscopy (SEM) images that is usually present in LIFT of solid films. The height profiles of these voxels were scanned by atomic force microscopy (AFM) and illustrate their high shape congruence and edge sharpness (acuity) as shown in Figure 10.1a,b. Since this first demonstration, the congruent nature of LDT has been verified elsewhere [24].

The LDT voxel can also be transferred with a wide range of heights by merely adjusting the donor layer thickness. Figure 10.1c shows a single voxel height from 1 to 5 μm and a voxel "side length" from a few micrometers to over 100 μm [25]. This wide range in voxel dimensions also means that a broad range of voxel volumes (from pico- to femtoliters) can be transferred. Note that these voxels were

Table 10.1 Demonstration of intrinsic and engineered characteristics of the congruent laser transfer process and measured properties of the transferred structures shown with references.

	LDT attribute	Demonstrator	References
Intrinsic	Shape and size congruence (wide range)	2–1000 μm features, arbitrary shapes	[15, 22–25, 27, 29–37, 39–41]
	High spatial resolution	2 and 5 μm squares, lines	[15]
	Wide thickness range	0.2–2.5 μm high squares (after curing)	[15, 25], Figure 10.1
	Absence of debris	EDX of 5 μm squares	[23]
	Edge acuity	Adjacent line separation of 2 μm	[23, 27]
	Transfer gap distance	5–50 μm	[15, 27, 29]
	Low substrate wettability	Transfers on glass, Si, polyimide	[15, 25]
	Strong elastic modulus	Freestanding structures, stacks, membranes	[23, 25, 30–32]
Engineered	Parallel processing (with SLM)	Concurrent transfer of large area (0.7 mm^2)	[33–36]
	Structured beam profile	Interconnects; lower transfer threshold	[36, 37]
	Conformal coverage	Transfers over a step	[39]
	Functional release layer (FRL)	Concurrent transfer of multilayers	[43]
	Laser curing	Continuous lines on glass	[15, 23]
Functionality	Electrical resistivity	2D and 3D interconnects	[15, 23, 25, 33, 34, 37, 39]
	Microwave transmission	CPW	[27]
	THz resonance	SRR	[40–42]
	Capacitance	Multilayer stack	[43]
	Material (static, dynamic)	Cantilevers, beams, membranes	[30–32]
	Mechanical stability	Au bonding; sonication	[25], Figure 10.6

EDX, energy dispersive X-ray spectroscopy; SLM, spatial light modulator; CPW, coplanar waveguide; SRR, split-ring resonator.

transferred from a *single* laser pulse with the same matching dimensions; no other direct-write tool can print such arbitrary features with such a height range from a single laser pulse. (Of course, the height of a voxel can be built up with successive laser transfers over the same location on the receiver substrate but could result in extra, unwanted voxel interfaces and extra processing time.)

Besides square voxels, this silver nanopaste donor material can be laser transferred as a linear array of individual rectangular voxels to form a continuous line [15, 23]. This line can then be oven- or laser-cured to yield measured

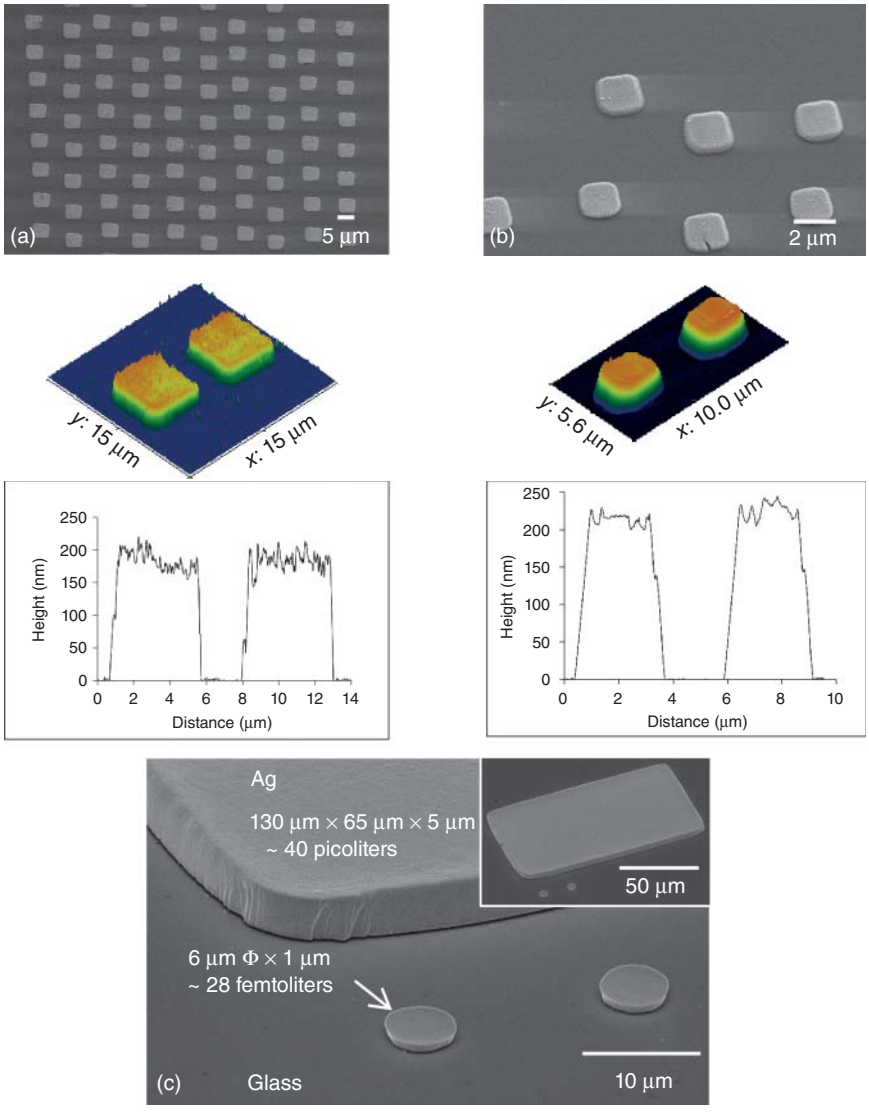

Figure 10.1 SEM images of an array of (a) 5 μm and (b) 2 μm square voxels on silicon as transferred by LDT. Representative AFM 3D and height profiles are shown below each respective image. (c) SEM images of uncured silver voxels made by LDT showing wide range in voxel size, thickness, and shape. Each shape is printed from a single laser pulse. (Panels (a,b): Piqué *et al*. 2008 [15]. Reproduced with permission from Proceedings of SPIE. Panel (c): Wang *et al*. 2010 [25]. Reproduced with permission from John Wiley and Sons.)

resistivities a few times that of bulk Ag. It will be shown in Section 10.3 that an entire continuous line could also be laser transferred with a single laser pulse, given sufficient energy and spatial uniformity.

The absence of debris and high edge acuity in LDT voxels allows the placement of features with high spatial resolution, which is important in fabricating

high-density interconnects and electrodes for organic thin-film transistors as well as minimizing conductor losses in microwave transmission lines [26]. As shown in Figure 10.2a, silver lines were transferred within 2 μm of each other and remained isolated from each other. However, the edge acuity of a successfully transferred voxel is inversely related to the thickness of the donor layer as shown in Figure 10.2b. In general, the thicker the transferred voxel, the less sharp are its edges, especially at the corners. This effect becomes more noticeable as the voxel size is decreased as shown by the more rounded corners for the 50 and 5 μm voxels.

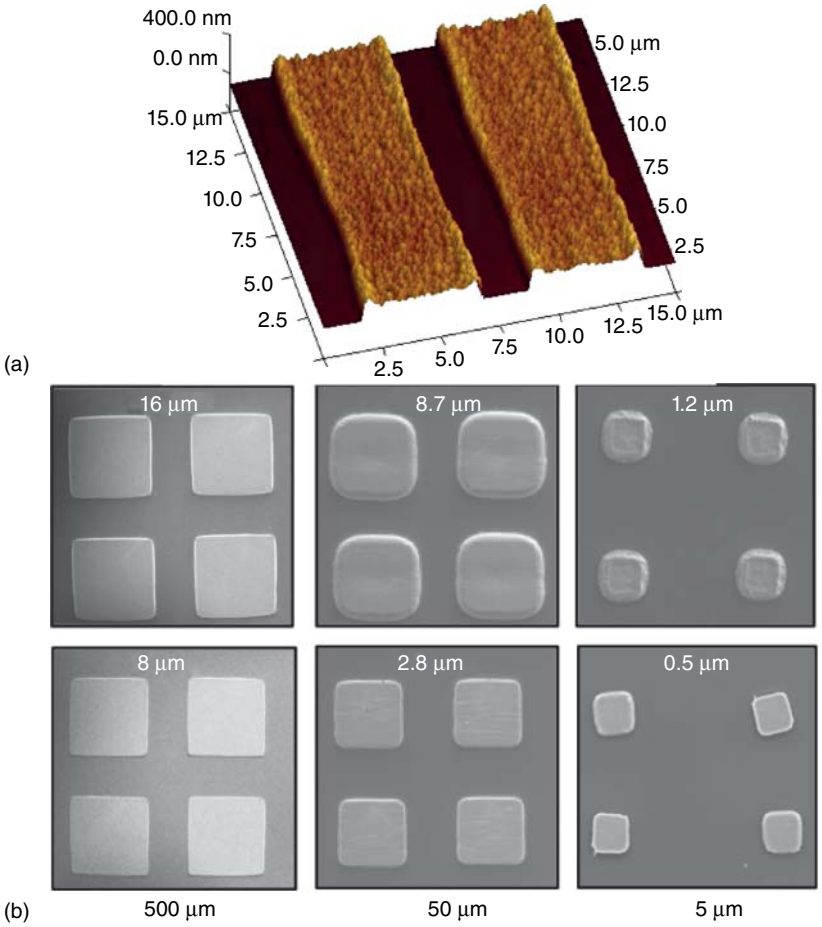

Figure 10.2 Edge acuity of LDT lines and voxels. Panel (a) shows an AFM image of two parallel lines separated by 2 μm. Panel (b) shows SEM images of the change in edge acuity for different voxel thicknesses (white labels) as a function of voxel size (shown below each column). (Panels (a): Piqué *et al*. 2008 [23]. Reproduced with permission from Journal of Laser Micro/Nanoengineering. Panel (b): Breckenfeld *et al*. 2015 [27]. Reproduced with permission from Applied Surface Science.)

In order for the LDT process to be commercially viable, there must be a reasonably wide gap between the donor and the receiver substrate in which the transfers remain intact, well-defined, and aligned. Figure 10.3 shows the LDT of 50 μm square voxels for different voxel thicknesses and transfer gap distances [27]. The minimum required laser fluence was used to transfer the voxels, but this value increased with thicker voxels. In general, the thicker the voxel, the more likely the voxel will transfer intact, with minimal rotation and misalignment on the receiving substrate. Note that a voxel thickness ≥3 μm can transfer reliably across

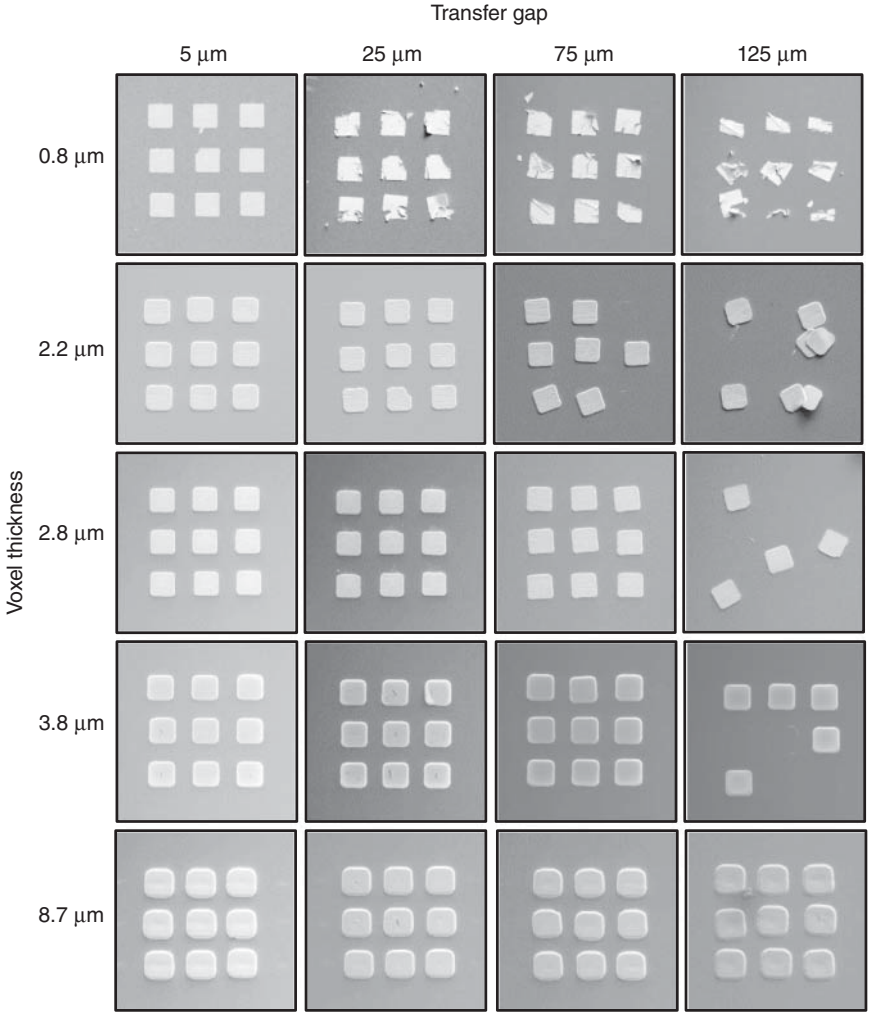

Figure 10.3 SEM images of LDT arrays of 50 μm square voxels on Si with increasing donor-to-receiving substrate distance (transfer gap) and increasing voxel thickness. Voxels were "soft-cured" at less than 100 °C. (Breckenfeld *et al*. 2015 [27]. Reproduced with permission from Applied Surface Science.)

a 75 μm gap, while a 2 μm thick voxel can only transfer successfully up to a 25 μm gap. Thinner voxels such as those below 1 μm can transfer successfully only at the closest gap of 5 μm. Thicker voxels such as those ≥8.5 μm can transfer successfully up to a gap of 125 μm albeit with some loss in edge acuity (rounded corners). These thicker voxels, by virtue of their greater mass and momentum, would resist any rotation or folding motion induced by nonuniformities in the laser beam profile or donor thickness during the transfer process. The thickness values of these partially cured voxels (<100 °C) were measured by confocal microscopy and were lower by 50% or more after a full cure at 220 °C. Maintaining a transfer gap maximum of approximately 25 μm for the LDT of an approximately 2 μm thick 50 μm square voxel should be easily accommodated in a commercial LDT tool as current hard disk drives have read/write heads only a few nanometers above the platter [28]. Note that a high-viscosity donor material also allows congruent transfers to occur over a wider gap distance than for low-viscosity ink [29].

The high viscosity of the donor material minimizes any wetting issues with the receiving substrate and was demonstrated in the successful transfers of silver lines on glass, silicon, and polyimide substrates [15, 25]. The high viscosity of the donor material in LDT also allows the transferred material to be self-supporting due to its high elastic modulus. As shown in Figure 10.4, high-aspect 3D stacks and freestanding structures were transferred onto Si substrates without using any sacrificial layers [23, 25, 30–32]. These structures were freestanding immediately

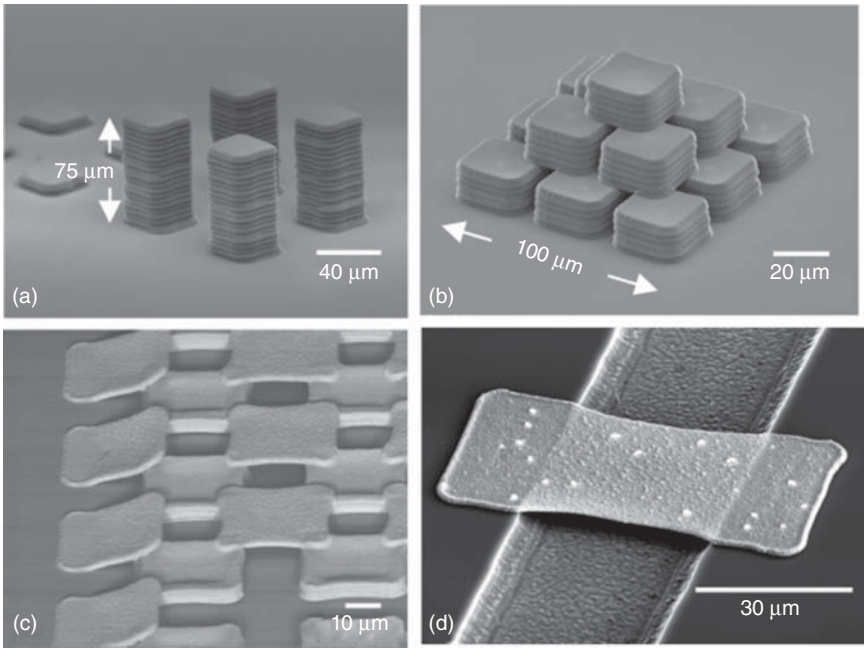

Figure 10.4 SEM images of self-supporting 3D stacks and a freestanding microbridge made by LDT without the use of any sacrificial layers. (Panels (a–c): Wang *et al*. 2010 [25]. Reproduced with permission from John Wiley and Sons. Panel (d): Piqué *et al*. 2013 [37]. Reproduced with permission from JIST.)

after the transfer and remained so after curing. The mechanical and electrical properties of these structures will be discussed in the next section.

These intrinsic properties of the transferred material make LDT unique among LIFT processes and place confidence in the design-to-manufacture process since the printed feature so closely matches the desired pattern. Since the pixels in a drawing correspond to voxels in a transferred feature, congruent laser transfer can be considered as a digital microfabrication process. Furthermore, since the thickness of the printed voxel can be varied (to an extent) and the voxel is able to support itself (without sacrificial layers), congruent laser transfer can also play a role in 3D microfabrication or laser additive micromanufacturing. The next section will describe how the LDT process can be engineered for specific applications, and some of the functional properties of the transfer will be showcased.

10.3 Applications

The many benefits of LDT allow the fabrication of microstructures that may be difficult or unrealistic to fabricate in other LIFT processes. The LDT process can be engineered for potential applications, and the functional properties of these substructures are shown in the lower portion of Table 10.1. Because these three aspects of LDT can be interrelated for a particular application, they are often discussed together in this section.

The most important advance in the LDT process is its ability to deposit material in a highly parallel, dynamically reconfigurable manner by using a spatial light modulator (SLM) [33–36]. This transfer of multiple voxels simultaneously is a parallel processing ability that represents a paradigm shift in laser additive printing technology. Traditionally, LDW techniques (as in other non-laser-based methods) deposited material in a serial manner by using an X–Y stage for a stationary laser beam or scanning the laser beam at high speed (with galvanometric mirrors) over a stationary sample. An SLM can structure the spatial profile of the incident laser pulse as determined from a drawing and combined with the high voxel congruence of LDT, a truly digital design-to-print process can be used to deposit large-area patterns with a single laser pulse.

The SLM used with LDT is a digital micromirror device (DMD) composed of a 2D array of approximately 14 μm square micromirrors (Figure 10.5a). Each micromirror can pixelate the spatial profile of the incident laser beam in a binary ("on–off") manner corresponding to the pixels in the bitmap image. This pattern on the DMD is then relayed by the laser beam profile and reimaged onto the donor layer for laser transfer. Because pixels in the original bitmap image can correlate into well-defined voxels in LDT, this ability allows the simultaneous laser printing of multiple voxels (of different sizes) over an extended area (limited by the available laser beam energy and spatial uniformity). In addition, the pattern on the DMD can be rapidly updated, thereby making DMD-LDT a dynamic, parallel processing direct-write technology.

Examples of transfers produced by DMD–LDT are shown in Figure 10.5b–g. Because the spatial profile of the laser pulse illuminating the DMD should

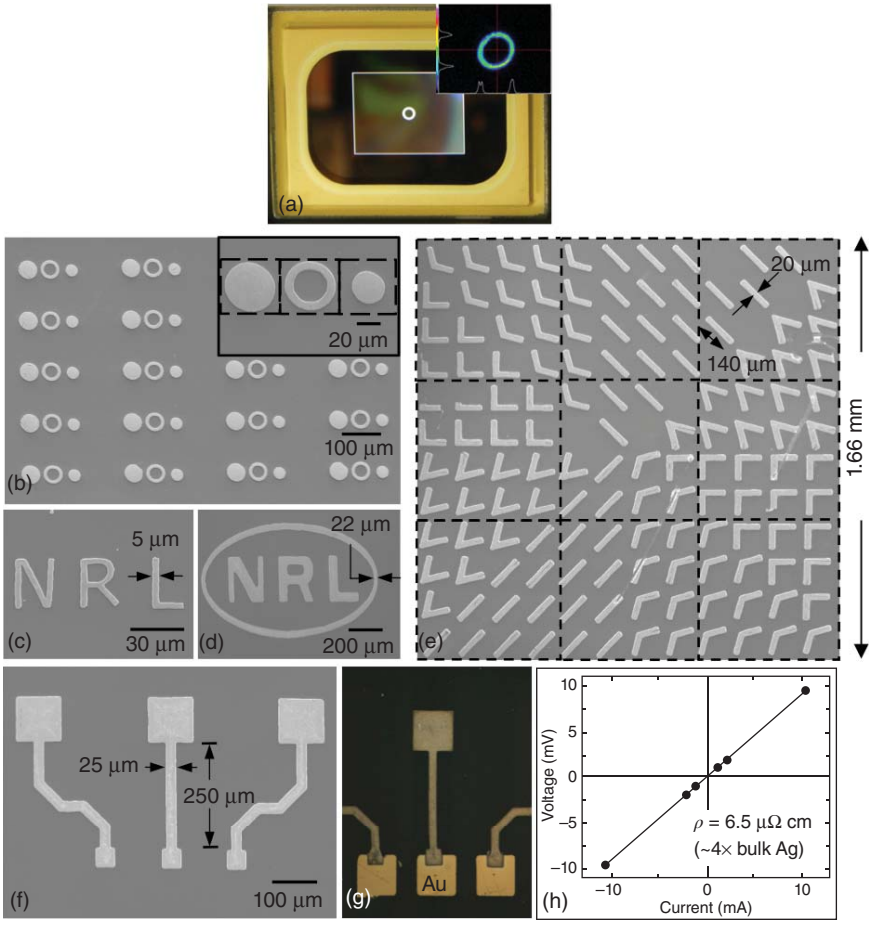

Figure 10.5 Transfers produced by DMD-LDT. (a) Optical image of an annulus pattern loaded onto a DMD array and its spatial beam profile (inset). SEM images of silver nanopaste transfers on Si produced by (b) UV ($\lambda = 355$ nm) laser and (c–f) green ($\lambda = 532$ nm) laser pulses. The dotted square outlines the pattern printed by a single laser pulse. A single laser pulse was used to transfer each letter in (c) and the entire logo in (d). (e) A metamaterial surface printed with nine different laser shots. (f) SEM image of three interconnect patterns, each one printed with a single laser pulse by DMD-LDT using an edge-enhanced beam profile. (g) Optical image of one of the patterns in (f) printed over Au pads on a glass substrate. (h) Measured *IV* plot of one interconnect. (Panel (a): Adapted from [35] and reproduced with permission from Applied Optics. © 2015 by Optical Society of America. Panels (b,c): Adapted from [33] and reproduced with permission from Applied Physics A. © 2011 by Springer. Panels (d,f,g,h): Adapted from [37] and reproduced with permission from Journal of Imaging Science and Technology. © 2013 by Society for Imaging Science and Technology. Panel (e): Adapted from [34] and reproduced with permission from Proceedings of SPIE. © 2013 by SPIE.)

be as uniform as possible, a refractive beam shaper was used to modify a UV laser spot from a Gaussian to a more "flat-top" profile for the transfers shown in Figure 10.5b, and a multimode green laser was used for the transfers shown in Figure 10.5c–g. The wide range in voxel sizes printed in an extended area by a single laser pulse is shown by the NRL logo in Figure 10.5d, which covers a 1×0.7 mm area and yet contains features down to approximately 22 μm in linewidth. The nine distinct patterns shown in Figure 10.5e show a dynamic "step-and-repeat" feature of DMD–LDT and represent an example of a metamaterial surface.

The DMD can also be used to impart grayscale intensities to the spatial structure of the laser beam used in LDT. By selectively turning "on" the pixels in the DMD, an edge-enhanced ("rabbit-eared") intensity profile can be created in the laser spot [36]. This altered beam profile resulted in a approximately 30% decrease in the laser fluence required to transfer a 13 μm square voxel as compared to a reference beam profile. This change in fluence threshold is important in the LDT of extended area patterns that contain different feature size resolutions. Figure 10.5f,g shows three complex interconnect patterns with feature sizes ranging from 25 to 250 μm where each one is transferred with a single laser pulse [37]. These interconnects were also transferred over a gold pad to verify its resistivity of 6.5 μΩ cm, which is approximately 4× bulk silver (Figure 10.5g,h). Structuring the spatial beam profile to produce enhanced edges has been used elsewhere to congruently transfer 400 nm thick polymer films, but it employs two apertures and a more complex beam path [38].

It is shown in Figure 10.4 that the elastic modulus of the donor nanopaste material was sufficiently high to support freestanding structures after laser transfer without the use of any sacrificial layers. By carefully adjusting the laser transfer fluence, a single voxel structure can also be transferred, which adapts or fully conforms to the receiving substrate's geometry. These structures are important in fabricating 3D interconnects in multilevel and sidewall circuit architectures. For example, two rectangular voxels were laser transferred to connect an embedded bare LED die to Au electrodes on a polyimide substrate (Figure 10.6a–c) [25]. The nanopaste material was flexible enough to bridge an approximately 15 μm height mismatch without damage (Figure 10.6a). After oven curing at 150 °C, LED emission was observed (Figure 10.6d), which continued even after 500 cycles of bending over a 13 mm radius (Figure 10.6e). A fuller conformal coverage of an LDT voxel to a receiving surface is shown in Figure 10.6f,g. Here, by carefully adjusting the laser fluence, a 10×70 μm voxel was laser transferred to conformally cover the top, side, and bottom of a 20 μm high SU-8 mesa [39]. An I–V plot of this interconnect voxel between Au electrodes on the top and bottom of the mesas (Figure 10.6g) shows a resistivity of 7.3 μΩ cm (Figure 10.6h). The conformal coverage of these voxels was very sensitive to laser fluence and is consistent with the shear thinning property of the silver nanopaste material. A reliable conformal transfer process would require laser pulse energies with less than 5% variation.

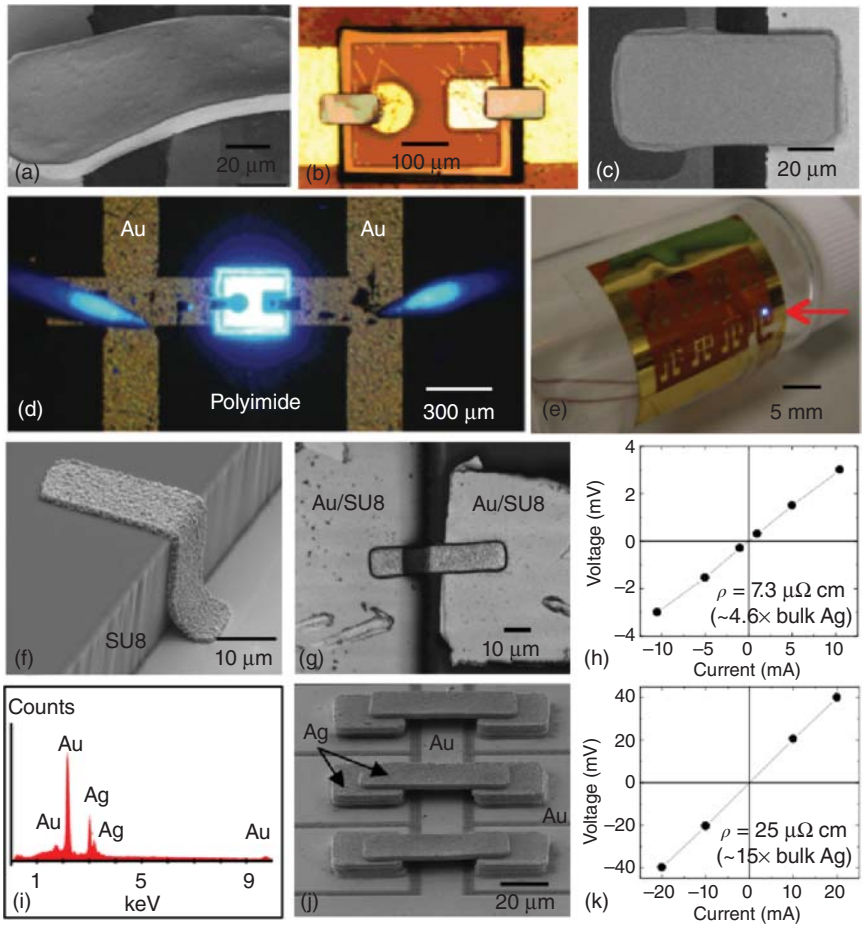

Figure 10.6 3D Ag interconnects fabricated by LDT with a (a–g) single voxel and (j) multiple voxels. (a,c) SEM images of LDT silver interconnects between an embedded LED die in polyimide to Au contact pads shown in the optical image (b). (d) LED Emission after oven curing at 150 °C and (e) after 500 bending cycles of 13 mm radius. (f) SEM image of an oven-cured (180 °C) LDT voxel conforming fully to a 20 µm high SU-8 mesa. (g) Confocal micrograph of a 10 µm × 70 µm voxel connecting two Au electrodes separated by a 20 µm high SU-8 mesa with (h) measured *I*–*V* plot. (j) SEM image of a 3D freestanding interconnect crossover made by LDT of a microbridge and pillars on a glass substrate. Panel (i) is the EDX spectrum of (j) showing Ag diffusion into the Au pad after oven curing at 250 °C. Panel (k) is the measured *I*–*V* plot of the interconnect in (j). (Panels (a–e,i): Adapted from [25] and reproduced with permission from Advanced Materials. © 2010 by Wiley. Panels (f–h): Adapted from [39] and reproduced with permission from Applied Physics A. © 2013 by Springer. Panels (j,k): Adapted from [29] and reproduced with permission from Applied Surface Science. © 2016 by Elsevier.)

Three-dimensional interconnects can also be fabricated with multiple instead of single voxels as shown in Figure 10.6j. An interconnect crossing over a 15 μm wide Au line was assembled from the LDT of a freestanding microbridge over two vertically stacked pillars at each end. No sacrificial layers were used. An I–V plot of the interconnect after curing at 250 °C (Figure 10.6k) showed ohmic behavior and a resistivity of 25 μΩ cm (~15× bulk Ag). The low form factor of this interconnect demonstrates its potential in increasing the fine pitch of bond pads and reducing the loop height, which are reaching their size limits in the current wire bonding technology.

An EDX analysis (Figure 10.6i) revealed diffusion of Ag in the Au electrodes near the Au/Ag interface, which is indicative of diffusion bonding occurring between the Ag transfers and the Au electrodes [25]. The mechanical stability of these bonds was tested by ultrasonically agitating five of these interconnects in isopropyl alcohol for 30 min. The measured resistivity of these interconnects was unchanged after the sonication and indicates effective bonding and mechanical stability between the cured Ag interconnects and the Au electrodes.

The self-supporting feature of these interconnects can also be exploited to the LDT of microcantilevers, microbridges, and membranes [30–32] directly onto substrates. These structures form the basis of many microelectromechanical systems (MEMS) and perform functions such as sensors, actuators, and filters. The measured resonant frequencies of these structures lie in the 1–3 MHz frequency range with quality factors (Q) ≈ 1400, which are comparable to structures made by photolithography. The fully cured silver nanopaste exhibited a nanoporous microstructure, and its static response showed a Young's modulus $E \approx 40$ GPa, residual tensile stress $\sigma_0 \approx 61$ MPa, and a density approximately 60% of bulk silver [31].

The electrical interconnects made by LDT not only have demonstrated DC performance but have been characterized for use in the microwave region. The steep sidewalls of an LDT feature (Figure 10.2) minimize conductor losses by maintaining a uniform current density profile along a microwave coplanar waveguide (CPW) [26]. Stitched Ag lines made by LDT were printed in a CPW geometry on silicon and sapphire substrates. A loss of −0.47 dB (10 GHz) was measured for a 1 mm long CPW double-layer line on sapphire, which approached the theoretical value calculated for a perfect Ag conductor [27].

Continuing up the frequency spectrum from the microwave region, silver split-ring resonators (SRR) were printed by LDT for a metamaterial application in the terahertz (THz) regime. SRRs are a common implementation of a THz metamaterial as their frequency response can be tuned by varying their dimensions. An array of 10 000 Ag SRRs was printed by LDT in a 1 cm^2 area on silicon, and their THz response is shown in Figure 10.7a–c [40]. The Ag SRRs made by LDT performed similarly as Au SRRs made by photolithography, and the measured spectra agreed well with that predicted for Ag SRRs. An alternative double-square SRR is shown in Figure 10.7d, and a D-ring meta-antenna designed to operate as an RF to optical modulator is shown in Figure 10.7e [41, 42].

Thus far, LDT has been used to fabricate structures originating from a single donor layer. In the introduction to this chapter, it was mentioned that a DRL

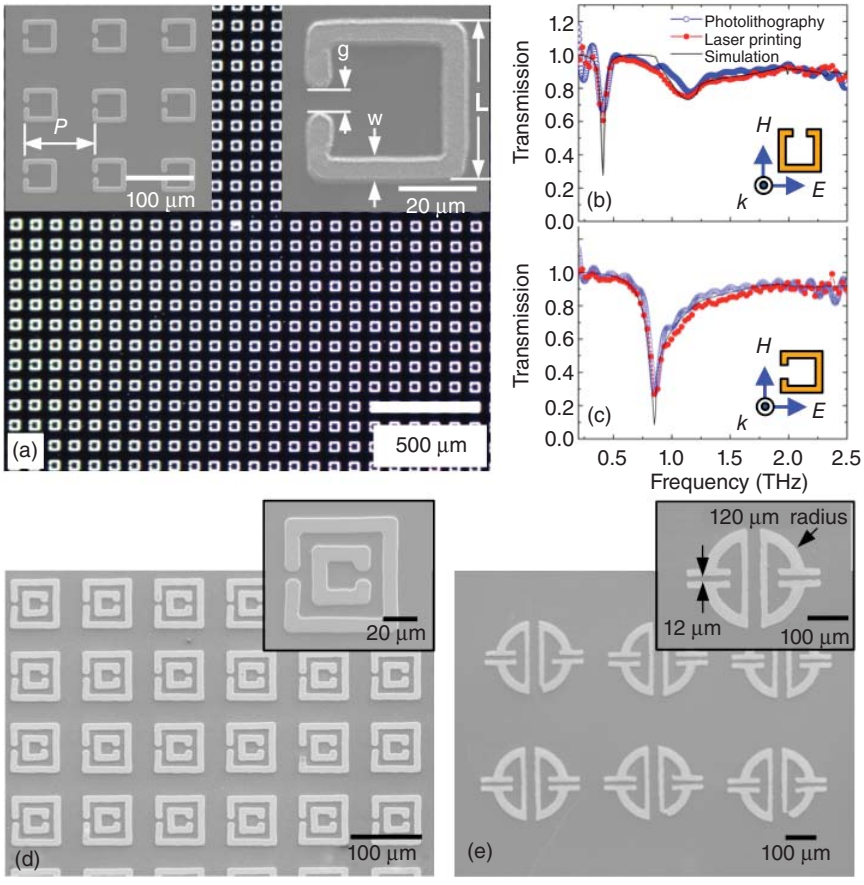

Figure 10.7 (a) Optical and SEM (insets) images of SRRs printed by LDT on silicon; $P = 100$ µm, $L = 48$ µm, $g = 8$ µm, $w = 6$ µm, and 0.7 µm thickness. Measured THz transmission spectra of Ag SRRs made by LDT (closed circle) and Au SRRs made by photolithography (open square) for (b) perpendicular ($E_{\perp}$) and (c) parallel ($E_{\parallel}$) electric field polarizations to the SRR gap. The simulated transmission spectra (solid line) are shown for both polarizations. SEM images of (d) double-square SRRs and (e) D-ring meta-antenna designed for an RF to optical modulator. (Panels (a–d): Kim et al. 2010 [40]. Reproduced from permission Optics Letters. Panel (e): Piqué *et al*. 2012 [41]. Reproduced with permission from Proceedings of SPIE.)

is often used to protect the donor material from high laser transfer fluences. However, since LDT requires such low laser fluences, the nanopaste material can be used as the first layer of a multilayer donor structure where it will absorb much of the laser energy and gently release and propel the entire stack to a receiving substrate. Because the nanopaste layer remains intact and possesses functional properties, it can be properly denoted as a *functional* release layer (FRL). For example, a donor layer consisting of a silver nanopaste layer (electrode) and a photoresist layer (dielectric) was transferred together onto a silicon substrate to form a capacitor (Figure 10.8) [43]. The cross section of the transferred stack showed sharp interfaces without any intermixing, bubbles, or voids

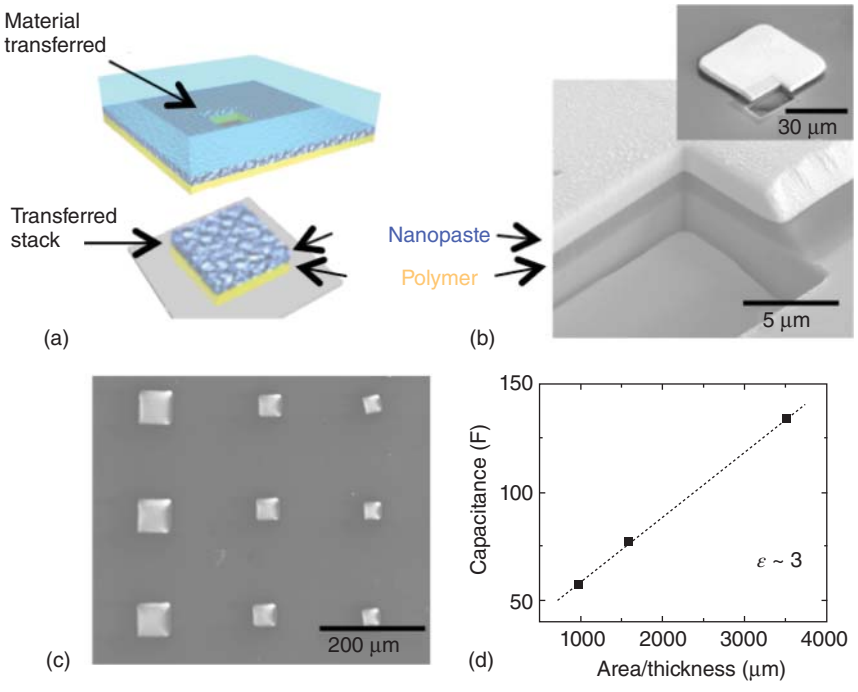

Figure 10.8 (a) Schematic diagram of an LDT multilayered stack. The FRL is a 2 μm thick Ag nanopaste layer spin-coated with a 1.8 μm thick photoresist layer. SEM image of (b) a cross section of a transferred multilayer stack (cured at 200 °C) on Si, part of which is exposed by focused ion beam (FIB) milling. SEM image (c) of Ag/polymer stacks with various planar areas transferred onto silicon. (d) Capacitance versus area/dielectric thickness for a Ag/photoresist (1818) stack. (Birnbaum *et al*. 2010 [43]. Reproduced with permission from Applied Physics A.)

(Figure 10.8b). Impedance measurements of these multilayer stacks showed a near-linear capacitance increase with transfer area/dielectric layer thickness (Figure 10.8c,d). A dielectric constant of ≈3 was extracted for the photoresist. Other schemes have been used to transfer entire multilayer stacks for organic thin-film transistor (OTFT) applications but have relied on a polymer DRL [44].

This section has presented many varied and unique structures that were produced nonlithographically by engineering the LDT process. The combination of LDT with a DMD is a major advance and potentially disruptive technology that enables parallel processing of a LDW process. The close congruence between the laser-printed voxels in LDT and the "designed" voxels minimizes "correction factors," builds reliability, and improves throughput in a dynamic, parallel writing process. The fabricated LDT features presented in this section include interconnects, waveguides, metamaterial surfaces, multilayer stacks (capacitors), and freestanding structures such as microcantilevers, microbridges, and membranes. These structures have demonstrated functional properties such as electrical transport (DC, microwave), THz resonance, capacitance, and mechanical resonance, all of which could find use in applications such as microelectronics, MEMS, and sensors.

10.4 Achieving Congruent Laser Transfers

In order for LDT to develop its potential in fabricating the unique structures presented in the previous section, a more complete understanding of the process must take place. This section examines the parameters, qualitative and quantitative, that affect LDT, which will then be used to formulate some general requirements for successful congruent transfers.

The most distinct difference between LDT and other solid-film LIFT processes is the high viscosity of the donor material. This high viscosity allows the released feature to resist deformation and maintain its shape and size as it travels to the receiving substrate. A comparison can be made of laser-transferred features from low- (0.01 Pa s) and high-viscosity (100 Pa s) ink using square, rectangular, and gridded beam spatial profiles (Figure 10.9) [37]. Note that only the high-viscosity ink produces a square-shaped voxel from a square beam profile (Figure 10.9d) and a sharp-edged line from a rectangular beam profile (Figure 10.9e). In Figure 10.9c, a grid feature was laser-printed with multiple voxels of low-viscosity nanoink, while a single (gridded) voxel of nanopaste was used in Figure 10.9f to print the entire grid with one laser shot. The clean and sharp overlap at the line intersections in Figure 10.9f, compared to Figure 10.9c, demonstrates the advantages of using high-viscosity ink for the transfer of complex features as well as the higher throughput achieved with parallel versus serial processing.

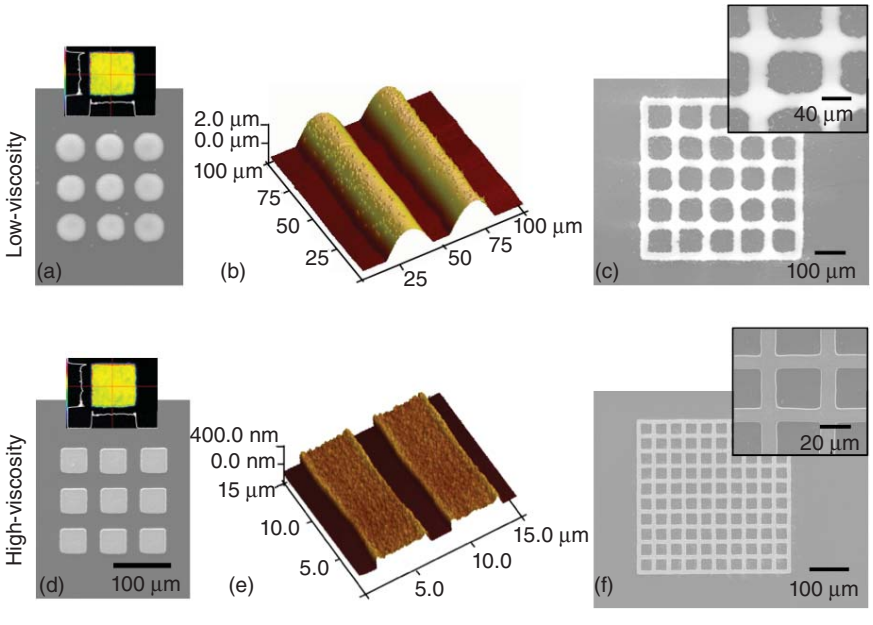

Figure 10.9 Comparison of laser transfers of low-viscosity Ag ink and high-viscosity Ag nanopaste on Si. SEM images of laser transfers of (a) nanoink and (d) nanopaste with a square laser beam profile (insets). AFM height profiles of laser transfers of (b) nanoink and (e) nanopaste with a rectangular beam profile. SEM images of a grid, laser printed with multiple voxels of (c) nanoink and with a single (gridded) voxel of (f) nanopaste. (Piqué *et al*. 2013 [37]. Reproduced with permission from JIST.)

Besides viscosity, another material property that is important in determining the nature of the laser–materials interaction and the success of LDT is its absorption coefficient. The donor material should have a high absorption coefficient, which will maximize the pressure generated to propel the donor feature across the gap to the receiving substrate with minimal phase transformation. It is known that the absorption efficiency (defined as the fraction of the incident light absorbed per unit cross-sectional area of a particle) increases as the particle size decreases below 100 nm [45]. Therefore, the donor material should ideally be comprised of a monodisperse distribution of sub-100 nm particles. The nanometer-sized particles bring an added benefit of significant melting point depression of its bulk value [46], which is important for processing on temperature-sensitive (i.e., flexible) substrates. The Ag nanopaste used for LDT contains approximately 12-nm-sized particles as specified by the manufacturer. In addition, the size of these nanoparticles should allow the laser printing of feature dimensions down to ≈10 times the particle size. By comparison, laser transfer of a silver paste containing 1–4 μm particles, although it is extremely viscous (>280 Pa s), does not produce congruent features as high quality as those in LDT [47].

A quantitative study of the dependence of the threshold transfer fluence on a round voxel thickness and size is shown in Figure 10.10a,b for LDT of Ag nanopaste [48, 49]. When a voxel separates from the donor layer by brittle fracture, energy is required to create the new surfaces at the perimeter of the voxel [50]. This energy, E, is proportional to the surface area of the new surfaces, as given by

$$E \propto Dt \tag{10.1}$$

where D is the voxel diameter, and t is the thickness. The laser fluence, F, in the voxel area, A, is given by

$$F(\equiv E/A) \propto Dt/A$$

$$\therefore \quad F \propto \begin{cases} 1/D, & \text{constant } t \\ t \quad , & \text{constant } D \end{cases} \tag{10.2}$$

As seen in Figure 10.10a, the fluence did indeed vary linearly with the reciprocal of the voxel diameter for three different voxel thicknesses as predicted by Eq. (10.2). However, for a fixed voxel size, the threshold fluence varied linearly only for voxel thicknesses $\lesssim$2 μm and saturated for thicknesses above that (Figure 10.10b). Using a rough estimate of 2 μm as the thermal penetration depth, this behavior was explained by an increase of thermal losses up to a donor layer thickness of 2 μm, above which the thermal losses saturated for higher thicknesses [49].

As a direct confirmation of the voxel separation mechanism during LDT, still frames captured from a high-speed (10^5 frames/s) video of a voxel released from the donor layer is shown in Figure 10.10c [48, 49]. No receiving substrate was present. The absence of any shock waves or deformation of the voxel anywhere in the LDT process indicates that the voxel separates from the donor layer by brittle fracture, which confirms the earlier assumptions made in Eq. (10.1). Note that

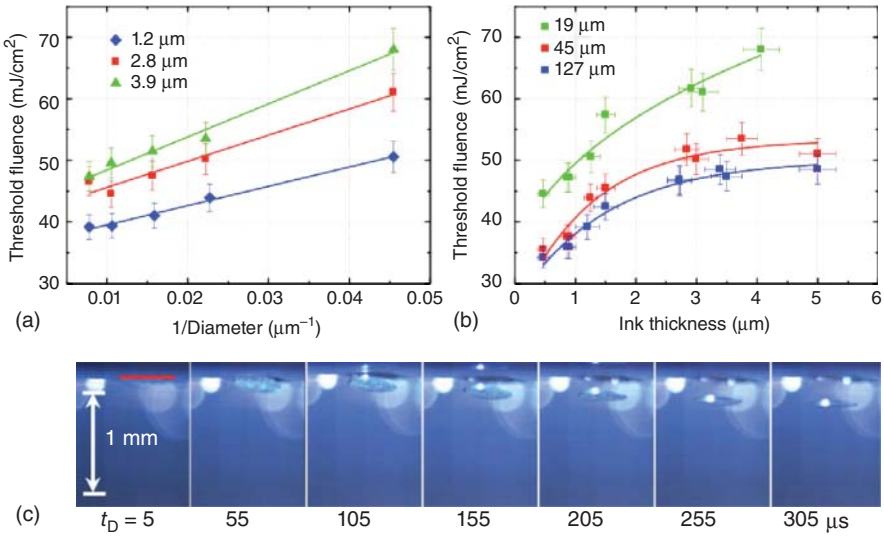

Figure 10.10 (a) Minimum laser transfer fluence versus 1/*D* (voxel diameter) for three different donor layer thicknesses. (b) Minimum laser transfer fluence versus donor layer thickness for three different voxel diameters. Error bars correspond to uncertainties in the measurement of the donor layer thickness and laser fluence. Lines are visual guides only. (c) Still frame images of a Ag nanopaste voxel released from the donor layer during LDT (with no receiving substrate). The red line in the first frame shows the location and size of the laser pulse (~475 µm diameter). Time delay (t_D) is measured from the start of the laser trigger. The laser transfer fluence was 52 mJ/cm^2, and the velocity of the voxel was calculated to be 0.9 m/s. (Mathews *et al*. 2013 [49]. Reproduced with permission from Journal of Applied Physics.)

the low velocity (0.9 m/s) of the released voxel in LDT, as calculated from the still frame images, is more than an order of magnitude lower than those seen in other LIFT processes [49].

From the characterization of the LDT process presented here, some general observations for its success can be summarized. These requirements for a successful congruent transfer are based on the donor material, laser beam, and transfer protocol.

First, the donor material in LDT must be both high-viscosity and strongly absorptive at the laser wavelength (usually achieved with nanoparticles). High-viscosity ink without nanoparticles does not produce congruent transfers [47], and obviously, nanoparticle ink of low viscosity (as for inkjet) produces droplets. (It is possible to "dry" low-viscosity ink to increase its viscosity (to ~0.4 Pa s) to achieve congruent-like transfers, but the operating window is narrower and the quality is lower than that of the features made by LDT.)

The donor material must be uniform in thickness and composition on the donor substrate. Since the absorbed laser energy is converted into a (small) expanding vapor pocket, any variation in donor layer thickness would affect the uniformity of release and even structural integrity of the voxel. The composition must also remain stable enough to perform LDT. The nanopastes used for the donor material often contain volatiles that must equilibrate with the ambient

conditions before attempting LDT. During this process, the nanoparticles must remain well dispersed and not agglomerate as this will affect its optical absorption properties.

The next requirement for successful congruent transfer is the optical and spatial quality of the laser beam. The wavelength of the laser beam must be chosen to be sufficiently absorbed by the donor material. Then, the spatial beam profile must be as uniform as possible since variations in fluence may cause uneven or broken release of the voxel. Typically, this uniformity can be achieved with a multimode laser or by using "beam shapers" with a Gaussian laser beam and carefully imaging this profile onto the donor layer. Finally, the laser must provide pulses of sufficiently stable energy and beam profile varying by less than $\pm$ 5%.

When the donor material and laser requirements are met, the donor layer thickness, laser fluence, and voxel or feature size must be chosen together as these three parameters are closely interrelated. These three parameters will then determine the operating fluence window and the donor-to-receiving substrate gap for the best-quality transfers. For a feature that has a wide range of feature sizes, some laser beam shaping with a SLM may be required to produce consistent congruent transfers.

The characterization of LDT operating parameters and the criteria for its success serve as general guidelines for producing congruent laser transfers. Although LDT was performed exclusively with silver nanopaste, its general concepts and process requirements should be applicable to congruent laser transfers of other materials as well.

10.5 Issues and Challenges

In order for congruent laser transfer to reach its full potential, some materials and processing issues must be addressed. The most important issue concerns the donor material and the donor substrate. As both the viscosity and the particle size are critical for the success of LDT, a wider range of viscosities (0.4–100 Pa s) and particle sizes (10–100 nm) needs to be examined to determine their effect on LDT. In addition, the donor material typically contains volatile components that must be removed before laser transfer. Active techniques such as forced air drying, vacuum oven, and hot plate, and a passive method such as storage in a desiccator have been used to remove the volatiles. Ideally, the composition of the donor material should be adjusted beforehand to the proper viscosity so it can be used immediately for LDT and remain useable with a reasonable lifetime afterward. Lastly, although LDT has met with great success with silver nanopaste, the donor source material should be expanded to include different metals, dielectrics, and other materials used in microfabrication. It is both promising and fortunate that the many successes of LDT were derived from the use of a commercially available screen-printing ink as the donor material. However, the process would be more straightforward and reliable if the donor material properties were specifically tailored for congruent laser transfer (e.g., viscosity, volatile content).

Next, there are engineering issues associated with the fabrication and implementation of the donor substrate. As the thickness of the donor layer is critical to

the success of LDT, the donor material must be applied uniformly to the donor substrate in depth and areal coverage. Automating this process by controlling the amount of donor material, blade pressure, and speed should result in a more uniform donor layer. In addition, the donor substrate is typically a glass plate or disk containing previously etched wells. An alternative donor substrate could be a flexible "ribbon" as long as it is wavelength-transparent. Finally, the placement, alignment, and positioning of the donor substrate above the receiving substrate must be automated in order to improve throughput, make efficient use of the donor layer, and maintain accurate gap distances between the donor and receiving substrates.

The last (but not least) element crucial to the success of LDT is, of course, the laser itself. The laser fluence window of congruent transfer can be very narrow under certain voxel size and thickness conditions, so the laser energy fluctuations should be minimized to a few percent. Just as importantly, the spatial profile of the laser beam should be stable as well. Currently, many laser manufacturers claim pulse energy fluctuations of less than 1% for Gaussian beams to a few percent for multimode beams; however, no specifications have been given for the spatial beam profile, which has been found to vary sufficiently to affect transfer quality. Further work is also needed to understand and design the spatial beam profiles for transferring features with varying-size resolutions since the laser transfer fluence is strongly affected by voxel size and thickness.

10.6 Summary

The transferred features and the processing conditions of congruent laser or laser decal transfer are unique among laser forward-transfer processes. The ability to laser print voxels that are congruent in shape and similar in size to the features of a user design builds confidence and increases reliability in the concept-to-product life cycle. The implementation of a SLM with congruent laser transfer enables dynamic parallel processing and laser beam structuring of a LDW process, which represents a major advance in this technology. As demonstrated with silver nanopastes the process can print sharp-edged features with voxel sizes from a few micrometers to over a 1 mm (limited by available laser energy) and voxel heights from a few hundred nanometers to over a few microns (limited by voxel size-to-height aspect ratio). Depending on the voxel size and thickness, the process can tolerate donor-to-receiving substrate gaps from 5 to greater than 75 μm. Furthermore, freestanding structures made of silver nanopaste can be made without the use of any sacrificial or release layers. The silver nanopaste structures made by LDT demonstrated functional properties such as electrical transport (DC to microwave), THz resonance, and dynamic mechanical response.

The congruent laser transfer process offers a compelling alternative to other (laser) direct-write processes for microfabrication. Although the results and characterization of LDT were demonstrated for silver nanopaste thus far, the concept and benefits of congruent laser transfer have been clearly established,

and research into its mechanism and development of materials specific to LDT should be further explored. Its ability to direct-write high-quality thin-film-like features with functional properties (and in a parallel manner) is a unique laser transfer process, which complements photolithography and provides an alternative tool for laser additive micromanufacturing.

Acknowledgment

This work was funded by the Office of Naval Research (ONR) through the Naval Research Laboratory Basic Research Program.

References

1 Braudy, R.S. (1969) Laser writing. *Proc. IEEE*, **57** (10), 1771–1772.
2 Bohandy, J., Kim, B., and Adrian, F.J. (1986) Metal deposition from a supported metal film using an excimer laser. *J. Appl. Phys.*, **60** (4), 1538–1539.
3 Piqué, A., Auyeung, R.C.Y., Kim, H., Charipar, N.A., and Mathews, S.A. (2016) Laser 3D micro-manufacturing. *J. Phys. D: Appl. Phys.*, **49** (22), 223001.
4 Tolbert, W.A., Lee, I.Y.S., Doxtader, M.M., Ellis, E.W., and Dlott, D.D. (1993) High-speed color imaging by laser-ablation transfer with a dynamic release layer - fundamental mechanisms. *J. Imaging Sci. Technol.*, **37** (4), 411–422.
5 Kattamis, N.T., Purnick, P.E., Weiss, R., and Arnold, C.B. (2007) Thick film laser induced forward transfer for deposition of thermally and mechanically sensitive materials. *Appl. Phys. Lett.*, **91** (7), 171120.
6 Kattamis, N.T., McDaniel, N.D., Bernhard, S., and Arnold, C.B. (2009) Laser direct write printing of sensitive and robust light emitting organic molecules. *Appl. Phys. Lett.*, **94** (10), 103306.
7 Piqué, A., Chrisey, D.B., Auyeung, R.C.Y., Fitz-Gerald, J., Wu, H.D., McGill, R.A., Lakeou, S., Wu, P.K., Nguyen, V., and Duignan, M. (1999) A novel laser transfer process for direct writing of electronic and sensor materials. *Appl. Phys. A Mater. Sci. Process.*, **69**, S279–S284.
8 Arnold, C.B., Serra, P., and Piqué, A. (2007) Laser direct-write techniques for printing of complex materials. *MRS Bull.*, **32** (1), 23–31.
9 Piqué, A., Arnold, C.B., Kim, H., Ollinger, M., and Sutto, T.E. (2004) Rapid prototyping of micropower sources by laser direct-write. *Appl. Phys. A Mater. Sci. Process.*, **79** (4–6), 783–786.
10 Kim, H., Auyeung, R.C.Y., and Piqué, A. (2007) Laser-printed thick-film electrodes for solid-state rechargeable Li-ion microbatteries. *J. Power Sources*, **165** (1), 413–419.
11 Kim, H., Kushto, G.P., Arnold, C.B., Kafafi, Z.H., and Piqué, A. (2004) Laser processing of nanocrystalline TiO2 films for dye-sensitized solar cells. *Appl. Phys. Lett.*, **85** (3), 464–466.
12 Ollinger, M., Kim, H., Sutto, T., and Piqué, A. (2006) Laser printing of nanocomposite solid-state electrolyte membranes for Li micro-batteries. *Appl. Surf. Sci.*, **252** (23), 8212–8216.

13 Piqué, A., Arnold, C.B., Pratap, B., Auyeung, R.C.Y., Kim, H.S., and Weir, D.W. (2003) Laser direct-write of metal patterns for interconnects and antennas. Proceedings of SPIE, vol. 4977, pp. 602–608.

14 Auyeung, R.C.Y., Kim, H., Mathews, S.A., and Piqué, A. (2007) Laser direct-write of metallic nanoparticle inks. *J. Laser Micro/Nanoeng.*, **2** (1), 21–25.

15 Piqué, A., Auyeung, R.C.Y., Metkus, K.M., Kim, H., Mathews, S., Bailey, T., Chen, X.H., and Young, L.J. (2008) Laser decal transfer of electronic materials with thin film characteristics. Proceedings of SPIE, vol. 6879, pp. 687911–1–687911–8.

16 Xu, J., Liu, J., Cui, D., Gerhold, M., Wang, A.Y., Nagel, M., and Lippert, T.K. (2007) Laser-assisted forward transfer of multi-spectral nanocrystal quantum dot emitters. *Nanotechnology*, **18** (2), 025403–1–025403–6.

17 Fardel, R., Nagel, M., Nuesch, F., Lippert, T., and Wokaun, A. (2007) Fabrication of organic light-emitting diode pixels by laser-assisted forward transfer. *Appl. Phys. Lett.*, **91**, 061103–1–061103–3.

18 Ko, S.H., Pan, H., Ryu, S.G., Misra, N., Grigoropoulos, C.P., and Park, H.K. (2008) Nanomaterial enabled laser transfer for organic light emitting material direct writing. *Appl. Phys. Lett.*, **93** (15), 151110.

19 Ihlemann, J. and Weichenhain-Schriever, R. (2010) Laser-induced congruent forward transfer of SiO (x) –layers. *Appl. Phys. A Mater. Sci. Proc.*, **101** (3), 483–486.

20 Ihlemann, J. and Weichenhain-Schriever, R. (2014) Patterned deposition of thin SiO_X-films by laser induced forward transfer. *Thin Solid Films*, **550**, 521–524.

21 Kaur, K.S., Feinaeugle, M., Banks, D.P., Ou, J.Y., Di Pietrantonio, F., Verona, E., Sones, C.L., and Eason, R.W. (2011) Laser-induced forward transfer of focussed ion beam pre-machined donors. *Appl. Surf. Sci.*, **257** (15), 6650–6653.

22 Breckenfeld, E., Kim, H., Auyeung, R.C.Y., and Piqué, A. (2016) Laser-induced forward transfer of Ag nanopaste. *J. Vis. Exp.*, **109**, e53728.

23 Piqué, A., Auyeung, R.C.Y., Kim, H., Metkus, K.M., and Mathews, S.A. (2008) Digital microfabrication by laser decal transfer. *J. Laser Micro/Nanoeng.*, **3** (3), 163–169.

24 Alloncle, A.P., Ailuno, J., Rapp, L., and Delaporte, P. (2012) Laser direct-printing for inter-connectivity and manufacturing of organic electronic components. *Int. Symp. High Power Laser Ablation*, **2012** (1464), 358–364.

25 Wang, J., Auyeung, R.C.Y., Kim, H., Charipar, N.A., and Piqué, A. (2010) Three-dimensional printing of interconnects by laser direct-write of silver nanopastes. *Adv. Mater.*, **22** (40), 4462–4466.

26 Coonrod, J. and Rautio, B. (2012) Comparing microstrip and CPW performance. *Microwave J.*, **55** (7), 74–86.

27 Breckenfeld, E., Kim, H., Auyeung, R.C.Y., Charipar, N., Serra, P., and Piqué, A. (2015) Laser-induced forward transfer of silver nanopaste for microwave interconnects. *Appl. Surf. Sci.*, **331**, 254–261.

28 Boettcher, U., Li, H., de Callafon, R.A., and Talke, F.E. (2011) Dynamic flying height adjustment in hard disk drives through feedforward control. *IEEE Trans. Magn.*, **47** (7), 1823–1829.

29 Piqué, A., Kim, H., Auyeung, R.C.Y., Beniam, I., and Breckenfeld, E. (2016) Laser-induced forward transfer (LIFT) of congruent voxels. *Appl. Surf. Sci.*, **374**, 42–48.

30 Auyeung, R.C.Y., Kim, H., Birnbaum, A.J., Zalalutdinov, M., Mathews, S.A., and Piqué, A. (2009) Laser decal transfer of freestanding microcantilevers and microbridges. *Appl. Phys. A*, **97** (3), 513–519.

31 Birnbaum, A.J., Auyeung, R.C., Wahl, K.J., Zalalutdinov, M., Laracuente, A.R., and Piqué, A. (2010) Laser printed micron-scale free standing laminate composites: process and properties. *J. Appl. Phys.*, **108** (8), 083526.

32 Birnbaum, A.J., Zalalutdinov, M.K., Wahl, K.J., and Piqué, A. (2011) Fabrication and response of laser-printed cavity-sealing membranes. *J. Microelectromech. Sys.*, **20** (2), 436–440.

33 Auyeung, R.C.Y., Kim, H., Charipar, N.A., Birnbaum, A.J., Mathews, S.A., and Piqué, A. (2011) Laser forward transfer based on a spatial light modulator. *Appl. Phys. A*, **102** (1), 21–26.

34 Piqué, A., Auyeung, R.C.Y., Smith, A.T., Kim, H., Mathews, S.A., Charipar, N.A., and Kirleis, M.A. (2013) Laser transfer of reconfigurable patterns with a spatial light modulator. Proceedings of SPIE, vol. 8608, UNSP 86080K.

35 Auyeung, R.C.Y., Kim, H., Mathews, S., and Piqué, A. (2015) Spatially modulated laser pulses for printing electronics. *Appl. Opt.*, **54** (31), F70–F77.

36 Auyeung, R.C.Y., Kim, H., Mathews, S., and Piqué, A. (2015) Laser forward transfer using structured light. *Opt. Express*, **23** (1), 422–430.

37 Piqué, A., Kim, H., and Auyeung, R.C.Y. (2013) Laser forward transfer of functional materials for digital fabrication of microelectronics. *J. Imaging Sci. Technol.*, **57** (4), 040404.

38 Rapp, L., Constantinescu, C., Larmande, Y., Alloncle, A.P., and Delaporte, P. (2014) Smart beam shaping for the deposition of solid polymeric material by laser forward transfer. *Appl. Phys. A*, **117** (1), 333–339.

39 Kim, H., Duocastella, M., Charipar, K.M., Auyeung, R.C.Y., and Piqué, A. (2013) Laser printing of conformal and multi-level 3D interconnects. *Appl. Phys. A*, **113** (1), 5–8.

40 Kim, H., Melinger, J.S., Khachatrian, A., Charipar, N.A., Auyeung, R.C.Y., and Piqué, A. (2010) Fabrication of terahertz metamaterials by laser printing. *Opt. Lett.*, **35** (23), 4039–4041.

41 Piqué, A., Charipar, N.A., Kim, H., Kirleis, M.A., Auyeung, R.C.Y., Smith, A.T., Metkus, K.M., and Mathews, S.A. (2012) Realization of metamaterial structures by non-lithographic processes. Proceedings of SPIE, vol. 8455, p. 845514.

42 Smith, A.T., Simonson, D., Charipar, N.A., and Piqué, A. (2012) Laser direct write fabrication of meta-antennas for electro-optic conversion. *J. Laser Micro/Nanoeng.*, **7** (3), 306–310.

43 Birnbaum, A.J., Kim, H., Charipar, N.A., and Piqué, A. (2010) Laser printing of multi-layered polymer/metal heterostructures for electronic and MEMS devices. *Appl. Phys. A*, **99** (4), 711–716.

44 Constantinescu, C., Diallo, A.K., Rapp, L., Cremillieu, P., Mazurczyk, R., Serein-Spirau, F., Lere-Porte, J.P., Delaporte, P., Alloncle, A.P., and

Videlot-Ackermann, C. (2015) Laser-induced forward transfer of multi-layered structures for OTFT applications. *Appl. Surf. Sci.*, **336**, 11–15.

45 Evanoff, D.D. and Chumanov, G. (2004) Size-controlled synthesis of nanoparticles. 2. Measurement of extinction, scattering, and absorption cross sections. *J. Phys. Chem. B.*, **108** (37), 13957–13962.

46 Buffat, P. and Borel, J.P. (1976) Size effect on melting temperature of gold particles. *Phys. Rev. A*, **13** (6), 2287–2298.

47 Munoz-Martin, D., Brasz, C.F., Chen, Y., Morales, M., Arnold, C.B., and Molpeceres, C. (2016) Laser-induced forward transfer of high-viscosity silver pastes. *Appl. Surf. Sci.*, **366**, 389–396.

48 Mathews, S.A., Auyeung, R.C.Y., and Piqué, A. (2012) Analysis and characterization of the laser decal transfer process. Proceedings of SPIE, vol. 8244, p. 82440A.

49 Mathews, S.A., Auyeung, R.C.Y., Kim, H., Charipar, N.A., and Piqué, A. (2013) High-speed video study of laser-induced forward transfer of silver nano-suspensions. *J. Appl. Phys.*, **114** (6), 064910.

50 Reed-Hill, R.E. (1973) *Physical Metallurgy Principles*, 2nd edn, PWS-KENT Publishing Co., Boston, MA, p. 758, (cited in Mathews, 2013).

11

Laser Printing of Nanoparticles

Urs Zywietz, Tim Fischer, Andrey Evlyukhin, Carsten Reinhardt, and Boris Chichkov

Leibniz Universität Hannover and Laser Zentrum Hannover e.V., Nanotechnology Department, Hollerithallee 8, Hannover 30419, Germany

11.1 Introduction, Setup, and Motivation

In this chapter, a laser-based printing process for the controlled fabrication of spherical nanoparticles is introduced. Spherical nanoparticles can have unique optical properties. Silicon nanoparticles, for example, provide strong electric and magnetic dipole responses within the visible range [1]. This property provides new possibilities for advanced light control at the nanoscale. The simultaneous excitation of both electric and magnetic dipoles within a single nanoparticle generates a strongly anisotropic scattering pattern [2]. For one wavelength, the scattering can be only in the forward direction while for another wavelength, scattering in the forward direction can be strongly suppressed.

Another important and interesting problem of modern nano-optics, where the concept of nanoparticles plays a principal role, is the creation of nanolasers for the generation of coherent electromagnetic fields at the subwavelength scale. Silicon nanoparticles that exhibit low ohmic losses within the visible and infrared spectral ranges are interesting candidates for use as nanolaser cavities. By coating them with an amplifying shell or doping them with laser active species, they can form a nanolaser with lasing modes associated to the Mie resonances of the nanoparticle [3, 4].

The wide range of new application opportunities of these nanoparticles cannot be exploited without a suitable method for a highly controlled fabrication of nanoparticles with precise positions, shapes, and sizes.

For the nanoparticle printing process, which is described in this chapter, femtosecond laser pulses are applied to generate and transfer single nanoparticles from a donor substrate to another receiver substrate. In this respect, thin films, as well as bulk materials, can be used as donor materials. In both cases, the irradiation by tightly focused femtosecond laser pulses results in the controlled melting of a defined volume and nanoparticle ejection.

It has been shown that femtosecond laser printing can be applied to controlled fabrication of metal (Au, Ag, Cu, Fe, etc.) and semiconductor (Si, Ge, etc.)

Laser Printing of Functional Materials: 3D Microfabrication, Electronics and Biomedicine,
First Edition. Edited by Alberto Piqué and Pere Serra.
© 2018 Wiley-VCH Verlag GmbH & Co. KGaA. Published 2018 by Wiley-VCH Verlag GmbH & Co. KGaA.

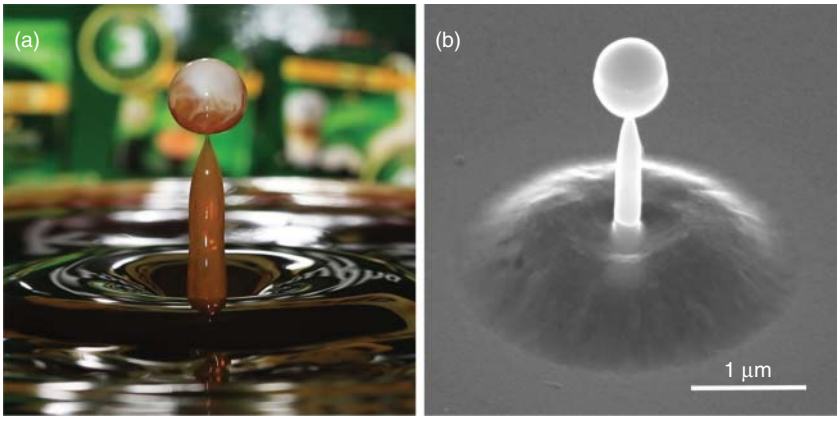

Figure 11.1 Laser printing of gold nanoparticles. (a) Photograph of a milk droplet in a coffee cup. (www.digifo-hka.de.) (b) SEM image of a gold surface subsequent to laser pulse irradiation.

nanoparticles with precisely adjustable radii between 100 and 800 nm and their accurate positioning on a desired substrate [5–8].

Furthermore, it has been demonstrated that the material phase of individual laser-printed Si nanoparticles can be varied from amorphous to crystalline. The Si nanoparticles generated by laser printing are initially in amorphous phase (a-Si). Using additional laser pulse irradiation, the amorphous nanoparticles can be controllably transformed into crystalline particles (c-Si) or into particles with more complex mixed amorphous/crystalline phases, providing possibilities to tune the optical properties of individual Si nanoparticles [5] (Figure 11.1).

11.2 Laser-Induced Transfer

Our printing process is based on the laser-induced transfer (LIT) technology and has been developed and used for the generation of monodisperse and spherical nanoparticles from different materials. The nanoparticle transfer can be realized in two directions. For the transfer of nanoparticles in the direction of laser beam propagation, the process is called laser-induced forward transfer (LIFT) while it is called laser-induced backward transfer (LIBT) for nanoparticles transferred in the opposite direction. Schematic representations of both processes are shown in Figures 11.2 and 11.3.

By using a thin gold layer as a donor material, the generation process can be described as follows. Due to the surface tension of molten material and the resulting pressure and temperature gradients, the liquid metal forms a nanobump with a jet-like protrusion at the center. On top of this protrusion, an almost perfectly spherical nanoparticle is produced. An example of this unique process is shown in Figure 11.1b. This figure demonstrates a SEM image of a 50 nm gold layer, which was irradiated with a single femtosecond laser pulse.

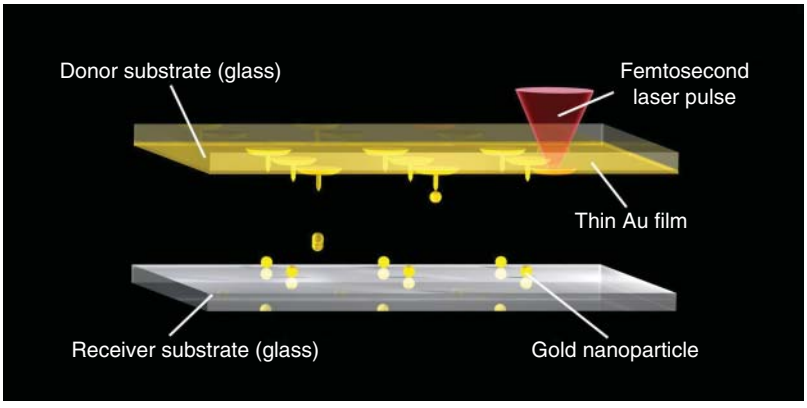

Figure 11.2 Schematic illustration of femtosecond laser printing of nanoparticles in forward direction (LIFT).

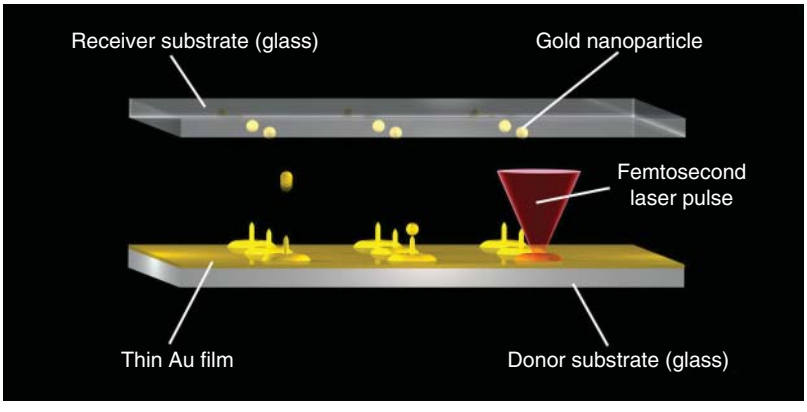

Figure 11.3 Schematic illustration of femtosecond laser printing of nanoparticles in backward direction (LIBT).

The hydrodynamic process taking place on the gold surface is comparable to that of a water droplet hitting the surface of a liquid (see Figure 11.1a). The evolving structures appear due to the strong surface tension at the liquid–air interface. By slightly increasing the laser pulse energy, a single spherical nanoparticle is ejected perpendicular to the gold surface toward another substrate. The size of the nanoparticle depends on the volume of laser–molten material and can be varied by changing the laser focusing conditions and film thickness. Laser-induced processes leading to the ejection of a liquid droplet from gold film surface have been studied in our previous publications [9–11].

In our experiments, a commercial femtosecond laser system (Tsunami Femtosecond Oscillator and Spitfire Amplifier, Spectra Physics) is used, providing laser pulses at 800 nm central wavelength, with maximum pulse energies of up to 3 mJ, and pulse duration of 50 fs at the repetition rate of 1 kHz. For the controlled fabrication of nanoparticles, single-laser pulses with energies in the range of

1–100 nJ are used. Laser pulses are tightly focused by a long-distance microscope objective (Nikon) with 50× magnification and a numerical aperture (NA) of 0.45. For the LIBT process, the long working distance of 17 mm allows irradiation of the target surface through the receiver glass substrate without noticeable distortion of the laser beam profile. According to the relation $d = \lambda/(2\mathrm{NA})$, the estimated FWHM-diameter of the laser pulse focus is $d = 890$ nm.

11.3 Materials for Laser Printing of Nanoparticles

As it was mentioned before, the laser printing process is suitable for the generation of nanoparticles from various materials. In this respect, it is beneficial when the donor material has strong absorption at the applied laser wavelength. In Figure 11.4, SEM images of the printing process for different materials are presented. The four images on the left side show the donor material surface after single-pulse laser irradiation. From left to right, the laser pulse energy is increased. The fourth image shows the donor substrate after the successful nanoparticle transfer. On the right side, the transferred nanoparticles on the receiver substrate are displayed. The graphic reveals that irradiation of different materials is accompanied by a broad variety of structural changes within the material. Thus, the transfer of nanoparticles is based on different melting dynamics for each material.

11.4 Laser Printing from Bulk-Silicon and Silicon Films

The generation of silicon nanoparticles has been strongly developed during the past years. The interest in silicon nanoparticles originates from their unique optical properties. With a size of 100–200 nm, they provide electric and magnetic dipole resonances within the visible spectral range. At the same time, they are characterized by very low optical losses compared to plasmonic nanoparticles. The generation of silicon nanoparticles with pronounced Mie resonances has been performed by different chemical [12–14] and physical [1, 2, 5, 6, 15] methods with a broad variety of results.

In this respect, the excitation of magnetic and electric dipole modes within the visible spectral range has also been observed in silicon nanodiscs and nanocylinders [16–19]. Such structures have been generated by a combination of electron lithography and reactive ion etching. Despite the fact that this method allows high precision, it is expensive and time-consuming. In contrast to our laser printing technique, lithographic methods require a series of processing steps.

The generation of silicon nanoparticles by laser printing can be realized using a polished silicon wafer as a donor substrate. The irradiation of the surface of the silicon wafer by single femtosecond laser pulses results in structural changes as they are shown in Figure 11.4 (row 4). Silicon is one of the few elements whose density increases during the phase transition (solid–liquid). This means that the material that has been melted by the laser pulse occupies less volume, which leads

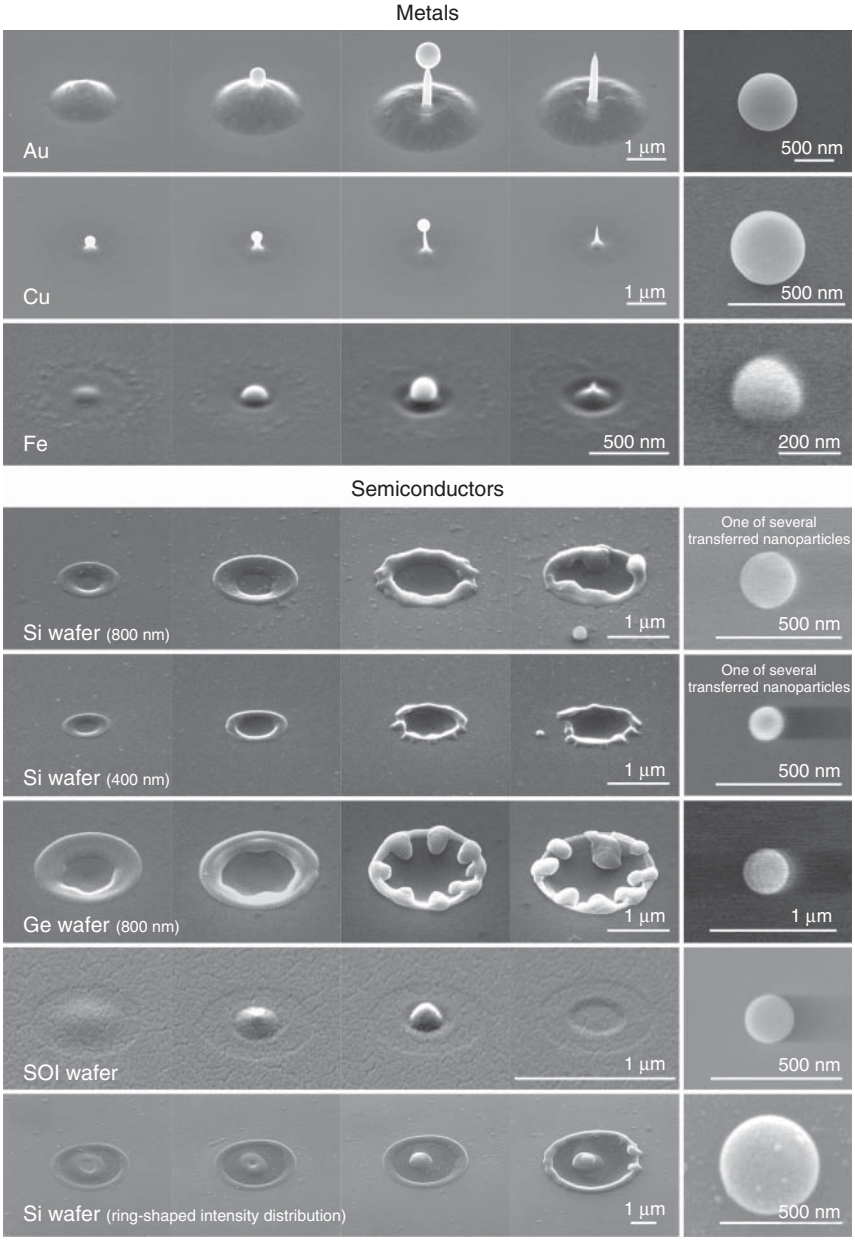

Figure 11.4 SEM images of the laser printing process of different materials. The four images on the left side show the donor material surface subsequent to single-pulse laser irradiation. From left to right, the laser pulse energy is increased. The fourth image shows the donor substrate after the successful nanoparticle transfer. On the right side, transferred nanoparticles on the receiver substrate are displayed.

to the material depression within the molten area. This depression is followed by the radial motion of liquid silicon toward the lower laser intensity edge of the focal spot. This motion appears due to the temperature-dependent differences in the surface tension of molten silicon. The more heated area in the center has lower surface tension [20]; therefore, molten silicon moves toward the colder regions. SEM analysis shows that the molten silicon forms a liquid ring at the edge of the focal spot (see Figure 11.4 row 4). At higher laser pulse energies, this liquid ring breaks up into several nanoparticles, which are ejected toward the receiver substrate. The breakup of the liquid ring has its origin in the Rayleigh–Plateau instability [21]. Surface tension is the driving force behind this phenomenon, as it tends to reduce the surface area by decreasing the radius of a fluid column.

For each pulse energy, the diameters of the ejected nanoparticles are statistically distributed. In order to determine the influence of the applied laser pulse energy as well as the laser wavelength on the size distribution of the ejected nanoparticles, diameters of 1000 transferred nanoparticles have been measured. Different laser pulse energies as well as two different laser wavelengths (800 and 400 nm) were applied, and the generated silicon nanoparticles subsequently analyzed with dark-filed microscopy and SEM. Results are shown in Figure 11.5. Computer-based image evaluation of the SEM images has been performed to determine the diameter of each individual nanoparticle. The normalized size distributions for both laser wavelengths (400 and 800 nm) are plotted in Figure 11.6. Experiments revealed that the applied laser pulse energy (in the range of 75–100 nJ) has no influence on the size distribution of the generated nanoparticles. For 800 nm laser wavelength, a pronounced maximum in the size distribution, for all considered pulse energies, is observed for particle diameters of 205 nm. The shorter laser wavelength (400 nm) results in a smaller average nanoparticle diameter. The maximum in the size distribution for 400 nm can be observed for particle diameters of 140 nm. To identify the origin of this surprising result, further investigations are required.

The described printing process of silicon nanoparticles is of course limited in its precision concerning the size and localization of nanoparticles. Each laser pulse ejects several nanoparticles with different diameters toward the receiver substrate. Therefore, it is not the method of choice for a controlled generation and precise deposition of single nanoparticles. The SEM images in Figure 11.4 show that the molten silicon forms a liquid ring at the edge of the focal spot. For the generation of single nanoparticles, concentration of liquid material at the center of the irradiated area is necessary. For this purpose, a ring-shaped laser beam profile within the focus has been used. This beam modification leads to the desired melting dynamics. By using a defined pulse energy, it enables the generation of single nanoparticles directly from a bulk silicon wafer. A schematic representation of the process is shown in Figure 11.7c. The melting dynamics on the donor substrate, as well as the resulting silicon nanoparticle, are shown in Figure 11.4 (row 8). With this method, silicon nanoparticles with a minimum diameter of 400 nm have been generated. In our experiments, the ring-shaped intensity distribution is realized by placing a chromium mask in the laser beam path. The image of this mask is 50× demagnified and projected onto the silicon surface by a 20 mm planoconvex lens and the long-distance microscope objective.

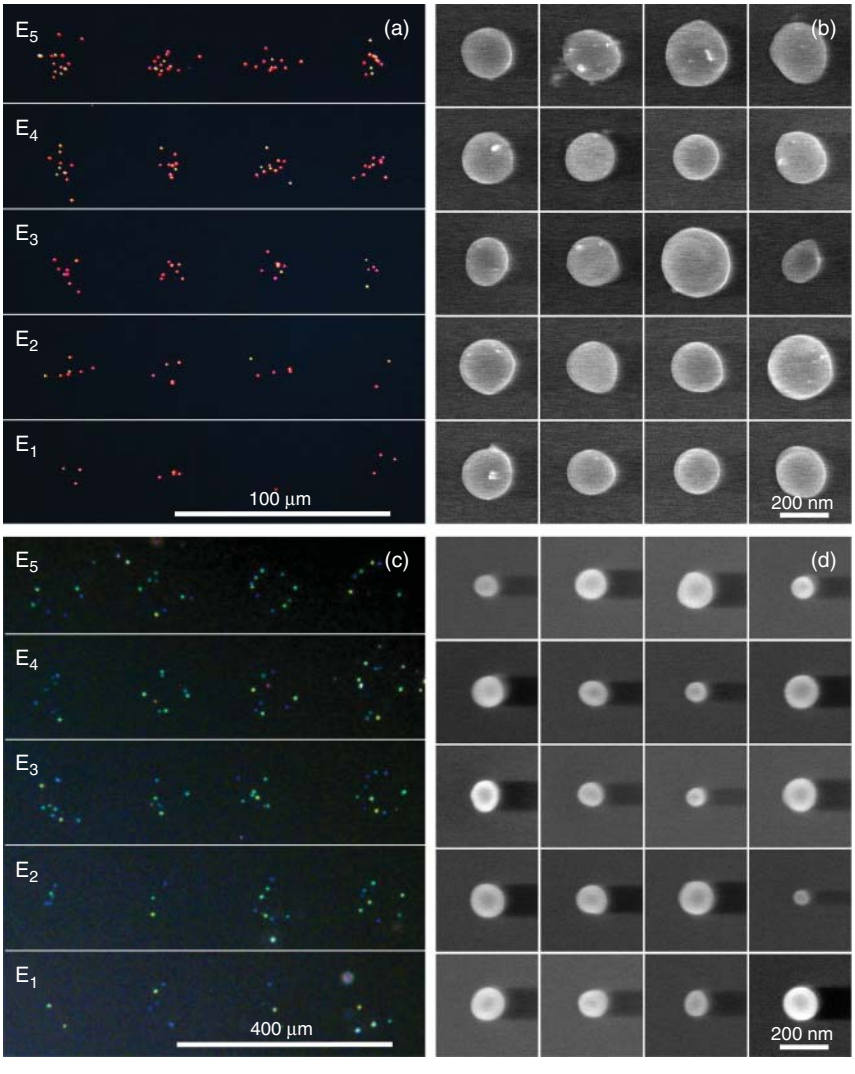

Figure 11.5 Laser-printed silicon nanoparticles on a glass substrate. For the printing process, 800 nm (a,b) and 400 nm (c,d) laser wavelengths have been used. The dark-field microscopic images reveal the different light scattering of the printed nanoparticles (a,c). The influence of the laser wavelength on the nanoparticle diameter can be seen in the SEM images (b,d).

Laser printing of single nanoparticles with a modified laser beam profile is also possible with germanium as a donor material. The ring-shaped intensity profile leads to comparable structural changes on the germanium wafer as they arise on the silicon wafer. In Figure 11.8, SEM images of the germanium donor and receiver substrates after the printing process are shown.

A unique property of silicon nanoparticles is their pronounced magnetic and electric dipole resonances. These resonances are located in the visible spectrum if the nanoparticle diameter is in the range of 100–200 nm. The previously

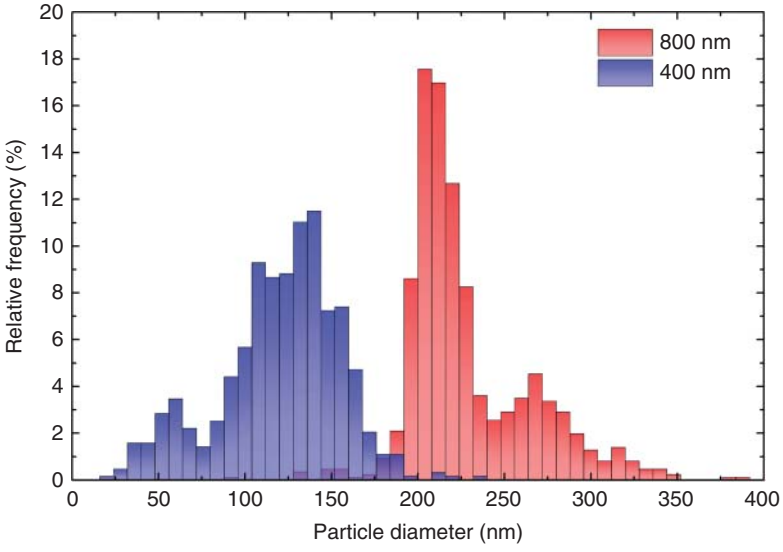

Figure 11.6 Size distribution of silicon nanoparticles that have been printed by two different laser wavelengths from a silicon wafer.

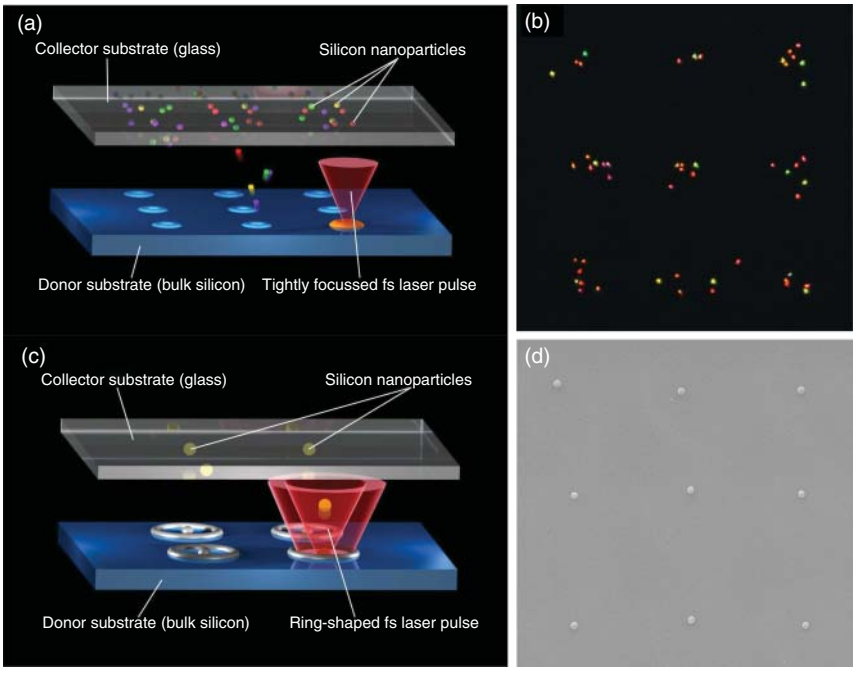

Figure 11.7 Schematic illustration of femtosecond laser printing of nanoparticles using Gaussian (a) and ring-shaped (c) intensity distribution on the target surface. Resulting nanoparticles on the receiver substrate are shown on the right side (b,d).

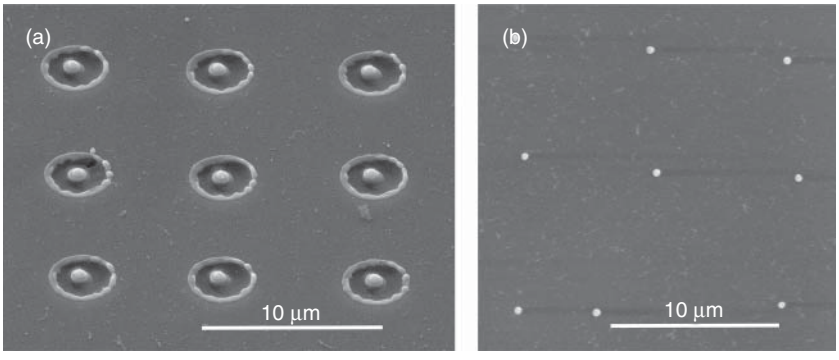

Figure 11.8 SEM images of the donor (a) and the receiver (b) substrate (Germanium) subsequent to laser printing using ring-shaped intensity profile.

described method is suitable for the controlled generation of single silicon nanoparticles with a minimum diameter of 400 nm. Another possibility to controllably generate single silicon nanoparticles with sizes in the range of 100–200 nm is to use a silicon-on-insulator (SOI) wafer as a donor substrate [5]. In Figure 11.9a, a schematic representation of the laser printing process of silicon nanoparticles from an SOI substrate is shown. Resulting nanoparticles on a glass receiver substrate are shown in the dark-field microscopic image in Figure 11.9b. Laser printing of silicon nanoparticles from an SOI substrate allows to controllably generate and precisely deposit nanoparticles on a receiver substrate. From the inset in Figure 11.9b, a nanoparticle diameter of 160 nm can be measured. During illumination of the SOI wafer by a single tightly focused Gaussian laser pulse, absorption in the top Si layer leads to ultrafast heating

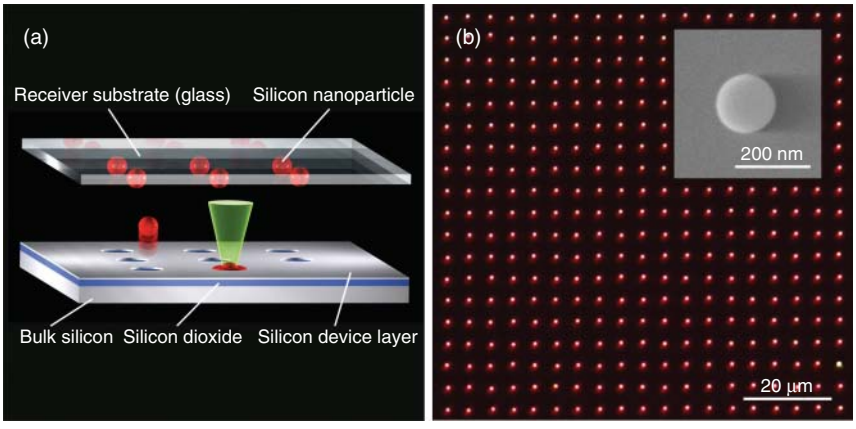

Figure 11.9 (a) Schematic illustration of femtosecond laser printing of nanoparticles. A silicon-on-insulator (SOI) wafer was used as a target to transfer spherical Si nanoparticles from 50 nm crystalline Si layer onto the transparent glass receiver substrate. (b) Array of several hundreds of amorphous Si nanoparticles (diameter of 160 nm) fabricated by this method and visualized with dark-field microscopy. The inset shows a SEM image of a single Si nanoparticle in this array.

and local melting of this layer. The oxide substrate (melting temperature of which is much higher) remains unaffected at these laser pulse energies. The liquid phase of silicon has higher density compared with its solid phase, leading to a volume reduction induced by melting. Owing to the surface tension, the molten region contracts to the center and forms a spherical droplet. The droplet acquires an upward-directed momentum, which drives it toward the receiver substrate placed on top of the SOI wafer, where the liquid material solidifies at the surface. The described process is performed in air at atmospheric pressure, and the distance between the receiver and the donor substrate is set to 5 µm. In Figure 11.4 (row 7), the remaining hole within the silicon layer after the transfer is visible. The hole has a diameter of approximately 250 nm. This diameter and the layer thickness of 50 nm result in a nanoparticle diameter of 160 nm. Therefore, the layer thickness is an important parameter to control the nanoparticle diameter. Another parameter that has influence on the diameter is the applied laser pulse energy. Within a certain range of pulse energies, a successful nanoparticle transfer can be realized. If the pulse energy is too low, the melted material remains on the donor substrate. If the laser pulse energy is too high, a fracture of the resulting nanoparticles on the receiver substrate takes place. In our experiments, silicon nanoparticles with diameters in the range of 165–240 nm have been generated. In Figure 11.10, SEM images, as well as dark-field microscopic images, of these nanoparticles are shown. The pulse energy that was used for printing of nanoparticles with the smallest diameter was set to 5 nJ and was increased in steps of 0.1 nJ for bigger nanoparticles. From the dark-field microscopic images, it can be seen that the first two rows of nanoparticles have pronounced dipole resonances within the visible spectral range.

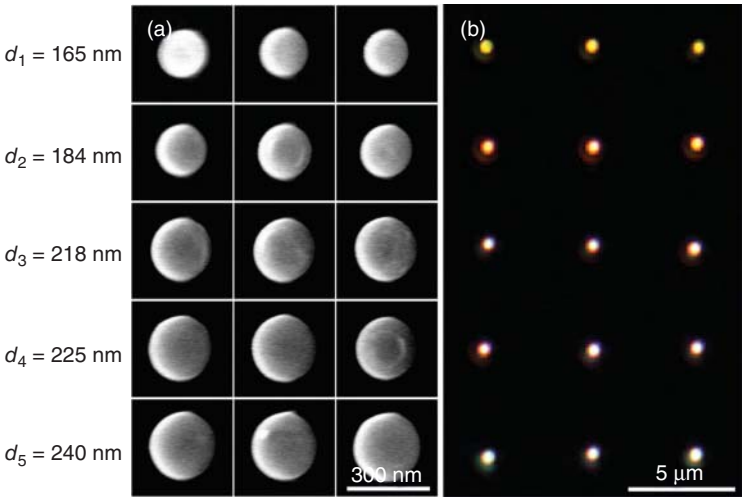

Figure 11.10 (a) SEM images of nanoparticles fabricated at slightly different laser pulse energies starting from 5 nJ. Each line, from top to bottom, corresponds to the laser pulse energy increase of 0.1 nJ. (b) Changes in the optical response of the generated nanoparticles are visualized by dark-field microscopic images. The given nanoparticle diameters represent an average value with a deviation of ±5 nm.

11.5 Magnetic Resonances of Silicon Particles

It is well known from Mie theory that the first and second lowest resonances in the light-scattering spectrum of dielectric spheres in the frequency domain correspond to the magnetic and electric dipole terms [22, 23]. Our group demonstrated for the first time experimentally strong resonant electric and magnetic light scattering by individual spherical Si nanoparticles [1, 5]. This is a very important step for the development of nanoparticle-based metamaterials. In Figure 11.11, a scattering spectrum of a single silicon nanoparticle with pronounced magnetic and electric dipole resonances is shown. The diameter of the nanoparticle is 160 nm. Characterization of the nanoparticle scattering properties has been performed by an optical fiber spectrometer (HR 2000, Ocean Optics), which was connected to a dark-field microscope setup. A dark-field condenser (Mueller Optronic, NA = 0, 9) was used to illuminate the generated Si nanoparticles from the bottom through the glass receiver substrate. Light scattered by individual nanoparticles is imaged by a microscope objective with 50× magnification and a NA of 0.55 (Zeiss) simultaneously on a CCD camera and an optical fiber end facet with an aperture of 200 μm. This setup allows studying light scattering by a single nanoparticle.

11.6 Laser Printing from Prestructured Films

The sizes of the laser-printed nanoparticles can be reduced drastically by using structured films consisting of islands of material. An example of this special kind of laser printing technique is shown in Figure 11.12. After laser irradiation, the material islands contract into spherical nanoparticles due to surface tension. The sizes of nanoparticles are precisely determined by the volume of the islands,

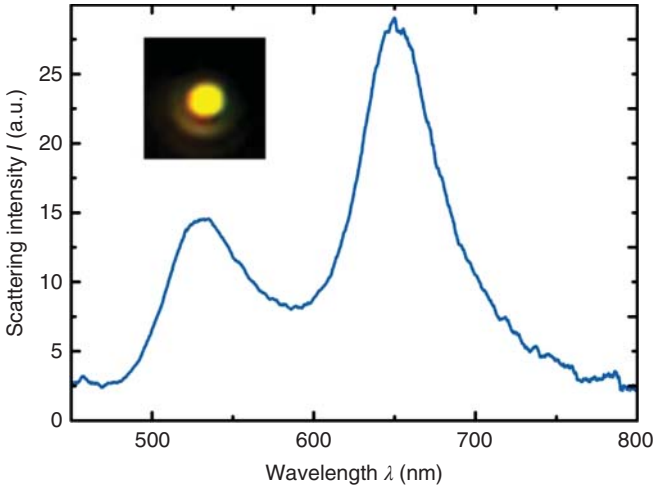

Figure 11.11 Experimentally measured scattering spectrum of a single silicon nanoparticle.

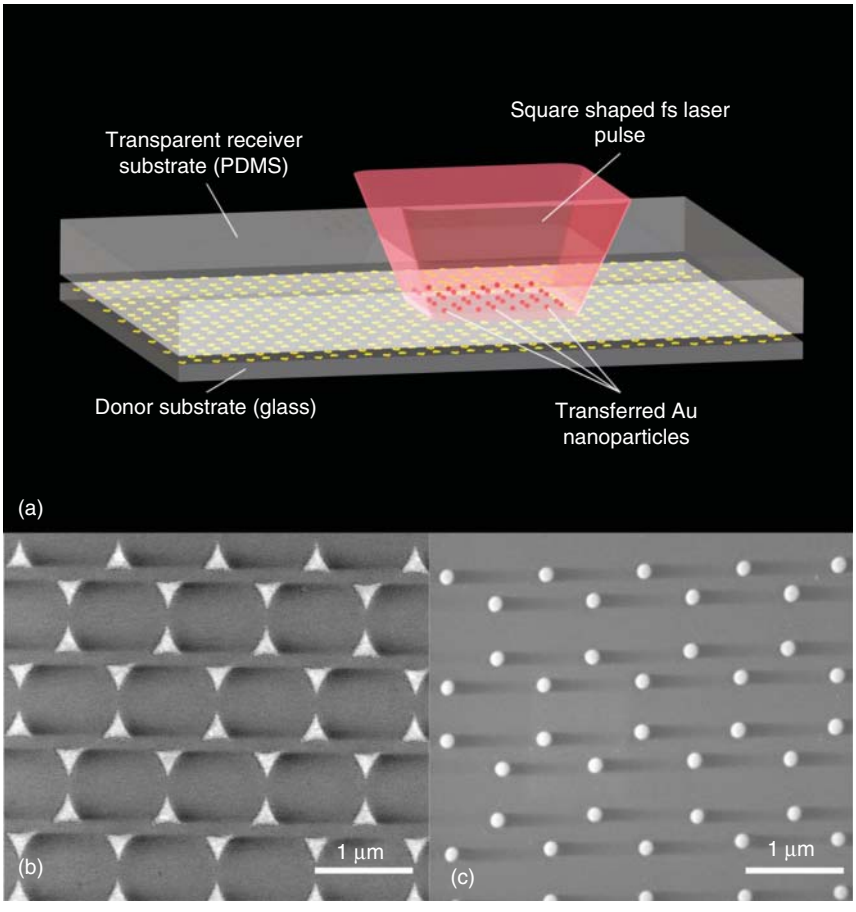

Figure 11.12 Schematic representation of laser printing from prestructured gold substrate; (a) SEM images of nanoparticle structures before (b) and after (c) laser printing. Due to the surface tension, the shape of the nanoparticles is changing from flat triangular prism type to spherical.

allowing generation of spherical particles with sizes of a few tens of nanometers. Positioning of the generated particles is determined by the lattice geometry. In a preliminary experiment, the nanoparticle arrangement has been limited to a hexagonal lattice due to a nanosphere lithography approach and gold islands [24]. However, high-speed fabrication of large-scale periodic arrays of nanoparticles (with diameters in the range of 40–200 nm) has been shown, and an optical sensor based on ordered gold nanoparticles with the sensitivity of 365 nm/RIU and a figure of merit of 21.5 in the visible spectral range has been demonstrated.

Another approach to realize arbitrarily designed prestructured films is to use simple UV lithography. In Figure 11.13a, an array of holes within a photoresist is shown. After coating the substrate with a thin layer of gold (50 nm) and a subsequent lift-off process, circular material islands with a diameter of 300 nm are

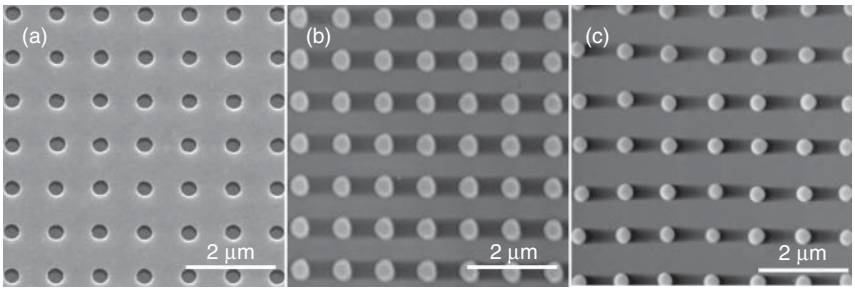

Figure 11.13 SEM images of gold island structures that have been transferred into a silicone polydimethylsiloxane (PDMS). (a) Array of holes within a photoresist covered by a thin layer of gold (50 nm). (b) After a lift-off process, circular material islands with a diameter of 300 nm remain on the substrate. (c) The gold islands have been laser printed into a silicone polydimethylsiloxane (PDMS). The transfer results in spherical nanoparticles partially embedded into the polymer substrate.

formed (Figure 11.13b). In Fig11.13c, these gold islands have been laser printed into a silicone polydimethylsiloxane (PDMS). The transfer results in highly ordered spherical nanoparticles partially embedded into the polymer substrate.

11.7 Applications: Sensing, Metasurfaces, and Additive Manufacturing

The unique optical properties of spherical nanoparticles generated from different materials enable a wide range of applications. Specially designed two-dimensional arrangements of nanoparticles with defined sizes, for example, can form new types of metasurfaces. In conventional refractive optical components, phase and polarization control are achieved through propagation effects. In contrast to this, metasurfaces can induce an abrupt change in the amplitude, phase, and polarization of an incoming electromagnetic wave. This property allows designing novel ultrathin optical components such as lenses [25] or wave plates [26] with unique functionalities [27, 28]. Metasurfaces can be made of arrays of anisotropic light scatterers with subwavelength dimensions or optically thin films. In the former case, abrupt and controllable changes of optical properties are achieved by engineering the interaction between light and optical scatterers [29, 30], which can take a variety of forms such as metallic or dielectric micro/nanoparticle structures [31, 32].

Laser printing of nanoparticles from prestructured films, which has been discussed in the previous section, can be used to generate an ultraflat optical element consisting of several hundreds of spherical nanoparticles. The element that is presented here is composed of concentrically arranged gold nanoparticles and is used to focus a linearly polarized laser beam. Each nanoparticle within this ultraflat lens contributes to the focusing effect. Final arrangement of the nanoparticles is obtained by iterative optimization of the focusing properties using Mie theory. A schematic drawing and the boundary conditions for the optimization are shown in Figure 11.14.

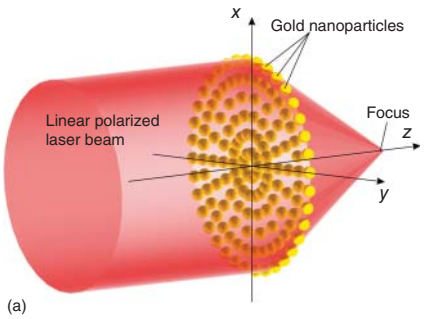

(b)

Wavelength	$\lambda = 780$ nm
Polarization	Linear in *x*-direction
Focal length	$f = 14{,}6$ µm
Number of rings	$N = 15$
Minimum nanoparticle distance	$d_{min} = 1$ µm
Maximum nanoparticle distance	$d_{max} = 2$ µm
Material	Gold
Nanoparticle diameter	$d_{sphere} = 200$ nm

Figure 11.14 (a) Schematic illustration of an ultraflat lens based on spherical gold nanoparticles. (b) Boundary conditions for the design calculations.

The generation process is the same as it has been described in the previous section. SEM images of each process step are shown in Figure 11.15. The final result of the ultraflat lens is shown in Figure 11.15c. Laser printing results in spherical nanoparticles partially embedded into the polymer substrate.

For optical characterization of this lens, the substrate is placed into a microscopic setup and is illuminated by a linear polarized and collimated laser beam ($\lambda = 780$ nm) from the backside. While the sample is gradually moved downward, the intensity pattern above the lens is measured by a CCD camera. In Figure 11.16, the resulting intensity pattern is compared to the theoretically calculated intensity pattern using Mie theory. Experimental evaluation showed very good agreement with the theoretically calculated properties.

The laser printing technique that has been presented in this chapter is not only capable of generating two-dimensional nanoparticle structures. Moreover, by independent movement of the donor and receiver substrates, it is possible to achieve a targeted stacking of several thousands of nanoparticles. A first demonstration of this approach is shown in Figure 11.17. The structure that is 60 µm in height and 3 µm in width consists of 10 000 silicon nanoparticles. Each nanoparticle within the structure has a diameter of about 250 nm. This proof of principal

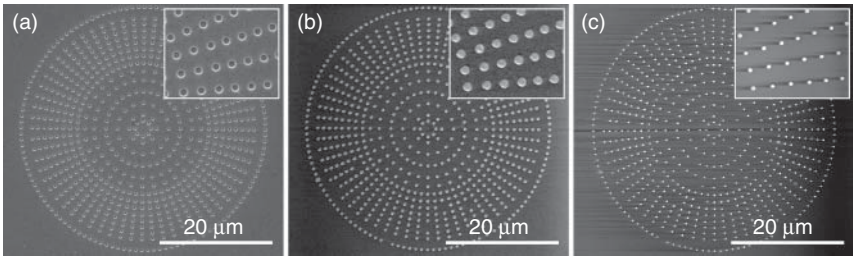

Figure 11.15 SEM images of the multistage process for the generation of an ultraflat lens based on spherical gold nanoparticles. (a) Array of holes within a photoresist covered by a thin layer of gold (50 nm). (b) After a lift-off process, circular material islands with a diameter of 300 nm remain on the substrate. (c) The gold islands have been laser printed into a silicone polydimethylsiloxane (PDMS). The transfer results in spherical nanoparticles partially embedded into the polymer substrate

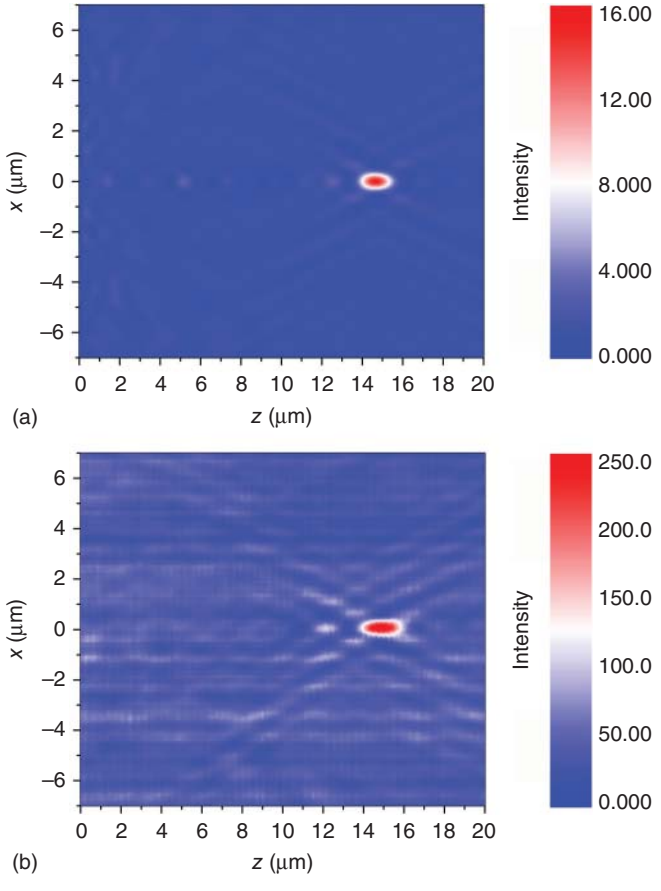

Figure 11.16 Focusing effect of an ultraflat lens based on spherical gold nanoparticles. Intensity pattern obtained by calculations based on Mie theory (a) compared to experimentally measured intensity pattern (b).

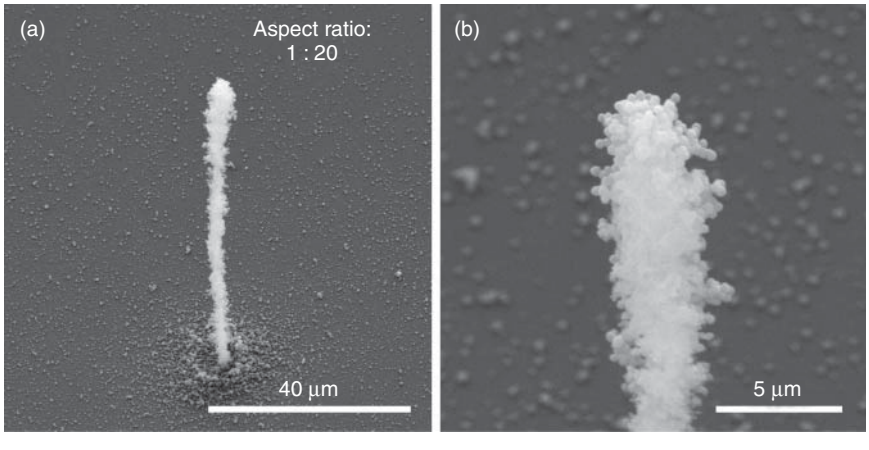

Figure 11.17 Three-dimensional structure consisting of several thousands of silicon nanoparticles generated by laser printing.

demonstrates the capabilities of the laser printing process and its applicability as a new additive manufacturing method for high-resolution structures. Only two-photon polymerization and FIB direct writing are able to generate submicrometer features for additive manufacturing [33]. With two-photon polymerization, no direct structuring of metals or semiconductors is possible, whereas FIB direct writing is expensive, slow, and must take place under high vacuum. Laser printing of nanoparticles works in air and can generate high-resolution structures directly from metals or semiconductors. This demonstrates that it can be a key technology for future additive manufacturing applications.

11.8 Outlook

Laser printing of nanoparticles with femtosecond laser pulses is a highly promising technology for the controlled generation and precise deposition of spherical nanoparticles. It has many advantages over the existing conventional methods. The process can be performed in air without any protective gas atmosphere. Nanoparticle diameter can be tuned by adjusting specific parameters. Nanoparticles can be printed from various materials and even arranged in three-dimensional structures.

First results have shown that laser printing of nanoparticles is a new technology for high-resolution additive manufacturing. In the future, it can be used as a highly flexible method for the generation of three-dimensional optical and electronic devices based on spherical nanoparticles.

References

1 Evlyukhin, A.B., Novikov, S.M., Zywietz, U., Eriksen, R.L., Reinhardt, C., Bozhevolnyi, S.I., and Chichkov, B.N. (2012) Demonstration of magnetic dipole resonances of dielectric nanospheres in the visible region. *Nano Lett.*, **12** (1), 3749–3755.

2 Fu, Y.H., Kuznetsov, A.I., Miroshnichenko, A.E., Yu, Y.F., and Luk'yanchuk, B. (2013) Directional visible light scattering by silicon nanoparticles. *Nat. Commun.*, **4**, 1527.

3 Baranov, D., Vinogradov, A., and Lisyansky, A. (2014) All-dielectric nanolaser, arXiv preprint arXiv:1408.5164.

4 Rodriguez-Oliveros, R., Höfner, K., Kuhlicke, A., Benson, O., Busch, K. et al. (2014) A fully nanoscopic dielectric laser, arXiv preprint arXiv:1412.4549.

5 Zywietz, U., Evlyukhin, A.B., Reinhardt, C., and Chichkov, B.N. (2014) Laser printing of silicon nanoparticles with resonant optical electric and magnetic responses. *Nat. Commun.*, **5**, 3402.

6 Zywietz, U., Reinhardt, C., Evlyukhin, A.B., Birr, T., and Chichkov, B.N. (2014) Generation and patterning of Si nanoparticles by femtosecond laser pulses. *Appl. Phys. A*, **114** (1), 45–50.

7 Kuznetsov, A., Koch, J., and Chichkov, B.N. (2009) Laser-induced backward transfer of gold nanodroplets. *Opt. express*, **17** (21), 18 820–18 825.

8 Kuznetsov, A.I., Evlyukhin, A.B., Reinhardt, C., Seidel, A., Kiyan, R., Cheng, W., Ovsianikov, A., and Chichkov, B.N. (2009) Laser-induced transfer of metallic nanodroplets for plasmonics and metamaterial applications. *J. Opt. Soc. Am. B*, **26**, B130–B138.

9 Kuznetsov, A., Koch, J., and Chichkov, B.N. (2009) Nanostructuring of thin gold films by femtosecond lasers. *Appl. Phys. A*, **94** (2), 221–230.

10 Korte, F., Koch, J., and Chichkov, B.N. (2004) Formation of microbumps and nanojets on gold targets by femtosecond laser pulses. *Appl. Phys. A*, **79** (4-6), 879–881.

11 Koch, J., Korte, F., Bauer, T., Fallnich, C., Ostendorf, A., and Chichkov, B.N. (2005) Nanotexturing of gold films by femtosecond laser-induced melt dynamics. *Appl. Phys. A*, **81** (2), 325–328.

12 Shi, L., Tuzer, T.U., Fenollosa, R., and Meseguer, F. (2012) A new dielectric metamaterial building block with a strong magnetic response in the sub-1.5-micrometer region: silicon colloid nanocavities. *Adv. Mater.*, **24**, 5934–5938.

13 Shi, L., Harris, J.T., Fenollosa, R., Rodriguez, I., Lu, X., Korgel, B.A., and Meseguer, F. (2013) Monodisperse silicon nanocavities and photonic crystals with magnetic response in the optical region. *Nat. Commun.*, **4**, 1904.

14 Abbarchi, M., Naffouti, M., Vial, B., Benkouider, A., Lermusiaux, L., Favre, L., Ronda, A., Bidault, S., Berbezier, I., and Bonod, N. (2014) Wafer scale formation of monocrystalline silicon-based Mie resonators via silicon-on-insulator dewetting. *ACS Nano*, **8** (11), 11 181–11 190.

15 Kuznetsov, A.I., Miroshnichenko, A.E., Fu, Y.H., Zhang, J., and Luk'yanchuk, B. (2012) Magnetic light. *Sci. Rep.*, **2**, 492.

16 Staude, I., Miroshnichenko, A.E., Decker, M., Fofang, N.T., Liu, S., Gonzales, E., Dominguez, J., Luk, T.S., Neshev, D.N., Brener, I. et al. (2013) Tailoring directional scattering through magnetic and electric resonances in subwavelength silicon nanodisks. *ACS Nano*, **7** (9), 7824–7832.

17 Shcherbakov, M.R., Neshev, D.N., Hopkins, B., Shorokhov, A.S., Staude, I., Melik-Gaykazyan, E.V., Decker, M., Ezhov, A.A., Miroshnichenko, A.E., Brener, I. et al. (2014) Enhanced third-harmonic generation in silicon nanoparticles driven by magnetic response. *Nano Lett.*, **14** (11), 6488–6492.

18 Spinelli, P., Verschuuren, M., and Polman, A. (2012) Broadband omnidirectional antireflection coating based on subwavelength surface Mie resonators. *Nat. Commun.*, **3**, 692.

19 Person, S., Jain, M., Lapin, Z., Saenz, J.J., Wicks, G., and Novotny, L. (2013) Demonstration of zero optical backscattering from single nanoparticles. *Nano Lett.*, **13** (4), 1806–1809.

20 Hardy, S. (1984) The surface tension of liquid silicon. *J. Crystal Growth*, **69** (2), 456–460.

21 Papageorgiou, D.T. (1995) On the breakup of viscous liquid threads. *Phys. Fluids*, **7** (7), 1529–1544.

22 Hulst, H.C. and Van De Hulst, H. (1957) *Light Scattering by Small Particles*, Courier Dover Publications.

23 Bohren, C.F. and Huffman, D.R. (1983) *Absorption and Scattering of Light by Small Particles*, Wiley-VCH Verlag GmbH & Co. KGaA.

24 Kuznetsov, A.I., Evlyukhin, A.B., Gonçalves, M.R., Reinhardt, C., Koroleva, A., Arnedillo, M.L., Kiyan, R., Marti, O., and Chichkov, B.N. (2011) Laser fabrication of large-scale nanoparticle arrays for sensing applications. *ACS Nano*, **5** (6), 4843–4849.

25 Ni, X., Ishii, S., Kildishev, A.V., and Shalaev, V.M. (2013) Ultra-thin, planar, babinet-inverted plasmonic metalenses. *Light: Sci. Appl.*, **2** (4), e72.

26 Yu, N., Aieta, F., Genevet, P., Kats, M.A., Gaburro, Z., and Capasso, F. (2012) A broadband, background-free quarter-wave plate based on plasmonic metasurfaces. *Nano Lett.*, **12** (12), 6328–6333.

27 Yu, N. and Capasso, F. (2014) Flat optics with designer metasurfaces. *Nat. Mater.*, **13** (2), 139–150.

28 Meinzer, N., Barnes, W.L., and Hooper, I.R. (2014) Plasmonic meta-atoms and metasurfaces. *Nat. Photonics*, **8** (12), 889–898.

29 Bharadwaj, P., Deutsch, B., and Novotny, L. (2009) Optical antennas. *Adv. Opt. Photonics*, **1** (3), 438–483.

30 Novotny, L. and van Hulst, N. (2011) Antennas for light. *Nat. Photonics*, **5** (2), 83–90.

31 Svirko, Y., Zheludev, N., and Osipov, M. (2001) Layered chiral metallic microstructures with inductive coupling. *Appl. Phys. Lett.*, **78** (4), 498–500.

32 Zou, L., Withayachumnankul, W., Shah, C.M., Mitchell, A., Bhaskaran, M., Sriram, S., and Fumeaux, C. (2013) Dielectric resonator nanoantennas at visible frequencies. *Opt. Express*, **21** (1), 1344–1352.

33 Vaezi, M., Seitz, H., and Yang, S. (2013) A review on 3D micro-additive manufacturing technologies. *Int. J. Adv. Manuf. Technol.*, **67** (5-8), 1721–1754.

Part III

Applications

12

Laser Printing of Electronic Materials

Philippe Delaporte[1], *Anne-Patricia Alloncle*[1], *and Thomas Lippert*[2,3]

[1] *Aix-Marseille University, CNRS, LP3 Laboratory, 163 Avenue de Luminy, 13288 Marseille Cedex 9, France*
[2] *Paul Scherrer Institute, Neutrons and Muons Research Division, Thin Films and Interfaces Group, 5232 Villigen PSI, Switzerland*
[3] *ETH Zürich, Laboratory of Inorganic Chemistry, Department of Chemistry and Applied Biosciences, Vladimir-Prelog-Weg 1-5/10, 8093 Zürich, Switzerland*

12.1 Introduction and Context

The development of printed electronics for industrial applications requires reliable and efficient digital printing techniques. For most of the applications, the challenge is no longer one of pitch size reduction, and the most relevant keywords are "flexible," "low cost," and "large area." In this context, the typical dimension of the elementary unit is of the order of a few microns (3–50 μm), and the integration of many functions on the same device via one unique process is of paramount importance. Moreover, organic compounds present very interesting performance characteristics and are becoming increasingly suitable for device production. Two immediate candidates are the organic light-emitting diode (OLED), which will be used for the next generation of displays and for smart lighting applications, and the organic thin-film transistor (OTFT), which also becomes very attractive for a wide range of applications.

Two approaches are developed to manufacture these printed electronic devices: first, mass printing technologies (gravure printing, flexography, screen printing, etc.), which are well known from the graphic arts industry and enable roll-to-roll or high-speed sheet-to-sheet processing but require the use of an impression cylinder, which is designed for only one application. Second, noncontact and digital printing methods, especially inkjet printing, which has become widespread in the graphics industry, are seeing significant use for organic and printed electronics. All these conventional techniques require the use of liquid inks, and the quality of the deposition is critically dependant on the ink properties, notably viscosity, adhesion and separation properties, and drying, which all have a strong influence on the stability, shape, and lateral resolution of the deposit. The realization of multilayer structures is also complex with such processes because of the solvent compatibility between two successive layers. Indeed, the solvent used during the top layer deposition should not damage the bottom layer. The development of a simple process allowing the deposition of

Laser Printing of Functional Materials: 3D Microfabrication, Electronics and Biomedicine,
First Edition. Edited by Alberto Piqué and Pere Serra.
© 2018 Wiley-VCH Verlag GmbH & Co. KGaA. Published 2018 by Wiley-VCH Verlag GmbH & Co. KGaA.

a wide variety of materials, with high spatial resolution (a few micrometers) is therefore of great interest for the manufacturing of future electronic devices.

As described in the previous chapters, laser-induced forward transfer (LIFT) allows printing a wide range of materials, organic or inorganic, in liquid or solid phase. LIFT is a single-step process, and dimensions of the printed pixels range typically from few micrometers to few millimeters, even if some submicrometer dots have already been LIFT-printed as described in Chapter 11. Moreover, this technique offers the possibility of transferring multilayer structures in a single step. Overall, LIFT appears as a very promising technology to overcome the challenges of printed electronic manufacturing.

Since the first experiment of LIFT performed by Bohandy *et al*. [1], for the deposition of copper film on a fused-silica substrate in vacuum using an ArF excimer laser (193 nm), many studies related to electronics applications have been reported. It is worth mentioning the use of LITI (see Chapter 1) for the fabrication of a functioning, large-area matrix backplane display circuits [2]. In 2004, Piqué *et al*. realized micropower sources [3] using a transfer process combining the advantages of LIFT and MAPLE (see Chapter 2). From 2007, the laser-induced forward transfer of organic materials led to the fabrication of functional organic electronic devices, such as polymer light-emitting diode (PLED) [4] and OTFT [5].

In this chapter, the pros and cons of LIFT as a manufacturing tool for printed electronics are discussed. First, the results of the studies dedicated to the fabrication of OTFT and OLED are presented. The main challenge relies on the ability of LIFT in transferring thin organic films without degrading their structural and electrical properties. The realization of passive components, such as capacitors, is also discussed. The last part is dedicated to the applications of LIFT for interconnection purposes, especially by transferring silver nanoparticle inks.

12.2 Organic Thin-Film Transistor

12.2.1 Operation and Characteristics of OTFTs

A growing interest in OTFTs has emerged due to their potential applications in electronics where low-cost, large-area coverage, and structural flexibility are required. The performance of OTFTs is often benchmarked against that of amorphous silicon (a-Si) TFTs with field-effect mobilities higher than $\mu = 1\,\mathrm{cm}^2/\mathrm{Vs}$ and on/off current ratios of $I_{\mathrm{on/off}} = 10^6 - 10^8$. However, there is currently more emphasis on developing soluble materials that allow the combination of high mobility with good stability under air, moisture, and light exposure [6]. Solubility in organic solvents has become a critical parameter with regard to the implementation of organic semiconductors in the solution deposition technologies developed for printable electronics. Indeed, new organic semiconductor materials are developed and allow the fabrication of TFTs with remarkably high performance and exceptional durability and operational stability. However, these compounds do not possess the solubility features required for their application in printable electronics. LIFT appears as a unique solution to achieve digital printing of these compounds in solid phase and for the fabrication of high-performance OTFTs.

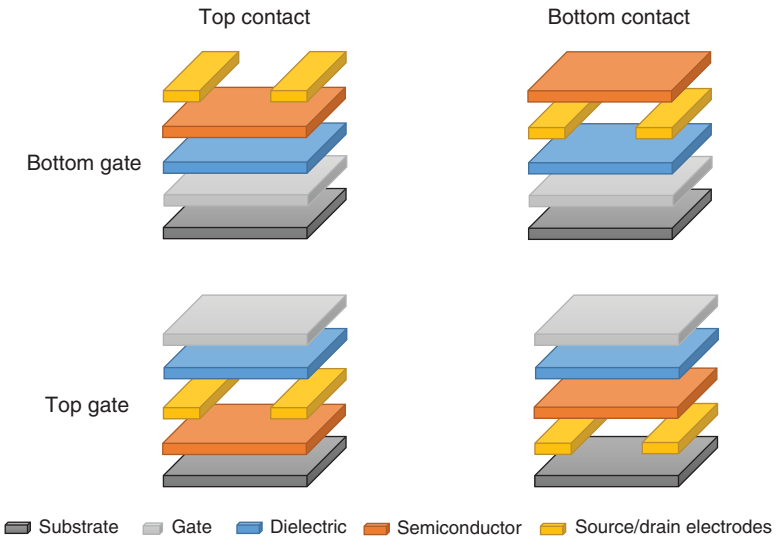

Figure 12.1 Schematic representation of the four configurations of a thin-film transistor structure.

Figure 12.1 shows the different layered structures of an OFET comprising a gate electrode, a dielectric layer, source/drain (S/D) electrodes, and a semiconductor (SC) film. Depending on the sign of the gate bias, charge carriers can accumulate or be depleted at the semiconducting layer near the dielectric interface. The accumulated charge carriers pass from the source to the drain electrode upon application of a potential deference across the electrodes. The main challenges of OFET processing are to transfer each layer by consecutive printing processes without modifying their structural and electrical properties. Most of the studies performed on LIFT printing of OTFTs address the bottom gate configurations.

Three parameters are considered to characterize the performances of thin-film transistors:

The mobility (μ), which represents the ability of the carriers to move in the active layer (semiconductor) when a voltage (V_D) is applied between the source and the drain electrodes. This physical parameter controls the current intensity at the drain electrode (I_D) and the commutation time (t_c), which defines the maximum operating frequency of the circuit. A higher mobility results in shorter commutation time, according to

$$t_c = \frac{L^2}{\mu V_D} \tag{12.1}$$

where L is the channel length or the gap between the source and drain electrodes. The value of the mobility depends of the structural properties of the semiconductor material, and this parameter is also sensitive to the modifications induced by the printing process in this layer.

The threshold voltage (V_T) is defined by the following equation:

$$V_T = \frac{qdn_0}{C_i} + V_{fb} \tag{12.2}$$

where d is the thickness of the semiconductor layer, C_i is the capacitance of the dielectric layer, q is the elementary charge, n_0 is the carrier density, and V_{fb} is the voltage from the charge at the interfaces of the dielectric layer. For OTFTs, the threshold voltage must be as close as possible to zero. However, some parameters can contribute to modify this value, and among them, we must consider the presence of defects in the semiconductor layer as they can be induced during the printing process by the laser irradiation of this layer.

The on/off current ratio (I_{on}/I_{off}) is the ratio of the currents measured when the gate voltage (V_G) switches from the Off state to the On state. The I_{OFF} current, corresponding to $V_G = 0$, should be, in theory, equal to zero as it characterizes the ability of the semiconductor layer to prevent the carrier flow between the source/drain electrodes when no seed carriers are injected. However, that is never the case for thin-film transistor because of the very small thickness of the layers and of the defects in the SC layer and at the interface with the dielectric layer. As these defects can be induced by the laser irradiation, this $I_{\text{on/off}}$ parameter is also important to characterize the printing process.

Two kinds of measurements are used to determine these parameters. First, the evolution of the drain current I_D as a function of the drain voltage V_D for different values of the gate voltage V_G provides a first characterization of the OTFT operation. As shown in Figure 12.2a, there is first a linear dependence of the current versus the voltage and a saturation regime for the highest voltages. The second measurement is the evolution of the drain current as a function of V_G for a given V_D. A larger slope of the curve (see Figure 12.2b) results in a higher gain of the transistor. The field effect mobility μ is extracted from the transfer characteristics in the saturation regime. The drain–source current (I_D) in the saturation regime is governed by the following equation:

$$(I_D)_{\text{sat}} = \left(\frac{W}{2L}\right) C_i \mu (V_G - V_T)^2 \tag{12.3}$$

where W is the channel width.

Then, because charge carriers pass through the semiconducting layer near the dielectric layer, the semiconductor–dielectric interface characteristics and the structural properties of the semiconductor (crystallinity, defects, etc.) play a crucial role in the achievement of high-performance OTFTs. The characteristics of the dielectric layer are also important as the layer must be free of defects and have a uniform thickness to prevent leakage current. Another main parameter for the OTFT performance is the current injection through the source/drain electrodes. The work function of the source/drain electrodes must match the organic semiconductor electrical properties. A small change in the work function of the source/drain, potentially induced by surface degradation, will modify the contact resistance and can dramatically reduce the current. The properties of these thin films and their interfaces can be modified by the laser printing process, and the measurements of the three parameters (μ, V_T, $I_{\text{on/off}}$) are used to determine the

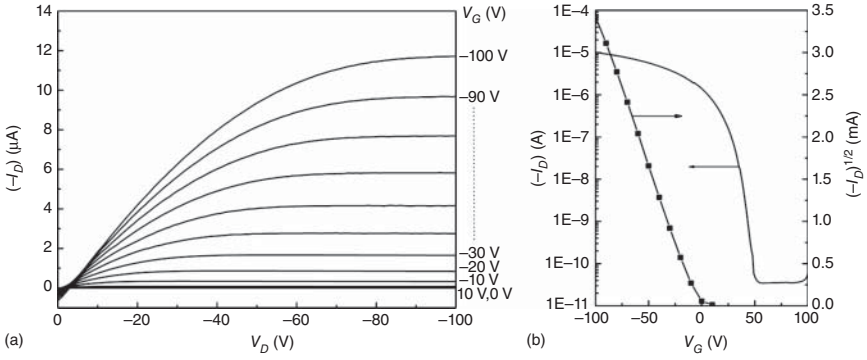

Figure 12.2 Typical output (a) and transfer (b) characteristics of a top contact OTFT.

impact of the laser-induced transfer on the material properties and the OTFT performance.

The most challenging part of the printing process is the transfer of thin organic films. As demonstrated by Kim *et al*., the realization of the conductive layers (source/drain electrodes and gate) by laser printing of silver nanoparticle (Ag-NP) inks does not degrade the OTFT performances, compared to other deposition processes. They fabricated bottom-gate OTFTs in top- and bottom-contact configurations. The SC (Pentacene) and dielectric (PVP) layers were deposited by spin coating, and they LIFT-printed Ag-NP ink to form the electrodes. They obtained field-effect mobilities of approximately 0.16 $cm^2/V/s$ and on/off current ratios of approximately 10^5 [7]. The following paragraphs are dedicated to the influence of laser printing on the organic layer properties.

12.2.2 Laser Printing of the Semiconductor Layer

The following examples presented the realization and characterization of OTFTs in which the deposition of nonsoluble semiconductor material is achieved by LIFT in solid phase.

The first realization of LIFT-printed functional OTFTs, including the transfer of SC layer and S/D electrodes, was performed by Rapp *et al.* [5]. The semiconductor layer was a 100 nm thin film of copper phthalocyanine (CuPc), and the source/drain electrodes were printed from a silver nanoparticle ink. The OTFTs have been realized in top-contact (TC) and bottom-contact (BC) on a doped silicon substrate, which plays the role of the gate, covered by a 300 nm thin silicon dioxide (SiO_2) film, which acts as the dielectric ($C_i = 12\,nF/cm^2$). Figure 12.3a shows an optical microscope image of this LIFT-printed structure. The electrical performances of these first LIFT-printed OTFTs were quite poor. For both BC and TC configurations, the mobilities were of few 10^{-5} $cm^2/V/s$, and the On/Off current ratio was few 10^{-2}. However, the performances of CuPc-based OTFTs realized by thermal evaporation under vacuum through a mask are only one order of magnitude better. These differences were probably due to the direct irradiation of CuPc film by the 355 nm picosecond laser that induced defects in the SC layer, and those defects can trap some of the carriers and reduce the mobility values.

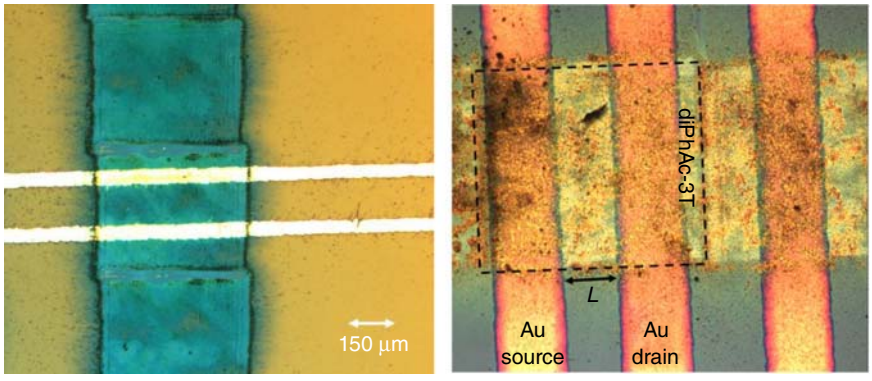

Figure 12.3 Optical microscope image of a LIFT-printed OTFT. The substrate is a doped silicon wafer (gate) covered by a thin SiO_2 layer (dielectric) on which are printed (a) CuPc SC pixels (blue–green) and Ag-NP ink lines (white) as S/D electrodes or (b) diPhAc-3T pixels, printed by LIFT, and gold electrodes evaporated with $L = 80\,\mu m$.

Small-molecule semiconductor films have also been used for laser-printed OTFTs. Especially, the p-type organic semiconductor distyryl-quaterthiophene (DS4T) was vacuum-deposited on a donor substrate and transferred with picosecond laser pulses on Si/SiO_2-based receiver substrates to form an organic active layer [8]. DS4T-based OTFTs realized by thermal evaporation showed a high field-effect mobility (0.02–0.04 $cm^2/V/s$) but were also found to be exceptionally long-lived and stable toward continuous operation, under atmospheric conditions. As the DS4T films are very fragile, the direct irradiation of these films with a picosecond UV laser led to strong damages of the material. The transfer of such small-molecule compounds requires the use of a dynamic release layer (DRL – see Chapter 3) that absorbs the laser energy, transforms it in mechanical energy that propels the film forward, and prevents direct interaction of the laser light with the SC film. OTFT devices were realized in TC and BC configurations with gold evaporated S/D electrodes. The measured mobilities were similar to those obtained with the evaporated DS4T, but the I_{ON}/I_{OFF} ratio was still low (few 10^3). These results show that the use of a DRL prevents the generation of light-induced defects in the semiconductor layer as the mobility is not degraded by the process. However, the strong mechanical effects due to the fast transfer (up to 500 m/s) of the pixel between the donor and the receiver lead to some modifications of the structure of the SC layer, which are probably responsible for the low current ratio. It is worth mentioning that these OTFTs exhibit very stable performances over time when stored in ambient conditions [8].

The diPhAc-3T (bis(2-phenylethynyl) end-substituted terthiophene) [9] compound has also been tested as organic semiconductor for the realization of thin-film transistors by means of laser printing. The specificity of this material is that the film growth is based on the island Volmer–Weber mechanism, which gives a structural cohesion to the film and makes it less sensitive to the mechanical damages potentially induced by laser irradiation. Indeed, atomic

force microscopy analysis confirmed that the laser transfer did not modify the material structure, even when a DRL is not used [10]. TC diPhAc-3T-based OTFTs were fabricated on Si/SiO_2 substrates with gold evaporated S/D electrodes (see Figure 12.3b). They exhibited good electrical performances ($\mu = 0.04\,cm^2/V/s$, $V_T = 0\,V$, $I_{ON}/I_{OFF} = 2.8 \times 10^5$), and the stability tests over 100 days were also very good [10]. These performances are similar to those obtained by thermal evaporation [9], which means that the laser printing process does not degrade the properties of the diPhAc-3T material.

In addition to these results obtained with nonsoluble SC compounds that suggest the great potential of LIFT for this application, other studies have been performed with soluble SC material, and the LIFT-printed OTFT performances were compared with those of inkjet-printed transistors. Among them, we would like to mention the poly-3-hexylthiophene (P3HT) semiconductor material [11, 12]. This semiconductor was printed on gold S/D electrodes sputtered on Si/SiO_2 substrates. The morphological properties of the SC pixel were improved when using a titanium DRL; however, to avoid any risk of contamination by the DRL, the OTFTs were realized without DRL but using a thicker P3HT layer (150 nm). High mobility values were obtained, comparable with, or even higher than, those of inkjet-printed OTFTs, but with a low current ratio and high threshold voltage. This is probably due to some damages created in the very thin SiO_2 layer (80 nm) by the impact of the transferred pixel or to some oxygen contamination at the SC–dielectric interface.

These different studies show that LIFT can be used to deposit SC pixels in solid phase for OTFT manufacturing. The irradiation parameters must be tuned to preserve the structural and electrical properties of the films. The use of a polymer DRL allows to prevent the direct irradiation of the film and therefore the generation of light- and thermally induced defects in the SC material. Another drawback of the laser printing process is the strong stress generated during the ejection from the donor and the landing on the receiver. This effect can modify the structural organization of the printed material and reduce the electrical performances of the OTFT devices. Then, organic semiconductors with high structural cohesion are the preferred choice if they are to be transferred by direct laser printing. For the tested materials, the mobilities of OTFTs with a laser-printed semiconductor were similar to those of OTFTs realized with a SC layer deposited by thermal evaporation.

12.2.3 Laser Printing of Dielectric Layers

Very few studies have been dedicated to laser printing of thin dielectric layers for the realization of OTFTs. The deposition of this layer is critical because both the interface with the semiconductor layer must be free of defects that could trap the carriers and its structure must be undamaged to avoid leakage currents. Diallo *et al.* performed an interesting experiment to investigate the effects of laser-printed dielectric layers on OTFT performances [13]. Figure 12.4 shows the three different OTFT configurations that have been realized and characterized. The substrate was a silicon (Si) wafer oxidized to form a 300 nm thick layer of SiO_2 that is used as gate and dielectric in the first configuration (BG-OTFT1),

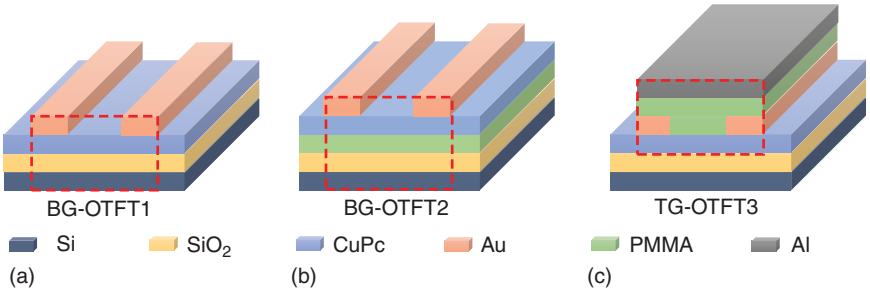

Figure 12.4 Schematic representation of the three OTFT configurations used to investigate the effects of laser printing of the dielectric layer on the OFTF characteristics. (a) BG-OTFT1: Si (gate)/SiO_2 (dielectric)/CuPc (SC)/Au (S/D); (b) BG-OTFT2: Si (gate)/SiO_2 + PMMA (dielectric)/CuPc (SC)/Au (S/D); (c) TG-OTFT3 CuPc (SC)/Au (S/D)/PMMA (dielectric)/Al (gate).

which is completed by a 100 nm thick CuPc p-type semiconductor, thermally evaporated under high vacuum (HV), and finally, a 50 nm gold S/D electrode also thermally evaporated. The second configuration (BG-OTFT2) is almost identical, but a 600 nm PMMA layer is spin-coated on the SiO_2 surface, which changes the dielectric capacitance from 12 to 5 nF/cm^2 and the nature of the dielectric/SC interface. The last configuration (TG-OTFT3) is a top-gate design that is made from BG-OTFT1 by laser printing a PMMA layer and covering it with thermally evaporated aluminum. Then, the Si/SiO_2 structure acts only as a substrate and the dielectric/SC interface is PMMA/CuPc as for BG-OTFT2.

Table 12.1 presents the main characteristics of the thin-film transistors in the three configurations.

The first observation is that the mobility value is almost the same for the three configurations. It is even slightly higher for the LIFT-printed PMMA, but that is probably due to the top-gate configuration. That means there is no degradation of the CuPc properties induced by the laser deposition of the PMMA layer on top of it. However, a large dispersion of the values of the threshold voltage (V_T), from −1 to +55 V is observed for TG-OTFT3, revealing that the density of trap states to be filled before the carrier transport becomes mobile is higher than that for the other two configurations. This higher density of trap states is directly related to the LIFT process. As PMMA is slightly absorbent at the laser wavelength, these modifications certainly occur not only at the interfaces but also within the bulk

Table 12.1 Main characteristics of the thin-film transistors in the three configurations.

OTFT reference	μ (cm^2/V s)	I_{On}/I_{Off}	V_T (V)
BG-OTFT1	$(1.7–2)\times10^{-3}$	$8\times10^2–8\times10^4$	(−1.8)–(+9)
BG-OTFT2	$(3.1–3.5)\times10^{-3}$	$(1.3–3.3)\times10^5$	(−11)–(−16)
TG-OTFT3	$(7.3–8.6)\times10^{-3}$	$(0.5–1)\times10^2$	(−1)–(+55)

material and close to the interface with the CuPc layer. Additionally, the low current ratio measured for the top-gate configuration, due to a high off-state current (I_{Off}), underlines the presence of charges in the conducting channel at $V_G = 0$ V. During the laser-induced transfer of PMMA layers, mechanical effects lead to some modifications of the morphology at the interface between the dielectric and the organic semiconductor, which is the interface where the charge transport occurs in such TG transistors.

The laser-induced transfer of dielectric layers is a critical step for the fabrication of thin-film transistors. It requires the use of a DRL to reduce the risk of material modifications, and as for SC layer, dielectric films with high structural cohesion are more suitable to improve the current ratio (I_{On}/I_{Off}) parameter.

12.2.4 Laser Printing of Conducting Layers

The main material used for laser printing gates or S/D electrodes is silver nanoparticle ink [3, 14] because the transfer is done in liquid phase, and then there are no risks of stress-induced damage of the previous layer (SC or dielectric). However, the ink needs to be heated for sintering the silver nanoparticles, and this step can limit the use of polymers or substrates sensitive to temperature. As with the dielectric layer, there are only few studies dedicated to the LIFT printing of organic conductors for OTFT applications [15, 16].

Rapp *et al*. reported the fabrication of fully polymeric OTFT devices based on PQT-12 poly(3,3‴didodecylquaterthiophene) as semiconductor and PEDOT:PSS (poly(3,4-ethylenedioxythiophene)/poly(styrenesulfonate)) as conductor [16]. Both layers were LIFT-printed in solid phase with a UV picosecond laser on Si/SiO_2 substrate acting as gate and dielectric. First, the OTFTs were printed PQT-12 transferred by laser and gold evaporated S/D electrodes. Their electrical characteristics showed a mobility of up to 5.10^{-3} cm^2/V/ s^{-1} with a threshold voltage V_T of −9 V and an I_{On}/I_{Off} ratio of 10^3. The second set of OTFTs was formed with laser-printed PEDOT S/D electrodes instead of the evaporated Au electrodes. Their electrical performances were slightly improved. Mobilities of up to 0.02 cm^2/V/s were measured with a threshold voltage V_T of −20 V and an I_{On}/I_{Off} ratio of 10^4. The semiconductor layer was the same for the two configurations of the transistors, and the increased mobility measured when PEDOT is used is attributed to a better interfacial contact between the two different polymer layers. Adequate contact between the printed PQT-12 and PEDOT:PSS is of prime importance, as it is essential for carrier's injection, which is the initial step to obtain operational OTFTs.

This result demonstrates that laser printing allows the fabrication of OTFT with conductor and semiconductor polymer materials transferred in solid phase. This approach gets rid of the solvent compatibility issue and opens the way of using a large set of organic materials.

12.2.5 Single-Step Printing of Full OTFT Device

LIFT offers the possibility of transferring a multilayer structure in a single step, and this approach has been used to print a full OTFT structure (gate/dielectric/SC) on S/D electrodes deposited on a substrate [17]. As shown

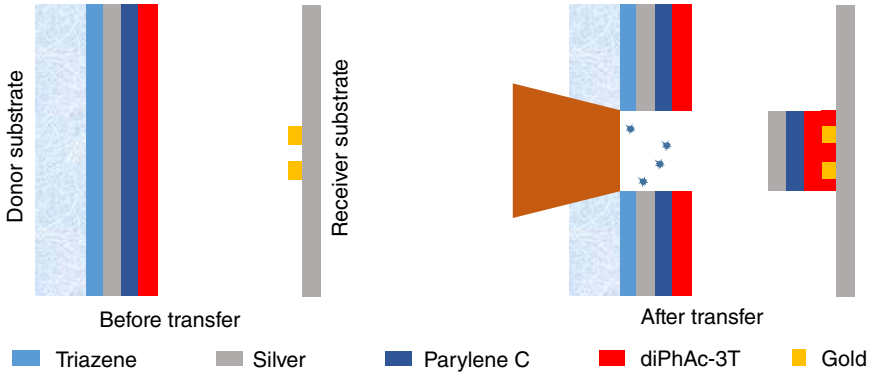

Figure 12.5 Schematic representation of the single-step LIFT process used in the fabrication of multilayer structure for OTFT applications.

in Figure 12.5, the donor substrate was composed of a triazene DRL [18], a silver layer (gate), a Parylene-C layer (dielectric), and a diPhAc-3T (SC). The receiver substrate was a silicon wafer with thermally evaporated gold electrodes. Under the laser irradiation of the DRL, the multilayer film (gate/dielectric/SC) is transferred over the electrodes to form a top-gate BC OTFT. Its electrical performances were a mobility 2×10^{-4} cm^2/V/s, a threshold voltage V_T of -4 V, and an I_{On}/I_{Off} ratio up to 4×10^4. These values are in the same range than those of transistors with similar structures and materials but fabricated by sequential evaporation steps. This single-step printing of a multilayer structure process offers the possibility to prepare large area donor film in a dedicated environment in which the interfaces between the different layers are optimized. Most of these interfaces are preserved as they do not interact with the atmosphere, and the realization of the transistor itself requires only the single step of laser transfer. For the transfer of very thick structures, the process can be optimized by using a smart beam shaping by increasing the fluence at the edges of the beam profile and reducing it in the center of the beam [19, 20].

In conclusion, the OTFTs realized by laser printing yielded good electrical performance characteristics, which are comparable to those of the OTFTs fabricated by other printing techniques. Moreover, this is the only digital process allowing the use of such large range of materials. However, there are also some drawbacks. This technique induces some mechanical stresses into the material and can significantly modify its structural organization, which means that LIFT is particularly well suited for printing organic materials with high structural cohesion. Finally, the ablation mechanism occurring in the donor film also leads to the generation of a small amount of debris that is also transferred on the receiver. Careful optimization of the process allows to significantly reduce these effects, but it is almost impossible to fully get rid of them, and the debris might not be acceptable for some applications in printed electronics.

12.3 Organic Light-Emitting Diode

OLEDs have become a promising candidate for lighting and display applications. High-efficiency OLEDs require a multilayer device architecture to provide exciton confinement and balanced charge transport, and conventional pixelated OLED displays are mainly evaporated in HV through shadow masks. However, vacuum thermal evaporation bears the drawbacks of low material utilization rates, poor scalability, high capital cost, and difficulties in patterning. Solution processing and digital printing provide a low-cost approach to fabricate OLEDs and address applications as flexible electronics or personalized devices. Both inkjet and laser printing technologies are investigated to develop a reliable digital printing process for OLED manufacturing. Especially, many studies have been dedicated to the LITI process for the fabrication of OLED displays. In 2003, Samsung SDI presented the first full-color active-matrix OLED display prototypes fabricated with a LITI process step [21]. Nevertheless, thermal transfer defects were observed during the LITI process of vacuum-coated OLED materials [22].

This application of laser transfer to OLED manufacturing faces the same challenges as OTFT fabrication. Indeed, conditions must be found to print thin organic layers without inducing significant modifications of their physical, chemical, and electrical properties. The first LIFT-printed OLED was reported in 2007 by Fardel *et al*. [4]. They fabricated PLED with poly[2-methoxy-5-(2-ethylhexyloxy)-1,4-phenylenevinylene] (MEH-PPV) as light-emitting polymer (LEP). The typical architecture of the devices used glass as substrate covered by an ITO layer on which the LEP (90 nm) and aluminum (70 nm) layers are deposited. A current flowing between the two electrodes (Al–ITO) leads to a broad light emission from the MEH-PPV around 600 nm. For the LIFT experiments, the receiver substrate was a glass substrate covered by the ITO layer and the donor substrate was composed of a quartz substrate covered by the multilayer stack triazene/Al/LEP. A triazene polymer was used as a sacrificial layer (DRL) to preserve the material to be transferred from thermal effects, such as melting of the aluminum layer or degradation of the LEP. Light-emitting organic layers are very sensitive to laser irradiation, and the positive impact of using a sacrificial layer on the OLED performances has been demonstrated for different configurations [23, 24] The functionality of operating devices was characterized by current–voltage and electroluminescence measurements, which prove that the integrity of the transferred materials has been fully preserved during the LIFT deposition process. This first experiment demonstrated that functional PLED pixels can be fabricated by the DRL-LIFT process, and a luminance of 6 cd/m^2 was measured at 14 V.

Based on the same device architecture and laser printing configuration, other materials and procedures have been investigated to realize RGB (red–blue–green) PLED devices with optimized performances [25]. Polyfluorene-based (PFO) polymers were studied as the electroluminescent

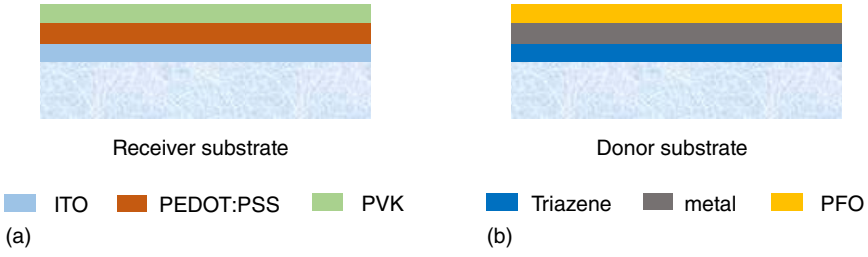

Figure 12.6 Structures of the receiver (a) and the donor (b) substrates.

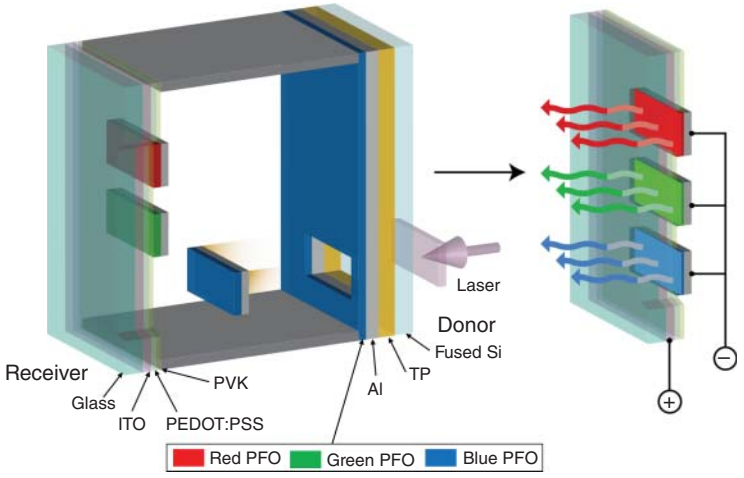

Figure 12.7 A scheme of the red–green–blue PFO pixel transfer. The left image shows the transfer of the third, blue, pixel after the other two colors have already been transferred. The right image shows the receiver substrate alone with a bias across the three pixels creating electroluminescence.

material, as that allows to generate the green and red emission by blending triplet emitters as dopants into the PFO matrix. Devices were based on the architecture glass/140 nm ITO/60 nm PEDOT:PSS/40 nm PVK/~50 nm LEP/cathode. The LEP was either plain for blue emission, or PFO doped with 5 wt% Ir(Me-ppy)3 for green emission, or with 5 wt% btp2Ir(acac) for red emission. Then donor substrates consisted typically of fused-silica/190 nm TP/80 nm cathode/PFO (<10 wt% triplet emitter dye, ~50 nm). The ITO-on-glass receiver substrates were all coated with 60 nm PEDOT:PSS and 40 nm PVK as a hole-transporting layer. Figure 12.6 shows the structure of both the receiver and donor substrates, and Figure 12.7 presents the procedure to transfer the multilayer film. For all of these experiments, an approximately 15 µm donor–receiver substrate gap was used with a reduced environmental pressure of 1 mbar. The control of the pressure value allows to get rid of the shock wave generated by the laser interaction process (compared to atmospheric pressure) and to limit the velocity of the pixel (compared to vacuum) [26, 27].

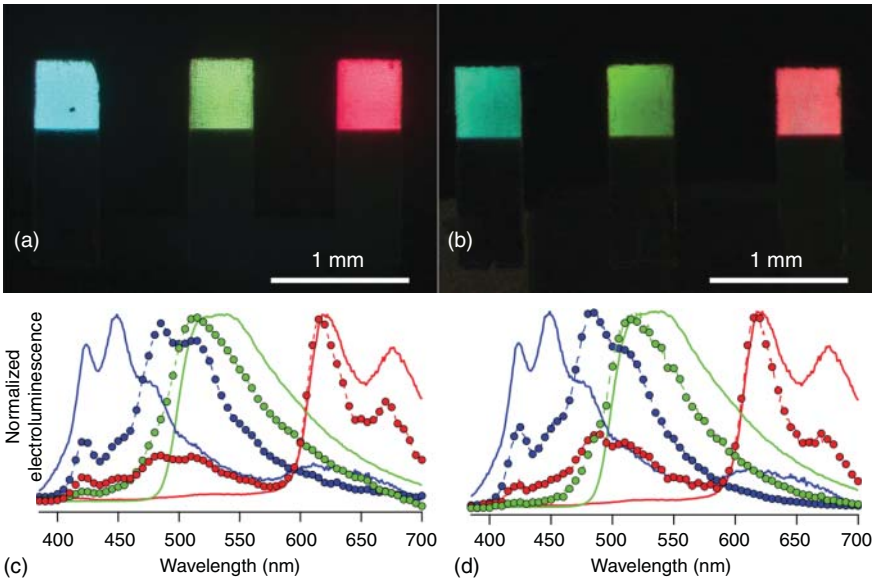

Figure 12.8 Tricolor pixels imaged using a light microscope are shown for an Al/TBA cathode at 20 V (a) and for an Al cathode at 24 V (b). Electroluminescence (EL) spectra of tricolor LIFT pixels with an Al/TBA cathode (c) and with an Al cathode (d). On both graphs, the EL spectra of the "conventionally fabricated devices" are shown with a solid line and a color corresponding to the relevant device, and the printed pixels are represented with dotted lines and circles of corresponding color. (Shaw-Stewart *et al*. 2012 [29]. Reproduced with permission of American Institute of Physics.)

Different cathode materials and irradiation conditions have been used to optimize the PLEDs' performances [28]: silver, aluminum, and aluminum with an ultrathin layer of the alkaline tetrabutylammonium hydroxide (TBA) directly deposited onto the electrode to help electron injection. Figure 12.8 shows microscopic images of the LIFT-printed RGB pixels with the Al and Al/TBA cathodes as well as the corresponding electroluminescent spectra.

Table 12.2 summarizes the performances of the PLED devices for different configurations. Luminance as high as 540 cd/m^2 for the blue pixel and 232 and 145 cd/m^2 have been obtained for the green and red pixel, respectively, after the optimization of the process, the materials, and the device configuration [29].

There is no doubt that laser printing is an appropriate process to realize PLED devices. Its ability to print multilayer films in a single-step process without reduction of the material performances is a great advantage over other printing technologies.

Sequential laser printing of the different layers has also been investigated for PLED fabrication and compared to single-step printing of multilayer films [30]. A 50 nm film of an alcohol-soluble polyfluorene (PFN) was transferred onto a receiver with a transparent anode, followed by the transfer of an aluminum cathode on top. Both printing steps were realized by the DRL-LIFT process under medium vacuum. The operation of the sequentially printed PLEDs requires higher voltages compared to the single-step printing PLEDs, and their

Table 12.2 Device performances for various device architectures, at a current density (CD) of approximately 40–50 mJ/cm^2.

Color	Fabrication process	Bias (V)	CD (mJ/cm^2)	Lum (cd/m^2)	LE (CD/A)	EQE (%)
Blue	LIFT Al	22	51	306.2	0.60	0.27
	LIFT Al/TBA	21	48.32	540	0.89	0.40
	Convent Al	18	51.16	25.4	0.05	0.042
	Convent Ca	13	49.23	102.3	0.21	0.17
Green	LIFT Al	26	37	134.5	0.36	0.11
	LIFT Al/TBA	24	43	232.4	0.54	0.18
	Convent Al	39	48.9	715.6	1.46	0.46
	Convent Ca	22	44.5	3311	7.44	2.31
Red	LIFT Al	19	35.67	84.7	0.24	0.15
	LIFT Al/TBA	22	44.33	145.2	0.33	0.23
	Convent Al	40	47.9	14.5	0.03	0.043
	Convent Ca	18	45.14	726.5	1.64	2.32

Blue, green, and red refer to the LEP layer, whether just plain PFO (blue) or doped PFO (red and green). The "LIFT Al" are the LIFTed pixels with plain Al electrodes, "LIFT Al/TBA" are the LIFTed pixels with Al/tetrabutylammonium electrodes, the "Convent Al" are the conventionally fabricated devices with Al electrodes, and "Convent Ca" are the conventionally fabricated devices with Ca electrodes.

efficiencies are slightly lower but still higher than those of the conventionally fabricated PLEDs with the same structure and materials. These differences are probably due to the higher roughness of the PFN surface induced by the LIFT process, and this surface corresponds to the interface with the aluminum cathode. However, this approach offers the advantage of transferring otherwise incompatible layers on top of one another and paves the way for the fabrication of more complex systems with improved device performances.

Small molecules have also been used to fabricate OLEDs by the LIFT process. This is more challenging than PLED printing because such small-molecule thin films have a much lower cohesion compared to polymeric films. A single-step transfer was used to deposit a multilayer film composed of TP-DRL/Al/TBA/Alq_3 on a glass receiver covered by an ITO/PEDOT/PVK multilayer film. The LIFTed Alq_3 pixels were functional, but their efficiencies were less than half the efficiencies of the conventionally fabricated Alq_3 OLED devices. This is attributed to the mechanical load applied to the fragile Alq_3 film during the transfer process [31]. This conclusion is consistent with the results previously discussed for OTFT fabrication where the laser printing process appears to have less of a negative influence for organic compounds with high structural cohesion.

Despite the interest of printing OLEDs in solid phase to avoid any solvent compatibility problems, laser printing has also been used to fabricate devices by transferring the compounds in liquid phase, similarly to the inkjet technique. Kattamis *et al*. [32] laser-printed different ionic transition metal complexes as

the active layer on patterned ITO deposited on glass, and the fabrication of the OLED device is completed by vapor depositing an aluminum electrode through a shadow mask. They used the BA-LIFT (blister actuated LIFT) approach, described in Chapter 5, to transfer the electroluminescent material [33]. The devices exhibit performances in terms of electroluminescence emission, diode behavior, and lifetimes similar to those of spin-coated devices fabricated in nitrogen environments. The main advantage of this technique is its ability to work in an atmospheric environment by using air- and moisture-tolerant materials, and since the transfer in liquid phase is mechanically softer than LIFT in solid phase, there is no risk of mechanical damage of the structural properties of the printed materials. Moreover, as for DRL-LIFT, the polymer layer used to absorb and transfer the energy to the layer to be transferred blocks the direct interaction with the laser beam and thus prevents the light- or thermally induced degradation of the sensitive film. Finally, the use of thin donor film and a small laser spot size resulted in the printing of small OLED pixels with sizes down to 10 μm [33].

Quantum-dot-based light-emitting diodes also represent an attractive opportunity to produce LED displays because of the high color purity and photophysical stability of quantum dots [34]. Triazene DRL-LIFT was used to print semiconductor nanocrystal quantum dots. As previously presented, the active quantum-dot-based film was transferred together with an aluminum electrode onto a glass slide covered by an ITO transparent electrode. No degradation was observed in the luminescent efficiencies of the transferred NQDs. Indeed, the fluorescence spectra of the transferred NQDs were identical to those of the NQD layers deposited on the fused-silica donor substrate prior to the transfer process. Two different sizes of CdSe(CdS) nanoquantum dots, 5 and 6 nm, have been used, leading to photoluminescence in the yellow and red spectral range [35].

In conclusion, different techniques of laser printing (LITI, LIFT, DRL-LIFT, BA-LIFT) have been used to fabricate light-emitting diodes by transferring a large range of materials in liquid or solid phase. As for OTFT realization, the main risk of material damage when printing solid thin films is linked to the mechanical load induced by the fast ejection of the film. Organic compounds with high structural cohesion are preferable for laser-printed OLEDs. Very promising results were also obtained with quantum-dot-based active materials and organometallic electroluminescent materials.

12.4 Passive Components

Since the first demonstration of laser-induced forward transfer of copper in 1986 by Bohandy *et al.* [1], laser printing of conductive structures attracted lot of attention because of the large amount of potential applications, especially in microelectronics. MAPLE DW has been used to print various powders, including metals [36]. LIFT of solid metal thin films [37], silver nanoparticle inks [38], and silver pastes [39] has also been widely investigated to fabricate conductive structures.

The simplest electronic passive components, based on conductive materials, are resistors and inductors. Nickel–Chrome (NiCr) resistors were LIFT printed

from NiCr donor films [36, 40]. Thicknesses up to 10 μm were obtained after 100 successive transfers. This parameter, as well as the planar geometry of the printed patterns and the material electrical properties, allows control of the resistance values. Laser printing resistors, with an accurate and easy-to-control value, can be considered as a postprocess to finely tune the operation of electronic circuits. When metal nanoparticle inks are used to print conductive patterns, the curing temperature of the deposited inks can also be used to control the resistive properties of the material [41]. Lasers are also used to achieve this sintering step, and an accurate selection of the irradiation parameters (wavelength, pulse duration, spatial distribution, fluence) provides a fine control of the resistivity value of the printed structures [42].

Capacitors have also been laser printed. In 2000, Chrisey *et al*. [40] transferred, by means of MAPLE DW, a 15 μm thick layer of $BaTiO_3$ onto an evaporated gold electrode. The top gold electrode was printed by LIFT to form a capacitor of few pF at 1 MHz. Later, a single-step approach was used to transfer the top electrode with the dielectric onto a substrate covered with the bottom electrode, with a single laser shot. Poly-4-vinylphenol (PVP) and Shipley 1818 were used as dielectric with low viscosity, while silver ink and high-viscosity silver pastes were used as top electrode and Au as bottom electrode to obtain capacitors of a few tens of fF, and these values are in good agreement with the theoretical values [43]. With the same approach, capacitors were realized by transferring PVP, PMMA, or Parylene as dielectric with silver top electrodes on previously laser-printed silver bottom electrode [44–46]. For these experiments, a polymer DRL was used to protect the materiel to be transferred. Again, the measurements of the capacitance were in good agreement with the theoretical values. A morphological analysis of the printed structure shows that the strong pressure applied to the dielectric layer when reaching the electrode on the receiver induces a slight increase of its surface beyond the electrode area, which prevents any risk of short circuit between the two electrodes. This effect has also been observed when printing multilayer films for OLED fabrication [4]. The fabrication of microcapacitors from organic and inorganic materials, by using a single step, opens up the way for fast and cost-efficient fabrication of a large range of electrical devices, from conducting lines to complex components.

One of the challenges of the development of autonomous smart cards, which is one of the major markets of printed electronics, is the energy management. This requires energy harvesting systems (piezoelectric devices, solar cells, etc.) and printable microbatteries. In this context, laser processes have been used to fabricate Zn-Ag_2O and Li-ion microbaterries [3]. Especially, the cathodes, Ag_2O and $LiMn_2O_4$, were printed by the MAPLE DW technique, and laser scribing was used to isolate the cathodes from the anodes. Laser direct-write was also used to fabricate stacked Li-ion cells with 3.80 V open-circuit potentials [3]. They operated for more than 50 charge/discharge cycles without significant performance degradation. Capacitance values of 110 μAh/cm^2 were obtained for batteries of 9.0 mm^2 surface area. More recently, thick-film electrodes ($LiCoO_2$ cathode and carbon anode) were laser-printed onto metallic current collectors for the fabricating Li-ion microbatteries. They exhibited a significantly higher

discharge capacity and power density than those made by sputter-deposition thin-film techniques. This result has been attributed to the porous structure of the laser-printed electrodes that allows improved ionic and electronic transport through the thick electrodes (up to ~100 μm) without a significant increase in internal resistance [47]. It has been proposed that the structuring effect of the printed $LiCoO_2$ surfaces is due to a preferred orientation of the $LiCoO_2$ particles that leads to a higher roughness when the number of layers increases [48].

12.5 Interconnection and Heterogeneous Integration

Printing conductive lines could appear as the simplest step of manufacturing printed electronic devices. However, the large number of applications requires a process that is able to print thin and thick lines (from 100 nm to 5 μm) with a minimum width of 10 μm and a width uniformity better than a few micrometers (±2 μm). Moreover, the process must be reliable and fast (>1 m/s). Inkjet is the most currently used digital process, but it suffers from drawbacks such as the high probability to get clogged nozzles and its limitation to transfer only low-viscosity inks, between 6 and 20 mPa s. Laser printing has been extensively investigated to address this topic. Two main approaches have been considered: first, the transfer of silver nanoparticle inks or pastes, and more recently, the printing of metal in liquid phase from a solid thin donor film.

The physics of printing lines by means of LIFT of liquids, such as inks, is presented in Chapter 4, and it will not be discussed here. The standard approach to deposit a continuous line is to print adjacent droplets with a controlled overlap. The value of this overlap must be high enough to guarantee the continuity of the line but not too high to avoid the formation of bulging. To avoid this bulging effect, one can use alternate printing of two overlapping sets of droplets with an intermediate drying step [49]. The morphological properties of the silver lines also depend on the surface energy of the receiver and the ink viscosity [38]. In order to increase the printing velocity, high-repetition-rate lasers, up to 1 MHz, were used to transfer microdroplets of silver inks [50]. It has been demonstrated, both experimentally [51] and numerically [52], that when two successive laser irradiations of the donor film are too close, in time and space, the cavitation bubbles generated in the liquid film interact and form tilted and instable jets. Based on this knowledge, continuous silver lines of 20 μm width have been printed with a three-pass approach at velocities up to 4 m/s [53]. In order to further increase the printing velocity, the distance between two consecutive laser spots can be decreased, leading to the formation of a large gas bubble and the transfer of a full continuous line instead of a set of liquid jets [54]. This approach allows printing silver lines in a single step at velocities up to 17 m/s without any risk of bulging. Figure 12.9 shows an illustration of this single-step transfer of a continuous line. After the transfer of the metal inks on the substrate, a sintering step is required to evaporate the solvent and sinter the particles in order to obtain conductive lines, and as mentioned previously, laser processes can be used to perform this step [41, 55, 56].

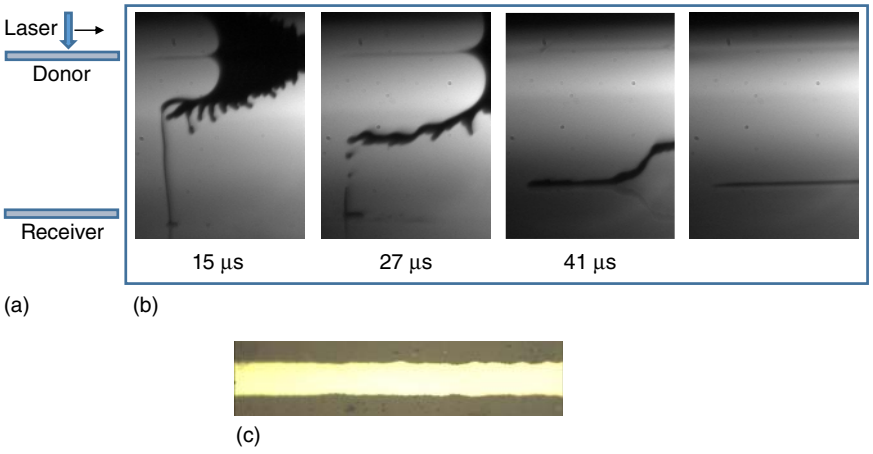

Figure 12.9 LIFT of a continuous line of silver inks in a single step at high velocity. The silver ink (Sun chemical U5714) has a viscosity of 11 mPa s and contains 40% of silver nanoparticle in weight. The UV picosecond laser operates at 1 MHz and scans the donor film at velocity of 17 m/s. (a) Schematic illustration of the setup. (b) Shadowgraphy images showing the formation of a large gas bubble in the donor film and the transfer dynamics of the continuous line toward the receiver substrate. (c) Optical microscopic image of the printed line showing a very uniform width of 25 µm.

These conductive lines are used to realize passive components as discussed previously, but also to connect the different devices of a printed circuit board. The integration of silicon-based circuits on smart cards or RFID cards requires the connection between the printed components (sensors, display, antenna, etc.) and the pads of the silicon chips. The width of these pads is typically around 50 µm, and the distance between two pads is of the order of 10 µm. To avoid any risk of short circuits, this step requires printing lines with small width (<40 µm) and with high resolution (better than 5 µm). To date, laser printing is the best candidate to realize this connection step at high velocity. Another important application of printing high-resolution conductive lines is the fabrication of interdigitized electrodes for sensors. Figure 12.10 shows two examples of such electrodes LIFT-printed at a velocity of 17 m/s on flexible PET substrates.

The laser printing of silver nanopastes also offers a wide range of possibilities. Indeed, this high-viscosity material (10^5 mPa s) combines the advantages of solids (preserve the shape of the beam, printing of thick layers) and those of liquids (no debris) [57, 58]. The realization of thick and narrow conducting lines is of great interest for applications that require high current [59], especially photovoltaic manufacturing [60]. Thanks to the mechanical properties and the soft nature of the nanopastes, freestanding structures, such as bridges or cantilevers, have been laser-printed in a single step [61], and that opens the way for the realization of MEMS devices on printed electronics cards. Printing bridges is also a unique single-step method to interconnect pads over another connection line without using an insulating intermediate layer [62].

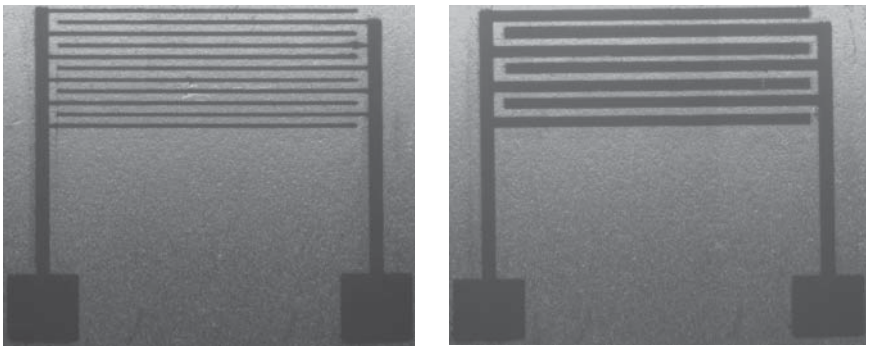

(a) (b)

Figure 12.10 Interdigitized electrodes LIFT-printed from silver nanoparticle inks with a UV picosecond laser operating at 1MHz and a scanner system to move the laser over the donor substrate. (a) Line width of 25 μm and distance between lines of 100 μm, (b) line width of 100 μm and distance between lines of 80 μm.

Flip-chip technology is used to connect the chip to the substrate via conductive bumps. Many bumping techniques are used, but they presented some drawbacks such as the high processing temperatures or the lack of flexibility. LIFT has been used to bond vertical-cavity surface-emitting lasers (VCSELs) to silicon grating couplers (GCs) [63] and single dies to gold contact pads deposited on glass [64]. For both experiments, indium metal pixels were LIFTed onto the receiver to form bumps of 20 μm diameter and few micrometers of thickness. Then, thermocompression bonding was used to ensure the final adhesion. The characteristics of the LIFT-bonded devices were similar to those assembled with other technologies, but the LIFT process is much simpler. In addition, LIFT enables the bumping and bonding down to chip scale, which is critical for fabricating ultraminiature circuitry. The realization of chip bonding on flexible substrate is even more challenging because of the mechanical stresses induced when the substrate is bent. Isotropic conductive adhesive (ICA) is often used to mount devices on conductive pastes deposited on plastic substrates. Sridhar *et al*. LIFT-printed ICA pixels and demonstrated the applicability of this process using RFID transponder integration and testing [65]. They performed the transfer experiment with and without polymer DRL, and no significant differences were observed. Some devices were realized with the LIFT process and others with the stencil printing technique. Their electrical and mechanical characteristics were compared, and the authors concluded that the LIFT process does not affect the electrical and reliability characteristics of the joints formed by the tested ICA. LIFT offers, therefore, a simple, highly accurate, and flexible solution to realize chip-level interconnections for applications requiring single-chip bumping, high-accuracy, and fine pitch for high-density flip-chip applications.

In 2006, Piqué *et al*. proposed and demonstrated a laser-based process to fabricate embedded circuits [66]. The heterogeneous integration consists in mixing

silicon chips and printed elements to realize low-cost smart cards. This requires to connect, as previously discussed, and embed chips in plastic. The authors used first laser ablation to realize the cavities in a plastic substrate, followed by the LIFT of different electronic chips into these cavities. Then an insulating layer is spin-coated to encapsulate the chips and access to the connections that are realized by means of LIFT of conductive pastes is realized by laser drilling. This approach is easy to implement compared to standard microelectronic techniques and opens the door for the fabrication of embedded electronic circuits, which are the building blocks for the development of 3D Systems-in-Package (3D-SiP) microelectronics.

All these ink- or paste-based approaches, developed to print conductive structures, present many advantages compared to other digital printing technologies, such as inkjet, but they still require a sintering step to obtain good conductivity. For the past few years, some groups have combined thin metal donor films with short laser pulses and small focal spot to transfer the metal in liquid phase. Indeed, an appropriate choice of the laser fluence and pulse duration allows to deliver an amount of energy in the thin metal film slightly higher than the energy required to melt it but lower than the energy that would induce its total vaporization [67]. This approach, discussed in greater detail in Chapter 17, has been successively used to print high-aspect-ratio gold pillars of 3–5 μm diameter and 2.1 mm long [68] and nanodots of silicon [69] and gold [70]. The great benefit of this process is that it removes the sintering step because the droplets solidify when reaching the receiver substrate. Conducting lines of copper, aluminum, and gold have been printed with a high resolution and minimum width down to 2 μm [71, 72]. Studies have been performed to investigate the effect of oxidation of melted metal droplets during their transfer on the conductivity of the printed lines. They showed that the electrical transport mechanism in the laser-printed copper structures is different than that in aluminum structures. Copper structures have resistivity as low as approximately 4× of bulk copper, and oxidation does not significantly increase this resistivity [73] as it does in aluminum structures, for which resistivity values have been measured between 4.9× and 470× of the bulk material [74]. For printed aluminum, the increase in resistivity is due to the formation of an aluminum-oxide shell surrounding each droplet. Smaller droplets result therefore in a higher resistivity increase, and printing in inert gas atmosphere prevents the oxidation of the droplets and low resistivity structures can be printed. It is worth mentioning that the company Orbotec has developed a laser printing process based on this approach to repair the interconnection defects of printed circuit board.

12.6 Conclusion

Laser printing has a huge potential for electronic applications. Its ability to deposit small amounts of a wide range of materials with very high resolution

makes it a unique tool for digital manufacturing of many electronic devices. The use of LIFT to transfer thin layers or multilayer stacks for the fabrication of OLEDs or OTFTs offers many possibilities but still has some drawbacks, for example, related to the generation of debris that can make the process irrelevant for ultraclean applications. Moreover, the generation of the shock wave induced by the transfer in solid phase requires the use of low gas pressure environment or/and a small gap between the receiver and the donor. When it is compatible with the application, a thin soft layer can be deposited on the receiver, and this lowers the impact and helps preserve the properties of the transferred material [75]. Despite these drawbacks, LIFT succeeds in printing OTFTs and OLEDs with performances similar or higher than those printed with conventional digital techniques.

The transfer of conductive structures, from metal inks or pastes or directly from solid thin films, is probably the most relevant application of this process for the microelectronics industry. Lines as narrow as 2 μm have been printed, and that is more than 10 times smaller than any other digital printing technology can achieve. All kinds of materials can be printed with very high resolution and at high velocities. The deposition of solid metals in liquid phase allows the printing of metal structures with low resistivity without the need for a sintering step. This process also offers the possibility to print very thick lines for high current flow and 3D structures such as bridges or MEMS and will be covered in more detail in Chapter 17.

Laser-based processes already addressed several manufacturing steps for electronics. In addition to drilling, scribing, cutting, and sintering, laser printing is becoming a mature process offering new opportunities for the development of electronic products [76]. Its ability to transfer a wide range of materials on various kinds of substrates and with high resolution makes it especially suitable for heterogeneous integration, which is considered a very relevant approach for the fabrication of low-cost electronic products, especially on flexible substrates. The digital and contact-free characteristics of the laser printing technology open new possibilities for the realization of personalized products or for adding new functions to standard products such as RFID tags. Furthermore, this technique is especially relevant to address the challenges of interconnection. That is a unique contact-free process for printing high-aspect-ratio conductive lines, narrower than 10 μm and thicker than few micrometers, to both increase the level of integration and enable the transmission of high currents, and for printing 3D structures for connecting the different levels of devices found in 3D-Systems-in-Package assemblies. As this chapter has shown, laser printing is poised to become a key technology for manufacturing the next generations of smart cards on plastic or flexible substrates.

References

1 Bohandy, J., Kim, B.F., and Adrian, F.J. (1986) Metal deposition from a supported metal film using an excimer laser. *J. Appl. Phys.*, **60** (4), 1538–1539.

2 Blanchet, G.B., Loo, Y.-L., Rogers, J.A., Gao, F., and Fincher, C.R. (2003) Large area, high resolution, dry printing of conducting polymers for organic electronics. *Appl. Phys. Lett.*, **82**, 463.

3 Piqué, A., Arnold, C.B., Kim, H., Ollinger, M., and Sutto, T.E. (2004) Rapid prototyping of micropower sources by laser direct-write. *Appl. Phys. A*, **79**, 783–786.

4 Fardel, R., Nagel, M., Nuesch, F., Lippert, T., and Wokaun, A. (2007) Fabrication of organic light-emitting diode pixels by laser-assisted forward transfer. *Appl. Phys. Lett.*, **91**, 061103.

5 Rapp, L., Diallo, A.K., Alloncle, A.-P., Videlot-Ackerman, C., Fages, F., and Delaporte, P. (2009) Pulsed-laser printing of organic thin film transistors. *Appl. Phys. Lett.*, **95**, 171109.

6 Kang, B., Lee, W.H., and Cho, K. (2013) Recent advances in organic transistor printing processes. *ACS Appl. Mater. Interfaces*, **5** (7), 2302–2315.

7 Kim, H., Auyeung, R.C.Y., Lee, S.H., Huston, A.L., and Piqué, A. (2009) Laser forward transfer of silver electrodes for organic thin-film transistors. *Appl. Phys. A*, **96**, 441–445.

8 Rapp, L., Diallo, A.K., Nénon, S., Alloncle, A.-P., Videlot-Ackerman, C., Fages, F., Nagel, M., Lippert, T., and Delaporte, P. (2012) Laser printing of a semiconducting oligomer as active layer in organic thin film transistors: impact of a protecting triazene layer. *Thin Solid Films*, **520**, 3043–3047.

9 Diallo, A.K., Videlot-Ackermann, C., Marsal, P., Brisset, H., Fages, F., Kumagai, A., Yoshimoto, N., Serein-Spirau, F., and Lere-Porte, J.P. (2010) Acetylenic spacers in phenylene end-substituted oligothiophene core for highly air-stable organic field-effect transistors. *Phys. Chem. Chem. Phys.*, **12**, 3845–3851.

10 Rapp, L., Serein-Spirau, F., Lère-Porte, J.-P., Alloncle, A.-P., Delaporte, P., Fages, F., and Videlot-Ackermann, C. (2012) Laser printing of air-stable high performing organic thin film transistors. *Org. Electron.*, **13** (10), 2035–2041.

11 Zergioti, I., Makrygianni, M., Dimitrakis, P., Normand, P., and Chatzandroulis, S. (2011) Laser printing of polythiophene for organic electronics. *Appl. Surf. Sci.*, **257**, 5148–5151.

12 Makrygianni, M., Verrelli, E., Boukos, N., Chatzandroulis, S., Tsoukalas, D., and Zergioti, I. (2013) Laser printing and characterization of semiconducting polymers for organic electronics. *Appl. Phys. A*, **110**, 559–563.

13 Diallo, A.K., Rapp, L., Nénon, S., Alloncle, A.P., Delaporte, P., Fages, F., and Videlot-Ackermann, C. (2011) Top gate copper phthalocyanine thin film transistors with laser-printed dielectric. *Synth. Met.*, **161**, 888–893.

14 Kim, H., Auyeung, R.C.Y., Lee, S.H., Huston, A.L., and Piqué, A. (2010) Laser-printed interdigitated Ag electrodes for organic thin film transistors. *J. Phys. D: Appl. Phys.*, **43**, 085101.

15 Thomas, B., Alloncle, A.-P., Delaporte, P., Sentis, M., Sanaur, S., Barret, M., and Collot, P. (2007) Experimental investigations of laser induced forward transfer process of organic thin films. *Appl. Surf. Sci.*, **254** (4), 1206–1210.

16 Rapp, L., Constantinescu, C., Delaporte, P., and Alloncle, A.P. (2014) Laser-induced forward transfer of polythiophene-based derivatives for fully polymeric thin film transistors. *Org. Electron.*, **15** (8), 1868–1875.
17 Constantinescu, C., Diallo, A.K., Rapp, L., Cremillieu, P., Mazurczyk, R., Serein-Spirau, F., Lere-Porte, J.P., Delaporte, P., Alloncle, A.P., and Videlot-Ackermann, C. (2015) Laser-induced forward transfer of multi-layered structures for OTFT applications. *Appl. Surf. Sci.*, **336**, 11–15.
18 Karnakis, D., Lippert, T., Ichinose, N., Kawanishi, S., and Fukumura, H. (1998) Laser induced molecular transfer using ablation of a triazeno-polymer. *Appl. Surf. Sci.*, **127–129**, 781.
19 Auyeung, R.C.Y., Kim, H., Mathews, S., and Piqué, A. (2015) Laser forward transfer using structured light. *Opt. Express*, **23** (1), 422–430.
20 Rapp, L., Constantinescu, C., Larmande, Y., Alloncle, A.P., and Delaporte, P. (2014) Smart beam shaping for the deposition of solid polymeric material by laser forward transfer. *Appl. Phys. A*, **117** (1), 333–339.
21 Lee, S.T., Suh, M.C., Kang, T.M., Kwon, Y.G., Lee, J.H., Kim, H.D., and Chung, H.K. (2007) 53.1: *invited paper*: LITI (laser induced thermal imaging) technology for high-resolution and large-sized AMOLED. *SID Int. Symp. Digest Tech. Pap.*, **38**, 1588–1591. doi: 10.1889/1.2785622.
22 Lamansky, S., Hoffend, T.R., Le, H., Jones, V., Wolk, M.B., and Tolbert, W.A. (2005) Laser induced thermal imaging of vacuum-coated OLED materials. *SPIE Proc.*, **5937**, 593702.
23 Kattamis, N.T., McDaniel, N.D., Bernhard, S., and Arnold, C.B. (2009) Laser direct write printing of sensitive and robust light emitting organic molecules. *Appl. Phys. Lett.*, **94**, 103306.
24 Ko, S.H., Pan, H., Lee, D., Grigoropoulos, C.P., and Park, H.K. (2010) Nanoparticle selective laser processing for a flexible display fabrication. *Jpn. J. Appl. Phys., Part 1*, **49**, 05EC03.
25 Shaw-Stewart, J., Lippert, T., Nagel, M., Nuesch, F., and Wokaun, A. (2011) Laser-induced forward transfer of polymer light-emitting diode pixels with increased charge injection. *ACS Appl. Mater. Interfaces*, **3** (2), 309–316.
26 Fardel, R., Nagel, M., Nuesch, F., Lippert, T., and Wokaun, A. (2010) Laser-induced forward transfer of organic LED building blocks studied by time-resolved shadowgraphy. *J. Phys. Chem. C*, **114**, 5617–5636.
27 Shaw-Stewart, J., Chu, B., Lippert, T., Maniglio, Y., Nagel, M., Nüesch, F., and Wokaun, A. (2011) Improved laser-induced forward transfer of organic semiconductor thin films by reducing the environmental pressure and controlling the substrate–substrate gap width. *Appl. Phys. A*, **105**, 713–722.
28 Shaw-Stewart, J., Mattle, T., Lippert, T., Nagel, M., Nüesch, F., and Wokaun, A. (2013) The optimisation of the laser-induced forward transfer process for fabrication of polyfluorene-based organic light-emitting diode pixels. *Appl. Surf. Sci.*, **278**, 341–346.
29 Shaw-Stewart, J., Lippert, T., Nagel, M., Nüesch, F., and Wokaun, A. (2012) Red-green-blue polymer light-emitting diode pixels printed by optimized laser-induced forward transfer. *Appl. Phys. Lett.*, **100**, 203303.

30 Shaw-Stewart, J., Lippert, T., Nagel, M., Nüesch, F., and Wokaun, A. (2012) Sequential printing by laser-induced forward transfer to fabricate a polymer light-emitting diode pixel. *Appl. Mater. Interfaces*, **4**, 3535–3541.
31 Shaw-Stewart, J., Mattle, T., Lippert, T., Nagel, M., Nuesch, F.A., and Wokaun, A. (2013) The fabrication of small molecule organic light-emitting diode pixels by laser-induced forward transfer. *J. Appl. Phys.*, **113**, 043104.
32 Kattamis, N.T., McDaniel, N.D., Bernhard, S., and Arnold, C.B. (2011) Ambient laser direct-write printing of a patterned organo-metallic electroluminescent device. *Org. Electron.*, **12**, 1152–1158.
33 Kattamis, N.T., Purnick, P.E., Weiss, R., and Arnold, C.B. (2007) Thick film laser induced forward transfer for deposition of thermally and mechanically sensitive materials. *Appl. Phys. Lett.*, **91**, 171120.
34 Lim, J., Bae, W.K., Kwak, J., Lee, S., Lee, C., and Char, K. (2012) Perspective on synthesis, device structures, and printing processes for quantum dot displays. *Opt. Mater. Express*, **2** (5), 594.
35 Xu, J., Liu, J., Cui, D., Gerhold, M., Wang, A.Y., Nagel, M., and Lippert, T. (2007) Laser-assisted forward transfer of multi-spectral nanocrystal quantum dot emitters. *Nanotechnology*, **18**, 025403.
36 Piqué, A., Chrisey, D.B., Auyeung, R.C.Y., Fitz-Gerald, J., Wu, H.D., McGill, R.A., Lakeou, S., Wu, P.K., Nguyen, V., and Duignan, M. (1999) A novel laser transfer process for direct writing of electronic and sensor materials. *Appl. Phys. A*, **69**, 279–284.
37 Zergioti, I., Mailis, S., Vainos, N.A., Papakonstantinou, P., Kalpouzos, C., Grigoropoulos, C.P., and Fotakis, C. (1998) Microdeposition of metal and oxide structures using ultrashort laser pulses. *Appl. Phys. A*, **66**, 579–582.
38 Rapp, L., Ailuno, J., Alloncle, A.-P., and Delaporte, P. (2011) Pulsed-laser printing of silver nanoparticles ink: control of morphological properties. *Opt. Express*, **19** (22), 21563–21574.
39 Duocastella, M., Kim, H., Serra, P., and Piqué, A. (2012) Optimization of laser printing of nanoparticle suspensions for microelectronic applications. *Appl. Phys. A*, **106**, 471–478.
40 Chrisey, D.B., Pique, A., Fitz-Gerald, J., Auyeung, R.C.Y., McGill, R.A., Wu, H.D., and Duignan, M. (2000) New approach to laser direct writing active and passive mesoscopic circuit elements. *Appl. Surf. Sci.*, **154–155**, 593–600.
41 Makrygianni, M., Kalpyris, I., Boutopoulos, C., and Zergioti, I. (2014) Laser induced forward transfer of Ag nanoparticles ink deposition and characterization. *Appl. Surf. Sci.*, **297**, 40–44.
42 Chung, J., Ko, S., Bieri, N.R., Grigoropoulos, C.P., and Poulikakos, D. (2004) Conductor microstructures by laser curing of printed gold nanoparticle ink. *Appl. Phys. Lett.*, **84** (5), 801–803.
43 Birnbaum, A. J., Kim, H., Charipar, N. A., Piqué, A. (2010) Laser printing of multi-layered polymer/metal heterostructures for electronic and MEMS devices, *Appl. Phys. A* **99**, 711–716.
44 Constantinescu, C., Rapp, L., Diallo, A.K., Videlot-Ackermann, C., Delaporte, P., and Alloncle, A.-P. (2015) Microcapacitors with controlled electrical

capacity in the pF–nF range printed by laser-induced forward transfer (LIFT). *Org. Electron.*, **20**, 1–7.

45 Constantinescu, C., Rapp, L., Delaporte, P., and Alloncle, A.-P. (2016) Investigation on laser printing of microcapacitors using poly (methyl methacrylate) dielectric thin films for organic electronics applications'. *Appl. Surf. Sci.*, **374**, 90–95.

46 Constantinescu, C., Rapp, L., Rotaru, P., Delaporte, P., and Alloncle, A.-P. (2016) Polyvinylphenol (PVP) microcapacitors printed by laser-induced forward transfer (LIFT): multilayered pixel design and thermal analysis investigations. *J. Phys. D: Appl. Phys.*, **49**, 155301.

47 Kim, H., Proell, J., Kohler, R., Pfleging, W., and Piqué, A. (2012) Laser-printed and processed $LiCoO_2$ CathodeThick films for Li-Ion microbatteries. *J. Laser Micro/Nanoeng.*, **7** (3), 320–325.

48 Atre, A.C. and Arnold, C.B. (2011) $LiCoO_2$ texturing by laser induced forward transfer for printed microbatteries. *SPIE Proc.*, **7921**, 79210O.

49 Florian, C., Caballero-Lucas, F., Fernández-Pradas, J.M., Artigas, R., Ogier, S., Karnakis, D., and Serra, P. (2015) Conductive silver ink printing through the laser-induced forward transfer technique. *Appl. Surf. Sci.*, **336**, 304–308.

50 Biver, E., Rapp, L., Alloncle, A.-P., and Delaporte, P. (2014) Multi-jets formation using laser forward transfer. *Appl. Surf. Sci.*, **302**, 153–158.

51 Biver, E., Rapp, L., Alloncle, A.-P., Serra, P., and Delaporte, P. (2014) High-speed multi-jets printing using laser forward transfer: time-resolved study of the ejection dynamics. *Opt. Express*, **22** (14), 17122–17134.

52 Brasz, C.F., Yang, J.H., and Arnold, C.B. (2015) Tilting of adjacent laser-induced liquid jets. *Microfluid. Nanofluid.*, **18**, 185–197.

53 Rapp, L., Biver, E., Alloncle, A.-P., and Delaporte, P. (2014) High-speed laser printing of silver nanoparticles ink. *J. Laser Micro/Nanoeng.*, **9** (1), 5–9.

54 Puerto, D., Biver, E., Alloncle, A.-P., and Delaporte, P. (2016) Single step high-speed printing of continuous silver lines by laser-induced forward transfer. *Appl. Surf. Sci.*, **374**, 183–189.

55 Son, Y., Yeo, J., Moon, H., Lim, T.W., Hong, S., Nam, K.H., Yoo, S., Grigoropoulos, C.P., Yang, D.-Y., and Ko, S.H. (2011) Nanoscale electronics: digital fabrication by direct femtosecond laser processing of metal nanoparticles. *Adv. Mater.*, **23**, 3176–3181.

56 Joo, M., Lee, B., Jeong, S., and Lee, M. (2012) Comparative studies on thermal and laser sintering for highly conductive Cu films printable on plastic substrate. *Thin Solid Films*, **520**, 2878–2883.

57 Auyeung, R.C.Y., Kim, H., Charipar, N.A., Birnbaum, A.J., Mathews, S.A., and Piqué, A. (2011) Laser forward transfer based on a spatial light modulator. *Appl. Phys. A*, **102**, 21–26.

58 Piqué, A., Auyeung, R.C.Y., Kim, H., Metkus, K.M., and Matthews, S.A. (2008) Digital microfabrication by laser decal transfer. *J. Laser Micro/Nanoeng.*, **3** (3), 163–169.

59 Breckenfeld, E., Kim, H., Auyeung, R.C.Y., Charipar, N., Serra, P., and Piqué, A. (2015) Laser-induced forward transfer of silver nanopaste for microwave interconnects. *Appl. Surf. Sci.*, **331**, 254–261.

60 Sanchez-Aniorte, M.I., Mouhamadou, B., Alloncle, A.-P., Sarnet, T., and Delaporte, P. (2016) Laser-induced forward transfer for improving fine-line metallization in photovoltaic applications. *Appl. Phys. A*, **122**, 595.

61 Auyeung, R.C.Y., Kim, H., Birnbaum, A.J., Zalalutdinov, M., Mathews, S.A., and Piqué, A. (2009) Laser decal transfer of freestanding microcantilevers and microbridges. *Appl. Phys. A*, **97**, 513–519.

62 Wang, J., Auyeung, R.C.Y., Kim, H., Charipar, N.A., and Piqué, A. (2010) Three-dimensional printing of interconnects by laser direct-write of silver nanopastes. *Adv. Mater.*, **22**, 4462–4466.

63 Kaur, K.S., Subramanian, A.Z., Cardile, P., Verplancke, R., Van Kerrebrouck, J., Spiga, S., Meyer, R., Bauwelinck, J., Baets, R., and Van Steenberge, G. (2015) Flip-chip assembly of VCSELs to silicon grating couplers via laser fabricated SU8 prisms. *Opt. Express*, **23** (22), 28264–28270.

64 Kaur, K. and Van Steenberge, G. (2015) Laser-induced forward transfer for flip-chip packaging of single dies. *J. Vis. Exp.*, **97**, e52623.

65 Sridhar, A., Perinchery, S.M., Smits, E.C.P., Mandamparambil, R., and van den Brand, J. (2015) Reliability investigations on LIFT-printed isotropic conductive adhesive joints for system-in-foil applications. *Microelectron. Reliab.*, **55**, 2324–2330.

66 Piqué, A., Mathews, S.A., Pratap, B., Auyeung, R.C.Y., Karns, B.J., and Lakeou, S. (2006) Embedding electronic circuits by laser direct-write. *Microelectron. Eng.*, **83**, 2527–2533.

67 Zenou, M., Sa'ar, A., and Kotler, Z. (2015) Laser jetting of femto-liter metal droplets for high resolution 3D printed structures. *Sci. Rep.*, **5**, 17265.

68 Visser, C.W., Pohl, R., Sun, C., Huis in 't Veld, B., Römer, G.-W., and Lohse, D. (2015) Towards 3D printing of pure metals by laser-induced forward transfer. *Adv. Mater.*, **27** (27), 4087–4092.

69 Zywietz, U., Evlyukhin, A.B., Reinhardt, C., and Chichkov, B.N. (2014) Laser printing of silicon nanoparticles with resonant optical electric and magnetic responses. *Nat. Commun.*, **5**, 3402.

70 Kuznetsov, A.I., Kiyan, R., and Chichkov, B.N. (2010) Laser fabrication of 2D and 3D metal nanoparticle structures and arrays. *Opt. Express*, **18**, 21198–21203.

71 Grant-Jacob, J.A., Mills, B., Feinaeugle, M., Sones, C.L., Oosterhuis, G., Hoppenbrouwers, M.B., and Eason, R.W. (2013) Micron-scale copper wires printed using femtosecond laser-induced forward transfer with automated donor replenishment. *Opt. Mater. Express*, **3** (6), 747–754.

72 Zenou, M. and Kotler, Z. (2016) Printing of metallic 3D micro-objects by laser induced forward transfer. *Opt. Express*, **24** (2), 1431.

73 Winter, S., Zenou, M., and Kotler, Z. (2016) Conductivity of laser printed copper structures limited by nano-crystal grain size and amorphous metal droplet shell. *J. Phys. D: Appl. Phys.*, **49**, 165310.

74 Zenou, M., Sa'ar, A., and Kotler, Z. (2016) Digital laser printing of metal/metal-oxide nano-composites with tunable electrical properties. *Nanotechnology*, **27**, 015203.

75 Feinaeugle, M., Horak, P., Sones, C.L., Lippert, T., and Eason, R.W. (2014) Polymer-coated compliant receivers for intact laser-induced forward transfer of thin films: experimental results and modelling. *Appl. Phys. A*, **116**, 1939–1950.

76 Zacharatos, F., Makrygianni, M., Geremia, R., Biver, E., Karnakis, D., Leyder, S., Puerto, D., Delaporte, P., and Zergioti, I. (2016) Laser direct write micro-fabrication of large area electronics on flexible substrates. *Appl. Surf. Sci.*, **374**, 117–123.

13

Laser Printing of Chemical and Biological Sensors

Ioanna Zergioti

National Technical University of Athens, Department of Physics, Heroon Polytehneiou 9, 15780 Zografou, Athens, Greece

13.1 Introduction

Today, there is a considerable necessity for depositing high-quality biological, organic, polymer thin films, multilayers, and composite materials. Furthermore, there is a need to find a method that could preserve the structural, morphological, and chemical composition of the film to be transferred. To be more specific, in biological and chemical sensor applications, high-quality thin films of bioselective or chemoselective materials must be processed so that the physiochemical properties are maintained. To take full advantage of the bulk properties of natural and synthetic polymers, the thin film must mimic these features. Various techniques have been established for the fabrication of biological and chemical sensors. For example, matrix-assisted pulsed laser evaporation (MAPLE) [1], dip-pen nanolithography [2], microcontact printing [3], or screen printing [4] and other techniques have been developed; however, some limitations exist in the aforementioned techniques.

Laser direct-write (LDW) techniques based on laser-induced forward transfer (LIFT) of functional materials offer unique advantages and capabilities for the rapid prototyping of electronic, optical, and sensor elements as opposed to other digital printing processes. The development of LIFT has grown steadily over a period of 30 years, and this chapter describes how the technique is used in many applications, especially for the fabrication of biological and chemical sensors. The ability to laser transfer and deposit a variety of materials without limitations at virtually any surface and conditions (ambient or vacuum) makes this technique an appropriate "tool" for the fabrication of sensor devices.

At this point, a brief introduction to the general principle of operation and some examples of chemical and biological sensors will be presented. One commonly cited definition by Higson *et al*. [5] regarding biosensors is: "a biosensor is a sensing device in which a biologically derived recognition entity is coupled to a transducer, to allow the quantitative development of some complex biochemical parameter." This sensing device is a combination of a recognition element and a sensor element. A general principle of biosensors operation is

Laser Printing of Functional Materials: 3D Microfabrication, Electronics and Biomedicine,
First Edition. Edited by Alberto Piqué and Pere Serra.
© 2018 Wiley-VCH Verlag GmbH & Co. KGaA. Published 2018 by Wiley-VCH Verlag GmbH & Co. KGaA.

that, a recognition element, such as enzymes, nucleic acids, antibodies, whole cells, recognizes a specific analyte and the sensor element transduces the change in the biomolecule into an electrical signal. The recognition element is very specific to the analyte to which it is sensitive, and it does not recognize other elements. Depending on the transducing mechanism used, the biosensors can be of many types such as resonant biosensors, optical detection biosensors, thermal-detection biosensors, ion-sensitive field-effect transistor (ISFET) biosensors, and electrochemical biosensors. The electrochemical biosensors, based on the parameter measured, can be further classified as conductimetric, amperometric, and potentiometric [6].

A chemical sensor can be defined as a device or instrument that detects the presence and quantity, in terms of concentration, of a given analyte, while the complexity of such a device is related to the technical difficulties associated with the specific nature (i.e., elemental or molecular) of the chemical substance to be analyzed. The chemical information may originate from a chemical reaction of a biomaterial, chemical compound, or a combination of both, attached onto the surface of a physical transducer, toward the analyte. According to the working principle, the chemical sensor can be classified into many types such as optical, electrochemical, mass, magnetic, and thermal. The optical chemical sensor is based on the changes in optical phenomena (reflection, deflection, refractive index variation) arising from the interaction between the analyte and the receiver. The electrochemical sensor utilizes the electrochemical effect among the analytes and the featured electrodes. The working principle of the mass sensor depends on the quality change induced by the mass loading, from the adsorption of the analyte on the special modification of the sensor surface. The magnetic device is based on the magnetic properties in analyte adsorption, whereas the thermal sensor utilizes the thermal effect generated by the specific chemical reaction or adsorption process [7, 8].

The following paragraphs briefly present various nonlaser printing techniques that have been investigated for the development of chemical and biological sensors. Furthermore, there is an extended analysis, especially for the LIFT technique as well as other laser-based techniques for the microdeposition of various materials with regard to biological and chemical sensor fabrication.

13.2 Conventional Printing Methods for the Fabrication of Chemical and Biological Sensors

Over the past years, there is an expanding need for the fabrication of simple, rapid, cost-effective, and field-deployable sensors. Sensors play an important role in industrial and safety-based applications. The aim of this chapter is to review and examine various challenges that are mentioned in the literature in the past decade related with the fabrication of chemical and biological sensors.

Various printing techniques have been investigated for the development of chemical and biological sensors, which may be separated into two major categories: contact and noncontact printing techniques, and they could also be classified into serial or parallel deposition. Specifically, in contact printing

methods, the printing device requires direct contact with the substrate while depositing materials. On the other hand, noncontact printing methods involve no physical contact between the device and the substrate but involve the transfer of the material to a receiving substrate via an ejection event (e.g., photolithography, inkjet printing, and laser writing). All printing methods have the same object: efficient deposition of uniform, dense arrays of small droplets of probe molecules.

13.2.1 Contact Printing Methods

Contact printing methods are utilized to fabricate microarrays by means of physical contact between the substrates. Contact printing approaches comprise solid pins, split pins, nanotips, and microcontact (or microstamps) technologies.

13.2.1.1 Pin Printing Approach

Over the past years, the pin printing approach has been employed as an appropriate technique for microfabrication and especially for sensor fabrication [9, 10], and the development of pin-printed sensor arrays has attracted great interest especially in the field of biological and chemical sensor applications. Generally, the methodology of pin printing approach relies on the transfer of one or more metallic pins from a microwell plate to a solid substrate, and the simplest approach is the solid pin contact printing, where the microarray spotter is being widely used. Pin printing method is ruled by the surface tension of the solution and the wettability of the solution on the substrate, while typical substrates for microarray printing include microscope slides, plastics, and polymer-coated glass. At this point, it is important to notice that the dispensed volume is also affected by the temperature. Additionally, contaminations and dust must be controlled if high-quality arrays are to be produced while the risk of split pin clogging should be minimized as well [11].

Many studies have been reported regarding the fabrication of sensors. For example, Cho *et al*. [12] were the first researchers who have fabricated biosensor arrays based on pin printing protein-doped xerogels for the simultaneous detection of glucose and O_2. They have observed that the combination of two major processes, namely (i) pin printing and (ii) sol–gel technique, demonstrates a simple approach to fabricate reusable biosensor arrays, which show good sensing properties and pave the way to integrated light source/biosensor arrays. Another work by the same research group presented the development of a reusable multianalyte chemical sensor for the simultaneous detection of O_2 and pH variations in aqueous samples using again the pin printing technology and the sol–gel process. They have reported that by utilizing the pin printing method, they could prepare reproducible chemical sensors with the following characteristics: 100 μm diameter, 1–2 μm thickness, at a rate of approximately 1 sensor element per second with a single pin. The aforementioned results have indicated the accuracy of the pin printing method for the fabrication of reusable chemical sensor arrays [13]. As mentioned earlier, except for solid pins, there are other printing techniques that are utilized in pin printing technology for the fabrication of sensors, that is, split pins and silicon pins.

Despite being an accurate printing technique, pin printing also faces various shortcomings. Specifically, pins are difficult to manufacture, also during machining, a pin experiences stresses that leave it vulnerable to corrosion and deformation. Furthermore, the mechanical fabrication procedure is not an appropriate method to form uniform surfaces, which are necessary for drop printing. Moreover, during machining, grind marks and polish lines are being created, affecting the pin surface area and the adhesive properties. In addition, these processes often leave residual surface impurities and contaminants.

13.2.1.2 Microcontact Printing (or Microstamping) Technique

An alternative method of the pin printing technique is the microcontact printing (or microstamps) for the fabrication of sensors [14]. The operating principle of this technique is simple, and the process may be characterized as simple and cost-effective since it can be conducted in a laboratory without the need for special or advanced equipment. To be specific, different types of materials are first adsorbed on the patterned large surface area of a polymer stamp, and then they are deposited on a substrate by physical contact. As a result, a large number of spots are printed in parallel, allowing high-throughput microarray fabrication. The most widely used materials to construct the stamps are the elastomeric ones, since they provide good contact. Polydimethylsiloxane (PDMS) is a commonly used material due to the fact that it is simple to be molded and it becomes a soft polymer. Consequently, this enables a well-defined contact between the stamp and the area to be modified, and the stamp is subsequently soaked in a molecular "ink" that is imprinted on the surface.

Many research groups have been involved with the fabrication of sensors using the microcontact printing. For example, Huang *et al*. [15] have designed and implemented a fully integrated humidity sensor device by using the microcontact printing for the transfer of sensing elements on top of a CMOS device. Analytically, the Fe–Al–polyaniline polymeric film was formed by the microstamping method so as to be deposited onto the integrated electrodes on top of the fabricated CMOS circuit and was selected due to the fact that this multisolution-based polyaniline humidity sensing material is a good candidate to achieve a stable and adequately selective humidity sensor. They have concluded that the developed sensor has exhibited low power consumption, fast response time of about 5 s, and high sensitivity of about 30 mV/%.

Despite the efficiency of this technique for the fabrication of sensors, it also presents some drawbacks. The main disadvantage of microcontact printing is based on the use of soft polymers. During the "stamping" process, swelling of the stamp is frequently observed and, as a result, an increased pattern size. Another aspect of soft lithography is the contamination of the patterns with unpolymerized low-molecular-weight siloxane from the stamp, while an excess of ink often results in enhanced diffusion of the imprinted molecules on the patterned surface. Finally, a major disadvantage is the reproducibility of the pattern, where an important parameter is the influence from the exerted forces, which derive from the contact of the stamp with the surface. In recent years, efforts were made to shrink the size of the structures to the nanoscale [10].

13.2.1.3 Nanotip Printing

The deposited feature spot size is an important parameter, which should be investigated in order to advance to more complex arrays for the fabrication of devices, and nowadays, the trend in the scientific community is heading toward the minimization of the printing resolution. The nanotip printing technique has many similarities with the pin printing technique, but it is based on atomic force microscopy (AFM) nanotips to transfer probes to the array substrate [2, 16]. This technique is also called "dip-pen lithography." One of the advantages of AFM printing is that the same tip is used to both print and detect so that the molecular and physical properties can be directly measured. When an AFM tip is brought in close proximity to the substrate, the probe solution flows from the coated tip to the substrate. The AFM tip also has the property (also known as *AFM grafting*) to eliminate parts of self-assembled monolayers (SAM) on a specific region (i.e., molecules resisting biomolecule adsorption). Using the nanotip printing technique, a solution that binds biological materials (e.g., proteins or other biomolecules), which is then transferred from the tip to the substrate, can achieve nanopatterns as well as more complex shapes [17, 18]. The rest of the substrate is blocked with molecules that do not bind the biomolecules under investigation, and the substrate is then exposed to the biomolecule solution. AFM printing technology is a serial printing method and, for that reason, is a slow-moving technique, compared to the microstamping method. Eventually, this technique tends to limit the device functionality because sample volumes are very small and they evaporate quickly.

13.2.2 Noncontact Printing Methods

According to the aforementioned, contact printing methods include a broad range of techniques, but all methods undoubtedly involve contact between the substrate surface and a stamp or pin. On the other hand, noncontact printing techniques vary between photochemistry-based methods to laser writing and fluid droplet dispensing, while the use of noncontact printing techniques presents two major benefits, which are the absence of contaminants and the higher throughput.

13.2.2.1 Photochemistry-Based Printing

This printing method relies on the chemical treatment of the substrate and the exposure with UV light through photomasks. In the photochemistry-based printing technique, the two major categories are photolithography [19–21] and direct photochemical patterning [22, 23]. These fabrication methods are a common practice to the design of protein and DNA arrays, although cell adhesion regions can also be fabricated in this way [24]. In the same way, as all the parallel printing methods, photochemistry features high throughput.

Despite the efficiency of this technique for patterning different samples, it also presents some drawbacks. The disadvantages involve the risk of biomolecule deterioration by photoresist solutions and the difficulty in patterning different samples in a single step [25].

13.2.2.2 Inkjet Printing Technique

This printing technique presents localized deposition and is offered readily to pattern structures without the need of a mask, providing a significant potential for the fabrication of reproducible patterns (especially of sensors). Among the many advantages of the technique, one may find the reduction of waste volumes and cross-contamination, as it is a noncontact deposition method, while it also provides high spatial resolution (<30 μm). Moreover, it is a promising method for depositing features on various substrates and transfer mainly biomaterials (i.e., nucleic acid and protein arrays), while in the last few years, it has been used as a free-form fabrication method for building three-dimensional parts and is currently being explored as a method of printing devices. This printing method is intrinsically compatible with flexible electronics, such as flexible printed circuit boards, and is expected to reduce the deterioration of the sensor characteristics. Its ability to deliver a precise amount of material in a quick, reproducible manner to predetermined locations under computer control is a desirable feature for applications, as in the production of sensors. In addition, it is scalable to large arrays and can coat arbitrary structures in a noncontact way.

In the work by Allain *et al*. [26], it was highlighted that biological materials (DNA) can be deposited using inkjet printers and remain intact; however, proteins that are more unstable may be more sensitive in the case that extreme conditions of inkjet printing are applied. The technique has also found application in patterning microarrays of *in situ* synthesized oligonucleotides, which is typically performed by photochemical means. In detail, different piezoelectric heads fabricated in various substrates (i.e., glass, silicon, or ceramics) have been used to synthesize DNA arrays [27, 28], and other solutions that have low volatility, high surface tension, and high viscosity are more desirable since they impede evaporation and contaminations between adjacent sites.

However, there are some significant limitations in this technique, which will not be discussed, thoroughly, in this chapter. Some significant disadvantages are (i) inkjet nozzles have the tendency to develop undesirable droplets (satellites). As a result, these surrounding spots reduce printing resolution [29] and (ii) the droplets experience high shear rates while passing through the nozzle, affecting the substrate surface. Under these shear rates or high temperatures, there is a risk of denaturing the biomolecules in the solution [25].

13.2.2.3 Electrospray Deposition (ESD)

Electrospray deposition (ESD) is, also, an alternative technique that allows for the parallel fabrication of microarrays. According to the vast number of studies that have been already reported, it is often used to transfer biological materials, semiconducting ceramics, and other materials [30–33] as well, as it provides the advantage of producing very small spots. However, there are some drawbacks as with inkjet printing. In more detail, the electrical field that is applied may result in degradation of the transferred material properties during the process, since, for example, the pH levels of the solution can be affected from the electrochemical reactions that occur. Finally, using this method, biological materials could deform under such conditions, because of the charging of the solution.

In summary, there is a variety of new technologies that are promising for faster, more efficient, less expensive microarray fabrication. In order for competing technologies to be viable in the long term, the microarray quality (e.g., spot uniformity and size) must also be evaluated alongside throughput and cost considerations. Although none of these new methods have yet supplanted the conventional method of contact pin printing, the continuing development of new materials and micromachining techniques may soon lead to an alternative technology, making the technique of biomolecular microarray analysis even more accessible to the scientific community. An ideal printing system should be capable of creating uniform, dense arrays of small droplets using minimum volumes of solutions, while preventing solution contamination and biomolecular damage. Furthermore, the system should be inexpensive, reliable, and durable. The aforementioned techniques do not meet all the required criteria, and this is why laser-based techniques are gaining increased interest for sensor applications.

13.3 Laser-Based Printing Techniques: Introduction

Modern laser micromachining offers several advantages in a wide field of applications, such as sensor devices, for chemical analysis as well as in the field of medicine. Owing to their great flexibility, laser-based techniques have been widely applied in many industrial applications, namely microelectronics and integrated devices such as those found in lab-on-a-chip and 3D printing. Nearly all applications require high resolution and high speed, while achieving high flexibility and full control of the quality, that is, morphology and size, of the deposited materials. Among the laser-based processes, laser ablation is widely used for selective material removal, both for laser cutting and drilling applications as well as for surface texturing. while laser printing has gained increased interest during the last decade due to its unique advantages since it provides fast, low-cost, and contact-free deposition in ambient conditions. Moreover, along with the variety of demanding applications that have been mentioned, a wide range of different materials may be transferred using laser printing. So far, several laser-based techniques have been developed to address the challenges of high resolution and printing speed, and given the continuous progress in additive manufacturing technologies, the fabrication of complex three-dimensional structures has also been achieved, as it will be presented in the next paragraphs.

13.3.1 Laser-Induced Forward Transfer

LIFT is a high-resolution 3D direct-write method that was first demonstrated in 1986 [34]. LIFT technique has a high potential for printing of various materials [35–38], mostly metals [39–42]. In this section, the general process of LIFT is discussed, where a more detailed description may be found in Chapters 1 and 2.

The fabrication of device structures requires the formation of complex high-resolution patterns in two-dimensions as well as three-dimensions. The

success of any microfabrication technique depends on its ability to direct-write a wide variety of materials over many different types of surfaces. A broad variety of device applications have been described in the literature involving organic and inorganic materials. Since the LIFT technique allows the deposition of complex and multicomponent materials in a direct way from a separately prepared donor film and without further development process of materials, this technique appears suitable for the fabrication of microdevices such as chemical and biological sensors, where functional and sensitive biomaterials such as proteins, enzymes, cells, nucleic acids, and microorganisms have to be accurately deposited in a controlled manner without degrading their desirable properties.

Despite the successful applicability of the LIFT technique, for the direct-laser printing of different types of metals, the actual uses of the LIFT technique are limited due to several shortcomings. In order to overcome several drawbacks of the traditional LIFT technique, novel approaches/modifications based on the original LIFT technique that enable a solvent-free (or "dry") direct-write deposition of solid and liquid thin films, necessary for the fabrication of devices with sensitive functional materials, have been developed.

One first variation to overcome some of LIFT's drawbacks was to deposit a multilayer film on the donor substrate. This modification has been called "laser ablation transfer" (LAT), a term that was first introduced by Tolbert *et al*. [43] in 1993 and was originally intended for high-speed color printing applications. In this approach, a thin absorbing layer, usually a metal, is firstly deposited on the transparent support followed by the deposition of a second layer that comprises the material under transfer. The thin absorbing layer was called "dynamic release layer" (or DRL) [43]. During laser printing, the laser pulse interacts with the laser-absorbing layer, causing vaporization of the metallic layer as in the case of traditional LIFT. DRL-LIFT is a highly flexible transfer technique, whose restrictions are mainly determined by the properties of the involved materials. So far, various materials [44, 45] including polymers [46] as well as liquids [47] and living cells [48, 49] have been successfully transferred for sensing applications. A more detailed analysis of LIFT using an intermediate laser-absorbing film has been described in Chapter 3. The following paragraphs present a compilation of "LIFT technique" examples for the microdeposition of various materials regarding the fabrication of biological and chemical sensors.

There are several examples in the literature on how the LIFT technique (with the intermediate-absorbing laser film DRL) is adapted for printing materials associated with sensor applications. For example, intermediate-absorbing titanium layers of about 50–60 nm thickness have been used in a LIFT setup to successfully deposit droplet of viscous DNA dispersions with the 355 nm emission of a frequency-tripled Nd:YAG laser [50]. For biosensor fabrication, where small amounts of delicate materials have to be manipulated, this modified LIFT approach opens up a promising orifice-free and noncontact deposition technique for the gentle and accurate direct-write of "bioinks" [51–53]. A number of bio-LIFT experiments were also reported with approximately 50–100 nm thick silver layers as absorbing layers in conjunction with 248 nm pulses (30 ns duration) using a KrF excimer laser and known as absorbing film-assisted

laser-induced forward transfer (AFA-LIFT) [54] for biosensor applications. Moreover, the accurate LIFT deposition of thin polymer films has recently been demonstrated for microsensor applications. Homogeneous and hole-free polyethyleneimine (PEI) pixels with a low surface roughness were deposited in the same way with a triazene photopolymer DRL after process optimization [55]. Meanwhile, LIFT of PEI thin films to sensing chip units allowed measurment of chemoresponsive signals [56]. The potential of photopolymers as laser-absorbing layers in LIFT applications was demonstrated with various highly sensitive materials: assisted by a approximately 100 nm thick sacrificial triazene polymer, DRL living mammalian neuroblast cells were transferred and gently deposited on a receiver substrate using a 193 nm ArF nanosecond excimer laser [57]. This opens up new possibilities for the manufacturing of biosensors, in which, living cells should be precisely deposited onto microchips.

13.3.2 LIFT of Liquid Films

The ability of LIFT to deposit materials from liquid films makes this technique especially suitable for the preparation of miniaturized biological and chemical sensors, since in this way material-containing solutions can be spotted with precision onto a solid substrate where the materials are immobilized to enable the subsequent sensing measurements. The potential of the LIFT technique to print a variety of liquid materials, such as inorganic inks, pastes, and biological solutions, has prompted many research groups to investigate the transfer process that takes place during the LIFT of liquids. The dynamics of the laser-induced ejection process have been studied through time-resolved imaging, and the mechanism of liquid-phase LIFT can be summarized as follows: Below a threshold laser fluence (low laser fluence), a bubble of vaporized material displaces the free surface but subsequently collapses back to the donor without releasing any material. Within an intermediate laser fluence range, the ejected material is confined to a narrow jet [58] suggesting an appropriate window of controlled and reproducible printing. As the laser fluence increases (high laser fluences), the deposition could be described as uncontrollable, presenting satellite droplets and material debris. Since the transferred material remains in the liquid state during the whole process, there is no biomolecule decomposition, and therefore, the deposited material preserves its bioactivity. The volume of the ejected material is determined by the dimensions of the laser beam; the high focusing power of lasers allows to obtain micron-sized droplets, and that provides this technique with a high degree of spatial resolution.

Barron *et al*. [59] have demonstrated time-resolved images of the LIFT technique for protein solution printing. In this experiment, a 355 nm Nd:YAG laser was used for the deposition of a protein solution from a metallic DRL substrate onto a glass-receiving substrate. It was assumed, using modeling calculations, that the ejection of protein solution from the donor occurs as a result of heat transfer through the intermediate laser-absorbing substrate and subsequent vaporization of a portion of the protein solution that is in direct contact with the heated layer. More recently, our group has studied the ejection behavior of complex solutions (silver nanoparticles (NP) inks) [60]. For the low-viscosity

silver NP inks, it was found that the use of a metallic DRL (titanium) resulted in smooth and low-velocity (9–77 m/s) jetting behavior, for a wide laser processing window, presenting well-defined transfer of silver droplets without undesirable satellite drops. For higher-viscosity inks, the printing behavior is similar to the behavior of solid-phase LIFT. The irradiated part of the viscous film that was ejected from the donor substrate was propelled slowly on the receiving substrate, which minimizes its deformation and fragmentation upon impact to the receiving substrate. In general, the understanding of the printing behavior of metallic NP inks provides an enhancement of the capabilities of the LIFT technique in industrial applications, especially on sensors fabrication. A further review on the LIFT technique of liquid transfer can be found in Chapters 4 and 5.

13.4 Applications of Direct Laser Printing

The continuing evolution of the laser transfer process, as presented in the previous sections, has been driven by the wide range of applications ready to benefit from the use of direct-write processes. In the following section, some selected examples in application areas ranging from biological arrays to chemical sensors are presented to indicate the versatility of the laser-based microfabrication techniques.

13.4.1 Biosensors

13.4.1.1 Background

In the past, sensors and biosensors were complex systems regarding the different types of parts and techniques that were required to fabricate them and more importantly their reusability. Nowadays, a variety of techniques have been developed for the fabrication of biosensors, which allow the controlled patterning of biological molecules and other related materials. Two procedures should be implemented in order to achieve fully functional sensors: (i) the transfer of the material from a donor substrate to the receiver substrate under specific circumstances and (ii) the precise and defined localization of the material on the receiver substrate. Two kinds of techniques have been developed to fabricate these sensors. Firstly, mass printing technologies: (i) gravure printing [61, 62], (ii) flexography [63], (iii) screen printing [64, 65], and (iv) roll-to-roll process, which are well-known approaches from the graphic techniques and enable roll-to-roll or high-speed sheet-to-sheet processing [66]; and secondly, the noncontact printing methods [67–70]. These methods have the main characteristic that involves an automated production system, based on a flexible, planar manufacturing technology inspired by the traditional print media industry.

The aforementioned (conventional) techniques, for printing sensors, present a number of drawbacks, where some of them have been described in Section 13.2. In the following paragraphs, we will focus on the laser-based printing techniques, which as we have already indicated present a number of advantages for the development of sensors.

13.4.1.2 Printing of Biological Materials for Biosensors

A rapidly growing field is considered for the fabrication of microarrays of biological molecules for the development of biosensors. Pharmaceutical companies, academia, and diagnostic firms employ massive analysis in order to develop products that improve the quality of life since the fabrication of advanced biological sensors will provide better health studies and faster detection of contagious and rare illnesses.

Different types of methods are currently established for depositing biopolymers in biosensor systems. As stated by most of the published works, biological materials are applied onto their binding or adsorbing substrates in solution by simple dispensing or soaking techniques. A number of methods, such as microfluidic, gel micro-casting, and localized activation methods, have been already reported for the successful localized deposition. The majority of these methods are liquid deposition processes. At this point, it is important to mention some critical parameters for the successful transfer of liquid microarrays. Among them, one may find the laser fluence and the beam-focusing parameters, which should be taken into consideration when it comes to laser printing and its suitability for biomaterial depositions [71].

A large number of biological materials have already been transferred by means of nanosecond and femtosecond LIFT, such as proteins [72, 73]. It should be noticed that both laser pulse regimes could be used for the transfer of proteins without considerable deterioration of their functionality.

Among the first works that have been published on the direct laser printing of biomaterials are those by Ringeisen *et al*. [74] as well as by Pique and Chrisey [75], who employed a direct-write technique for the laser writing of active protein patterns, viable *Escherichia coli*, and mammalian Chinese hamster ovary cells using nanosecond pulses. The crucial point during biological laser printing is the survival of the transferred cells and the preservation of their structural and physical properties upon irradiation. After the revolution of sensor fabrication through laser-based techniques and especially LIFT, many research groups have been involved with the development of biological sensors.

Serra *et al*. [76] proposed a protein-based biological device for protein detection and identification. This research group fabricated a single-protein-based microarray through the LIFT method in order to show the effect of the transfer technique on the protein integrity and reactivity. Specifically, an Nd: YAG laser (355 nm wavelength, 10 ns pulse duration) was utilized to deposit droplets of a solution containing the *Treponema pallidum* 17 kDa protein antigen on a nylon-coated glass slide, and they mentioned that the solution preserved its antigenic reactivity and diagnostic properties. The results obtained from the immunostaining assay when the array was incubated with a human serum positive for syphilis indicated that the antigen conserved its immunological reactivity after having been transferred. This study revealed that the LIFT method is an appropriate "tool" for the deposition of a diagnostically relevant antigen onto solid substrates. This work proved that the LIFT technique is a promising method for manufacturing protein microarrays of diagnostic interest.

Our group first studied the laser microprinting of different biomaterial patterns, such as DNA and proteins (bovine serum albumin), with spatial resolution,

which was achieved due to the use of femtosecond laser pulses, down to 50 μm, and we showed that they were also functional after printing and, thus, could be used as biosensors. This work demonstrated that ultrashort laser pulses reduce the thermal effects, allowing the effective deposition of sensitive biomaterials at high spatial resolution for microfabrication patterns [77, 78]. Figure 13.1, depicts a scanning electron microscopy (SEM) picture of the printed features of lambda phage DNA on glass substrate by LIFT using 500 fs pulses.

Figure 13.2, shows the scanning laser confocal fluorescence microscopy of the Alexa 594 labeled lambda phage DNA pattern.

In another study we demonstrated [79] the development of a capacitive DNA biosensor, where single-stranded DNA droplets have been transferred using the LIFT technique. Furthermore, in the same work, in order to enhance the immobilization of the thiol-modified oligonucleotides, 3-glycidoxypropyl-trimethoxy silane (GOPTS) has been used, for the surface functionalization of

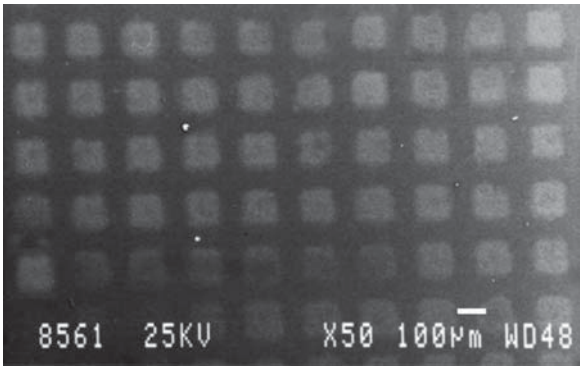

Figure 13.1 Scanning electron microscopy (SEM) picture of the printed features of lambda phage DNA on glass substrate by laser-induced forward transfer (LIFT) using 500 fs. (Karaiskou *et al*. 2003 [78]. Reproduced with permission of Elsevier.)

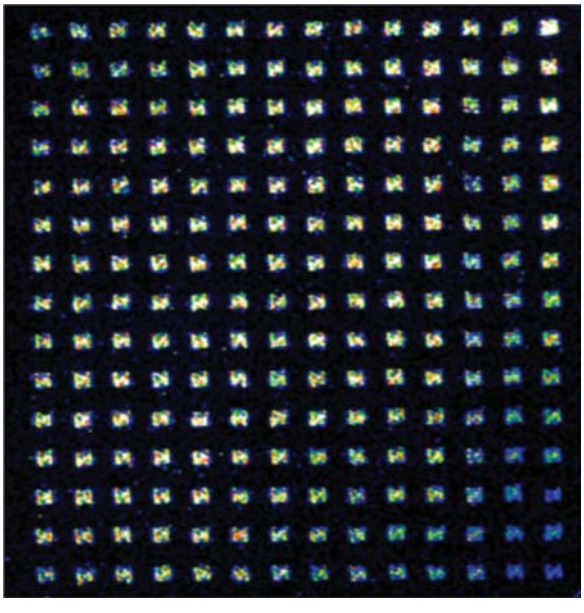

Figure 13.2 Scanning laser confocal fluorescence microscopy of the Alexa 594 labeled lambda phage DNA pattern. (Karaiskou *et al*. 2003 [78]. Reproduced with permission of Elsevier.)

a low-temperature oxide (LTO)/silicon substrate. Finally, validation tests after laser irradiation showed that the GOPTS-functionalized surfaces were stable when stored at 40 °C over a period of 1 month.

In another work, we have also reported the development of an amperometric biosensor, sensitive toward phenolic compounds, using the enzyme laccase as recognition element [80]. The enzyme was successfully immobilized through the LIFT technique in active form onto nonfunctionalized screen-printed electrodes. The immobilized laccase was characterized toward catechol in solution, which is a typical phenolic compound. It was observed that this biosensor permits the detection of catechol in aqueous solution, without the need of any type of functionalization, at concentrations in the nanomolar range. In Figure 13.3, we can discern the wetting variation in relation to the laser printing energy that leads to the direct immobilization of the biomaterial on the screen-printed electrodes. This type of biosensor exhibited good sensitivity toward the catechol compound and preserved its activity for 35 days.

Palla-Papavlu *et al*. [81] presented the development of surface acoustic wave (SAW) biosensors for odor detection in the food industry. Specifically, a wild-type bovine odorant-binding protein was laser-transferred on the SAW biosensor, while evaluation of the sensor performance under exposure to different concentrations of octenol presented high sensitivity and a detection limit of 2 ppm. Fernández-Pradas *et al*. [58] demonstrated, through the LIFT technique and using the third harmonic ($\lambda = 355$ nm) of an Nd: YAG laser, regular microarrays of double-stranded DNA of salmon sperm onto poly-L-lysine-coated slides. To achieve this, a laser intermediate-absorbing layer (titanium) was used between the laser-transparent substrate and the solution film. In another work,

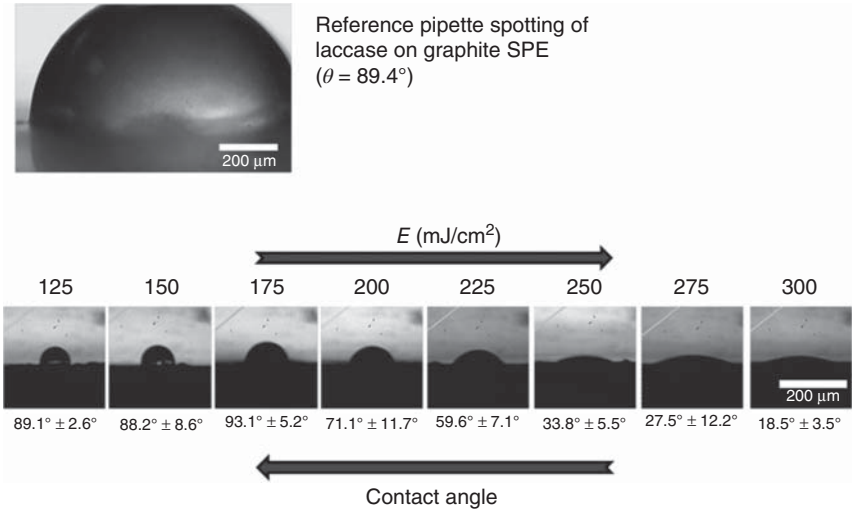

Figure 13.3 Wetting variation in relation to the laser printing energy that leads to the direct immobilization of the biomaterial on the screen-printed electrodes. (Touloupakis *et al*. 2014 [80]. Reproduced with permission of Elsevier.)

they compared the fabrication of cDNA microarrays onto poly-L-lysine-treated glass slides by LIFT and pin microspotting [52]. The produced microarrays were hybridized with the complementary strands of the spotted cDNAs, each one tagged with a different fluorochrome. Analysis protocols revealed that, through LIFT, the transferred microarrays are equivalent to those transferred through pin microspotting in terms of signal intensity and gene discrimination capacity.

In another study, Duocastella *et al*. [82] have demonstrated immunoglobulin (IgG) microarrays prepared through the LIFT technique by varying the laser pulse energy. During their experiment, they have tested the bioactivity of the transferred proteins, showing no loss of their activity along the whole laser pulse energy range. In Figure 13.4, an optical microscopy image of a microarray of the IgG solution at different laser pulse energies is presented.

It is important to mention that the optical absorption characteristics of the material under deposition is a critical step, and in the case where a specific wavelength is absorbed, thermal effects that can cause degradation of the deposited material should be taken into consideration. The plurality of biological moieties are dissolved in aqueous media, which means that the solutions, which are mainly utilized, are transparent to many laser wavelengths that are commonly used, thus laser printing under such terms is considered prohibitive. On this occasion, to bring this restriction under control, especially on biological material printing as well as other materials, a DRL should be used between the donor substrate and the thin material to be transferred during LIFT.

In case of biological material printing, the term *DRL LIFT* in the literature is also called biological laser printing (BioLP) technique [83] or AFA-LIFT [84]. In the modified LIFT techniques, BioLP and AFA-LIFT, the donor substrate is coated with a (1–100 nm) thick metal or metal oxide layer. In the past, one of

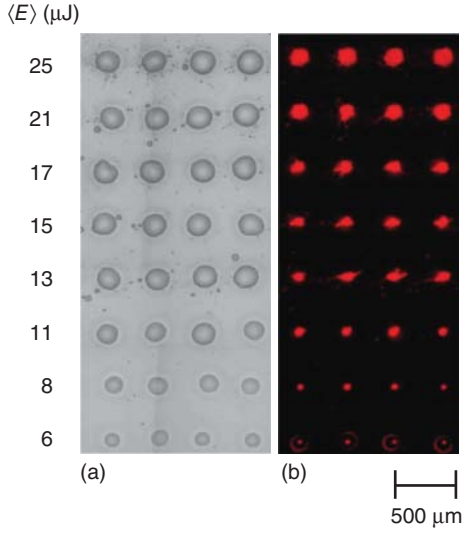

Figure 13.4 Optical microscopy image of microarray (IgG solution) at different laser pulse energies. (Duocastella *et al*. 2008 [82]. Reproduced with permission of National Technical University of Athens.)

LIFT variations, namely BioLP, was employed for the laser printing of human osteosarcoma cells [85].

A recent work for the detection of heavy metal ions using a DNAzyme-functionalized capacitive micromechanical sensor has been presented by our group [86]. The fabricated sensor operation is based on the catalytic activity of the "8–17" DNAzyme, which undergoes self-cleavage in the presence of Pb^{+2} and is capable of selectively detecting the aforementioned heavy metal. For the immobilization of the catalytic strand with high spatial resolution onto the micromembrane surfaces, the LIFT technique was employed. Following the deposition of the catalytic strand, the substrate strand was then applied with the use of a pipette, thus covering a number of micromembrane sensors as shown in Figure 13.5.

Furthermore, in Figure 13.6, we can observe the sensor capacitance variation for those sensing elements that were first spotted with the catalytic strand and then allowed to hybridize with their complementary substrate strand.

Recently, Duocastella *et al*. [87] reported an alternative approach on laser printing for the transfer of DNA microarrays for biosensor fabrication, similarly to LIBT [88]. The idea of this technique is based on the transparency of the receiver substrate to the laser wavelength. In addition, when using this modified technique, some substantial differences appeared (i.e., no donor film is utilized for the coating of the material under transfer, the deposition takes place in the direct opposite to the incident laser beam direction), compared to the original LIFT. A more thorough description of film-free laser printing may be found in Chapter 6.

In other works [78, 89], we have also demonstrated how the deposition of biomaterials, avoiding the use of any matrix material, through laser direct transfer could be performed. This method reaches high spatial resolution given the ultrafast laser pulses that it employs, avoiding melting and vaporization and

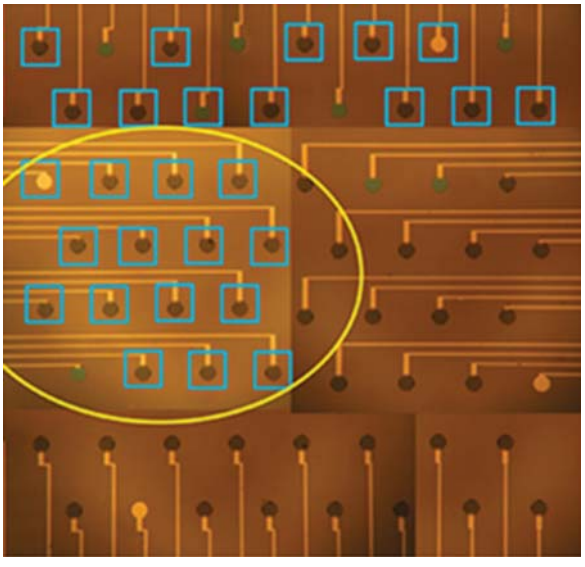

Figure 13.5 Optical microscope image of the micromembrane array following modification with the biological material. (Tsekenis *et al*. 2015 [86]. Reproduced with permission of Elsevier.

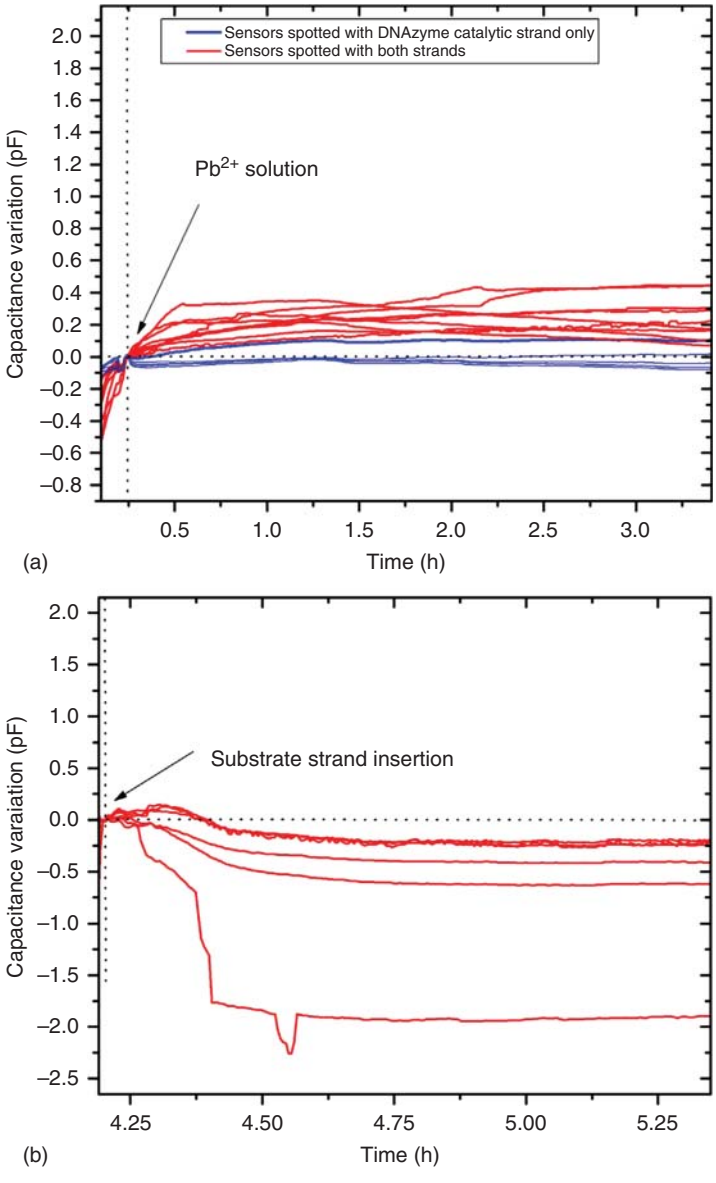

Figure 13.6 Heavy metal ion detection using the capacitive sensor. (a) Sensors that were first spotted with the catalytic strand and then allowed to hybridize with their complementary substrate strand (red) increase their capacitance upon the insertion of heavy metal, contrary to the sensors with only the catalytic strands immobilized on their surface (blue). (b) After cleavage in the presence of heavy metal, all the sensing elements decrease their capacitance. (Tsekenis *et al*. 2015 [86]. Reproduced with permission of Elsevier.)

allowing material transfer with narrow angular divergence. Therefore, sensitive biomaterials are deposited without significant damage due to the use of ultrafast laser pulses, which minimize the adverse thermal effects.

Another interesting study for a low-cost biosensor using a paper platform was initially proposed by Whitesides *et al*. [90]. After that, Eason *et al*. [91] motivated by the previous work, investigated the development of such biosensors due to the fact that paper is available in a range of different grades, also it is biocompatible and presents a variety of promising properties such as wettability and porosity to liquid solutions, factors that contribute in making paper an interesting tool for the fabrication of biosensing devices. This research group presented a point-of-care paper-based diagnostic sensor using the LIFT printing technique to transfer a solution that contained either enzyme-tagged or enzyme-untagged antibodies. To test the effectiveness of the functionality and the immunological reactivity of the LIFT-printed structures, an ELISA (Enzyme-Linked Immunosorbent Assay) protocol was developed and confirmed the validation of the LIFT-printed solution. This work highlighted that LIFT is an accurate method to transfer biological solutions onto a paper substrate with minimal loss of their biochemical functionality for the fabrication of point-of-care diagnostic sensors. Finally, it was presented that the immobilized enzymes were maintained during the whole wet-bench process, which is something that confirms the successful deposition of the LIFT-printed antibodies.

Moreover, in another study by our group [92], we have reported the fabrication of an efficient and sensitive photosynthetic-based biosensor for detecting herbicides as well as an interesting method about how the LIFT technique can enable efficient electron transfer from photosynthetic biomaterials immobilized on screen-printed electrodes, since current electrochemical biosensors present a limitation in the stability and the junctions efficiency between biomaterial and solid-state devices. It was shown that the efficiency of energy production of a photosynthetic system can be strongly enhanced by the LIFT technique (Figure 13.7: SEM analysis of the Au working electrode printed with thylakoid droplets, using (i) pipette and (ii) LIFT).

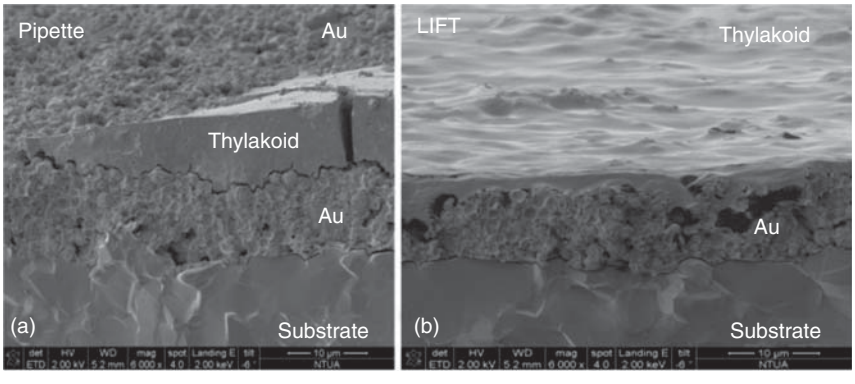

Figure 13.7 SEM analysis of the Au working electrode printed with thylakoid droplets, using (a) pipette and (b) laser-induced forward transfer (LIFT). (Touloupakis 2012 [92]. Reproduced with permission of Elsevier.)

It is important to notice that the interest for the fabrication of sensors is not limited only in the academia. Companies have also been involved with the fabrication of biological sensors. For instance, a research group from "Fraunhofer Institute for Laser Technology (ILT)," in collaboration with GeSiM GmbH, developed a new system for biological sensing. In more detail, they manufactured a table-top "Protoprinter" system for transferring proteins and DNA on any given surface that can also be used in the manufacturing of microarrays. The utility of the LIFT technique was decisive for this small-scale application. This system is capable of transferring high-viscous and solid materials without damaging them, while achieving a spot size of 10 μm.

13.4.2 Chemical Sensors

The continuing evolution of the laser transfer process and the demand of society for flexible technologies that are useful for manufacturing chemical sensors for the detection of extremely small amounts of chemical vapors have rapidly increased in recent years.

Chemical sensors are available for a broad range of applications including: (i) detection and diagnosis of infections, (ii) identification of spilled chemicals, (iii) quality of foods and drinks, (iv) water and wastewater analysis, and (v) air quality monitoring.

The need for portable, low-cost, and easily deployable chemical sensors has become even more urgent due to the increased number of harmful chemical agents. Recent advances in sensors in conjunction with the use of both organic and inorganic active layers, such as porous metallic oxides, polymers, or metal porphyrins, has led to the development of chemical sensors with improved performances. The recent revolution in laser processing of a wide range of materials such as polymers, carbon nanotubes, and derivatives of graphene proves that laser processing techniques are suitable for the fabrication of accurate chemical sensors.

Recently, a work on the fabrication of chemical sensors using graphene oxide has been presented by our group [93]. This work presented the pulsed laser printing of graphene oxide and a subsequent thermal reduction step, using the LIFT technique. The evaluation of the reduction efficiency was made by Fourier transform reflectance spectroscopy and electrical characterization of the thermally reduced devices. The response of the sensor upon exposure to water vapors was evaluated, and sensitivities down to 0.22%/%RH were recorded.

Apart from the aforementioned biological sensors, LIFT has also been used for the fabrication of chemical sensors using laser-printed oxides (SnO_2) [94] for the detection of ethanol, methanol, acetone, and capacitive sensor arrays [95] based on various polymers such as polyacrylic acid (PAA), poly(4-vinylpyridine) (P4VP), poly(hydroxyl styrene) (PHS), poly(methyl methacrylate) (PMMA), and poly(2-hydroxyethyl methacrylate) (PHEMA), as shown in Figure 13.8.

In this study, the sensor device was able to measure 256 sensing sites, with each sensing site comprising a polymer/silicon membrane, passivated with a LTO allowing the use in liquid environments. Assessment of the sensor showed quick

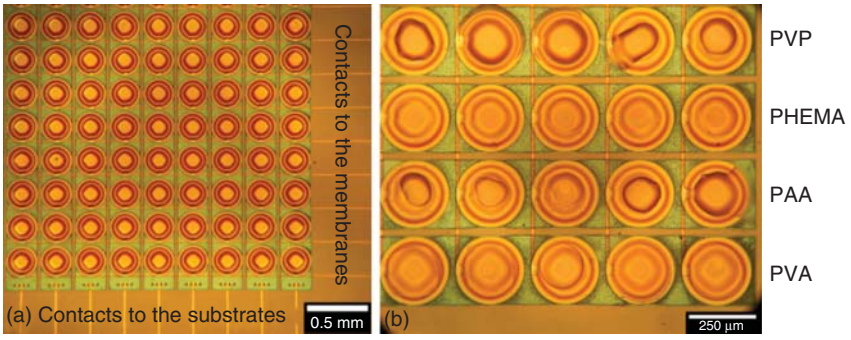

Figure 13.8 Capacitive sensor arrays. (a) Al contacts on the membranes. (b) Sensitive polymers (PVP-, PHEMA-, PAA-, and PVA-) printed in sensor device using LIFT. (Mattle *et al*. 2013 [94]. Reproduced with permission of Springer.)

response upon exposure to different analytes, emphasizing the potential of the LIFT technique for multisensing purposes.

A recent work on the fabrication of chemical sensors using composite layers has been presented by our group [96]. In this study, the use of LIFT as an alternative and promising technique for the dry printing of polymer/carbon nanotubes (CNTs) composite layers has been presented. These composites have been reported to exhibit significant electrical response toward a wide range of chemical compounds. Furthermore, TEM analysis (Figure 13.9: TEM images of PVP/f-MWCNT and PAA/f-MWCNT composite layers through LIFT) revealed that the LIFT-deposited PVP/f-MWCNT and PAA/f-MWCNT composite layers exhibited a high degree of dispersion of the carbon nanotubes into the polymer matrices.

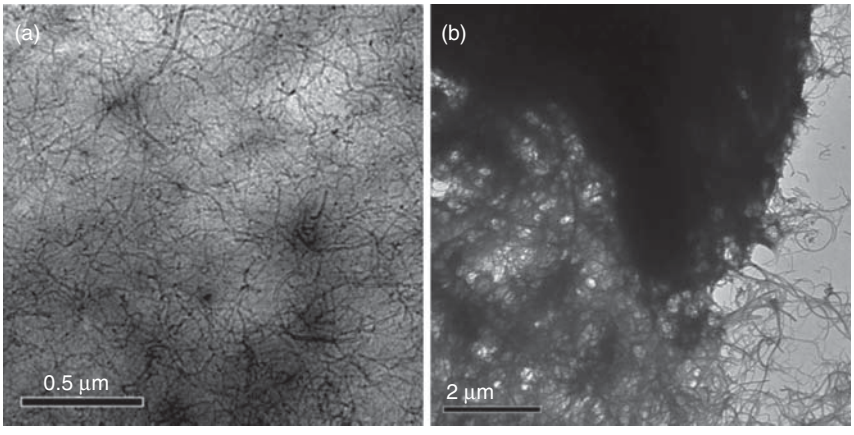

Figure 13.9 TEM images of PVP/f-MWCNT and PAA/f-MWCNT composite layers through LIFT. (Boutopoulos *et al*. 2010 [96]. Reproduced with permission of American Institute of Physics.)

Another type of chemical sensors, also using carbon nanotubes, was investigated by Palla-Papavlu *et al*. [97] The aim of their work was to fabricate a chemoresistor onto different flexible substrates, appropriate for the fabrication of intelligent clothing. Using the LIFT technique, they have transferred single-walled carbon nanotubes (SWCNTs) in a range of different laser fluences, that is, from sufficient conditions to eject the donor films up to high irradiation. Their experiment showed a repeatable response, and they have also made an additional study through Raman spectra where the results were satisfactory. This showed that after the LIFT process, the material (SWCNTs) did not present any decomposition.

Additionally, the work by Dinca *et al*. [98] revealed how polymers could be used to fabricate chemical sensors. The purpose of their work was to improve the laser printing of active polymer pixels onto surface acoustic waves (SAW) chemical sensors. This kind of devices are able to measure gas, vapor concentration. Specifically, pixels of polyisobutilene (PIB) polymers were transferred through the LIFT technique onto glass at different fluences.

An alternative laser-based direct-write technique, called MAPLE DW, for matrix-assisted pulsed laser evaporation–direct write, which uses all of the benefits associated with LIFT and the primary version of MAPLE-DW, which is known as *MAPLE* [99–101], has been used for the direct-write of materials for sensor applications, since it operates in air and at low temperatures. The MAPLE-DW technique relies on the transfer of materials in powder form mixed with an organic binder. Such mixtures or matrices are then applied as a uniform coating on the transparent donor substrate. The advantage of this procedure resides in the fact that the transfer of thick films from the donor substrate can be achieved in lower laser fluences than with the LIFT technique. Various types of miniature sensor designs have been fabricated incorporating different materials such as metals, polymers, biomaterials, or composites as multilayers or discrete structures on a single substrate. The MAPLE DW is a computer-controlled process that allows the sensor design to be easily modified and adapted to any specific application.

The first work employing laser printing for sensing applications was mentioned by Pique *et al*. [102] where chemoresistor gas sensors were fabricated using the MAPLE-DW technique. The operating principle of chemoresistor gas sensors relies on the ability of a chemoselective polymer to reversibly change its volume after exposure to various concentrations of analyte vapors. Then the fluctuation in volume is converted into electrical resistance variations, whose absolute values depend on the analyte concentrations in the sensor chamber. In MAPLE-DW, the laser fluences are below the ablation threshold of the powders under transfer. As a result, no vaporization of the materials takes place, enabling the transfer of complex patterns and avoiding undesirable structural transformations. However, this technique was not developed exactly for biological materials. There has been some concern for the safety of the biological material during the laser transfer and its effects in biological properties after the exposure.

Moreover, in another work, Piqué *et al*. [103] have reported the development of a chemical sensor using polyepichlorohydrin (PECH) polymer/carbon.

The polymer was successfully deposited through the MAPLE-DW technique onto silver interdigitated electrodes. In order to evaluate the performance of the chemical sensor made by MAPLE DW, similar PECH/carbon pads were fabricated by spray coating onto NaCl substrates and placed side by side and exposed to calibrated concentrations of analyte vapors. The results of the vapors tests showed that the response of the MAPLE DW and that of the spray-coated chemical sensors were similar and showed sensitivities of the order of parts per million (ppm).

13.5 Conclusions

This chapter presented how the LIFT technique has evolved into different LDW techniques and found use in many applications, especially in the sensor fabrication. The ability to laser transfer a variety of materials on virtually any surface without the need of masks or molds, both in ambient and vacuum conditions, shows the potential of the technique in microfabrication processes. LIFT is a noncontact microfabrication technique that offers opportunities for the generation of patterns, structures, and devices, which was not possible with traditional photolithographic tools in the previous years. Due to the fact that LIFT is a nonlithographic microfabrication method, it can be used for many prototyping applications, allowing the design, fabrication, and testing of a given structure to be completed quickly. This chapter demonstrated that LIFT can be utilized for many different types of sensor devices, including various types of materials.

List of Abbreviations

AFA-LIFT	Absorbing film-assisted laser-induced forward transfer
AFM	Atomic force microscopy
BioLP	Biological laser printing technique
CAD/CAM	Computer-aided design/computer-aided manufacturing
CNT	Carbon nanotubes
DRL	Dynamic release layer
ELISA	Enzyme-linked immunosorbent assay
ESD	Electrospray deposition
GOPTS	3-Glycidoxypropyl-tri-methoxy silane
IgG	Immunoglobulin
LAT	Laser ablation transfer
LDW	Laser direct write
LIFT	Laser-induced forward transfer
LTO	Low-temperature oxide
MAPLE	Matrix-assisted pulsed laser evaporation
MAPLE-DW	Matrix-assisted pulsed laser evaporation–direct write
PDMS	Polydimethylsiloxane
SAM	Self-assembled monolayer

References

1 Piqué, A., Wu, P., Ringeisen, B.R., Bubb, D.M., Melinger, J.S., McGill, R.A., and Chrisey, D.B. (2002) Processing of functional polymers and organic thin films by the matrix-assisted pulsed laser evaporation (MAPLE) technique. *Appl. Surf. Sci.*, **186** (1–4), 408–415.

2 Lee, K.-B., Park, S.-J., Mirkin, C.A., Smith, J.C., and Mrksich, M. (2002) Protein nanoarrays generated by Dip-Pen nanolithography. *Science*, **295**, 1702–1705.

3 Graber, D.J., Zieziulewicz, T.J., Lawrence, D.A., Shain, W., and Turner, J.N. (2003) Antigen binding specificity of antibodies patterned by microcontact printing. *Langmuir*, **19**, 5431.

4 Schuler, T., Asmus, T., Fritzsche, W., and Moller, R. (2009) Screen printing as cost-efficient fabrication method for DNA-chips with electrical readout for detection of viral DNA. *Biosens. Bioelectron.*, **24**, 2077.

5 Higson, S.P.J., Reddy, S.M., and Vadgama, P.M. (1994) Enzyme and other biosensors: evolution of a technology. *Eng. Sci. Educ. J.*, **3** (1), 41–48.

6 Swapna, G., Ajaysushanth, K., Erfana Begum, P., Chandrakiran, P., and Bharat, M. (2015) Biosensor general principles and applications a review. *Int. J. Curr. Sci. Technol.*, **3** (10), 90–93.

7 Sekhar, P.K., Brosha, E.L., Mukundan, R., and Garzon, F.H. (2010) Chemical sensors for environmental monitoring and homeland security. *Electrochem. Soc. Interface*, **19** (4), 35–40.

8 Hulanicki, A., Glab, S., and Ingman, F. (1991) Chemical sensors definitions and classification. *Pure Appl. Chem.*, **63** (9), 1247–1250.

9 Schena, M., Shalon, D., Davis, R.W., and Brown, P.O. (1995) Quantitative monitoring of gene expression patterns with a complementary DNA microarray. *Science*, **270** (5235), 467–470.

10 Sheehan, P.E., Edelstein, R.L., Tamanaha, C.R., and Whitman, L.J. (2003) A simple pen-spotting method for arraying biomolecules on solid substrates. *Biosens. Bioelectron.*, **18**, 1455–1459.

11 Barbulovic-Nad, I., Lucente, M., Sun, Y., Zhang, M., Wheeler, A.R., and Bussmann, M. (2006) Bio-microarray fabrication techniques—a review. *Crit. Rev. Biotechnol.*, **26**, 237–259.

12 Cho, E.J., Tao, Z., Tehan, E.C., and Bright, F.V. (2002) Multianalyte pin-printed biosensor arrays based on protein-doped xerogels. *Anal. Chem.*, **74** (24), 6177–6184.

13 Cho, E.J. and Bright, F.V. (2002) Pin-printed chemical sensor arrays for simultaneous multianalyte quantification. *Anal. Chem.*, **74** (6), 1462–1466.

14 Gopal, A., Hoshino, K., and Zhang, J.X. (2012) Microcontact printing. *Encycl. Nanotechnol.*, **1**, 1397–1404.

15 Huang, C.-W., Huang, Y.-J., Lu, S.-S., and Lin, C.-T. (2012) A fully integrated humidity sensor system-on-chip fabricated by micro-stamping technology. *Sensors*, **12**, 11592–11600.

16 Piner, R.D., Zhu, J., Xu, F., Hong, S.H., and Mirkin, C.A. (1999) "Dip-pen" nanolithography. *Science*, **283** (5402), 661–663.
17 Wadu-Mesthrige, K., Xu, S., Amro, N.A., and Liu, G.Y. (1999) Fabrication and imaging of nanometer-sized protein patterns. *Langmuir*, **15** (25), 8580–8583.
18 Xu, S. and Liu, G.Y. (1997) Nanometer-scale fabrication by simultaneous nanoshaving and molecular self-assembly. *Langmuir*, **13** (2), 127–129.
19 Blawas, A.S. and Reichert, W.M. (1998) Protein patterning. *Biomaterials*, **19** (7–9), 595–609.
20 Lom, B., Healy, K.E., and Hockberger, P.E. (1993) A versatile technique for patterning biomolecules onto glass coverslips. *J. Neurosci. Methods*, **50** (3), 385–397.
21 Mooney, J.F., Hunt, A.J., McIntosh, J.R., Liberko, C.A., Walba, D.M., and Rogers, C.T. (1996) Patterning of functional antibodies and other proteins by photolithography of silane monolayers. *Proc. Natl. Acad. Sci. U.S.A.*, **93**, 12287–12291.
22 Hengsakul, M. and Cass, A.E.G. (1996) Protein patterning with a photoactivatable derivative of biotin. *Bioconjugate Chem.*, **7** (2), 249–254.
23 Pritchard, D.J., Morgan, H., and Cooper, J.M. (1995) Patterning and regeneration of surfaces with antibodies. *Anal. Chem.*, **67** (19), 3605–3607.
24 Britland, S., Clark, P., Connolly, P., and Moores, G. (1992) Micropatterned substratum adhesiveness—a model for morphogenetic cues controlling cell behavior. *Exp. Cell. Res.*, **198** (1), 124–129.
25 Tseng, F.-G., Lin, S.-C., Yao, D.-J., Huang, H., and Chieng, C.-C. (2005) in *Protein Microarrays* (ed. M. Schena), Jones and Bartlett Publishers, Inc., Sudbury, MA, pp. 305–338.
26 Allain, L.R., Stratis-Cullum, D.N., and Vo-Dinh, T. (2004) Investigation of microfabrication of biological sample arrays using piezoelectric and bubble-jet printing technologies. *Anal. Chim. Acta*, **518** (1–2), 77–85.
27 Butler, J.H., Cronin, M., Anderson, K.M., Biddison, G.M., Chatelain, F., Cummer, M., Davi, D.J., Fisher, L., Frauendorf, A.W., Frueh, F.W., Gjerstad, C., Harper, T.F., Kernahan, S.D., Long, D.Q., Pho, M., Walker, J.A., and Brennan, T.M. (2001) In situ synthesis of oligo nucleotide arrays by using surface tension. *J. Am. Chem. Soc.*, **123** (37), 8887–8894.
28 Hughes, T.R., Mao, M., Jones, A.R., Burchard, J., Marton, M.J., Shannon, K.W., Lefkowitz, S.M., Ziman, M., Schelter, J.M., Meyer, M.R., Kobayashi, S., Davis, C., Dai, H.Y., He, Y.D.D., Stephaniants, S.B., Cavet, G., Walker, W.L., West, A., Coffey, E., Shoemaker, D.D., Stoughton, R., Blanchard, A.P., Friend, S.H., and Linsley, P.S. (2001) Expression profiling using microarrays fabricated by an inkjet oligonucleotide synthesizer. *Nat. Biotechnol.*, **19** (4), 342–347.
29 Tseng, F.G., Kim, C.J., and Ho, C.M. (2002) A high-resolution high-frequency monolithic top-shooting micro injector free of satellite drops - Part I: concept, design, and model. *J. Microelectromech. Syst.*, **11** (5), 427–436.

30 Avseenko, N.V., Morozova, T.Y., Ataullakhanov, F.I., and Morozov, V.N. (2001) Immobilization of proteins in immunochemical microarrays fabricated by electrospray deposition. *Anal. Chem.*, **73** (24), 6047–6052.

31 Moerman, R., Frank, J., Marijnissen, J.C.M., Schalkhammer, T.G.M., and van Dedem, G.W.K. (2001) Miniaturized electrospray in gas a technique for the production of microarrays of reproducible micrometer-sizedproteinspots. *Anal. Chem.*, **73** (10), 2183–2189.

32 Morozov, V. and Morozova, T.Y. 2002 Electrospray apparatus for mass fabrication of chips and libraries. US Patent 6,350,609.

33 Morozov, V.N. and Morozova, T.Y. (1999) Electrospray deposition as a method for mass fabrication of mono-and multicomponent microarrays of biological and biologically active substances. *Anal. Chem.*, **71**, 3110–3117.

34 Bohandy, J., Kim, B., and Adrian, F.J. (1986) Metal deposition from a supported metal film using an excimer laser. *J. Appl. Phys.*, **60** (4), 1538–1539.

35 Fogarassy, E., Fuchs, C., Kerherve, F., Hauchecorne, G., and Perrière, J. (1989) Laser induced forward transfer of high-Tc YBaCuO and BiSrCaCuO superconducting thin films. *J. Appl. Phys.*, **66** (1), 457–459.

36 Narazaki, A., Sato, T., Kurosaki, R., Kawaguchi, Y., and Niino, H. (2008) Nano- and microdot array formation of FeSi2 by nanosecond excimer laser-induced forward transfer. *Appl. Phys Express*, **1**, 057001.

37 Veiko, V.P., Shakhno, E.A., Smirnov, V.N., Miaskovski, A.M., and Nikishin, G.D. (2006) Laser induced film deposition by lift physical mechanisms and applications. *Laser Part. Beams*, **24**, 203–209.

38 Röder, T.C. and Köhler, J.R. (2012) Physical model for the laser induced forward transfer process. *Appl. Phys. Lett.*, **100**, 071603.

39 Mogyorósi, P., Szörényi, T., Bali, K., Tóth, Z., and Hevesi, I. (1989) Pulsed laser ablative deposition of thin metal films. *Appl. Surf. Sci.*, **36**, 157–163.

40 Tóth, Z., Szörényi, T., and Tóth, A.L. (1993) Ar^+ laser-induced forward transfer (lift): a novel method for micrometer-size surface patterning. *Appl. Surf. Sci.*, **69**, 317–320.

41 Esrom, H., Zhang, J.-Y., Kogelschatz, U., and Pedraza, A.J. (1995) New approach of a laser-induced forward transfer for deposition of patterned thin metal films. *Appl. Surf. Sci.*, **86**, 202–207.

42 Yang, L., Wang, C.Y., Ni, X.C., Wang, Z.J., Jia, W., and Chai, L. (2006) Microdroplet deposition of copper film by femtosecond laser-induced forward transfer. *Appl. Phys. Lett.*, **89**, 161110.

43 Tolbert, W.A., Lee, I.Y.S., Doxtader, M.M., Ellis, E.W., and Dlott, D.D. (1993) High-speed color imaging by laser ablation transfer with a dynamic release layer: fundamental mechanisms. *J. Imaging Sci. Technol.*, **37**, 411.

44 Fardel, R., Nagel, M., Nuesch, F., Lippert, T., and Wokaun, A. (2007) Laser forward transfer using a sacrificial layer: influence of the material properties. *Appl. Surf. Sci.*, **254**, 1322–1326.

45 Shaw Stewart, J., Fardel, R., Nagel, M., Delaporte, P., Rapp, L., Cibert, C., Alloncle, A.P., Nuesch, F., Lippert, T., and Wokaun, A. (2010) The effect of laser pulse length upon laser-induced forward transfer using a triazene polymer as a dynamic release layer. *Optoelectron. Adv. Mater.*, **12**, 605–609.

46 Mito, T., Tsujita, T., Masuhara, H., Hayashi, N., and Suzuki, K. (2001) Hollowing and transfer of polymethyl methacrylate film propelled by laser ablation of triazeno polymer film. *Jpn. J. Appl. Phys.*, **40** (8A), L805.

47 Colina, M., Duocastella, M., Fernández-Pradas, J.M., Serra, P., and Morenza, J.L. (2006) Laser-induced forward transfer of liquids study of the droplet ejection process. *J. Appl. Phys.*, **99**, 084909.

48 Koch, L. (2010) Laser printing of skin cells and human stem cells. *Tissue Eng. Part C*, **16**, 847–854.

49 Hopp, B., Smausz, T., Kresz, N., Barna, N., Bor, Z., Kolozsvári, L., Chrisey, D.B., Szabó, A., and Nógrádi, A. (2005) Survival and proliferative ability of various living cell types after laser-induced forward transfer. *Tissue Eng.*, **11** (11–12), 1817–1823.

50 Fernandez-Pradas, J.M., Colina, M., Serra, P., Dominguez, J., and Morenza, J.L. (2004) Laser induced forward transfer of biomolecules. *Thin Solid Films*, **453–454**, 27–30.

51 Serra, P., Colina, M., Fernandez-Pradas, J.M., Sevilla, L., and Morenza, J.L. (2004) Preparation of functional DNA microarrays through laser-induced forward transfer. *Appl. Phys. Lett.*, **85** (9), 1639–1641.

52 Colina, M., Serra, P., Fernandez-Pradas, J.M., Sevilla, L., and Morenza, J.L. (2005) DNA deposition through laser induced forward transfer. *Biosens. Bioelectron.*, **20**, 1638–1642.

53 Serra, P., Fernandez-Pradas, J.M., Colina, M., Duocastella, M., Dominguez, J., and Morenza, J.L. (2006) Laser-induced forward transfer: a direct- writing technique for biosensors preparation. *J. Laser Micro/Nanoeng.*, **1** (3), 236–242.

54 Hopp, B., Smausz, T., Antal, Z., Kresz, N., Bor, Z., and Chrisey, D. (2004) Absorbing film assisted laser induced forward transfer of fungi (Trichoderma conidia). *J. Appl. Phys.*, **96** (6), 3478–3481.

55 Dinca, V., Fardel, R., Di Pietrantonia, F., Cannata, D., Benetti, M., Verona, E., Palla-Papavlu, A., Dinescu, M., and Lippert, T. (2010) Laser-induced forward transfer: an approach to single-step polymer microsensor fabrication. *Sens. Lett.*, **8**, 1–5.

56 Dinca, V., Fardel, R., Shaw-Stewart, J., Di Pietrantonio, F., Cannata, D., Benetti, M., Verona, E., Palla-Papavlu, A., Dinescu, M., and Lippert, T. (2010) Laser-induced forward transfer: an approach to single-step polymer microsensor fabrication. *Sens. Lett.*, **8**, 436–440.

57 Doraiswamy, A., Narayan, R.J., Lippert, T., Urech, L., Wokaun, A., Nagel, M., Hopp, B., Dinescu, M., Modi, R., Auyeung, R.C.Y., and Chrisey, D.B. (2006) Excimer laser forward transfer of mammalian cells using a novel triazene absorbing layer. *Appl. Surf. Sci.*, **252**, 4743–4747.

58 Duocastella, M., Fernández-Pradas, J.M., Morenza, J.L., and Serra, P. (2009) Time-resolved imaging of the laser forward transfer of liquids. *J. Appl. Phys.*, **106**, 084907.

59 Barron, J.A., Young, H.D., Dlott, D.D., Darfler, M.M., Krizman, D.B., and Ringeisen, B.R. (2005) Printing of protein microarrays via a capillary-free fluid jetting mechanism. *Proteomics*, **5**, 4138.

60 Boutopoulos, C., Kalpyris, I., Serpetzoglou, E., and Zergioti, I. (2014) Laser-induced forward transfer of silver nanoparticle ink: time-resolved imaging of the jetting dynamics and correlation with the printing quality. *Microfluid. Nanofluid.*, **16**, 493–500.

61 Li, D.W. and Guo, L.J. (2008) Organic thin film transistors and polymer light-emitting diodes paterned by polymer linking and stamping. *J. Phys. D: Appl. Phys.*, **41**, 105115.

62 Tuomikoski, M., Suhonen, R., Valimakia, M., Sauer, M., and Rogin, P. (2006) Manufacturing of polymer light-emitting device structures. *Org. Optoelectron. Photonics II*, **6192**, 19204.

63 Makela, T., Haatainen, T., Majander, P., and Ahopelto, J. (2007) Continuous roll to roll nanoimprinting of inherently conducting polyaniline. *Microelectron. Eng.*, **84**, 877–879.

64 Albareda-Sirvent, M., Merkoci, A., and Alegret, S. (2000) Configurations used in the design of screen-printed enzymatic biosensors. A review. *Sens. Actuators, B*, **69**, 153–163.

65 Tudorache, M. and Bala, C. (2007) Biosensors based on screen-printing technology, and their applications in environmental and food analysis. *Anal. Bioanal. Chem.*, **388**, 565–578.

66 Makela, T., Haatainen, T., Majander, P., and Ahopelto, J. (2006) Nickel stamp fabrication using step & stamp imprint lithography. *Microelectron. Eng.*, **83**, 948–950.

67 Setti, L., Fraleoni-Morgera, A., Ballarin, B., Fillippini, A., and Frascaro, D. (2005) *Biosens. Bioelectron.*, **20**, 2019–2026.

68 Ngamna, O., Morrin, A., Killard, A.J., Moulton, S.E., Smyth, M.R., and Wallace, G.G. (2007) *Langmuir*, **23**, 8569–8574.

69 Fuller, S.B., Wilhelm, E.J., and Jacobson, J.A. (2002) *J. Microelectromech. Syst.*, **11**, 54–60.

70 Xu, T., Jin, J., Gregory, C., Hickman, J.J., and Boland, T. (2005) *Biomaterials*, **26**, 93–99.

71 Dinca, V., Kasotakis, E., Catherine, J., Mourka, A., Mitraki, A., Popescu, A., Dinescu, M., Farsari, M., and Fotakis, C. (2007) Development of peptide-based patterns by laser transfer. *Appl. Surf. Sci.*, **254**, 1160–1163.

72 Dinca, V., Farsari, M., Kafetzopoulos, D., Popescu, A., Dinescu, M., and Fotakis, C. (2008) Patterning parameters for biomolecules microarrays constructed with nanosecond and femtosecond UV lasers. *Thin Solid Films*, **516**, 6504–6511.

73 Dinca, V., Ranella, A., Farsari, M., Kafetzopoulos, D., Dinescu, M., Popescu, A., and Fotakis, C. (2008) Quantification of the activity of biomolecules in microarrays obtained by direct laser transfer. *Biomed. Microdevices*, **10**, 719–725.

74 Ringeisen, B.R., Chrisey, D.B., Pique, A., Young, H.D., Modi, R., Bucaro, M., Jones-Meehan, J., and Spargo, B.J. (2002) Generation of mesoscopic patterns of viable *Escherichia coli* by Ambien tLaser transfer. *Biomaterials*, **23**, 161–166.

75 Pique, A. and Chrisey, D.B. (2002) *Direct-Write Technologies for Rapid Prototyping Applications*, Academic Press, pp. 93–116.

76 Serra, P., Fernández-Pradas, J.M., Berthet, F.X., Colina, M., Elvira, J., and Morenza, J.L. (2004) Laser direct writing of biomolecule microarrays. *Appl. Phys. A*, **A79**, 949–952.

77 Zergioti, I., Karaiskou, A., Papazoglou, D.G., Fotakis, C., Kapsetaki, M., and Kafetzopoulos, D. (2005) Femtosecond laser microprinting of biomaterials. *Appl. Phys. Lett.*, **86**, 163902.

78 Karaiskou, A., Zergioti, I., Fotakis, C., Kapsetaki, E., and Kafetzopoulos, D. (2003) Microfabrication of biomaterials by the sub-ps laser induced forward transfer process. *Appl. Surf. Sci.*, **208–209**, 245–249.

79 Tsekenis, G., Chatzipetrou, M., Tanner, J., Chatzandroulis, S., Thanos, D., Tsoukalas, D., and Zergioti, I. (2012) Surface functionalization studies and direct laser printing of oligonucleotides toward the fabrication of a micromembrane DNA capacitive biosensor. *Sens. Actuators, B*, **175**, 123–131.

80 Touloupakis, E., Chatzipetrou, M., Boutopoulos, C., Gkouzou, A., and Zergioti, I. (2014) A polyphenol biosensor realized by laser printing technology. *Sens. Actuators, B*, **193**, 301–305.

81 Palla-Papavlu, A., Patrascioiu, A., Di Pietrantonio, F., Fernandez-Pradas, J.-M., Cannata, D., Benetti, M., D'Auria, S., Verona, E., and Serra, P. (2014) Preparation of surface acoustic wave odor sensors by laser-induced forward transfer. *Sens. Actuators, B*, **192**, 369–377.

82 Duocastella, M., Fernández-Pradas, J.M., Serra, P., and Morenza, J.L. (2008) Laser-induced forward transfer of liquids for miniaturized biosensors preparation. *J. Laser Micro/Nanoeng.*, **3** (1), 1–4.

83 Barron, J.A., Wu, P., Ladouceur, H., and Ringeisen, B.R. (2004) Biological laser printing: a novel technique for creating heterogeneous 3-dimensional cell patterns. *Biomed. Microdevices*, **6**, 139–147.

84 Hopp, B., Smausz, T., Kresz, N., Barna, N., Bor, Z., Kolozsvari, L., Chrisey, D.B., Szabo, A., and Nogradi, A. (2005) Survival and proliferative ability of various living cell types after laser induced forward transfer. *Tissue Eng.*, **11**, 1181.

85 Barron, J.A., Krizman, D.B., and Ringeisen, B.R. (2005) Laser printing of single cells: statistical analysis, cell viability, and stress. *Ann. Biomed. Eng.*, **33** (2), 121–130.

86 Tsekenis, G., Filippidou, M.K., Chatzipetrou, M., Tsouti, V., Zergioti, I., and Chatzandroulis, S. (2015) Heavy metal ion detection using a capacitive micromechanical biosensor array for environmental monitoring. *Sens. Actuators, B*, **208** (1), 628–635.

87 Duocastella, M., Fernandez-Pradas, J.M., Morenza, J.L., Zafra, D., and Serra, P. (2010) Novel laser printing technique for miniaturized biosensors preparation. *Sens. Actuators, B*, **145**, 596–600.

88 Patrascioiu, A., Fernandez-Pradas, J.M., Palla-Papavlu, A., Morenza, J.L., and Serra, P. (2014) Laser-generated liquid microjets: correlation between bubble dynamics and liquid ejection. *Microfluid. Nanofluid.*, **16**, 55–63.

89 . Fotakis K, Thireos G, Zergioti I, Kafetzopoulos D. (2002) Fabrication of biopolymer patterns by means of laser transfer. Patent: 1004059 (15-NOV-2002). International patent Application PCT/EP 02/14761 (24-DEC-02)
90 Martinez, A.W., Phillips, S.T., Butte, M.J., and Whitesides, G.M. (2007) Patterned paper as a platform for inexpensive, low-volume, portable bioassays. *Angew. Chem. Int. Ed.*, **46**, 1318–1320.
91 Katis, I.N., Holloway, J.A., Madsen, J., Faust, S.N., Garbis, S.D., Smith, P.J.S., Voegeli, D., Bader, D.L., Eason, R.W., and Sones, C.L. (2014) Paper-based colorimetric enzyme linked immunosorbent assay fabricated by laser induced forward transfer. *Biomicrofluidics*, **8**, 036502.
92 Touloupakis, E., Boutopoulos, C., Buonasera, K., Zergioti, I., and Giardi, M.T. (2012) A photosynthetic biosensor with enhanced electron transfer generation realized by laser printing technology. *Anal. Bioanal. Chem.*, **402**, 3237–3244.
93 Papazoglou, S., Tsouti, V., Chatzandroulis, S., and Zergioti, I. (2016) Direct laser printing of graphene oxide for resistive chemosensors. *Opt. Laser Technol.*, **82**, 163–169.
94 Mattle, T., Hintennach, A., Lippert, T., and Wokaun, A. (2013) Laser induced forward transfer of SnO2 for sensing applications using different precursors systems. *Appl. Phys. A*, **110**, 309–316.
95 Tsouti, V., Boutopoulos, C., Goustouridis, D., Zergioti, I., Normand, P., Tsoukalas, D., and Chatzandroulis, S. (2010) A chemical sensor microarray realized by laser printing of polymers. *Sens. Actuators, B*, **150**, 148–153.
96 Boutopoulos, C., Pandis, C., Giannakopoulos, K., Pissis, P., and Zergioti, I. (2010) Polymer/carbon nanotube composite patterns via laser induced forward transfer. *Appl. Phys. Lett.*, **96** (4), 041104.
97 Palla-Papavlu, A., di Pietrantonio, F., Cannata, D., Benetti, M., Veron, E., Dinca, V., Lippert, T., and Dinescu, M. (2014) Gas sensors fabricated by laser-induced forward transfer. International Conference of Scientific paper AFASES 2014, Brasov, 22–24 May, 2014.
98 Dinca, V., Palla-Papavlu, A., Dinescu, M., Shaw Stewart, J., Lippert, T.K., Di Pietrantonio, F., Cannata, D., Benetti, M., and Verona, E. (2010) Polymer pixel enhancement by laser-induced forward transfer for sensor applications. *Appl. Phys. A*, **101**, 559–565.
99 McGill, R.A. and Chrisey, D.B. (1997) Method of producing thin film coating by matrix assisted pulsed laser evaporation. Patent W09853767.
100 McGill, R.A., Chung, R., Chrisey, D.B., Dorsey, P.C., Matthews, P., Pique, A., Mlsna, T.E., and Stepnowski, J.L. (1998) Performance optimization of surface acoustic wave chemical sensors. *IEEE Trans. Ultrason. Ferroelectr. Freq. Control*, **45**, 1370.
101 Pique, A., Auyeung, R.C., McGill, R.A., Chrisey, R.B., Callahan, J.H., and Mlsna, T.E. (1998) Matrix assisted pulsed laser evaporation (maple) of polymeric materials: methodology and mechanistic studies. *MRS Proc.*, **526**, 375.

102 Pique, A., Auyeung, R.C.Y., Stepnowiski, J.L., Weir, D.W., Arnold, C.B., McGill, R.A., and Chrisey, D.B. (2003) Laser processing of polymer thin films for chemical sensor applications. *Surf. Coat. Technol.*, **163–164**, 293–299.

103 Piqué, A., Weir, D.W., Wu, P.K., Pratap, B., Arnold, C.B., Ringeisen, B.R., McGill, R.A., Auyeung, R.C.Y., Kant, R.A., and Chrisey, D.B. (2002) Direct-write of sensor devices by a laser forward transfer technique. Proceedings of SPIE LASER 2002, vol. 4637, 19–25 January, 2002, San Jose, CA, pp. 361–368.

14

Laser Printing of Proteins and Biomaterials

Alexandra Palla Papavlu, Valentina Dinca, and Maria Dinescu

Lasers Department, National Institute for Lasers, Plasma, and Radiation Physics, Atomistilor 409, 077125 Magurele, Romania

14.1 Introduction

Today, a strong research effort is directed toward the development and integration of new materials, especially of polymers and biomolecules, which are essential in pharmaceutical, bioengineering, and sensing applications. In fact, patterning of organic and inorganic materials, in particular enabling precise positioning of different materials with nano- and microscale resolution over large areas, is the main demand in the development of next-generation sensors, biosensors, and microarray chip devices [1].

Biomicrodevices are miniaturized devices based on biologically derived components (e.g., DNA, proteins, and cells) combined or integrated with microfabricated substrates. The methods that had been originally developed for the microelectronics industry, such as photolithography, and for the fabrication of microelectromechanically systems, such as silicon micromachining, were the first to be adapted to the fabrication of biomicrodevices.

Research in this field started in the late 1970s and resulted in the development of the first miniaturized gas chromatography system on a silicon chip [2]. However, the last 10 years have witnessed a truly exponential growth in the research focused on the development of biomicrodevices. Today, this field of research represents one of the most important sectors of the biotechnology and biomedical industry, with applications ranging from drug discovery studies to tissue engineering. Research in this area has been motivated by the numerous advantages conferred by miniaturization, such as the reduction of device size, use of smaller volumes and consequent reduction of waste, high throughput, and batch processing [3, 4].

Before a biomicrodevice can be fully developed, many specific fabrication and biointeraction challenges must be addressed. Compared to silicon-based electronic devices, the challenges for the fabrication of biomicrodevices are much more diverse due to the large variety of biomaterials, fluids, and chemicals involved, as well as the spotting method. Among these challenges, we emphasize the spatial immobilization and bioactivity preservation of the

Laser Printing of Functional Materials: 3D Microfabrication, Electronics and Biomedicine,
First Edition. Edited by Alberto Piqué and Pere Serra.
© 2018 Wiley-VCH Verlag GmbH & Co. KGaA. Published 2018 by Wiley-VCH Verlag GmbH & Co. KGaA.

selected biomolecules in the specific place on a surface. Different approaches regarding spotting/printing methods, printing media preparation, optimization of printing buffer for high binding efficiency of molecules to different microarray surfaces, and the evaluation of the produced microarrays performance must be considered.

Direct patterning methods have attracted an increasing attention in the last few years, in particular since their demonstrated ability to reach nanoscale patterning. The major concerns within this area of applications are related to protein malfunction after patterning, as proteins easily lose their activity due to various factors (denaturation, dehydration, or oxidation) [5]. Nowadays, simple methods such as dispensing or soaking techniques are used for depositing biological molecules in solution onto their binding or adsorbing substrates [6]. In addition, a multitude of contact and noncontact patterning methods have been developed for localized biomolecules patterning. For example, in contact methods, in order to generate high densities of biomolecule micropatterns on porous or solid materials, the factors to be considered include the nature of the liquid samples, the diameters of the pins or capillary dispensers, and the pin impact [7]. As miniaturization represents a requirement of biomicrodevice manufacturing, techniques such as dot blotting are unsuitable for depositions onto nonporous substrates as dots with diameters of/or larger than 1 mm are being produced with this technique [8]. Robotic microneedle array fabrication allows specific and localized antibody–antigen interactions as defined cognate spots in the array, with antibody–antigen pairs allowing detection of the cognate ligands at concentrations below 1 ng/ml [9]. Despite its ability to print hundreds of specific antibody or antigen solutions in an array, it is a time-consuming and costly technique with additional issues related to cross-contamination during tip cleaning [10]. Biocompatibility and the relatively expensive processing equipment are the main issues in the alternative photolithographic and/or microfluidic methods [11, 12].

Furthermore, microfluidic patterning is a versatile patterning technique that allows immobilizing multiple types of proteins on a variety of substrates [13]. The main limitation of this technique is the fabrication of an array where the same protein (or other analyte) is placed obligatory along one line. Microcontact printing (μCP) allows parallel and fast printing of bioreagents in hundreds of spots. μCP and, more recently, nCP offer a simple and convenient method to stamp a variety of "inks," from proteins to peptides and other macromolecules. The method is parallel; however, as previously discussed, it can also be used to print different types of inks, even if this might require laborious alignment processes. The disadvantages of protein denaturation, contamination, and noncontrollability of the patterning process limit its use [14].

Spotting biological liquid samples onto different substrates may use also *noncontact printing* approaches such as the "inkjet" printing [15, 16]. Uniform patterning of different types of proteins using high-speed printing requires precise pressure control for each nozzle, preventing cross-contamination, and controlled but limited range of viscoelastic properties of the samples. In particular, the fast growing field of protein and cell microarrays demands for a fast and reliable noncontact printing technology. The multitude of printing samples often shows very different liquid properties, which highly influence the

deposition behavior. In addition, the surface properties of microarray substrates vary in a wide range. As a result, different applications need specifically adopted printing systems, printing media, coupling chemistry of microarray slides, and surface properties. Thus, the production of custom microarrays requires a very flexible microarrayer technology.

In materials science, laser techniques revolutionized our understanding of materials by making it possible to design and integrate new materials with tailored properties for novel technology developments. The next step beyond conventional direct writing techniques, that is, inkjet printing, is the laser-induced forward transfer (LIFT) technique.

LIFT first appeared as a new deposition method for the direct writing of different dried inks to a glass substrate for the graphic industry [17–19]. At that point, it was called laser writing (LW) or material laser recording (MTR). In 1986, Bohandy *et al*. [20] deposited copper metal patterns onto fused-silica substrates under vacuum conditions by the same method and called it LIFT. Two years later, the same group demonstrated the same process under atmospheric conditions [21]. Detailed information on the origins of LIFT is given in Chapter 2.

In LIFT, a laser beam is focused through a transparent support plate onto a precursor thin film of the material to be transferred. Every single pulse promotes the transfer of the thin film material onto a substrate that is usually placed parallel and facing the thin film at very short distances (<100 μm). A pattern of the transferred material can be "written" on the substrate with multiple shots by displacing the substrate and the thin film with respect to the laser beam. This technique was proven to be appropriate for printing patterns of different materials, both in solid phase (including metals [22–31], oxides [32–35], and high-temperature superconductors [36]) and in liquid phase (proteins [37–39], DNA [38–42], cells [43], and tissue [44]). In addition, LIFT is a technique that requires the use of small quantity of sample, which represents an advantage over conventional pin printing methods that often induce significant sample waste. Please refer to Chapter 1 for a detailed description of the LIFT and other direct-write techniques.

Conventional LIFT is well suited for the transfer of metals, but in the case of soft, sensitive materials, the energetic laser pulses may damage these materials and result in the loss of functionality, for example, in the case of proteins, or damage of the structural integrity (as in the case of cells or other biomolecules such as liposomes). Therefore, in order to reduce the risk of damaging the layer to be transferred and to improve the process efficiency, the donor substrate can be precoated with an intermediate layer, which is called dynamic release layer (DRL) or sacrificial layer. In most studies in the literature, metallic layers [45, 46] have been used as sacrificial layers, and more recently, UV-sensitive photopolymers, such as triazene polymers (TPs) (see Chapter 3) [47, 48], or thick polymer layers (i.e., polyimide) (see Chapter 5) have also been used to transfer "soft" materials [49].

This chapter reviews the advancements in LIFT for the spatial immobilization of different biomolecules such as proteins (i.e., protein patterning), DNA, and liposomes. In addition, a detailed analysis of the characteristics and process parameters of the LIFT process is reviewed, with emphasis on the possible applications of LIFT of biomolecules in microarrays and biosensors.

14.2 LIFT of DNA in Solid and Liquid Phase

During the past years, laser technology was firmly established in many fields of basic research, such as diagnostics in the biomedical field, as well as in functional biocoatings and in microarray technology. While many experiments are performed with commercial oligonucleotide microarrays (e.g., Affymetrix, Agilent, Eppendorf), custom-made microarrays extend the researchers toolbox when the DNA sequence is not known or fast and different layout changes of microarrays are required.

The transfer of biomolecules, for example, DNA, is interesting both to compare the solid-phase LIFT to the liquid-phase LIFT and also because of the potential applications of these biomolecules in biosensors and microarray chip devices. A detailed presentation of LIFT of liquids is given in Chapter 4. In addition, a review of DNA (and other biomolecules) printing by LIFT is presented in [50].

One of the first studies on the laser transfer of biological compounds (DNA) involved the use of a femtosecond laser [40, 41] where the biomaterials were deposited on a substrate without the assistance of any transferring matrix material or absorbing film from a dried target. Further on, studies aimed at understanding the LIFT transfer processes by means of nanosecond laser pulses were carried out by Serra *et al*. using a liquid target and the assistance of an absorbing metal film [38, 42]. In [38], the authors deposit microdroplets of a solution containing double-stranded DNA of salmon sperm onto poly-L-lysine-coated glass substrates. This was the first report on DNA printing, a proof-of-concept for future works in which the actual fabrication of a DNA microarray was reported. DNA microarray fabrication was demonstrated in [42], where solutions containing DNA strands corresponding to different human genes were successfully transferred by LIFT. To prove the functionality of the microarrays, they were submitted to hybridization protocols, and it was shown that the LIFTed microarrays were specific in gene discrimination.

More recently, the transfer of DNA solutions (at 266 nm) with Ti films was analyzed, and the quantification of the preservation of the biological activity of DNA transferred by LIFT was investigated. Regular DNA transferred patterns were obtained for a narrow range of laser fluences (1–3 mJ/cm^2). An optical image of a DNA microarray printed onto glass substrates is shown in Figure 14.1a, while a digital image of agarose gel electrophoresis is shown in Figure 14.1b, demonstrating that no fragmentation of the DNA occurred as a result of the laser transfer. These images prove the feasibility of LIFT for printing regular DNA microarrays and that the activity of the spotted DNA was maintained only for relatively low laser fluences (<3 mJ/cm^2) compared to the DNA control ladder.

Furthermore, in order to surmount the difficulties characteristic of the conventional LIFT, an original idea, which allows the direct printing of biological solutions without the need for preparing the liquid in thin-film form, has been developed [52]. This technique, called film-free LIFT (a detailed description is provided in Chapter 6) relies on strongly focusing a femtosecond pulsed laser beam inside the liquid to be printed just below the free surface. A cavitation bubble is generated, which projects a small fraction of the liquid beyond the

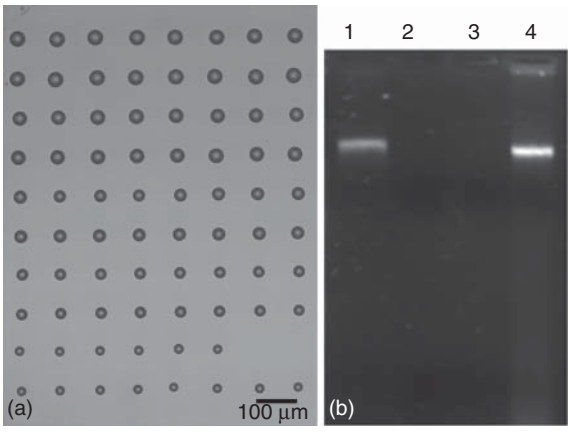

Figure 14.1 (a) Optical microscopy image of a DNA microarray printed by LIFT on glass. Laser fluence increases from bottom to top of the image: each laser fluence (1, 1.5, 2, 2.5, 3 mJ/cm^2) is applied to deposit two rows of droplets. (b) Agarose gel electrophoresis (1) 3 mJ/cm^2, (2) 4 mJ/cm^2, (3) 5 mJ/cm^2 laser fluence, and (4) DNA control 12 ng/µl [51].

free surface, thus the liquid being deposited on a substrate as a printed droplet. The displacement of the substrate with respect to the free surface allows the realization of micropatterns. This technique has been proved to be feasible for biomolecules printing, that is, functional DNA and protein microarrays [53, 54].

14.3 LIFT of Biomolecules

14.3.1 Streptavidin and Avidin–Biotin Complex

Among the numerous biomolecules involved in the development of a controlled immobilization in a biomicrodevice configuration, proteins are particularly challenging. In contrast with DNA, for which suitable immobilization technologies have been developed and DNA microchips commercialized, technology allowing uniform and global attachment of a wide variety of proteins to different surfaces is not currently available. This lag in technology arises from the fundamental structural difference between DNA and proteins, the latter being complex three-dimensional biomolecules with many attachment sites, which can lose their bioactivity if their structure is disrupted during the immobilization process or due to random orientation of the immobilized protein.

The first works on protein printing are presented in [55, 56], where the authors report on an alternative to LIFT, that is, matrix-assisted pulsed laser evaporation–direct write (MAPLE-DW) (for details on LIFT basics and its alternatives, please refer to Chapter 1) for the deposition of (i) a mixture of banana tissue with mineral oil and graphite powder for the fabrication of electrochemical sensors and (ii) a functional bovine serum albumin (BSA) biomolecule microarray. In [57], the same group from the Naval Research Laboratory reports on the application of MAPLE DW for the fabrication of bioactive and regular microarrays of streptavidin. In the same work, a comparison with the soft lithography microprinting technique is provided. The authors explored the direct immobilization, morphology, and function of the deposited protein at the interface with an aqueous environment and in the presence of controlled ligand–receptor reactions. The advantages of the laser techniques applied in

comparison with the soft lithography microprinting were evident, that is, the patterns obtained via laser-based techniques showed a reduction in size and well-defined patterns.

These first successes on biomolecule printing prompted an extensive number of different protein types being printed through LIFT, as, for example, the biotin–avidin complex.

Avidin is a glycoprotein found in egg whites that contains four identical subunits, each having one binding site for biotin (or vitamin H). Streptavidin is a biotin-binding protein isolated from *Streptomyces avidinii*, which contains four subunits, each with a single biotin-binding site [58]. Both proteins are very stable and can tolerate a wide range of buffer conditions, pH, and chemical modifications and can be conjugated to other proteins or labeled with various detection agents without loss of binding activity.

Further on, based on the fact that the biospecificity and strength of the biotin–avidin noncovalent interaction make this system very useful for the micropatterning of biomolecules [59], nanosecond and femtosecond lasers were used to obtain micron-size patterns of biotin and avidin. The laser parameters, the influence of the solution viscosity, and the receiving surface wettability on the formed patterns were investigated and optimized. The size of the transferred patterns was controlled by the spot dimensions and energy of the laser beam, thickness of the donor (liquid) layer, glycerol percentage in the composition of the donor, and surface wettability. Moreover, a regular transfer of droplets was possible for distances greater than few micrometers, and different percentages of glycerol could be added without the risk of contamination. The pattern functionality after laser transfer was confirmed by using a three-step strategy: (i) direct transfer of coupling molecules using LIFT, (ii) immobilizing an active complementary protein on it, and (iii) performing direct and/or indirect labeling by fluorescence microscopy assay [60]. In order to exploit the direct labeling interaction, biotin was linked to the surface of the substrate using LIFT and then used as a site for the specific recognition of the Atto-565-Streptavidin as shown in Figure 14.2.

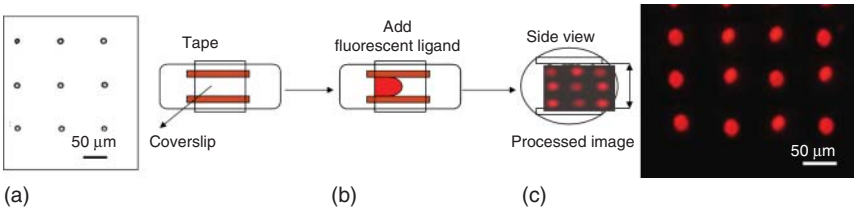

Figure 14.2 Strategy implying the direct and indirect labeling by fluorescence microscopy assays for the functional biotin patterns obtained by LIFT in a perfusion chamber. (a) The perfusion chamber was built from cleaned Corning cover glass and the patterned cover glass separated by a double-side tape spacer (red). (b) The direct labeling was based on one-step antibody–biotin coupling. (c) The indirect labeling was based on the fluorescent marked Atto-565-Streptavidin–biotin coupling. After incubation with the fluorescence labeling solution, all the samples were rinsed with PBS and distilled water. Fluorescence was detected using a Zeiss fluorescence microscope equipped with a Laser Scanning System Radiance 2100 (400–700 nm) and with a Carl Zeiss Axio Camera HR, and the signal intensity was quantified.

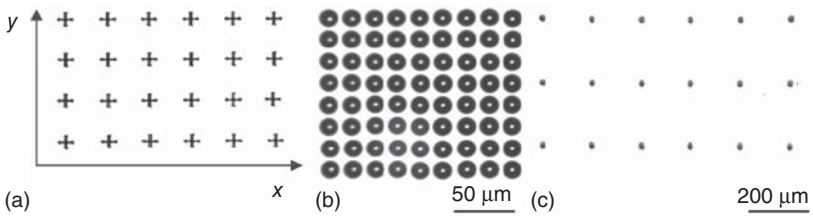

Figure 14.3 (a) Pattern diagram for obtaining spots onto different surfaces, that is, hydrophilic/hydrophobic. (b) 10 μm spot spacing on hydrophilic surfaces (glass). (c) 200 μm or more on hydrophobic surfaces (Ormocer). The spots were captured immediately after printing, the spot diameter and their spacing on the substrate were measured.

For the indirect labeling strategy, two different protein–ligand systems were used: avidin, biotin, and Atto-565-Streptavidin, and titin I band fragment human recombinant – monoclonal anti-titin antibody-cy 5 goat anti-mouse IgG conjugate antibody [60] respectively.

An important aspect in the miniaturization of the patterns was given by the wetting properties of the receiving surfaces (see Figure 14.3).

The wettability aspect enabled reproducible printing of microarrays with spacing between spots from 10 to 200 μm or more as it can also be seen in Figure 14.3. The diameter of the spots on the hydrophilic surfaces was 20 μm resulting in a theoretical spot-to-spot distance of less than 10 μm. In the case of the hydrophobic surfaces (Ormocer), this distance could be optimized. However, this parameter was tolerable, because even in the worst case, no mixing of spots could occur.

Furthermore, by varying the laser energy and the donor solution viscosity (from 0% to 70% (v/v) of a glycerol/water solvent) together with the receiver substrates (hydrophobic surfaces), micropatterns with droplets as small as 8 μm could be obtained [37, 61]. Therefore, enzyme solution properties, that is, viscosity and surface tension enable LIFT as a suitable method for biological compound patterning. The efficiency of LIFT was not affected by the addition of glycerol in a percentage up to 70%, which contributed to the stabilization of the microarray patterns and the increase of their resolution.

Another important key factor in protein patterning is the spot uniformity. Depending on the solutions used for donor preparation, especially when glycerol and surfactants are missing, a ring-like morphology can appear within the printed spots (see Figure 14.4). The ring structure in the spot morphology is commonly seen in protein or antibody microarrays, and it results from the transport of protein molecules that are accumulated at the air/water interface in the perimeter of the droplet on a solid surface. This effect becomes increasingly significant as the droplet size decreases. One can eliminate the ring structure by adding competitive surfactants to the protein solution or by designing facile surface reactions for protein immobilization.

The effect of the nanosecond and femtosecond laser pulse lengths has been studied in relation to the preservation of the activity of the transferred biomolecules. LIFT has been employed for microarray printing of liquid solutions of both the enzyme Horseradish Peroxidase (HRP) and the titin protein on nitrocellulose solid surfaces, as shown in Figure 14.5 [37]. The quantification

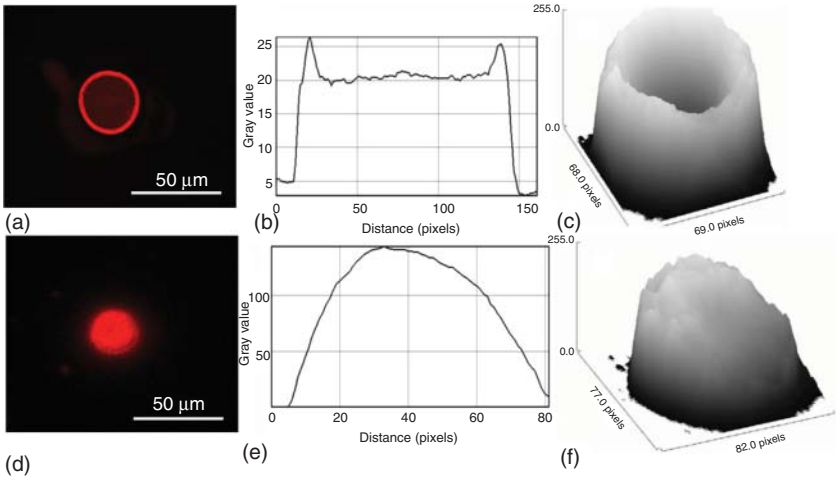

Figure 14.4 From left to right (a–c) without SDS, (d–f) with SDS. (a) and (d) Fluorescence microscopy images of photobiotin spots immobilized onto an Ormocer slide. (b) and (e) Cross-sectional profiles of the images (a) and (d), respectively. (c) and (f) Profiles of the surfaces shown in (a) and (d).

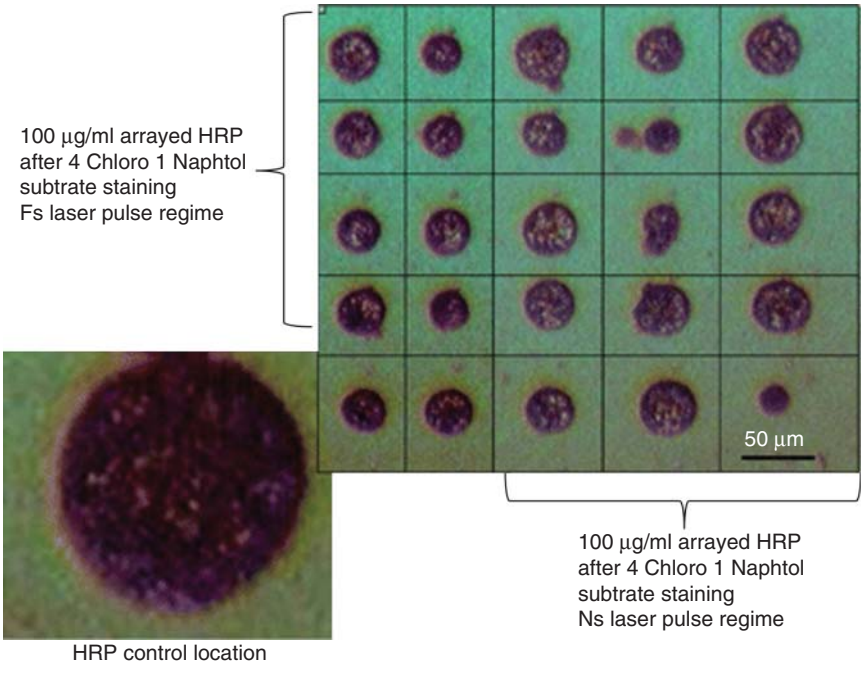

Figure 14.5 HRP transfer at a laser fluence of 260 mJ/cm^2. (Dinca *et al*. 2008 [37]. Reproduced with permission of Springer.)

of the active biomolecules has been carried out by Bradford assay, quantitative colorimetric enzymatic assay, and fluorescence techniques. Spectrophotometric measurements of the HRP and the titin activity as well as chromatography and fluorescence assay studies have revealed a connection between the properties of the deposited biologically active biomolecules, the experimental conditions, and the target composition. The bioassays have shown that up to 78% of the biomolecules remained active after femtosecond laser transfer, while this value was reduced to 54% after ns laser transfer.

In a more recent paper, [62] the authors present the successful transfer of untagged and enzyme-linked antibodies on cellulose-based filter paper receivers for future developments in point-of-care diagnostic devices. The functionality of the laser transferred biomolecules (mouse IgG and anti-mouse IgG tagged with HRP) was demonstrated by carrying out a colorimetric enzyme-linked immunosorbent assay (ELISA), which proved that LIFT is a technique capable of transferring antibodies accurately and with high reproducibility onto unconventional substrates for the fabrication of immunologic paper-based sensors.

Not only 2D but also 3D biomolecule patterning using laser-based techniques, which enable the construction of arbitrary two- and three-dimensional shapes, not restricted to array-based shapes, was demonstrated in [63]. 3D patterning implied the immobilization and activation of photobiotin on the surface of the 3D Ormocer structures and further binding specifically to fluorescently labeled streptavidin.

Avidin was also used as homobifunctional protein adapter for directed three-dimensional patterning of self-assembled amyloid fibrils. In this case, each protein molecule could simultaneously bind to a photobiotin-functionalized substrate, and the biotinylated molecules on the opposite face were exposed to solution as seed, or "anchoring point." The covalent bond formation between the iodoacetamide group in the biotin derivative and the thiol group in the fibrils containing cysteine allowed specific 3D peptides patterning [64].

14.3.2 Amyloid Peptides

Amyloid peptides have the characteristic of self-assembling, and in addition, they may be deposited by LIFT on specific positions and different surfaces. Therefore, it is possible to enable the specific fabrication of a huge number of different structures aiming at many important applications in medicine and biology [65].

LIFT was used for microarray fabrication of self-assembled octapeptides derived from sequences of a natural fibrous protein (i.e., the adenovirus fiber). No influence on the peptide fibril self-assembly process and/or fibril stability at the solid/solution interface has been observed after LIFT.

As previously mentioned, the transferred patterns' size and shape are directly correlated to the laser pulse energy used; for energies close to the threshold energy, the transfer was uniform and no splashes were observed as shown in Figure 14.6.

Well-defined patterns of peptides on gold-coated glass were obtained, and the larger spots, with diameters of 120 μm, allowed a better observation of the peptide fibril formation during drying, as shown in Figure 14.7.

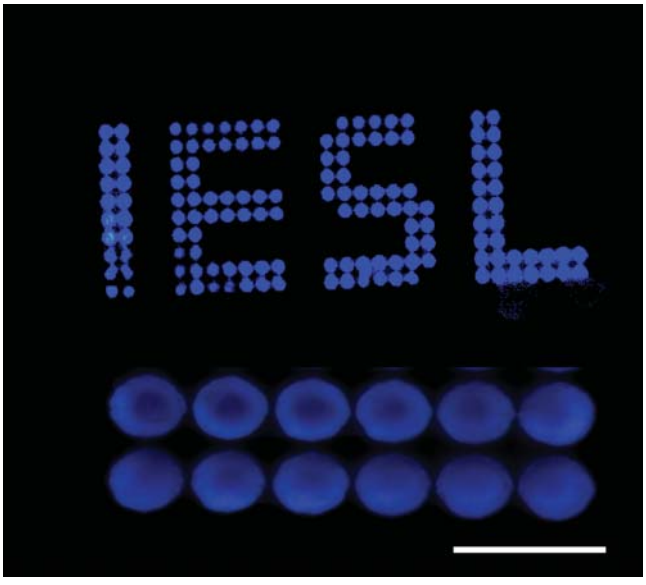

Figure 14.6 Peptide micropatterns transferred by LIFT and stained using Thioflavin T diagnostic tests. Scale bar is 50 μm.

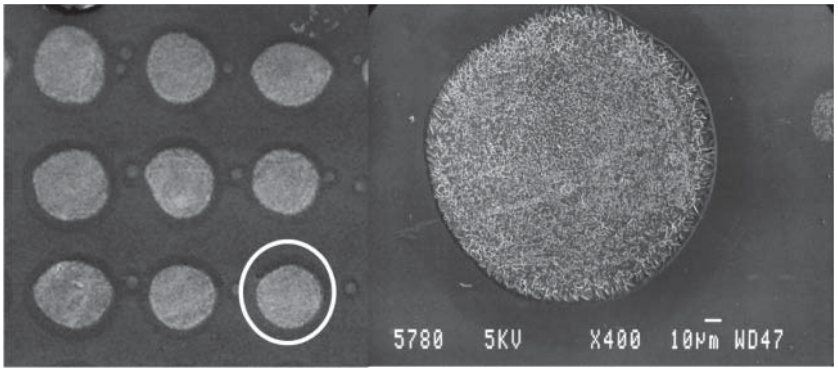

(a) (b)

Figure 14.7 Scanning electron microscopy image of part of (a) a printed peptide array and (b) one peptide droplet transferred by LIFT on a gold surface when the samples is left to dry in air, at room temperature after deposition. The presence of flat and elongated aggregates, 2–6 μm long and 0.2–0.5 μm thick peptide tapes can be noticed.

LIFT provides the possibility to pattern peptide-based arrays, which could be used as flexible and powerful tool in basic biology studies of protein recognition and function, peptides–other biocompounds (enzymes, proteins, DNA, small molecules) interactions, but also for the 2D and 3D templating of inorganic materials and incorporation and display of ligands critical for cell attachment and growth.

14.3.3 Odorant-Binding Proteins

Protein printing is important for applications aiming at the fabrication of not only functional microarrays but also biosensors, in particular for the detection of contaminants in food, essential to avoid risks for humans [66]. An extensive review of laser printing of chemical and biological sensors is presented in Chapter 13. In recent studies [67, 68], the possibility of depositing biomolecule-containing solutions, that is, odorant-binding proteins (OBPs), through LIFT onto the active area of a surface acoustic (SAW) device for the development of a bioelectronic nose was presented. The sensing system proposed by the authors exploited the high sensitivity and fast response time typical of SAW-based sensors in combination with the adaptable selectivity of the OBPs [60]. OBPs are small extracellular proteins that belong to the lipocalin superfamily [69, 70]. They have an important role in odor detection by carrying, deactivating, and/or selecting the odorant molecules [71, 72].

The "bioelectronic nose" fabricated in [67] was based on three SAW resonators coated through LIFT with three different OBPs, characterized by different binding specificities, plus an uncoated SAW device used as reference. The selected proteins were the wild-type OBP from bovine (wtbOBP), a double mutant of the OBP from bovine (dmbOBP), and the wild-type OBP from pig (wtpOBP). To demonstrate the functionality of the biosensor arrays, the SAW devices coated by LIFT were exposed to different concentrations of octanol and carvone, two odorant compounds largely used in the food industry.

It was found that LIFT it is an appropriate technique for OBP deposition with a very high lateral resolution (Figure 14.8a,b), which allowed the fabrication of functional SAW biosensor arrays. The SAW biosensor arrays fabricated by

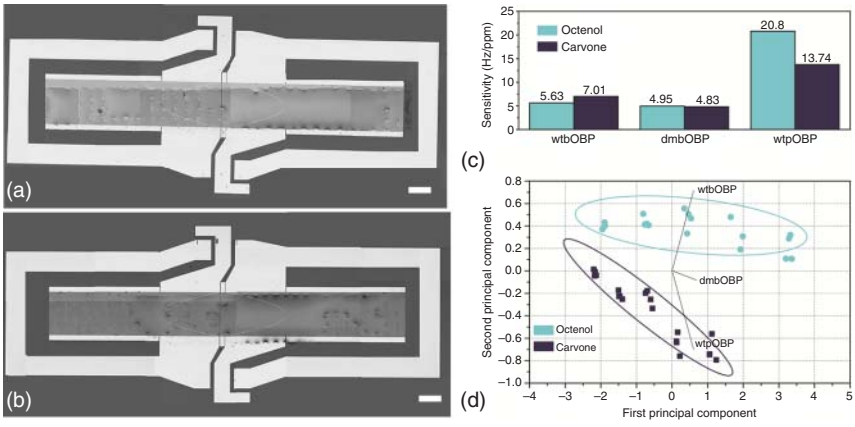

Figure 14.8 Optical microscopy images of SAW sensors printed by LIFT, by overlapping individual droplets at different center-to-center distances (ratio of overlapped length between two neighboring droplets to the individual droplet diameter (a) 30% overlap, (b) 50% overlap. (c) Comparison between sensitivities to octanol and carvone detection of the wtbOBP-, dmbOBP-, and wtpOBP-based biosensors. (d) Biplot of loadings and scores using the first two components of the principal component analysis. (Reproduced with permission from [67].)

LIFT were capable of detecting specific odors with sensitivity and detection limit similar to those that could be obtained with more conventional methods, but with a much lower consumption of detecting agent (Figure 14.8c,d). These results demonstrate that LIFT is a powerful technique to fabricate biosensors with ultimate applications in the assessment of food contamination by molds or for the evaluation of indoor air quality in buildings.

14.3.4 Liposomes

Similarly to DNA and protein printing, liposome printing also represents an important area of research. Liposome patterns are used in applications such as carrier systems of drugs or other functional substances and miniaturized biosensors.

Liposomes are molecular structures consisting of lipid bilayers that enclose an aqueous core. The most important properties of liposomes are, for example, non-toxicity, biodegradability, the easy preparation (or production), and stability in solution for a long period of time.

In [73], liposome-containing solutions were printed by LIFT assisted by a DRL (or sacrificial layer). This layer consists of a photodegradable polymer, namely a TP. For details on LIFT assisted by a TP, please refer to Chapter 3. The TP was chosen as DRL layer, due to the fact that the emission wavelength of the lasers used for LIFT matches the absorption maxima of the TP. The specific TP was synthesized following the procedure published previously [74].The TP was deposited by spin coating. TP films with a thickness of 60, 150, and 350 nm were obtained with this procedure and subsequently used for transfer experiments.

The donor solutions used for LIFT in [73] contained giant liposomes with diameters of tens of micrometers, which were obtained by the "gentle hydration method" and by the rotoevaporation method. A phase-contrast microscopy image and a fluorescence microscopy image of giant liposomes in solution, that is, the donor solution prior to LIFT, are shown in Figure 14.9. The transfer was performed using two laser systems, a XeCl (308 nm) and an ArF (193 nm) excimer laser.

It was found that a major role in the transfer process of the liposome-containing solution was played by the thickness of the TP layer. The data suggested that in the case of TP-LIFT with the 193 nm laser system, it was not possible to print a regular array with a 60 nm intermediate TP layer, and that only a 150 nm thick TP layer was sufficient to minimize the damages to the transferred liquid layer. In addition, the laser fluences necessary to transfer regular droplets need to be higher than the fluences needed for the complete vaporization of the TP layer (35 mJ/cm^2). Further experiments, with a XeCl, laser system operating at 308 nm, showed that circular droplets with a well-defined contour could be obtained even for a 60 nm thick TP layer. Another important parameter for printing droplets with high resolution, reproducibility, and integrity of the biomolecules was the laser fluence. Fluorescence microscopy was used to determine whether the integrity of the liposomes was altered after laser transfer. A fluorescence image of a microarray obtained at different laser fluences (for ArF laser irradiation) is presented in

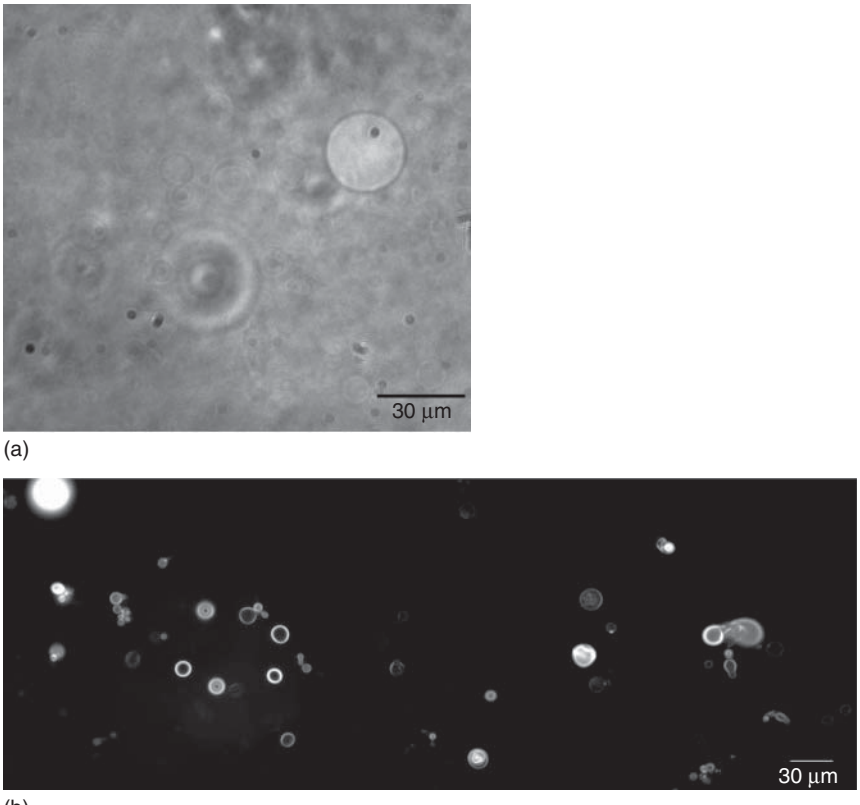

Figure 14.9 Phase-contrast microscopy image (a) and fluorescence microscopy image (b) of giant liposomes in solution. (Palla-Papavlu *et al*. 2011 [73]. Reproduced with permission of Springer.)

Figure 14.10. Only at fluences between 40 and 80 mJ/cm^2, the transferred spots exhibited fluorescence with an intensity corresponding to the target solution. The transferred spots were not surrounded by splashes for fluences between 40 and 60 mJ/cm^2, while for fluences up to 80 mJ/cm^2, random droplets appeared on the substrate. Above 80 mJ/cm^2, no fluorescence was detected anymore, suggesting that in this case, the liposomes may have degraded due to the high laser fluences.

In addition, to further investigate the chemical composition of the liposomes after the laser transfer, micro-Raman spectroscopy was used. The μ-Raman reference spectrum (Figure 14.11) of the liposomes agrees well with literature data, although it had a lower signal-to-noise ratio than for reported data [75]. Raman spectra of transferred liposomes using different laser fluences (Figure 14.11) showed a clear trend: the intensity of characteristic Raman peaks decreased with increasing laser fluence. In addition, there were no indications of TP or TP fragments being present in the transferred liposomes. The Raman analysis suggested that the liposomal membranes were not damaged for laser fluences below 60 mJ/cm^2 and that the TP did probably not contaminate the lipids.

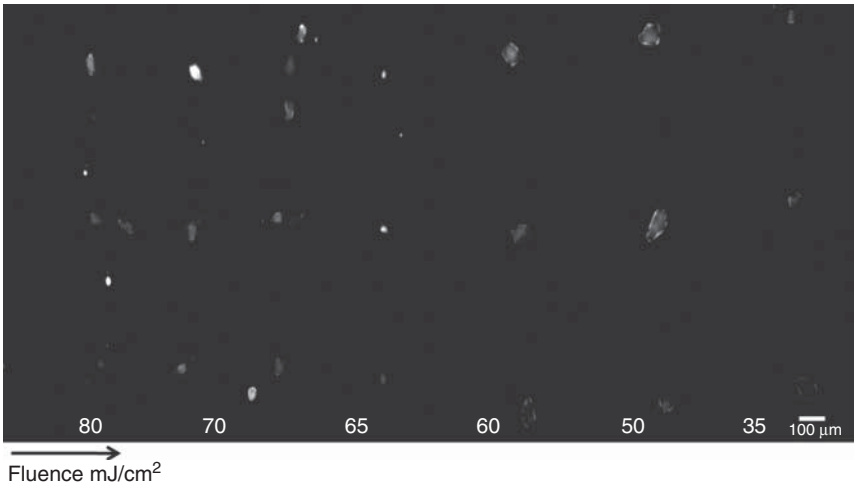

Figure 14.10 Fluorescence image of a microarray of liposome solution obtined at different laser fluences. (Palla-Papavlu *et al*. 2011 [73]. Reproduced with permission of Springer.)

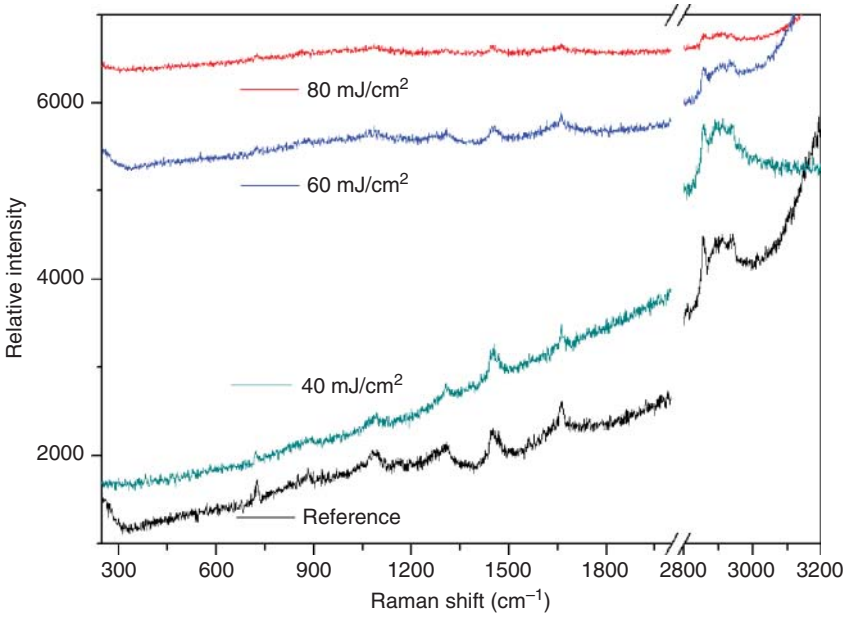

Figure 14.11 Raman spectra of the liposome solution after transfer at different laser fluences. (Palla-Papavlu *et al*. 2011 [73]. Reproduced with permission of Springer.)

The fact that liposome arrays could be produced in a cost- and time-effective way with a minimum sample volume suggested that LIFT is a promising technique for transferring liposome solutions, which could therefore be used for *in vitro* and *in vivo* applications.

14.4 Conclusions and Perspectives

For many applications in the area of biosensors, tissue engineering, and regenerative medicine, it is important to develop a new generation of high-performance biomaterials, where their interfacial properties could be controlled and modulated toward the required application. Although significant progress has been achieved in the field of material printing and patterning, the materials and methods discussed within this chapter still have limitations in practical applications that need to be overcome in the future.

This chapter summarizes some applications and developments in the field of LIFT of biomolecules. The data shown suggest that LIFT is a promising approach for printing DNA, proteins (avidin, streptavidin), peptides, and lipids either in solution or as dry thin films that can be utilized for the fabrication of functional microarrays, biosensors, or drug delivery systems. The transfer process of the biological materials can be optimized by modifying the process parameters, that is, laser wavelength, laser fluence, applying intermediate DRLs with varying thickness, or using different types of substrates. As it has been shown in different studies, the target–substrate distance is a parameter that does not influence the morphology of the obtained micropatterns.

Considering the aforementioned advantages of the LIFT technique on depositing materials with very high resolution onto different types of substrates, one could envision that this approach could provide a new strategy to engineer functional multicompositional platforms to be used for regenerative biomedicine and tissue engineering studies, which could ultimately be extended toward industrial applications.

Future research in the field of LIFT could also be directed toward biomimetic biointerfaces, with integrated analysis platforms able to address the complexity of bioenvironments according to the desired application.

Acknowledgments

This work was supported by the National Program 4N/2016 and grants of the Romanian National Authority for Scientific Research and Innovation, CNCS – UEFISCDI, project number PN-II-RU-TE-2014-4-2311, PN-II-PT-PCCA-2013-4-1643, PNII-PT-PCCA-2013-4-1992, and PN-II-RU-TE-2014-4-2434.

Conflict of Interest

The authors declare no competing interests.

References

1 Ozbolat, I.T., Peng, W., and Ozbolat, V. (2016) Application areas of 3D bioprinting. *Drug Discovery Today*, **21** (8), 1257–1271.
2 Terry, S.C., Jerman, J.H., and Angell, J.B. (1979) A gas chromatography air analyzer fabricated on a silicon wafer. *IEEE Trans. Electron. Dev.*, **26**, 1880–1886.
3 Voldman, J., Gray, M.L., and Schmidt, M.A. (1999) Microfabrication in biology and medicine. *Annu. Rev. Biomed. Eng.*, **1**, 401–425.
4 Gaharwar, A.K., Arpanaci, A., Andersen, T.L., and Dolatshahi-Pirouz, A. (2016) 3D biomaterial microarray for regenerative medicine: current state of the art, emerging directions and future trends. *Adv. Mater.*, **27**, 771–781.
5 Vo-Dinh, T. (2005) *Methods in Molecular Biology*, Protein Nanotechnology, Protocols, Instrumentation, and Applications, vol. **300**, Humana Press Inc., Totowa, NJ, p. 101.
6 Borini, S., Staiano, M., Rocchia, M., Rossi, A.M., and D'Auria, S. (2007) Advanced nanotechnological approaches for designing protein-based "Lab-on-Chips" sensors on porous silicon wafer. *Recent Pat. DNA Gene Seq.*, **1**, 1–7.
7 Gutmann, O., Niekrqwietz, R., Steinert, C.P., Sandmaier, H., Messner, S., de Heij, B., Daub, M., and Zengerle, R. (2003) Droplet release in a highly parallel pressure driven nanoliter dispenser. *IEEE Trans.*, 364–367.
8 Ekins, R. and Chu, F.W. (1999) Microarrays: their origins and applications. *Trends Biotechnol.*, **17** (6), 217–218.
9 Haab, B.B., Dunham, M.J., and Brown, P.O. (2001) Protein microarrays for highly parallel detection and quantitation of specific proteins and antibodies in complex solutions. *Genome Biol.*, **2** (2), 0004.1–0004.13.
10 Seong, S. and Choi, C. (2003) Current status of protein chip development in terms of fabrication and application. *Proteomics*, **3**, 2176–2189.
11 Blawas, A.S. and Reichert, W.M. (1998) Protein patterning. *Biomaterials*, **19**, 595–609.
12 Blawas, A.S., Oliver, T.F., Pirrung, M.C., and Reichert, W.M. (1998) Step-and-repeat photopatterning of protein features using caged-biotin-BSA: characterization and resolution. *Langmuir*, **14**, 4243–4250.
13 Khademhosseini, A., Eng, G., Kucharczyk, P.A., Langer, R., Vunjak-Novakovic, G., and Radisic, M. (2007) Microfluidic patterning for fabrication of contractile cardiac organoids. *Biomed. Microdevices*, **9**, 149–157.
14 Martin, B.D., Gaber, B.P., Patterson, C.H., and Turner, D.C. (1998) Direct protein microarray fabrication using a hydrogel "stamper". *Langmuir*, **14**, 3971–3975.
15 Roda, A., Guardigli, M., Russo, C., Pasini, P., and Baraldini, M. (2000) Protein microdeposition using a conventional ink-jet printer. *BioTechniques*, **28**, 492–496.
16 Howard, E.I. and Cachau, R.E. (2002) Ink-jet printer heads for ultra-small-drop protein crystallography. *BioTechniques*, **33**, 1302–1306.
17 Braudy, R.S. (1969) Laser writing. *Proc. IEEE*, **57**, 1771–1772.

18 Levene, M.L., Scott, R.D., and Siryj, B.W. (1970) Material transfer recording. *Appl. Opt.*, **9** (10), 2260–2265.

19 Brisbane, A.D. (1971) Pattern deposit by laser. US Patent 3,560,258, filed and issued May 31, 1967 issued Feb. 2, 1971.

20 Bohandy, J., Kim, B.F., and Adrian, F.J. (1986) Metal deposition from a supported metal film using an excimer laser. *J. Appl. Phys.*, **60** (4), 1538–1539.

21 Bohandy, J., Kim, B.F., Adrian, F.J., and Jette, A.N. (1988) Metal deposition at 532 nm using a laser transfer technique. *J. Appl. Phys.*, **63** (4), 1158–1162.

22 Baseman, R.J., Froberg, N.M., Andreshak, J.C., and Schlesinger, Z. (1990) Minimum fluence for laser blow-off of thin gold films at 248 and 532 nm. *Appl. Phys. Lett.*, **56**, 1412–1414.

23 Schultze, V. and Wagner, M. (1991) Laser induced forward transfer of aluminium. *Appl. Surf. Sci.*, **52**, 303–309.

24 Kantor, Z., Zs, T., and Szorenyi, T. (1992) Laser induced forward transfer: the effect of support-film interface and film to substrate distance on transfer. *Appl. Phys. A*, **54**, 170–175.

25 Kantor, Z., Zs, T., Szorenyi, T., and Toth, A.L. (1994) Deposition of micrometer-sized tungsten patterns by laser transfer technique. *Appl. Phys. Lett.*, **64**, 3506–3508.

26 Sano, T., Yamada, H., Nakayama, T., and Miyamoto, I. (2002) Experimental investigation of laser induced forward transfer process of metal thin films. *Appl. Surf. Sci.*, **186**, 221–226.

27 Toth, Z., Szorenyi, T., and Toth, A.L. (1993) Ar+ laser induced forward transfer (LIFT): a novel method for micrometer size surface patterning. *Appl. Surf. Sci.*, **69**, 317–320.

28 Zergioti, I., Mailis, S., Vainos, N.A., Papakonstantinou, P., Kalpouzos, C., Grigoropoulous, C.P., and Fotakis, C. (1998) Microdeposition of metal and oxide structures using ultrashort laser pulses. *Appl. Phys. A*, **66**, 579–582.

29 Zergioti, I., Papazoglu, D.G., Karaiskou, A., Fotakis, C., Gamaly, E., and Rode, A. (2003) A comparative schlieren imaging study between ns and sub-ps laser induced forward transfer of Cr. *Appl. Surf. Sci.*, **208-209** (1), 177–180.

30 Banks, D.P., Grivas, C., Mills, J.D., Eason, R.W., and Zergioti, I. (2006) Nanodroplets deposited in microarrays by femtosecond Ti:sapphire laser induced forward transfer. *Appl. Phys. Lett.*, **89**, 19107-(1–3).

31 Papakonstantinou, P., Vainos, N.A., and Fotakis, C. (1999) Microfabrication by UV femtosecond laser ablation of Pt, Cr and indium oxide thin films. *Appl. Surf. Sci.*, **151**, 159–170.

32 Greer, J.A. and Parker, T.E. (1988) Laser induced forward transfer of metal oxides to trim the frequency of surface acoustic wave resonator devices. *SPIE Proc.*, **998**, 113–125.

33 Zergioti, I., Papazoglu, D.G., Karaiskou, A., Vainos, N.A., and Fotakis, C. (2002) Laser microprinting of InO_x active optical structures and time resolved imaging of the transfer process. *Appl. Surf. Sci.*, **197–198**, 868–872.

34 Chakraborty, S., Sakata, H., Yokoyama, E., Wakaki, M., and Chakravorty, D. (2005) Laser induced forward transfer technique for maskless patterning of amorphous V_2O_5 thin film. *Appl. Surf. Sci.*, **254**, 638.

35 Klini, A., Mourka, A., Dinca, V., Fotakis, C., and Claeyssens, F. (2007) ZnO nanorod micropatterning via laser induced forward transfer. *Appl. Phys. A*, **87** (1), 17–22.

36 Fogarassy, E., Fuchs, C., Kerherve, F., Hauchecorne, G., and Perrière, J. (1989) Laser-induced forward transfer: a new approach for the deposition of high T_c superconducting thin films. *J. Mater. Res.*, **4**, 1082–1086.

37 Dinca, V., Ranella, A., Farsari, M., Kafetzopoulous, D., Dinescu, M., Popescu, A., and Fotakis, C. (2008) Quantification of the activity of biomolecules in microarrays obtained by direct laser transfer. *Biomed. Microdevices*, **10**, 719–725.

38 Fernandez-Pradas, J.M., Colina, M., Serra, P., Domınguez, J., and Morenza, J.L. (2004) Laser induced forward transfer of biomolecules. *Thin Solid Films*, **27**, 453–454C.

39 Chrisey, D.B. (2000) The power of direct writing. *Science*, **289** (5481), 879–881.

40 Karaiskou, A., Zergioti, I., Fotakis, C., Kapsetaki, M., and Kafetzopoulos, D. (2003) Microfabrication of biomaterials by the sub-ps laser induced forward transfer process. *Appl. Surf. Sci.*, **208**, 245–249.

41 Zergioti, I., Papazoglou, D.G., Karaiskou, A., Fotakis, C., Kapsetaki, E., and Kafetzopoulos, D. (2005) Femtosecond laser microprinting of biomaterials. *Appl. Phys. Lett.*, **86**, 163902-(1–3).

42 Serra, P., Colina, M., Fernandez-Paras, J.M., Sevilla, L., and Morenza, J.L. (2004) Preparation of functional DNA microarrays by laser induced forward transfer. *Appl. Phys. Lett.*, **85**, 1639–1641.

43 Doraiswamy, A., Narayan, R.J., Lippert, T., Urech, L., Wokaun, A., Nagel, M., Hopp, B., Dinescu, M., Modi, R., Auyeung, R.C.Y., and Chrisey, D.B. (2006) Excimer laser forward transfer of mammalian cells using a novel triazene absorbing layer. *Appl. Surf. Sci.*, **252**, 4743–4747.

44 Chrisey, D.B., Piqué, A., McGill, R.A., Horwitz, J.S., Ringeisen, B.R., Bubb, D.M., and Wu, P.K. (2003) Laser deposition of polymer and biomaterial films. *Chem. Rev.*, **103** (2), 553–576.

45 Dinca, V., Fardel, R., Di Pietrantonio, F., Cannatà, D., Benetti, M., Verona, E., Palla-Papavlu, A., Dinescu, M., and Lippert, T. (2010) Laser induced forward transfer: an approach to single-step polymer microsensor fabrication. *Sens. Lett.*, **8** (3), 436–440.

46 Boutopoulos, C., Tsouti, V., Goustouridis, D., Chatzandroulis, S., and Zergiotti, I. (2008) Liquid phase direct laser printing of polymers for chemical sensing applications. *Appl. Phys. Lett.*, **93**, 191109-(1–3).

47 Fardel, R., Nagel, M., Nuesch, F., Lippert, T.K., and Wokaun, A. (2007) Laser forward transfer using a sacrificial layer: Influence of the material properties. *Appl. Surf. Sci.*, **254**, 1322–1326.

48 Nagel, M., Fardel, R., Feurer, P., Häberli, M., Nüesch, F., Lippert, T.K., and Wokaun, A. (2008) Aryltriazene photopolymer thin films as sacrificial release layers for laser-assisted forward transfer systems: study of photoablative decomposition and transfer behavior. *Appl. Phys. A*, **92**, 781–789.

49 Kattamis, N.T., Purnick, P.E., Weiss, R., and Arnold, C.B. (2007) Thick film laser induced forward transfer for deposition of thermally and mechanically sensitive materials. *Appl. Phys. Lett.*, **91**, 171120-(1–3).

50 Serra, P., Duocastella, M., Fernandez-Pradas, J.M., and Morenza, J.L. (2010) in *Cell and Organ Printing* (eds B.R. Ringeisen *et al.*), Springer, pp. 53–80.

51 Palla-Papavlu, A., Dinca, V., Lippert, T., and Dinescu, M. (2011) Laser induced forward transfer for materials patterning. *Rom. Rep. Phys.*, **63**, 1285–1301.

52 Duocastella, M., Patrascioiu, A., Fernandez-Pradas, J.M., Morenza, J.L., and Serra, P. (2010) Film-free forward printing of transparent and weakly absorbing liquids. *Opt. Express*, **18** (21), 21815–21825.

53 Duocastella, M., Fernandez-Pradas, J.M., Morenza, J.L., Zafra, D., and Serra, P. (2010) Novel laser printing technique for miniaturized bisosensor preparation. *Sens. Actuators, B*, **145** (1), 596–600.

54 Patrascioiu, A., Duocastella, M., Fernandez-Pradas, J.M., Morenza, J.L., and Serra, P. (2011) Liquids microprinting through a novel film-free fs laser based technique. *Appl. Surf. Sci.*, **257** (12), 5190–5194.

55 Wu, P.K., Ringeisen, B.R., Callahan, J. *et al.* (2001) The deposition, structure, pattern deposition, and activity of biomaterial thin-films by matrix-assisted pulsed-laser evaporation (MAPLE) and MAPLE direct write. *Thin Solid Films*, **398–399**, 607–614.

56 Ringeisen, B.R., Wu, P.K., Kim, H. *et al.* (2002) Picoliter-scale protein microarrays by laser direct write. *Biotechnol. Progr.*, **18**, 1126–1129.

57 Dinu, C.Z., Dinca, V., Howard, J., and Chrisey, D.B. (2007) Printing technologies for fabrication of bioactive and regular microarrays of streptavidin. *Appl. Surf. Sci.*, **253** (19), 8119–8124.

58 Wilchek, M. and Bayer, E.A. (eds) (1990) *Introduction to avidin–biotin technology*, vol. **184**, Elsevier, pp. 3–15.

59 Green, N. (1975) Avidin. *Adv. Protein Chem.*, **29**, 85–133.

60 Dinca, V., Farsari, M., Kafetzopoulos, D., Popescu, A., Dinescu, M., and Fotakis, C. (2008) Patterning parameters for biomolecules microarrays constructed with nanosecond and femtosecond UV lasers. *Thin Solid Films*, **516** (18), 6504–6511.

61 Dinca, V., Ranella, A., Popescu, A., Dinescu, M., Farsari, M., and Fotakis, C. (2007) Parameters optimization for biological molecules patterning using 248-nm ultrafast lasers. *Appl. Surf. Sci.*, **254**, 1164–1168.

62 Katis, I.N., Holloway, J.A., Madsen, J., Faust, S.N., Garbis, S.D., Smith, P.J.S., Voegeli, D., Bader, D.L., Eason, R.W., and Sones, C.L. (2014) Paper-based colorimetric enzyme linked immunosorbent assay fabricated by laser induced forward transfer. *Biomicrofluidics*, **8**, 036502-(1–9).

63 Farsari, M., Dinca, V., Dinescu, M., Georgiou, S., and Fotakis, C. (2007) Construction of 2D and 3D biomolecules structures using fs lasers. *Int. J. Nanomanuf.*, **1** (6), 762–770.

64 Dinca, V., Kasotakis, E., Catherine, J., Mourka, A., Ranella, A., Ovsianikov, A., Chichkov, B.N., Farsari, M., Mitraki, A., and Fotakis, C. (2008) Directed

three-dimensional patterning of self-assembled peptide fibrils. *Nano Lett.*, **8** (2), 538–543.

65 Dinca, V., Kasotakis, E., Catherine, J., Mourka, A., Mitraki, A., Popescu, A., Dinescu, M., Farsari, M., and Fotakis, C. (2007) Development of peptide-based patterns by laser transfer. *Appl. Surf. Sci.*, **254** (4), 1160–1163.

66 McGrath, T.F., Andersson, K., Campbell, K., Fodey, T.L., and Elliott, C.T. (2013) Development of a rapid low cost fluorescent biosensor for the detection of food contaminants. *Biosens. Bioelectron.*, **41**, 96–102.

67 Di Pietrantonio, F., Benetti, M., Cannatà, D., Verona, E., Palla-Papavlu, A., Fernández-Pradas, J.M., Serra, P., Staiano, M., Varriale, A., and D'Auria, S. (2015) A surface acoustic wave bio-electronic nose for detection of volatile odorant molecules. *Biosens. Bioelectron.*, **67**, 516–523.

68 Palla-Papavlu, A., Patrascioiu, A., Di Pietrantonio, F., Fernández-Pradas, J.-M., Cannatà, D., Benetti, M., D'Auria, S., Verona, E., and Serra, P. (2014) Preparation of surface acoustic wave odor sensors by laser-induced forward transfer. *Sens. Actuators, B*, **192**, 369–377.

69 Ramoni, R., Bellucci, S., Grycznyski, I., Grycznyski, Z., Grolli, S., Staiano, M., De Bellis, G., Micciulla, F., Pastore, R., and Tiberia, A. (2007) The protein scaffold of the lipocalin odorant-binding protein is suitable for the design of new biosensors for the detection of explosive components. *J. Phys. Condens. Matter*, **19**, 395012-(1–7).

70 Lobel, D., Jacob, M., Volkner, M., and Breer, H. (2002) Odorants of different chemical classes interact with distinct odorant binding protein subtypes. *Chem. Senses*, **27**, 39–44.

71 Spinelli, S., Ramoni, R., Grolli, S., Bonicel, J., Cambillau, C., and Tegoni, M. (1998) The structure of the monomeric porcine odorant binding protein sheds light on the domain swapping mechanism. *Biochemistry*, **37**, 7913–7918.

72 Tegoni, M., Ramoni, R., Bignetti, E., Spinelli, S., and Cambillau, C. (1996) Domain swapping creates a third putative combining site in bovine odorant binding protein dimer. *Nat. Struct. Biol.*, **3** (10), 863–867.

73 Palla-Papavlu, A., Paraico, I., Shaw-Stewart, J., Dinca, V., Savopol, T., Kovacs, E., Lippert, T., Wokaun, A., and Dinescu, M. (2011) Liposome micropatterning based on laser-induced forward transfer. *Appl. Phys. A*, **102**, 651–659.

74 Lippert, T., Wokaun, A., Stebani, J., Nuyken, O., and Ihlemann, J. (1993) Triazene polymers designed for excimer laser ablation. *Angew. Makromol. Chem.*, **206**, 97–110.

75 Cherney, D.P., Conboy, J.C., and Harris, J.M. (2003) Optical-trapping Raman microscopy detection of single unilamellar lipid vesicles. *Anal. Chem.*, **75** (23), 6621–6628.

15

Laser-Assisted Bioprinting of Cells for Tissue Engineering

Olivia Kérourédan, Murielle Rémy, Hugo Oliveira, Fabien Guillemot, and Raphaël Devillard

Université de Bordeaux, Bioingénierie Tissulaire (BioTis), INSERM U1026, 146, rue Léo-Saignat, Case 45, 33076 Bordeaux Cedex, France

During the past decades, many technologies have been developed or modified in the field of laser-assisted bioprinting (LAB) in order to achieve the ability to print living cells. Cell bioprinting by LAB provides significant advantages in terms of precision, reproducibility, rapidity, creation of two- or three-dimensional patterns, and potential *in vitro* or *in vivo* applications, if compared to other printing technologies. Many studies have also demonstrated its excellent capacity to preserve cell viability and proliferation after printing. These properties make LAB a useful tool for cell biology studies and a promising technology for tissue engineering applications, as it will be described in the following chapter.

15.1 Laser-Assisted Bioprinting of Cells

15.1.1 The History of Cell Bioprinting and Advantages of Laser-Assisted Bioprinting for Tissue Engineering

Three-dimensional printing has grown considerably in many areas in recent years, including manufacturing, consumer products, microengineering, art, food industry, and aeronautics [1]. Regenerative medicine is no exception, and tissue engineering now incorporates "bioprinting" technologies as relevant tools to develop biological substitutes of native tissues or organs.

Bioprinting is currently defined as "computer-aided, automatic, layer-by-layer deposition, transfer, and patterning of biologically relevant materials" [2, 3]. Among these biological materials, cells can be organized using bioprinting technologies in order to develop a tissue, with a better control of its structure and function [4]. This ability of reproducing cell microenvironment and tissue organization makes bioprinting a shift in paradigm compared to traditional approaches of tissue engineering.

During the last few years, many experiments have been conducted in the field of biofabrication, with an increasing development of cell bioprinting methods. However, cell bioprinting is far from being recent.

Laser Printing of Functional Materials: 3D Microfabrication, Electronics and Biomedicine,
First Edition. Edited by Alberto Piqué and Pere Serra.
© 2018 Wiley-VCH Verlag GmbH & Co. KGaA. Published 2018 by Wiley-VCH Verlag GmbH & Co. KGaA.

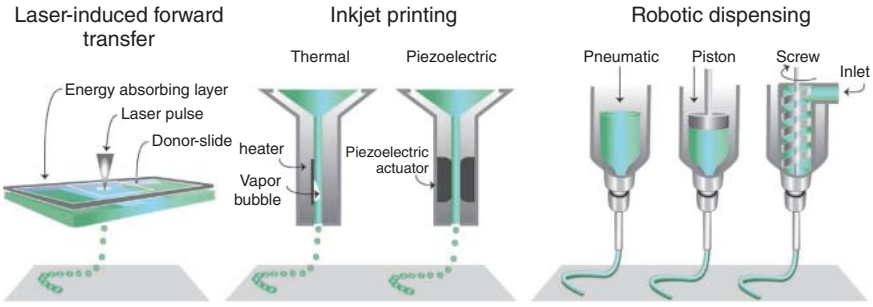

Figure 15.1 Schematic representation of the different biofabrication approaches. (Malda *et al*. 2013 [7]. Reproduced with permission from John Wiley and Sons.)

In 1988, Klebe described for the first time a technique called "cytoscribing" allowing for the micropositioning of cells according to defined patterns [5]. Following this first study, a large number of cell printing technologies have been developed. Parallel to traditional approaches of tissue engineering, such as homogeneous seeding of cells into prefabricated scaffolds or lithographic methods, novel approaches have emerged based on inkjet, microextrusion, and laser-assisted bioprinting [6, 7] (Figure 15.1). These new and promising technologies have quickly excited the media, who more willingly used the term "organ printing" than "cell printing", since they showed the ability to print viable cells in three dimensions [2]. In reality, major advances are still needed in order to obtain not only a mere cellular construct but also a fully functional printed tissue or organ.

Inkjet- and microextrusion-based technologies were derived from existing systems that were not primarily developed for biological applications [8]. The first inkjet printers used for printing biological materials were obtained from modified commercially available inkjet printers [9]. Initially limited to two-dimensional constructs, the development of novel biomaterials, such as thermosensitive gels, allowed for creating three-dimensional constructs [10]. This technology has the advantage of being simple to use and low cost; however, it has several drawbacks, especially when applied to cell printing, namely nozzle clogging, exposition of cells to mechanical stress at the orifice (shear stress), risk of contamination, and low droplet directionality [11]. Following the development of inkjet bioprinters, extrusion-based techniques (i.e., syringe, micropen, bioplotter) were also adapted to cell bioprinting, allowing for the generation of a large variety of tissue models such as liver or neural tissue, aortic valves, or vascular networks [12–16]. Although this technology is also easy to use and low cost, it shares the same disadvantages as inkjet printing related to the presence of an orifice.

Besides inkjet- and extrusion-based bioprinting techniques, laser-based printing technologies involve rapid and resoluted prototyping methods allowing organization of biomaterials in a defined conformation for tissue-engineering applications. In particular, LAB has emerged as a relevant method to print living cells. Technical characteristics and methodology of each LAB method applied to cell printing are discussed in more detail in Section 15.1.2.

The first study involving laser printing applied to living cells was conducted by Odde and Renn [17]. They used a near-infrared diode laser to print individual embryonic chick spinal cord cells and named this technology "laser-guided direct writing" (LGDW). They demonstrated the possibility to use this technology with biological materials by printing clusters of hundreds of cells, such as human umbilical vein endothelial cells (HUVECs) [18–20]. Nahmias *et al*. also showed that bioprinting of multipotent adult progenitor cells was equally feasible through LGDW [21].

Besides LGDW, other laser-based technologies were developed, derived from the laser-induced forward transfer (LIFT) effect [22, 23], and have demonstrated their capacity to print biological materials, especially cells (for specific description of the general principles of the different laser-induced transfer processes, please see Chapters 1 and 2).

The first ones involved matrix-assisted pulsed laser evaporation–direct write (MAPLE-DW), derived from matrix-assisted pulsed laser evaporation (MAPLE), and allowed creation of patterns of viable eukaryotic cells and *Escherichia coli* [24–26]. Then, MAPLE-DW was widely used for printing proteins and living cells [27–29]. Multiple cell types have been deposited using this technology, demonstrating the possibility to build two- or three-dimensional cellular constructs and offering potential applications for tissue engineering [4]. As examples: Chinese hamster ovary (CHO) cells [24], B35 neuronal cells [30], human dermal fibroblasts, mouse myoblasts, rat neural stem cells, human breast cancer cells, and bovine pulmonary artery endothelial cells [31] were printed using MAPLE-DW technology.

There are two other technologies based on the LIFT technique that consist of a three-layer approach: absorbing film assisted–laser-induced forward transfer (AFA-LIFT) and biological laser printing (BioLP). The main difference with MAPLE-DW resides on the presence of an absorbing layer that avoids the direct interaction of the laser with the bioink. Another advantage is an improvement of reproducibility of the transfer, as the interaction of the beam onto the absorbing layer is further standardized.

AFA-LIFT was employed for cell printing by Hopp *et al*. in 2005. They used four different cell types: human neuroblastoma, chronic myeloid leukemia, osteogenic sarcoma cell lines, and primary astroglial rat cells [29]. Nonetheless, its use for cell printing is yet less widespread in the literature than BioLP.

BioLP was developed by Barron *et al*. and permits to create patterns of various biological components, including cells, with high speed and reproducibility [28]. A large variety of cell types have been printed using BioLP: human osteosarcoma cells [32], rat cardiac cells [33], bovine aortic endothelial cells [34], olfactory ensheathing cells [35], mouse NIH3T3 fibroblast cells [36], and human endothelial cells [37]. This ability to print multiple types of cells, associated to a precise control of cell density and organization, suggests the relevance of this technology for applications in tissue engineering (Figure 15.2). BioLP has shown to be more efficient than other methods for cell printing and tissue engineering, making its employment more widespread in the field of cell printing [37].

LAB has significant assets for applications in tissue engineering and offers many advantages compared to other bioprinting techniques and more widely

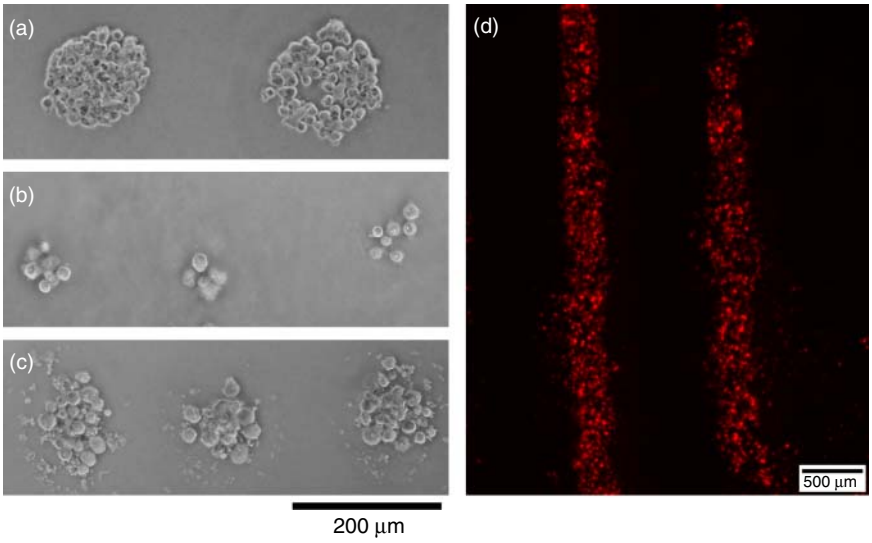

Figure 15.2 Patterning of different cell types by laser-assisted bioprinting with a range of cell concentrations. Observation of printed patterns of (a) mouse D1 mesenchymal stromal cell line, (b) human umbilical vein endothelial cells, (c) human progenitor endothelial cells, in phase-contrast microscopy, and (d) tdTomato-labeled human endothelial cells in fluorescence microscopy.

compared to traditional cell patterning techniques. LAB allows for a rapid and highly precise printing pattern formation, at a micron level [38]. The processes employ computer-aided design and computer-aided manufacturing (CAD/CAM) systems leading to an increased resolution (single cell or near single cell) compared to related technologies [33]. In particular, BioLP technology leads to smaller and more resolute patterns, with higher reproducibility.

The ability to precisely organize the printed cells is one of the major advantages of LAB in order to obtain cell arrays and for tissue engineering applications, since it permits to mimic the tissue heterogeneity and complexity by appropriately combining cells and specific biological factors [32]. Indeed, tissues present a specific and complex architecture, characterized by cell–cell and cell–microenvironment interactions, depending on a three-dimensional organization of the different components [39]. LAB allows precise deposition of the different components of a tissue, especially cells, in order to reproduce their spatial organization [18, 40]. This approach could reproduce native tissues and organs with accurate architecture and function [37]. Moreover, precise cocultures and multicultures, as more complex cellular constructs, can be created by controlling the spatial positioning of the different cell types, for example, in the field of vascular engineering (Figure 15.3). This ability to print multiple types of cells, to precisely control cell positioning, relative to one another, is of major importance for regenerative medicine approaches, where the reproduction of the local microenvironment of the cells plays a crucial role.

Moreover, as an orifice-free and noncontact technique, LAB overcomes problems related to the orifice clogging, nonreproducibility due to solution viscosity,

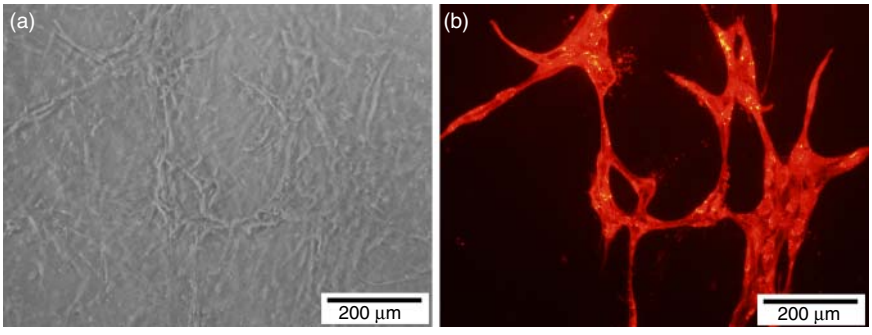

Figure 15.3 Coculture of human stem cells from the apical papilla (SCAPs) and tdTomato-labeled human endothelial cells created by laser-assisted Bioprinting. Observation of vascular-like network formation on day 6 (a) in phase-contrast microscopy and (b) in fluorescence microscopy.

cross-contamination, and damage to the substrate. Compared to inkjet printers or bioplotters, this technology allows to deposit different varieties of biomaterials with smaller volume aliquots (nl to fl) and with greater accuracy [26]. Additionally, and in contrast to orifice-based techniques, LAB enables to print patterns with high cell densities, thus reducing the maturation culture time of the engineered constructs [41].

Furthermore, LAB has already shown the capacity to create multilayered cellular constructs. In 2004, Barron *et al*. demonstrated the capacity of LAB to participate in the formation of three-dimensional cell constructs, using a multistep process, based on a layer-by-layer approach, by coating the printed cells with a thin layer of extracellular matrix and by repeating this operation several times [42]. Based on a bottom-up approach, spatial patterning enabled by LAB could lead to the introduction of structures such as vascular networks into tissue-engineered constructs, thus overcoming problems of poor vascularization in large-size grafts [4].

Finally, another advantage of LAB is its possible application for direct *in situ* and *in vivo* printing. LAB has already been used for *in situ* bioprinting in mice. In 2010, for the first time, Keriquel *et al*. demonstrated the capacity of LAB to directly print nanohydroxyapatite particles on a critical-size bone defect (calvaria model) in mice [43]. It was the first step toward computer-assisted medical interventions, using LAB. In the same way, cells, such as endothelial cells, could be printed *in situ* by LAB in order to promote tissue regeneration (Figure 15.4). This technology may be helpful to improve precision of surgical procedures, while reducing the required volume of deposited biomaterials, enabling higher resolution, and reducing the risks of contamination. In this sense, LAB offers new perspectives and innovative therapeutic solutions to clinicians.

15.1.2 Technical Specifications of Laser-Assisted Bioprinting of Cells

LAB technologies are noncontact, orifice-free techniques that can allow the precise deposition of biomaterials onto a substrate. When applied specifically to cell

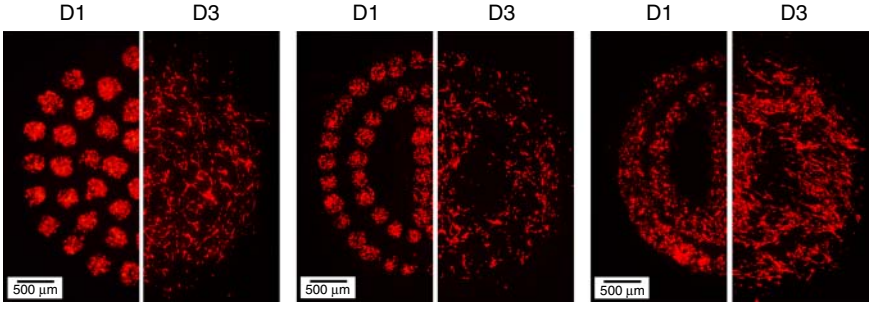

Figure 15.4 Fluorescence microscopy images of human endothelial cell printed patterns, for future *in vivo* application in bone calvaria defect in mice. Observation of three relevant patterns of tdTomato-labeled endothelial cells on days 1 and 3 (D1 and D3, respectively) after laser-assisted bioprinting.

bioprinting, dedicated systems have similar general principles, but each method also presents some specificities.

Cell printing experiments imply the placement of CAD/CAM workstation in a cell culture room in order to simplify cell manipulation and enable a sterile environment. A large variety of workstations have been developed or modified in order to micropattern cells, involving different technologies mentioned previously: LG DW, LIFT, MAPLE-DW, AFA-LIFT, and BioLP.

The first one, LG DW, differs from the other methods since it involves the use of a weakly focused continuous laser (i.e., tunable diode laser beam at a wavelength of about 800 nm) [19]. For cellular suspensions, near-infrared wavelengths are used to avoid cell damage [6]. Individual cells are propelled from a liquid cell suspension toward a receiving surface through optical forces [18].

The last four cited technologies (i.e., LIFT, MAPLE-DW, AFA-LIFT, BioLP) have similar principles in what regards the cell bioprinting procedure, which is based on a print ribbon and on a pulsed laser. Cells to be printed, embedded in a biological polymer or suspended in culture medium or hydrogel, are spread onto a laser-transparent glass slide (termed *ribbon* or *donor slide*) using a pipette or a micrometric film blade. The receiving substrate (termed *collector slide*) is generally coated with a hydrogel, in order to minimize cell damage upon impact and to allow cell adhesion and proliferation. The laser pulse induces the propulsion of cells from the donor slide toward the collector slide. Computer control and CCD cameras allow to specifically select the cell area to be targeted for printing [4] (Figure 15.5).

LIFT is characterized by the use of a high-powered pulsed laser, which implies interposing a thin absorbing layer between the donor slide and the cell bioink, in order to preserve cell viability. The laser beam is focused through the ribbon, onto the absorbing layer, and induces the propulsion of cells by vaporization from the donor slide toward the collector slide [4].

Modified-LIFT techniques, comprising MAPLE-DW, AFA-LIFT, and BioLP, involve the same three components: a pulsed laser beam, a donor slide, and a collector slide. The donor slide is composed of two or three layers: a glass slide, the cell bioink (transfer layer), and optionally a conversion layer interposed between

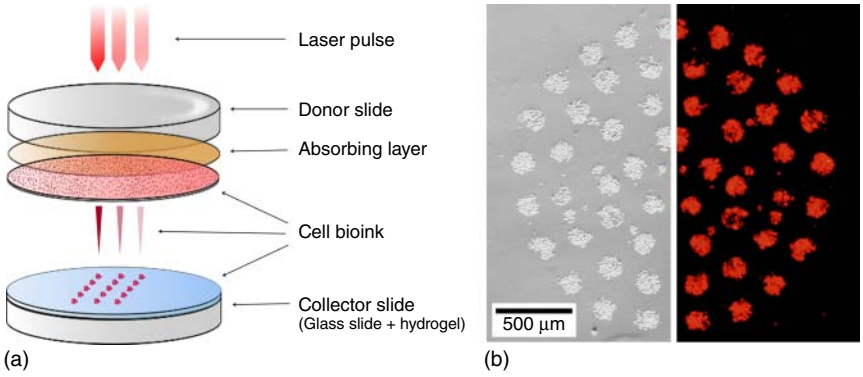

Figure 15.5 (a) Schematic representation of laser-assisted bioprinting setup; (b) Observation of TdTomato-positive mouse mesenchymal stromal cells (D1 cell line) patterns printed by LAB, in phase-contrast and fluorescence microscopy.

the two previous layers [44]. For cell bioprinting, the laser beam is focused at the interface between the glass slide and the cell bioink [6].

MAPLE-DW utilizes laser–biomaterial interactions and involves a low powered, pulsed laser at ultraviolet (UV) or near-UV wavelengths. The donor slide is coated with a sacrificial water-based polymer layer onto which cells adhere. This UV-absorbent matrix material promotes light absorption and energy transfer. The laser is focused at the interface between the glass slide and the biolayer [28]. After local vaporization of the sacrificial layer and formation of a vapor pocket, a small spot (including cells and matrix) is transferred onto the collector slide [4, 33]. In 2002, Ringeisen *et al*. used MAPLE-DW technology (argon fluoride (ArF) excimer laser 193 nm, 20 ns) to transfer *E. coli*, embedded in a matrix, at a concentration of 10^7 cells/ml [25]. In 2004, Barron *et al*. transferred mammalian cells (human osteosarcoma and rat cardiac cells) included into a matrix made from Matrigel^{TM}/Dulbecco's Modified Eagle Medium (DMEM) or glycerol/DMEM mixtures, at concentrations varying between 2 and 100×10^6 cells/ml [33]. However, MAPLE-DW has shown limitations in terms of resolution and reproducibility and is now less frequently used. Reproducibility was improved by the addition of an energy conversion layer between the glass slide and the cell bioink, allowing the use of more diverse solutions and materials to mix with the cells to be transferred. Besides increasing reproducibility, addition of a conversion (or absorbing) layer led to a better protection of cells from the incident laser beam by preventing interactions between the laser and the biomaterial. These three-layer approaches were called "AFA-LIFT" and "BioLP" [6, 28].

AFA-LIFT closely resembles LIFT but involves the use of a thick absorbing layer on the donor slide. BioLP derives directly from AFA-LIFT and comprises motorized receiving stages and a CCD camera in order to target the cell area for printing. This technology has been developed by Barron *et al*., in a study involving a krypton fluoride (KrF) excimer laser (248 nm, 2.5 ns) [28]. The absorbing layer consisted of a 75–100 nm thick metal layer, into which the laser pulse was focused, generating a high gas pressure that propelled the subjacent bioink,

Table 15.1 Summary of the different LAB techniques used for cell printing.

Technologies	Major characteristics	First references related to cell printing
Laser guided direct writing (LGDW)	Weakly focused continuous laser (800 nm wavelength) Propulsion of individual cells from a liquid cell suspension toward a receiving surface through optical forces	[17]
Laser induced forward transfer (LIFT)	High-powered pulsed laser Print ribbon coated with a thin layer of metal	[45]
Modified LIFT techniques		
Matrix assisted pulse laser evaporation direct write (MAPLE-DW)	Low-powered pulsed laser (UV, near-UV) Matrix-embedded transfer layer to promote light absorption and energy transfer	[24]
Absorbing film assisted-LIFT (AFA-LIFT)	Presence of a thick absorbing layer between the ribbon and the cells (100 nm)	[29]
Biological laser printing (BioLP)	Presence of a thick absorbing layer between the ribbon and the cells (75–100 nm) Motorized receiving stages and CCD camera	[28]

constituted by cells and culture medium or hydrogel, toward the collector slide with little heating of the cell suspension [26] (Table 15.1).

Specific technical precautions have to be taken into account for cell printing. Near-infrared lasers should be favored in order to avoid potential DNA damage, relevant when considering higher energy lasers such as UV lasers. Pulse duration and repetition rate have to be tuned in order to achieve high-throughput procedures. Beam quality has to be optimized in order to achieve high reproducibility and resolution. Finally, adjustment of laser parameters is a critical step since they can vary the function of the rheological properties of cell bioink, especially viscosity [37].

15.1.3 Effect of Laser Process and Printing Parameters on Cell Behavior

Many studies have been conducted in order to investigate the effect of each process (i.e., LG DW, MAPLE-DW, BioLP) and printing parameters on cell viability, proliferation, and differentiation.

In 2000, Odde and Renn printed embryonic chick spinal cord cells using LGDW technology and demonstrated the preservation of cell viability after printing [18]. In 2001, Wu *et al*. printed CHO cells, using MAPLE-DW, and showed normal cell

growth and proliferation, what could imply the lack of genotype alteration [24]. Cell viability of *E. coli* patterns, created using MAPLE-DW, was also assessed through live/dead assays and GFP expression analysis. No alteration of viability and functionality could be observed due to laser pulses or the transfer process [25]. In 2004, Ringeisen *et al*. conducted another study involving MAPLE-DW on pluripotent embryonic carcinoma cells. Near 100% viability was observed, and both genotype and phenotype were preserved postprinting [27]. In the same way, Barron *et al*. assessed postprinting viability using live/dead viability and cytotoxicity assays. They showed viability near 100% for rat cardiac cells posttransfer [33]. In addition, Patz *et al*. used TUNEL staining in order to determine the apoptosis rate of B35 cells postprinting and showed that only 3% of cell underwent apoptosis [30].

Similar investigations on posttransfer cell viability were conducted using the BioLP process. Barron *et al*. showed, through the live/dead assay, that 100% of human osteosarcoma cells and MG63 cells retained their viability after printing by BioLP [28]. They also measured cell damage postprinting and showed very low expression of stress-induced proteins (i.e., Heat Shock Proteins) by the deposited cells. They demonstrated that BioLP allowed the preservation of cell viability and maintained their ability to establish cell-to-cell communication and to differentiate.

On the basis of the results obtained, some authors made hypotheses and provided explanations related to the influence of laser process on cell damage. In one of the experiments mentioned earlier, Ringeisen *et al*. suggested that the little cell damage observed postprinting was due to the incident laser energy, heat stress, shear stress during acceleration (cell droplet formation) and deceleration (cell droplet landing on collector slide) phenomena. The thickness of hydrogel coating on the collector slide was found to be a critical parameter in order to reduce cell injury after landing. Viability of cells increased from 50% to 95% when the hydrogel coating was increased from 20 to 40 μm in thickness [27]. Indeed, during cell droplet landing, the impact between the cells and the substrate can lead to membrane rupture and cell death. But cell damage could be the result of a combination of mechanical and biochemical (thermal and UV damages) effects [4]. Thermal injury could affect enzymes and proteins and be responsible for the vaporization or carbonization of cells, and UV could lead to DNA alterations. Lin *et al*. showed that laser parameters had a direct effect on cell viability. They demonstrated that printed yeast (*Saccharomyces cerevisiae*) cell viability decreased as the laser energy increased and that postprinting cell recovery was a function of the laser energy. However, in what concerns thermal and UV damage, they concluded that they were negligible [46]. In 2010, the same group investigated the effect of laser fluency on printed human colon cancer cell (HT-29) viability after MAPLE-DW process and derived the same conclusions: the viability decreased as the laser energy increased, cell damage was mostly due to shear stress occurring during jet formation and cell landing, and thermal and UV damages were considered negligible. In what regards the effects drawn by the UV laser, most of the UV energy is absorbed by the coating on the donor slide. They estimated that only 5% of the coating was altered by UV radiation, for a total of 100 μm thickness, explaining the negligible damage effect to cells [47]. In another study, regarding

the excellent preservation of cell viability with BioLP, Barron *et al*. hypothesized that the low damaging levels of stress obtained could be due to the fact that laser-based technologies are high-throughput processes subjecting the cells to a very quick stress [32, 34]. Indeed, similarly to UV damage described previously by Lin *et al*., in laser-based technologies used for cell printing, the incident laser pulse induces a very low thermal penetration (a few micrometers), compared to 100 μm thick coating, as jet formation occurs in a few microseconds. And, as such, the thermal damage can be considered negligible [4]. Finally, other authors demonstrated that, in addition to laser energy and hydrogel film thickness, viscosity of cell bioink had an important influence on the preservation of cell viability after printing. EA.hy926 endothelial cells were printed using different laser energies and different concentrations of sodium alginate (0.5% or 1% (w/v)), and the results showed that viability was higher for cells printed with the highest alginate concentration. Increasing the bioink viscosity would thus contribute to improve cell survival [48].

To conclude, laser-based technologies allow for successful printing of a large variety of cells, while permitting to preserve their viability, genotype, and phenotype [49–51]. Laser parameters have been optimized in order to protect the cells from the potential damaging effects of the process. As such, it seems to be an efficient and safe method for biofabrication processes.

15.2 Laser-Assisted Bioprinting for Cell Biology Studies

15.2.1 Study of Cell–Cell and Cell–Microenvironment Interactions

Laser-assisted bioprinting can be a useful method to study cellular interactions and to fabricate cell-based biosensors due to its capacity to spatially control cell position and cell density [2]. Moreover, it has the ability to create cellular constructs that can mimic native tissue architecture.

This technology, by its resolution, is particularly relevant to investigate cell–cell and cell–microenvironment interactions *in vitro* since it is well known that spatial organization of cells has an impact on cell behavior. Cell functions are completely different under two- or three-dimensional culture conditions [50]. Then, if we consider potential applications for therapies in regenerative medicine, it seems to be fundamental to organize cells in three dimensions in order to reproduce complex interactions as they occur *in vivo*. This spatial arrangement of cells has been shown to have a critical effect on cellular differentiation both *in vivo* and *in vitro* [52–55].

LAB is an interesting tool to create spatially defined coculture or multiculture models by precisely depositing biomaterials or different cell types, allowing studies of cell communication, focusing on the cues that might steer specific cell differentiation and on understanding of cell–environment impact (for additional information related to the contribution of laser printing of biomolecules to the study of cell–environment interactions, please refer to Chapter 14). In 2011, Gruene *et al.* used LAB for printing human adipose-derived stem cells (ASCs) and endothelial colony-forming cells

(ECFCs), layer by layer, in a three-dimensional array and investigated the cell–cell and cell–microenvironment interactions. They demonstrated that stable vascular-like networks were promoted by direct cell–cell interactions [56].

As a potential application in the field of pharmaceutics and drug development, laser-assisted bioprinting of cells could lead to the replacement or at least reduction of animal testing by generating complex three-dimensional constructs that could reproduce native tissues or organs [41]. In addition, this ability to allow studies of cell interactions could be applied to biomaterial testing and development, by enabling multiple array tests to investigate cell-to-biomaterial interactions [4].

15.2.2 Cancer Research

The ability of laser-based technologies to reproduce *in vitro* cell microenvironments is a major attribute that could lead to advances in cancer research [31]. *In vitro* cocultures of cells, reproducing *in vivo* organization of biological components with high resolution, can allow to study cell signaling with a higher degree of complexity, further approaching the *in vivo* scenario. This could have potential applications for diagnostic and pharmaceutical assays [57].

One point of focus is cancer research, as cell patterning could permit to accurately reproduce the microenvironment of tumors. Indeed, cell communication, between tumor cells and the surrounding microenvironment, including normal cells, plays a critical role in tumor development mechanisms, stressing the importance of the influence of spatial organization of cells, further mimicking the *in vivo* scenario, in this field of research. Metastatic mechanisms, cancer cell dynamics and neoangiogenesis, which play a key role in cancer development, can then favor from these new tools, based on LAB, to establish novel experimental models [58]. In this sense, several types of cancer- and tumor-derived cells have been used for laser printing experiments. Ringeisen *et al*. demonstrated the capacity of laser-based technologies to print pluripotent embryonic carcinoma cells (P19) while maintaining cell viability and differentiation capacity [27]. Barron *et al.* showed the feasibility to generate three-dimensional constructs with human osteosarcoma cells (MG63) and rat cardiac cells by using MAPLE-DW and BioLP technologies [33, 42].

The fabrication of engineered tumor models can be a novel tool, with the potential to assist in the understanding of crucial mechanisms of cancer, such as the processes of cancer induction, proliferation, metastasis, and treatment [4].

15.3 Laser-Assisted Bioprinting for Tissue-Engineering Applications

Laser-based technologies are promising approaches in the field of tissue engineering and regenerative medicine. Tissue engineering takes place at the encounter of engineering and living sciences. In this field, biofabrication through bioprinting and bioassembly try to create structures as close as possible to the organs in order to provide functional biological tissue constructs, which can

be used for drug testing or regenerative medicine applications. By allowing the fabrication of complex three-dimensional constructs with both living cells and biomaterials, they enable the fabrication of functional tissue models that can mimic native tissue. In this sense, LAB, combined with other bioprinting techniques, seems to be a relevant tool for tissue or organ replacement/regeneration [41] or at least for a better understanding of healing process. Many studies using LAB, described next, have been conducted focusing on several clinical applications. This technology could lead gradually to the elaboration of functional tissues by overcoming the limitations of other current techniques. Indeed, the main challenges of tissue engineering and regenerative medicine are related to the lack of consistent vascularization of biofabricated tissues, the control of the maturation process, the behavior of cells in an unnatural environment. Even *in vitro* culture of small 3D structures reveals to be challenging due to the lack of interaction between the cells, the scaffold, and the surrounding medium. Moreover, it is known that the extracellular matrix (ECM) composition differs within different specific regions of a complex organ. The mechanical properties of the ECM are paramount to control the behavior or fate of immature stem cells, and reciprocally, cells will modify the ECM depending on their maturation stage. Accordingly, the precise control of cell organization within the construct is essential for the function of the final model tissue. In this sense, LAB allows to precisely control cell positioning, at the micron scale, enabling the creation of cellular models that can streamline the development of further complex tissue-engineering applications.

15.3.1 Skin

One of the major potential applications of LAB is the fabrication of skin substitutes for burned patients [45]. Current therapeutic solutions exist, such as autologous skin grafts or diverse skin substitutes, but they present limitations such as in extensive or ulcerative burns and risks related to the sampling procedure. Engineering skin substitutes by LAB, with the patient's own cells, could lead to the creation of tailor-made grafts with fewer postoperative complications.

For that purpose, Koch *et al*. printed skin cell lines (NIH3T3 fibroblasts and HaCaT keratinocytes) and human mesenchymal stem cells (hMSCs) using LAB in the perspective of promoting skin tissue repair and regeneration. LAB has the advantage to be able to reproduce, by a layer-by-layer approach, the complex three-dimensional architecture of the native tissue. The different types of cells were patterned according to the specific organization of skin tissues [47]. In 2012, and using LAB, they developed a three-dimensional *in vitro* model of skin composed of fibroblasts and keratinocytes embedded in a collagen matrix. They succeeded in mimicking the layered architecture of skin, namely the formation of a dermis and epidermis, and showed the capacity of such constructs to form cell–cell adhesion and communication, with the presence of zonula adherens and gap junctions [60] (Figure 15.6).

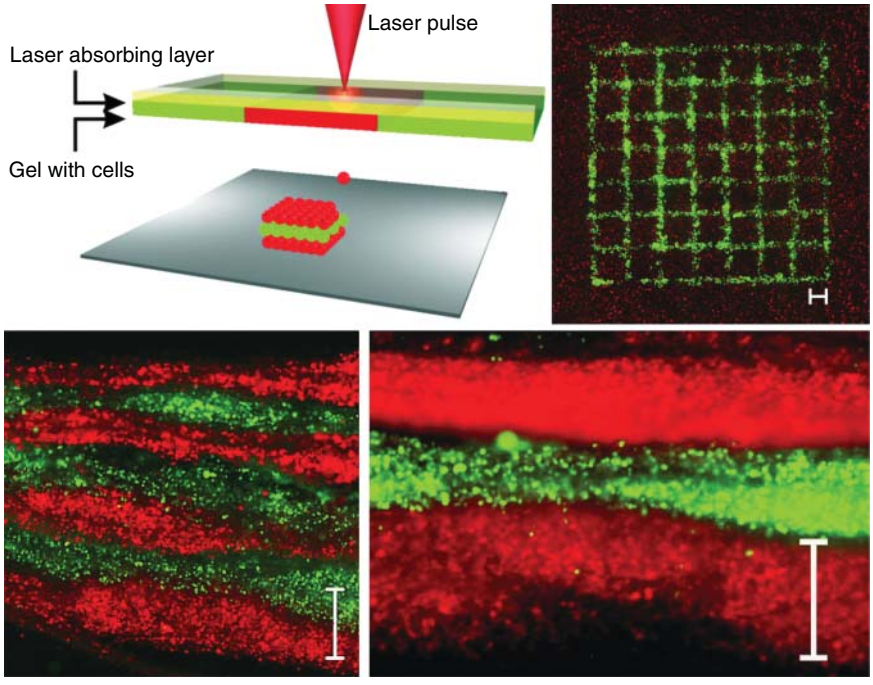

Figure 15.6 *Top*: Schematic representation of the laser printing setup and the layer-by-layer approach. Laser printing technology allows for printing a grid structure (top view) of fibroblasts (green) and keratinocytes (red). *Bottom*: A seven-layer construct of red and green keratinocytes was obtained by laser printing (left; detail right). Scale bars are 500 µm. (Koch *et al*. 2012 [60]. Reproduced with permission of ACS Publications.)

In another study, Michael *et al.* also printed fibroblasts and keratinocytes by LAB on MatridermH in order to create a three-dimensional construct mimicking the skin tissue. They transplanted these cellularized skin substitutes into full-thickness skin wounds in nude mice and showed the formation of skin tissue, with the organization of a multilayered epidermis, by the deposited keratinocytes, emergence of the stratum corneum, and the formation of blood vessels in the direction of printed cells [61].

These results show promise for the development of novel regenerative medicine approaches for clinical application. They can constitute relevant models for pharmaceutical or cosmetics studies, for *ex vivo* assays or *in vivo* testing in animal models. Advanced constructs could also be generated from the perspective of personalized medicine: pathological skin, such as melanoma, could be printed in order to study susceptibility of patient cells prior to treatment in order to improve the tolerance. Moreover, increased complexity of these three-dimensional constructs can be achieved by integrating other cell types, such as melanocytes or hair follicle cells, increasing the mimicry to

native tissues. The addition of endothelial cells would also permit to introduce microvascularization into the generated skin tissue and enable the formation of thicker tissue without the problem of insufficient perfusion [60].

15.3.2 Blood Vessels

Considering that, *in vivo*, cell survival is limited to a diffusion distance of 150–200 μm from the supplying blood vessels, one of the major challenges of tissue engineering is the creation of perfusable tissue substitutes. Many studies aiming to improve the generation of a functional vasculature, focusing on different strategies, namely the use of growth factors (e.g., vascular endothelial growth factor, platelet-derived growth factor-BB, angiopoietin-1 and angiopoietin-2), pericyte and smooth muscle cells, coculture with different cell types or gene transfer [62] have been reported (Figure 15.7).

Additionally, tissue perfusion could be achieved by cell printing and by the prevascularization of engineered tissues using biofabrication methods. Indeed, several studies involving LAB have been focusing on this challenging task.

Nahmias *et al.* succeeded in patterning HUVECs on Matrigel™, through LGDW technology, in two and three dimensions. They showed the formation of vascular structures consistent with the initial pattern [19]. Wu and Ringeisen also demonstrated the ability of BioLP to direct the architecture of a vascular network according to a defined pattern. They organized HUVECs and HUVSMCs in branch/stem structures in order to promote a network organization, similar to an *in vivo* vasculature [63]. Moreover, Pirlo *et al.* used BioLP in order to print HUVECs onto biopapers of PLGA/hydrogel (Collagen type I from rat tail or Matrigel™). They showed that cell self-assembled into networks, following the defined pattern, resembling the vascularization of native tissue. The use of "biopapers" makes the fabrication of three-dimensional prevascularized constructs feasible, by overlaying the printed layers supporting the HUVEC networks [64].

So far, this technology has shown the capacity to orient the formation of microvascular networks, and when associated with a layer-by-layer approach, it may be used to attain complete 3D constructs (Figure 15.8).

In view of these results, laser-assisted cell printing seems to be a promising technology to introduce prevascularization throughout engineered constructs, but further developments need to be attained in order to obtain fully functional and perfusable tissue constructs. Connection to host vascular and lymphatic system is the most important hurdle to tackle. It is essential to elaborate a microenvironment favorable to vascular network expansion, morphological and functional changes of endothelial cells, in order to control the prevascularization of three-dimensional substitutes prior to implantation. In particular, this reproduction of cell microenvironment is critical since it allows for specific communication with surrounding cells. Indeed, it is well known that endothelial cells, more than dynamic regulators of vasculature, have a major role in the development of functional tissues by communicating with nearby cells. For example, in cardiac surgery, it has been demonstrated that endothelial cells had to be coupled with cardiomyocytes in order to regulate cardiac development and also cardiomyocyte function, especially myocardial contractility [65].

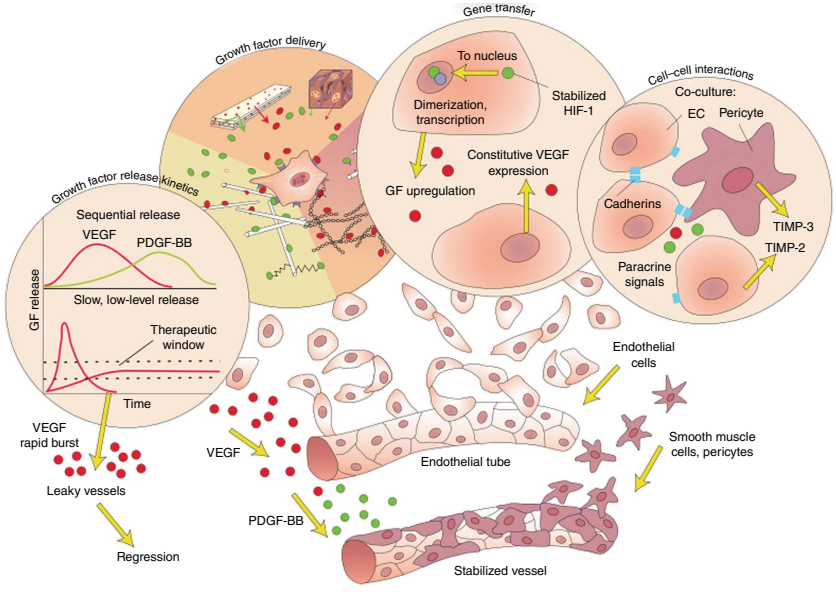

Figure 15.7 Vascularization of tissue-engineering scaffolds. Schematic representation of the different strategies used for the formation and maturation of vessels in tissue-engineered constructs. (Place *et al*. 2009 [62]. Reproduced with permission of Nature Publishing Group.)

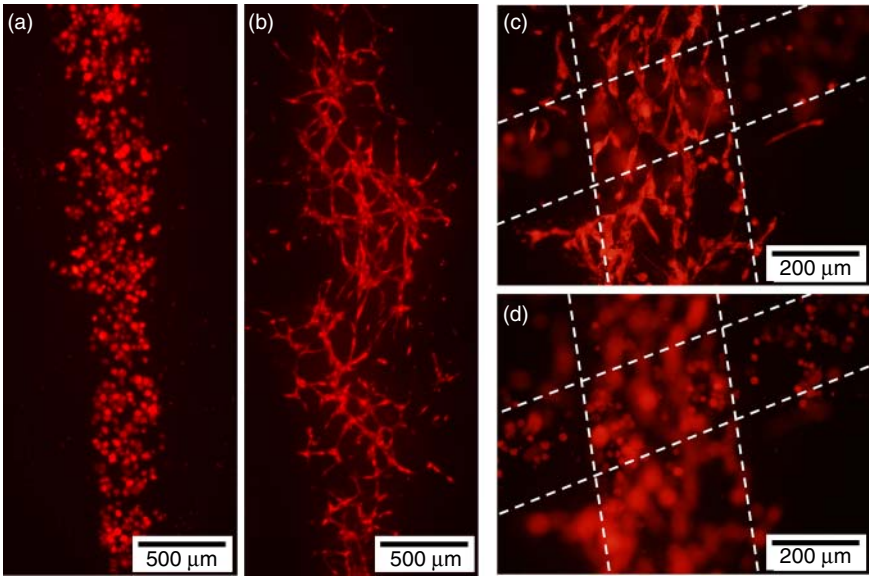

Figure 15.8 Creation of an organized multilayered construct of vascular-like network by laser-assisted bioprinting. observation of patterns of tdTomato-labeled endothelial cells in fluorescence microscopy (a) postprinting, (b) at D3; (c,d) observation of multilayered construct with patterns of tdTomato-labeled endothelial cells in fluorescence microscopy.

15.3.3 Heart

Laser-assisted bioprinting of cells has great potential for the creation of cardiac tissue, as cardiomyocytes are contractile cells with a specific tridimensional organization. Currently, one of the major limitations, regarding therapeutic solutions offered after myocardial infarction, such as cardiac patch, is insufficient neovascularization. In this sense, several studies have reported the use of laser bioprinting technology, showing important prospects in the field of cardiac surgery.

Gaebel *et al.* printed squared patterns of HUVEC and hMSC on a polyester urethane urea (PEUU) cardiac patch in order to promote cardiac regeneration. The rational on using hMSC was based on their capacity to stimulate angiogenesis. Indeed, the authors demonstrated that the preorganization of HUVEC and hMSCs in coculture patches promoted vascularization and improved functional recovery of the infarcted hearts, in comparison to randomly seeded cells, in a rat infarction model. As such, cell printing could be an efficient approach to treat myocardial infarction, leading to wound healing and to increased preservation of cardiac functions [66] (Figure 15.9).

As MSCs have been shown to contribute to cardiac regeneration, through several cell interactions, several studies have focused on the establishment of cocultures between MSCs and cardiomyocytes, but these conventional coculture systems do not accurately reproduce native cardiac muscle architecture. In this scope, Ma *et al*. proposed the use of laser-based technologies to create a well-organized MSC–cardiomyocyte coculture model, by reproducing cardiomyocyte alignment as it is found *in vivo*. They investigated if this cell

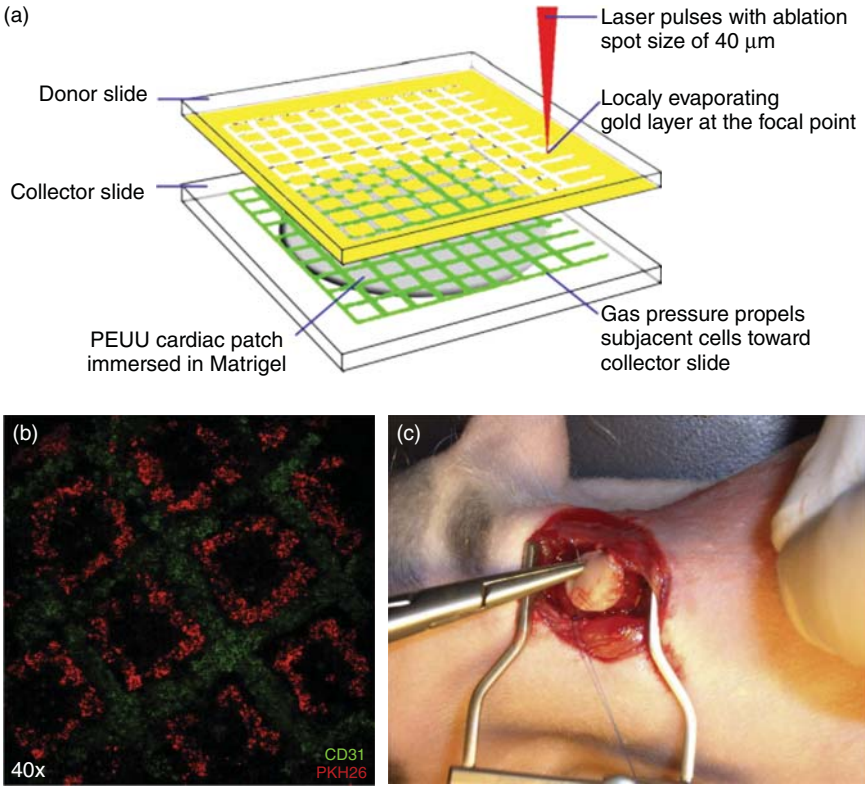

Figure 15.9 (a) Schematic representation of laser bioprinting setup. (b) Observation of printed patterns of human MSC and HUVEC on cardiac patch 24 h after bioprinting, (c) Patch implantation *in vivo* in a rat infarction model. (Gaebel *et al*. 2011 [66]. Reproduced with permission of Elsevier.)

arrangement had an impact on MSC cardiogenic differentiation. The results showed that this cell alignment promoted stem cell differentiation toward the cardiac phenotype (i.e., contractile cytoskeleton, electrophysiological properties, cardiogenic transcription factors, connexin 43 distribution) [67].

In this medical field of research, in addition to its benefits for cardiac repair, LAB can enable the fabrication of more complex *in vitro* models, as to further understand the cellular mechanisms leading to cardiac disorders such as arrhythmia, contractility issues, hypoxia resistance, and sensibility by accurately reproducing the cardiac tissues in three dimensions.

15.3.4 Bone

Currently, bone tissue regeneration represents a major public health issue. Indeed, diseases inducing bone loss affect a growing number of patients due to the aging of the population. A large variety of therapeutic solutions exist, but all present limitations and risks, including pain, infections, and morbidity. One of the most important limitations is the sufficient perfusion of bone grafts or

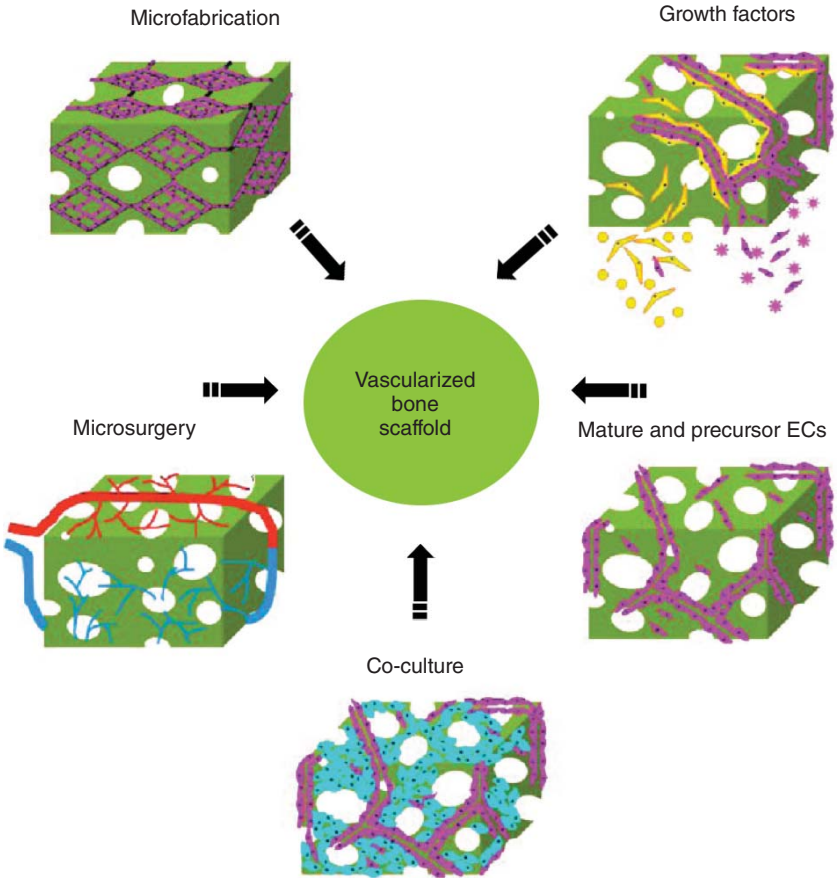

Figure 15.10 Illustration of the five major approaches used to support perfusion in bone constructs [68]. (Santos and Reis 2009 [68]. Reproduced with permission of John Wiley & Sons.)

bone substitutes, leading to graft failure [68]. This explains why bone repair, particularly in cases of critical size defects, still represents a big challenge. Different strategies have been proposed in order to induce the development of a microvasculature into tissue-engineered constructs (Figure 15.10). If scaffolds based on synthetic or natural biomaterials can be used to improve bone injury healing, they lack osteogenic and osteoinductive properties, which can be found in bone autograft strategies [69]. In this sense, different studies have focused on this problematic, namely improving vascularization and several biological functions, using laser-assisted cell printing, with the aim of promoting bone regeneration.

Doraiswamy *et al.* printed patterns of bioceramics and MG63 osteoblast-like cell through MAPLE-DW, based on the knowledge that hydroxyapatite sustains bone formation. The layer-by-layer engineering of these composite structures allowed the design of a three-dimensional construct, with controlled porosity, and allowed the vascularization of the bone substitute [70].

For the same purpose, Catros *et al.* printed nanohydroxyapatite (nHA) and human osteoprogenitors (isolated from human bone marrow stromal cells) by LAB to create two- and three-dimensional composite structures, thus demonstrating the ability of LAB to preserve nHA functionality and cell proliferation and differentiation properties postprinting [71]. This is particularly interesting since the same group demonstrated the feasibility to adapt the laser workstation for *in vivo* printing, by transferring *in situ* nHA particles onto bone calvaria defect in mice [43]. Then, *in situ* bioprinting could guide bone regeneration by directly printing cells or other biomaterials onto the injured area.

From the perspective of bone tissue engineering applications, Gruene *et al.* printed MSCs embedded in a matrix biomaterial (plasma and alginate) and demonstrated the preservation of MSC differentiation capacities into osteogenic and chondrogenic lineages. They fabricated three-dimensional constructs that led to autologous bone and cartilage tissue grafts after being cultured for 2 weeks, giving the possibility to transplant them *in vivo* [51].

To conclude, laser-assisted bioprinting could have interesting applications in orthopedic and dental tissue engineering, by allowing the structure of bone to be reproduced as accurately as possible. Indeed, bone tissue is a complex tissue at different scales. At a cellular scale, the collaboration between vascular, osteoblastic, osteoclastic, and neural cells needs a better understanding. At a tissue scale, the macroscopic organization of bone differs from the periphery to the center. If we want to reproduce an embryonic environment to optimize bone healing after injury, we have to keep in mind that ossification is completely different between endochondral and membranous bone. Then, LAB is an interesting technology that could lead to the development of bone models specific to each type of ossification and healing. More elaborated models could also be produced by adding other cell types, such as nerve cells, which play an important role in bone regeneration.

15.3.5 Nervous System

Avoiding irreversible loss of function due to damage of the central and peripheral nervous systems remains a challenge for tissue engineering, as nervous tissue presents limited healing capacity, particularly the central nervous system. In this sense, LAB technologies have been used to pattern neurons or glial cells in three dimensions in order to promote nerve repair. Patz *et al*. printed neuronal cells in order to create three-dimensional cellularized scaffolds, by *in situ* depth-controlled transfer within Matrigel™, for peripheral nerve regeneration [30] (Figure 15.11).

Othon *et al.* used BioLP in order to print relevant-size patterns of olfactory ensheathing cells (OECs) throughout a multilayer hydrogel scaffold. These cells have demonstrated the capacity to favor neurite outgrowth in spinal cord injury models [72]. In this study, the authors showed the creation of a three-dimensional cellularized scaffold, with a defined microorganization of OECs, which enhanced cell interactions. These cellularized matrices could be transplantable *in vivo* in order to promote axonal regeneration in an animal model of spinal cord injury [35].

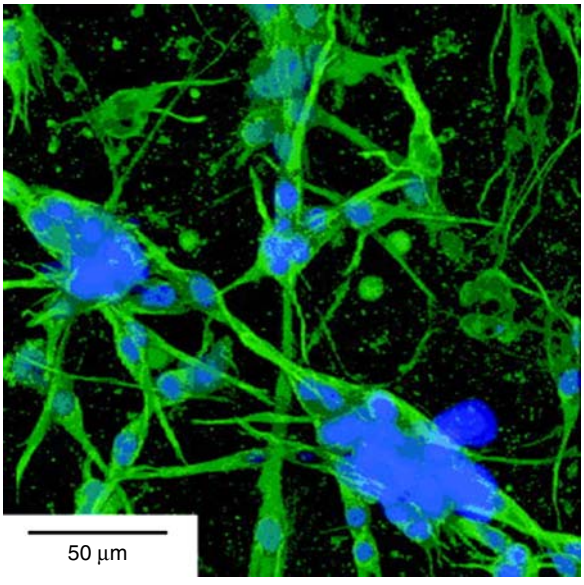

Figure 15.11 Observation of printed B35 neuronal cells in confocal microscopy, with the presence of axonal extensions between neuronal cells on different deposition planes. (Patz 2006 [30]. Reproduced with permission of John Wiley and Sons.)

In addition, studies on neural stem cell proliferation and differentiation could be conducted thanks to laser technologies, by organizing the cells along a specific architecture within a construct, and lead to advances in nerve damage treatment or drug testing [31]. Recently, Curley *et al.* organized the dorsal root ganglion neurons by laser direct write in order to reproduce a neural microenvironment, offering interesting prospects in neurophysiology and neuroregeneration [73]. Indeed, and due to the inherent complexity of the nervous system, biofabrication techniques such as LAB may hold the promise for further complex cellular models with unprecedented cellular organization, widening the field of regenerative medicine.

15.4 Conclusion

Laser-assisted bioprinting is a versatile technology allowing for printing a large variety of biological materials, including cells, and biomaterials such as hydrogels. Its ability to accurately reproduce the microenvironment of cells and the microarchitecture of native tissues, *in vitro,* makes this technique a promising tool for fundamental research, tissue engineering, and regenerative medicine. *In vitro* models can be generated for pharmaceutical studies, disease-related research, biomaterial testing, toxicity assays, and studies focusing on cell interactions. Moreover, several clinical applications may be considered, ranging from prevascularization of transplantable substitutes for bone regeneration to nerve, cardiac, and skin repair. Over the coming years, advances in robotics and automation could allow for the transition of LAB technologies from bench to the bedside.

References

1 Murphy, S.V. and Atala, A. (2014) 3D bioprinting of tissues and organs. *Nat. Biotechnol.*, **32** (8), 773–785.
2 Mironov, V., Boland, T., Trusk, T., Forgacs, G., and Markwald, R.R. (2003) Organ printing: computer-aided jet-based 3D tissue engineering. *Trends Biotechnol.*, **21** (4), 157–161.
3 Mironov, V., Trusk, T., Kasyanov, V., Little, S., Swaja, R., and Markwald, R. (2009) Biofabrication: a 21st century manufacturing paradigm. *Biofabrication*, **1** (2), 22001.
4 Schiele, N.R., Corr, D.T., Huang, Y., Raof, N.A., Xie, Y., and Chrisey, D.B. (2010) Laser-based direct-write techniques for cell printing. *Biofabrication*, **2** (3), 32001.
5 Klebe, R.J. (1988) Cytoscribing: a method for micropositioning cells and the construction of two- and three-dimensional synthetic tissues. *Exp. Cell. Res.*, **179** (2), 362–373.
6 Ringeisen, B.R., Othon, C.M., Barron, J.A., Young, D., and Spargo, B.J. (2006) Jet-based methods to print living cells. *Biotechnol. J.*, **1** (9), 930–948.
7 Malda, J., Visser, J., Melchels, F.P., Jüngst, T., Hennink, W.E., Dhert, W.J.A. *et al.* (2013) 25th anniversary article: engineering hydrogels for biofabrication. *Adv. Mater.*, **25** (36), 5011–5028.
8 Wilson, W.C. and Boland, T. (2003) Cell and organ printing 1: protein and cell printers. *Anat. Rec. A Discovery Mol. Cell. Evol. Biol.*, **272** (2), 491–496.
9 Xu, T., Kincaid, H., Atala, A., and Yoo, J.J. (2008) High-throughput production of single-cell microparticles using an inkjet printing technology. *J. Manuf. Sci. Eng.*, **130** (2), 021017.
10 Boland, T., Mironov, V., Gutowska, A., Roth, E.A., and Markwald, R.R. (2003) Cell and organ printing 2: fusion of cell aggregates in three-dimensional gels. *Anat. Rec. A Discovery Mol. Cell. Evol. Biol.*, **272** (2), 497–502.
11 Zhu, W., Ma, X., Gou, M., Mei, D., Zhang, K., and Chen, S. (2016) 3D printing of functional biomaterials for tissue engineering. *Curr. Opin. Biotechnol.*, **40**, 103–112.
12 Cohen, D.L., Malone, E., Lipson, H., and Bonassar, L.J. (2006) Direct freeform fabrication of seeded hydrogels in arbitrary geometries. *Tissue Eng.*, **12** (5), 1325–1335.
13 Faulkner-Jones, A., Fyfe, C., Cornelissen, D.-J., Gardner, J., King, J., Courtney, A. *et al.* (2015) Bioprinting of human pluripotent stem cells and their directed differentiation into hepatocyte-like cells for the generation of mini-livers in 3D. *Biofabrication*, **7** (4), 44102.
14 Hsieh, F.-Y. and Hsu, S. (2015) 3D bioprinting: a new insight into the therapeutic strategy of neural tissue regeneration. *Organogenesis*, **11** (4), 153–158.
15 Duan, B., Hockaday, L.A., Kang, K.H., and Butcher, J.T. (2013) 3D bioprinting of heterogeneous aortic valve conduits with alginate/gelatin hydrogels. *J. Biomed. Mater. Res. A*, **101** (5), 1255–1264.
16 Norotte, C., Marga, F.S., Niklason, L.E., and Forgacs, G. (2009) Scaffold-free vascular tissue engineering using bioprinting. *Biomaterials*, **30** (30), 5910–5917.

17 Odde, D.J. and Renn, M.J. (1999) Laser-guided direct writing for applications in biotechnology. *Trends Biotechnol.*, **17** (10), 385–389.

18 Odde, D.J. and Renn, M.J. (2000) Laser-guided direct writing of living cells. *Biotechnol. Bioeng.*, **67** (3), 312–318.

19 Nahmias, Y., Schwartz, R.E., Verfaillie, C.M., and Odde, D.J. (2005) Laser-guided direct writing for three-dimensional tissue engineering. *Biotechnol. Bioeng.*, **92** (2), 129–136.

20 Nahmias, Y. and Odde, D.J. (2006) Micropatterning of living cells by laser-guided direct writing: application to fabrication of hepatic-endothelial sinusoid-like structures. *Nat. Protoc.*, **1** (5), 2288–2296.

21 Nahmias, Y.K., Gao, B.Z., and Odde, D.J. (2004) Dimensionless parameters for the design of optical traps and laser guidance systems. *Appl. Opt.*, **43** (20), 3999–4006.

22 Bohandy, J., Kim, B.F., and Adrian, F.J. (1986) Metal deposition from a supported metal film using an excimer laser. *J. Appl. Phys.*, **60** (4), 1538–1539.

23 Levene, M.L., Scott, R.D., and Siryj, B.W. (1970) Material transfer recording. *Appl. Opt.*, **9** (10), 2260–2265.

24 Wu, P.K., Ringeisen, B.R., Callahan, J., Brooks, M., Bubb, D.M., Wu, H.D. *et al.* (2001) The deposition, structure, pattern deposition, and activity of biomaterial thin-films by matrix-assisted pulsed-laser evaporation (MAPLE) and MAPLE direct write. *Thin Solid Films*, **398–399**, 607–614.

25 Ringeisen, B.R., Chrisey, D.B., Piqué, A., Young, H.D., Jones-Meehan, J., Modi, R. *et al.* (2002) Generation of mesoscopic patterns of viable *Escherichia coli* by ambient laser transfer. *Biomaterials*, **23** (1), 161–166.

26 Barron, J.A., Rosen, R., Jones-Meehan, J., Spargo, B.J., Belkin, S., and Ringeisen, B.R. (2004) Biological laser printing of genetically modified *Escherichia coli* for biosensor applications. *Biosens. Bioelectron.*, **20** (2), 246–252.

27 Ringeisen, B.R., Kim, H., Barron, J.A., Krizman, D.B., Chrisey, D.B., Jackman, S. *et al.* (2004) Laser printing of pluripotent embryonal carcinoma cells. *Tissue Eng.*, **10** (3–4), 483–491.

28 Barron, J.A., Wu, P., Ladouceur, H.D., and Ringeisen, B.R. (2004) Biological laser printing: a novel technique for creating heterogeneous 3-dimensional cell patterns. *Biomed. Microdevices*, **6** (2), 139–147.

29 Hopp, B., Smausz, T., Kresz, N., Barna, N., Bor, Z., Kolozsvári, L. *et al.* (2005) Survival and proliferative ability of various living cell types after laser-induced forward transfer. *Tissue Eng.*, **11** (11–12), 1817–1823.

30 Patz, T.M., Doraiswamy, A., Narayan, R.J., He, W., Zhong, Y., Bellamkonda, R. *et al.* (2006) Three-dimensional direct writing of B35 neuronal cells. *J. Biomed. Mater. Res. B Appl. Biomater.*, **78B** (1), 124–130.

31 Schiele, N.R., Koppes, R.A., Corr, D.T., Ellison, K.S., Thompson, D.M., Ligon, L.A. *et al.* (2009) Laser direct writing of combinatorial libraries of idealized cellular constructs: biomedical applications. *Appl. Surf. Sci.*, **255** (10), 5444–5447.

32 Barron, J.A., Krizman, D.B., and Ringeisen, B.R. (2005) Laser printing of single cells: statistical analysis, cell viability, and stress. *Ann. Biomed. Eng.*, **33** (2), 121–130.

33 Barron, J.A., Ringeisen, B.R., Kim, H., Spargo, B.J., and Chrisey, D.B. (2004) Application of laser printing to mammalian cells. *Thin Solid Films*, **453–454**, 383–387.

34 Chen, C.Y., Barron, J.A., and Ringeisen, B.R. (2006) Cell patterning without chemical surface modification: cell–cell interactions between printed bovine aortic endothelial cells (BAEC) on a homogeneous cell-adherent hydrogel. *Appl. Surf. Sci.*, **252** (24), 8641–8645.

35 Othon, C.M., Wu, X., Anders, J.J., and Ringeisen, B.R. (2008) Single-cell printing to form three-dimensional lines of olfactory ensheathing cells. *Biomed. Mater.*, **3** (3), 34101.

36 Kaji, T., Ito, S., Miyasaka, H., Hosokawa, Y., Masuhara, H., Shukunami, C. *et al.* (2007) Nondestructive micropatterning of living animal cells using focused femtosecond laser-induced impulsive force. *Appl. Phys. Lett.*, **91** (2), 023904-1–023904-3.

37 Guillemot, F., Souquet, A., Catros, S., Guillotin, B., Lopez, J., Faucon, M. *et al.* (2010) High-throughput laser printing of cells and biomaterials for tissue engineering. *Acta Biomater.*, **6** (7), 2494–2500.

38 Serra, P., Fernandez-Pradas, J.M., Colina, M., Duocastella, M., Dominguez, J., and Morenza, J.L. (2006) Laser-induced forward transfer: a direct-writing technique for biosensors preparation. *J. Laser MicroNanoeng.*, **1** (3), 236–242.

39 Griffith, L.G. and Naughton, G. (2002) Tissue engineering--current challenges and expanding opportunities. *Science*, **295** (5557), 1009–1014.

40 Guillemot, F., Souquet, A., Catros, S., and Guillotin, B. (2010) Laser-assisted cell printing: principle, physical parameters versus cell fate and perspectives in tissue engineering. *Nanomedicine*, **5** (3), 507–515.

41 Koch, L., Gruene, M., Unger, C., and Chichkov, B. (2013) Laser assisted cell printing. *Curr. Pharm. Biotechnol.*, **14** (1), 91–97.

42 Barron, J.A., Spargo, B.J., and Ringeisen, B.R. (2004) Biological laser printing of three dimensional cellular structures. *Appl. Phys. A [Internet]*, [cited 2015 Feb 19], , **79** (4–6), 1027–1030. doi: 10.1007/s00339-004-2620-3

43 Keriquel, V., Guillemot, F., Arnault, I., Guillotin, B., Miraux, S., Amédée, J. *et al.* (2010) In vivo bioprinting for computer- and robotic-assisted medical intervention: preliminary study in mice. *Biofabrication*, **2** (1), 14101.

44 Hopp, B. (2012) Femtosecond laser printing of living cells using absorbing film-assisted laser-induced forward transfer. *Opt. Eng.*, **51** (1), 14302.

45 Koch, L., Kuhn, S., Sorg, H., Gruene, M., Schlie, S., Gaebel, R. *et al.* (2010) Laser printing of skin cells and human stem cells. *Tissue Eng. Part C Methods*, **16** (5), 847–854.

46 Lin, Y., Huang, Y., Wang, G., Tzeng, T.-R.J., and Chrisey, D.B. (2009) Effect of laser fluence on yeast cell viability in laser-assisted cell transfer. *J. Appl. Phys.*, **106** (4), 043106.

47 Lin, Y., Huang, G., Huang, Y., Tzeng, T.-R.J., and Chrisey, D. (2010) Effect of laser fluence in laser assisted direct writing of human colon cancer cell. *Rapid Prototyp. J.*, **16** (3), 202–208.

48 Catros, S., Guillotin, B., Bacáková, M., Fricain, J.-C., and Guillemot, F. (2011) Effect of laser energy, substrate film thickness and bioink viscosity on viability of endothelial cells printed by Laser-Assisted Bioprinting. *Appl. Surf. Sci.*, **257** (12), 5142–5147.

49 Raof, N.A., Schiele, N.R., Xie, Y., Chrisey, D.B., and Corr, D.T. (2011) The maintenance of pluripotency following laser direct-write of mouse embryonic stem cells. *Biomaterials*, **32** (7), 1802–1808.

50 Gruene, M., Pflaum, M., Deiwick, A., Koch, L., Schlie, S., Unger, C. *et al.* (2011) Adipogenic differentiation of laser-printed 3D tissue grafts consisting of human adipose-derived stem cells. *Biofabrication*, **3** (1), 15005.

51 Gruene, M., Deiwick, A., Koch, L., Schlie, S., Unger, C., Hofmann, N. *et al.* (2010) Laser printing of stem cells for biofabrication of scaffold-free autologous grafts. *Tissue Eng. Part C Methods*, **17** (1), 79–87.

52 Hurtley, S. (2009) Spatial cell biology. Location, location, location. Introduction. *Science*, **326** (5957), 1205.

53 Chang, H.Y. (2009) Anatomic demarcation of cells: genes to patterns. *Science*, **326** (5957), 1206–1207.

54 Ruiz, S.A. and Chen, C.S. (2008) Emergence of patterned stem cell differentiation within multicellular structures. *Stem Cells (Dayt Ohio)*, **26** (11), 2921–2927.

55 Vunjak-Novakovic, G. (2008) Patterning stem cell differentiation. *Cell Stem Cell*, **3** (4), 362–363.

56 Gruene, M., Pflaum, M., Hess, C., Diamantouros, S., Schlie, S., Deiwick, A. *et al.* (2011) Laser printing of three-dimensional multicellular arrays for studies of cell-cell and cell-environment interactions. *Tissue Eng. Part C Methods*, **17** (10), 973–982.

57 Kasili, P.M., Cullum, B.M., Griffin, G.D., and Vo-Dinh, T. (2002) Nanosensor for in vivo measurement of the carcinogen benzo[a]pyrene in a single cell. *J. Nanosci. Nanotechnol.*, **2** (6), 653–658.

58 Phamduy, T.B., Sweat, R.S., Azimi, M.S., Burow, M.E., Murfee, W.L., and Chrisey, D.B. (2015) Printing cancer cells into intact microvascular networks: a model for investigating cancer cell dynamics during angiogenesis. *Integr. Biol.*, **7** (9), 1068–1078.

59 MacNeil, S. (2007) Progress and opportunities for tissue-engineered skin. *Nature*, **445** (7130), 874–880.

60 Koch, L., Deiwick, A., Schlie, S., Michael, S., Gruene, M., Coger, V. *et al.* (2012) Skin tissue generation by laser cell printing. *Biotechnol. Bioeng.*, **109** (7), 1855–1863.

61 Michael, S., Sorg, H., Peck, C.-T., Koch, L., Deiwick, A., Chichkov, B. *et al.* (2013) Tissue engineered skin substitutes created by laser-assisted bioprinting form skin-like structures in the dorsal skin fold chamber in mice. *PLoS ONE*, **8** (3), e57741.

62 Place, E.S., Evans, N.D., and Stevens, M.M. (2009) Complexity in biomaterials for tissue engineering. *Nat. Mater.*, **8** (6), 457–470.

63 Wu, P.K. and Ringeisen, B.R. (2010) Development of human umbilical vein endothelial cell (HUVEC) and human umbilical vein smooth muscle cell (HUVSMC) branch/stem structures on hydrogel layers via biological laser printing (BioLP). *Biofabrication*, **2** (1), 14111.

64 Pirlo, R.K., Wu, P., Liu, J., and Ringeisen, B. (2012) PLGA/hydrogel biopapers as a stackable substrate for printing HUVEC networks via BioLP. *Biotechnol. Bioeng.*, **109** (1), 262–273.

65 Hsieh, P.C.H., Davis, M.E., Lisowski, L.K., and Lee, R.T. (2006) Endothelial-cardiomyocyte interactions in cardiac development and repair. *Annu. Rev. Physiol.*, **68**, 51–66.

66 Gaebel, R., Ma, N., Liu, J., Guan, J., Koch, L., Klopsch, C. *et al.* (2011) Patterning human stem cells and endothelial cells with laser printing for cardiac regeneration. *Biomaterials*, **32** (35), 9218–9230.

67 Ma, Z., Liu, Q., Yang, H., Runyan, R.B., Eisenberg, C.A., Xu, M. *et al.* (2013) Laser patterning for the study of MSC cardiogenic differentiation at the single-cell level. *Light Sci. Appl.*, **2** (5), 68.

68 Santos, M.I. and Reis, R.L. (2009) Vascularization in bone tissue engineering: physiology, current strategies, major hurdles and future challenges. *Macromol. Biosci.*, **10** (1), 12–27.

69 Petite, H., Viateau, V., Bensaïd, W., Meunier, A., de Pollak, C., Bourguignon, M. *et al.* (2000) Tissue-engineered bone regeneration. *Nat. Biotechnol.*, **18** (9), 959–963.

70 Doraiswamy, A., Narayan, R.J., Harris, M.L., Qadri, S.B., Modi, R., and Chrisey, D.B. (2007) Laser microfabrication of hydroxyapatite-osteoblast-like cell composites. *J. Biomed. Mater. Res. A*, **80A** (3), 635–643.

71 Catros, S., Fricain, J.-C., Guillotin, B., Pippenger, B., Bareille, R., Remy, M. *et al.* (2011) Laser-assisted bioprinting for creating on-demand patterns of human osteoprogenitor cells and nano-hydroxyapatite. *Biofabrication*, **3** (2), 25001.

72 Ramón-Cueto, A. and Valverde, F. (1995) Olfactory bulb ensheathing glia: a unique cell type with axonal growth-promoting properties. *Glia*, **14** (3), 163–173.

73 Curley, J.L., Sklare, S.C., Bowser, D.A., Saksena, J., Moore, M.J., and Chrisey, D.B. (2016) Isolated node engineering of neuronal systems using laser direct write. *Biofabrication*, **8** (1), 15013.

16

Industrial, Large-Area, and High-Throughput LIFT/LIBT Digital Printing

Guido Hennig[1], *Gerhard Hochstein*[2], *and Thomas Baldermann*[1]

[1] *Daetwyler Graphics AG, Flugplatz, 3368 Bleienbach, Switzerland*
[2] *Terra Incognita Innovationsmanagement GmbH, Kastanienweg 8, 57392 Schmallenberg-Bad, Fredeburg, Germany*

16.1 Introduction

The graphics industry has been facing its digital revolution since the 1990s, resulting in digital printing systems replacing partly conventional printing machines. A broad range of digital printing techniques is available today. Nevertheless, a lot of demands for the printing of special inks have been not yet fulfilled by today's digital printing methods, leaving space for the introduction of new technologies. Identifying suitable business models for industrial use of LIFT/LIBT applications is an ongoing process. Initial approaches have been undertaken in the area of graphical and functional printing within the first and early second decades of the 2000s. Emerging markets of this era such as mass production of solar cells bore challenges for advanced coating technologies for conductive and semiconductive layers. Functional applications such as heating elements or antennas on automotive glass windshields and windows require transfer technologies for printing of conductive structures with high solid content, high viscosity, and high volume transfer. Traditional printing techniques such as screen printing cause high fixed costs prior to the first copy, thus prototyping, low volume orders, and individualization of functional goods are cost-ineffective. Typical digital printing systems are rather limited in terms of big volume transfer of conductive and other technical materials, which might be an area for implementation of the here described LIFT/LIBT-production solutions. Meanwhile, the development of industrial solutions for the aforementioned applications left the status of venture capital investments. Nowadays, small and medium enterprises (SME) are trying to enter markets with highly specified LIFT/LIBT machine concepts. However, there has still been no breakthrough in the industrial use of LIFT/LIBT applications, neither in functional nor in graphical printing applications. However, some industries for printed electronics and decor printing have already discovered LIFT/LIBT as one of their potential future technologies for process optimization and showed willingness to invest. The following discussion aims to encourage the LIFT/LIBT community to

Laser Printing of Functional Materials: 3D Microfabrication, Electronics and Biomedicine,
First Edition. Edited by Alberto Piqué and Pere Serra.
© 2018 Wiley-VCH Verlag GmbH & Co. KGaA. Published 2018 by Wiley-VCH Verlag GmbH & Co. KGaA.

intensify contact to the early industrial adopters of this technology and to search for further opportunities.

16.1.1 State of the Art in Digital Printing

For the past two decades, the printing industry has been facing dramatic changes. Nowadays, former mass application printing markets such as packaging, illustration, or décor printing, traditionally served by classical rotogravure-, offset- or flexo-printing, require additional production methods for personalized/customized products or fixed-cost-optimized low-volume orders. Since digital printing technologies reached industrial practicability, today's task, addressing special reader or user groups with selected, targeted, and individually adopted content, has allowed digital printing machines to gain substantial market share. Common digital printing methods, such as Inkjet printing or Xerography, show 100% flexibility regarding print-on-demand and CTP (computer-to-press) workflow. However, there are still some barriers toward competitive industrial scales. To achieve high printing quality comparable to offset or rotogravure printing, the common digital printing techniques require costly specially coated substrates. In many cases, each of the typical digital printing techniques needs expensive and specialized printing inks. Those inks are rarely approved by the US Food and Drug Administration (FDA) for use in the printing of food packaging. Moreover, the small inkjet nozzles or the toner-based Xerography is not able to print large pigments with a size of up to 100 µm as those used in rotogravure inks in order to achieve brilliant silver or gold gloss or mother-of-pearl effects. Furthermore, comparability with classical printing methods, using standard inks on standard substrates, is still a requirement in some markets or at least a strong asset. Therefore, there is a demand in the printing industry for a versatile digital CTP printing method, which enables printing with any common low-cost inks on any common low-cost substrates and producing some thousands of units within a reliable time frame. The direct LIFT/LIBT transfer of liquid inks gives a new option for this and has the potential to fill up some not yet addressed areas in the landscape of digital printing.

16.1.2 History of Lasersonic® LIFT

Already in the 1960s, first scientific and industrial approaches have been developed in the United States, Japan, and Russia to design printing machines utilizing LIFT methods. Fundamental studies of the LIFT (laser-induced forward transfer) process of liquid materials are reported in [1–10]. In 1969, Browning and Johnson filed their patent titled "Recording method and apparatus utilizing light energy to move record forming material onto a record medium" [11], which represents a kind of LIFT method for the writing of large data. In 1989, Kohyama, from KK Toshiba, Kawasaki, Japan, filed his patent of a "Laser actuated recording apparatus" using LIFT printing with continuously refreshed donor and acceptor substrates [12]. In their patent applications of 1995 and 1997 [13, 14], Maximovsky and Radutzki from the Polygraphical Institute in Moscow, Russia, described several solutions for LIFT-based printing unit configurations.

Similar but advanced ideas have been described by Lehmann, the founder of Aurentum GmbH, Germany, in his patents [15–17]. Since 1997, Aurentum developed several LIFT- and LIBT-based printing machine prototypes, for example, from 2003 to 2006 within the project cluster "Propolytec," which was supported with research funding by the German government ministry BMBF. The project scope contained the development of a prototype device for digital LIFT printing of organic and metallic layers on foils. This device was able to print digitally as well as to structure the layers locally by ablation [18]. Aurentum used the name Lasersonic® for this special LIFT approach. In 2009, DI Projekt AG (Bleienbach/CH) was founded as joint venture by Daetwyler AG, Switzerland, and Interprint GmbH, Germany, in order to industrialize the results of the Lasersonic® studies by Aurentum and to realize a niche application for the printing of short-run decor products with LIFT and LIBT. A first industrial four-color printing machine for decor applications was built, and printing trials were started in 2011 [19].

16.2 Potential Markets and their Technical Demands on Lasersonic® LIFT

16.2.1 Digital Printing Market Expectations and Challenges

In the meantime, digital printing technologies reached industrial standards in several applications. Classical mass-printing markets such as brochures, forms, and other office demands, in the past, dominated by offset printing, have been partly occupied by digital printing techniques. However, the growth curve for digital printing machine sales has been flat in those markets. In fact, industrial digital printing market share is still said to remain at a one-digit percentage as referred to offset printing. Despite this, in some specialized markets, for example, printing of tiles, inkjet printing has reached a market share of about 35% (status: 2016) and is competing successfully against screen printing [20].

Nowadays, digital printing equipment suppliers are focusing on new markets. Growth potential is seen in large-scale printing markets such as flexible packaging, printing on corrugated board, label or niche markets such as décor printing. Here, inkjet dominates the technical solutions. The technical approach is quite higher compared to the current digital printing markets. Packaging printing markets are forcing suppliers to deal with strong legal and hygienic requirements. Challenges are to be found in applications such as food packaging or pharmaceutical packaging. Typical inkjet inks contain ingredients that are legally banned from direct and indirect contact with food or drugs. European authorities are moving toward banning more and more chemicals for use in package printing. The "positive list," stated in the "Commission Regulation (EU) No 10/2011" is an example of such kind of restrictions [21]. Current amendments of relevant German regulations, for example, the "Bedarfsgegenstände-Verordnung/Druckfarbenrichtlinie" [22, 23], are raising the bar for digital printing system design. Meanwhile, big players in the digital printing equipment market are focusing their development resources

on those applications. The influence of both printing head suppliers and ink manufacturers is growing more and more because both those parts of an inkjet-printing system have to match perfectly. Otherwise, access to explicit safety-driven applications will not be possible.

Niche markets in decorative applications are more driven by the special physical, mechanical, and chemical properties of the inks or the envisaged use of the printed products. Tile printing inks contain high abrasive ceramic pigments, thereby posing demanding challenges to the inkjet printing heads. The printed inks and pigments have to survive temperatures of about 900 °C during production process of tiles. The off-standard inks used for digital décor printing of furniture and laminate flooring applications have to perfectly match the standard gravure inks to avoid metamerism with rotogravure décor-printing products.

The LIFT/LIBT process offers new options for the digital printing of inks, which are not well suited for inkjet printing but are preferred because they fulfill the new legal requirements or have special required technical properties. However, LIFT/LIBT is a serial writing process, and the overall speed of the process is limited and not competitive in the range of today's inkjet printing speeds, which performs up to some hundred meters/min web speed. Therefore, it is not able to compete directly with inkjet or Xerography in their common markets. However, niche applications exist, for example, for "low number of runs" jobs, where speed is not the dominant factor, but other features such as the use of common rotogravure inks or the independent choice of the substrate are appreciated. For example, digital proof printing with standard inks for the creation of new designs of personalized packaging solutions – that is, for the so-called mock-up – process of new packaging designs – could lead to final results in a faster and more economical way by LIFT/LIBT than by traditional rotogravure printing, which requires a complete new set of print forms for each substep of the design evaluation, which is today a very costly and time-consuming process. Using the digital LIFT/LIBT process, the evaluation of the color management of a new product can be made by computer-controlled variations of the print parameters, using *ab initio* the same inks as in later mass production by rotogravure. Other examples are personalized "low number of runs" jobs in packaging or decor applications.

16.2.2 Demands on a LIFT/LIBT Printing Unit for Special Printing Markets

The specifications and the functional performance of the Lasersonic® digital LIFT/LIBT printing machine to be described in this chapter aim at the requirements of special decor market applications and proof printing processes in packaging and include the definition of following key parameters: a screen resolution of 300–600 dpi (physically true pixels as in rotogravure, each pixel must have a full 8-bit grayscale range), a minimum print size of 530 mm (minimum scanline length), and a minimum feeding speed of the substrate web of 2.5 m/min. That is equivalent to an area rate of 1.325 m^2/min and requires at 600 dpi resolution – with a duty cycle of about 50% of the line scanner

device – a pixel rate of about 25 MHz and a high-power laser source as described to closer details in Section 16.4. Such a fast rate of modulation is a challenge for high-power laser beams with several hundred watts.

16.3 Lasersonic® LIFT/LIBT Printing Method

With respect to the performance requirements and standards of industrial printing applications, the Lasersonic® LIFT process is characterized by specific features:

1) The ink materials are mostly solvent or water-based fluids with dispersed pigments exhibiting different absorption characteristics, ranging from strongly absorbing black pigments to colored pigments (e.g., blue, magenta, yellow), which are transparent materials for the NIR laser wavelength (in our case, at 1070 nm). As described in Section 16.3.1, this implies two different approaches for the LIFT process, the laser-induced forward transfer (LIFT) for laser absorbing inks and the laser-induced backward transfer (LIBT) for transparent inks.
2) In contrast to many other LIFT applications, which use pulsed laser sources (ns, ps pulses), this approach is based on a polarized cw-TEM_{00} NIR laser source at high power level of several hundred watts.
3) The laser beam is fast intensity-modulated by an external acousto-optical modulator (AOM) device in order to generate pulses per pixel. This concept allows to control pulse length, timing, peak power, and pulse energy of each individual pulse by appropriately designed electronic signals up to extremely high repetition rates (as the required 25 MHz) and down to minimized short pulse lengths (16 ns FWHM). The high repetition rate is essential to achieve the required throughput for ultrafast direct writing of large areas.
4) The data flow has to be boosted by a fast data calculation and data transfer rate.
5) When writing pixel by pixel in a sequential manner, the coverage of large areas within a reasonable time requires precise and stable methods of ultrafast laser beam scanning. This is achievable with a high-speed laser scanning polygon wheel and at the same time a precisely synchronized and well-aligned feed rate of the substrate.
6) To run the LIFT process R2R without interruption, the donor layer must be refreshed continuously. This requires appropriate donor substrates and inking units including a stable control of pigment concentration and rheological parameters of the ink (see Section 16.5).

These conditions are the guidelines and represent the key components for a concept of an industrial LIFT printing unit. Over the entire run, all these components must be precisely controlled and strongly coordinated.

16.3.1 LIFT for Absorbing and LIBT for Transparent Inks

In case of an absorptive ink (Figure 16.1), the laser beam passes through a transparent donor substrate (film or ribbon) and is focused with a spot size $2w_o$ of

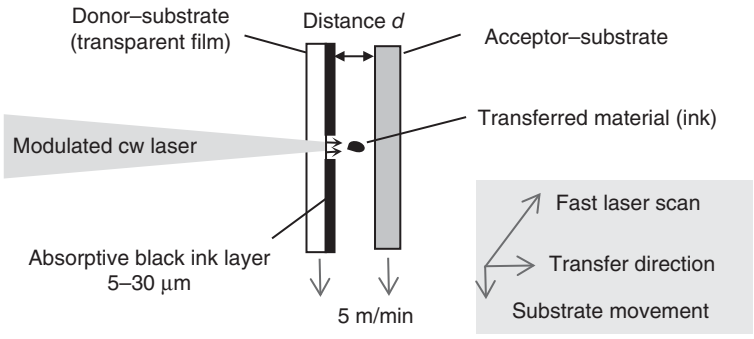

Figure 16.1 Scheme of Lasersonic® LIFT printing of black (absorptive) ink.

about 60 µm exactly at the interface between the donor substrate and the absorptive black ink layer. The laser beam energy is absorbed by the black ink and converted into thermal energy. This induces a small vapor bubble with high expansive pressure at this spot. An explosive expansion, followed by a breakdown of the bubble, leads to forces, which push the liquid ink to move forward to the acceptor substrate.

This scheme is in essence similar to a lot of other LIFT applications. However, the difference is that the laser beam can be scanned at ultrafast speeds (with 400 m/s up to 2116 m/s, depending on the operation mode) across the donor substrate in order to achieve an acceptable area throughput for the application. Additionally, the acceptor substrate can be moved with a speed of up to 5 m/min in a cross-scan direction in order to perform a reel-to-reel process, and the donor film must be continuously moved forward in order to provide a fresh ink layer for each printed spot. Currently, the maximum area production rate is 2.65 m^2/min for 300 dpi (limited by the acceptor substrate movement) and 1.325 m^2/min for 600 dpi screen resolution, according to the requirements considered earlier.

The distance d between the donor and the acceptor substrates must be large enough to avoid mechanical contact between the donor and the acceptor, especially, when both are moving, and as small as possible in order to receive a precise ink transfer and to avoid, for instance, excessive spreading of satellite droplets. Typical values for d in R2R printing are in the range of $0.3\,\text{mm} < d < 0.6\,\text{mm}$.

A full-color print requires – apart from black – at least primary inks such as cyan, magenta, and yellow. Usually, if made up by standard pigments, these inks are not absorptive at the laser wavelength of 1070 nm, though exceptions may eventually be posed by certain types of blue phtalocyanine pigments. This means that a different approach for the Lasersonic® printing of near-infrared (NIR)-transparent colors is required. The solution, the LIBT process, is shown in Figure 16.2. The donor substrate is coated by an absorption material, which is able to efficiently convert photonic energy into heat, and the ink is applied on top of this converting layer. The laser beam propagates through the transparent ink layer and is absorbed at the surface of the absorption layer, which faces the ink. The absorbed energy heats up the ink at this interface zone and generates an

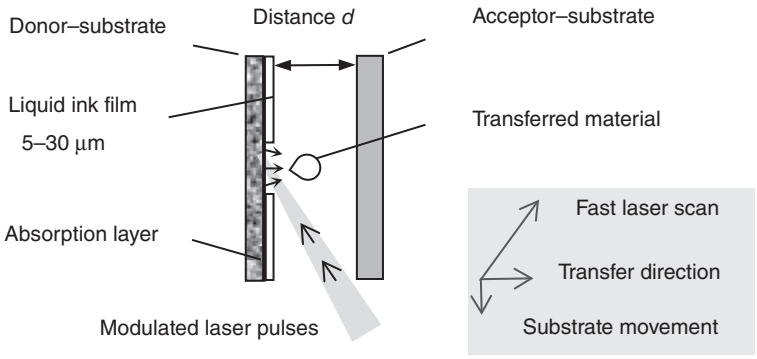

Figure 16.2 Lasersonic® LIBT printing of transparent inks.

explosively expanding vapor bubble, pushing the ink toward the acceptor. Due to the inverse direction of the laser, this process is named LIBT (laser-induced backward transfer). The scanning scheme of the laser beam and the substrate movement is analoguous to that shown in Figure 16.1. More details about the absorption layer are described in Section 16.5.4.

In order to avoid blocking or shadowing of the incident laser beam by the acceptor substrate, the spatial arrangement of the color printing unit has been designed as shown in Figure 16.3. The laser beam hits the donor substrate surface with an angle of incidence of 60° referring to the normal direction. This is close to the Brewster angle of the fluidic ink layer, and an appropriately polarized laser beam shows only reduced reflection losses at the ink surface. The size of the laser focus is shaped elliptically at the scanline with a diameter of 30 µm in cross-scan

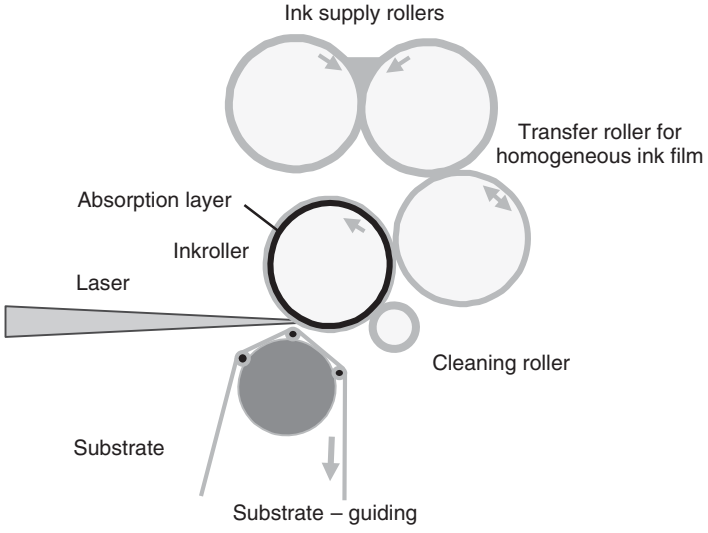

Figure 16.3 Printing unit for continuous R2R printing of color pigmented NIR-transparent inks; the ink roller is precoated with a laser-absorbing material.

direction and 60 µm in scan direction. For 60° of incidence, the projection on the surface of the donor roller results in a 60 µm round laser spot.

The laser beam scans a 530 mm long line on the surface of the ink roller parallel to the roller axis with up to 2 kHz line frequency, and the substrate is synchronously moving in cross-scan direction. The ink roller is coated with ink by a precise inking system as described in Section 16.5.3.

16.4 Optical Concept and Pulse Control of the Lasersonic® Printing Machine

The optical beam path of the laser scan unit is shown in Figure 16.4. A high-power cw fiber laser beam with 300 W is modulated by an acousto-optical modulator (AOM), scanned by a fast rotating polygon mirror and focused by an f-theta lens system onto the scanline at the ink roller surface, respectively, at the absorption layer.

16.4.1 Ultrafast Pulse Modulation at High Power Level

For the described printing applications, a fast writing speed of at least 1.3 m^2/min with 600 dpi pixel resolution is desired. That corresponds for a one-color printing unit to 1.5 gigapixel per minute and a high modulation rate of up to 25 MHz, which is very challenging at this high power range. For the Lasersonic® approach, acousto-optical modulation has been used because it turned out that a tailored AOM was less expensive and easier to push to high pulse rates than high-voltage-driven electro-optical modulation. With a cw-power of 300 W from the laser, an efficiency of more than 56% in the first diffracted order could be achieved at 25 MHz. The dynamical contrast ratio of the AOM is the ratio of the minimum to the maximum power signal of the first diffracted order when an on/off modulated input signal is applied. It was measured with a fast photodiode. The dynamical contrast ratio depends strongly on the modulation rate, if – in the

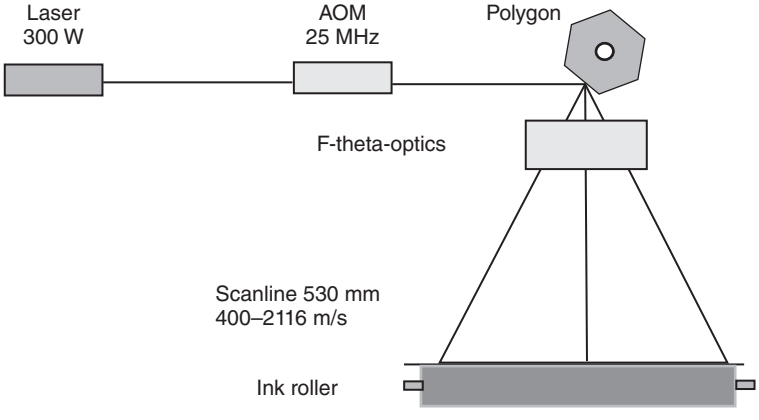

Figure 16.4 Optical laser beam path of the printing unit (one-color).

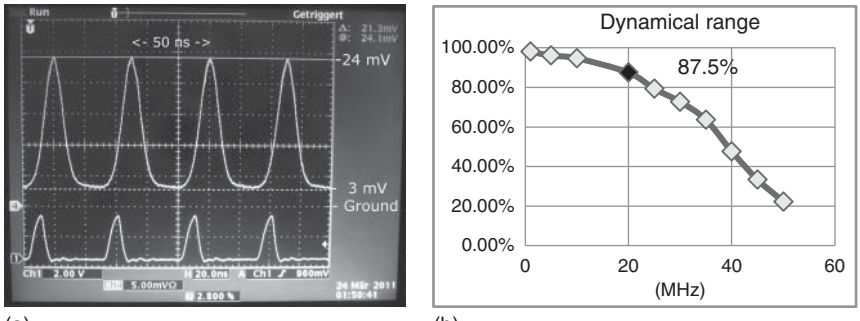

(a) (b)

Figure 16.5 (a) Laser power signal of first diffracted order at 20 MHz (AOM input signal is displayed at screen bottom), (b) frequency response of the dynamical range for on/off.

high-frequency regime – the modulation rate is as fast as that permitted by the minimum rise and fall times of the AOM sound field. At 20 MHz, the measured contrast ratio has been 1 : 8 and enables for a dynamical modulation range of 87.5% of the laser peak power. The example illustrated in Figure 16.5 shows that the photodiode signal of the power in the first AOM order can be varied from 12.5% to 100% of the full signal (3–24 mV) by changing the input signal from 0% to 100%. This power modulation hub of 87.5% enables for an on/off pulse control of the LIFT process at each single pixel of the printed image. The residual power of 12.5% in the first diffracted order does not have any impact on the transfer because the value is below the process threshold of the LIFT process if the laser is scanned as fast as that described in Section 16.4.4.

At a modulation rate of 25 MHz, the contrast ratio drops down to 1 : 5. This is equivalent to a modulation range of only 80%. Even this is sufficient to modulate the LIFT/LIBT process. The increased residual power of now 20% is again below the process threshold because the threshold power increases as well due to a shorter time of impact of the laser at higher frequency and higher scan speed. At lower frequencies, that is, at 5 MHz, the contrast ratio exceeds 1 : 25 according to a dynamical modulation range of 96% (Figure 16.5) with a residual power of only 4%. Therefore, the process steering by modulation works well over a large frequency range.

16.4.2 Time Schemes

The concept of the *modulated cw-laser beam* allows the application of various time schemes with variable pulse length and pulse height control.

The default scheme is the simple *on/off switching* of the RF power in order to generate separated pulses, as shown in Figure 16.5. The number of peaks/s represents the pulse rate or pixel rate. If using an AOM, the lower limit of a minimum pulse length is given by the sum of rise and fall times of the AOM sound field along the cross section of the laser beam. For example, for a sound velocity of 5×10^3 m/s within the AOM crystal and for a laser beam diameter of 100 µm, a time of about 20 ns is needed for rise time and again for fall time of the RF field

across the beam. Without plateau, the on/off time for the whole pulse sums up to about 40 ns, according to a maximum repetition rate of separated pulses of 25 MHz.

Another modulation scheme is the *direct switching between subsequent power levels*: The power level of the RF input signal is switched just from one value to the next value without intermediate zero level according to the change of the grayscale value from one pixel of an image to the next in the input data (Figure 16.6, P_{RF} input signal). This suggests that a doubling of the data pixel rate of up to 50 MHz (20 ns per pixel) might be possible. However, the sound field that is induced by the RF signal in the AOM needs about 40 ns time to propagate across the laser beam cross section, so that the effective pulse energy that is irradiated to a pixel at the scanline becomes a mixture (a weighted sum) of the pulse energies of its correlated data pixel and neighbored data pixels (calculable by integration of P_{eff_laser} over the exposure time). For a screen of 600 dpi with a pixel size of 42 µm and for a scan speed of 2100 m/s, the scan time across a pixel is only 20 ns (minimum exposure time). In that case, at least two data pixels contribute partly to the effective pulse energy impact at that pixel. The size of 60 µm of the laser focus at the scanline is still neglected in this model and leads to an additional elongation of the exposure time to 50 ns at 2100 m/s with partial contribution of four data pixels, which are differently weighted according to the changing spatial overlap of the laser spot and the pixel area during scanning. Therefore, the grayscale values of the printed dots become blurred and incorrect. We learn from Figure 16.6 that a crucial criterion for the printing speed is the switching speed of the power level of the laser beam by the modulator. The direct switching scheme is not well suited for acousto-optical modulation of a cw-laser due to the slow slope of the laser pulse. However, if a ps-laser or sub-ns laser is used and the RF field in the modulator is synchronized

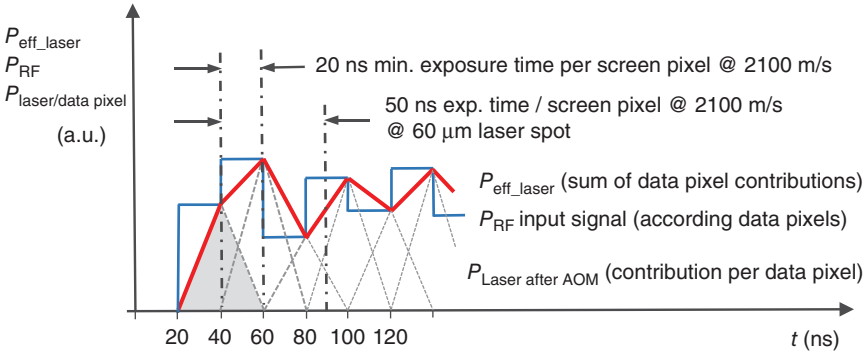
P_{eff_laser}
P_{RF}
$P_{laser/data\ pixel}$
(a.u.)
20 ns min. exposure time per screen pixel @ 2100 m/s
50 ns exp. time / screen pixel @ 2100 m/s
@ 60 µm laser spot
P_{eff_laser} (sum of data pixel contributions)
P_{RF} input signal (according data pixels)
$P_{Laser\ after\ AOM}$ (contribution per data pixel)
20 40 60 80 100 120
t (ns)

Figure 16.6 Schematic diagram of *direct switching between power levels*. The RF input signal is switched each 20 ns according to the image data. The resulting laser pulses in the first diffracted order after the AOM need a rise time of 20 ns and a fall time of 20 ns (simplified shown as triangles with dashed lines). At the falling edge of these laser pulses, the next data pixel is already set and the next RF field has been started to propagate through the laser beam and already contributes to the effective laser power in the first diffracted order. The power curves of all pulses (dashed lines) are summed up to the effective laser power in the first diffracted order (bold curve).

in such a way that it covers the whole laser beam cross section exactly at the time when the laser pulse appears, this scheme can be applied and power level values are correct. (Here the question remains, if the ps pulses does not destroy the modulator crystal.) In addition, in case of electro-optical modulation, which might be performed by high technical effort with faster rise and fall times of the resulting high power laser pulses than acousto-optical modulation (required are smaller than 1 ns rise and fall times), this time scheme might be an option to boost the data pixel rate up to 50 MHz without mixing of data pixel grayscale values.

Nevertheless, this kind of modulation scheme is helpful in order to study the mechanism and limits of correct pixel reproduction. For example, it can be used for the investigation of the transfer process of the ink, especially in case of drawing a line in the scan direction with a constant power level all over the line without intermediate zero level. In Section 16.7, how the LIFT transfer process is being affected by the modulation time schemes is described.

16.4.3 Data Flow

Data sources in printing are typically files such as bitmaps or tiff files, which provide an 8-bit or 12-bit grayscale value for each pixel of an image. The data output has to be synchronized along the scanline according to the master clock pulses of the polygon encoder and corrected for facet angle errors or other discontinuities in scan direction. The data output scheme must be edited and recalculated according to the correct timing information, for instance, for the purpose of introducing adopted time delays for each facet in the case of a nonideal polygon, defining starting points and compensating flatness deviations of the facets (convexity) by rescaling the scanline length in order to finally determine the correct pixel positions at the donor substrate. At a data rate of 20 MHz to 25 MHz, this requires fast FPGA processors with reference clock rates of up to some hundred MHz. After calculation (and digital–analog conversion), the data are sent sequentially to the AOM driver electronics.

16.4.4 Ultrafast Scan of the Laser Beam

As described in Section 16.2.2, the market aims for a productive printing speed of at least several m^2/min, even at a screen resolution of 600 dpi. This can be satisfied only with a beam scanning strategy, which allows for a scan speed of more than 1000 m/s over the whole scanline.

Therefore, the scanning unit was designed based on a fast spinning polygon wheel and a new concept for an f-theta lens unit. A solution for the correction of polygon errors as pyramidal error and facet-to-facet angle tolerances is commonly obtained by additional galvoscanner mirrors. However, at the high line frequency of 1–2 kHz, this is no more possible in a satisfactory precise manner. In order to minimize the impact of pyramidal errors of the polygon facets onto distance variations of subsequent scanlines on the donor substrate, an anamorphic optical system with cylindrical lenses was designed, which allows to separate the propagation properties of the laser beam in two independent (orthogonal) components, one in the horizontal-scan direction (x-axis) and the other in the vertical

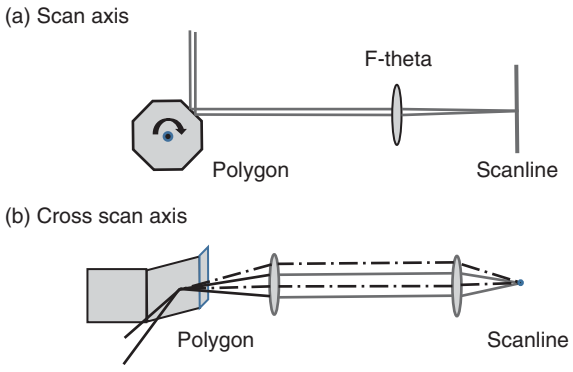

Figure 16.7 Purpose of anamorphic optics: (a) scan direction with far field at polygon surface, (b) cross-scan direction with near field at polygon surface, insensitive against pyramidal error; if the polygon facet is slightly tilted, the beam follows the dashed line, but the focus point stays stable at the scanline.

cross-scan direction (y-axis). The laser beam has been transformed by cylindrical lenses in such a way that at a certain z-position the x component of the laser beam is in the far field with respect to the scanline and the y component is at the same z-position in the near field with respect to the scanline (Figure 16.7). If the polygon facet is placed at this z-position, both laser beam components behave in different ways: for the far-field component, a change of the angle of the polygon facet (as during rotation or also due to polygon shape errors) leads to a change of the focus position along the scanline. Fabrication tolerances of the polygon facet angle from facet to facet in the scan direction can be corrected by appropriate time delays of the modulation signal, which generates the laser pulses at each new scanline.

On the other hand, for the near-field component, the focus position on the substrate in cross-scan direction is insensitive to variations of the polygon facet angle in the y-direction, and the focus position remains stable on the donor substrate. This is a passive stabilization of the focus position in the cross-scan direction and a passive suppression of the pyramidal error of the polygon. However, this has strong consequences for the design of the f-theta unit, which must be built up as an anamorphic lens system as well. On the other hand, this concept opens the way for different focus spot sizes in scan and cross-scan directions, especially, to achieve a $2w_0$-spot size of only 30 µm in the cross-scan direction and of 60 µm in the scan direction. This was very helpful to realize the 60° angle of incidence and to achieve at the same time a round projection of the spot with 60 µm diameter on the absorption layer, as described in Section 16.3.1. We achieved a scan speed of more than 2000 m/s over a scanline length of 530 mm and with a pixel-to-pixel distance of 84 µm (300 dpi). The alignment of the components of this anamorphic optical beam path has to be carried out very accurately using tools such as autocollimator and Shack–Hartmann wavefront sensor. The duty cycle of a polygon is the percentage of the revolution time that can be used effectively for the scan of the beam. During transit time, when the extended diameter of the laser beam crosses one of the edges of the polygon, the laser beam must be interrupted. Usually, the laser energy is wasted during this time. To continuously use nearly the whole power delivered by one laser source, we switched the laser beam between two different printing units on opposite sides of a two-color double print unit. This works as follows (see Figure 16.8): the duty cycle of the polygon was chosen

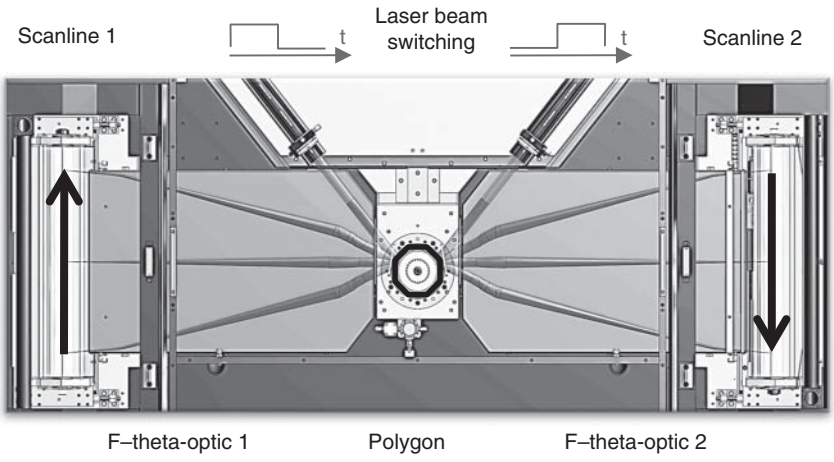

Figure 16.8 Two-color double-printing unit for transparent inks. The laser beam alternates between left and right scanline.

closely below 50%. As long as the beam from the right side hits on top of a facet of the rotating polygon, the right printing unit is scanned by this beam. However, just before the beam starts to run over the edge from one facet to the other, the beam path is switched to hit the polygon from its other side (again on a facet) in order to serve the left printing unit. By this method, only one laser source and one polygon are needed to generate two timely alternating scanlines, each with a line frequency of up to 2 kHz and a scan length of 530 mm.

16.5 The Four-Color Lasersonic® Printing Machine

16.5.1 Large-Area, High-Throughput LIFT/LIBT Inline R2R Printing System

The four-color Lasersonic printing machine is built up as a combination of two two-color double print units as shown in Figure 16.9. The combination concept is scalable to three or four double print units for printing with six or eight colors. The substrate passes the four printing units one after the other with intermediate ink drying devices and automated corrections of path deviations (web guide control). Some features of the substrate guiding system are shown in Table 16.1.

Multicolor printing with several printing units requires a precise synchronization between the time-dependent local position of the fast scanned laser beams on each scanline, the *x*-, *z*-feed position of the substrate at each printing unit and the exact timing of each AOM signal for the laser modulation based on the data flow.

For this purpose, the angular position of the fast rotating polygon – which represents the laser spot position at the scanline – is detected by a rotary encoder at each double-print unit. The clock signal of the encoder is used as a master trigger of the unit. Steering signals, which are synchronized to this master, regulate the feedforward of the substrate and control the image data output processing for the

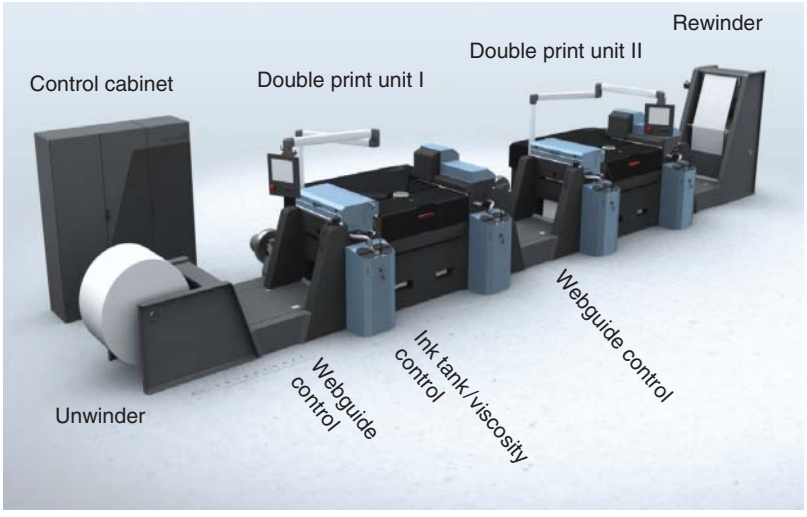

Figure 16.9 Four-color Lasersonic® printing machine with unwinder and rewinder unit of the substrate, ink mixing and supply tanks, printing units, and human interfaces. The inking modules on top can be exchanged within a few minutes to vary between different inks or ink sequences.

Table 16.1 Web characteristics.

Parameter	Range
Maximum web size	630 mm
Web speed (synchronized with polygon scan)	0–5 m/s
Gap width between ink roller and paper	0–1.5 mm
Maximum print width	530 mm
Maximum paper reel diameter	1000 mm
Maximum paper reel weight	500 kg

laser power modulation with the AOM. The laser beam position, the transversal and longitudinal control of the correct substrate movement, and the start position of the scanline are essentially "to be matched" parameters. Multiple control systems and more than 50 motor-driven axes are involved. Moreover, the mixture and viscosity of the ink can be actively adjusted to optimize the conditions for the LIFT process.

16.5.2 Printing Heads for Absorptive (Black) and for Transparent (Colored) Inks

As mentioned in Section 16.3.1, two technical approaches for the donor substrate have been realized, an circulating transparent endless ribbon for the black ink printing unit and an ink roller, coated by an absorption layer, for each of the color printing units.

The design of a machine for industrial use should be based as much as possible on the integration of identical components or modules, especially if these are highly performing parts, which require major efforts in development. The optical system for the creation of the 530 mm long scanline is such a module. In order to avoid the development of two different scan modules, the same one should be used for the black ink printing unit and for the color printing units. In both cases, a passive cross-scan correction is helpful to ensure equal distances from scanline to scanline, especially at high scan speeds when galvomirror correction of the pyramidal error is not fast enough. Hence, the f-theta unit is designed as an anamorphic system (Figure 16.7). Moreover, in case of the LIBT color printing unit, an angle of incidence of the laser beam on the ink roller of 60° is used in order to avoid collision with the paper. The anamorphic approach allows not only the passive cross-scan correction but also to generate an *elliptical* focus spot at the scanline of the f-theta unit (60 µm spot diameter in scan direction, 30 µm in cross-scan direction) in order to finally achieve a round projection of this elliptical focus on the ink roller. When using the same f-theta module, the same projection should also be applied to the printing unit for absorbing (black) ink. Therefore, the donor ribbon is arranged under 60° instead of being perpendicular to the laser beam. An additional advantage is that the beam is coupled near the Brewster angle through the donor ribbon. It is a challenge to handle a 530 mm wide flexible donor ribbon and to ensure equal ink layer thickness and density over the whole width. In order to make this easier, the donor ribbon is designed much smaller than the scanline length, but the feeding direction is under an angle of only less than 10° to the scanline instead of 90°. By this, the whole scanline can be covered by a narrower donor substrate with a width less than 100 mm. Figure 16.10 shows a scheme of the print unit for absorbing inks. The feed rate of the donor ribbon has to be fast enough to provide a complete fresh ink layer for the next scanline.

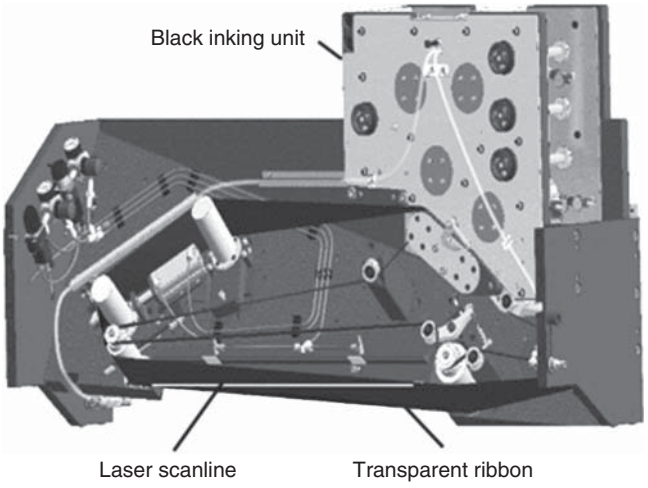

Figure 16.10 Print unit for absorbing ink, the scanline is covered over the whole length by the donor ribbon, the laser comes from the backside, hits the ribbon under 60°, and is scanned along the scanline.

The geometry of the color printing unit has already been explained in Section 16.3.1 and by means of Figure 16.3. The unit is shown in Figure 16.11 in raised position for maintenance in order to allow a view to the ink roller and the substrate. In operation mode, the ink roller and the substrate are closer to each other with a gap in the range of 0.3–0.6 mm.

16.5.3 Inking Units

Both of the described printing head types include an appropriate inking unit, a roller inking unit for the IR-transparent inks (Figure 16.12), and a ribbon inking unit for the IR-absorptive inks (Figure 16.13). The machine concept contains the flexibility to use each inking unit module on each one of the four scanline positions in order to vary between different inks or color sequences (Figure 16.9). The quality and function of the LIFT/LIBT printing units are highly dependent on a uniform and homogeneous ink layer on the donor surface of the converting roller or of the ribbon along the scanline. The most important design approach for both kinds of ink coating systems is the capability to generate a precisely defined, homogeneous, and isotropic thin ink layer at the printing zone.

There are several different kinds of classical inking concepts, each of them in use for industrial processes. For the ink transport toward the printing zone, a conventional "4/5 roller system" has been selected. In this concept, the first two rollers are acting as pond rollers with a small, thin adjustable gap for predosing and preforming the ink layer and ink volume (Figure 16.12). The third roller is equalizing the ink layer and is the handover roller for either the LIBT roller or the LIFT ribbon (Figure 16.3).

The machine requires quite thin ink layers (5–30 μm thick). An ink thickness deviation of even 1 μm or little more on the circumference of the inking roller or on the ink ribbon could already lead to a color density deviation on the printed substrate, which might be detected by the human eye. This indicates the challenge presented to the mechanical engineering, parts manufacturing, and assembling.

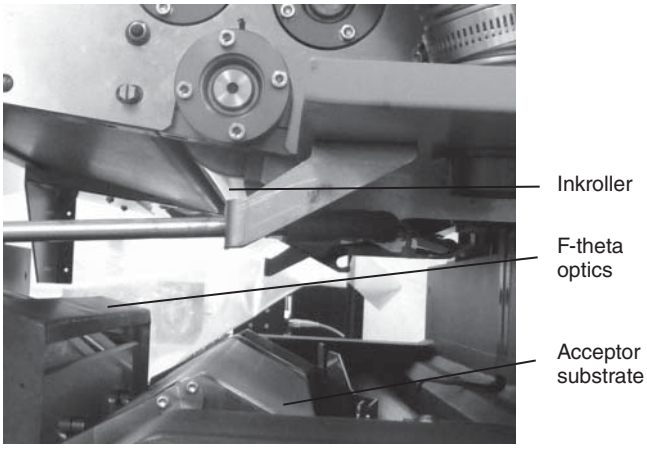

Figure 16.11 Printing unit for transparent inks lifted up for maintenance; in operation, the ink roller is positioned about 0.5 mm close to the substrate.

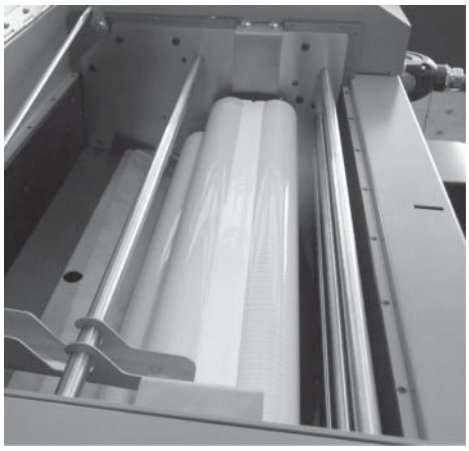

Figure 16.12 Roller inking unit for NIR-transparent inks.

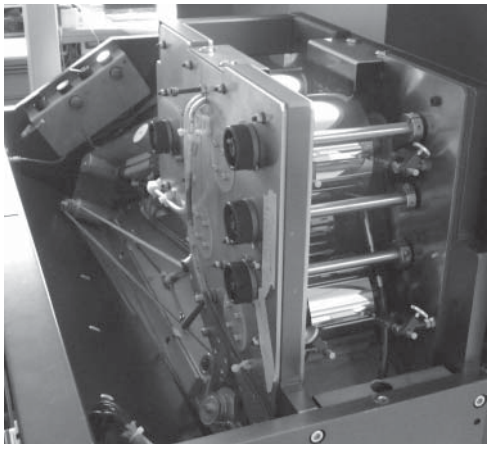

Figure 16.13 Ribbon inking unit for NIR-absorptive inks.

To have the chance to adjust to different rheological ink behavior in the inking unit, a high level of flexibility in roller gap distances, drive speeds of the rollers, rotating directions, and ink flow volume was incorporated in the engineering and operating concept. Evidence of an imperfect ink distribution on the roller or ribbon surface are stripes, rings, clouds, and all other visible structures. Any anisotropic appearance of the ink on the surface of the carrier roller or ribbon would lead to unacceptable quality defects in the visual appearance of the final print. Summing up all the factors of physical, mechanical, or chemical origin, which influence the even ink laydown, is beyond the scope of this chapter. One major factor is the ink's complex viscosity, which takes into consideration the dynamical physical effects caused by changing shear rates during ink transport within the inking unit, that is, shear thinning effects in non-Newtonian fluids also named structural viscosity effects. As temperature and solvent content are major factors that influence the ink viscosity, the described machine and its inking units are equipped with viscosity sensors and were designed to operate with an automatic viscosity control system. According to the results and experience gathered during the trials and process development with the machine, each different kind

of ink or liquid to be printed or transferred by this machine requires its individual and specific set of operating parameters in the inking unit. This has to be taken into account for future concepts of LIFT/LIBT printing units, which will be designed for more than one single type of ink or material suspension.

16.5.4 Synthetic Approaches to the Absorption Layer of the LIBT Donor Surface

In the course of prior experiments, the absorption layer of the donor roller was realized by use of various types and qualities of carbon black as absorbing agents. The carbon black pigments were dispersed in heat-resistant matrices and afterward used to cover the donor. However, these layers were rapidly worn out by the mechanical stresses as exerted by sudden and steep local temperature changes and by cavitation erosion caused by the collapses of jet driving vapor bubbles. Service life has been restricted to several hours of operation only, and the rollers had to be exchanged after that. More wear-resistant converter layers with considerably prolonged service life have been designed by synthesizing highly efficient organic NIR absorbers, which – after dispersing them into high-temperature-withstanding silicon resins – have been equally spread as an even and isotropic layer over the cylindrical surface of the converter roller. Afterward, this coating was burned at a temperature of 120 °C over a period of 4 h in a homogeneously air-vented oven.

16.6 Print Experiments and Results

In order to study the LIFT/LIBT transfer process in the regime of high pulse repetition rates and at high scan speeds and in order to demonstrate the functionality of the print unit concept, the first printing experiments were run with one print unit (one color) only. During these tests, various customary paper webs and foil substrates as well as different ink materials were evaluated. The range of process parameters of the machine and the ones regarded as most practical are listed in Table 16.2. Some of these parameters (such as the laser power, web tension, web speed, ink viscosity) could be varied and controlled directly during the running print process and have been optimized for every ink–substrate combination by on-the-fly reference to print results.

They have been measured in real time and displayed at the monitor. Viscosity readings were taken with a 3 mm Frickmar-efflux cup at 20 °C and have been converted to dynamical viscosity. Automated viscosity control was performed with a vibrating rod device. The print results show that the LIFT/LIBT process with an acousto-optical-modulated cw-laser beam is well suited to transfer inks with different pigment sizes, attributes, and features such as habitus, coatings, and organic/inorganic nature. Tests have been run with highly scattering TiO_2 pigmented inks as well as inks with large and flaky pigment sizes of the leaving and nonleaving type for metallic or mother-of-pearl effect as well as trials with various types of widespread, standard pigmented inks used in bulk quantities all over the gravure- and flexo-, décor- and packaging-printing industries worldwide. Most prominent among the standard inks for decor and

Table 16.2 Parameter ranges of the machine and of used consumables.

Parameter	Range	Mainly used setting (best results)
Area screen resolution	300–600 dpi	600 dpi
Laser power (pulse peak)	0–154 W	Gray scale value dependent
Pulse repetition rate PRR	5–25 MHz	23.6 MHz
Pulse width (FWHM)	16 ns to several microseconds	16 ns
Scan speed laser focus	400–2116 m/s	1000 m/s
Line frequency	0.5–2 kHz	0.943 kHz
Web speed	0–5 m/s	2.4 m/s
Gap donor roller/substrate	0–1500 µm	350–600 µm
Web tension paper	0–300 N	50–150 N (300 µm)
Web tension thin foils	0–300 N	30–70 N
Sort of ink (water-based)	Rotogravure décor ink with organic pigments and casein binders or with pearlescent pigments and casein binders	8 < Visc < 20 mPa s Ink pigment size 5–100 µm
Sort of Ink (solvent-based)	PVB ink, CN ink	8 < Visc < 20 mPa s
Types of substrate/thickness	Décor paper	60 µm
	LWC paper	70 µm
	OPP film, PE film	90, 50 µm

packaging applications are water-dilutable decor inks based on casein as binding system, alcohol- or ester-based CN inks for packaging with various types of cellulose nitrate binders as well as polyvinyl butyral (PVB) inks for packaging, which are diluted with organic solvents as well (Figures 16.14 and 16.15).

All these inks may be tinted with both organic or inorganic pigments. Undesired side effects of the LIFT/LIBT process, affecting the quality of the print, have been observed, such as satellite drops sputtered on the substrate or haze and fog of the ink along the scanline, reappearing on the substrate and also drifting backward into the optics compartment. Parts of the haze condensation may have electrostatic origin. Whiskers due to electrostatic discharge may be occasionally discerned on the print. The charge-generating mechanism of the LIBT/LIFT elementary drop-generating process seems to be quite prone to parasitic charge accumulation by a very sudden material separation and hence depending on the material's work functions. CN-ink systems showed slightly more of these unwanted side effects (clouds of haze and whiskers) compared to the other inks.

To at least partly avoid these electrostatic effects, different additives were tested with moderate success.

Other types of additives to improve the rheology of the inks, thereby preventing the generation of satellite drops, were tried with considerable success. Further

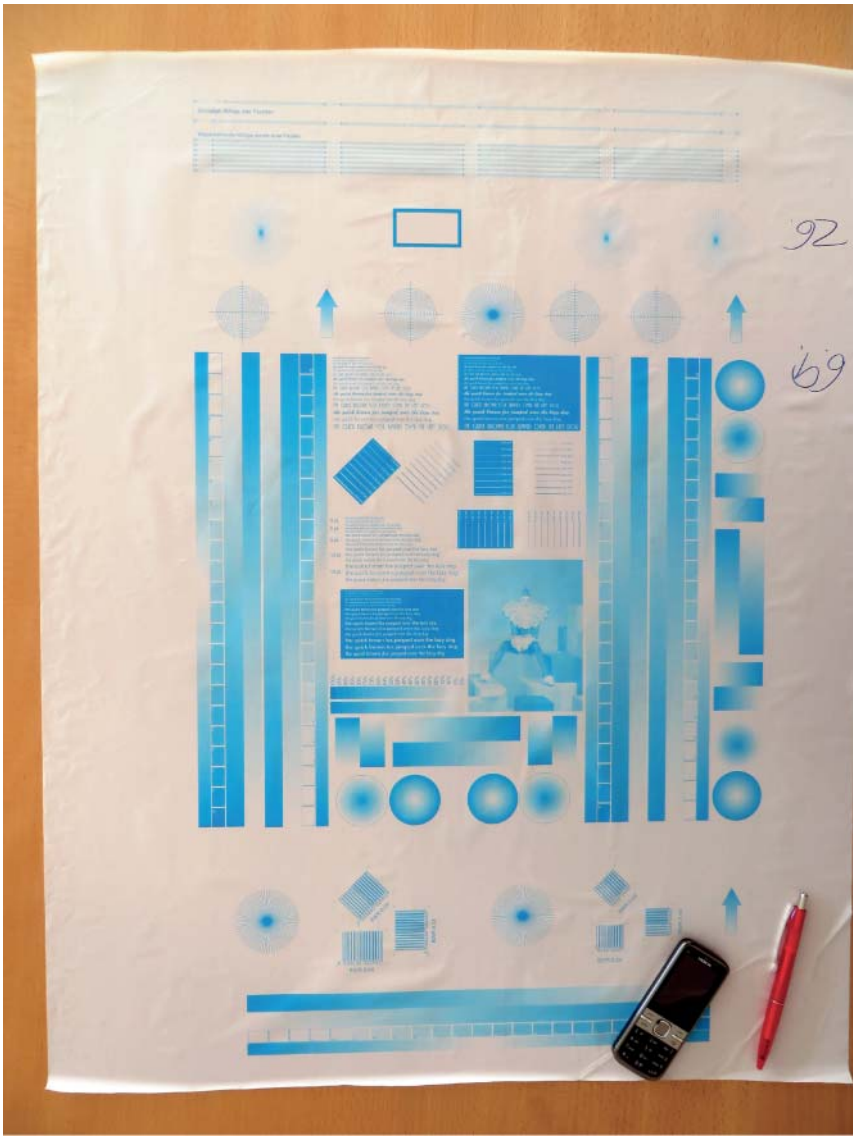

Figure 16.14 Test print example with PVB ink on OPP film, web size 630 mm, width of printed area 435 mm, length 730 mm, resolution 600 dpi, feeding speed 2.39 m/min, scan speed 1000 m/s, printing time 18 s for the complete sheet.

reduction of satellites, haze, and fog has been achieved by reducing the laser power to a level just above the process threshold. With all the aforementioned additions to and slight alterations of the base inks, the general principle was strictly observed, not to bring a new and special ink into play, but instead rely on the standard range of commonly used additives in common printing business with the aforementioned types of inks.

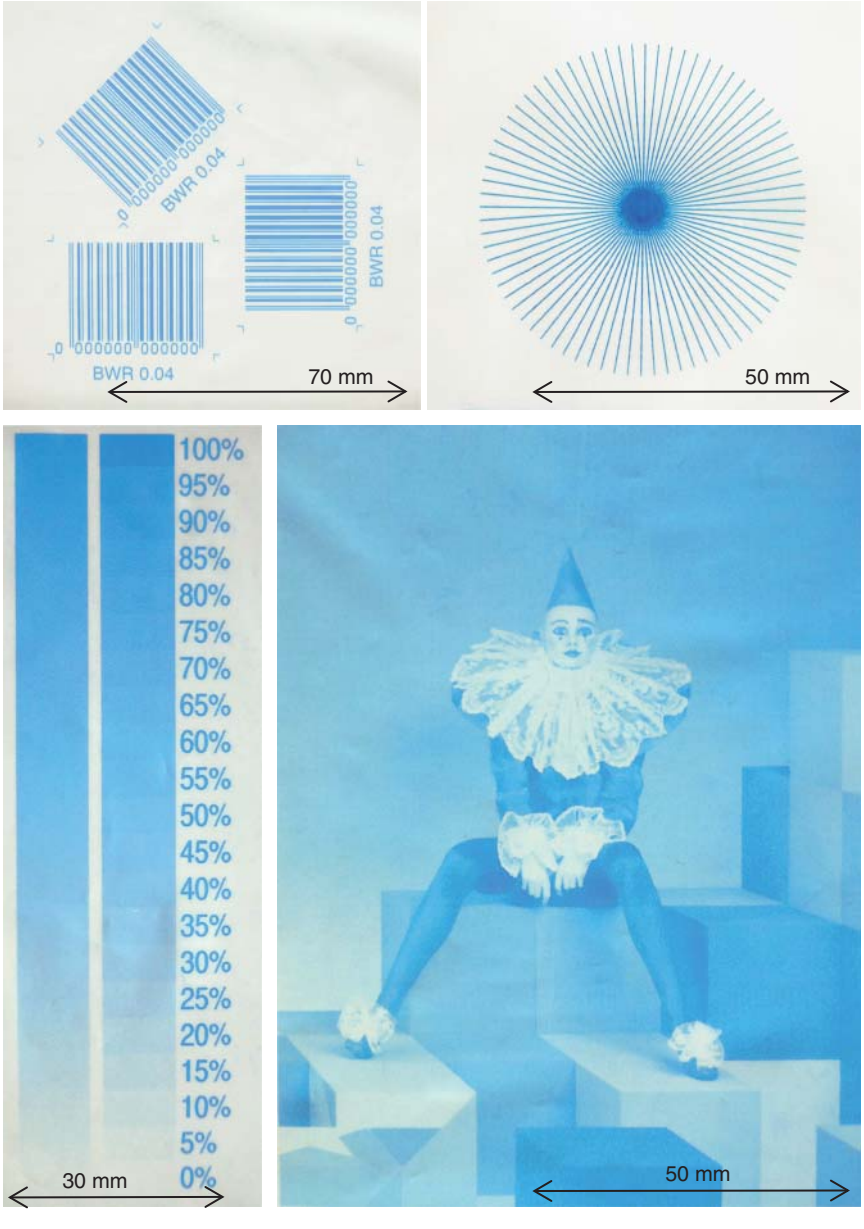

Figure 16.15 Details of the print example of Figure 16.14: bar codes with various orientations, line stars for resolution proof, continuous and stepped grayscales and a grayscale test image (600 dpi).

The best LIFT/LIBT results were realized with polyvinyl butyral (PVB) inks on OPP foil, when using drying-time-retarding additives and solvents. Optical densities of the printouts have been achieved as required for the printing industry (i.e., OD > 1.95 for magenta, OD > 2.5 for cyan). The distance between the ink roller and the substrate should be as small as possible in order to achieve optimized transfer results. For the test results shown in Figures 16.14 and 16.15, this distance was fixed at 0.5 mm, thereby leaving enough space between the ink roller and the running web to avoid any contact. The feed rate of the substrate was 2.39 m/min, the scan speed was 1000 m/s, and the modulation rate was 23.6 MHz.

A closer insight into the LIFT transfer process with modulated cw laser can be gained by analyzing the printing of lines along the scan direction. The fast modulation method of the high-power cw-laser beam allows the application of various time schemes in order to understand and optimize the LIFT/LIBT process. The question is, how to write a line in the scan direction with best precision and reproducibility of the image data input. Figure 16.16 shows several scanlines, one below the other. Dots printed by short modulated single pulses ($t = 42$ ns and $t = 84$ ns) occur for each scan at the same position of the scanline. This means their position is controllable. The length of the single pulses defines the amount of ink volume that is transferred by the droplet. The 84 ns long pulses generate dots with a larger diameter (dot size <100 μm) than the 42 ns long pulses (dot size <50 μm). The entire volume of ink transferred by these single pulses is collected in a single dot. Fine structures must be printed with short pulses.

For long "laser on periods," the dots are randomly distributed along the scanline with the exception of the first dots of the long periods, which are aligned accordingly to the rising edge of the "laser on period." This disruptive behavior

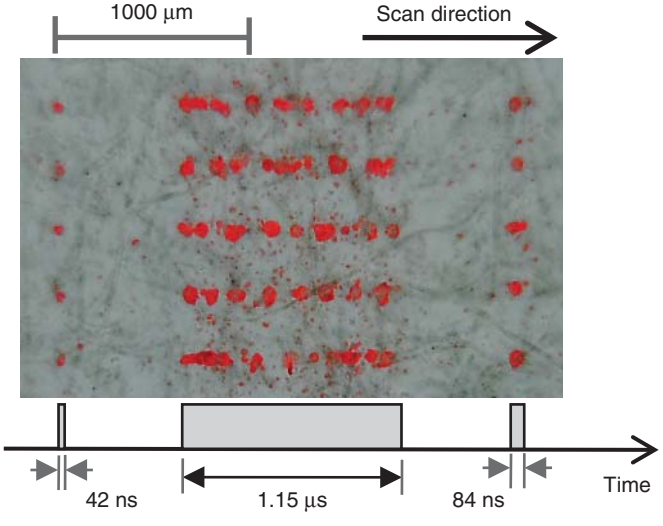

Figure 16.16 Effects of different durations of "laser on" periods: long "laser on" periods over some microseconds show uncontrollable separation of droplets; for single shots in the ns range, the dot size increases with the pulse length. The on-level of the AOM input signal was of equal height for all pulse lengths and "laser on" periods.

along the lines shows that the ink transfer is not simply correlated to the time pattern of the laser impact but is influenced by fluid dynamics and the dynamics of heat dissipation on the converter surface as well. As described in Section 16.7, the correct alignment and positioning of the transferred LIFT dots and the correct and precise reproduction of the grayscale values of an image require the development of appropriate modulation and timing algorithms for the laser beam, which must refer to the detailed physics of the elementary processes behind the transfer.

16.7 Discussion of Effects

16.7.1 LIFT Process with Continuous-Wave Laser Source and Fast Modulation

To understand and control the LIFT transfer process with a fast scanned and modulated cw-laser focus, we have to take into account the following aspects:

1) Due to the fast scan velocity of the laser beam within the range of 1000–2000 m/s, even a not pulse-modulated cw-laser beam has locally (at one point of the scanline) only a timely short impact resulting in a "single quasi laser pulse" at this point. The transient field of the fast-passing laser gives a pulsed energy input to the absorption layer where the pulse duration τ is approximately given by the speed and the diameter of the laser spot (i.e., $\tau = 60$ ns at 1000 m/s for a 60 µm spot size).
2) The timescale for excitation and energy impact is in the ns regime, whereas the transfer process itself, that is, the bubble and jet formation, takes 1–100 µs [3, 4]. On the timescale of the jet formation and transfer process, the energy impact to neighboring, closely spaced pixels along the scanline is done quasi simultaneously by the fast scanning laser beam. At a scan speed of 1000 m/s and with a screen resolution of 600 dpi (42 µm screen pitch), a line section of about 24 pixels can be activated per 1 µs.
3) In our case, the screen resolution is defined and limited by the achieved local precision of the power modulation of the scanned laser focus at a given scan velocity, that is, at $v = 1000$ m/s. Due to the fast acousto-optical modulation (see Section 16.3.1), we are able to control the positioning of the center of single dots with a screen resolution of 600 dpi (42 µm screen pitch for addressability of single pixels). The spot size of the laser beam (60 µm) and also the diameter of the printed dot may be even larger than 42 µm because in printing, an overlap of the dots is allowed, and for full-color applications, it is even necessary to avoid white, uncovered areas. The diameter of a printed dot depends mainly on the volume of the transferred ink and not directly on the screen resolution. The ink layer thickness on the ink roller has an important influence on the dot diameter.

In order to write continuous lines in the scan direction, tests were conducted to do this by writing with a "continuous laser on" mode by setting the laser modulation gray level permanently on a value above the threshold for the LIFT process

(Figure 16.17). However, the resulting bubble formation and the ink transfer are not as continuous as the laser beam, but show droplets and interruptions, which lead to an irregular pattern of separated dots along this line. This separation into droplets must be investigated by numerical modeling of the interaction between shock wave forces during bubble expansion and tension forces of the ink during bubble collapse (see Chapters 4 and 5). As a first approach to an explanation, we assume that the different timescales of the fast excitation by the laser (60 ns) and the slow transfer process (1 – 100 µs) result in a quasi-simultaneous start of the bubble formation over many pixels along the scanned line. Over a line section of a few mm, the ink is transferred quasi simultaneously. Tension forces inside of the flowing ink lead to a separation into single droplets of various sizes during bubble formation and collapse and during the transfer process between the ink roller and the substrate. The separations do not occur periodically along the scan direction, but rather randomly with a large spatial jitter (Figure 16.17, left side). Important parameters for this effect are the viscosity and rheology (elastic forces, creep compliance) of the ink, the scanning speed, the laser beam intensity, and the distance d between the donor and the acceptor. During this process, it is likely that not only the ink region, which is directly excited by the laser, is pushed away, but also, due to tension and elastic forces, ink from the surrounding area is taken off and contributes to a droplet.

To eliminate this random behavior of the droplet formation, an active on/off switching as well as power level grayscale modulation of the laser beam was investigated. The modulation signal was synchronized to the local position of the laser spot along the scanline (Figure 16.17, right side). The results show evidence that it is possible to realign the starting point of the droplet evolution by switching the laser beam off and on again in order to introduce controlled separations for the droplet formation while moving along the scan direction. For example, instead of line writing in scan direction with continuous "laser on" and with randomly droplet separation and irregular dots as shown in Figure 16.18, scanning with a "1-pixel on / 2-pixel off "- pattern leads to the periodical dot patterns of Figure 16.19. Due to the off time, less overall ink volume is

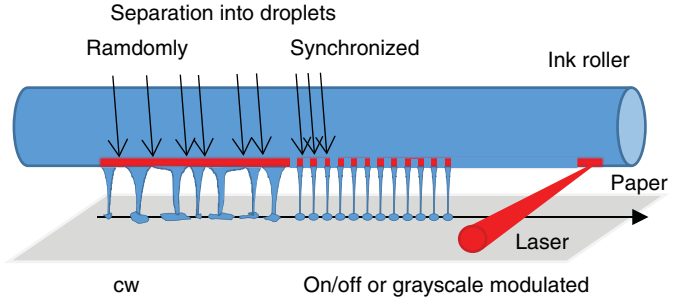

Figure 16.17 Line writing in scan direction with cw-"laser-on" mode compared to an on/off-modulated laser. At cw mode, an ink-layer stripe of a few millimeters length is quasi simultaneously transferred and separates due to tension forces of the ink randomly into droplets of various sizes. On/off modulation of the laser synchronizes the droplet separation with the pixel screen along the scanline.

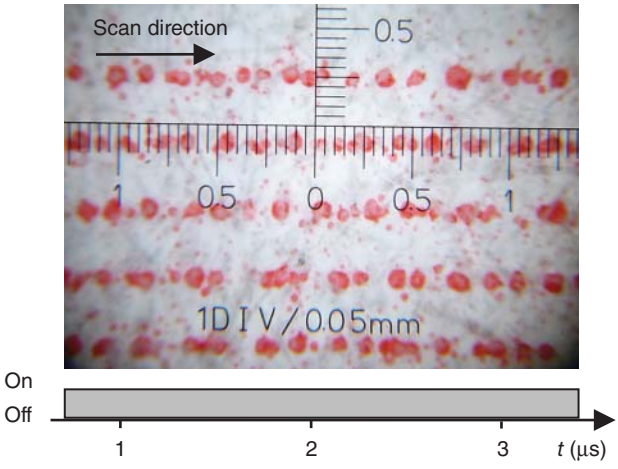

Figure 16.18 Line writing in scan direction with continuous "laser on" and $v = 1000$ m/s shows irregular patterns of dots along the scanline; a lot of small satellite drops are seen between the lines.

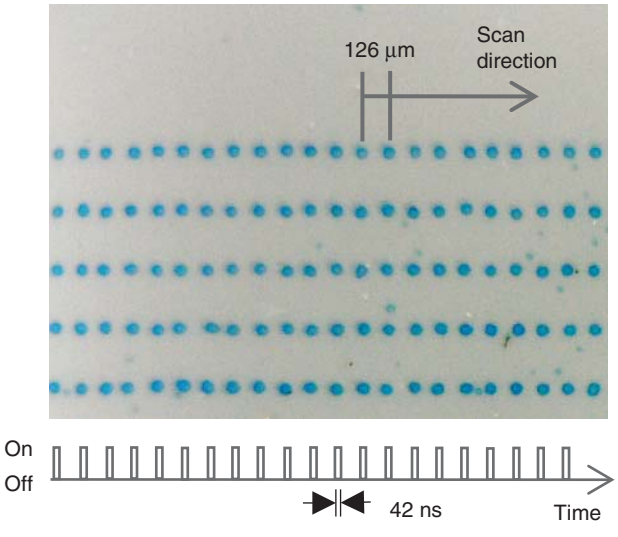

Figure 16.19 Pulsed laser operation leads to reproducible, separated single dots at defined position according to the screen, for example, line writing in scan direction with an one-pixel on/two-pixel off modulation shows regular patterns of dots.

transferred and the dot diameters (about 50 µm) are smaller than those shown in Figure 16.18. In addition, less satellite drops are generated between the lines.

16.7.2 Special Test Pattern to Study the Transfer Behavior at High Pixel Rate

To learn more about the conditions of the separation process, we tried to find out:

1) how long the laser pulse length may be at maximum, so that the whole ink volume of the corresponding laser excited line section is still flowing into only one single-transfer filament and one round spot;
2) when the spot starts to become elliptical;
3) when it will split into several dots.

As shown in Figure 16.20, a special data file (bitmap) was created, containing the following test pattern, which was repeated for statistic reasons each 30 pixels along the scanline: after a line with only a single "on pixel" (position marker function) and a few void lines for distance a line with 2 "on pixels" follows. After a gap, again a line with 1 "on pixel" (next position marker) and then a line with 3 on pixels was written.This scheme of alternating 1 "marker pixel" and n "on pixel" ($n = 2, \ldots, 20$) was continued up to $n = 20$ and allows to detect the following effects (under the geometrical conditions and with scan parameters of this experiment):

1) The printed single-pixel dots follow exactly the vertical line a) and represent a feasible marker line of the scan position.
2) For the printed line segments with $n < 8$, the transferred ink was collected in only one jet, resulting in one printed dot with increasing diameter according

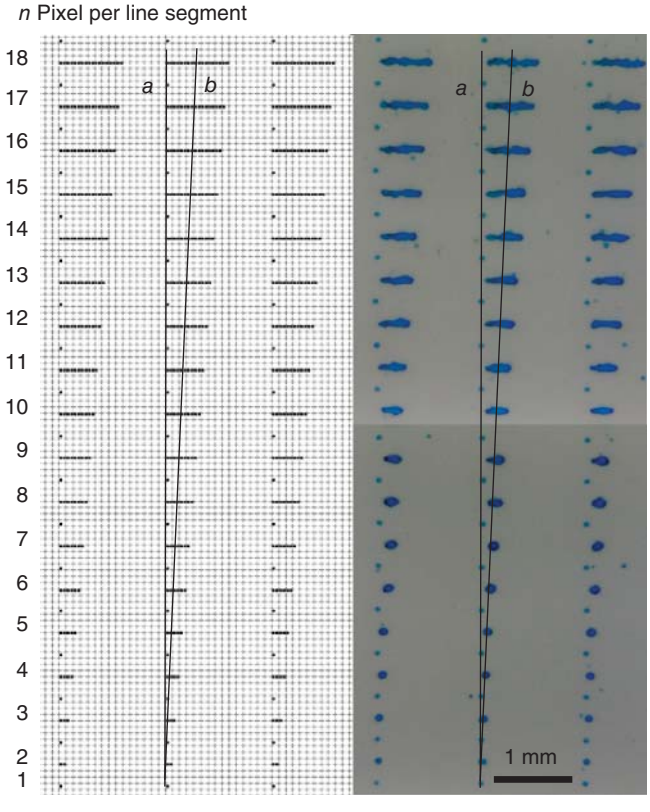

Figure 16.20 Test bitmap with increasing "on-pixel" line sections (left side) and print results (right side).

to the number of excited pixels and with linearly shifted position. The position of this dot is nearly exactly at the center of mass of each excited "laser on" line segment, in Figure 16.20 indicated by line (b). The shape of the dot remains still round.

3) For $8 \leq n \leq 11$, the printed dots become more and more elliptical. The homogeneity of the elliptical dots suggests that there is still only one common transfer jet collecting the ink of the whole line segment. The position is still at the center of mass of the bitmap line.
4) For $n \geq 12$, the printed dots start to form two and (for higher n) also more subspots (nuclei) along the scanline, probably due to the evolution of more than one transfer jet. These subspots have different sizes and are irregularly positioned along the line segment. For longer line segments, they separate into several nuclei. These experiments have been done with a scan speed of 1000 m/s, at 23.6 MHz. Other scan parameters and ink properties may lead to different bubble and jet formations and to other numbers of combined pixels. It would be helpful to study the transfer process by shadowgraphy directly on the machine in order to confirm these observations, but the scanline region is not accessible for such equipment.

However, for the case $n = 2$, similar experiments have been performed by Patrascioiu *et al.* at the University of Barcelona ([24] and Chapter 4). These experiments focused on the jet evolution and interactions during the LIFT transfer of a fluidic material with low viscosity in case of simultaneous excitation by two laser spots, which have been positioned on the donor substrate with only a short distance to each other. Shadowgraphs show the timely development of bubbles and transfer jets for different laser spot distances. The key result is that only one jet is created and only one dot is printed just at the position in the middle between the two laser spots (the center of mass), when their distance is small enough. This is consistent with the print result in Figure 16.20.

For an accurate reproduction of the image data, these jetting effects must be eliminated. The obvious way to avoid coalescence of several pixels is to print with spatially enough separated pulses. If the distance of two consecutive "laser on spots" is large enough, no interaction between the separately excited jets is observed and the print results show regular dots. This is the case for, for example, the "1 pixel on – 2 pixel off" pattern along the scanline, as already shown in Figure 16.19. In order to fill the gaps without jet interactions, the pixels between the on-pixels should be printed with enough timely separation, for example, in a second and a third scan process making multiple passes with the same laser beam or using simultaneously a multispot arrangement with enough distance of the spots.

16.8 Future Directions

LIFT/LIBT solutions in graphical art applications may find their niche in the current trends to functionalize printing products. Major trends driven by market demands are applications such as smart labels and packaging solutions with

integrated functions. In particular, the fabrication of printed organic electronics may open additional opportunities. Still there is a tough competition between the different fabrication methods, traditional and advanced ones, to establish themselves as major production techniques in those emerging product segments. Associations such as the OE-A (Organic and Printed Electronics Association) offer platforms [25] to learn about markets, requirements, and solutions. In the classical graphical art markets, digital printing techniques are entering more and more markets such as label printing or packaging printing. Still many of the special requirements of those applications are not suitably solved by the current digital printing techniques, for example, printing of pearlescent or metallic pigments with particle sizes of 2–100 μm. Here still indirect solutions such as hybrid production techniques with digital printing and conventional or semidigital transferring techniques for pearlescent or metallic printing are state of the art. As the "pain" of the unresolved customer requirements regarding digital printing of special inks is going on and additional requirements regarding functionalization of printed products are rising, this may open new opportunities to implement LIFT/LIBT solutions in the form of special printing units for fully digital hybrid production environments.

16.9 Summary

The Lasersonic® LIFT/LIBT process is suited to be used for fast, large-area direct-writing processes in industrial applications such as commercial digital printing. The physical properties of the laser-induced transfer process open new digital printing features, which are difficult to realize by other digital printing methods such as inkjet or Xerography. High area throughput can be achieved by using a high-power cw-laser beam, which is scanned at high speed (>1000 m/s) over the substrate. A fast modulation of this beam with a data rate of 20–25 MHz allows even at this speed for screen resolutions of 600 dpi. Large-area printing up to 2.6 m^2/min was demonstrated with common liquid inks on different common substrates. Inks with small (<1 μm) and large (100 μm) pigments could be transferred by this fast LIFT/LIBT process. The investigation of dynamic effects during the transfer of such liquid materials at high scan rates with simultaneous excitation of many pixels leads to a new understanding of how to operate the machine. Appropriate modulation time schemes such as the "1 pixel on – 2 pixel off scheme" with multiple passes are suited to achieve high-quality printing results. LIFT/LIBT solutions in printing applications may find their niche in the current trends to functionalize printing products and may be used to promote applications such as smart labels, packaging solutions with integrated functions and new upcoming function requirements on printing products.

Acknowledgments

The authors give special thanks to the project team of the DI Project AG, namely Peter Daetwyler, René Hartmann, Rudolf Griebel, Christian Nussbaum, Marcel Rossier, Andreas Brockelt, and Lorenz Schuler, for their restless work, precious contributions, ideas, and their commitment for this Digital Imaging project. Also special thanks go to Craig Arnold, Princeton University, Pere Serra, University of Barcelona, and Philippe Delaporte, Marseille University, for many discussions on the dynamics of the liquid ink transfer.

References

1 Young, D., Auyeung, R.C.Y., Piqué, A., Chrisey, D.B., and Dlott, D.D. (2001) Time-resolved optical microscopy of a laser-based forward transfer process. *Appl. Phys. Lett.*, **78** (21), 3169–3171.
2 Young, D., Auyeung, R.C.Y., Piqué, A., Chrisey, D.B., and Dlott, D.D. (2002) Plume and jetting regimes in a laser based forward transfer process as observed by time-resolved optical microscopy. *Appl. Surf. Sci.*, **197**, 181–187.
3 Brown, M.S., Kattamis, N.T., and Arnold, C.B. (2011) Time-resolved dynamics of laser induced microjets from thin liquid films. *Microfluid. Nanofluid.*, **11**, 199–207.
4 Duocastella, M., Fernandez-Pradas, J., Morenza, J., and Serra, P. (2009) Time-resolved imaging of the laser forward transfer of liquids. *J. Appl. Phys.*, **106** (8), 084907.
5 Duocastella, M., Fernandez-Pradas, J., Serra, P., and Morenza, J. (2008) Jet formation in the laser forward transfer of liquids. *Appl Phys A*, **93** (2), 453–456.
6 Minsier, V., De Wilde, J., and Proost, J. (2009) Simulation of the effect of viscosity on jet penetration into a single cavitating bubble. *J. Appl. Phys.*, **106** (8), 084906.
7 Colina, M., Duocastella, M., Fernandez-Pradas, J., Serra, P., and Morenza, J. (2006) Laser induced forward transfer of liquids: study of the droplet ejection process. *J. Appl. Phys.*, **99** (8), 084909.
8 Serra, P., Duocastella, M., Fernández-Pradas, J., and Morenza, J. (2009) Liquids microprinting through laser-induced forward transfer. *Appl. Surf. Sci.*, **255**, 5342–5345.
9 Duocastella, M., Fernández-Pradas, J., Morenza, J., and Serra, P. (2010) Sessile droplet formation in the laser-induced forward transfer of liquids: a time-resolved imaging study. *Thin Solid Films*, **518**, 5321–5325.
10 Unger, C., Gruene, M., Koch, L., Koch, J., and Chichkov, B. (2011) Time-resolved imaging of hydrogel printing via laser-induced forward transfer. *Appl. Phys. A*, **103**, 271–277.

11 Browning, I. and Johnson, P. (1974) Recording method and apparatus utilizing light energy to move record forming material onto a record medium. US Patent 3.798.365, filed July, 14, 1969, granted March 19, 1974.

12 Kohyama, M. (1991) Laser actuated recording apparatus. US Patent 5.021.808, filed 1989, granted 1991.

13 Maximovski, S. and Radutzki, G. (2000) Method of ink-jet printing and an ink-jet printing head for carrying out the method. US Patent 6.056.388, filed 1995, granted 2000.

14 Maximovski, S. and Radutzki, G. (2001) Printing method and printing device for realizing the same. US Patent 6.270.194 B1, filed 1997, granted 2001.

15 Lehmann, U. and Meyer, D. (2006) Aurentum GmbH. US Patent 7.154.522 B2.

16 Lehmann, U. (1999) Aurentum GmbH, Druckverfahren und Einrichtung zu dessen Durchführung. DE Patent 19746174 C1.

17 Lehmann, U. (2003) Aurentum GmbH, Method of printing and corresponding print machine. US Patent 2003/0156178.

18 Ferchner, H.G., Gerner, H., and Lehmann, U. (2006) Aurentum Innovationstechnologien GmbH: Digitale Druck und Strukturierungsverfahren. 18th Workshop "Mikrotechnische Produktion - ProPolyTec – Produktionstechnik für die Polymerelektronik", Fürth 2006, published in "Abschlussbericht BMBF Project ProPolyTech", editor G. Klink, Fraunhofer IZM, Munich, p. 103.

19 Hennig, G., Baldermann, T., Nussbaum, C., Rossier, M., Brockelt, A., Schuler, L., and Hochstein, G. (2012) Lasersonic® LIFT process for large area digital printing. *J. Laser Micro/Nanoeng.*, **7** (3), 299–305.

20 Homepage Durst Phototechnik AG http://www.durst.it/index.php/durst/article/digital-decoration-die-stille-revolution (accessed 25 October 2016).

21 http://eur-lex.europa.eu/legal-content/EN/ALL/?uri=CELEX%3A32011R0010 (accessed 25 October 2016).

22 http://ec.europa.eu/growth/tools-databases/tris/de/search/?trisaction=search.detail&year=2016&num=333 (accessed 25 October 2016).

23 https://www.gesetze-im-internet.de/bundesrecht/bedggstv/gesamt.pdf (accessed 25 October 2016).

24 Patrascioiu, A., Florian, C., Fernández-Pradas, J.M., Morenza, J.L., Hennig, G., Delaporte, P., and Serra, P. (2014) Interaction between jets during laser-induced forward transfer. *Appl. Phys. Lett.*, **105** (014101).

25 Homepage Organic and Printed Electronics Association http://www.oe-a.org/home (accessed 25 October 2016).

17

LIFT of 3D Metal Structures

Ralph Pohl[1], Claas W. Visser[2], and Gert-willem Römer[3]

[1] Demcon B.V., Institutenweg 25, 7521 PH Enschede, The Netherlands
[2] Harvard University, John A. Paulson School of Engineering and Applied Sciences, Cambridge, MA 02138, USA
[3] University of Twente, Department of Mechanics of Solids, Surfaces & Systems (MS[3]), Chair of Laser Processing, Drienerlolaan 5, 7522NB, Enschede, The Netherlands

17.1 Introduction

This chapter presents and discusses detailed aspects of pure metal laser-induced forward transfer (LIFT) printing of 3D (micro)structures as opposed to the discussions of LIFT of various other materials under the framework of printing 3D (see Chapters 11, 13, 14, and 16) or 2D and $2\frac{1}{2}$D structures (see Chapters 8 and 11). In this chapter, 3D structures are defined as freestanding, out-of-plane (micro)structures, such as 3D stacks. Furthermore, here it is assumed that these structures are created by repeating the LIFT process over the same location by the stacking of liquid droplets, see Figure 17.1a. Note that LIFT of solid-phase metal layers or pastes, see Figure 17.1b and Chapter 8, can also be applied to create 3D structures, as is illustrated in Figure 17.2, examples of which are discussed in Chapter 11. However, this chapter addresses only pure metals, which have distinct advantages in terms of properties such as strength, conductivity, and corrosion rate.

Until now, LIFT of 3D (micro)structures of (pure) metals has been achieved by research groups from The Hebrew University of Jerusalem in Israel [3–7] and research groups from the University of Twente in the Netherlands [1, 8–12]. A wide range of structures and devices were demonstrated. However, LIFT of metals suffers from several problems, which still limit its application to printing 3D (micro)structures. First, LIFT of metals suffers from "debris," that is, besides ejection of a (main) droplet, the process suffers from "fragments" originating from the donor, which deposit on the (micro)structure being printed, as well as around it, on the receiver. Second, a prerequisite for the printing of 3D (micro)structures is that the droplet must be deposited close (< 1 μm) to its targeted landing position on the receiving substrate or the previously deposited droplets. Unfortunately, the directionality of the LIFT-ejected metal droplet and, as a result, the geometrical accuracy of the deposits are rather poor. That is, unless the donor is brought into very close proximity, typically a few

Laser Printing of Functional Materials: 3D Microfabrication, Electronics and Biomedicine,
First Edition. Edited by Alberto Piqué and Pere Serra.
© 2018 Wiley-VCH Verlag GmbH & Co. KGaA. Published 2018 by Wiley-VCH Verlag GmbH & Co. KGaA.

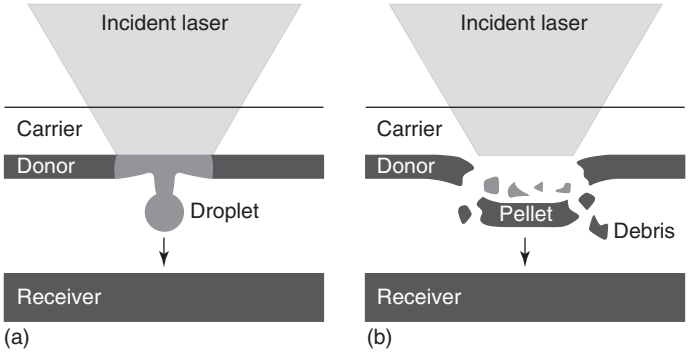

Figure 17.1 Schematic representation of LIFT, where a focused laser (a) melts the donor layer resulting in droplet formation or (b) transfers a solid-phase pellet. (Pohl *et al*. 2015 [1]. Reproduced with permission of Springer.)

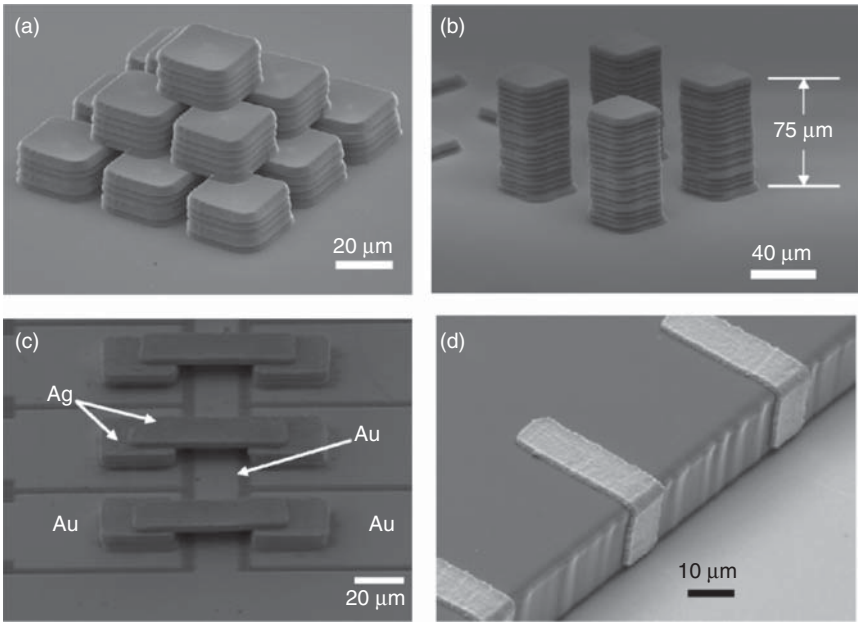

Figure 17.2 SEM images corresponding to examples of 3D microfabricated structures produced by LIFT of *solid*-phase metal layers or *pastes* (or the like). (a) Printed pyramid stacks. (b) Printed vertical interconnects generated by repeated solid transfers. (c) Crossover interconnects made by combining the printing of vertical stacks capped with freestanding crossovers. (d) Folded interconnects. (Piqué *et al*. 2016 [2]. Reproduced with permission of IOP.)

tens of micrometers, to the receiving substrate [5]. The geometrical accuracy of LIFT of metals is also limited by the relatively high surface roughness of the printed structures, which is about one order of magnitude smaller than the diameter of an ejected droplet. This roughness can be mainly attributed to the solidification phenomena of the droplet upon impact of the (still liquid) droplet on the previously deposited droplet(s). Last, but not least, in some cases, LIFT

of metals may be hindered by poor adhesion between deposits and/or between a first deposit and the receiving substrate. Good adhesion between the deposited and subsequently stacked droplets is required for dense, mechanically strong, and electrically conductive 3D (micro)structures.

Therefore, in the remainder of this chapter, first, the basic aspects of metal LIFT are presented, which will unveil the physical origin of the aforementioned problems. These basic aspects include the characteristics of the ejection of the donor material at different fluence levels/regimes, the origin of debris, and last, but not least, droplet impact and solidification. Next, in Section 17.3, the properties of LIFT-printed freestanding metal pillars are discussed, including the reproducibility of the process, the mechanical properties, and the electrical properties. Finally, in Section 17.4, existing and potential applications of (pure) metal LIFT-printed pillars are presented and discussed.

17.2 Basic Aspects of LIFT of Metals for 3D Structures

The results presented in this chapter were obtained with two laser setups of which the main characteristics are summarized in Table 17.1. The two setups mainly differ in the pulse duration and spot size. The wavelengths of the two systems are nearly equal, and therefore, no processing differences due to this quantity are expected. Despite the differences, both groups using the setups targeted debris-free printing. Due to the relative novelty of (pure) metal LIFT printing of 3D (micro)structures, only a few metals, namely gold, copper, platinum, and aluminum, have been investigated by the two research groups. However, this does not necessarily exclude other pure metals or metal alloys to be used for metal LIFT printing of 3D (micro)structures.

The governing physics related to the ejection phenomena are still under debate [13–17]. Nevertheless, (pure) metal LIFT of 3D (micro)structures is typically performed at laser fluence levels just above the "transfer threshold fluence" of the donor layer, that is, the smallest fluence level at which ejection of the donor material occurs. For these relatively low fluence levels, three different ejection phenomena have been reported, depending on the thickness of the donor layer and the laser pulse duration, namely:

Table 17.1 Laser system and processing parameters.

No.	Research group	Laser source	Wavelength (nm)	Pulse duration (ps)	Focal spot diameter (μm)	Fluence (mJ/cm^2)
1.	Hebrew University of Jerusalem, Israel	Freq. doubled Nd:YAG	532	400	4–32	≈740–920
2.	University of Twente, The Netherlands	Freq. doubled Yb:YAG	515	6.7	16.6 ± 1.2	≈314–480

1) the formation, and subsequent breakup, of a liquid metal jet, during nanosecond LIFT [10, 18],
2) the formation of a so-called thermally induced nozzle, during picosecond LIFT [5],
3) and the ejection of a so-called cap of liquid donor material, during picosecond LIFT [9].

All these ejection regimes are suitable for (pure) metal LIFT of 3D (micro) structures [5, 10]. The third regime was investigated in detail, which will be discussed in the next subsection. Next, the velocity of these donor ejections is discussed, followed by the origin of debris and droplet impact and solidification.

17.2.1 Ejection Regimes of Pure Metal Picosecond LIFT

Figure 17.3 shows the typical ejection dynamics of a 200 nm copper film at different fluence levels, using laser system 2, listed in Table 17.1 [8, 9, 12]. For low fluence levels between 320 and 600 mJ/cm^2, the ejection of a hemispherical-shaped "cap" was observed, see Figure 17.3a–c. This fluence regime is referred to as the "cap"-ejection regime in the following. For fluence levels between 600 and 740 mJ/cm^2, "jet ejection" was identified. These jets were characterized by a narrow jet, protruding from an ejected cap, see Figure 17.3d,e. For higher fluence levels, that is, over 740 mJ/cm^2, a cloud (or spray) of particles was observed, see Figure 17.3f,g. Therefore, these ejections were referred to as "spray ejection."

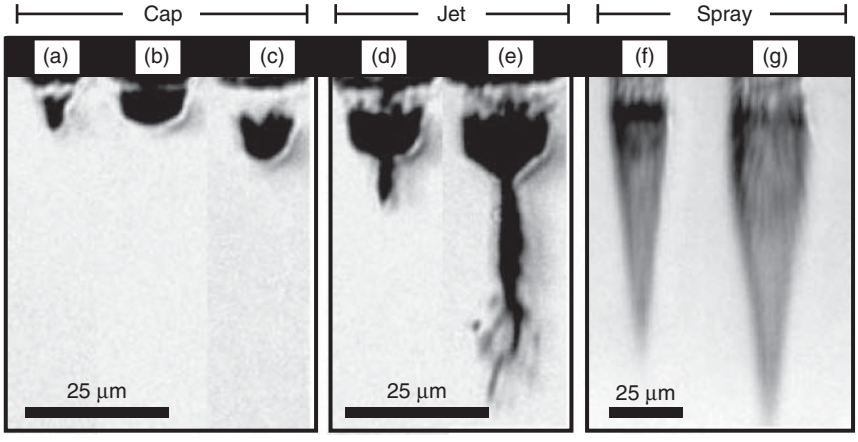

Figure 17.3 Ejection of a 200 nm copper film, visualized 125 ns after the incident laser pulse using laser system 2, listed in Table 17.1 . Images (a–g) correspond to increasing fluence values of 314, 392, 480, 660, 864, 1060, and 1576 mJ/cm^2, respectively. The black bar (not to scale) at the top of the images schematically shows the location of the donor layer. Images (a–c) illustrate the cap-ejection regime observed at low fluence levels; (d,e) show the formation of a jet from the apex of the cap at intermediate fluence levels, and (f,g) show the ejection of a fast copper spray. In image (g), some droplets are visible as lines, as their high velocity results in strong motion blur, as the tip speed is 700 m/s. (Pohl *et al*. 2015 [11]. Reproduced with permission of American Physical Society.)

Further insights into the driving mechanisms of the observed ejection regimes were gained from numerical temperature simulations, including a two-temperature model [11]. The modeling was used to estimate the temporal evolution and spatial distribution of the electron and lattice temperatures in the donor layer. Based on the temperature simulation results, the observed ejection regimes (cap, jet, spray) were found to be related to phase changes within the donor layer. It was claimed that, in the cap-ejection regime, the relaxation of elastic stresses within the melted donor film are the driving mechanism of ejection of the donor material. Further, it was reported that in both the jet- and spray-ejection regimes, the expansion of a vapor bubble is the driving mechanism of the ejection process.

17.2.1.1 Velocity of the Ejected Donor Material

In general, the velocity of the ejected donor material determines the morphology of the deposit on the receiving substrate or on prior deposited material, see Section 17.2.2. Therefore, the velocities of copper and gold ejections were experimentally determined from numerous observations such as in Figure 17.3. Figure 17.4 shows the measured ejection velocities for copper and gold donor layers. The graphs also include the velocity estimated by a simple model, based on the energy balance of the absorbed laser energy and the kinetic energy of the ejections [11]. The trend of the experimental results was found to be consistent with the calculated velocity values [11]. The graphs show that a minimum ejection velocity of about 20 m/s was found. This value was compared to the Weber number (We), indicating whether inertia or surface tension is dominating the ejection of the donor material from the liquified donor layer [19], see also Section 17.2.2. It was shown that for droplets with an ejection velocity of about 20 m/s, the Weber number corresponds to $We \approx 1$. For smaller velocities, the Weber number would be $We < 1$, implying that surface tension dominates over the inertia of the droplet. That is, for $We < 1$, the melted donor layer will retract and no ejection will occur. This is in agreement with the measured velocities, see Figure 17.4. Based on these results, it was also claimed that the Weber number can be used to quantitatively determine the ejection threshold fluence and vice versa, see also Section 17.2.2.

The insights gained earlier allow for the selection of proper processing parameters, which in turn allows for (a more) controlled deposition of micron-sized metal droplets relevant for 3D printing. That is, not only the first two ejection phenomena mentioned on page 408, but also cap ejection, characterized by its specific range of achievable droplet sizes and velocities, can be exploited for metal LIFT printing of 3D (micro)structures.

17.2.1.2 Origin of Fragments in Cap-Ejection Regime

Applying fluence levels in the cap-ejection fluence regime allows to control the velocity and size of droplets but was found to suffer from the creation of additional small droplets, next to the ejected cap [9]. That is, not only a single droplet is ejected from the donor layer, but also multiple smaller droplets, also referred to as "fragments" or "satellites," are ejected. As a result, LIFT printing exploiting the cap regime will result in debris on the receiver around the main

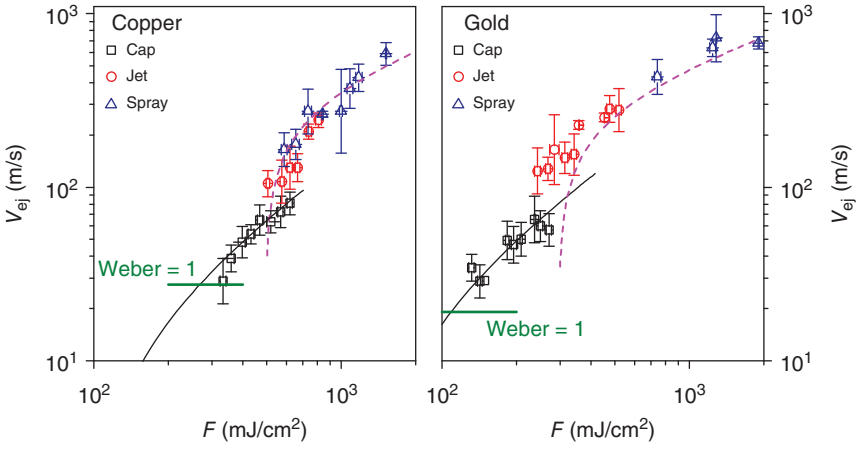

Figure 17.4 Experimentally determined and calculated velocity of LIFT ejections, as a function of laser fluence, using laser system 2, listed in Table 17.1. (a) 200 nm copper donor layer, (b) 160 nm gold donor layer. The different markers indicate the measured velocities of the three ejection regimes corresponding to the regimes in Figure 17.3. The short horizontal line in the lower left indicates the predicted minimum velocity corresponding to a Weber number of $We = 1$. The curved solid lines show the calculated cap-ejection velocity. The curved dashed line indicates the calculated velocities of ejections in the jet- and spray regime. (Reprinted figure with permission from Ref. [11]. Copyright (2015) by the American Physical Society.)

deposit and therefore also on the structure being printed. In order to unveil the origin of these undesired satellites, the ejection dynamics during cap ejection were recently studied in more detail [9].

To this end, high-speed imaging was employed to visualize the ejection process of a 200 nm copper layer, see Figure 17.5. The cap ejections were captured at two time instances of 50 ns (top row in Figure 17.5) and 400 ns (bottom row in Figure 17.5), with respect to the time instance of the first visible deformation of the donor layer. It was found that the initially well-defined cap ejections are contracted, but many relatively small droplets are observed at the second time instance, that is, after 400 ns. Typically, those observations consisted of a main droplet, which was identified as the contracted cap, and additional smaller droplets. The latter were referred to as "satellites," which are indicated by white arrows in Figure 17.5d (bottom row). It should be noted in Figure 17.5d (top row) that after 50 ns, the ejected cap seems to be partly attached to the donor layer by thin "threads." These threads are indicated in Figure 17.5d (top row) by white arrows. The formation of these threads was frequently observed during the experiments. Remnants of these threads were also found in the postmortem SEM images of the ejection crater in the donor layer, see Figure 17.6. These kinds of thread formations are often discussed in the context of capillary thinning and breakup, referred to as *necking* [9, 20]. Careful statistical analysis of numerous images such as in Figure 17.5 was performed. It was claimed that the number of observed satellites correlates to the number of threads visible along the rupture of the rim in the donor layer [9]. From these results, it was concluded that origin of the observed satellites is an in-flight phenomenon, caused by the breakup of

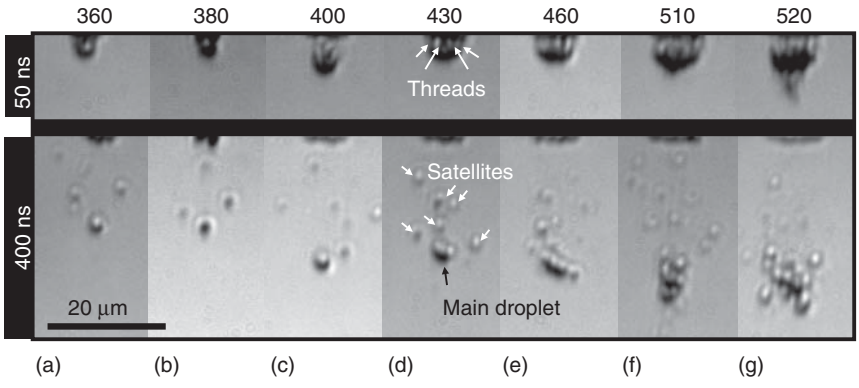

Figure 17.5 Cap-ejection events of a 200 nm copper donor layer at different fluence levels, using laser system 2, listed in Table 17.1. The events were captured at time instances of 50 ns (top row) and 400 ns (bottom row) with respect to the time instance of the first visible deformation of the donor layer. In image (d), top row, liquid threads between the donor layer and the cap during the ejection process are indicated by arrows. The time instance of 400 ns shows multiple droplets, which are identified either as satellites or as a main droplet. Here, the main droplet is assumed to be the contracted droplet of the ejected cap. (Reprinted figure with permission from Ref. [9]. Copyright (2015) by Pohl.)

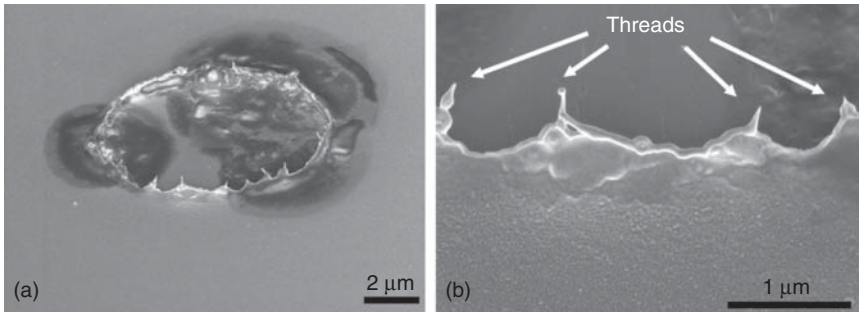

Figure 17.6 SEM images of the ejection crater in a 200 nm thick copper donor layer obtained at laser fluence of 444 mJ/cm^2, corresponding almost to the fluence level shown in Figure 17.5d, using laser system 2, listed in Table 17.1. (a) Tilted view (45°) of the ejection crater. (b) Close-up of the rim formation at the edge of the crater and indications of solidified liquid threads along the rim. (Reprinted figure with permission from Ref. [9]. Copyright (2015) by Pohl.)

liquid threads. It was further concluded that threading during cap ejection cannot be avoided entirely, but only be minimized. Nevertheless, the cap-ejection regime was still found to be of high interest for printing applications, as will be discussed in more detail in Section 17.3.

17.2.2 Droplet Impact and Solidification

The impact and solidification of a droplet on a receiver determine the morphology and size of the deposit. Therefore, these two aspects are discussed here in more

detail, as a function of the fluence levels applied and the velocity of the ejected donor material.

It was reported by several authors [13, 17, 22–28] that for fluence levels just above the ejection threshold of the donor material, spherical solidified droplets are typically found on the surface of the receiving substrate, as shown in Figure 17.7a. Moreover, intermediate fluence levels were found to generate disk-like droplets on the surface of a receiver, as shown in Figure 17.7b,c. In addition, toroids [17] and the fragmentation of droplets [13, 29] were reported, whereas splashing was only scarcely observed. For even higher fluence levels, a transition occurs toward the spray ejection regime, in which many similarly sized droplets are ejected and deposited. Still, each of these droplets was found to solidify as an individual sphere, disk, or toroid as shown in Figure 17.7d and also reported by Banks *et al*. [17].

As discussed on page 409 in Section 17.2.1, ejection of donor material will only occur if the inertia of the ejected material exceeds the surface tension of the liquified donor layer, that is, if the corresponding Weber number is $We > 1$. For a donor layer with a thickness d, density ρ, surface tension σ, and ejection velocity V_{ej}, the Weber number reads

$$We_{ej} = \frac{\rho\, d\, V_{ej}^2}{\sigma} \tag{17.1}$$

Next, to determine the droplet shape during impact, an impact Weber number We_{im} was defined as

$$We_{im} = \frac{\rho\, D_0\, V_{im}^2}{\sigma} \tag{17.2}$$

in which the droplet diameter D_0 is generally one order of magnitude larger than the film thickness d. If the effect of air drag is neglected, and it is assumed

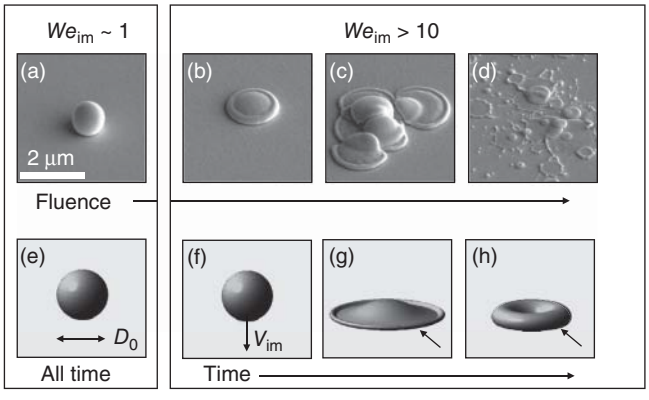

Figure 17.7 Shapes of deposits as a function of the laser fluence, impact Weber number We_{im}, and time. SEM images (a–d) show solidified droplets deposited on a copper-coated surface, for laser fluence levels of 380, 440, 630, and 820 mJ/cm^2, respectively, using laser system 2, listed in Table 17.1. Figures (e–h) show numerical simulations of impact dynamics onto nonwetting surfaces. For numerical details, see [21]. (Visser *et al*. 2015 [12]. Reproduced with permission of John Wiley & Sons.)

that $V_{im} = V_{ej}$, a typical impact Weber number of $We_{im} \approx 10$ is found. For these low Weber numbers, droplets hardly spread during impact [30] as shown in Figure 17.7e and thus could only solidify in a spherical shape. Since fluence levels just above the ejection threshold also correspond to the smallest droplets [13, 17, 22–28], increasing the printing resolution using smaller droplets and control of the droplet shape were found to be conflicting requirements [12].

Further, it was shown that for higher laser fluence levels, the impact velocity increases, that is, $We_{im} \gtrapprox 10$. The resulting inertial impact under these conditions is illustrated in Figure 17.7f–h. An additional requirement for inertial impact was found to be a high ratio of kinetic impact energy to viscous dissipation of the droplet. This ratio is described by the dimensionless Reynolds number $Re = \rho D_0 V_{im}/\eta$, in which η denotes the viscosity of the liquid donor material. In LIFT, the requirement that Re should be high is fulfilled since usually $Re \gtrsim 100$. Based on this conclusion, it was claimed that the initially spherical droplet spreads out into a disk, until a certain maximal spreading diameter is reached as shown in Figure 17.7g. Meanwhile, the edge of the droplet is contracting due to surface tension, which would result in the formation of an initially small "rim," as shown in Figure 17.7g. This rim keeps growing until the droplet reaches an essentially toroidal shape as shown in Figure 17.7h. Eventually, the droplet contracts back into a spheroid that can even bounce away from the surface [21]. Hence, the spheres, disks, and toroids observed in LIFT (see Figure 17.7a–d) correspond to droplet shapes for nonsolidifying impact.

Based on the aforementioned analysis, it was concluded that the particular shape of the solidified droplet depends on the solidification timescale with respect to the spreading and retraction timescales of the droplet. However, the research regarding the impact of liquid metal droplets is still under debate, and the solidification timescale cannot yet be calculated reliably. Therefore, an empirical approach is still required to optimize the droplet shape.

As discussed earlier, a trade-off exists between the shape of the solidified droplet, its impact location, and the formation of debris. Typical process parameters for LIFT lead to low ejection velocities at the ejection threshold fluence. For small Weber numbers, corresponding to these low velocities, this leads to the relatively clean deposition of droplets, forming spherically shaped deposits [13, 17, 22–28], which is expected to lead to generation of significant voids in LIFT-printed 3D (micro)structures. In contrast, cap-like ejections exhibit large(r) ejection velocities, and consequently, these droplets primarily solidify in a disk-like shape, as shown in Figure 17.7c. Pillars, which are presented and discussed in the next section, have been printed in this regime, since the solidification phenomena are reproducible, and the location of impact is robust with respect to the ejection location.

17.3 Properties of LIFT-Printed Freestanding Metal Pillars

In order to reliably and accurately fabricate pure metal 3D (micro)structures with LIFT, it is necessary that the spatial deposition of individual droplets

be controlled to a fraction of their diameter. In addition, the adhesion of the droplets to the receiving substrate and to each other must be sufficiently strong to withstand mechanical and thermal forces during printing and during use [2]. Therefore, in this section, the reproducibility of LIFT of pure metals is discussed when printing freestanding, out-of-plane, 3D microstacks (pillars). In addition, the typical metallurgical microstructures of these pillars, as well as their mechanical and electrical properties, are presented.

17.3.1 Reproducibility

If the laser parameters are accurately controlled, the geometrical accuracy (reproducibility) of pure metal LIFT structures, using picosecond laser sources and donor layers with a thickness of few hundred nanometers, is in the (sub)micrometer regime [9].

The reproducibility is illustrated in Figure 17.8a, showing high-aspect-ratio pillars, which were created by stacking of various numbers of copper LIFT droplets [12], using laser system 2, listed in Table 17.1. For the first number of droplets, the pillar growth rate was nonlinear, due to deviations in the ejection angle of the droplet resulting in a spread of the impact location. Therefore, the diameter of the bottom of the pillar is slightly larger than the rest of the pillar. This larger diameter at the bottom of the pillar could be easily prevented by reducing the donor–receiver distance, for the bottom part of the pillar. Alternatively, the larger diameter of the bottom of the pillar could be exploited in the case a strong pillar–receiver adhesion is required. At pillar heights of about 70 μm and higher (corresponding to about 80 droplets and more), the growth rate per deposited droplet was found to be constant as indicated by the inclined line in Figure 17.8a. From about 30 μm up, the diameter of the pillar was found to be constant.

The reproducibility of LIFT printing of pillars is illustrated in Figure 17.8b, showing five pillars. These pillars were deposited by repeating a series of LIFT ejection events with identical laser parameters. Printing pillars with extreme aspect ratios requires accurate control of the ejection angle of the LIFT droplet. This was found to be feasible, as demonstrated by the gold pillar (diameter ≈ 10 μm, length ≈2100 μm) in Figure 17.8c with an aspect ratio of more than 1 : 200.

The reproducibility of copper LIFT printing is also illustrated in Figures 17.9 and 17.10. These pillars were printed using laser system 1, listed in Table 17.1. Figure 17.9a shows large-aspect-ratio copper pillars. Each pillar was created by depositing 400 droplets over a donor–tip distance of 300 μm. The four pillars shown in Figure 17.9a were each printed at a different fluence level, resulting in pillar diameters ranging from 7 to 10 μm, respectively. The length of the pillars ranged from 150 to 220 μm for the four fluence levels. The increase of the dimensions of the pillars is attributed to the increase in droplet volume as the laser fluence increases. In order to estimate the volume of a single droplet, the pillars were approximated as perfect cylinders. From the measured volume of these cylinders, droplet volumes of 15, 22, 34, and 45 fl were found respectively, for the four fluence levels applied.

Yet another example of the achievable reproducibility of metal LIFT is depicted in Figure 17.10. This figure shows an array of 70 identical, high-aspect-ratio

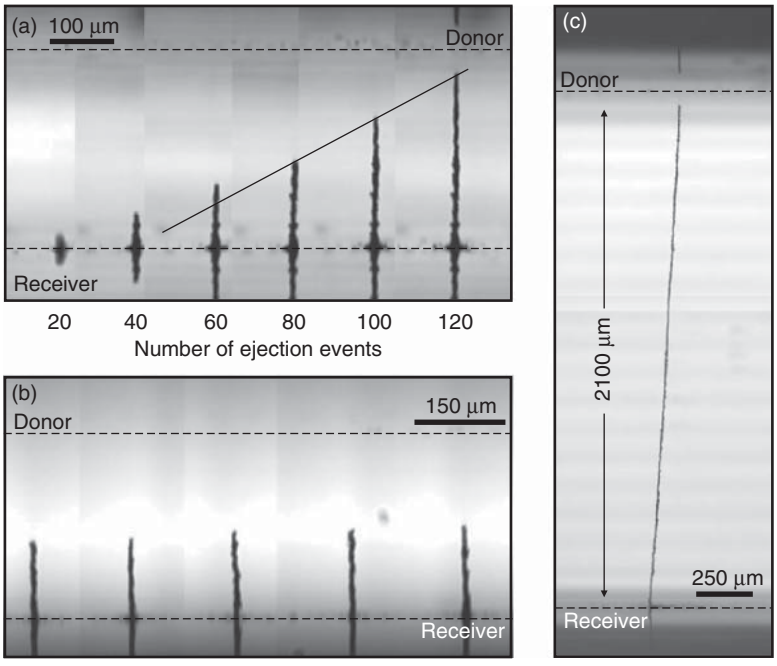

Figure 17.8 (a) Optical microscopy images of copper pillars after a number of deposited droplets. The solid line indicates a constant pillar growth rate of 2.3 µm/droplet, which is observed if the pillar tip is sufficiently close to the donor surface and all droplets land on the tip. (b) Images of five LIFT-printed copper pillars on the same receiver, while using identical process parameters. The dashed lines indicate the donor and receiver surfaces. The features in the images, below the lower dashed line, representing the receiver, are optical reflections of pillars on top of the receiver. (c) Gold pillar with a height of 2100 µm, illustrating the potential for fabrication of freestanding structures. (Visser *et al*. 2015 [12]. Reproduced with permission of John Wiley & Sons.)

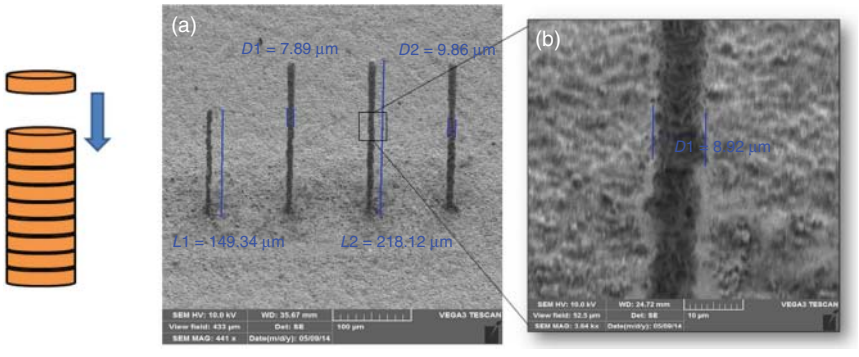

Figure 17.9 (a) SEM image of printed pillars each made up by a pileup of 400 droplets printed on a copper foil. The four pillars were each printed at a different fluence level, from left to right: F_p = 0.8, 0.84, 0.88, and 0.92 J/cm^2, using laser system 1, listed in Table 17.1.(b) A zoom-in on the third pillar from left of (a). (Reproduced and adapted from Ref. [5]. Creative Commons Attribution 4.0 International License.)

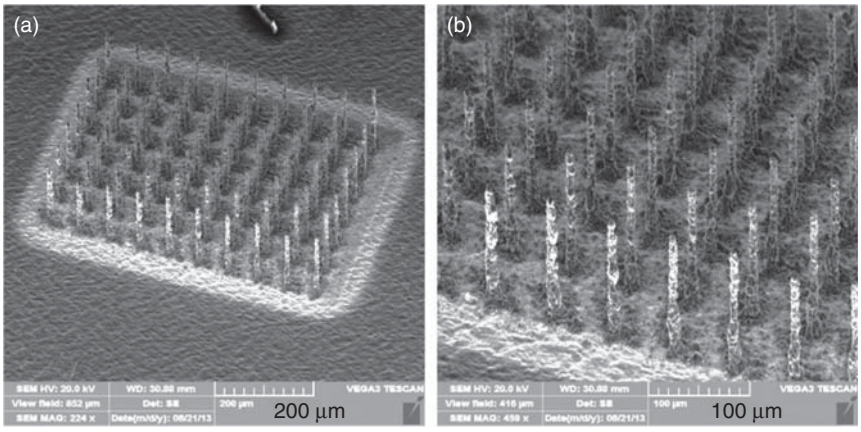

Figure 17.10 (a) SEM image of an array of LIFT-printed copper metal pillars (7 × 10 pillars) with width of 9 µm and height of 106 µm; (b) zoom-in on (a). (Zenou and Kotler 2016 [7]. Reproduced with permission of The Optical Society.)

(AR ≫ 10) copper pillars created by LIFT of a copper donor layer of a thickness of 500 nm, using laser system 1, listed in Table 17.1, at a fluence level of 0.8 J/cm^2 [7]. Each high-aspect-ratio pillar was printed by stacking 200 copper droplets.

17.3.2 Metallurgical Microstructure

The copper pillar shown in Figure 17.11a was printed using laser system 2, listed in Table 17.1. The pillar has a height of about 80 µm and a diameter of 5.3 ± 0.7 µm, implying a height–diameter ratio of about 15. The pillar tip is magnified in Figure 17.11b, showing the last-deposited droplet, which has spread out over the pillar tip and subsequently solidified. Below this droplet, the edges of several solidified droplets can be observed. To assess whether such edges result in pores within the pillar, a cross section of pillar was prepared using a focused ion beam (FIB) and subsequently imaged using a scanning electron microscope (SEM). As shown in Figure 17.11c,d, the individual deposits are hardly visible and only a few small pores are observed. Using a through-lens detector in the SEM, the grains within the pillar were visualized. Grain sizes between 50 and 200 nm were observed and seem to constitute most of the pillar volume. Furthermore, several long, horizontally aligned grain boundaries are identified, as illustrated by the dashed lines in Figure 17.11e. At the outer surface of the pillar, the ends of these boundaries frequently coincide with voids (pores) corresponding to the edge of the solidified droplets. This suggests that the impacting droplets do not melt the pillar surface during impact, but instead crystallize onto the previously deposited droplets. Therefore, these horizontal interfaces could be weak or brittle. This mechanical aspect will be accessed in Section 17.3.3.

Another example of the metallurgical microstructure obtained by metal LIFT can be observed in the cross-sectional image of a LIFT-printed aluminum track, shown in Figure 17.12 [4]. This track was printed using laser system 1, listed in Table 17.1. As shown in Figure 17.11c–e, porosities can be observed in this cross

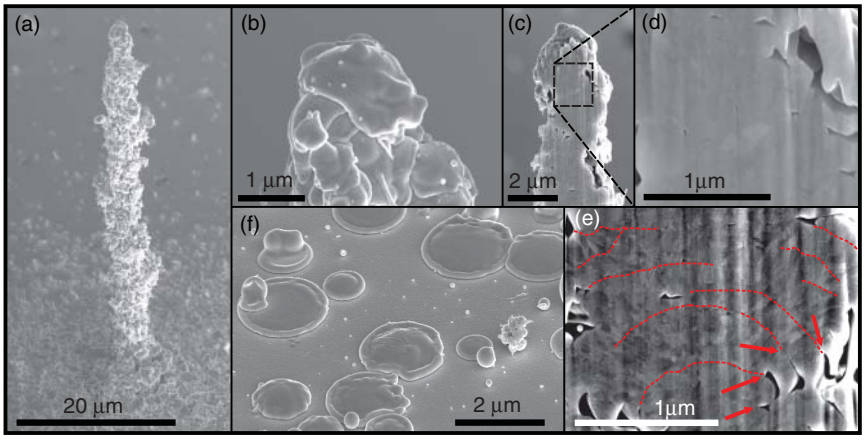

Figure 17.11 SEM images of a LIFT-printed copper pillar. (a) Isometric overview image. (b) Pillar tip, clearly showing the final droplet, which had spread over the top prior to solidifying. The nanodroplets visible (white) on top of this resolidified droplet originate from satellite droplets caused during the ejection process, see Figure 17.5. Image (c) shows the cross section of the pillar tip, obtained by cutting with a focused ion beam (FIB); the region in the rectangle is magnified in figure (d), showing that the interior of the pillar is almost pore-free. (e) Detail of pillar cross section, showing different grain orientations in different gray levels. Grain boundaries with a length spanning multiple grains are indicated by dashed lines. (f) Example view of solidified droplets deposited next to the base of a pillar. (Visser *et al*. 2015 [12]. Reproduced with permission of John Wiley & Sons.)

section. When assuming that the pores are equally distributed in the volume of the track, the total void volume, relative to the "bulk" volume, can be determined from the void "area" in the cross section in Figure 17.12. In this way, Zenou *et al*. [4] found an average total void area percentage of less than 3% of the total printed volume and an average void radius of 143 nm. This low void percentage was attributed to the high droplet kinetic energy and high impact on the surface followed by conformal spreading.

17.3.3 Mechanical Properties

The mechanical properties of the pillars presented earlier were assessed by applying a force to its tip, using an atomic force microscope (AFM), and measuring the subsequent deflection δ_{pi}, as shown in Figure 17.13a. To determine the effective pillar radius r_{pi}, the deflection δ_{pi} of the pillar was determined as a function of the force F_{AFM}. After each measurement, the pillar was allowed to relax to its original position to verify that no plastic deformation of the pillar occurred. The measured deflection as a function of the applied force is depicted in Figure 17.13b. As can be observed, the deflection increases linearly with the applied force, as is expected for elastic deformation/deflection δ_{pi} of a thin homogeneous pillar,

$$\delta_{pi} = \frac{F_{AFM}\, L^3}{3\, E\, I_{pi}}, \text{ in which } I_{pi} = \frac{\pi}{4}\, r_{pi}^4 \tag{17.3}$$

and L and I_{pi} being the probe distance (to the bottom of the pillar) and the moment of inertia, respectively. Since the metallurgical microstructure of the

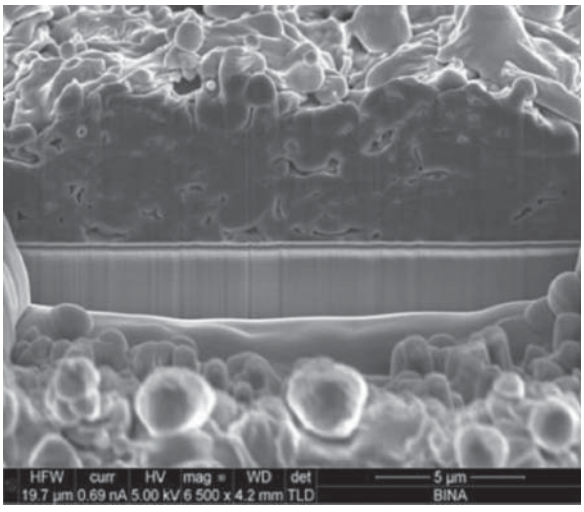

Figure 17.12 Focused-ion-beam (FIB) cross section of a LIFT-printed aluminum track. Thickness of the donor layer 500 nm, laser fluence 0.74 J/cm^2, and a donor–receiver distance of 300 µm. (Reproduced from Ref. [4]. Reprinted figure with permission from Ref. [4]. © IOP Publishing. Reproduced with permission. All rights reserved.)

pillar is unknown, a (bulk) Young's modulus E of 117 GPa was assumed. The effective thickness of the pillar was calculated to be equal to 0.9 ± 0.15 µm. Finally, to cross-check this approach and to assess whether the pillars are homogeneous in diameter, the shape of the deflected pillar was compared to the theoretical solution for a bent beam of constant diameter according to Eq. (17.3). The dashed line in Figure 17.13a indicates a deflected beam of homogeneous diameter, which nearly exactly overlays the deflected pillar. This confirms that the pillar is effectively homogeneous in diameter, despite its surface roughness and internal voids. The deformation of the pillar was found to be elastic, illustrating that the pillar can be significantly deformed prior to plastic deformation.

17.3.4 Electrical Properties

Because conductive pillars are highly relevant for electronic applications, for example, out-of-plane interconnects between different layers of stacked electronics, the electrical properties of the pillars, discussed earlier, were assessed.

The electrical properties were determined by connecting electrodes to the donor- and receiver substrates and gently pressing the donor layer onto the tip of the pillar, such that electrical contact with the pillar is guaranteed. The resistance measured by this approach consists of the contact resistance R_c of the contacts with the substrates and the resistance of the pillar itself. The resistance was measured for different pillar heights and is illustrated in Figure 17.13c. The slope of the linear fit of the resistance curve as a function of height, that is, $R_{\mathrm{pi}}(h)$, which was corrected for the contact resistance R_c, provides the pillar resistance per unit length. When normalizing the pillar resistance per unit length with the cross-sectional area of the pillar, the effective bulk electrical resistance ρ_E of the pillar material was obtained.

For copper pillars printed in air at room conditions, a resistance of $\rho_E = 35.3 \times 10^{-8}$ Ωm was found. This value exceeds the resistance of pure bulk copper, which is 1.6×10^{-8} Ωm, by a factor of 22. As oxidation of the metal

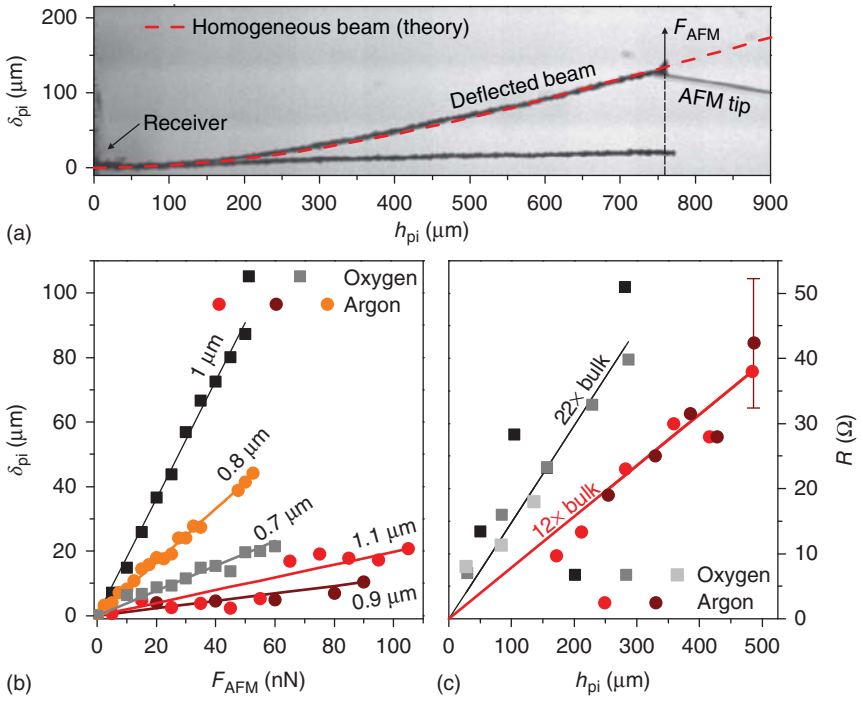

Figure 17.13 (a) Optical microscopic image of a pillar with a height of $h_{pi} \approx 800$ µm, which is deflected by the tip of an AFM. The arrow at the tip of the AFM lever indicates the force (here $F_{AFM} = 90$ nN). The dashed line represents the modeled deflection of a theoretical homogeneous pillar. (b) Measured deflection of the pillar tip as a function of the AFM force applied. The shown linear dependency of the deflection on the applied force corresponds to elastic deformation/defelction of a beam with a homogeneous diameter. The deflection Δ_{pi} is measured at a different pillar height for each pillar, as indicated next to each line. (c) Electrical resistance of pillars processed in air and argon as a function of the pillar height. The slope of the fitted lines indicates the resistance per unit length, which is 22 and 12 times higher than for bulk copper for the air- and argon-processed pillars, respectively. The error resulting from the ≈ 20% uncertainty in pillar diameter is indicated and scales proportional to R_{pi}. (Visser *et al*. 2015 [12]. Reproduced with permission of John Wiley & Sons.)

droplets or the pillar tip during deposition was expected to cause this relatively high resistance, a next set of pillars was printed in an argon environment, see Figure 17.13c. These pillars exhibit about half the resistance as compared to the pillars printed in air. The resistance of pure bulk copper, however, was not obtained. This was attributed due to the transfer of copper oxide from the donor film or hard-to-detect nanometer-scale inhomogeneities within the pillar. Those inhomogeneities were argued to originate from gas bubbles entrapped during droplet deposition [21]. Moreover, electrical resistivity is increased by electron scattering from grain boundaries and nanoamorphous layers at the droplet boundaries, which also contribute to the overall resistivity [31]. These ρ_E values are several orders of magnitude below the values of other metals used for printing of conductive wires, for example, Gallium–Indium ($\rho_E = 3 \times 10^{-3}$

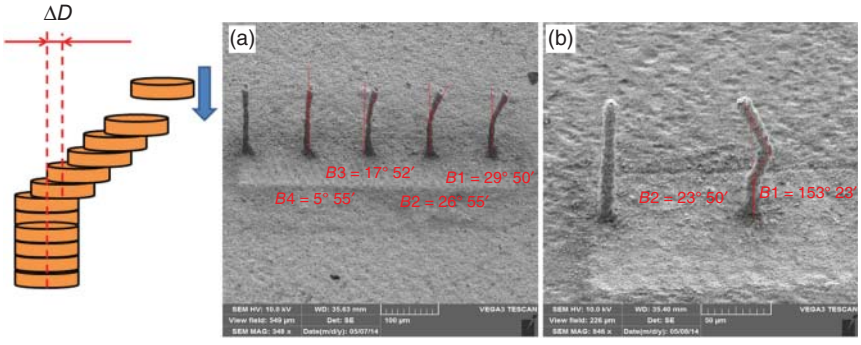

Figure 17.14 (a) SEM image of two-segment, bent pillars; 100 droplets each, with shift ΔD of 0, 0.1, 0.2, 0.3, 0.4 µm (left to right). (b) SEM image of an upright pillar and a three-segment bent pillar for which the second segment is composed of 50 droplets, each shifted by $\Delta D = 0.3$µm, and in the third segment, there are 100 droplets each shifted by $\Delta D = -0.3$ µm. (Reproduced and adapted from Ref. [5]. Creative Commons Attribution 4.0 International License.)

Ωm [32]), and the pillars printed in this manner are suitable for out-of-plane electrode manufacturing.

17.3.5 Inclined Pillars

In 3D additive manufacturing, horizontal structures are traditionally produced using support structures [33]. Up to a certain angle, slanted structures can be produced with (pure metal) LIFT without support material. This section addresses the limit of producing slanting pillars using LIFT, without support structures.

Figure 17.14 shows SEM images of several inclined copper pillars [5]. As shown in Figure 17.9, these copper pillars were created using laser system 1, listed in Table 17.1. Figure 17.14a shows an upright pillar part, composed of 100 droplets. Next, 100 droplets were deposited, where each subsequent droplet was shifted by a distance ΔD compared with the last deposited droplet. The maximum angles in these pillars are limited by the droplet volume, its solidification rate and adhesion to prior deposits, and of course, the strength of the material. For droplets with a volume of 45 fl, a maximum bent angle of 30° was found [5]. Figure 17.14b depicts a two-segment pillar with two consecutive deflection angles. First, 50 droplets were deposited with zero shift ($\Delta D = 0$), followed by 50 droplets with a shift of $\Delta D = 0.3$ µm. Finally, 100 droplets were deposited with a shift of $\Delta D = -0.3$ µm. This figure illustrates the achievable reproducibility and the accuracy of pure metal LIFT.

17.4 Demonstrators and Potential Applications

In semiconductor industry, out-of-plane interconnects, usually referred to as through-silicon vias (TSVs), between different layers of stacked electronics are used. These metal pillars are currently manufactured using conventional lithographic processes requiring vacuum, which are limited to specific (mainly

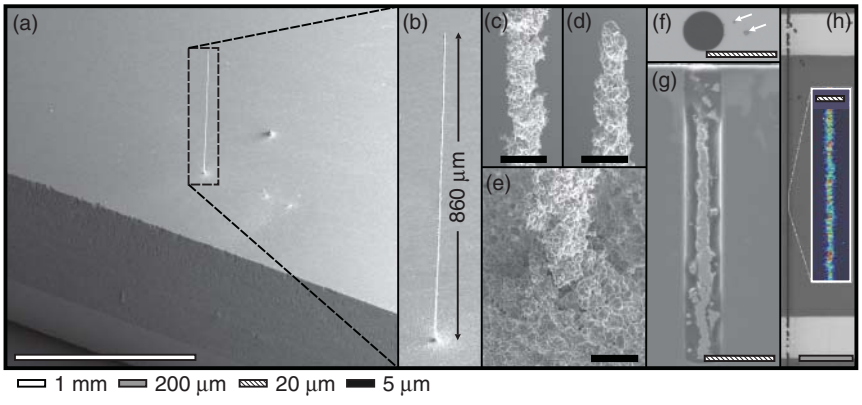

Figure 17.15 High-aspect-ratio examples of copper LIFT. (a) 860 µm long pillar close to the clearly visible edge of a microscope slide. (b) Close-up of the pillar, showing that the pillar has a virtually homogeneous thickness: the center (c) and top (d) of the pillar are approximately 4 µm in diameter, whereas the bottom diameter (e) is about 6 µm, due to droplets landing next to the pillar. Panels (f) and (g) show a top view and a cross section of a filled TSV, respectively. The dark area next to the pillar (also visible from top) is a polymer for fixating the pillar, to avoid any damage due to polishing. The arrows in (f) indicate droplets that landed next to the TSV. The cross section in image (g) shows that the pillar extends to the bottom of the hole. Finally, by moving the receiver substrate while depositing droplets, conductive lines can be fabricated as shown in (h). The inset shows a close-up of the line, in which the colors represent a height map. (Visser *et al*. 2015 [12]. Reproduced with permission of John Wiley & Sons.)

semiconductor) materials. Moreover, the height of the pillars produced by lithographic processes is limited to a few (tens of) microns [5]. As LIFT can print multiple materials in air, it is a promising technology to produce TSVs. Figure 17.15a shows a 860 µm long copper pillar that was deposited, by moving the receiver down during droplet deposition, while maintaining a distance between the donor and the pillar tip in the range of 20–50 µm. Even higher pillars could easily be created, until at some height, the position of the tip is no longer exactly over the base of the pillar. That is, small vibrations or light airflows result in a "waving" motion of the tip. Therefore, a wider distribution in the droplet impact location with respect to the tip was observed, resulting in a tip with a larger diameter. Nonetheless, these pillars can also be deposited to fill TSVs. A top view and cross section of such a filled TSV are shown in Figure 17.15f,g, respectively. The top view shows the virtually clean deposition process. That is, only a few droplets landed next to the TSV as indicated by the arrows. These could easily be removed by a postprocessing step, such as etching. The cross section of the TSV shown in Figure 17.15g verifies that the pillar extends to the 100 µm deep bottom. So far, only a single filled TSV was prepared for visualization, as its preparation without damaging the pillar proved to be challenging; for example, the defect close to the top in Figure 17.15g might be caused by accidentally cutting the intact pillar. Zenou *et al*. [5] suggested further fields of application for metal pillars including photonics [34, 35], biology [36], micromechanics [37, 38], and microbatteries [39, 40].

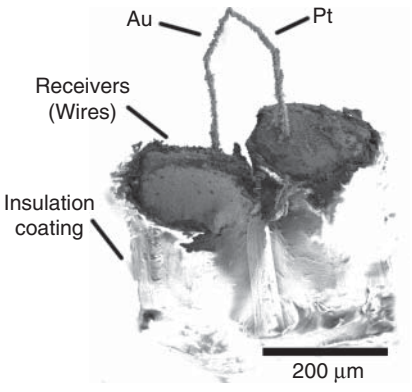

Figure 17.16 A 220 μm high Pt–Au joint, acting as a thermocouple, LIFT printed on the top of a Pt–Au wire pair, using a 4 ns pulsed Nd:YAG laser with a wavelength of 532 nm and a laser spot diameter of 16 μm. The copper wires on which the Pt and Au pillar are printed have an electrical insulation coating. (Reprinted figure with permission from Ref. [18]. ©2017 Wiley-VCH Verlag. All rights reserved.)

LIFT printing of a sensing device is demonstrated in Figure 17.16, showing an out-of-plane thermocouple [18]. The platinum and gold inclined pillars, which join at the tops, were LIFT printed on the top of two receivers, which are also a Pt and an Au wire. The functionality of the thermocouple was confirmed by applying a temperature over its legs and measuring the voltage differential over its legs.

High aspect ratios of LIFT-printed structures can also be achieved in the horizontal plane, for example, printing of a conductive copper line, shown in Figure 17.15h. This conductive line was achieved by moving the receiver substrate, while repeatedly ejecting droplets. By combining this approach with out-of-plane printing, rapid prototyping of fully 3D electronics becomes within reach.

Finally, Figure 17.17 shows an example of LIFT printing of mechanical applications, that is, a "microgear" composed of a copper–silver alloy [7]. Here, the donor consisted of a layer of copper and a layer of silver, each with a thickness ratio resulting in a printed structure with a composition of 98% copper and 2% silver [6].

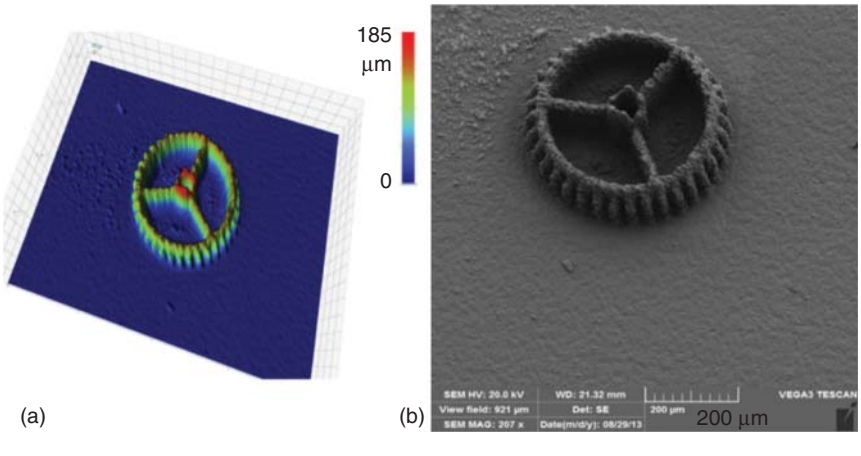

Figure 17.17 (a) 3D measurement of the printed "gear." (b) A SEM image of the same structure. The printed gear-like structure is 400 μm wide, and the finest metal feature resolution is 20 μm. (Zenou and Kotler 2016 [7]. Reproduced with permission of The Optical Society.)

17.5 Conclusions and Outlook

It is shown in this chapter that (pure) metal LIFT can be applied to print 3D freestanding, out-of-plane (micro)structures, such as high-aspect-ratio copper or gold pillars. By the selection of the appropriate processing parameters, metal LIFT allows a high level of control over the size, velocity, and solidification morphology of the deposited droplets.

Pillars of diameters as small as a few micrometers can be manufactured by picosecond LIFT to a height over 2000 μm. The surface-finish geometrical accuracies (reproducibility) of the pillars were found to be in the (sub)micrometer regime. At this accuracy, an array of 70 copper pillars of width of 9 μm and height of 106 μm was shown to be feasible. Unfortunately, it was found that debris, that is, fragments originating from the donor, which also deposits on the (micro)structure being printed, cannot be avoided entirely, but only be minimized. Per micrometer pillar height, about 0.45 LIFT deposits (droplets) are required, when using a picosecond laser source and metal donor layers with a thickness of the order of magnitude of 200 nm. This implies that when donor refreshment and laser beam positioning are optimized, a theoretical pillar print rate of more than 1 m/s is used, when assuming a laser source with a pulse repetition rate of 500 kHz.

Further, it was shown that the maximum bent angle, without support, in a metal pillar is limited to about 30°. This implies that, unless the structure to be printed can be rotated relative to the laser beam by a manipulator, overhang structures cannot be produced. This limits the achievable complexity of LIFT-printed 3D (micro)structures. However, a common approach in additive manufacturing to print complex 3D structures is the use of a sacrificial support material, for example, a dissolvable polymer, or a selectively etchable metal, which is subsequently selectively removed in a postprocessing step. As LIFT allows printing of various materials with essentially the same laser equipment, future research results may prove that this is a valid approach for metal LIFT printing of complex metal 3D structures.

When compared to traditional powder bed methods, using selective laser melting (SLM) for 3D additive manufacturing, LIFT of 3D metal (micro)structures demonstrates to be a more accurate as well as a much more flexible technology in terms of variety of substrates and surrounding materials that can be used to print multimaterial structures. Therefore, LIFT is particularly interesting for rapid prototyping of high-aspect-ratio microstructures as well as manufacturing metals with resolutions between the nanometer scale, as accessible by lithography, and about 30 μm, as accessible by alternative 3D printing techniques.

References

1 Pohl, R., Jansink, M., Römer, G., and Huis in 't Veld, A. (2015) Solid-phase laser-induced forward transfer of variable shapes using a liquid-crystal spatial light modulator. *Appl. Phys. A: Mater. Sci. Process.*, **120** (2), 427–434.

2 Piqué, A., Auyeung, R.C.Y., Kim, H., Charipar, N.A., and Mathews, S.A. (2016) Laser 3D micro-manufacturing. *J. Phys. D: Appl. Phys.*, **49**, 24.

3 Zenou, M., Sa'ar, A., and Kotler, Z. (2015) Supersonic laser-induced jetting of aluminum micro-droplets. *Appl. Phys. Lett.*, **106**, 181 905.

4 Zenou, M., Sa'ar, A., and Kotler, Z. (2015) Digital laser printing of aluminum micro-structure on thermally sensitive substrates. *J. Phys. D: Appl. Phys.*, **48**, 205 303.

5 Zenou, M., Sa'ar, A., and Kotler, Z. (2015) Laser jetting of femto-liter metal droplets for high resolution 3D printed structures. *Sci. Rep.*, **5**, 17 265.

6 Zenou, M., Sa'Ar, A., and Kotler, Z. (2015) Laser transfer of metals and metal alloys for digital microfabrication of 3D objects. *Small*, **11** (33), 4082–4089.

7 Zenou, M. and Kotler, Z. (2016) Printing of metallic 3D micro-objects by laser induced forward transfer. *Opt. Express*, **24** (2), 1431–1446.

8 Pohl, R., Visser, C., Römer, G., Sun, C., Huis in 't Veld, A., and Lohse, D. (2014) High-resolution imaging of ejection dynamics in laser-induced forward transfer. *Proceedings of the SPIE Conference on Laser Applications in Microelectronic and Optoelectronic Manufacturing (LAMOM) XIX, 4-6 February, San Francisco, CA, USA*.

9 Pohl, R. (2015) Laser-induced forward transfer of pure metals– towards 3D printing. PhD thesis. University of Twente, The Netherlands, doc.utwente.nl/97060 (accessed 10 June 2017).

10 Pohl, R., Visser, C.W., Römer, G., Sun, C., Huis in 't Veld, A., and Lohse, D. (2015) Imaging of the ejection process of nanosecond laser-induced forward transfer of gold. *J. Laser Micro Nanoeng.*, **10** (2), 154–157.

11 Pohl, R., Visser, C.W., Römer, G.W., Lohse, D., Sun, C., and Huis in 't Veld, B. (2015) Ejection regimes in picosecond laser-induced forward transfer of metals. *Phys. Rev. Appl.*, **3** (2), 024 001.

12 Visser, C.W., Pohl, R., Sun, C., Römer, G.W., Huis in 't Veld, B., and Lohse, D. (2015) Toward 3D printing of pure metals by laser-induced forward transfer. *Adv. Mater.*, **27** (27), 4087–4092.

13 Yang, L., Wang, C.-Y., Ni, X.-C., Wang, Z.-J., Jia, W., and Chai, L. (2006) Microdroplet deposition of copper film by femtosecond laser-induced forward transfer. *Appl. Phys. Lett.*, **89**, 161 110.

14 Veiko, V.P., Shakhno, E.A., Smirnov, V.N., Miaskovski, A.M., and Nikishin, G.D. (2006) Laser-induced film deposition by lift physical mechanisms and applications. *Laser Part. Beams*, **24**, 203–209.

15 Röder, T.C. and Köhler, J.R. (2012) Physical model for the laser induced forward transfer process. *Appl. Phys. Lett.*, **100**, 071 603.

16 David, A. and Willis, V.G. (2004) Evaporation and phase explosion during laser-induced forward transfer of aluminum. Porceedings of SPIE.

17 Banks, D.P., Grivas, C., Mills, J.D., Eason, R.W., and Zergioti, I. (2006) Nanodroplets deposited in microarrays by femtosecond Ti:sapphire laser-induced forward transfer. *Appl. Phys. Lett.*, **89**, 193 107.

18 Luo, J., Pohl, R., Qi, L., Römer, G.W., Sun, C., Lohse, D., and Visser, C.W. (2017) Printing functional 3D microdevices by Laser-induced forward transfer. *Small*, **13**, 1602553.

19 Li, D. (ed.) (2008) *Encyclopedia of Microfluidics and Nanofluidics*, Springer-Verlag.
20 Mckinley, G.H. (2005) Visco-elasto-capillary thinning and break-up of complex fluids. *Br. Soc. Rheol.*, **3**, 1–49.
21 Visser, C.W., Frommhold, P.E., Wildeman, S., Mettin, R., Lohse, D., and Sun, C. (2015) Dynamics of high-speed micro-drop impact: numerical simulations and experiments at frame-to-frame times below 100 ns. *Soft Matter*, **11**, 1708–1722.
22 Kuznetsov, A.I., Unger, C., Koch, J., and Chichkov, B.N. (2012) Laser-induced jet formation and droplet ejection from thin metal films. *Appl. Phys. A*, **106**, 479–487.
23 Li, Y. and Ching-Yue, W. (2009) Experimental study on microdeposition of the copper thin film by femtosecond laser-induced forward transfer. *Chin. Phys. B*, **18**, 4292.
24 Oosterhuis, G., Prenen, A., and Huis in 't Veld, A.J. (2012) Laser induced forward transfer of interconnects for 3D integration. *ECS Trans.*, **41** (43), 81–90.
25 Othon, C.M., Laracuente, A., Ladouceur, H., and Ringeisen, B.R. (2008) Sub-micron parallel laser direct-write. *Appl. Surf. Sci.*, **255** (5), 3407–3413.
26 Palla-Papavlu, A., Dinca, V., Luculescu, C., Shaw-Stewart, J., Nagel, M., Lippert, T., and Dinescu, M. (2010) Laser induced forward transfer of soft materials. *J. Opt.*, **12** (12), 124 014.
27 David, A. and Willis, V.G. (2005) Microdroplet deposition by laser-induced forward transfer. *Appl. Phys. Lett.*, **86**, 244 103.
28 Zergioti, I., Mailis, S., Vainos, N.A., Papakonstantinou, P., Kalpouzos, C., Grigoropoulos, C.P., and Fotakis, C. (1998) Microdeposition of metal and oxide structures using ultrashort laser pulses. *Appl. Phys. A*, **66**, 579–582.
29 Klini, A., Loukakos, P.A., Gray, D., Manousaki, A., and Fotakis, C. (2008) Laser induced forward transfer of metals by temporally shaped femtosecond laser pulses. *Opt. Express*, **16**, 11 300.
30 van Dam, D.B. and Clerc, C.L. (2004) Experimental study of the impact of an ink-jet printed droplet on a solid substrate. *Phys. Fluids*, **16**, 3403–3414.
31 Winter, S., Zenou, M., and Kotler, Z. (2016) Conductivity of laser printed copper structures limited by nano-crystal grain size and amorphous metal droplet shell. *J. Phys. D: Appl. Phys.*, **49** (16), 165310.
32 Zrnic, D. and Swatik, D. (1969) On the resistivity and surface tension of the eutectic alloy of gallium and indium. *J. Less Common Met.*, **18**, 67–68.
33 Gibson, I., Rosen, D.W., and Stucker, B. (2015) *Additive Manufacturing Technologies - 3D Printing, Rapid Prototyping, and Direct Digital Manufacturing*, Springer-Verlag.
34 Joannopoulos, J., Villeneuve, P., and Fan, S. (1997) Photonic crystals: putting a new twist on light. *Nature*, **386** (6621), 143–149.
35 Grigorenko, A., Geim, A., Gleeson, H., Zhang, Y., Firsov, A., Khrushchev, I., and Petrovic, J. (2005) Nanofabricated media with negative permeability at visible frequencies. *Nature*, **438** (7066), 335–338.
36 LaVan, D., McGuire, T., and Langer, R. (2003) Small-scale systems for in vivo drug delivery. *Nat. Biotechnol.*, **21** (10), 1184–1191.

37 Ko, S., Chung, J., Hotz, N., Nam, K., and Grigoropoulos, C. (2010) Metal nanoparticle direct inkjet printing for low-temperature 3D micro metal structure fabrication. *J. Micromech. Microeng.*, **20** (12), 125010.

38 Ahn, B., Duoss, E., Motala, M., Guo, X., Park, S.I., Xiong, Y., Yoon, J., Nuzzo, R., Rogers, J., and Lewis, J. (2009) Omnidirectional printing of flexible, stretchable, and spanning silver microelectrodes. *Science*, **323** (5921), 1590–1593.

39 Sun, K., Wei, T.S., Ahn, B., Seo, J., Dillon, S., and Lewis, J. (2013) 3D printing of interdigitated Li-ion microbattery architectures. *Adv. Mater.*, **25** (33), 4539–4543.

40 Ho, C., Murata, K., Steingart, D., Evans, J., and Wright, P. (2009) A super ink jet printed zinc-silver 3D microbattery. *J. Micromech. Microeng.*, **19** (9), 094013.

18

Laser Transfer of Entire Structures and Functional Devices

Alberto Piqué, Nicholas A. Charipar, Raymond C. Y. Auyeung, Scott A. Mathews, and Heungsoo Kim

Materials Science and Technology Division, Code 6360, U.S. Naval Research Laboratory, 4555 Overlook Ave. SW, Washington, DC 20375, USA

18.1 Introduction

For commercial, aerospace, and military applications, miniaturization and functionality are key factors. In all these applications, the driving force is the need to achieve higher functionality in increasingly smaller packages. As a result, traditionally packaged electronic components such as integrated circuits (ICs) and surface-mount devices (SMDs) are reaching the point where their individual packaged size is too large to achieve the required device density on the available circuit board surface. Other approaches such as application-specific ICs or ASICs can be used in place of an entire microelectronic circuit board, replacing all the individual components with a single IC. However, development of these single-chip designs is extremely expensive and time-consuming and, once designed and fabricated, very difficult to change, thus they are not suitable for the rapid prototyping of circuits at a reasonable cost and in a short time.

A better solution is to be able to place all the required passive components and semiconductor devices onto or within the substrate, that is, the circuit board, in order to achieve higher component densities. This type of hybrid circuits, where the interconnects are printed while the devices are embedded, have had limited success when implemented with unpackaged or bare-die semiconductor devices. This is because bare dice are very fragile and can be damaged easily by the robotic systems, known as *pick-and-place* tools, used to place the devices on a circuit board. Despite these difficulties, the implementation of embedded hybrid electronic circuits comprising SMDs, interconnects, and ICs in bare-die form promises to make possible levels of miniaturization well beyond the capabilities of current circuit manufacturing techniques. In order to realize these gains, novel approaches to the assembly and interconnection of passives and bare-die ICs need to be considered.

This chapter describes the adaptation of laser direct-write processes originally developed for printing predetermined patterns without lithography or

Laser Printing of Functional Materials: 3D Microfabrication, Electronics and Biomedicine,
First Edition. Edited by Alberto Piqué and Pere Serra.
© 2018 Wiley-VCH Verlag GmbH & Co. KGaA. Published 2018 by Wiley-VCH Verlag GmbH & Co. KGaA.

masks to the assembly and interconnection of microelectronic circuits [1]. These laser-based nonlithographic processes can be used for the transfer or placement of entire structures and functioning devices on a substrate and connecting them afterward. For example, these processes can be used to first laser micromachine a pocket or recess on a substrate, then to laser transfer a device or component inside the pocket without damaging the device's functionality, and finally, laser print the metallic electrical interconnects required by each device in order to complete the circuit [2]. Discussion of the laser-induced transfer of metal droplets or metal inks for the printing of patterns can be found in earlier chapters of this book, while the use of laser ablation for micromachining purposes is well established for microfabrication applications [3]. However, the use of laser direct-write techniques such as laser induced forward transfer (LIFT) for the placement of whole structures or functional devices has only been recently explored by a few groups and is the subject of recent attention given the potential offered by embedding components and devices within flexible substrates.

This chapter begins with an overview of early reports of the use of LIFT to release and place microelectromechanical system (MEMS)-like structures and more recent results demonstrating the laser-mediated release of semiconductor devices. Next, it describes the use of LIFT to release, transfer, and place a wide range of structures including whole parts, passive components, and semiconductor devices. This variant of LIFT developed at the U.S. Naval Research Laboratory (NRL) is known as *lase-and-place*. The chapter then discusses the application of these laser-based tools in the fabrication of hybrid circuits and provides a series of examples from NRL's work. Finally, the chapter concludes with a discussion of laser-based transfer processes for the digital microfabrication of next-generation microelectronics whose design and geometry can be customized and implemented in less time and at lower cost than with any other currently available circuit fabrication technique.

18.2 Early Demonstrations of LIFT of Entire Structures

The use of LIFT processes for the transfer and placement of prefabricated parts or components onto a receiving substrate was first reported by Holmes and Saidam [4]. In their work, the authors describe the laser-driven release of Si-based microstructures from a UV-transparent substrate with an intermediate polymer sacrificial layer. Upon irradiation with an excimer laser pulse, a thin fraction of the sacrificial layer is vaporized, releasing the microstructure. This technique was later used to demonstrate the laser-assisted assembly of rotors for electrostatic MEMS micromotors and transfer of contact bumps for ICs in bare-die form [5]. These initial results showed how to apply the laser transfer process as an alternative to conventional MEMS assembly techniques for placement of both fixed and moving parts of a wide range of materials over both planar and nonplanar surfaces. The basic concept relies in the use of a

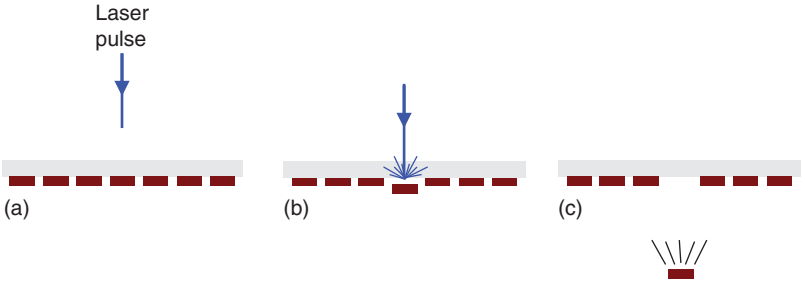

Figure 18.1 Schematic (not to scale) of the laser transfer process of a device or solid component (rectangular blocks). (a) A single UV laser pulse is aimed at the interface between the device and the transparent carrier (gray rectangle). (b) As the polymer layer vaporizes, it releases and launches the device from the substrate. (c) The device is forward transferred away from the donor substrate, landing on the receiving substrate (not shown).

laser-absorbing sacrificial release layer such as the polymer layer described by Holmes to attach the individual components to a UV-transparent support. A laser pulse then ablates the sacrificial layer, generating gases that release and propel the component toward a receiving substrate placed in close proximity. This laser device transfer process is contactless and thus allows the transfer of very small and very thin components, which could easily be damaged by pick-and-place tools. This process is illustrated schematically in Figure 18.1, where individual blocks representative of a device or component are shown attached to the laser-transparent carrier, which forms the donor substrate. Notwithstanding the success achieved with MEMS structures, no reports since have been published by this group describing the use of LIFT with other types of structures such as functional semiconductor devices.

More recently, other groups have shown that LIFT can be adapted for the transfer of entire semiconductor bare dies. One approach reported by Karlitskaya and coworkers from the University of Twente relies on the thermal decomposition of the sacrificial layer to release and transfer individual RFID devices [6]. The Twente group has developed a simple model that predicts the fluence threshold for the release of $200 \times 200\ \mu m^2$ by 150 μm thick Si dies held with various types of semiconductor carrier tapes [6, 7]. Their model shows that the release threshold in terms of laser intensity is below the thermal damage threshold of silicon for the reverse side of the die (<673 K) based on heat diffusion of the absorbed laser pulse through the silicon substrate. In this case, the authors applied the laser transfer process to devices with the active region facing opposite to the laser pulse to minimize thermal damage. However, no reports from the Twente group can be found indicating if the devices survived the transfer process and remained functional afterwards. Perhaps this was due to the difficulty in trying to make electrical contact between the device pads on the laser-transferred devices and the acceptor substrate for testing purposes. A better solution is to transfer the die with its active surface facing up, facilitating access to the contact pads to interconnect the device with the receiving substrate using wire bonding tools or

direct-write approaches to enable testing and connecting to form a circuit. The challenge, however, is to be able to illuminate the active region of the die with the transfer laser pulse without causing any damage.

At NRL, this capability was demonstrated for the laser forward transfer of individual InGaN LED semiconductor substrates (250 μm × 350 μm) in bare-die form, that is, unpackaged, using a series of low fluence (≈150–200 mJ/cm^2) 10 ns pulses from either excimer (248 nm) or YAG (355 nm) lasers [8]. Once laser transferred, the LEDs were electrically tested and their operation verified. This laser-driven pick-and-place of electronic devices named "lase-and-place" has been shown to be compatible not only with bare-die semiconductor devices but also with a wide range of devices and structures independent of their size, thickness, and mass as displayed in the image in Figure 18.2. The optical micrograph shows examples of various objects transferred into laser micromachined pockets on the surface of an ULTEM-1000 receiving substrate. They range from two types of structures (a polyimide laser micromachined gear and two silicon beams) to unpackaged semiconductor devices of various sizes (a LM555 timing chip and four InGaN LEDs) and illustrate the range and capabilities of lase-and-place. As reported by the NRL group and discussed in the following sections, the devices are not damaged upon laser illumination of their active surface and subsequent transfer demonstrating the ability of this LIFT technique to effectively provide a noncontact alternative to mechanical pick-and-place tools.

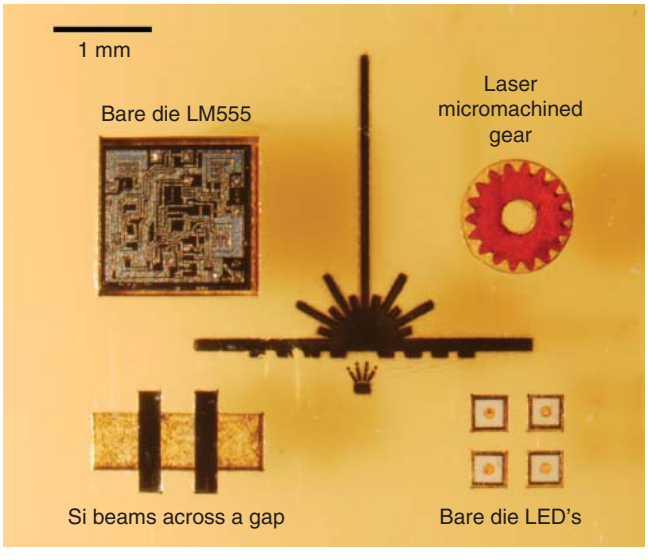

Figure 18.2 Optical micrograph showing an arbitrary arrangement of various types of components and parts all transferred onto a plastic substrate (ULTEM-1000) using "lase-and-place." The artwork in the center corresponds to the laser transfer schematic and was laser-printed by LIFT of a silver metallic nanoink (see chapter 4).

18.3 Process Dynamics

LIFT techniques offer a practical alternative to conventional, that is, mechanically driven, pick-and-place methods for release, transfer, placement, and/or embedding of different types of millimeter- to micrometer-sized structures such as MEMS and similar structures, solid interconnects, passive components, sensors, actuators, semiconductor bare dice, and optoelectronic devices onto any 2D or 3D surface. The concept is simple in principle: have each component mounted on a laser-transparent support using an intermediate support layer. Upon exposure to one or several laser pulses, the support layer releases the component, and in the process, the component moves away from the support. This mechanism, however, can be initiated through various laser-induced effects ranging from thermal heating to full ablation of the support layer. The Twente group was the first to systematically study this range of effects [9] and compare/contrast the thermal and ablative release mechanisms. Their analysis applied to the transfer of silicon substrates based on the assumption that the process was driven by the substrate's absorption of the laser radiation rather than the intermediate layer. Relying on heating or ablation of the silicon substrate can lead to its transfer but also can cause its damage. Despite their technique's narrow implementation (only with silicon substrates), this work demonstrated the potential of LIFT of devices as an alternative to pick-and-place tools and investigated how the laser parameters (wavelength, pulse length, energy, and spatial characteristics) together with the nature of the intermediate layer (various types of laser-transparent carrier tapes with thermal adhesive films) and the donor-to-receiving substrate gap influenced the transfers. The results of Karlitskaya's work showed that for their optimized configuration, that is, using laser pulses from a frequency-doubled Nd:YAG ($\lambda = 532$ nm, $\tau = 0.2$ ms) with a laser-transparent tape/thermal adhesive layer as carrier for silicon substrates, transfers with low release velocities (<1 m/s) were possible. Their goal was to avoid damage of the substrate upon landing and reduced tumbling to improve placement accuracy. Their statistical analysis of the transferred silicon substrates showed that with a gap between the donor and receiving substrates of 0.2 mm, it was possible to obtain a placement accuracy of ± 35 μm [7].

Although the thermal release showed the possibility of achieving reasonable placement precision, accuracies of the order of less than ± 20 μm are required in order to compete with pick-and-place tools [10]. Given the fact that LIFT of devices involves the release of gases of much lower densities compared to the objects being launched, these processes are expected to be highly sensitive to the initial conditions. That is, small variations in the absorption mechanisms or even nonuniformities in the homogeneity and/or thickness of the support layer will lead to very unstable transfers with poor overall reproducibility, as observed by the Twente group with both their ablative- or thermal-mediated release from adhesive tapes. An alternative approach using a multilayer support comprising of a blistering polymer layer and a pressure-sensitive layer (PSA), known as *thermomechanical selective laser-assisted die transfer* (*tm*SLADT), has been

reported to achieve better placement accuracy by a group at North Dakota State University [11]. This process uses a combination of a polyimide blistering layer (along the lines of the BA-LIFT process discussed in Chapter 5 of this book) with a spin-coated PSA layer to which 680 μm × 680 μm silicon tiles 65 μm thick are attached. UV laser pulses from a frequency tripled Nd:YVO_4 ($\lambda = 355$ nm, $\tau = 30$ ns) strike the polyimide layer forming a blister that causes the PSA layer to release the attached die. The process results in complete release and transfer of devices most of the times (transfer rates up to 93.5% were reported) with placement accuracy of ±25 μm on average and under optimized conditions [12]. The difficulties in transfer yield and part placement accuracy can be found in the choice of carrier layer. For example, the use of chip carrier tapes as release layers limits further optimization of the process, as evidenced by the results obtained by the University of Twente group due to the fact that these tapes do not exhibit the uniformity required by the LIFT process. Similarly, the multilayer approach explored by the group at North Dakota State University led to an unnecessarily complex carrier support that resulted in less than 100% transfer yields. Notwithstanding these results, it is possible to achieve 100% transfer yields with better than ±25 μm placement accuracy using a single carrier layer that fully absorbs the laser pulses, as described in the next section.

18.3.1 Lase-and-Place

The polymer sacrificial layer is critical for achieving reproducible release and transfer of a given structure or device during lase-and-place. In its simplest form, it needs to absorb the laser and decompose into volatile components with little or no residue left afterward. Given that many polymers decompose cleanly upon irradiation with UV laser pulses, their use in lase-and-place allows high reproducibility in the transfers. In fact, the polymers used to hold the components or devices in the donor substrate fulfill the same role as that of the dynamic release layer discussed in Chapter 3 of this book. In general, the use of polymer solutions applicable via spin coating such as photoresists, semiconductor wafer protective coatings, and polyimide precursors works well in conjunction with sources producing nanosecond pulses in the UV, that is, excimer or frequency-tripled diode-pumped solid-state lasers. When done correctly, the polymer absorbs the entire laser pulse and fully decomposes, leaving no residue on the device while shielding it from laser damage. This has been demonstrated by the NRL group for devices ranging in size from 0.1 to over 6 mm^2 [8, 13–15].

Using stroboscopic imaging techniques, snapshots of the actual launch, release, and travel away from the donor substrate have been reported as shown in the sequence of micrographs in Figure 18.3a–c. These images can be used to calculate the velocity as a function of laser fluence, and the results are plotted in Figure 18.3d. From this data, it is clear that for a given laser fluence, the lighter components are transferred at a higher velocity compared to the heavier ones [8]. The solid line for the 1 mm^2 device corresponds to a fit based on the following relationship [5]

$$v = \sqrt{\frac{2\eta(E - E_T)}{m}} \tag{18.1}$$

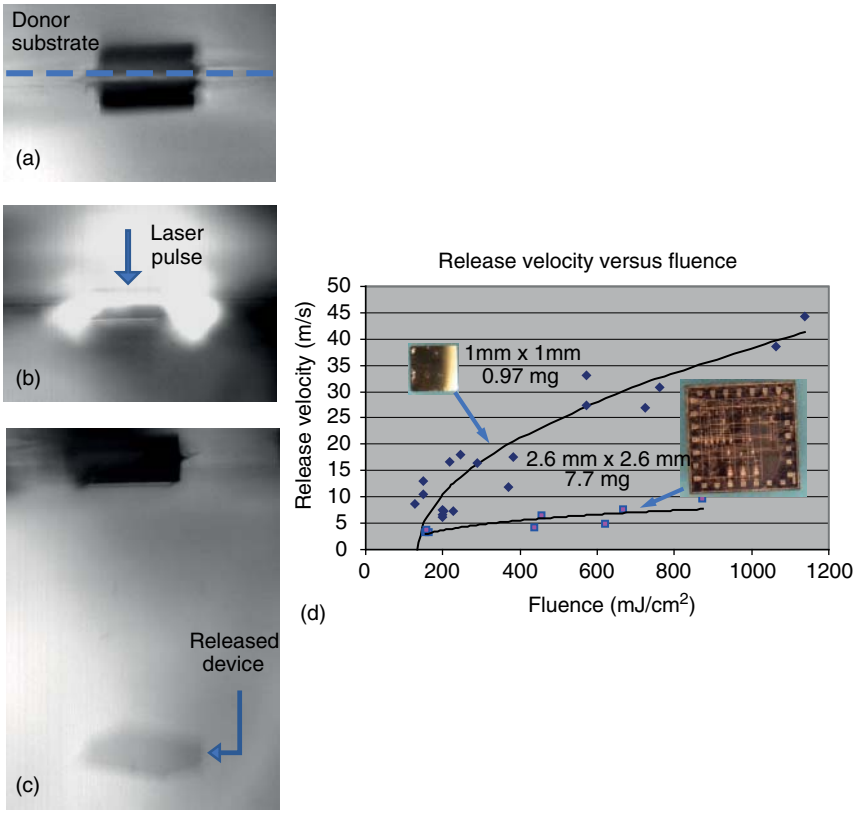

Figure 18.3 Stroboscopic micrographs showing three stages in the transfer of 1 mm × 1 mm Si substrates (laser pulse is ≈100 mJ/cm^2). (a) shows the device prior to launch at $t < 0$; (b) shows the laser as it vaporizes the polymer layer at $t \approx 0$; and (c) shows the device moving away at $t < 100$ µs. (d) Plot of release velocity versus laser fluence for two different sizes (1 mm^2 vs 6.8 mm^2) of unpackaged devices (bare die). The line fitting the data points for the 1 mm^2 substrates represents a fit to Eq. (18.1) in the text, while the line for the 2.6 mm × 2.6 mm ASIC bare die is only a guide to the eye.

where v is the velocity, η is the fraction of available energy converted into kinetic energy, E is the laser fluence, E_T is the ablation threshold of the sacrificial polymer layer, and m is the mass per unit area of the device. Note that the solid curve for the 2.6 mm × 2.6 mm ASIC bare dies is a visual aid and not a fit to the aforementioned formula. While (18.1) is reasonably consistent with the experimental results obtained with the 1 mm^2 samples, the energy conversion efficiency η is not necessarily constant over a wide range of laser fluences due to numerous other mechanisms responsible for energy losses. In fact, only a very small fraction of the incident laser energy is converted into kinetic energy responsible for the release and launch of the part or device. However, near the fluence threshold of 150 mJ/cm^2, this is sufficient to release a part with velocities of a few meters per second without causing damage during launch or upon landing on the receiving substrate.

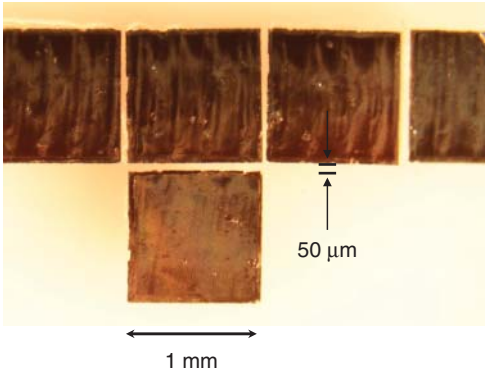

Figure 18.4 Optical micrograph showing transfers with lase-and-place of 1 mm × 1 mm ultrathin (9 μm thick) silicon die onto a glass receiving substrate with placement accuracy of ±25 μm and no signs of damage after laser transfer.

The lase-and-place technique has also been used successfully to laser transfer ultrathin (≈10 μm) silicon substrates, which despite their fragility, can be inserted with extreme placement accuracy on the surface of an acceptor substrate without being damaged or fractured [13, 14]. This type of ultrathin devices are representative of the class of components required for next generation of RFID tags and other flexible electronic applications. Furthermore, with lase-and-place, it is possible to place devices next to each other with sufficient precision to fabricate assemblies or arrays of components. Figure 18.4 shows an image of five 1 mm × 1 mm ultrathin (9 μm thick) Si substrates, transferred next to each other along a grid and spaced 50 μm apart to demonstrate the device placement control achievable with lase-and-place. A few of the substrates exhibit minor rotation from the grid arrangement. However, the overall placement accuracy is of the order of ±25 μm, despite minor rotation and tilting-away from the transfer axis. In fact, fine-tuning the transfer laser parameters, adjusting the device ribbon-to-substrate gap, and increasing the polymer layer uniformity in the donor substrate can further improve the overall placement control and reproducibility. The image in this figure also shows that despite their very low thickness (<10 μm), these Si substrates were laser-transferred intact (no cracks or fractures). Finally, the combination of lase-and-place with self-assembly techniques provides another way to achieve precise placement. For example, the application of magnetic fields to trap and align magnetically susceptible devices onto a substrate has been reported for ultrathin chip placement by Kuran *et al.* [16].

The aforementioned results demonstrate that LIFT techniques can place individual structures or device over a given location with sufficient precision for applications involving component assembly. Furthermore, since the donor substrate onto which the devices are attached is optically transparent, registration and alignment of the device with the receiving substrate are rather straightforward and can be performed via machine vision. This process can be carried out at great speeds (>10 devices/s) with great lateral precision (<25 μm) for short travel distances away from the support (<0.2 mm). The following sections discuss the use of lase-and-place with structures and components of different sizes, shapes, and robustness. This is an important attribute since the ability to handle delicate parts, that is, ultrathin semiconductor bare die, as well as very robust and oversized structures, that is, SMD resistors can only

be achieved with dedicated nozzle tips when using mechanical tools such as pick-and-place. The ease by which the lase-and-place process can be adjusted allows it to handle a wide range of components both in terms of shape, size, overall mass, and type of device without degrading their mechanical or electrical functionality, which is ideal for applications in printed electronics.

18.4 Laser Transfer of Intact Structures

As mentioned earlier, the original work by Holmes *et al*. demonstrated the use of LIFT to release prefabricated individual MEMS components held onto a donor substrate with a polymer sacrificial layer [4]. The laser-driven release of individual or multiple components is fast and is largely independent of geometry, size, or mass. This enables the fabrication of hybrid assemblies comprising a wide variety of structures, which cannot be produced using either chemically (wet) or plasma (dry) driven traditional etching techniques. As the transfers shown in Figure 18.2 show, the LIFT of whole structures can be applied to a broad range of shapes, sizes, and materials beyond silicon-based MEMS components. That is, the lase-and-place process works with structures made from silicon (bare die and beams), plastic (polyimide), and also metal (as discussed next).

Lase-and-place can also be applied to structures ranging in size from a few microns to millimeters as shown by the images in Figure 18.5. These results

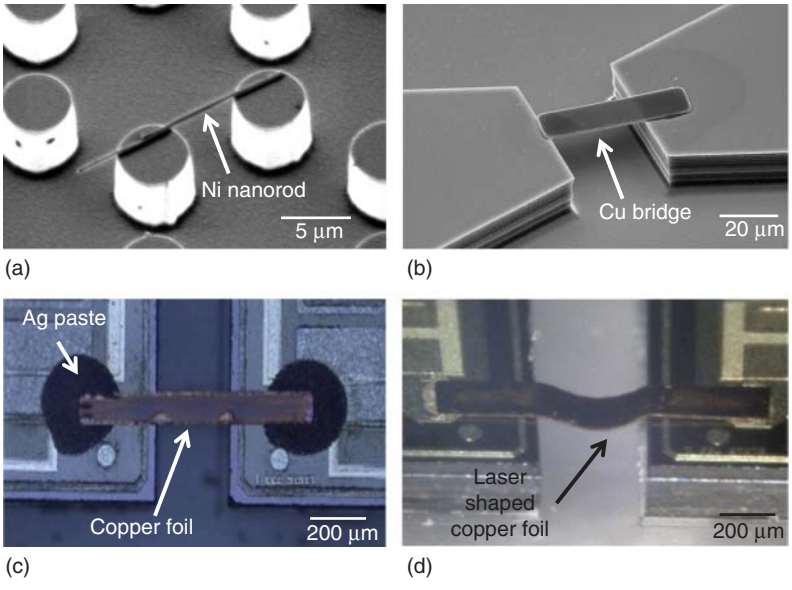

Figure 18.5 Images of representative structures transferred by lase-and-place. (a) SEM of nickel nanorod (200 nm diameter and 10 μm long) across silicon pods. (b) SEM of a copper film (10 μm wide, 50 μm long and 500 nm thick) over SU-8 pads. (c) Optical micrograph of a copper foil (150 μm wide, 1 mm long and 25 μm thick) connecting two capacitors using silver paste. (d) Similarly to (c), this time the copper foil was laser-shaped while attached to the donor substrate prior to its transfer.

do not represent the technique's lower or upper limit for transferable sizes but rather illustrate its potential and versatility. As shown in Figure 18.5a, a 10 μm long, 200 nm diameter nickel nanorod was laser transferred without deformation or fracture above two posts etched on a silicon substrate. This capability offers great potential for the precise placement of discrete nanoscale structures, which would otherwise require handling via more complex and time-consuming techniques such as AFM-tips or laser tweezers. Patterned thin films can also be laser transferred as shown in Figure 18.5b, where a prepatterned 500 nm thick copper film 50 μm long by 10 μm wide was placed to form a bridge between two SU-8 pads. Alternatives for placing these relatively large but thin structures on a particular location on a substrate without damage can be found using self-assembly techniques. However, self-assembly becomes impractical when working with a few components of varying size requiring placement at arbitrary locations.

18.4.1 Laser Transfer of Metal Foils for Electrical Interconnects

Figure 18.5c,d shows much larger structures also handled by lase-and-place. The copper foils are 1 mm long and are attached with silver paste to the contact pads at the edges of the two devices for the purpose of serving as electrical interconnects. In general, wire bonding is the most common approach for fabricating interconnects. Wire bonding offers the greatest flexibility in terms of matching different device sizes, varying package form factors, and cost per interconnect. However, as circuits are implemented onto flexible substrates or 3D configurations, wire bonding is not practical given the large volume required to accommodate the wire loop as it connects from one pad to another [17]. Low profile, freestanding interconnects can be fabricated by dispensing conductive pastes or polymers [18]. These printed interconnects can accommodate flexing of the substrate, but given their composite nature (usually a mix of a polymer binder and metal particles), they are not well suited for handling high currents and their electrical performance degrades with time [19]. The laser transfer of copper foils allows the fabrication of low-profile interconnects as shown in Figure 18.5c which are much more robust and durable than printed inks or pastes.

The laser transfer of copper foils allows the fabrication of low-profile interconnects, but it does not address the challenges presented by flexible circuits where displacement of the devices due to flexing and thermal expansion mismatch can cause strains in the interconnects, which may cause their detachment or fracture, resulting in failure. It is thus necessary to consider alternatives to the simple flat geometries shown so far. One option explored by the NRL group is to use shaped metal beams that can flex in order to accommodate deflections under strain. An example of a laser-shaped copper beam is shown in the micrograph in Figure 18.5d where its placement over the pads of two individual devices with the shaped beam facing down between the devices is demonstrated for a low-profile yet flexible interconnect. Details on the fabrication, transfer and testing of these laser-shaped copper beams can be found in the work by Beniam *et al*. [20]. Overall, the ability to shape and print metal foils onto the pads of existing devices allows for low-profile interconnects of greater cross section, while minimizing the

occupied volume. In wire bonding, especially on the ball bond side, the contact area between the wire and the die pad is $\approx 5 \times 10^2$ μm^2. In contrast, the copper interconnect from a metal beam can have a contact area of $\approx 4 \times 10^4$ μm^2 enabling lower contact resistance [20]. Overall, the use of flat or shaped metal beams or foils enables a new way to print low-profile, low-resistance, and mechanically compliant interconnects, which will play an important role in the development of next-generation flexible hybrid electronics comprising different types of electronic components, interconnects, and printed structures.

18.5 Laser Transfer of Components for Embedded Electronics

Embedded, that is, below the surface, passive components such as resistors, capacitors, and inductors have enjoyed widespread use for many years driven by high-density and high-speed applications. Current trends require the use of flexible substrates such as polyimide, polyester, or other polymer films, which allow the fabrication of thinner circuits capable of higher interconnect densities than traditional rigid substrates. The use of laser-based direct-write or LDW techniques offers an alternative for the fabrication of such embedded structures at a fraction of the cost and in less time than with traditional approaches, thus enabling the development of a full embedding capability for hybrid circuits.

In previous publications, the NRL group has demonstrated how LIFT techniques can be used to perform various circuit fabrication steps such as embedding the devices [14], laser transfer of individual devices into pockets on a substrate [13, 15], laser transfer of silver nanopastes to form 3D interconnects [21, 22] (see Chapter 10 for more details), and laser shaping and transfer of copper foils [20]. The objective of these reports was to investigate the use of laser processing techniques to carry out most of the steps required for the rapid prototyping of functional electronic circuits. By embedding bare die and unpackaged devices and wiring them using low-profile interconnects, significant reduction in thickness in the connections to the devices can be achieved with an overall reduction in footprint of about 80% and requiring substrates less than 1/10 of the thickness of a typical printed circuit board. If the savings from using bare die and other types of unpackaged devices are taken into consideration, volume reduction factors of 10–100 times, depending on the type of circuit design, become possible. Embedding components also result in shorter interconnects, which reduce parasitic inductance, thereby enhancing the electrical performance.

The use of laser microfabrication in combination with LIFT techniques to micromachine pockets, lase-and-place SMDs (resistors, capacitors, and LEDs) and bare die chips (i.e., a LM-555 timer chip), and laser transfer silver paste to form interconnects has been reported by NRL [23]. The steps required for laser fabricating a sample functional circuit in this manner are shown schematically in Figure 18.6a–c with micrographs from a sample circuit fabricated this way shown in Figure 18.6d–f. The circuit with planar interconnects shown in

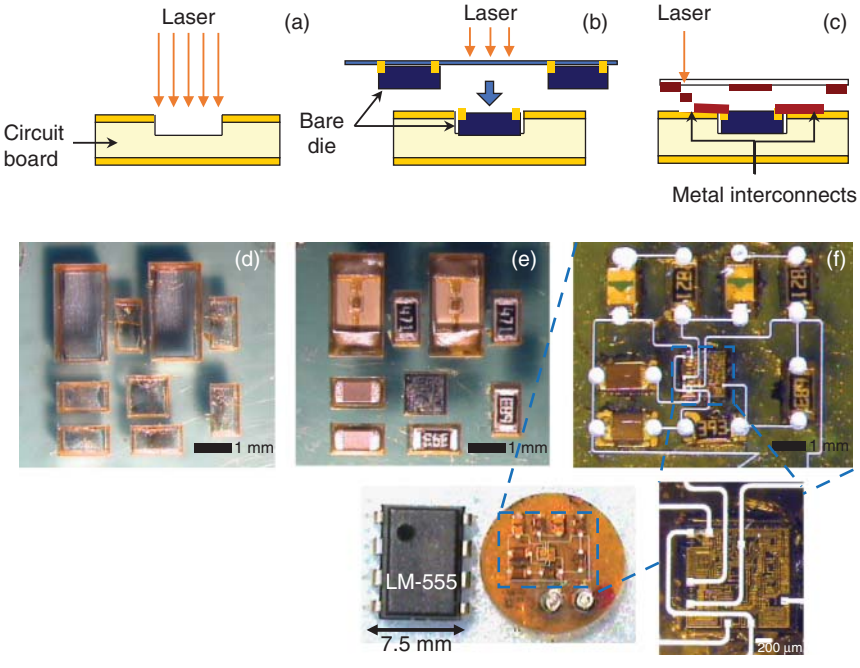

Figure 18.6 (a–c) Schematic (not to scale) showing the steps involved for LIFT of components and printing their interconnects for an embedded device. Optical micrographs of (d) an ULTEM 1000 substrate showing the laser-machined trenches, (e) the populated trenches with the blinker circuit components, including the LM-555 bare die in the center, and (f) the printed metal traces and interconnects for the embedded 555 blinker circuit. Bottom insets show the embedded circuit next to a packaged LM-555 chip for size comparison (left) and the LM-555 bare die and laser-printed interconnects (right)

Figure 18.6f exemplifies the level of miniaturization achievable with footprints of less than 20% of that of existing layouts. This is illustrated by the insets in Figure 18.6f showing the actual size of the LIFT-fabricated circuit against a single packaged LM-555 chip (on the left) and details of the embedded LM-555 bare die showing the LIFT-printed interconnects (on the right). In principle, the same approach can be used to develop three-dimensional embedded circuits, where the components are placed at various depths or levels and their interconnects extend in 3D rather than 2D, so as to fully utilize the available space.

18.6 Outlook

The need for implementing electronic systems that are compatible with additive manufacturing, 3D printing, and direct-write processes is pushing electronic manufacturing techniques beyond their current capabilities. In particular, traditional approaches to the manufacture of printed circuit boards are not compatible with the needs of a new generation of electronic systems that call for electronic circuits to be conformal, flexible, and hybrid in nature as

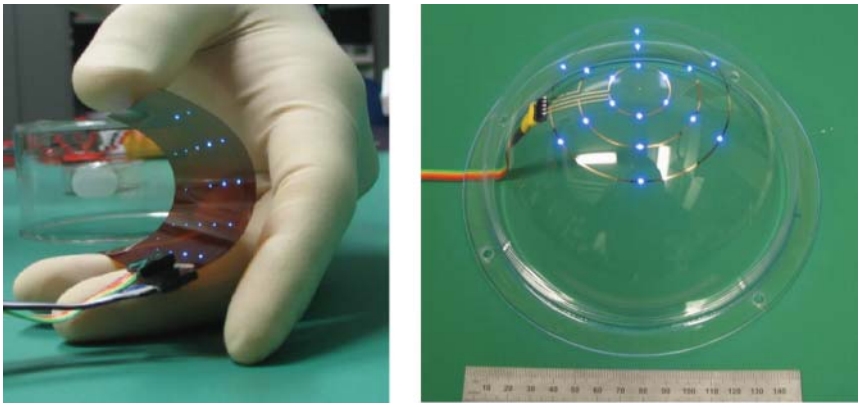

(a) (b)

Figure 18.7 Photos of a laser embedded array of LEDs on (a) a flexible polyimide substrate and (b) on an acrylic hemisphere.

the LED array made by laser transfer of bare-die LEDs on a polyimide foil in Figure 18.7a illustrates. Conformal circuits are needed to realize electronics in 3D rather than standard planar or 2D configurations, as shown in Figure 18.7b, a requirement that is becoming more urgent as 3D printed electronics mature and become more reliable. Flexible circuits require the integration of components into substrates or packages that are mechanically compliant so that they can conform, bend, stretch, or fold to a predesigned level without causing the circuit to fail. Hybrid circuits are comprised of distinct discrete components integrated into single or multilayer architectures assembled on nontraditional substrates as opposed to printed circuit boards. Examples of such components include logic, communication, memory, sensing, and power elements all integrated into a functional system or module. The need for new fabrication techniques capable of handling these new types of circuits cannot be ignored.

The design of such circuits will require the use of more sophisticated computer-based circuit layout tools, which will need to take into consideration issues such as power dissipation and stresses generated due to differences between the thermal expansion coefficients of the substrate and devices, in order to guarantee the circuit's long-term reliability. The implementation of such 3D circuit layouts represents a paradigm shift to the traditional planar approach to circuit manufacture and opens the possibility to further miniaturization and placement of electronics in locations considered impractical until now. Presently, the development of fully embedded electronic circuits has been limited at best, due to the lack of viable and practical fabrication techniques; however, the application of laser transfer techniques such as lase-and-place and other techniques for printed electronics will enable the development and implementation of fully functional 3D conformal electronic systems for applications ranging from distributed sensors to wearable devices.

From a circuit fabrication perspective, in order for any technique to be able to replace existing mechanically driven pick-and-place tools, it must be able to

reliably place devices (i.e., with 100% transfer yields without damage) at the exact location with little variation (near-zero placement error) and precise orientation (little if any rotation). Furthermore, any new technique must be able to work with the new generation of small and ultrathin bare-die ICs. Finally, the technique in question must be capable of throughputs compatible with high-volume fabrication, meaning that device placement rates of over 10 components per second must be achievable. Manufacturers of mechanical pick-and-place tools are struggling to satisfy all these requirements, and the need for alternative processes cannot be ignored. The lase-and-place technique – LIFT-and-place maybe a better term – is capable of satisfying all these requirements, as described in the previous sections. Since it is laser-driven, it does not rely on the travel of pins or nozzles, which require translation stages constrained by mechanical acceleration/deacceleration limits. A laser beam can be pulsed and scanned at much higher rates, and the only mechanical movement required involves the alignment between the donor and receiving substrates, which can be greatly optimized to minimize acceleration/deacceleration steps. This noncontact feature is what enables lase-and-place to reach component transfer rates well above today's target of 10 devices/s and is perhaps the greatest advantage of the LIFT technique.

Other benefits of lase-and-place include cost reduction for prototyping and production, manufacture simplification (through the reduction of production steps), and greater design freedom due to the inherent geometrical versatility allowed by the laser transfer processes. LIFT of structures and functional devices offers a wide window of applications ranging from R&D and prototyping to high-throughput production. Many applications have already been identified with many more awaiting developments. However, many challenges for LIFT of hybrid electronics remain besides the establishment of design rules, such as process modeling and optimization, integrating and connecting large numbers of devices, metrology and evaluation of the performance of the printed patterns and circuits, and long-term reliability of the LIFT-made assemblies. Solving these challenges will require a considerable effort but as commercial applications develop and the electronics and aerospace industries embrace laser-based digital microfabrication processes, these issues will have to be addressed sooner or later. With increasing development and opportunities in micro- and mesosystems combining electronics, photonics, fluidics, and bioactivity, LIFT will play a significant role in the new paradigm offered by digital microfabrication.

18.7 Summary

The recent development of LIFT techniques for the transfer of preformed devices such as metal foils and functional devices such as semiconductor bare die opens the door for their use as unique tools for laser-based microelectronics fabrication. These lase-and-place systems will be capable of fabricating and embedding electronic circuits with their interconnects and printed conductive traces and perhaps even incorporate the required power storage and power harvesting components within the same substrate. The resulting fully integrated

circuits could easily be reconfigured to fit within a desired form factor, thus allowing the placement of electronic systems in places inconceivable today.

As discussed in this chapter, laser-based device-transfer processes are a novel alternative to conventional mechanically driven pick-and-place methods for placement and embedding millimeter- to micrometer-sized structures such as semiconductor bare die, SMDs, optoelectronic devices, sensors, actuators, and MEMS onto any surface. Application of this technique to various types of semiconductor bare dies has shown that it is possible to transfer complete devices with the active surface facing the laser pulse without damage. This presents the device with its contact pads facing up, which greatly facilitates the printing or transfer of the metallic patterns required to connect it to the rest of the circuit using planar interconnects, thus replacing traditional wire bonding processes while minimizing space requirements. As the examples presented in this chapter demonstrate, the use of LIFT techniques allows the rapid prototyping of embedded microelectronics, which is not possible using current circuit board fabrication tools. In fact, the functionality of these laser-printed circuits could be customized for a particular application by choosing the appropriate electronic modules or building blocks from a circuit library available in the lase-and-place tool. Such a laser-based digital microfabrication system does not yet exist, but it is just a matter of time before LIFT-and-place tools are developed that make this vision a reality. Based on LIFT's success to date, it is highly probable that the laser-based printing techniques described in this chapter and the rest of this book will play a significant role in making embedded sensors and electronics and hybrid systems a reality in the not so distant future.

Acknowledgments

This work was funded by the Office of Naval Research (ONR) through the Naval Research Laboratory Basic Research Program.

References

1 Piqué, A., Mathews, S.A., Auyeung, R.C., Ollinger, M., Kim, H., Pratap, B., Arnold, C.B., and Sutto, T.E. (2004) Application of laser direct-write techniques for embedding electronic and micropower components. *SPIE Proceedings, vol. 5662*, pp. 564–569.

2 Piqué, A., Mathews, S.A., Auyeung, R.C., and Sood, B.P. (2011) Laser-based technique for the transfer and embedding of electronic components and devices. US Patent 8,056,222.

3 Piqué, A., Auyeung, R., Kim, H., Charipar, N., and Mathews, S. (2016) Laser 3D micro-manufacturing. *J. Phys. D: Appl. Phys.*, **49** (22), 223001.

4 Holmes, A.S. and Saidam, S.M. (1998) Sacrificial layer process with laser-driven release for batch assembly operations. *J. Microelectromech. Syst.*, **7** (4), 416–422.

5 Holmes, A.S. (2002) Laser processes for MEMS manufacture. *SPIE Proceedings, vol. 4426*, pp. 203–209.

6 Karlitskaya, N.S., Lange, D.F.D., Sanders, R., and Meijer, J. (2004) Study of laser die release by Q-switched Nd:YAG laser pulses. *SPIE Proceedings, vol. 5448*, pp. 935–943.

7 Karlitskaya, N.S., Meijer, J., Lange, D.F.D., and Kettelarij, H. (2006) Laser propulsion of microelectronic components: releasing mechanism investigation. *SPIE Proceedings, vol. 6261*, p. 62612P.

8 Mathews, S.A., Auyeung, R.C.Y., and Piqué, A. (2007) Use of laser direct-write in microelectronics assembly. *J. Laser Micro/Nanoeng.*, **2** (1), 103–107.

9 Karlitskaya, N.S. (2011) Laser die transfer: laser-induced transfer of microcomponents. PhD thesis. Faculty of Engineering Technology, University of Twente, The Netherlands.

10 Gilleo, K. (2004) *Area Array Packaging Processes: For BGA, Flip Chip, and CSP*, McGraw Hill Professional, New York.

11 Miller, R., Marinov, V., Swenson, O., Chen, Z., and Semler, M. (2012) Noncontact selective laser-assisted placement of thinned semiconductor dice. *IEEE Trans. Compon. Packag. Manuf. Technol.*, **2** (6), 971–978.

12 Marinov, V., Swenson, O., Atanasov, Y., and Schneck, N. (2013) Laser-assisted ultrathin die packaging: insights from a process study. *Microelectron. Eng.*, **101**, 23–30.

13 Piqué, A., Charipar, N.A., Auyeung, R.C.Y., Kim, H., and Mathews, S.A. (2007) Assembly and integration of thin bare die using laser direct-write. *SPIE Proceedings, vol. 6458*, p. 645802.

14 Piqué, A., Charipar, N.A., Kim, H., Auyeung, R.C.Y., and Mathews, S.A. (2007) Applications of laser direct-write for embedding microelectronics. *SPIE Proceedings, vol. 6606*, p. 66060R.

15 Mathews, S.A., Charipar, N.A., Metkus, K., and Piqué, A. (2007) Manufacturing microelectronics using 'lase-and-place'. *Photonics Spectra*, **41** (10), 70–74.

16 Kuran, E., Berg, Y., Tichem, M., and Kotler, Z. (2015) Integration of laser die transfer and magnetic self-assembly for ultra-thin chip placement. *J. Micromech. Microeng.*, **25** (4), 45 008.

17 Dixit, V., Davis, H., and Clark, M. ([Online]) Wire Bonding Considerations, http://electroiq.com/blog/2006/07/wire-bonding-considerations/ (accessed 24 February 2017).

18 Ahn, B.Y., Duoss, E.B., Motala, M.J., Guo, X., Park, S.I., Xiong, Y., Yoon, J., Nuzzo, R.G., Rogers, J.A., and Lewis, J.A. (2009) Omnidirectional printing of flexible, stretchable, and spanning silver microelectrodes. *Science*, **323** (5921), 1590–1593.

19 Perelaer, J., Smith, P.J., Mager, D., Soltman, D., Volkman, S.K., Subramanian, V., Korvink, J.G., and Schubert, U.S. (2010) Printed electronics: the challenges involved in printing devices, interconnects, and contacts based on inorganic materials. *J. Mater. Chem.*, **20**, 8446–8453.

20 Beniam, I., Mathews, S., Charipar, N., Auyeung, R., and Piqué, A. (2016) Laser printing of 3D metallic interconnects. *SPIE Proceedings, vol. 9738*, p. 97380I.

21 Wang, J., Auyeung, R., Kim, H., Charipar, N.A., and Piqué, A. (2010) Three-dimensional printing of interconnects by laser direct-write of silver nanopastes. *Adv. Mater.*, **22** (40), 4462–4466.
22 Kim, H., Duocastella, M., Charipar, N.A., Auyeung, R.C.Y., and Piqué, A. (2013) Laser printing of conformal and multi-level 3D interconnects. *Appl. Phys. A: Mater. Sci. Process.*, **113** (1), 5–8.
23 Piqué, A., Mathews, S.A., Pratap, B., Auyeung, R.C.Y., Karns, B.J., and Lakeou, S. (2006) Embedding electronic circuits by laser direct-write. *Microelectron. Eng.*, **83** (11-12), 2527–2533.

Index

a

absorbing-film assisted laser-induced forward transfer (AFA-LIFT) 66, 351
absorption efficiency 243
acousto-optical modulator (AOM) 382
active-matrix OLED (AMOLED)
  displays 7
  prototype devices 30
additive manufacturing 266
Alexa 594 labeled lambda phage DNA 310
amperometric biosensor 311
amyloid peptides 337, 338
avidin 334

b

BA-LIFT *see* blister-actuated laser-induced forward transfer (BA-LIFT)
ballistic laser-assisted solid transfer (BLAST) 177–179
bio-electronic nose 339
Biological Laser Printing (BioLP) 66, 351
BioLP process 357
biomicrodevices 329
bioprinting 349
biosensors 299
blade coating 23, 129–130
blister-actuated laser-induced forward transfer (BA-LIFT) 66, 92
  blister formation
    dynamics 97–102
    finite element modeling 102–105
  cavitation bubble collapse 96
  delicate materials 113–117
  experimental setup 92
  jet formation 92
  jet formation and expansion
    computational fluid dynamics model 106–108
    ink film properties 111–113
    laser energy 108–111
  laser absorption 96
  liquid ejection 95
  liquid jets 97
  mechanism 92
  penetration or absorption depth 94
  polyimide 93
  polymer laser-absorbing layer 93
  pump-probe imaging 94
  solvent orthogonality 93
  thick polymer layer 92
  time-resolved imaging 92
  vapor cavity 96
blister formation
  dynamics 97–102
  finite element modeling 102–105
    boundary deformation function 244
    domain perturbation method 239–40, 239–40
    kinetic energy 242, 243
    velocity components 240, 241
"blow-off time" 166

Laser Printing of Functional Materials: 3D Microfabrication, Electronics and Biomedicine,
First Edition. Edited by Alberto Piqué and Pere Serra.
© 2018 Wiley-VCH Verlag GmbH & Co. KGaA. Published 2018 by Wiley-VCH Verlag GmbH & Co. KGaA.

c

cancer research 359
capacitive DNA biosensor 310
CdSe(CdS) nanoquantum dots 285
cell printing 350
centripetal acceleration 37
chalcogenide thin films 189–190
chemical and biological sensors
  applications 316
  background of biosensors 308
  carbon nanotubes 318
  electrospray deposition 304, 305
  inkjet printing technique 304
  laser-Induced forward transfer (LIFT) 305, 307
  LIFT of liquid films 307, 308
  microcontact printing 302
  nano-tip printing technique 303
  photochemistry-based printing 303
  pin printing approach 301, 302
  polyepichlorohydrin (PECH) polymer/carbon 318
  printing of biological materials 309, 316
chemoresistor gas sensors 318
colorimetric enzyme linked immunosorbent assay (ELISA) 337
congruent LIFT, *see* laser decal transfer (LDT)
contact printing methods
  microcontact printing 302
  nano-tip printing technique 303
  pin printing approach 301, 302
coplanar waveguide (CPW) 239
cytoscribing 350

d

digital micromirror device (DMD) 176, 235, 236
  advantages 181
  experimental setup 182
  pattern 181
  polymer films 181
digital printing 376
dip coating 23, 129, 130
diPhAc-3T (Bis(2-phenylethynyl end-substituted terthiophene) 276
dip-pen lithography 303
direct-matrix absorption (DMA) 92
direct patterning methods 330
"direct-write" approaches 27
dispensing or soaking techniques 330
distyryl-quaterthiophene (DS4T) 276
DMD-based pulse shaping, LIBT 195
"8–17" DNAzyme 313
doctor blading, *see* blade coating
dot-blotting 330
drawdown rods method 23
droplet mode deposition
  contact and non-contact configurations 160
  copper droplets 162
  donor film 161
  droplet velocity 163
  femtosecond excimer LIFT 160
  jet instability 162
  jetting phenomena 163
  liquid jets 67, 163
  mechanism 69, 163
  microscale 3D printing 163
  multiple droplets per laser pulse 162
  nanosecond LIFT of aluminum 161
  printing lines 78–81
  transfer droplet 69, 72, 161
dynamic release layer (DRL) 24, 92, 306, 331
  advantage 124
  explosive polymers 124
  laser absorption 124
  trace material 124
dynamics process 431
  lase-and-place 432–435
  laser transparent carrier tapes 431
  polyimide blistering layer 432
  silicon substrates 431
  thermo-mechanical selective laser-assisted die transfer 431

e

electrical resistivity 164
electrochemical biosensors 300

electron lithography 254
electrospray deposition 304, 305
energy harvesting 286
  chalcogenide thin films 189–190
  thermoelectric generator 190–193
enzyme linked immunosorbent assay 315
explosive polymers 124

f

femtosecond laser
  printing 251
  system 178, 180
FF-LIFT, *see* film-free LIFT (FF-LIFT)
film-formation methods 23
film-free laser printing (FF-LP) technique 5, 67
film-free LIFT (FF-LIFT) 125
  applications 140
    micro-optical elements fabrication 140
    printing biomaterials 139–140
  forward (inverted) *vs.* backward (upright) systems 137
  fundamentals of
    cavitation-induced phenomena 131–132
    jet formation 132–133
    vs. LIFT 134
  implementation and optical considerations
    forward (inverted) *vs.* backward (upright) systems 136–137
    laser source 135–136
    spherical aberration and chromatic dispersion 137–138
  jet formation 132–134
  vs. LIFT 135
  micro-optical elements fabrication 141
  receiver substrate 130–131
  spherical aberration and chromatic dispersion 137–138
  thin liquid film preparation
    blade coating 129, 130
    dip coating 129, 130
    external instabilities 125–126, 128–129
    rheological parameters 126
    spin coating 129, 130
    spontaneous instabilities 125, 126–128
  traditional LIFT 123, 124
  transparent liquids 124, 125
finite-element analysis software 187
finite element modeling 102–105
flexography 271
flip-chip technology 289
fluence threshold value 178
fluids 63
  ejection and deposition
    droplet deposition 69–71
    jet formation 67–69
  printing continuous patterns 78
  printing droplets
    fluid properties 76, 77
    laser parameters 69, 72–75
    setup parameters 76–78
  printing lines 78–81
fluorescently tagged complementary proteins 27
focussed ion beam (FIB) 180, 416
Fresnel diffraction 178
fs-LIFT technique 25
fully polymeric OTFT devices 279
functional release layer (FRL) 240

g

Gaussian/'top-hat' spatial intensity beam profile 181
gentle hydration method 340
gravure printing 271

h

horizontally-aligned grain boundaries 416
horseradish peroxidase (HRP) 335
hybrid circuits 427
hydrodynamic process 253
hydrogen-assisted laser-induced forward transfer (HA-LIFT) 28

i

immunoglobulin (IgG) microarrays 312
inclined pillars 420
inkjet printing 38, 304, 330, 350
intact polymer molecules 8
interconnection and heterogeneous integration 287, 288, 290
interdigitized electrodes 289
interference effects 177
isotropic conductive adhesive (ICA) 289

j

jet-and spray-ejection regime 409
jet formation dynamics 67, 201
  experimental set up 201
  Newtonian glycerol solutions
    experimental design 202
    fluid properties and laser fluence 204, 205
    jettability phase diagram 206–208
    typical jetting regimes 202, 203
  viscoelastic alginate solutions
    alginate concentration effects 214, 216
    experimental design 208, 209
    ink coating preparation 208
    jettability phase diagram 215, 217
    laser fluence effects 212, 215
    material properties 209
    non-dimensional numbers 209
    typical jetting regimes 209, 210
jet formation mechanism 67, 96, 200
jet morphology 200
JetXpert imaging system 202

l

large area, high throughput LIFT/LIBT inline R2R-printing system 387, 388
lase-and-place 428, 432–435, 440
laser ablation transfer (LAT) 7, 24, 306
laser-assisted bioprinting (LAB) 66
  blood vessels 362
  bone 365, 367
  cancer research 359
  effect of laser process and printing parameters 356, 358
  heart 364, 365
  history of cell bioprinting 349, 354
  nervous system 367, 368
  skin 360, 362
  technical specifications 353, 356
laser-based non-lithographic processes 428
laser-based printing/marking process 6
laser decal transfer (LDT) 66, 228
  arrays 233
    high viscosity donor material 234
    thicker and thinner voxels 233
  absorption efficiency 243
  congruent laser transfer 244, 245
  CPW 239
  DMD 235–237
  edge acuity 232
  EDX analysis 239
  fabricated LDT features 241
  FRL 240
  high-aspect 3D stacks and freestanding structures 234
  intrinsic and engineered characteristics 230
  laser system and experimental setup 229
  low-viscosity Ag ink *vs.* high-viscosity Ag nanopaste 242
  mechanical stability 239
  multi-layered stack 240, 241
  operating parameters 245
  OTFT 241
  potential applications and functional properties 235
  properties 229
  quantitative study 243
  self-supporting feature 239
  SRR 239
  steep sidewalls 239
  three complex interconnect patterns 237–239
  threshold fluence 243
  voxel separation mechanism 243
  voxels transfer 229

laser direct-write (LDW)
process 228
techniques 235, 299
laser forward transfer process 6
laser-guided direct writing (LGDW) 351
laser-induced backward transfer (LIBT) 5, 252
beam-shaping 183
experimental setup 194
nanoimprinting approach 194
structured carrier substrate 195
transparent carrier 193
transparent receiver and transparent donor 193
unstructured carrier substrate 195
laser-induced cavitation bubble 5
laser induced forward transfer (LIFT) 3, 17, 252, 305, 307
advantages 20, 343
amyloid peptides 337, 338
composite-matrix-based materials 27
of DNA in solid and liquid phase 332, 333
donor substrate 22–23
DRL 24
early work 17–19
film-free laser printing 5
fluids, *see* fluids
HA-LIFT 28
limitations 22
liposomes 340, 343
liquid donor films 5
LITI 30–31
LMI 29
LP-LIFT 28, 29
MAPLE-DW 27
material transfer 19, 21, 22
of metals, *see* metals
odorant binding proteins 339
principle of operation 4, 5
printable inks 5
repairing damaged photomasks 19
soft materials, *see* soft materials
solid donor films 4
solid films (ceramics and polymers), *see* solid films (ceramics and polymers)
steps 20
streptavidin and avidin-biotin complex 333, 337
ultra-short laser pulses 25–26
viscosity and size of particles 5
laser-induced molecular implantation technique (LIMIT) 8, 29
laser-induced patternwise sublimation (LIPS) 7
laser induced thermal imaging (LITI) 7, 30
laser induced transfer process technique, *see* laser induced forward transfer (LIFT) technique
laser-induced transfer technology (LIT)
gold nanoparticles 252
hydrodynamic process 253
LIBT 252
LIFT 252
laser molecular implantation (LMI) 8, 29
laser pressure catapulting (LPC) 8
laser printing 3
additive manufacturing method 266
bulk-silicon and silicon films
beam modification 256
computer-based image evaluation 256
femtosecond laser printing 258, 259
laser pulse energy 260
layer thickness 260
nanoparticle scattering properties 261
nanoparticles fabrication 260
normalized size distributions 256
processing steps 254
ring-shaped intensity distribution 256
ring shaped laser beam profile 256
scattering spectrum 261

laser printing (*contd.*)
silicon wafer 254
SOI 259
of conducting layers 279
of dielectric layers 277–279
metasurfaces 263
multi-stage process 264
nanoparticles 254
pre-structured films 261–263
ribbon 199
of semiconductor layer 275–277
spherical nanoparticles 251, 263
ultraflat optical element 263
Lasersonic® LIFT
continuous wave laser source and fast modulation 397–399
data flow 385
digital printing market expectations and challenges 377–378
future directions 401
history of 376–377
inking units 390–392
large area, high throughput LIFT/LIBT inline R2R-printing system 387, 388
print experiments and results 392–397
printing heads 388–390
special printing markets 378
special test pattern 399–401
synthetic approaches 392
time schemes 383–385
transparent inks 379–382
ultrafast pulse modulation 382–383
ultrafast scan 385–387
laser transfer, structures and functioning devices
chemically/plasma driven traditional etching techniques 435
dynamics process *see* dynamics process
early demonstrations 428–430
electronic systems 438
embedded electronics 437–438
flexible circuits 439
hybrid circuits 439
individual or multiple components 435
metal foils 436–437
patterned thin films 436
pick-and-place tools 440
self-assembly techniques 436
lase-and-place 428, 432–435, 437, 440
laser transfer universe 5–8
laser writing (LW) 331
LDT, *see* laser decal transfer (LDT)
LIFT, *see* laser induced forward transfer (LIFT)
LIFT of liquid films 307, 308
LIFT of 3D metal structures
adhesion 407
characteristics 407
definition of 3D structures 405
demonstrators and potential applications 420–422
droplet impact and solidification 411–413
ejection phenomena 407
ejection regimes of pure metal picosecond 408–411
electrical properties 418–420
inclined pillars 420
mechanical properties 417–418
metal LIFT printed pillars 407
metallurgical microstructure 416–417
copper pillars 415
pulse duration and spot size 407
reproducibility 414
schematic representation of LIFT 406
solidification phenomena 406
surface roughness 406
thermally induced nozzle 408
transfer threshold fluence 407
LIFT printed copper pillar 417
LIFT-printed OTFT 276
light-to heat-conversion (LTHC) 30
liposomes 340, 343
long-pulsed LIFT (LP-LIFT) 28

m

mass printing technologies 271
material laser recording (MTR) 331
Matrigel™ 362
matrix-assisted pulsed laser evaporation (MAPLE) 38
matrix-assisted pulsed laser evaporation direct write (MAPLE DW) 27, 39, 318, 333, 351
metals 149
  numerical modeling of LIFT for metals 165–167
  applications 150
  beam pattern 149
  deposited structures 163–165
  deposition 150
  droplet mode deposition
    contact and non-contact configurations 160
    copper droplets 162
    donor film 161, 162
    droplet velocity 163
    fs excimer LIFT 160
    jet instability 162
    jetting phenomena 163
    liquid jets 163
    mechanism 163
    microscale 3D printing 163
    multiple droplets per laser pulse 162
    nanosecond LIFT of aluminum 161
    transfer droplet 161, 162
  feature characteristics 149
  metal films 149
  parametric effects
    donor-film gap spacing 156, 157
    laser fluence and film thickness 154–156
    pulse width 157–160
  resolution 150
  single-step process 150
  thermal processes 151–153
  time scale and fluence 167–169
  transfer 150
microbatteries 286
micro-contact printing (μCP) 302, 330
microelectromechanical systems (MEMS) 239
microfluidic patterning 330
microscale 3D printing 163
Mie theory 261, 263
mobility (μ) 273
multilevel computer-generated holographic structure 25

n

nanocrystal quantum dots (NCQDs 46
nano-hydroxyapatite (nHA) 367
nanoimprinting approach 194
nanolasers 251
nanomaterial enabled laser transfer (NELT) 8
nanoparticles 251
  laser printing 254
  printing process 251
nano-tip printing technique 303
nervous system 367
Newtonian glycerol solutions
  experimental design 202
  fluid properties and laser fluence 204, 205
  jettability phase diagram 206–208
  typical jetting regimes 202, 203
nickel-chrome (NiCr) resistors 285
non-contact digital technology 38
non-contact printing methods
  electrospray deposition 304, 305
  inkjet printing technique 304
  photochemistry-based printing 303

o

odorant binding proteins (OBPs) 339
one-dimensional thermal model 155
on/off current ratio (I_{on}/I_{Off}) 274, 275
optical chemical sensor 300
organic electronic devices 7
organic light-emitting diodes (OLEDs) 7, 30, 281, 282, 285
  TP-LIFT 47–49

organic thin film transistor (OTFT) 241
  laser printing of conducting layers 279
  laser printing of dielectric layers 277–279
  laser printing of semiconductor layer 275–277
  operation and characteristics 272, 273, 275
  single step printing 279, 280
organ printing 350

p

passive components 285, 287
photochemistry-based printing 303
photoinduced decomposition 21
photolithography 123
pin printing approach 301, 302
platinum and gold inclined pillars 422
pluming/splashing regime 202, 203
poly(butyl methacrylate) (PBMA) 8
poly(3,4-ethylenedioxythiophene) polystyrene sulphonate (PEDOT:PSS) 48
poly(ethyl methacrylate) (PEMA) 8
poly-3-hexylthiophene (P3HT) semiconductor material 277
polyimide blistering layer 432
polymer laser-absorbing layer 93
polymer sacrificial layer 432
poly[2-methoxy-5-(2-ethylhexyloxy)-1,4-phenylenevinylene] (MEH-PPV) 281
poly(methylmethacrylate) (PMMA) 181
polymethyl methacrylate polymer layer 44
polyvinyl butyral (PVB) inks 396
power-law relaxation time model 208
pulsed laser deposition (PLD) 38
pump-probe imaging 94

q

quantum dot-based light emitting diodes 285

r

Rayleigh–Plateau instability 96
reactive ion etching 254
reactive LIFT (rLIFT) 52–54
red-green-blue PFO pixel transfer 282
robotic micro-needle array fabrication 330

s

satellites 410
SAW biosensor arrays 339
"Scotch tape" test 164
screen printing 271
Seebeck coefficient 192
selective laser melting (SLM) 423
sequential laser printing 283
shadowgraphy studies 42, 45, 184, 288
  ceramic thin films 184–186
  compliant receivers 186–188
silicon-on-insulator (SOI) 259
silver split-ring resonators (SRR) 239
single step printing, OTFT device 279, 280
slot-die approach 23
soft materials 199
  jet formation, *see* jet formation dynamics
  jet formation mechanism 200
  jet morphology 200
  jet velocity 200
  laser printing applications 218, 219
  multilayer hydrogel-cell planar structure 201
sol–gel technique 301
solid films (ceramics and polymers) 175
  energy harvesting
    chalcogenide thin films 189–190

micro-scale thermoelectric generator 188
thermoelectric generator 190–193
laser pulse interference-assisted LIFT
BLAST 177–179
standing wave interference from multiple layers 176–177
LIBT
experimental setup 194
ion beam milling/UV beam machining 194
nanoimprinting approach 194
structured carrier substrate 195
transparent carrier 193
transparent receiver and transparent donor 193
unstructured carrier substrate 195
polymer films, 181–183
pre-machined ceramic micro-discs, LIFT printing of 180–181
shadowgraphy studies
ceramic thin films 184–186
compliant receivers 186–188
solvent orthogonality 93
spatial light modulator (SLM) 235
spin coating 23, 37, 129, 130
spray coating technology 38
streptavidin 334
and avidin-biotin complex 333, 337
stroboscopic imaging techniques 432
surface acoustic waves (SAW)
biosensors 311
chemical sensors 318
surface tension 256

t

tert-butyl acrylate (TBA) 49
thermoelectric generator 190–193
thermo-mechanical selective laser-assisted die transfer 431
thin-film transistor-liquid crystal displays (TFT-LCD) 228
3D structures 405
through silicon vias (TSVs) 420
time-resolved imaging of jet formation 67–69
time-resolved imaging of droplet deposition 69–71
tissue engineering
blood vessels 362
bone 365, 367
heart 364, 365
nervous system 368
skin 360, 362
traditionally packaged electronic components 427
triazene DRL-LIFT 285
triazene polymers (TP) 331
chemical structure 40, 41
front and back side ablation 41–42
higher ablation rates 41
LIFT
application 46
aryltriazene photopolymers 44
biomembrane model system 45
materials 44
OLEDs, 47–49
polystyrene microbeads 45
sensors, 49–52
PS-microbead pixel 46
UV–vis absorption spectrum 41
tri-color pixels 283
two-dimensional thermal model 166
two-temperature model 166

u

ultra flat lens 264
ultra-short laser pulses 25–26
UV photolysis 150

V
viscoelastic alginate solutions
alginate concentration effects 214, 216
experimental design 208, 209
ink coating preparation 208
jettability phase diagram 215, 217
laser fluence effects 212, 215
material properties 209
non-dimensional numbers 209
typical jetting regimes 209, 210
voxel separation mechanism 243

W
Wenzel wetting 71
wild-type OBP from bovine (wtbOBP) 339

WILEY END USER LICENSE AGREEMENT

Go to www.wiley.com/go/eula to access Wiley’s ebook EULA.